Universität Potsdam

ALFRED-WEGENER-INSTITUT
HELMHOLTZ-ZENTRUM FÜR POLAR-
UND MEERESFORSCHUNG

Carbon Cycle of Arctic Lagoons

Greenhouse Gas Production During the Transition from Terrestrial to Marine Permafrost

DISSERTATION

Maren Jenrich

Carbon Cycle of Arctic Lagoons

Greenhouse Gas Production During the Transition from Terrestrial to Marine Permafrost

Publikationsbasierte Dissertation

zur Erlangung des akademischen Grades

"doctor rerum naturalium"

(Dr. rer. nat.)

in der Wissenschaftsdisziplin

Geochemie

eingereicht an der

Lehreinheit Geowissenschaften der

Mathematisch-Naturwissenschaftlichen Fakultät an der

Universität Potsdam

angefertigt am

Alfred-Wegener-Institut

Helmholtz-Zentrum für Polar- und Meeresforschung

vorgelegt von

Maren Jenrich

Potsdam, den 26. November 2024

Hauptbetreuer: Prof. Dr. Guido Grosse [1,2]
Betreuer: Dr. Jens Strauss [1]

Gutachter*innen: Prof. Dr. Guido Grosse [1,2]
Prof. Dr. Susanne Liebner [3,4]
Prof. Dr. Craig Tweedie [5]

[1] Alfred-Wegener-Institut Helmholtz Zentrum für Polar- und Meeresforschung, Sektion Permafrost Forschung, Potsdam, Germany
[2] Institute of Geoscience, University of Potsdam, Potsdam, Germany
[3] Geoforschungszentrum Potsdam (GFZ), Sektion Geomikrobiologie, Potsdam, Germany
[4] Institute of Biochemistry and Biology, University of Potsdam, Potsdam, Germany
[5] Department of Environmental Science and Engineering, University of Texas at El Paso, USA

Published online on the
Publication Server of the University of Potsdam:
https://doi.org/10.25932/publishup-67929
https://nbn-resolving.org/urn:nbn:de:kobv:517-opus4-679293

Abstract

Permafrost, defined as ground that has been frozen for more than two consecutive years, underlies 15% of the land area of the Northern Hemisphere, storing vast amounts of organic carbon accumulated over millennia. Over 30% of global coastlines are shaped by permafrost, which is particularly sensitive to climate change. The rapid reduction in sea ice, rising air and sea temperatures, and more intense storm activity amplify erosion along these ice-rich coasts, leading to land loss of up to 25 meters per year at the Beaufort Sea. Coastal erosion taps lakes and drained lake basins formed during permafrost thaw, transforming them into so-called thermokarst lagoons. These lagoons serve as transition zones between terrestrial and subsea permafrost. Entering seawater accelerates thawing, making previously frozen or lacustrine organic carbon available for microorganisms to decompose into greenhouse gases (GHGs) such as carbon dioxide and methane, which contributes to further climate warming. So far, only a few studies have focused on the geology and evolution of these Arctic lagoons, and little is known about the role of thermokarst lagoons in the permafrost carbon cycle. To address this research gap, the key research questions of this thesis are:

- What is the spatial pan-Arctic extent of thermokarst lagoons, how are they distributed and how can they be classified according to their development stages?
- What is the effect of increasing seawater influence on GHG production and microbial community composition?
- Does GHG production of inundated Arctic coastal lowlands differ between landscape features and regions?

To answer these research questions, a combination of remote sensing and laboratory analyses was conducted. High-resolution satellite imagery and geographic information system tools were used for mapping and classifying thermokarst lagoons, providing a pan-Arctic context. The effect of seawater inundation on GHG production in thawed permafrost sediments was studied through four long-term anaerobic incubation experiments (at 4°C for up to 415 days) using permafrost, active layer, thermokarst lake, and lagoon sediment from three distinct Arctic coastal regions under various saline conditions to simulate increasing seawater influence. Microbial analyses were conducted before and after two of the experiments to understand how microorganisms respond to changing seawater influence.

Along the Arctic coast between the Taimyr Peninsula (Siberia) and the Tuktoyaktuk Peninsula (Canada), 520 lagoons originating from former lakes and lake basins were identified and mapped with remote sensing and cover an area of 3,457 km^2, which is only a

fraction of the area occupied by thermokarst lakes. Based on their connectivity to the sea, the lagoons were categorized into five classes, with the majority (55%) in early transition stages (very low and low connected).

Incubation studies consistently revealed that under the prevailing brackish conditions, methane production is highest in these low-connected lagoons and decreases during the ongoing transition into a marine environment. Due to the higher global warming potential of methane, the climate impact of these low-connected lagoons is up to 18 times greater than that of open lagoons, where CO_2 is the dominant GHG produced. The microbial diversity is found to be higher in lagoon sediments than in terrestrial sediments, underlining the uniqueness of these transitional systems. However, the shift from terrestrial to marine conditions involves changes in oxygen availability and salinity, both of which disrupt the initial terrestrial microbial community, leading to a decrease in GHG production in the short term. Over time, as salt-tolerant, anaerobic microbial communities establish, CO_2 production increases, reaching levels as high as eight times those found in terrestrial permafrost.

Combining data from all incubation experiments revealed that GHG production varies significantly during the transition from newly thawed terrestrial permafrost to established lagoons. GHG production is highest in lagoon sediments compared to the terrestrial landscape features (permafrost, active layer, lake). Although regional variations in GHG production exist, they are less pronounced than the variations between different landscape features. The combination of incubation and mapping results enabled the first rough estimate of potential carbon release from all mapped pan-Arctic lagoons, showing that, on average, 3 Tg CO_2eq could be released per year from all mapped thermokarst lagoons by 2100.

In conclusion, these results show that, while the total thermokarst lagoon area is relatively small (3,457 km^2), thermokarst lagoons release more than four times the CO_2-equivalent per unit area compared to thermokarst lakes, and even more than gradually thawing permafrost. This indicates that thermokarst lagoons are hotspots of carbon cycling and may play a more significant role in the carbon budget of rapidly thawing Arctic landscapes than previously anticipated. This role may become even more critical, as current climate scenarios suggest accelerating permafrost coastal erosion and rising sea levels. The incubation experiments were useful for understanding the impact of changing salinities on microbial dynamics and GHG production in seawater-inundated terrestrial and lagoon sediments, but it is not possible to reproduce all processes occurring in natural environments. To confirm and verify the presented incubation results, *in situ* measurements of GHG fluxes during the land-sea transition are needed.

Zusammenfassung

Permafrost, definiert als Untergrund, der länger als zwei aufeinanderfolgende Jahre gefroren bleibt, erstreckt sich über 15 % der Landfläche der Nordhalbkugel und enthält große Mengen organischen Kohlenstoffs, die sich über Jahrtausende angesammelt haben. Mehr als 30 % der weltweiten Küstenlinien sind von Permafrost geprägt, und daher besonders anfällig gegenüber den Auswirkungen des Klimawandels. Der Rückgang des Meereises, steigende Luft- und Wassertemperaturen sowie vermehrte Sturmaktivität verstärken die Erosion dieser eisreichen Küsten, was etwa in der Beaufortsee zu einem jährlichen Landverlust von bis zu 25 Metern führt. Durch das Fortschreiten der Erosion entstehen Thermokarstlagunen, da Seen und drainierte Seebecken, die durch das Tauen des Permafrosts gebildet wurden, vom Meer angeschnitten werden. Diese Lagunen stellen Übergangszonen zwischen terrestrischem und submarinem Permafrost dar. Das in den Boden eindringende Meerwasser beschleunigt das Auftauen und macht organischen Kohlenstoff, der zuvor gefroren war, für Mikroorganismen verfügbar. Dieser wird dann in Treibhausgase wie Kohlendioxid und Methan umgewandelt, was die globale Erwärmung weiter antreibt.

Bislang gab es nur wenige Studien zu Thermokarstlagunen und diese beschränkten sich vornehmlich auf die Geologie und Entstehungsgeschichte dieser arktischen Lagunen, wobei ihre Rolle im Permafrost-Kohlenstoffkreislauf weitgehend unerforscht blieb. Diese Arbeit soll diese Wissenslücke schließen und folgende zentrale Fragen beantworten:

1. Welches räumliche Ausmaß haben Thermokarstlagunen in der Arktis, wie sind sie verteilt, und wie lassen sie sich anhand ihrer Entwicklungsstadien klassifizieren?
2. Wie beeinflusst der zunehmende Meerwassereinfluss die Treibhausgasproduktion und die Mikroorganismen?
3. Unterscheidet sich die Treibhausgasproduktion zwischen verschiedenen Landschaftselementen überfluteter Küstenregionen und in verschiedenen Regionen?

Zur Beantwortung dieser Fragen wurden Fernerkundungsmethoden und Laboranalysen kombiniert. Für die Kartierung und Klassifizierung der Thermokarstlagunen im pan-arktischen Kontext kamen hochauflösende Satellitenbilder und geografische Informationssysteme zum Einsatz. Um die Wirkung von Meerwasser auf die Treibhausgasproduktion zu simulieren, wurden in sauerstofffreien Langzeit-Inkubationsexperimenten Sedimente aus Permafrost, Auftauschicht, Thermokarstseen und Lagunen aus drei arktischen Küstenregionen unter verschiedenen Salzwassereinflüssen bis zu 415 Tage lang bei 4°C inkubiert. Dabei wurden mikrobiologische Analysen vor und nach

zwei dieser Experimente durchgeführt, um die Reaktionen der Mikroorganismen auf den Einfluss von Meerwasser zu untersuchen.

Entlang der arktischen Küste, von der Taimyr-Halbinsel in Sibirien bis zur Tuktoyaktuk-Halbinsel in Kanada, wurden mittels Fernerkundung 520 Lagunen identifiziert und kartiert, die aus ehemaligen Seen und Seebecken entstanden sind, über sich über eine Fläche von 3.457 km^2 erstrecken. Im Vergleich dazu nehmen Thermokarstseen eine deutlich größere Fläche ein. Die Lagunen wurden basierend auf ihrer Verbindung zum Meer in fünf Klassen unterteilt. Die Mehrheit (55 %) dieser Lagunen sind weitgehend geschlossene Systeme und befinden sich in frühen Stadien des Übergangs zwischen Land und Meer.

Die Ergebnisse zeigen, dass die Methanproduktion in diesen weitgehend geschlossen Lagunen am höchsten ist und während des Übergangs zum marinen Umfeld abnimmt. Aufgrund des höheren globalen Erwärmungspotenzials von Methan ist der Einfluss dieser Lagunen auf das Klima bis zu 18-mal höher als bei offenen Lagunen, in denen hauptsächlich Kohlenstoffdioxid produziert wird. Die mikrobielle Vielfalt in Lagunensedimenten ist höher als in terrestrischen Sedimenten, was die Einzigartigkeit dieser Systeme verdeutlicht. Beim Übergang von terrestrischen zu marinen Bedingungen verändern sich sowohl die Sauerstoffverfügbarkeit als auch die Salinität, was die ursprüngliche mikrobielle Gemeinschaft aus dem Gleichgewicht bringt und kurzfristig zu einer Abnahme der Treibhausgasproduktion führt. Im Laufe der Zeit etablieren sich jedoch salztolerante, anaerobe Mikroorganismen, und die CO_2-Produktion steigt auf Werte, die bis zu achtmal höher sind als in terrestrischem Permafrost.

Die Zusammenführung der Daten aller Inkubationsexperimente zeigt, dass die THG-Produktion im Verlauf des Übergangs von frisch aufgetautem terrestrischem Permafrost zu etablierten Lagunen stark variiert. Die Produktion ist in Lagunensedimenten höher als in den terrestrischen Sedimenten von Permafrost, Auftauschicht und Thermokarstseen. Obwohl es regionale Unterschiede in der THG-Produktion gibt, sind diese weniger stark ausgeprägt als die Unterschiede zwischen den verschiedenen Landschaftselementen. Die Kombination von Inkubations- und Kartierungsergebnissen ermöglichte eine erste grobe Schätzung der potenziellen Kohlenstofffreisetzung aus allen kartierten pan-arktischen Lagunen. Es wird deutlich, dass bis zum Jahr 2100 durchschnittlich 3 Tg CO_2 Äquivalente pro Jahr aus diesen Thermokarstlagunen freigesetzt werden könnten.

Diese Ergebnisse zeigen, dass Thermokarstlagunen trotz ihrer relativ kleinen Gesamtfläche (3.457 km^2) pro Flächeneinheit mehr als das Vierfache an CO_2-Äquivalent freisetzen als Thermokarstseen und weit mehr als langsam auftauender Permafrost. Dies deutet darauf hin, dass Thermokarstlagunen Hotspots im Permafrost-Kohlenstoffkreislauf sind und eine größere Rolle im Kohlenstoffhaushalt der sich rasch erwärmenden arktischen Landschaften spielen könnten als bisher angenommen. Diese Bedeutung könnte weiter zunehmen, da aktuelle Klimaszenarien eine beschleunigte Erosion der Permafrostküsten und steigende Meeresspiegel vorhersagen. Die Inkubationsexperimente waren hilfreich, um den Einfluss von steigender Salinität auf die mikrobielle Dynamik und Treibhausgasproduktion in durch Meerwasser überfluteten Küstensedimenten zu verstehen. Dennoch ist es nicht möglich, mit den Laborinkubationen alle in natürlichen Umgebungen auftretenden Prozesse vollständig nachzubilden. Zur Validierung der Inkubationsergebnisse sind daher *in situ*-Messungen der Kohlenstoffflüsse während des Übergangs von Land zu Meer erforderlich.

Für meine Familie und all die, die sich anfühlen wie Familie.

TABLE OF CONTENTS

LIST OF FIGURES

LIST OF TABLES

LIST OF ABBREVIATIONS

%	Percent	FWL	Fresh water lake	OC	Organic carbon
‰	Promille	g	Gram	OM	Organic matter
°C	Degree Celsius	gdw	Gram of dry weight	p	Significance value
ABS	Alaskan Beaufort Sea	GFZ	Geoforschungszentrum Potsdam	PCA	Principal component analyses
ACP	Arctic coastal plain	GHG	Greenhouse gas	PCR	Polymerase chain reaction
AL	Active Layer	GIS	Geographic information system	Pg	Petagrams (10^{15} g)
ANME	Anaerobic methanotrophic archaea	GSW	Global surface water	ppm	Parts per million
AOM	Anaerobic oxidation of methane	GWP	Global Warming Potential	QGIS	Geographic information Software
ASV	Amplicon sequence variants	inc	Incubation	r	Correlation factor
AWI	Alfred Wegener Institute	IPCC	Intergovernmental Panel on Climate Change	RGB	Red-Green-Blue

B	Brackish	kaBP	1000 years before present	s	Seconds
B2-B8	Satellite bands 2-8	KCl	Potassium chloride	SD	Standard deviation
BWL	Brackish water lake	km	Kilometer	SDLAG	Semi drained lagoon
C	Carbon	L	Liter	SIPRE	Snow, Ice, and Permafrost Research Establishment
c	Concentration	LAG	Lagoon	SOC	Soil organic carbon
$CaCl_2 \times 2H_2O$	Calcium chloride dihydrate	LS	Laptev Sea	SRB	Sulfate reducing bacteria
CBS	Canadian Beaufort Sea	M	Marine	Tg	Terragrams (10^9 g)
CH_4	Methane	m	Meter	TKL	Thermokarst lake
CO_2	Carbon dioxide	MAR	Marine / Offshore	TN	Total nitrogen
CS	Chukchi Sea	$MgCl_2 \times 6H_2O$	Magnesium chloride hexahydrate	TOC	Total organic carbon
d	Day	mL	Milliliter	TPF	Terrestrial permafrost
$d^{13}C$	Stable carbon isotopes	mM	Milli mol	UPL	Upland
DEM	Digital elevation model	mS	Milli Simens	US	United States
DLAG	Drained lagoon	Mt	Mega tones	UTM	Universal Transverse Mercator Coordinate System
DNA	Deoxyribonucleic acid	Na_2SO_4	Sodium sulfate	V	Volume
DOC	Dissolved organic carbon	NaCl	Sodium chloride	WGS 84	World Geodetic System 1984
EC	Electrical conductivity	$NaHCO_3$	Sodium bicarbonate	$\delta^{13}C$	Stable carbon isotope
eq	Equivalent	NIR	Near infrared	µg	Microgram
ESS	East Siberian Sea	NSIDC	National Snow and Ice Data Center	µm	Micro meter
F	Fresh water	Ø	Diameter	µm	Micro meter

1

Introduction

1.1. Scientific Background

1.1.1. Arctic Warming and Rising Sea Levels

Climate change is causing rapid warming in the Arctic, with rates of temperature increase nearly four times faster than the global average (Rantanen et al., 2022). The phenomenon known as Arctic amplification describes the accelerated warming of the Arctic compared to other regions of the earth (Figure 1.1), driven by processes such as reductions in sea ice and snow cover, which decrease the albedo effect and increase heat absorption leading to further warming and ice and snow loss (Cohen et al., 2020). Additionally, increased atmospheric water vapor and shifting cloud patterns further amplify warming in this region (Richter-Menge et al., 2017). Rising air temperatures are leading to rising land surface temperatures. During the Arctic winters of 2016 and 2018 ground temperatures were recorded as being up to 6 °C above the long-term average (from 1981 to 2010; IPCC, 2023). This rapid warming accelerates permafrost thaw and leads to substantial shifts in Arctic coastal and terrestrial ecosystems (Schuur et al., 2009).

Sea levels in the Arctic Ocean are currently rising at an average rate of 2.3 mm per year, slightly faster than the global average, with the most significant increases observed in the Beaufort Sea (Jin et al., 2023). The rise in sea levels in combination with extended open water seasons intensifies coastal wave energy and increases erosion of coastal bluffs that were previously unaffected (Irrgang et al., 2022). Additionally, storm events can cause temporary surges in sea level, leading to immediate coastal erosion, increased sediment mobilization (Hequette et al., 2001), shoreline shifts, and flooding of coastal lowlands with saline water, which accelerates permafrost thawing in submerged areas (Kim et al., 2021) and affecting human infrastructure, as recently happened in the Kotzebue area (Hagen, 2024).

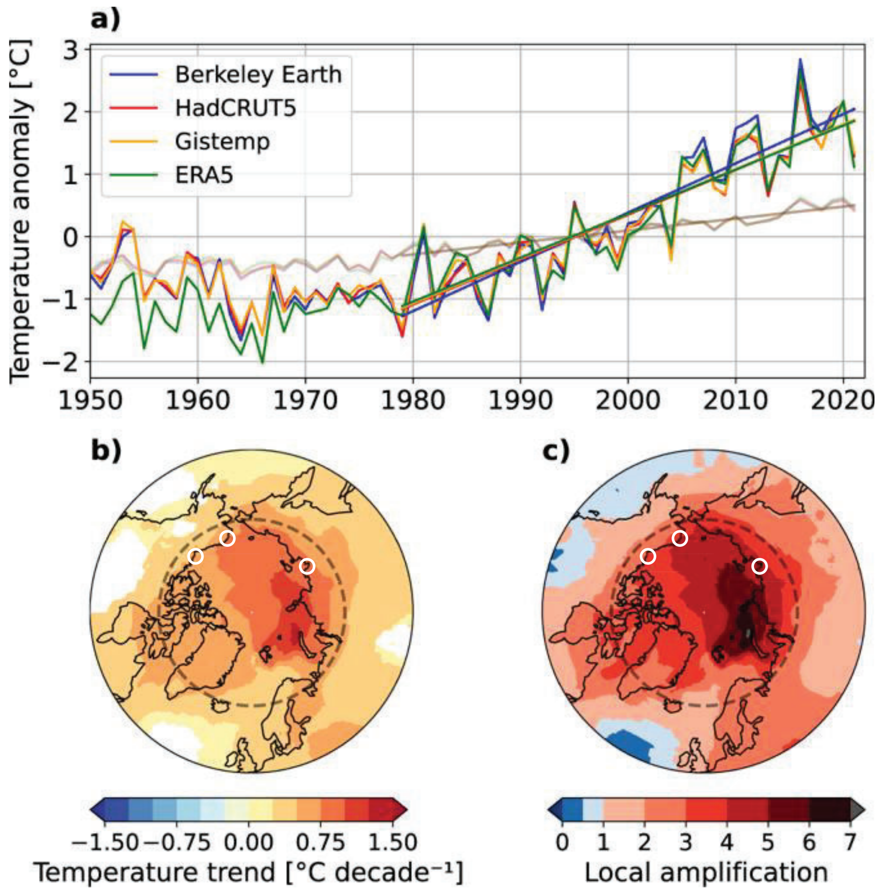

Figure 1.1 Arctic amplification. **a)** Annual mean temperature anomalies in the Arctic (66.5°–90°N) (dark colours) and globally (light colours) during 1950–2021, linear temperature trends for 1979–2021. Berkeley Earth: temperature dataset from weather stations and other sources; HadCRUT5: Met Office Hadley Centre/Climatic Research Unit version 5.0.1.0 integrates sea surface and land air temperature data; GISTEMP: NASA's Goddard Institute for Space Studies Surface Temperature version 4 dataset, provides a long-term record of global surface temperature changes; ERA5: reanalysis dataset that uses a combination of historical weather observations and model outputs; **b)** Annual mean temperature trends for the period 1979–2021. **c)** Local amplification ratio calculated for the period 1979–2021. The dashed line in (**b**) and (**c**) indicate the Arctic Circle (66.5°N), the white circles indicate study site locations of this thesis. Modified after Rantanen et al. (2022).

1.1.2. Permafrost Distribution and Carbon Pools

Permafrost, defined as ground that has been frozen for at least two consecutive years, underlies approximately 13.9 × 10^6 km² (around 15%) of the exposed land area (Obu, 2021) and extends over about 2.5 × 10^6 km² of subsea terrain along the Arctic shelves of the Northern Hemisphere (Figure 1.2; Overduin et al., 2019). About 407 680 km of the Arctic coasts are classifies as permafrost coasts, which are 34% of the world coastline (Lantuit et al., 2012).

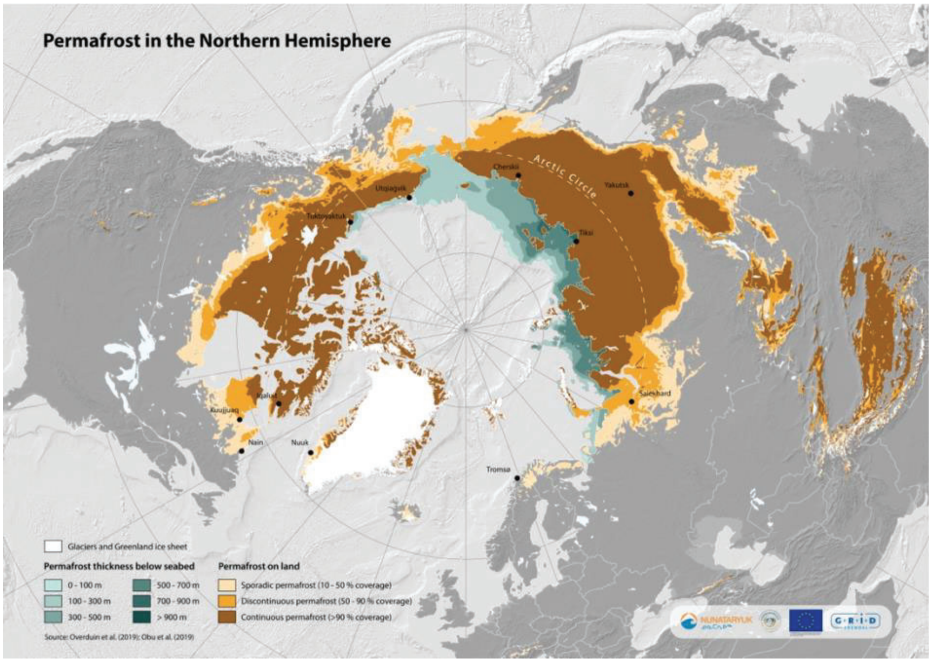

Figure 1.2 Terrestrial and subsea permafrost extent on the Northern Hemisphere. This map was created by G. Fylakis from GRID-Arendal based on data from Overduin et al. (2019) and Obu et al. (2019) as a product of the NUNATARYUK project in collaboration with GRID-Arendal.

Permafrost is a significant carbon reservoir. The permafrost region, which includes both permafrost and non-permafrost deposits, is estimated to store approximately 1,700 petagrams (Pg) of organic carbon (OC) in active layer soils, frozen ground (Lindgren et al., 2018; Miner et al., 2022; Schuur et al., 2022), and lake taliks (Strauss et al., 2021; Walter Anthony et al., 2014). This amounts to nearly 50% of the total OC stored in global soils, which is around 3,350 Pg (Strauss et al., 2024), a large part of it in the Yedoma domain. Yedoma deposits are ice-rich, silty sediments from the late Pleistocene (Kanevskiy et al., 2011, Schirrmeister et al. 2025) that cover approximately 480,000 km^2, with the largest area in north-eastern Siberia (81%) and the smallest in North America (19%) (Strauss et al., 2021, 2022). These deposits can be up to 50 meters thick, providing a substantial source of ancient carbon stored within the Arctic landscape (Strauss et al., 2017). Model simulations suggest that beneath the Arctic seafloor, subsea permafrost stores an additional ~2,800 Pg OC (Miesner et al., 2023).

1.1.3. Thermokarst Development and Carbon Cycle

The thawing of ice-rich permafrost causes surface subsidence, which alters the landscape, affecting ecosystems and infrastructure (Figure 1.3). This thaw also leads to the formation of thermokarst features such as ponds and lakes and contributes to further, rapid permafrost degradation (Grosse et al., 2013; Walter Anthony et al., 2014). Below lakes the locally thawed sediment, called talik, can reach several tens of meters in depth (Ulrich et al., 2010), making the stored organic matter (OM) available for microbial decomposition and resulting in the release of GHGs like carbon dioxide (CO_2) and methane (CH_4) into the atmosphere, further heating the climate (Schneider von Deimling et al., 2012; Schuur et al., 2022). Anaerobic conditions in these waterlogged environments promote archaeal methanogenesis (e.g. Heslop et al., 2020; Townsend-Small et al., 2016). Methanogens utilize simple substrates such as acetate, methanol, methylamines, or hydrogen (H_2) to decompose organic carbon (OC), with methane (CH_4) produced as a metabolic byproduct (Fenchel et al., 2012). However, methanogens compete for substrates with other microbes, such as sulfate-reducing bacteria (SRB), and are suppressed in environments containing more energy-efficient electron acceptors (e.g., Fe^{3+}, Mn^{4+}) (Vincent et al., 2021). In contrast, methanotrophs oxidize CH_4 to CO_2, thereby mitigating methane emissions. Studies have shown that thermokarst lakes are hotspots for methane emissions, as CH_4 is released both through ebullition and diffusion through the water column (Elder et al., 2021; Walter Anthony et al., 2006, 2014). The collapse and erosion of lake edges continuously exposes fresh permafrost to thaw and degradation. Matthews et al. (2020) estimated that thermokarst lakes release between 14 and 18 Tg C per year, contributing substantially to regional carbon budgets.

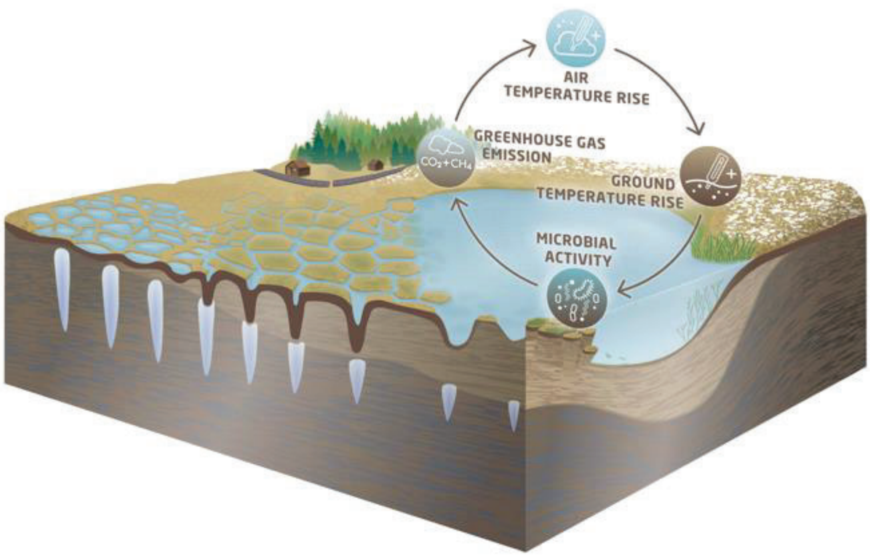

Figure 1.3 Carbon cycle and permafrost thaw. Illustration by Alfred Wegener Institute.

Rising sea surface temperatures, the reduction in sea ice (Jahn et al., 2024; Kwok and Rothrock, 2009; Notz and Stroeve, 2016), and increasing storm intensities are driving enhanced coastal erosion and the inland migration of the Arctic shoreline (Günther et al., 2013; Jones et al., 2018; Malenfant et al., 2022; Whalen et al., 2022), leading to land loss of up to 25 meters per year at the Beaufort Sea (Irrgang et al., 2022) and inundating lowland coastal permafrost landscapes. In this process coastal thermokarst lakes or basins can become connected to the sea, forming thermokarst lagoons (Schirrmeister et al., 2018). The stages of lagoon formation are visualized in Figure 1.4. Two primary pathways of formation are observed: in the first, permafrost transitions into a freshwater lake, which then develops directly into a brackish or saltwater lagoon; in the second, permafrost transitions to a freshwater lake, followed by drainage and the formation of a drained lake basin with renewed permafrost development, before subsequent seawater inundation leads to brackish or saltwater lagoon formation. These thermokarst lagoons, influenced by seawater, form a highly dynamic biogeochemical transition zone at the interface between terrestrial and marine ecosystems. A special role in these transitional zones from land to the marine realm has sulfate. In marine environments, sulfate-reducing microorganisms, including sulfate-reducing bacteria and sulfate-dependent archaea, utilize sulfate as an electron acceptor to produce sulfide (S^{2-}) or to oxidize CH_4. Elevated sulfate concentrations lead to a competitive advantage for these sulfate reducers over methanogens, resulting in generally low CH_4 production in marine sulfate-rich sediments (Holmes et al., 2017; Kristjansson and Schönheit, 1983; Lovley et al., 1982). However, the specific effects of sulfate presence in permafrost environments on the activity of sulfate-reducing microorganisms and their influence on microbial community composition and metabolic activities remain poorly studied and understood.

Figure 1.4 Stages of thermokarst lagoon formation: ① initial situation: thermokarst lake in distance to the sea, ② lake enters the flooding area due to inland-migrating coastlines; initiation of lagoon formation: ③ lake is tapped by the sea or ④ gets permanently connected to the sea via a drainage channel, ⑤ connection of lagoons and surrounding lakes lead to the formation of complex lagoon systems. Example for the northern tip of the Tuktoyaktuk Peninsula (Canadian Beaufort Sea); false-color infrared Sentinel-2 satellite image from July 27, 2019, available at https://apps.sentinel-hub.com/sentinel-playground (modified after Jenrich, 2020).

Looking at their total count, around 40% of the lagoons along the Arctic coast have originated from thermokarst lakes and contain carbon-rich former permafrost deposits (Jenrich, 2020). The formation and evolution of thermokarst lagoons represent a critical step in the mobilization of terrestrial permafrost and thermokarst lake carbon pools along rapidly changing Arctic coastlines, yet they remain largely uninvestigated. Currently, the spatial extent (area) of these lagoons, and whether they function as sources or sinks of GHGs is unclear.

1.2. Research Questions

With this thesis I aim to quantify the greenhouse gas production during the process of permafrost land-sea transition, and more specifically to understand the role of thermokarst lagoons in the permafrost carbon cycle and to estimate the potential carbon release from pan-Arctic thermokarst lagoons.

I aim to answer the following research questions:

- What is the spatial pan-Arctic extent of thermokarst lagoons, how are they distributed and how can they be classified according to their development stages?
- What is the effect of increasing seawater influence on GHG production and microbial community composition?
- Does GHG production of inundated Arctic coastal lowlands differ between landscape features and regions?

1.3. Methods

1.3.1. Study Sites

To explore the potential spatial variability of GHG production in thermokarst lagoons on a maximum geographical spread of the selected field sites, I examined Arctic coastal lowlands across three distinct regions: Northeast Siberia, Northern Alaska, and Northwestern Canada (Figure 1.5). These regions are highly impacted by the amplified warming of the Arctic, as shown in Figure 1.1, with the Bykovsky site in Siberia experiencing the greatest temperature increase. Each region presents unique environmental conditions and formation histories. In each study area, surface sediment samples were collected from permafrost and/or active layer to serve as terrestrial endmember for the thermokarst settings, as well as from thermokarst lakes to reflect the initial state before lagoon formation. Additionally, samples were taken from lagoons with varying connectivity to the sea to represent different stages of lagoon evolution. Furthermore, deep talik and permafrost sediment samples (up to 31 m deep) were collected from one lake and two lagoons in Siberia to investigate potential future GHG release from these deep sediments (Chapter 5). All study sites are situated at the Arctic permafrost coast in highly thermokarst affected regions of the continuous permafrost zone. Sediment and water samples were collected during three expeditions in April 2017 (Siberia), August 2021 (Canada) and April 2022 (Alaska).

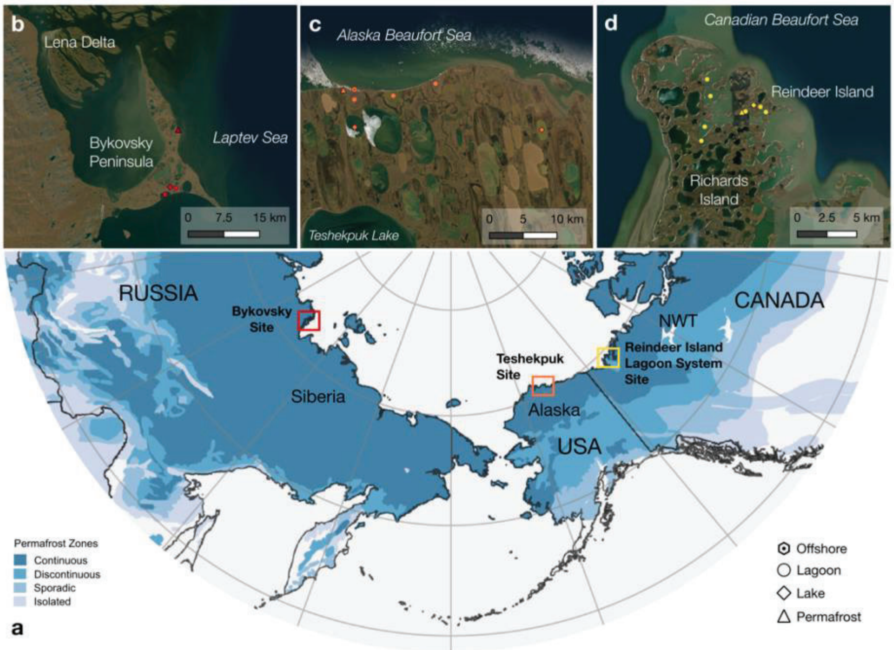

Figure 1.5 Location of the three study sites on a circum-Arctic map (a) and detailed maps with the coring locations on Bykovsky Peninsula (b, Chapter 3, 5), Teshekpuk coast (c, Chapter 6) and Reindeer Island lagoon system (d; Chapter 4). Sources: (a) Permafrost extent regions based on Brown et al. (1997), (b-d): ESRI Satellite

The Bykovsky Peninsula (see Chapter 3 and 5), located along the Laptev Sea southeast of the Lena Delta, Siberia, is shaped by Yedoma uplands, thermokarst lakes and older basins, some of them transitioned into thermokarst lagoons after seawater inundation (Angelopoulos et al., 2020b). Three about 30-meter-long sediment cores were collected from beneath a thermokarst lake and two lagoons of different openness using a drilling rig positioned on the ice (Figure 1. a, b). Further, permafrost samples from the headwall of a retrogressive thaw slump were collected with a hand drill.

Reindeer Island (see Chapter 4) in the northern Mackenzie Delta, Northwest Territories, Canada, is separated from Richards Island by a thermokarst lagoon system, which evolved due to rising sea levels. The shallow lagoon system consists of at least 14 distinguishable former lake basins of which we sampled seven. The sampling covered lagoons with varying connectivity with the sea and therefore varying influence of marine processes and fluvial inputs from the Mackenzie River. Cores were taken from the boat with a gravity corer (Figure 1.6 c). Further, we sampled one thermokarst lake and lowland permafrost and active layer from the island (Figure 1.6 d, e).

The third study area is located on Alaska's North Slope north of Teshekpuk Lake (see Chapter 6), approximately 125 km east of Utqiaġvik along the Beaufort Sea coast. Here, frozen and unfrozen cores of seven distinct sites along a land-sea transect were drilled: a permafrost core from an upland site as an endmember, two lake cores from a freshwater lake and a brackish lake, and three nearly closed lagoons separated from the sea by a sand barrier. These lagoons vary in connectivity and drainage status, with one lagoon being semi-drained, another covered by a thick ice layer with an underlying unfrozen brine-sediment layer, and a third fully drained at the time of coring. Additionally, a marine core was taken offshore in a part of the original basin of the semi-drained lagoon that already transitioned into a subsea state. Frozen cores were drilled using a Snow Ice and Permafrost Research Establishment (SIPRE) corer, while for unfrozen cores a push corer was used (Figure 1.6 f-h).

Figure 1.6 Sediment coring methods. (a) Drilling rig and (b) core description on the Bykovsky Peninsula; (c) gravity coring of unfrozen lagoon sediments at Reindeer Island lagoon system; (d) cryoturbated active layer and permafrost table and (e) drilled ice-rich permafrost on

Reindeer Island; (f) coring of (g) frozen sediments using SIPRE drill and (h) unfrozen sediments using a push corer at Teshekpuk coast. Pictures by (a, b) J. Strauss, (c-h) M. Jenrich.

1.3.2. Key Laboratory Analyses and Experiments

Sediment cores were analyzed in the laboratories of AWI and GFZ in Potsdam. After thawing the cores, I extracted pore water and analyzed it for pH, electrical conductivity (EC), and major anions and cations. The homogenized sediment samples were measured for total organic carbon (TOC), dissolved organic carbon (DOC), total nitrogen (TN), and stable carbon isotopes ($d^{13}C$).

Four anaerobic incubation experiments were conducted at 4°C for 7.5 to 12 months. I designed three of the four experiments (Chapters 3, 4 and 6) as following: Surface samples from permafrost and active layer sediments were treated with: (1) sterilized tap water to simulate fresh lake conditions, (2) artificial brackish water to represent a newly formed lagoon, and (3) artificial seawater (marine) to reflect subsea conditions after inundation. Similarly, surface sediment from thermokarst lake taliks was incubated under these three conditions. Freshwater conditions simulated GHG production in established lakes, while brackish conditions simulated early-stage lagoons and marine incubation conditions simulated either highly saline lagoons or newly submerged coastal sediments transitioning to subsea states. Lagoon surface sediments were incubated under brackish and marine conditions to simulate a young, less connected state and an open setting or the subsea transition. For comparability it was crucial to keep the seawater boundary conditions (fresh: c = 0 g/L, brackish: c = 13 g/L, marine: c = 36 g/L) and the total water volume of 10.5 mL constant for each sample.

In the fourth experiment (Chapter 5), I incubated sediments from Bykovsky Peninsula from three different sampling depths reaching down to 30m below ground with 20 mL artificial seawater (36 g/L) to investigate the potential future GHG production in deep layers after seawater inundation.

I manually measured anaerobic CO_2 and CH_4 production in the headspace of incubation bottles (in triplicate) using gas chromatography, initially on a daily basis, followed by weekly and then biweekly intervals. In total, this process resulted in over 5 000 measurements, requiring more than 400 hours of work.

The microbial analyses conducted on the Bykovsky samples included DNA extraction, PCR, and sequencing (see Chapter 3.3.3).

1.3.3. Remote Sensing

The mapping and classification of thermokarst lagoons to answer research question 1 (for details see Chapter 2) were conducted using high-resolution satellite imagery and geographic information system (GIS) tools. Water masks derived from the Global Surface Water (GSW) dataset, spanning from 1984 to 2021, were applied to assess the presence of water bodies. These masks, processed in Google Earth Engine, were used to define lagoon areas and to understand past water coverage patterns. Lagoon classifications, based on connectivity to the sea, were developed to reflect different stages of the lake-to-sea transition. The openness of the lagoon and whether the lagoons are connected to another were visually identified based on geomorphological features, without incorporating bathymetric data. Statistical analysis, including linear trend calculations, were performed to analyse lagoon area changes over time.

1.3.4 Upscaling Carbon Loss from Thermokarst Lagoons

Using CO_2 and CH_4 production data from the incubation experiments described in Chapters 3 (Jenrich et al., 2024a), Chapter 4 (Jenrich et al., 2024d), and Chapters 5 and 6 and the pan-Arctic lagoon extend from Chapter 2 (Jenrich et al., in review), I estimated carbon loss for all lagoons under both brackish and marine treatments. I did this for low, medium, and high connectivity lagoons under both treatments and an average carbon loss for thermokarst lagoons across all connectivity classes and treatments, based on the following equation, modified from (Dolle et al., in review; see Appendix E):

$$C_{loss}(Tg) = \bar{x}\left(DBD(kg\ m^{-1}) \cdot P_c\left((\mu gCgdw^{-1} \cdot 10^{-3}) \cdot \frac{365}{244}\right)\right) \cdot LT(m) \cdot A(m^2) \cdot 10^{-9}$$

where C_{loss} is the soil carbon loss, DBD is the dry bulk density, P_c is the cumulative GHG production after 244 days of incubation interpolated to 365 days (one year), LT is the layer thickness and A is the lagoon area (Table 4.2). As pan-Arctic data on the area and duration of bottom-fast ice formation for lagoons is missing, for this first upscaling approach I calculate the maximum C loss assuming the lagoon sediment is unfrozen year-round. Using a 100-year GWP of 36 for CH_4 (IPCC, 2014), the warming effect of CH_4 can be compared to CO_2 emissions. Since GWP is expressed in terms of tons of CH_4 per ton of CO_2, a molar mass correction is required to relate it to total carbon losses. With this correction, the warming effect of CH_4 per unit of soil carbon lost is approximately 12.4 times that of CO_2, which is given as CO_2eq. This is a rough estimation which accounts only for aerobic and anaerobic CH_4 oxidation in the sediment (discussed in Chapter 3 and Appendix C), but not in the water column and under the ice cover in winter (Elder et al., 2019; Greene et al., 2014; Martinez-Cruz et al., 2015). Even at temperatures below 0°C, which is common for salty sediments, 41-83 % of the produced CH_4 can be oxidized as shown by Winkel et al. (2019) for deeper thawed sediments (3-5 m) beneath an Alaskan lake.

1.4 Thesis Structure and Overview of Publications

This cumulative dissertation consists of seven main chapters. The introductory Chapter 1 provides the scientific background and relevance of thermokarst lagoons as crucial transitional systems in rapidly changing Arctic coastal permafrost landscapes, particularly in the context of the carbon cycle. Additionally, it outlines the research questions, provides a brief overview of the main methods, and introduces the research articles, along with their contributions.

Chapters 2–4, as well as Appendices A to E, contain three original research articles, which have been published or are currently under review in international peer-reviewed journals (Table 1.1). Specifically, Chapter 2 presents remote sensing data on the distribution, extent, and classification of thermokarst lagoons, alongside with an analysis of the dynamics in permafrost-to-marine transitions. Chapter 3 focuses on the incubation of sediment samples from the Bykovsky Peninsula in Siberia. This chapter investigates CO_2 and CH_4 production, as well as short- and long-term microbial responses to varying salinities. Chapter 4, which focusses on the incubation of sediment samples from the Reindeer Island lagoon system in Canada, examines variations in CO_2 and CH_4 production within lagoon systems and along a land-sea transition gradient.

Chapter 5 contains the draft of a manuscript presenting the results from the deep Bykovsky sediment incubation and the corresponding microbial analysis. Chapter 6 covers another draft of a manuscript including the results of the incubation experiment with sediment samples from the Teshekpuk Lake region in Alaska and focuses on the simulation of the inundation of an Arctic coastal plain.

Finally, Chapter 7 synthesizes and discusses the results of the individual studies. This chapter highlights the drivers of GHG production, discusses variations in GHG production during the transition from terrestrial to marine environments, and estimates carbon loss on a pan-Arctic scale.

Table 1.1 Overview of publications and drafts included in this thesis.

	Publication
Chapter 2	**Jenrich, M.**, Prodinger, M., Nitze, I., Grosse, G., and Strauss, J.: Thermokarst Lagoons: Distribution, Classification, and Dynamics in Permafrost-to-Marine Transitions, under review in *Permafrost and Periglacial Processes*
Chapter 3	**Jenrich, M**., Angelopoulos, M., Liebner, S., Treat, C., Knoblauch, C., Yang, S., Grosse, G., Giebeler, F., Jongejans, L. L., Grigoriev, M., and Strauss, J.: Greenhouse Gas Production and Microbial Response During the Transition From Terrestrial Permafrost to a Marine Environment, *Permafrost and Periglacial Processes*, https://doi.org/10.1002/ppp.2251, 2024.
Chapter 4	**Jenrich, M.**, Wolter, J., Liebner, S., Knoblauch, C., Grosse, G., Giebeler, F., Whalen, D., and Strauss, J.: Rising Arctic Seas and Thawing Permafrost: Uncovering the Carbon Cycle Impact in a Thermokarst Lagoon System in the outer Mackenzie Delta, Canada, *Biogeosciences*, 1–30, https://doi.org/10.5194/egusphere-2024-2891, preprint, 2024.
Chapter 5	Potential Future Greenhouse Gas Production in Deep Thawing Permafrost Sediments Under Saltwater Impact *(not yet submitted manuscript draft)*
Chapter 6	Simulated Inundation of a Coastal Plain: An Incubation Study of the Teshekpuk Coast Region, Alaska *(not yet submitted manuscript draft)*
Appendix A	**Jenrich, M.**, Angelopoulos, M., Grosse, G., Overduin, P. P., Schirrmeister, L., Nitze, I., Biskaborn, B. K., Liebner, S., Grigoriev, M., Murray, A., Jongejans, L. L., and Strauss, J.: Thermokarst Lagoons: A Core-Based Assessment of Depositional Characteristics and an Estimate of Carbon Pools on the Bykovsky Peninsula, Front. Earth Sci., 9, 637899, https://doi.org/10.3389/feart.2021.637899, 2021.
Appendix B	Angelopoulos, M., Overduin, P. P., **Jenrich, M.**, Nitze, I., Günther, F., Strauss, J., Westermann, S., Schirrmeister, L., Kholodov, A., Krautblatter, M., Grigoriev, M. N., and Grosse, G.: Onshore Thermokarst Primes Subsea Permafrost Degradation, *Geophysical Research Letters*, 48, e2021GL093881, https://doi.org/10.1029/2021GL093881, 2021.
Appendix C	Yang, S., Anthony, S. E., **Jenrich, M.**, in 't Zandt, M. H., Strauss, J., Overduin, P. P., Grosse, G., Angelopoulos, M., Biskaborn, B. K., Grigoriev, M. N., Wagner, D., Knoblauch, C., Jaeschke, A., Rethemeyer, J., Kallmeyer, J., and Liebner, S.: Microbial methane cycling in sediments of Arctic thermokarst lagoons, *Global Change Biology*, 29, 2714–2731, https://doi.org/10.1111/gcb.16649, 2023.
Appendix D	Giest, F., **Jenrich, M.**, Prodinger, Grosse, G., Jones, M., Mangelsdorf, K., Windirsch, T., and Strauss, J.: Organic Carbon, Mercury, and Sediment Characteristics along a land – shore transect in Arctic Alaska, in review *Biogeosciences*
Appendix E	Dolle, M. L., Laurent, M., Schaller, J., Seemann, F., **Jenrich, M.**, Strauss, J., and Treat, C.: Effect of Sea Water Inundation on CO_2 and CH_4 Production of Thawing Coastal Permafrost near Utqiaġvik, Alaska, submitted to *Permafrost and Periglacial Processes*

1.5 Contributions to Publications

1.5.1 Publication "Thermokarst Lagoons: Distribution, Classification, and Dynamics in Permafrost-to-Marine Transitions"

M. Jenrich designed the study. M. Prodinger led the mapping, which was used by M. Jenrich and M. Prodinger to compile the first draft of the manuscript. I. Nitze led the lagoon change analysis and created these figures. J. Strauss created Figure 5. M. Jenrich generated the remaining figures and tables. All authors contributed by revising and reviewing the manuscript drafts.

1.5.2 Publication "Greenhouse Gas Production and Microbial Response During the Transition From Terrestrial Permafrost to a Marine Environment"

M. Jenrich and J. Strauss designed this study. J. Strauss, G. Grosse, and M. Grigoriev developed the overall coring plans for the Bykovsky Peninsula field campaign. J. Strauss, M. Grigoriev, M. Angelopoulos, S. Liebner, and G. Grosse conducted the field work. M. Jenrich and F. Giebeler performed laboratory analyses. S. Liebner and S. Yang conducted the microbial work and data the microbial data interpretation. M. Jenrich led the writing of the first draft of the manuscript. All co-authors contributed within their specific expertise to data interpretation as well as manuscript writing.

1.5.3 Publication "Rising Arctic Seas and Thawing Permafrost: Uncovering the Carbon Cycle Impact in a Thermokarst Lagoon System in the outer Mackenzie Delta, Canada"

M. Jenrich and J. Strauss designed this study. M. Jenrich and J. Strauss developed the overall coring plans for the Reindeer Island field campaign. M. Jenrich and J. Strauss conducted the field work. D. Whalen enabled field work due to his logistical support. M. Jenrich and F. Giebeler performed laboratory analyses. S. Liebner supported the incubation experiments by supplying GC facilities. J. Wolter conducted statistical analyses. M. Jenrich led the writing of the first draft of the manuscript. All co-authors contributed within their specific expertise to data interpretation as well as manuscript writing.

Contributions to the publications in the appendix are given in the section "author contribution" of the corresponding publication.

2

Thermokarst Lagoons: Distribution, Classification, and Dynamics in Permafrost-to-Marine Transitions

Maren Jenrich[1,2*], Maria Prodinger[1,3*], Ingmar Nitze[1], Guido Grosse[1,2] and Jens Strauss[1]

[1]Alfred Wegener Institute Helmholtz Centre for Polar and Marine Research, Permafrost Research Section, Potsdam, 14473, Germany

[2] University of Potsdam, Institute of Geosciences, Potsdam, 14469, Germany

[3] Universität Hamburg, Institute of Geosciences, Hamburg, 20148, Germany

* contributed equally to this work

This publication is under review in *Permafrost and Periglacial Processes*

Abstract The transition of permafrost landscapes to marine environments, driven by climate change, plays a crucial role in the global carbon cycle. Thermokarst lagoons, formed along permafrost coasts when thermokarst lakes get connected to the sea, are key features in this transition. Using remote sensing imagery, we manually mapped and classified 520 thermokarst lagoons along the coastline of five Arctic shelf seas (Laptev, East Siberian, Chukchi, Alaskan Beaufort, and Canadian Beaufort seas) between the Taymyr and Tuktoyaktuk peninsulas, and most were located along the Canadian Beaufort Sea. These lagoons cover a total area of 3,457 km², with strong regional variations in both size and distribution. Based on their sea connectivity, we categorized the lagoons into five classes, with 55% in early transition stages (very low to low-connected). From 2000 to 2021, lagoon area increased in all regions, with the Alaska Beaufort Sea coast showing the most growth (+1.34%). Smaller and isolated lagoons expanded faster than those in lagoon systems or deltas. Our analysis links thermokarst lagoon distribution to coastal erosion, land cover, ground ice, and organic carbon, showing that most lagoons are located in areas of thermokarst lake coverage and high coastal erosion. This unique pan-Arctic dataset serves as a foundation for understanding thermokarst lagoon dynamics and their role in the rapidly changing Arctic environment.

2.1 Introduction

The transition of permafrost landscapes to marine environments due to climate change is a critical process with significant implications for the global carbon cycle (Fritz et al., 2017; Jenrich et al., 2024b; Nielsen et al., 2022; Vonk et al., 2012). Permafrost holds a vast amount of organic carbon (~1460–1600 gigatons; Hugelius et al., 2014; Mishra et al., 2021; Strauss et al., 2025) and permafrost thaw leads to the partial mobilization and degradation of this previously sequestered organic carbon, potentially creating a feedback loop that exacerbates climate change (Koven et al., 2015; Schuur et al., 2022). Especially vulnerable are deposits including excess ice, which are prone to surface subsidence and also high coastal erosion rates (Irrgang et al., 2022; Nitzbon et al., 2020). Understanding the dynamics of these transitions is important for predicting future climate scenarios and mitigating their impacts. Both permafrost coastal erosion and inundation of low-lying areas are important processes that result in terrestrial permafrost transitioning to a marine environment. In the Arctic, lagoons are providing a unique setting where these types of transitions and their consequences can be studied in detail.

Arctic lagoons are critical habitats that support diverse and highly productive ecosystems, playing a key role in the structure and functioning of the Arctic coastal environment (Craig, 1984; Dunton et al., 2012). These shallow, semi-enclosed water bodies act as ecological buffers between terrestrial and marine environments, providing crucial habitats for a wide variety of species, including migratory birds, fish, and marine mammals (Craig, 1984; Dunton et al., 2006, 2012; McMahon et al., 2021). For example, in Alaska the Beaufort Lagoon LTER (Long Term Ecological Research) program has emphasized the importance of these ecosystems, highlighting their sensitivity to changes in freshwater input, sea ice dynamics, and coastal erosion (Dunton et al., 2023; "LTER Core Research Areas," 2019). Studies show that more sheltered lagoons foster greater biodiversity, while less protected lagoons exhibit lower diversity of trophic niches among fish populations (Stanek et al., 2022). Research from Siberia and Canada highlighted the role of lagoons in shaping coastal geomorphology and influencing sediment fluxes, nutrient cycling, carbon storage, and their complex hydrochemistry (Grasby et al., 2013; Romanovskii et al., 2000; Solomon et al., 2000). Across Alaska, Canada, and Russia, studies consistently show that lagoons may serve as hotspots of biological activity, supporting both local biodiversity and subsistence practices of Indigenous communities (e.g., Fraley et al., 2022).

Unlike barrier-island lagoons, which develop when spits or sandbars enclose a waterbody, thermokarst lagoons form exclusively in Arctic thermokarst coastal lowland environments when thermokarst lakes or basins are inundated by the sea (Figure 2.1). These lagoons have distinct geomorphological features, including a round to oval shape and well-defined shorelines distinguishing them from other coastal lagoons. They maintain at least intermittent connections to the sea through inlets or visible channels formed after thermokarst lake drainage or regular water exchanges driven by tides or storm surges (Angelopoulos et al., 2021; Jenrich, 2020). Thermokarst lagoon formation is driven by coastal erosion, sea-level rise, and permafrost thaw induced ground subsidence (Creel et al., 2024). Previous thermokarst lagoon research focused for example on coastline evolution and drowning of thermokarst-affected landscapes (Hequette et al., 1995; Romanovskii et al., 2000; Ruz et al., 1992) or lagoon sediment characteristics (Cheverev et al., 2007; Jenrich et al., 2021; Schirrmeister et al., 2018; Solomon et al., 2000, Giest et al., 2025). We here develop a broader generalization scheme for thermokarst lagoons and a pan-Arctic assessment of their distribution and classification, because they are key features in the permafrost-to-marine transition and a generalized scheme will help better understanding of thermokarst lagoon development and the environmental settings.

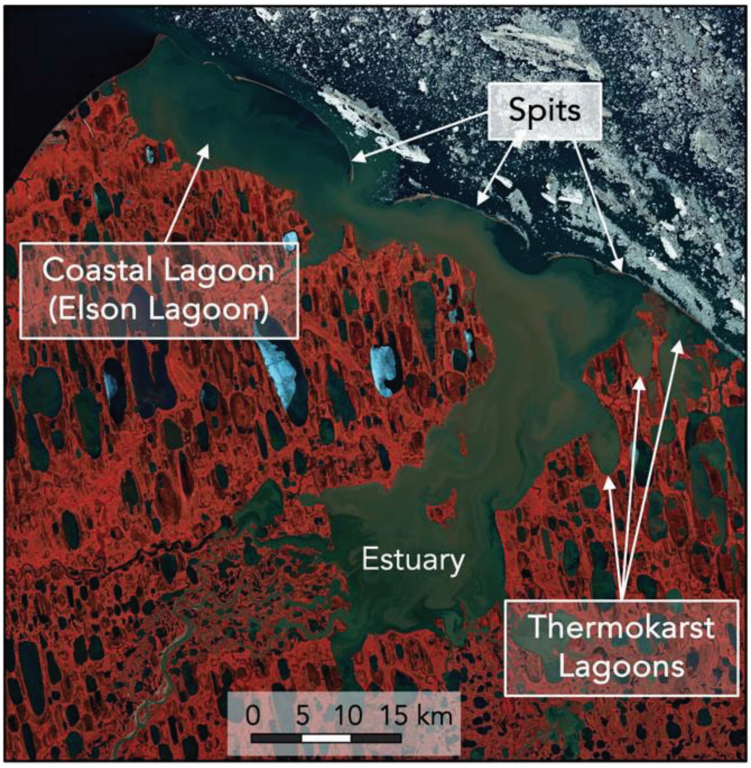

Figure 2.1. Sentinel-2 satellite image of northern Alaska showcasing different coastal waterbody types along a typical Arctic lowland coastline. Thermokarst lagoons, formed from inundated thermokarst lakes and drained lake basins, are distinct from the larger, barrier island-separated coastal lagoon (here, Elson Lagoon) and a wide river estuary. Image source: ESA, false-color Sentinel 2 image from 2024-07-11.

Previous research has laid the groundwork for categorizing Arctic lagoons based on their connectivity to the marine environment (Fraley et al., 2022). The classification of Arctic lagoons into “barrier island”, “stable connection”, “intermittent connection”, and “closed” on a gradient from high to low connectivity is comparable to the initial thermokarst lagoon classification by Jenrich et al. (2021), though Fraley et al. (2022) focused on coastal lagoons without taking thermokarst processes into account. Specifically for thermokarst lagoons, the initial classification system by Jenrich et al. (2021) categorized lagoons into "open", "semi-closed", and "nearly closed" systems based on their connectivity and coastal erosion gradients. Angelopoulos et al. (2021) provided a first distribution map, and the first total area estimation was conducted by Jenrich et al. (2021), followed by an extensive pan-Arctic lagoon area estimation by Yang et al. (2023). This research showed that thermokarst lagoons occupy approximately 2,579 km², an area roughly equivalent to the country of Luxembourg.

Despite these advances, several knowledge gaps remain. In particular, lagoon connectivity is an important parameter that determines water exchange, hydrochemistry and biogeochemistry, as well as ecological exchange (Fraley et al., 2021; Young et al., 2022). Connectivity might be affected by spatial constraints such as channel length and depth or by temporal constraints for example due to seasonal ice formation that restricts or seals connecting channels (Spangenberg et al., 2021). Hence, the subdivision of interconnected lagoon systems into individual lagoons needs more precision, also impacting the accurate estimation of their number and area. The existing classification system remains insufficient for the detailed categorization required for complex or nested lagoon systems. Moreover, the biogeochemical and hydrochemical diversity within these systems, influenced by differences in connectivity, sediment input, and salinity, needs a more refined classification approach. Furthermore, while thermokarst lagoon area change has not yet been studied, it is conceivable that the nature of lagoons, i.e. the openness or closedness of their connection, could impact erosion of their shorelines since it impacts salinity, water temperatures, as well as wave and current dynamics, all which are factors known to affect coastal erosion. Some of the most prominent changes in permafrost-affected areas are due to coastal erosion (Günther et al., 2015; Irrgang et al., 2018; Jones et al., 2020) and widespread thermokarst lake changes (Marsh et al., 2009; Nitze et al., 2017). While those have been widely studied using remote sensing techniques, research concerning area change dynamics of thermokarst lagoons is lacking.

This paper addresses these above-mentioned gaps by aiming to provide a unique dataset that includes the count, area, and classification of thermokarst lagoons on a pan-Arctic scale and further the change in lagoon area over 20 years. By employing manual mapping techniques and an improved classification system, this study aims to offer a comprehensive understanding of thermokarst lagoon dynamics and their role in the permafrost-to-marine transition.

2.2 Methods

Thermokarst lagoons were differentiated from other types of lagoons based on their high roundness that suggest an origin as thermokarst lake or basin, their presence along a lowland coast dominated by thermokarst lake and basin systems, and the absence of wide spits and barrier islands enclosing a coastal water body, which is typical for other coastal lagoon types.

2.2.1 Improved Lagoon Mapping Approach

Building on previous mapping efforts (Jenrich, 2020; Angelopoulos et al., 2021), we refined the classification of thermokarst lagoons by distinguishing interconnected sub-lagoons as individual entities where the original basin shape was still recognizable. This distinction acknowledges differences in geomorphological legacy, hydrochemistry, biogeochemistry, and sedimentology among sub-lagoons.

A water body was classified as a thermokarst lagoon if it met the following criteria:

1. Located in a thermokarst environment;
2. Round to oval-shaped depression with a discernible shoreline;
3. Minimum of 500 m in diameter;
4. At least intermittent connection with the sea either through:
   a) a visible channel with a maximum length of 1 km;
   b) separation only by a narrow beach;
   c) or a maximum elevation difference to the sea of ≤1.5 m which ensures regular water exchange via spring tides or storm surges.

Differences in altitude between land and sea were determined using the ArcticDEM digital elevation model and hillshade (Porter et al., 2018) in combination with ESA Sentinel-2 false color satellite imagery. A median image composite from August and September 2018 with a spatial resolution of 10 m served as the base imagery.

The methodological approach of the mapping and the datasets used are shown in Figure 2.2. Mapping was conducted in QGIS version 3.34 using Sentinel-2 imagery accessed via the Copernicus Browser (Copernicus Sentinel data). Images were selected with a cloud cover of less than 30% from 2023-07-01 to 2023-08-30, utilizing true color (B4: red, B3: green, B2: blue) and false color composites (B8: NIR, B4: red, B3: green) to enhance visibility of natural boundaries. Features such as sand spits, sandbanks, and shoals were used as visual references for delineation. Additional imagery basemaps, including Google Satellite layer and ESRI Satellite/ArcGIS World Imagery (Esri, Maxar, Earthstar Geographics, and the GIS User Community), provided supplementary context but were secondary due to unclear acquisition dates.

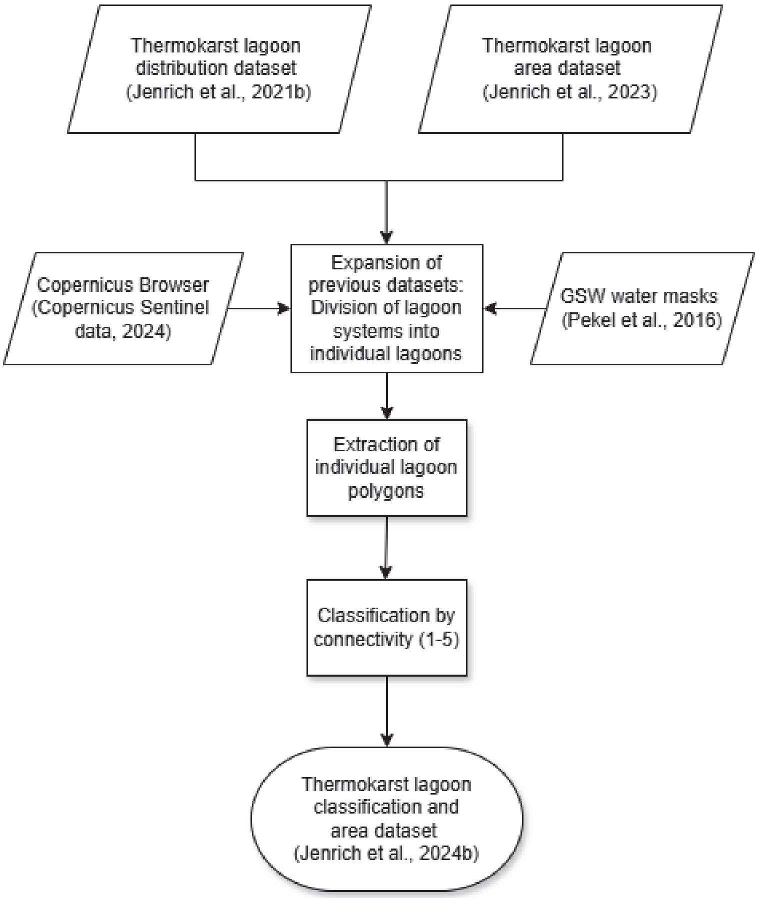

Figure 2.2. Flowchart depicting the datasets (parallelogram) that contributed to this study, the main methodological steps (boxes) of the lagoon mapping, as well as the dataset which the study is based on (oval). Datasets: Copernicus Sentinel, 2024; Jenrich et al., 2024b, 2023, 2021b; Pekel et al., 2016

Water masks for sub-lagoon delineation were derived from the Global Surface Water dataset (GSW) (Pekel et al., 2016), which utilizes Landsat-5, -7, and -8 data from 1984-2021 at 30 m resolution. These masks were generated in Google Earth Engine (Gorelick et al., 2017) based on the occurrence dataset from GSW in version 1.4 (Pekel et al., 2016) using a threshold of >75%. The resulting raster images were vectorized in QGIS to guide lagoon mapping. The basin shapes from the water masks provided crucial reference points for accurate boundary determination based on which lagoon polygons where (Figure 2.3).

Figure 2.3. Exemplary lagoon extraction for individual lagoons (blue circles) and connected lagoons in lagoon systems (white circles) at the Northern Head of the Mackenzie Delta, Richards Island, Canadian Beaufort Sea. *CBS 213* and *CBS 214* are examples of newly formed lagoons that have been shrinking in recent years due to drainage. Water mask is based on the Global Surface Water dataset (Pekel et a., 2016) and coalesced water bodies have been split with a straight by line at the narrowest part between visually identifiable sub-basins. Source imagery: true-color Sentinel-2 satellite image from 2023-08-26.

Pre-existing thermokarst lagoon boundaries from Jenrich et al. (2023), were integrated and refined where necessary. Adjustments were made in cases where the original mapping did not align with expected lagoon morphology, leading to slight variations in area size. For example, in *Tesh 15 (ABS_010)*, the current study mapped the lagoon based solely on its distinct round shape, whereas Jenrich et al. (2023) included an elongated, estuary-like outlet. This refinement led to improved accuracy in lagoon size estimation.

Water mask datasets in Jenrich et al. (2023) were based on data spanning 1984-2018, while this study incorporated an updated range of 1984-2021. The resulting difference in total lagoon area was 0.33 ± 0.94% (median: 0.04%), also pointing at the dynamic nature of Arctic coastal water surfaces. The use of an updated dataset has increased the precision of area calculations.

By implementing these refinements and developing clear criteria for manual mapping, this study ensures a more consistent and accurate assessment of thermokarst lagoon distribution and area in permafrost regions.

To define lagoon boundaries and create distinct polygons, the "split with lines" function in QGIS was used. This step was particularly crucial in complex landscapes like the Lena Delta, where a Sentinel-2 RGB composite (acquisition date 2023-06-08) provided additional clarity. Lagoon boundaries were delineated based on:

(1) Water masks: Boundaries were set at the narrowest points of lagoon openings, as derived from the GSW dataset.

(2) Satellite imagery: Sentinel-2 imagery allowed identification and tracking of natural morphological features such as sandbanks, barriers, and shoals.

To ensure consistency in area calculations, we used the EPSG:3413 coordinate reference system (WGS 84 / NSIDC Sea Ice Polar Stereographic North), avoiding discrepancies from re-projection into UTM Zones. This approach differs from Jenrich (2020), where UTM-based calculations were used.

2.2.2 Classification

The 520 mapped thermokarst lagoons were then classified manually into five distinct classes based on their connectivity to the sea (Table 2.1), using a geomorphological approach that did not account for bathymetry. This classification reflects different stages of the lake-to-sea transition and considers the presence of natural barriers such as sand banks and spits, the length of a channel or width of a lagoon opening, as well as the distance from the sea. Exemplary ranges from lagoons of each class are presented in Table 2.1. A table with additional examples can be found in the supplementary material (Table S1).

Class 1: This class is characterized by lagoons with very low connectivity to the sea. Exchange is strongly limited by a long and/or narrow channel. These lagoons may exhibit temporary lake characteristics and represent the least advanced stage in the lake-to-sea transition. In some cases, they are subsequent lagoons with very limited exchange due to the restrictive nature of the channel and/or the high distance to the sea.

Class 2: Lagoons in this class have low connectivity, with exchange limited by a very small opening or narrow channel. These may be subsequent lagoons with less connection to the primary lagoon, either due to the small channel size or high distance from the sea.

Class 3: This class represents lagoons with medium connectivity. Exchange is limited either temporally or spatially by larger barrier islands or sand spits compared to class 4. These lagoons can also be subsequent lagoons that are well connected to the previous lagoon.

Class 4: Lagoons classified as class 4 exhibit high connectivity to the sea. Exchange is only slightly limited by the presence of barrier islands or sand spits which constrict the inlet slightly. This class also includes subsequent lagoons that are very well connected to the previous lagoon, with minimal obstruction to seawater exchange.

Class 5: Representing the most advanced stage in the lake-to-sea transition, class 5 lagoons have very high connectivity to the sea. The inlet is not limited by sand banks or spits, allowing for unrestricted exchange with the sea.

Table 2.1 Thermokarst lagoon classification by connectivity to the sea, based on a geomorphological approach. The classes increase with the growing openness of the lagoon and the stronger connection to the sea. Characteristics of classes are CL: channel length, W: width of channel/lagoon opening, D: distance to open sea, and B: coastal barriers like beaches or spits. Examples of the classification are provided in the satellite image of the eastern tip of Tuktoyaktuk Peninsula, NWT, Canada. Imagery source: False-color Sentinel 2 image from 2023-08-05.

Class	Connectivity	Openness	Characteristics	Examples
1	Very Low	Nearly Closed	CL: 430-1000 m W: 70-2000 m D: 15-19000 m B: <100m in width if no channel present or none	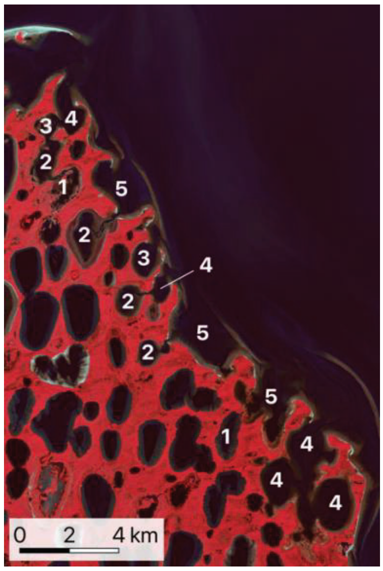
2	Low	Limited Open	CL: 150-1000 m W: 40-2000 m D: 0-12000 m B: leaky or none	
3	Medium	Semi-Open	CL: no channel W: 80-2600 m D: 0-4500 m B: with wide openings or none	
4	High	Mostly Open	CL: no channel W: 420-5000 m D: 0-7000 m B: almost absent or none	
5	Very High	Always Open	CL: no channel W: 500-2700 m D: 0-1500 m B: none	

This classification framework allows for a detailed understanding of the connectivity levels of thermokarst lagoons and their respective stages in the transition from lake to marine environments, and works for single lagoons, but also for lagoon systems.

2.2.3 Lagoon Area Change

2.2.3.1 Water area Extraction

In order to explore thermokarst lagoon area changes on a larger scale, the GSW dataset (Pekel et al., 2016) and its annual data availability were used. Area information for individual years from 2000 through 2021 was extracted through Google Earth Engine using the existing lagoon polygons. We extracted all four layers of the GSW data, including permanent and seasonal water area, as well as land and no data area for debugging and data filtering with values in square kilometers (km^2) per lagoon for each year. We refrained from using data before 2000 due to highly limited data availability, particularly over Siberia.

2.2.3.2 Data Cleaning

The extracted annual surface water data for each lagoon required preprocessing before data analysis. Many lagoons contained NoData pixels in the original surface water dataset due to missing data, primarily resulting from lower acquisition frequencies before 2013 prior to the launch of Landsat-8, limited downlink capacities of Landsat, and challenging acquisition conditions for optical satellite data in Arctic coastal regions (Beamish et al., 2020; Loveland and Irons, 2016; Wulder et al., 2019).

To ensure complete surface water information, we flagged and removed data points for each year and lagoon with a NoData fraction exceeding 2%. After this cleanup, the fraction of lagoons with NoData ranged from 1.0% in 2019 to 87.4% in 2003, with a notably higher fraction of missing data before 2013 (see Figure S3).

Subsequently, we merged the permanent and seasonal water classes into a single water class. For further time-series analysis, we implemented data imputation strategies to fill the gaps. Assuming that lagoon areas are comparably stable with minimal interannual variation and that the remaining data points are of good quality, we first applied linear interpolation to fill gaps based on local linear functions of the nearest data points in time. For NoData at the edges of the time series, we used forward- and backward-filling techniques, taking the nearest data point before or after the gap, respectively. As a result, we obtained a complete annual surface water area time series for all lagoons from 2000 to 2021.

2.2.3.3 Data Aggregation and Change Analysis

We calculated the linear trends of area for each lagoon using ordinary least-squares regression over the entire period, which included the slope, intercept, p-value, and r^2. Next, we aggregated the results by region, class and lagoon type to identify commonalities and differences in lagoon connectivity.

For the grouped statistics, we summarized the mean area per year. Additionally, we computed the mean normalized change, which represents the average percentage change for individual lagoons from 2000 to 2021, as well as the overall normalized change, reflecting the total change within each region or class.

2.2.3.4 Statistical Analyses

We assessed the statistical significance of lagoon area change rates (slope values) across regions and lagoon classes using a two-step approach. First, the Shapiro-Wilk test identified non-normal distributions in our samples, precluding the use of parametric t-tests. We therefore implemented non-parametric alternatives: the Kruskal-Wallis test for regional pairwise comparisons, which is practically the Mann-Whitney U test. Next, we compared single regions (adjacent seas) and lagoon classes against the total lagoon population using Wilcoxon signed-rank tests. All analyses were conducted in Python using SciPy's statistical module (scipy.stats).

2.3 Relationship between Thermokarst Lagoon and Lake Area

We analyzed the relationship between lagoon and lake area. Lakes were extracted from the Global Lake and Wetland Database (Lehner and Döll, 2004). Lakes ≥0.1 km² within a 30 km coastal buffer (ARCADE database; Speetjens et al., 2023) were included, without filtering for thermokarst characteristics. All lakes fell within continuous or discontinuous permafrost zones and were grouped by sea (Obu et al., 2019). We visualized the size distribution using histograms with fixed bins of 3 km² to ensure comparability.

Lakes and lagoons for each coast were categorized by size using quartiles: small (0.1 – <0.8 km²), medium (0.8 – <1.2 km²), large (1.2 – <2.4 km²), and very large (≥2.4 km²). Afterwards the difference between lake and lagoon quartiles was calculated, and the deviation (absolute values) further grouped in quartiles: small (1.2 – <11.1 %), medium (11.1 – <21.0 %), large (21.0 – <30.9 %), and very large (≥30.9 %).

2.4 Results

2.4.1 Distribution and Size of Thermokarst Lagoons

In total, we identified 520 thermokarst lagoons along the Arctic coast between the Taymyr Peninsula and Tuktoyaktuk Peninsula (Figure 2.4). Table 2.2 provides an overview of lagoon distribution across various Arctic coastal regions, lagoon types and lagoon classes. The Canadian Beaufort Sea has the highest lagoon count with 243, including 63 in the Mackenzie Delta, comprising nearly half of the total. These lagoons are also the smallest on average, at 2.0 km². In contrast, lagoons along the coast of the Chukchi Sea present the largest average size at 23.9 km². The coast of the East Siberian Sea shows the lowest density of thermokarst lagoons. Most lagoons along the Laptev Sea Coast are located in the Lena Delta (87).

Figure 2.4 a) Pan-Arctic permafrost map of the 520 thermokarst lagoons located along the Arctic coast between the Taimyr Peninsula (Siberia, Russia) and the Tuktoyaktuk Peninsula (Northwest Territories, Canada); number of lagoons in brackets. Detailed map of examples of thermokarst lagoons within lagoon systems located in the Lena Delta (b) and at the Northern Head of Richards Island, Mackenzie Delta, Canada (c). Imagery sources: a) service layer credits: Permafrost distribution: (Obu et al., 2019); other layer: Natural Earth; b) Sentinel 2 image from 08.08.2023, natural colors. c) Sentinel 2 image from 16.08.2023 in natural colors.

In summary, there are 152 lagoons in delta regions, accounting for 29% of the total lagoons, occupying 78% of the total lagoon area. Lagoons in delta environments are larger on average (17.8 km²) compared to lagoons outside of delta environments (2.0km²). In contrast, most lagoons (69%) are part of a lagoon system and account for 80% of the total lagoon area. Single lagoons (see example in Figure 2.3) along straight coastlines are fewer and smaller on average (4.2 km²) compared to lagoons in lagoon systems (7.7 km²).

Table 2.2 Number, size, and spatial distribution of thermokarst lagoons, classified by type and connectivity, along the Arctic coast from the Taymyr Peninsula (Siberia) to the Tuktoyaktuk Peninsula (Canada). The deviation between Delta and non-Delta lagoons is based on data published by Tessler et al. (2015).

Category		Lagoon Number	Lagoons Distribution per Category	Lagoon Area km²	Mean Lagoon Area per Category km²	Share of Lagoon Area Category
Total		520	100 %	3457	6.6	100 %
Region	**Canadian Beaufort Sea**	243	47 %	592	2.4	17 %
	Alaska Beaufort Sea	70	13 %	277	4.0	8 %
	Chukchi Sea	57	11 %	1362	23.9	39 %
	East Siberian Sea	46	9 %	353	7.7	10 %
	Laptev Sea	104	20 %	872	8.4	25 %
Type	**Delta ***	152	29 %	2712	17.8	78 %
	non-Delta *	368	71 %	744	2.0	22 %
	Single Lagoon	159	31 %	675	4.2	20 %
	Part of Lagoon System	361	69 %	2782	7.7	80 %
Connectivity Class	**1**	167	32 %	792	4.7	23 %
	2	119	23 %	658	5.5	19 %
	3	117	23 %	989	8.5	29 %
	4	74	14 %	819	11.1	24 %
	5	43	8 %	199	4.6	6 %

* based on Tessler et al. 2015

Additionally, the classification of lagoons into different connectivity classes further highlights variations in distribution. More than half (55%) are very low and low connected lagoons (Class 1 and 2). Highly connected lagoons (Class 4) have the largest average area of 11.1 km². Very highly connected Class 5 lagoons are the fewest and smallest (on average 4.6 km²).

We extracted the length of the coastlines from the pan-Arctic catchment database (ARCADE) and calculated the average lagoon and lake density per 100km coastline length, which was highest for the Canadian Beaufort Sea with 8.3 lagoons and 51.0 lakes per 100km, followed by the Alaskan Beaufort Sea (2.6 and 35.8). Lagoon and lake density were similar for the Chukchi Sea (1.2 and 17.9) and Laptev Sea with (1.3 and 17.0). The East Siberian Sea has the lowest lagoon density (0.9) but a higher lake density (22.6) than Chukchi and Laptev seas.

2.4.2 Lagoon Area Change

Here, we present the results of the lagoon area change analysis from 2000 to 2021. The data were aggregated by region, class, and lagoon type to identify similarities and variations in lagoon connection. The most intense lagoon shrinking and growing was observed for two single Class 1 and Class 2 lagoons located at the Alaska Beaufort Sea (Table 2.3).

Table 2.3. The table summarizes across various Arctic regions and categories including maximum negative (shrinking) and positive (growing) area changes. Mean change represents the average percentage change for individual lagoons, with a standard deviation (SD) indicating variability. Overall change reflects the total change within each region, type, or class.

Category		Initial Lagoon Area (km^2)	Absolute Change (km^2)	Maximum Negative Change (km^2)	Maximum Positive Change (km^2)	Mean Change (%)	SD of Change (%)	Overall Change (%)
Region	**Canadian Beaufort Sea**	584.4	2.9	-0.04	0.05	0.75	0.97	0.49
Region	**Alaska Beaufort Sea**	227.0	3.0	-0.28	0.14	1.23	5.49	1.34
Region	**Chukchi Sea**	563.8	4.7	-0.01	0.05	1.16	1.09	0.84
Region	**East Siberian Sea**	135.7	1.5	-0.19	0.13	1.91	4.65	1.08
Region	**Laptev Sea**	522.4	5.2	-0.04	0.09	0.68	2.02	1.00
Type	**Lena Delta**	421.0	1.7	-0.04	0.04	0.15	1.39	0.39
Type	**Mackenzie Delta**	205.6	0.4	-0.04	0.03	0.54	0.94	0.19
Type	**non-Delta**	1406.6	15.3	-0.28	0.14	1.19	3.08	1.09
Type	**Single Lagoon**	510.6	7.6	-0.28	0.14	1.21	4.51	1.49
Type	**Part of Lagoon System**	1522.6	9.7	-0.04	0.07	0.82	1.25	0.64
Co	**1**	451.2	5.1	-0.18	0.14	1.38	2.73	1.13

2	428.1	2.0	-0.28	0.1	0.45	4.09	0.47
3	520.0	5.9	-0.04	0.06	0.87	1.48	1.14
4	426.9	2.4	-0.01	0.13	0.96	1.71	0.56
5	196.6	1.0	-0.01	0.03	0.65	0.66	0.50

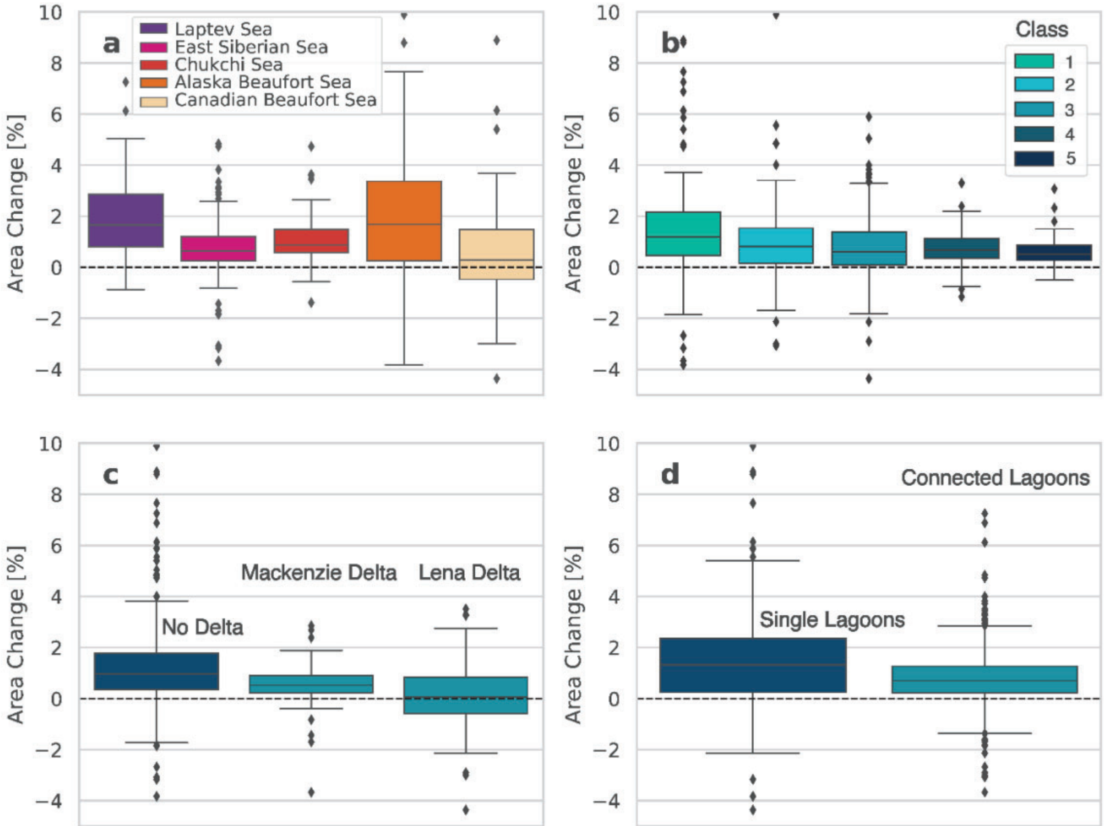

Figure 2.5 Boxplots of normalized lagoon area change trends (% change 2000-2021) per (a) region, (b) class, (c) Delta, and (d) Lagoon System.

2.4.2.1 Regional Changes

The analysis of thermokarst lagoon area changes revealed growth across all five regions (Table 3) with significant differences ($p < 0.05$) in lagoon area trends (Figure S4). Specifically, the lagoon area change at the Laptev Sea differed significantly from the East Siberian, Chukchi, and Alaska Beaufort Seas, while the Canadian Beaufort Sea also showed distinct trends compared to these three regions.

The strong change was observed for the Alaska Beaufort Sea, with a growth of 1.34%, followed by the East Siberian Sea at 1.08%, Laptev Sea at 1.00%, Chukchi Sea at 0.84%, and Canadian Beaufort Sea, which experienced the lowest increase at 0.49%. The Wilcoxon Signed-Rank Test revealed that the East Siberian, Chukchi, and Alaska Beaufort Seas showed significant deviations ($p < 0.05$), while the Laptev and Canadian Beaufort Seas were statistically similar to the entirety of lagoon change. The variance per region, represented by the standard deviation (SD), correlates directly with overall regional change, suggesting that regions with substantial increases also exhibit greater variability among lagoons.

In the category "single lagoons", the highest average increase of 1.91 ± 4.65% was observed for lagoons located at the East Siberian Sea. However, due to their smaller size, these lagoons have a limited impact on the overall regional budget. In contrast, thermokarst lagoons in other regions exhibit mean change rates ranging from 0.68% to 1.23% (Table 2.3). Notably, lagoons along the Alaska Beaufort Sea and East Siberian Sea coasts display the greatest variability in area changes (Figure 2.5a).

Temporal variation in lagoon area shows a general increase over time, with short-term fluctuations of varying degrees (Figure 2.6). However, due to the inherent noise in the input data, making definitive assumptions about these fluctuations is challenging. Nonetheless, the long-term trend of area increase is clearly evident.

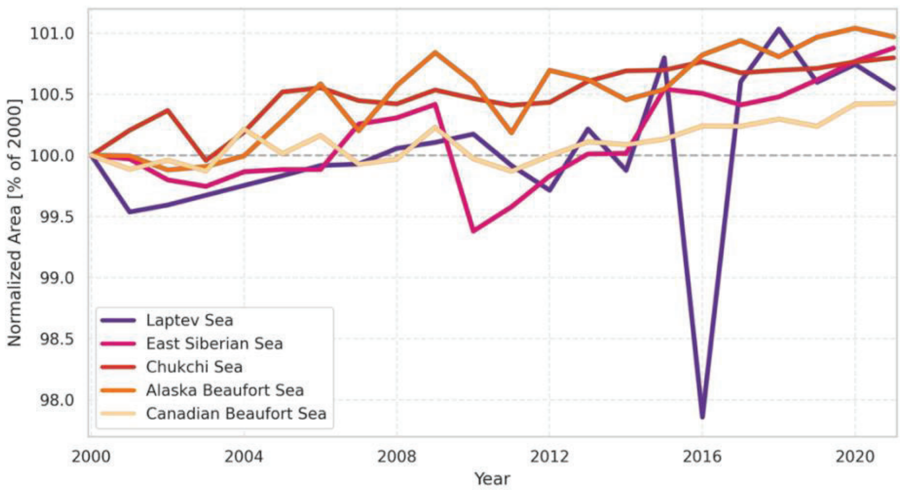

Figure 2.6 Annual lagoon area per region for the years 2000 to 2021, as area anomaly in % in reference to the base year 2000.

2.4.2.2 Lagoon Change by Class

Among lagoon classes, Class 4 differed significantly from Classes 1–3, though these results were markedly weaker ($p > 0.027$; Figure S5) than the regional comparisons ($p >$

1.8×10^{-8}). Analysis of individual lagoon classes revealed marginal significance for Class 1 ($p = 0.037$) and Class 3 ($p = 0.049$), while Class 4 was highly significant ($p < 0.001$). Classes 1 and 3 demonstrate the strongest overall growth (Figure 2.5b), with increases of 1.13% and 1.14%, respectively (Table 2.3). However, individual lagoons within these classes show average growth rates of 1.37 ± 2.73% and 0.87 ± 4.09%, indicating that smaller lagoons are expanding more rapidly. Despite this, the expansion of smaller lagoons does not significantly affect the overall area change.

2.4.2.3 Lagoon Change in River Deltas

Non-deltaic lagoons exhibit stronger growth compared to lagoons within the Lena and Mackenzie Deltas (Figure 2.5c). Non-deltaic lagoons show an overall area increase of 1.09% and a mean increase of 1.19 ± 3.08% (Table 2.3). In contrast, lagoons in the deltas grew significantly slower, with an overall increase of 0.39% in the Lena Delta and 0.19% in the Mackenzie Delta. However, when looking at individual lagoons, those in the Mackenzie Delta grew slightly faster but with less variability, on average, at 0.54 ± 0.94%, compared to the Lena Delta at 0.15 ± 1.39%. This suggests that non-deltaic lagoons are expanding faster, but there are also differences in the growth rates of individual lagoons between both Delta regions.

2.4.2.4 Change in Connected Lagoon Systems

Lagoons that are part of larger connected systems exhibit weaker growth with less variability than non-connected lagoons (Figure 2.5d). The overall area of connected lagoons grew by 0.63% and, on average, by 0.82 ± 1.25% per individual lagoon (Table 2.3). In contrast, the overall area of non-connected lagoons grew by 1.49% and, on average, by 1.21 ± 4.51% per individual lagoon, signifying the much stronger variation of non-connected lagoons.

2.4.2.5 Individual Lagoon Examples

Most lagoons exhibit a slow growth over the observed period. Here, we highlight the case of lagoon ABS_024 (Figure S6) on the Alaska Beaufort Sea coast at Cape Halkett, northeast of Teshekpuk Lake, which lost up to 36.1 % of its area between 2012 and 2016, though it recovered to over 85 % of the maximum area. The drainage of this particular water body was extensively covered by Jones and Arp (2015), and will be discussed in the context of lagoon formation.

More detailed case studies can be found in the supplementary material, highlighting some thermokarst lagoons which deviate from the general trends, showing especially strong increase or decrease in water area.

2.4.3 Comparison between thermokarst lagoon and lake area

The comparison of lake and lagoon sizes across all study regions show revealed that both lakes and lagoons follow a strongly right-skewed size distribution, with the majority of features being relatively small (Figure S8). Although lakes are far more numerous than lagoons, the overall shape of the size distributions is very similar, especially in the Canadian and Alaskan Beaufort Seas. In total, 55% of lagoons are similar in size to nearby lakes, with a maximum deviation of 11%, and 95% differ by less than %. Many of them are located along the Beaufort Sea Coast (Figure S9). Additionally, 40% show moderate size differences of up to 21%, while only 5% exhibit large deviations ranging from 31% to 41%. Most lagoons are smaller than the surrounding coastal lakes, with the exception of the "very large" size only in the category, where “very large”, lagoons tend to be mainly larger. This pattern is particularly prominent along the Beaufort Sea coast (Figure S9).

2.5 Discussion

Our methodological study employed for calculating the distribution, classification, and area estimation of thermokarst lagoons along the Arctic coast provides a comprehensive overview of these unique water bodies across the Arctic coastal regions. To the best of our knowledge, no similar approach concerning thermokarst lagoons has been undertaken. The approach presented by Fraley et al. (2022) aligns largely with our classification. Four out of five Arctic lagoons examined in both studies were classified as Class 1 or “intermittent connection”, which both emphasize the temporary nature of their limited connection.

2.5.1 Geographical Distribution of Thermokarst Lagoons

The geographical distribution of thermokarst lagoons shows strong regional variation, primarily shaped by the interplay of coastal erosion dynamics, the presence of thermokarst lakes, and local geomorphological conditions. Lagoon densities are highest along the Beaufort Sea coast, a region characterized by extensive lake-rich lowlands and rapid coastal erosion - reaching up to 48.8 meters per year in extreme events (2007–2008; Irrgang et al., 2022) and averaging around 1.15 to 1.12 meters per year for the Alaska and Canadian Beaufort Seas (Lantuit et al., 2012). These high erosion rates, combined with widespread ground-ice and low-lying terrain, promote frequent inland migration of the coastline, increasing the likelihood of coastal lakes being breached by the sea and transformed into lagoons. In contrast, the Chukchi Sea region, with significantly lower erosion rates - averaging just 0.20 to 0.49 meters per year (Irrgang et al., 2022; Lantuit et al., 2012) - shows much lower lagoon density, suggesting that slower coastal retreat reduces the frequency of lagoon formation.

The distribution of lagoons also strongly correlates with areas of high lake thermokarst activity. Based on regional thermokarst coverage data (Olefeldt et al., 2016), 90% of lagoons are found in areas where lake thermokarst affects 60–100% of the landscape, while only 5% occur in regions with low thermokarst presence (1–30%) (Figure S2). This highlights the critical role of pre-existing thermokarst lakes in enabling lagoon development. However, this relationship is not uniform across the Arctic. For example, the western East Siberian Sea coast, despite high lake thermokarst coverage, shows a surprisingly low density of lagoons. This could be caused by elevation differences between former lake basins and the sea, which, if larger than spring tide heights, inhibit effective flooding and thus prevent lagoon formation.

In addition to spatial patterns, size comparisons further support the close link between lakes and lagoons. Across all regions, both features exhibit strongly right-skewed size distributions dominated by small waterbodies (Figure S7). This similarity indicates that lagoon size is closely tied to the size of the original lakes, with most lagoons being slightly smaller than nearby lakes. The exception is the "very large" category, where lagoons often exceed lake sizes (Figure S8) - potentially due to local geomorphic processes or post-formation changes such the connection of neighboring lagoon and the formation of larger lagoon systems.

These patterns suggest that lagoon formation is primarily controlled by the distribution and size of thermokarst lakes, while coastal erosion modulates the timing and frequency of their transformation into lagoons.

We connected the mapped thermokarst lagoons with ground ice and organic carbon content data from the Arctic Coastal Database (Lantuit et al., 2020). The findings reveal that 38% of all mapped thermokarst lagoons are located in areas with low ground ice content (0-20%). The majority - about 53% - are found in regions with medium ground ice content (21-50%). Only 9% of thermokarst lagoons are situated in areas with high ground ice content (>50%), primarily located along the Alaska Beaufort Sea and the US Chukchi Sea.

Additionally, nearly 80% of the lagoons are located in areas where the organic carbon content is low (0-2%) to medium (2-5%). At thermokarst-affected coasts, permafrost thaw has already advanced significantly, and the stored organic matter has been decomposed over a long period. Furthermore, mixing with mineral-rich, OC-poor marine sediments could lead to a reduction in OC content in thermokarst lagoon sediments. However, field data suggests high variability in OC content between lagoons (Jenrich et al., 2024b, 2021; unpublished data; Schirrmeister et al., 2018). Young, less connected lagoons tend to retain terrestrial OC-rich sediment for longer periods, while more open lagoons experience faster sediment export due to stronger currents transporting material into the open ocean. About 21% of thermokarst lagoons are located in regions with high OC content (> 5%). In these lagoons, present mostly along the coasts of the Beaufort and Chukchi seas, the potential for elevated GHG production is particularly high.

Regional Distribution of Lagoon Classes

Our classification of lagoons based on connectivity revealed important trends. More than half of the lagoons (55%) were classified as nearly-closed (Class 1) and limited open (Class 2), indicating very low connectivity. These lagoons are critical in understanding the initial stages of the lake-to-sea transition and their potential for organic carbon degradation. Highly connected lagoons (Class 4) had the largest average area (11.1 km²), highlighting the advanced stages of the transition process. Interestingly, Class 5 lagoons, representing the most advanced stage, were the fewest and smallest (average 4.6 km²), suggesting that as lagoons become more connected to the sea, their overall area may decrease due to factors such as increased erosion and sediment redistribution.

When normalized to account for the total number of lagoons in each region, the distribution of lower-connected lagoons (Class 1 to Class 3) appears more consistent across different regions (Figure S1 a-c). In contrast, the more open and highly connected lagoons (Class 4 and Class 5) are primarily concentrated in deltas and areas with high thermokarst activity, particularly along the Beaufort Sea and Laptev Sea coasts (Figure S1 d-e). In these lowland regions, which are highly shaped by thermokarst processes, the combination of surface subsidence, sea-level rise and elevated erosion rates are drivers for the rapid drowning of thermokarst lakes (Creel et al., 2024). This process results in large lagoon systems (Figure 2.3), which account for more than two-thirds of the mapped lagoons and take up 80% of the total lagoon area.

These patterns highlight the interplay between geomorphological setting, lagoon connectivity, and sediment composition, underscoring the potential for substantial spatial variability in carbon cycling and greenhouse gas emissions across Arctic thermokarst lagoons.

2.5.2 Patterns of Thermokarst Lagoon Area Change

As thermokarst lagoon area is likely closely linked to coastal erosion rates, patterns of thermokarst lagoon area change might correlate with those of Arctic coastal erosion rates. Along the Alaskan Beaufort Sea coast, coastal erosion rates are especially high (Irrgang et al., 2022). The high variability and strong growth found in the thermokarst lagoons of this region may be especially influenced by coastal erosion. In contrast, the East Siberian Sea, Chukchi Sea, and Laptev Sea generally exhibit slightly lower area growth. The stability of thermokarst lagoons along the Canadian Beaufort Sea stands in contrast to the erosivity along this coast. The overall trend of coastal erosion rather than progradation does not explain the observed stability, which may be coupled to other environmental factors. Importantly, many of these lagoons are part of larger lagoon systems, which can mitigate the expected impacts of coastal erosion due to reduced wave energy in these more sheltered environments. Overall, the analysis of the influence of coastal erosion would benefit greatly from a more in-depth quantitative assessment, which could be conducted with the help of the presented dataset.

At class level, the lack of a clear trend of change rates based on connectivity, may be due to the highly variable distribution of lagoon classes along Arctic coasts, especially for classes 1-3. Meanwhile, the location of many Class 4 and 5 lagoons in delta environments could point towards lower change in these delta environments. Nevertheless, the argument of subjectivity with classification based on geomorphology is one that should not be ignored and may have a slight influence on the lack of a clear trend. The inherent complexity of thermokarst lagoons indicates that while they can be classified based on their connectivity to the sea, each lagoon may still display different characteristics such as sediment grain size, shoreline elevation, or ground ice content of the surrounding permafrost, which influences area changes. The implication here is that river delta and lagoon system environments are more influential on lagoon area change than classification.

Lagoons within systems may experience less change due to reduced wave energy, as the interconnected lagoons act as natural buffers. In particular, subsequent lagoons in these systems are shielded from wave action by the preceding ones, functioning like natural breakwaters. This is comparable to how Tuktoyaktuk Island, though actively eroding, serves as a protective barrier for the coastal Hamlet of Tuktoyaktuk located further inland on the Tuktoyaktuk Peninsula (Whalen et al., 2022). Exemplary own field observations during a very stormy boat ride from Reindeer Island (located near the outer Mackenzie Delta) back to Inuvik after finishing field work revealed very low wave activity in this specific lagoon system. These observations from 2021 are supported by Hill and Solomon (1999), who report low wave frequency in the system, with the presence of eolian deposits on lagoon shorelines indicating low erosional energy.

Overall, Arctic wave energy is projected to increase (Malito et al., 2022), driven by factors such as a longer open-water season (Stroeve et al., 2012) and higher storm intensity (Lim et al., 2020). This raises the question of how thermokarst lagoons will be affected. Malito et al. (2022) modelled wave energy along the Alaskan Beaufort Sea, finding that shelf geometry plays a crucial role - the steeper the shelf, the higher the wave energy reaching the coast. Generally, the shelves of the Beaufort, Chukchi, Laptev, and East Siberian seas are characterized by low relief (Harris et al., 2014) and tend to be less impacted by high wave energy (Malito et al., 2022). Previous studies at Reindeer Island and Bykovsky Peninsula (Laptev Sea) have shown that the depth of Class 3 to Class 5 lagoons ranges from 2 to 2.5 m (Schirrmeister et al., 2018; Solomon et al., 2000). These shallow lagoons, combined with low-relief shelves, may be less vulnerable to coastal erosion from breaking waves than steeper or more exposed coastlines. While this may not represent all pan-Arctic lagoons, we hypothesize that, although wave energy is an important factor, it may play a lesser role in lagoon growth compared to other drivers – particularly thermal erosion, which occurs on a much larger scale along permafrost coasts (Lim et al., 2020; Malito et al., 2022).

Climate change-induced sea-level rise could drive lagoon growth and formation. Although this rise occurs at a rate of only millimeters per year (Malito et al., 2022), rising sea levels in Arctic lowlands – combined with factors such as increased storm intensity (Lim et al., 2020) – could flood coastal thermokarst lakes if the elevation difference between the lake and the sea is small enough. Over time, thermokarst lagoons may progress through different connectivity stages, from Class 1 to Class 5, creating a complex, evolving shoreline. These lagoons are gradually eroded over long timescales, eventually contributing to shoreline smoothing (Ruz et al., 1992).These lagoons are gradually eroded over long timescales, eventually contributing to shoreline smoothing. The potentially cyclical nature of thermokarst lagoons, along with the influence of sea-level rise, remains understudied, highlighting an important field for future research.

Individual lagoons that exhibit exceptional area changes may be influenced by local environmental processes and are not necessarily connected to global trends. However, lagoons such as ABS_024 (Figure S2.7), which formed after a major lake drainage event in July 2014 (Jones and Arp, 2015), may represent the earliest stage in the lake-to-lagoon transition.

When drainage channels form due to the thermo-erosion of ice wedges (Fortier et al., 2007; Nicu et al., 2022) thermokarst lakes can drain into the sea, causing water levels to equalize with sea level. These connecting channels are commonly observed in many Class 1 and Class 2 lagoons (e.g., *Polar Fox Lagoon SLS_003* and other lagoons listed in Table 1) and may have formed through thermo-erosion (Angelopoulos et al., 2020b). Further thermo-erosion could potentially widen these channels, though this process has not yet been studied specifically in the context of thermokarst lagoons.

Coastal erosion can also erode the barrier between the lakes or drained lake basins and the sea – particularly in lowland areas (Mackay 1988; Hinkel et al., 2007). This appears to be the case for *ABS_024*, where surrounding elevations are less than 1 meter, according to ArcticDEM data (Porter et al., 2018). As erosion breaches the barrier, a connection to the sea is established, allowing seawater intrusion.

As reported, *ABS_024* expanded its surface area to nearly match its pre-drainage maximum lake size, likely driven by enhanced seawater inflow. We propose that *ABS_024* serves as a prime example of an early-stage thermokarst lagoon formation.

2.5.3 Implications

Even though the majority of thermokarst lagoons are located in areas where the organic carbon content is low, most (55 %) of the mapped thermokarst lagoons are young, less connected lagoons (Class 1 and 2), which may have higher GHG emissions (Figure 2.7). Incubation and microbiology studies have revealed that under the occurring brackish conditions, methane production is highest in these first stages of land-sea transition (Jenrich et al., 2024d, b; Yang et al., 2023). More connected thermokarst lagoons (3, 4) gradually receive more seawater and experience more sediment exchange with the sea, causing a decrease in organic matter availability and a shift toward marine microbial communities (Jenrich et al., 2024b). In this course CH_4 production decreases drastically. Fully connected, open lagoons (5) show more marine characteristics. GHG production shifts from a CH_4 ratio of 1:1 in low connected lagoons to pure CO_2 production (Figure 2.7 and Jenrich et al., 2024a, 2024b).

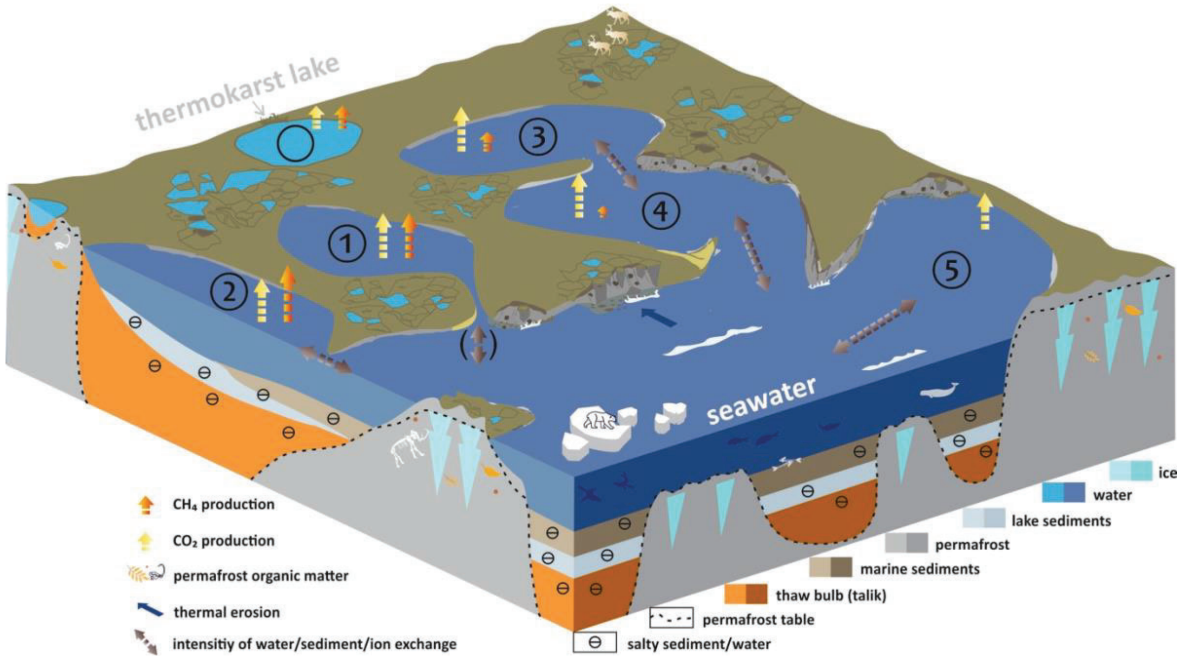

Figure 2.7. Schematic representation of the transformation of thermokarst lakes into lagoons and their progression towards fully marine systems due to permafrost thaw and coastal erosion in the Arctic. The diagram illustrates different stages of lagoon connectivity with the sea (1-5), highlighting methane (CH_4) and carbon dioxide (CO_2) production (red and yellow arrows) as a result of the breakdown of permafrost organic matter. Younger, less connected lagoons show higher CH_4 production, while more marine-influenced systems have increased CO_2 production. Subsurface features such as thaw bulbs (talik) and the permafrost table are depicted, along with sediment, water, and ion exchange processes (black-grey arrows). The ongoing thermal erosion and seawater intrusion contribute to the thawing of permafrost and the migration of Arctic coastlines. This process may result in increased greenhouse gas emissions from Arctic coastal systems. Figure modified after Romanovskii et al. (2000), information on CO_2 and CH_4 production rates is based on Jenrich et al., 2024a and Jenrich et al., 2024b.

Our comprehensive dataset provides a robust foundation for future research on the biogeochemical processes within Arctic thermokarst lagoons. The detailed classification and area calculations provide a basis for extrapolation of more detailed local studies and enable more precise assessments of organic carbon degradation and nitrogen cycling – both of which are critical for understanding the broader implications of permafrost thaw at the land-ocean frontier with climate change. Beyond openness, local factors – particularly freshwater (Harris et al., 2017; McClelland et al., 2012), sediment (Chalov et al., 2023; Gordeev, 2006; Vonk et al., 2015b), and organic matter inputs (Jung et al., 2022; Tank et al., 2012; Zhang et al., 2024) in deltaic and estuarine environments - shape the hydrochemistry and biogeochemical properties of these lagoons, highlighting their variability and complexity.

There is also progress in other related fields covering Arctic land-to-sea frontier environments, such as studies assessing the specific ecology of Arctic lagoons (Dunton et al., 2012; Fraley et al., 2021; Laske et al., 2024), the carbon and nitrogen pools of Arctic delta deposits (Fuchs et al., submitted; Vonk et al., 2016), or modelling the morphodynamics of Arctic river deltas where many thermokarst lagoons were found (Chan et al., 2023; Piliouras and Rowland, 2020).

While our analysis provides insight into the modern (~20-year) variability of lagoon area, the extent to which these changes fall within long-term natural variability remains uncertain. Over longer timescales, Holocene climate fluctuations and postglacial transgression have likely influenced lagoon formation and change rates. (Romanovskii et al., 2000; Ruz et al., 1992),, potentially leading to different patterns of variability compared to today. Future research incorporating paleoenvironmental reconstructions and sea-level change modelling could help determine whether the observed trends align with past lagoon evolution or if recent changes reflect a shift beyond natural variability.

Further research should focus actual rates of transition from thermokarst lake to lagoon and the associated environmental impacts. A special focus should be placed on thermokarst lagoon systems, as they cover large areas with likely a high portion of organic carbon and nitrogen included (Strauss et al., 2025), but have been scarcely studied so far. Additionally, expanding the analysis to include the Kara and Barents Sea coasts can help identify broader patterns and regional differences, enhancing our understanding of these dynamic ecosystems.

2.6 Conclusion

This study provides the first comprehensive pan-Arctic assessment of thermokarst lagoons, including an updated analysis of their distribution and size, the introduction of a new classification approach, and the first 20-year lagoon area change analysis. Our refined mapping revealed a detailed dataset of lagoon distribution and size, uncovering significant regional patterns in lagoon density – highest along the Beaufort Sea coast and lower across the Laptev, Chukchi, and East Siberian Sea coasts.

Categorizing thermokarst lagoons by their degree of openness provides new insights into the evolution of these dynamic coastal systems. This framework supports future research on how biogeochemical, hydrochemical, and ecological processes change throughout the permafrost land-to-sea transition. Beyond openness, local factors – particularly freshwater, sediment, and organic matter inputs in deltaic and estuarine environments – shape the hydrochemistry and biogeochemical properties of these lagoons, highlighting their variability and complexity.

Our time series analysis of annual surface water area reveals both overall lagoon area expansion and marked regional differences. The greatest variability emerged along the Alaskan Beaufort Sea and East Siberian Sea coasts. Local processes like drainage events and thermal erosion appear to drive rapid changes. Coastal erosion, intensified by longer ice-free seasons, increasing sea water temperatures and increased storm intensity is hypothesized to be a key driver of lagoon formation, while rising sea levels may further amplify the creation of new lagoons in Arctic lowlands.

At a broader scale, this study highlights how Arctic climate change is reshaping the Arctic coastline, fostering the formation of thermokarst lagoons and therefore potentially altering local hydrology and impacting ecosystems. These lagoons serve as critical transition zones between terrestrial and marine environments, playing a unique role in permafrost carbon cycling. Notably, 55% of the mapped lagoons are young and low-connected lagoons, where OC-rich terrestrial sediments get trapped longer compared to more open, connected lagoons, resulting in a high potential for increased GHG production in the first stages of land-sea-transition. Understanding the distribution and evolution of thermokarst lagoons is essential for predicting future landscape transformations and their global climate implications, making this research a crucial step toward better understanding the Arctic's response to climate change.

2.7 Acknowledgements

Ideas for this research were initially developed in the German Federal Ministry of Education and Research (BMBF) research projects KoPF (Carbon in Permafrost; #03F0764B), KoPF-Synthesis (03F 0834B), and CACOON (Changing Arctic Carbon cycle in the Coastal Ocean Near-shore; #03F0806A). We thank Sebastian Laboor for helping to improve Figure 2.1.

2.8 Supplementary Material

Table S2.1 Detailed thermokarst lagoon classification based on connectivity to the sea with definitions for thermokarst lagoon classes, labels, and examples for single lagoons and lagoons located in systems. Lagoon IDs for single and system lagoons: SLS_003 and CBS_077 (Class 1), ABS_066 and CBS_024 (Class 2), CBS_220 and CBS_081 (Class 3), CBS_060 and CBS_034 (Class 4), CBS_020 and CBS_196 (Class 5). Source imagery: True-color Sentinel-2 imagery with acquisition dates from 2023-07-01 to 2023-08-30.

Class	Connectivity	Label	Single Lagoon	Lagoon System
1	Very low - Exchange strongly limited due to long and narrow channel, or subsequent lagoon with very limited exchange. Temporary lake characteristics are possible.	Lagoon, nearly-closed (L_{nc})	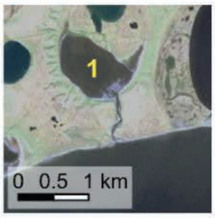	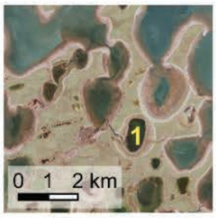
2	Low - Exchange very limited due to very small opening or narrow channel or subsequent lagoon which is less connected to primary lagoon due to small channel or high distance.	Lagoon, limited open (L_{lo})	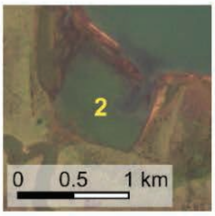	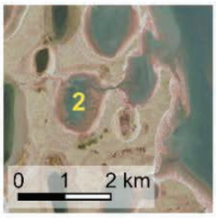
3	Medium - Exchange limited either temporally or spatially due to barrier islands and sand spits or subsequent lagoon which is well connected to the primary lagoon.	Lagoon, semi-open (L_{so})	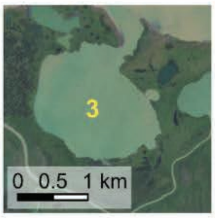	
4	High - Barrier islands or sand spits only slightly block exchange with the sea or subsequent lagoon which is very well connected to the primary lagoon.	Lagoon, mostly open (L_{mo})		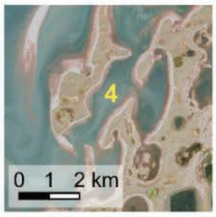
5	Very high - Lagoon in direct exchange with the sea.	Lagoon, always open (L_{ao})		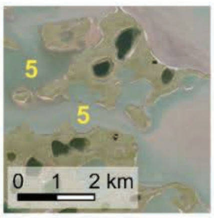

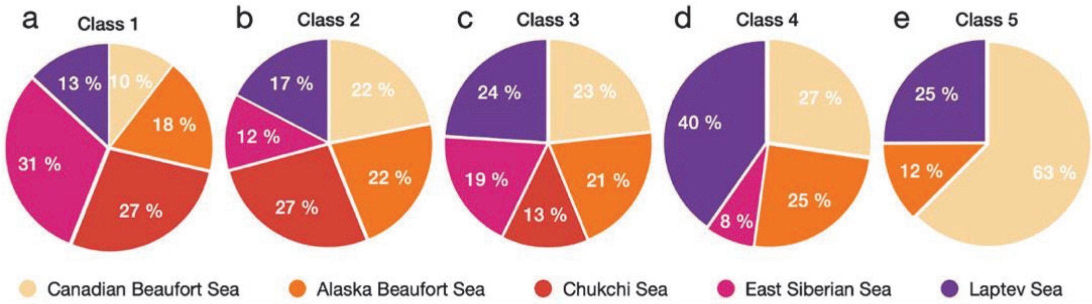

Figure S2.1 Regional Distribution of Lagoons by Classes normalized to the total number of lagoons per region.

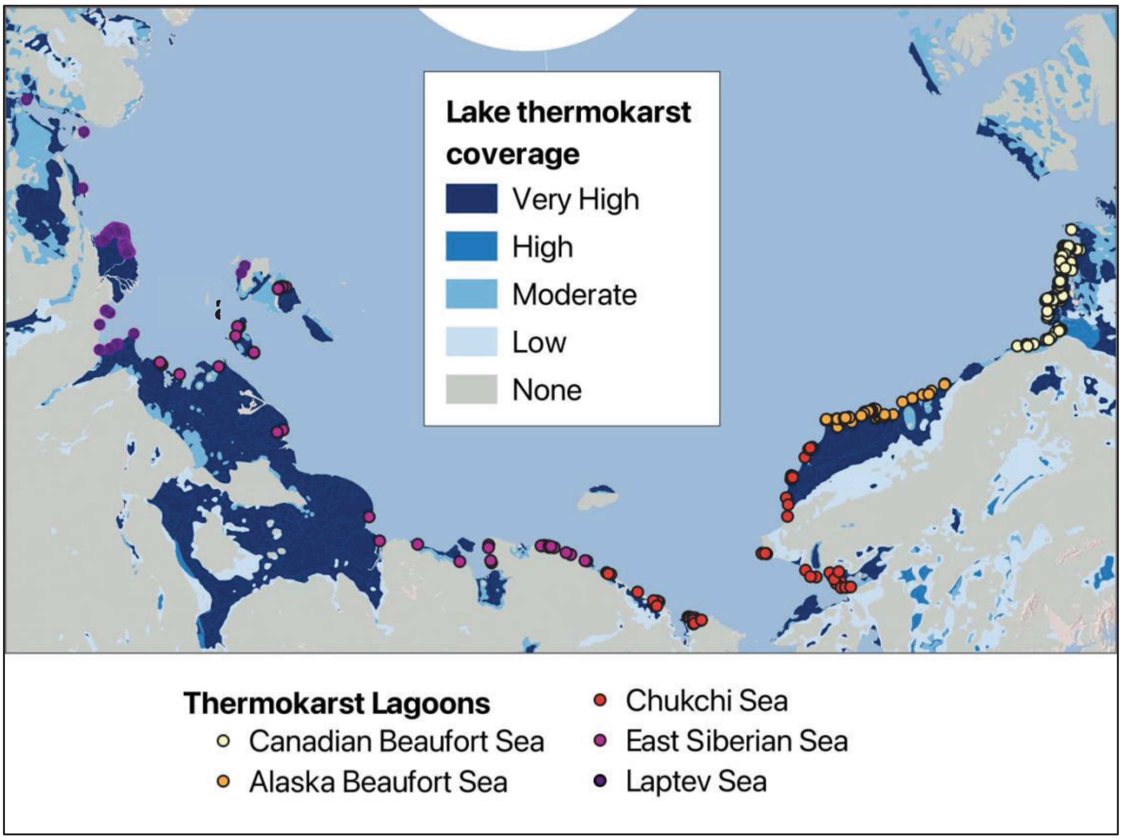

Figure S2.2 Thermokarst lagoons in relation to the regional lake thermokarst coverage. Modified after Olefeldt et al., 2016.

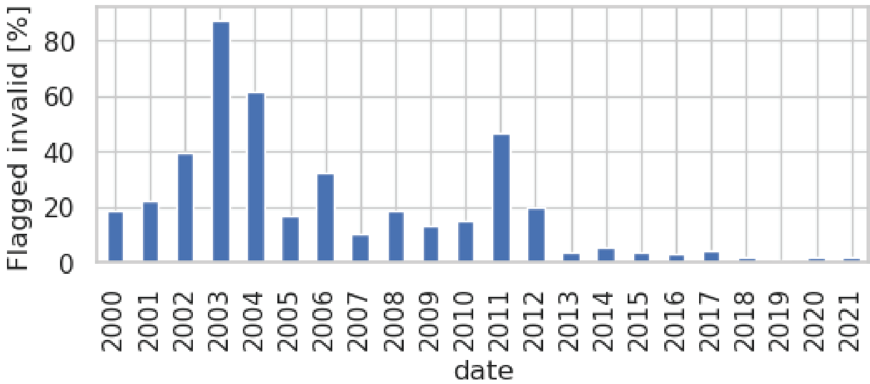

Figure S2.3 Percentage of data points flagged as invalid per year due to exceeding the NoData threshold of 2%. The fraction of flagged and removed data was highest between 2000 and 2012, peaking at 87.4% in 2003, and decreases significantly after 2013. This reflects improvements in data availability and quality over time.

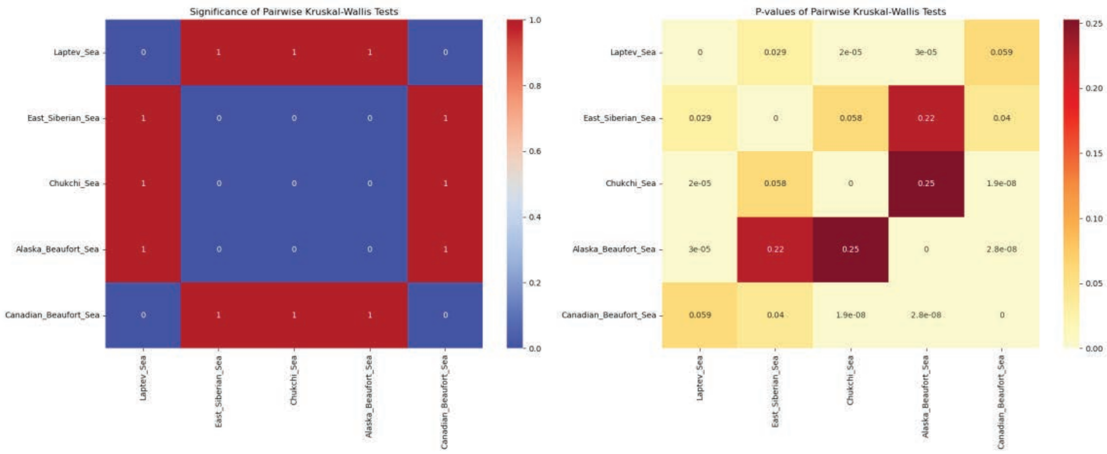

Figure S2.4. Results of the Kruskal-Wallis test for regional pairwise comparisons between lagoons of different regions. Lagoon area change rates are significant if p < 0.05.

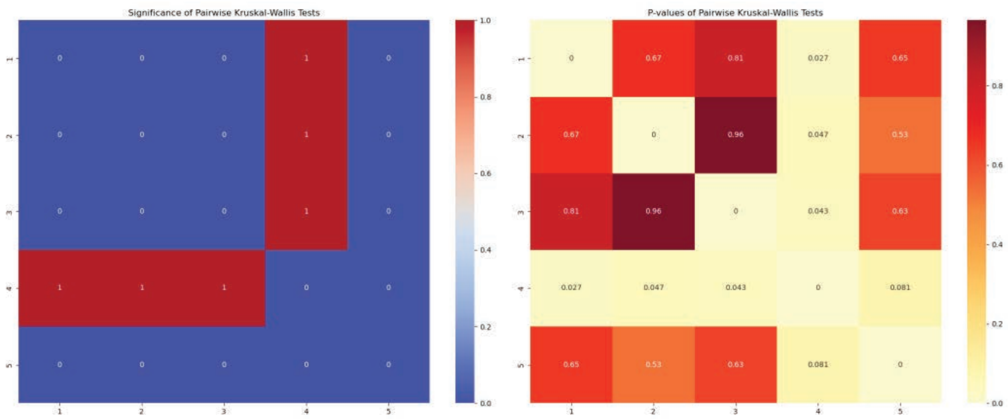

Figure S2.5. Results of the Kruskal-Wallis test for pairwise comparisons between lagoons of different connectivity classes. Lagoon area change rates are significant if p < 0.05.

Table S2.2. Results of the Wilcoxon Signed-Rank Test to assess whether lagoon area trends in individual regions or connectivity classes differed significantly ($p < 0.05$) from overall lagoon population.

Category		p-value	Significance
Region	Laptev_Sea	0.9479	Not Significant
	East_Siberian_Sea	0.0166	Significant
	Chukchi_Sea	0.0000	Significant
	Alaska_Beaufort_Sea	0.0000	Significant
	Canadian_Beaufort_Sea	0.6998	Not Significant
Class	1	0.0370	Not Significant
	2	0.0166	Significant
	3	0.0634	Significant
	4	0.0001	Significant
	5	0.5299	Not Significant

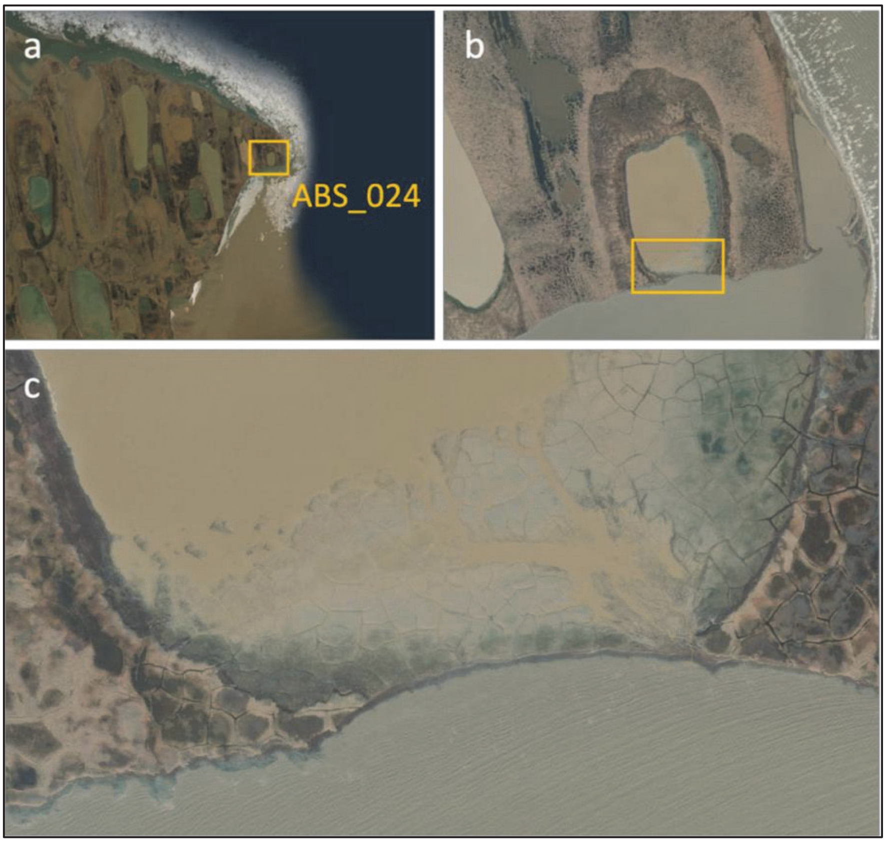

Figure S2.6. Lagoon ABS_024 located at Alaska Beaufort Sea (panel a and b; - 70.79664°N, -152.23941°W) formed on 05 July 2014 due to drainage towards the sea. After the event, the connecting channel was 9 m wide, 2 m deep, and 70 m long (Jones and Arp, 2015). c: Close-up of the current sea-connection. ABS_024 is a prime example of early-stage lagoon formation with high variations in area due to regular shrinking and expansion events. Data Sources: a: ESA-CCI Land-Ocean Map (provided by DLR), World Imagery (ESRI): Esri, Maxar, Earthstar Geographics, and the GIS User Community; b, c: Arctic Landscape Explorer (Nitze et al., 2024)

Supplementary Text S1: Additional Information to Section 3.2.5 "Individual Lagoon Examples"

Shrinking Lagoons

Although most lagoons were growing in size, some were affected by a loss of surface water area. Two of the most significant changes (lowest trend p-value) were observed for the young lagoons CBS_213 and CBS_214, which are located on Reindeer Island in the CBS (Figure 2). The lagoons were affected by area loss of up to 2.5 % and 3.5 %, respectively. Both lagoons are connected, and were seemingly both affected by some drainage mechanisms similar to thermokarst lakes (Grosse et al., 2013; Jones et al., 2022).

Growing Lagoons

Lagoon growth was more widespread than shrinkage, though still some specific lagoons showed a much stronger expansion. For example, lagoon WCS_020 (68.145°N, 177.125°W), located west of Vankarem, a settlement in the Russian District of Chukotka Autonomous Okrug at the West Chukchi Sea coast, showed gradually increasing water area by around 2.9 % or 0.88 km^2. Both lagoons, ABS_031 (70.849°N, 152.454°W) and ABS_045 (70.874°N, 153.666°W) are located at the Alaskan Beaufort Sea close to Drew Point north of Teshekpuk Lake, which is one of the fastest eroding Arctic coasts. Figure S2.7 exemplarily shows the strong growth of ABS_045 in more detail, which may be due to variations in water level rather than lagoon area expansion.

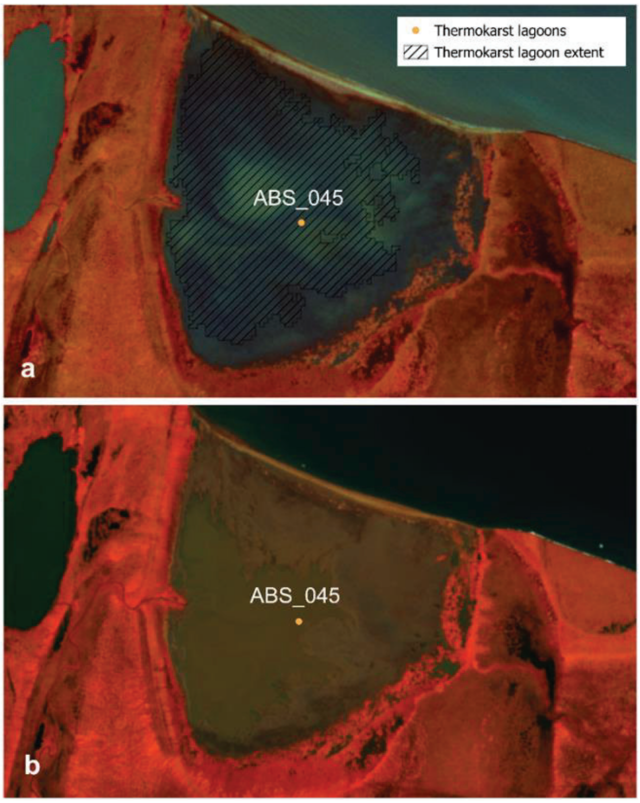

Figure S2.7. Exemplary comparison of thermokarst lagoon water levels in different years with the thermokarst lagoon extent represented by the water mask created from the GSW dataset (Pekel et al., 2016) to show how changing water levels may impact the extent of the water mask with data from 1984-2021. Source imagery: (a) False-color Sentinel 2 imagery from 2023-09-14 (b) False-color Sentinel-2 imagery from 2020-07-08.

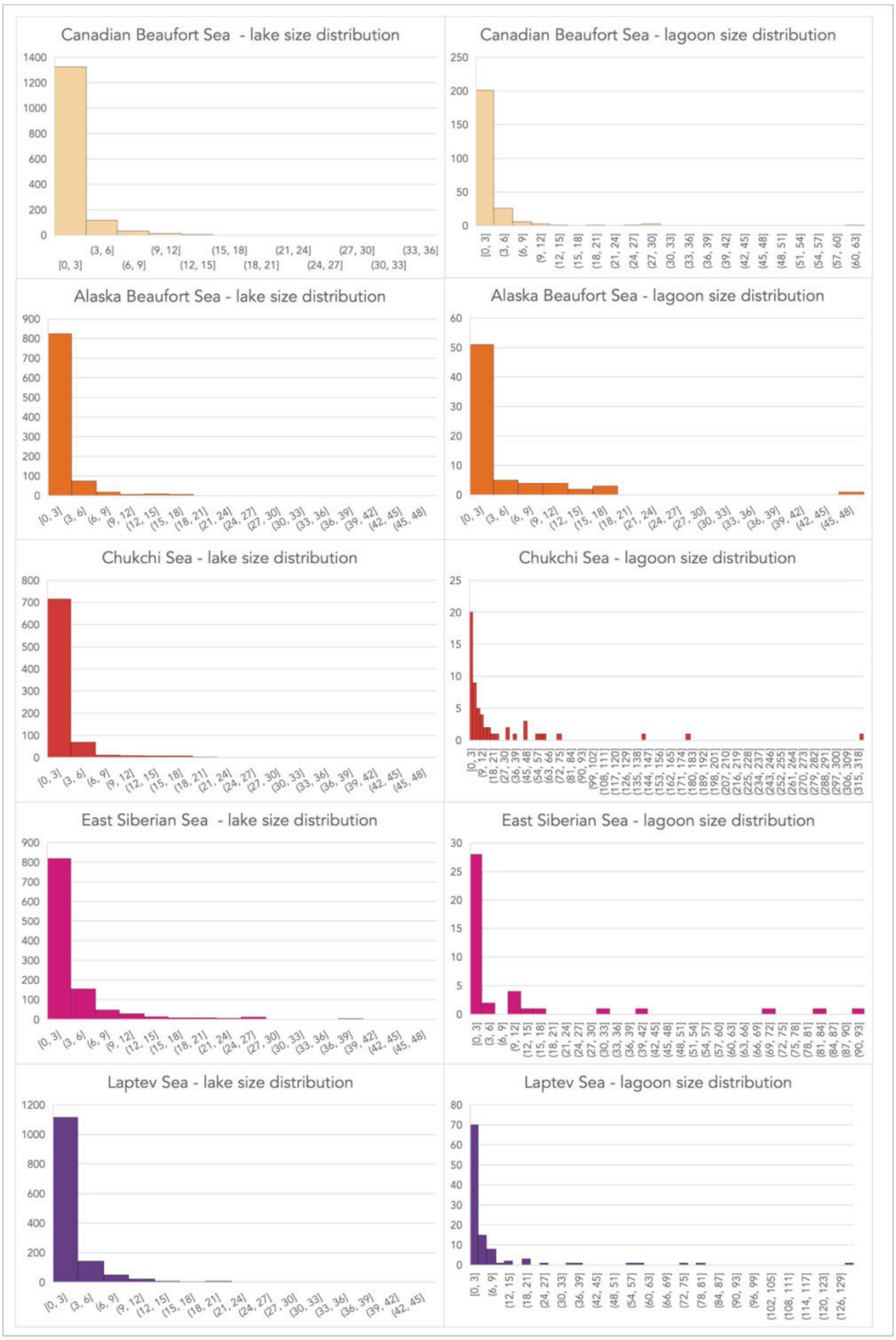

Figure S2.8. Size distribution of lakes (left panel) and lagoons (right panel) by region. The x-axis shows surface area classes (km^2), and the y-axis indicates the number of lakes or lagoons per class. All distributions are strongly right-skewed, highlighting that the majority of both lakes and lagoons are small in size. Despite differences in absolute numbers, the shape of the distributions is similar across regions, suggesting a relationship between lake and lagoon sizes.

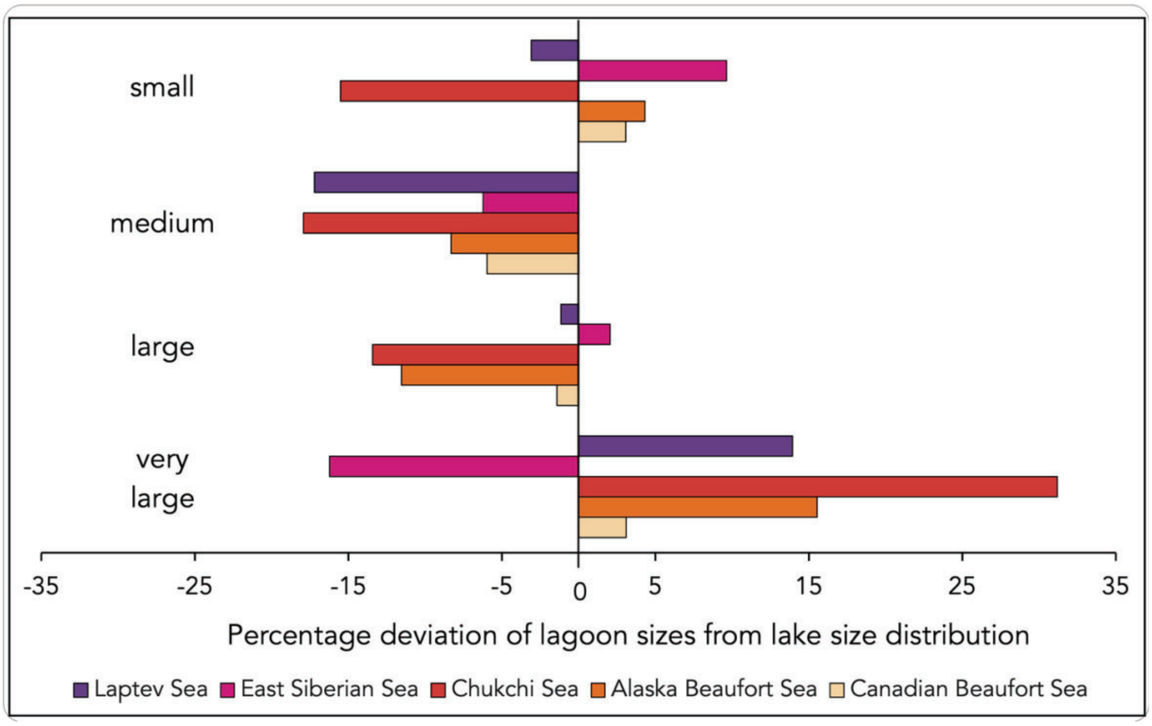

Figure S2.9. Percentage deviation of lagoon size relative to the size of coastal lakes located within 30km of the coast. Categories are based on quartiles: small (0.1–<0.8 km^2), medium (0.8–<1.2 km^2), large (1.2–<2.4 km^2), and very large (≥2.4 km^2). In the medium category, lagoons in all regions are smaller than the surrounding lakes.

3

Greenhouse Gas Production and Microbial Response During the Transition from Terrestrial Permafrost to a Marine Environment

Maren Jenrich[1,2], Michael Angelopoulos[1], Susanne Liebner[3,4], Claire Treat[1,2], Christian Knoblauch[5,6], Sizhong Yang[3], Guido Grosse[1,2], Fiona Giebeler[1,2], Loeka Jongejans[1], Mikhail Grigoriev[7] and Jens Strauss[1]

[1] Alfred Wegener Institute Helmholtz Centre for Polar and Marine Research, Permafrost Research Section, Potsdam, Germany

[2] University of Potsdam, Institute of Geosciences, Potsdam, Germany

[3] GFZ German Research Centre for Geosciences, Section Geomicrobiology, Potsdam, Germany

[4] University of Potsdam, Institute of Biochemistry and Biology, Potsdam, Germany

[5] Universität Hamburg, Institute of Soil Sciences, Faculty of Mathematics, Informatics and Natural Sciences, Germany

[6] Universität Hamburg, Center for Earth System Research and Sustainability, Germany

[7] Melnikov Permafrost Institute, Russian Academy of Sciences, Siberian Branch, Yakutsk, Russia

This chapter is published in: *Permafrost and Periglacial Processes*; Special Issue: Land-Ocean Interactions in Polar Regions: Landforming Processes, and Fluxes of Energy and Matter

DOI: https://doi.org/10.1002/ppp.2251, 2024

Abstract Arctic permafrost coasts, affected by rising sea levels and increasing coastal erosion in a warming climate, undergo significant changes. Simulating how permafrost is impacted by inundation with fresh, brackish and marine water enhances our understanding of permafrost carbon stock responses to increasingly marine conditions. We investigated CO_2 and CH_4 production during key transitions in a coastal thermokarst landscape on Bykovsky Peninsula, Siberia, assessing short- and long-term microbial responses to varying salinities in anaerobic one-year incubation experiments. Initially, CO_2 production from saltwater-inundated permafrost was low due to the low abundance of salt-tolerant microbial communities. Over the long term, after simulated lagoon formation and the growth of sulfate-reducing bacteria, CO_2 production surpassed the terrestrial permafrost by 8 times. CO_2 and CH_4 production were lowest under marine conditions, suggesting incomplete adaptation of microbes. Rapid ecosystem changes stress microbial communities, with greenhouse gas production highest under near-natural conditions. With an increase in lake drainage events and rising sea levels, thermokarst lagoon distribution on Arctic coasts will escalate, resulting in a further increase of carbon mineralization and CO_2 release. With

this study, we provide first estimations on greenhouse gas production during the transition from terrestrial to submarine conditions in permafrost affected aquatic systems.

3.1. Introduction

Approximately 15 % of the land area of the Northern Hemisphere (Obu, 2021), and about 80 % of the Arctic Beaufort, Chukchi, East Siberian, Laptev, and Kara Seas (Overduin et al., 2019), are underlain by permafrost. The terrestrial permafrost area is estimated to contain a reservoir of 1700 petagrams (Pg; 10^{15} grams) of organic carbon (OC) deposited in frozen soil, the active layer (Lindgren et al., 2018; Miner et al., 2022; Permafrost and Climate Change: Carbon Cycle Feedbacks From the Warming Arctic, 2024), and onshore taliks (Strauss et al., 2021; Walter Anthony et al., 2014), in addition to 2800 Pg of OC below the seafloor (Miesner et al., 2023). The Arctic is warming nearly four times faster than the global average (Rantanen et al., 2022), and so the terrestrial permafrost is thawing. Subsea permafrost is already in thermal disequilibrium because of the overlying seawater, but warming shelf waters and a shrinking sea ice extent can increase the thawing rate (Wilkenskjeld et al., 2022). Permafrost thawing unlocks ancient organic matter (OM), which can be decomposed by microorganisms into greenhouse gases (GHG) such as carbon dioxide (CO_2) and methane (CH_4), further fueling the warming of the Earth's climate. During winter, the terrestrial permafrost region loses 1.66 Pg OC in the form of CO_2 from Arctic and boreal soils (Natali et al., 2019). This is higher than the carbon uptake during the growing season in summer, converting the terrestrial Arctic into a carbon source (Miner et al., 2022). In contrast, subsea permafrost thaw is more resistant to climate warming and OM decomposition rates are lower, in part because the OM has already been exposed to multiple marine transgression and regression cycles (Miesner et al., 2023).

The thaw of ice-rich permafrost is causing substantial land surface subsidence. This process is called thermokarst and leads to the formation of thermokarst features such as ponds, lakes, drained lake basins, and lagoons. Thermokarst lagoons form when thermokarst lakes or basins with bottom elevations below the sea level are breached along Arctic coasts by the sea due to coastal erosion (Günther et al., 2013; Jones et al., 2018; Nielsen et al., 2022), sea-level rise (Guimond et al., 2021; Nerem et al., 2018; Proshutinsky et al., 2001; Watson et al., 2015) or become connected to the sea by their drainage channels (Jenrich et al., 2021b). Because of continued high rates of coastal erosion along ice-rich permafrost coasts (Irrgang et al., 2022; Jones et al., 2018), thermokarst lagoons are transitional and dynamic coastal landforms that combine traits of both terrestrial and over time increasingly marine systems (Harris et al., 2017; Jenrich et al., 2021b; Kjerfve, 1994; Tagliapietra et al., 2009; Yang et al., 2023). The connectivity with the sea and thus water and sediment exchange are dependent on the size of the inlet and the ice dynamics of the inlet. The degree of connectivity has an impact on the physicochemical state (for example, salinity, ionic composition, temperature, turbidity, nutrients) (Tagliapietra et al., 2009), the erodibility of the shore, and therefore also the mobilization of soil OC from land to the ocean. Lagoons with a narrow inlet channel (nearly-closed lagoons) are characterized by a low exchange with seawater and have lower salt concentrations in the water in summer than more open lagoons (semi-open/open lagoons) (Jenrich et al., 2021). With increasing connectivity, surface water salinity increases from brackish to marine conditions. When seawater enters a freshwater system, the ionic composition of surface and pore water is changing, altering the environmental conditions for macro- and microorganisms. In the case of nearly-closed lagoons, ice formation in winter can temporarily seal off the inlet and disconnect the lagoon from the sea (Jenrich et al., 2021b; Spangenberg et al., 2021). Within lagoons, salt diffuses into the sediment, forming unfrozen and saline ground (Angelopoulos et al., 2020a; Jenrich et al., 2021b). Beneath shallow lagoons, hypersalinity can develop in the sediment when bedfast ice injects salts into the sediment (Jenrich et al., 2021). Since lagoon ice formation expels salts into the underlying liquid water, the salinity of the sediment can become much higher than the lagoon water salinity at the onset of freeze. Thus, shallow lagoons are niche environments in which only highly salt tolerant microorganisms (halophiles) survive.

So far, there is only a limited understanding of how carbon cycling behaves under the complex hydrochemical conditions in such coastal transitional environments. With the help of incubation experiments, it is possible to mimic OM decomposition processes and the measure the production of CO_2 and CH_4 in the course of landscape changes under laboratory conditions (e.g. Laurent et al., 2023; Tanski et al., 2019). The decomposition of OM is influenced by various factors, including the OC content (Knoblauch et al., 2013; Treat et al., 2015), quality of OM (Jongejans et al., 2021), temperature (Schädel et al., 2016), salinity, and the availability of oxygen (Laurent et al., 2023; Schädel et al., 2016) within the soil. Previously, a simulation of an Arctic coastal erosion setting was achieved by incubating permafrost from a coastal outcrop with seawater, for 120 days, which approximates the time of an average Arctic open-water season (Tanski et al., 2019). The results demonstrated that the production of CO_2 from permafrost OC remains equally high under freshwater and marine conditions, which indicates that at least under these specific laboratory conditions, salinity does not significantly reduce CO_2 production.

While many studies focus on GHG production in soils from terrestrial permafrost and thermokarst landscapes (Galera et al., 2023; Heslop et al., 2015, 2019, 2020; Jongejans et al., 2021; Knoblauch et al., 2013, 2018; Kuhry et al., 2020; Lee et al., 2012) only little is known about OC decomposition, GHG production and changes in microbial communities during the transition from land to subsea permafrost and subsequent thaw.

Especially in marine environments, sulfate-reducing microorganisms, such as sulfate-reducing bacteria (SRB) and sulfate-dependent archaea, use sulfate as electron acceptors to produce sulfide (S^{2-}) or to oxidise CH_4. Since sulfate-reducers outcompete methanogens under elevated sulfate concentrations, CH_4 production in marine, sulfate-containing sediments is generally low (Holmes et al., 2017; Kristjansson and Schönheit, 1983; Lovley et al., 1982; Olefeldt et al., 2013; Schönheit et al., 1982). During lagoon formation, seawater intrusion introduces sulfate ions (SO_4^{2-}) into former freshwater lake or permafrost environments, likely resulting in complex changes of CH_4 production, oxidation and emissions from these settings. For example, when sulfate is depleted, methanogenic archaea may increase their activity, leading to increased methane production. The net effect of seawater intrusion on methane emissions depends on the balance between sulfate reduction and methanogenesis. The presence of sulfate in permafrost environments can stimulate the activity of sulfate-reducing microorganisms, leading to changes in microbial community composition and metabolic activities (Gutekunst et al., 2022; Jansson and Hofmockel, 2018; Yang et al., 2023).

The OM inventory of Arctic coastal areas is thus potentially exposed to large thermal and chemical changes with so far unknown consequences on GHG production. In our study, we are simulating the CO_2 and CH_4 production during the most important direct transitions that occur in a coastal thermokarst landscape: (I, II) ice-bonded permafrost transitioning into a thermokarst lake, a thermokarst lagoon, or into the subsea environment through block erosion; (III) thermokarst lakes transitioning into lagoons of different salinities and (IV) lagoons becoming part of the shelf by using controlled laboratory incubation experiments. With that we aim to answer the question: What is the potential local response of anaerobic CO_2 and CH_4 production to salinity changes in the short- and in the long-term? In our approach, we monitored CO_2 and CH_4 concentrations in one-year long anaerobic incubations (short-term response) of sediment samples from terrestrial permafrost, lake, and lagoons under different salt concentrations (freshwater, brackish and marine) and compared the microbial communities before and after the incubation. By using a space-for-time approach studying terrestrial aquatic systems and lagoons of different age and levels of connectivity, we mimic the long-term response to an increasingly marine influence.

3.2. Study Area

The Bykovsky Peninsula is located southeast of the Lena Delta in the Buor-Khaya Gulf of the Laptev Sea in northeastern Siberia, Russia (Figure 3.1a). The peninsula is covered by largely fine-grained deposits of the late Pleistocene, ice-rich Yedoma and by Holocene thermokarst lake and basin sediments (Schirrmeister et al., 2011, 2002; Sher et al., 2005). Thermokarst processes resulting from thaw of these ice-rich deposits play a significant role in shaping the landscape in this region, with thermokarst lakes covering approximately 15 % of the peninsula (Grosse et al., 2008) and thermokarst-affected areas, including drained lake basins, making up over 50 % of the total land area (Grosse et al., 2005). The presence of Yedoma uplands, thermokarst depressions, and thermal erosional valleys contribute to the diverse topography of the Bykovsky Peninsula.

We chose a terrestrial permafrost (TPF) outcrop located at the west coast (sampled in 2014) and three sediment cores below water bodies (cored in 2017) located at the south coast of the peninsula for our investigation (Figure 3.1b).

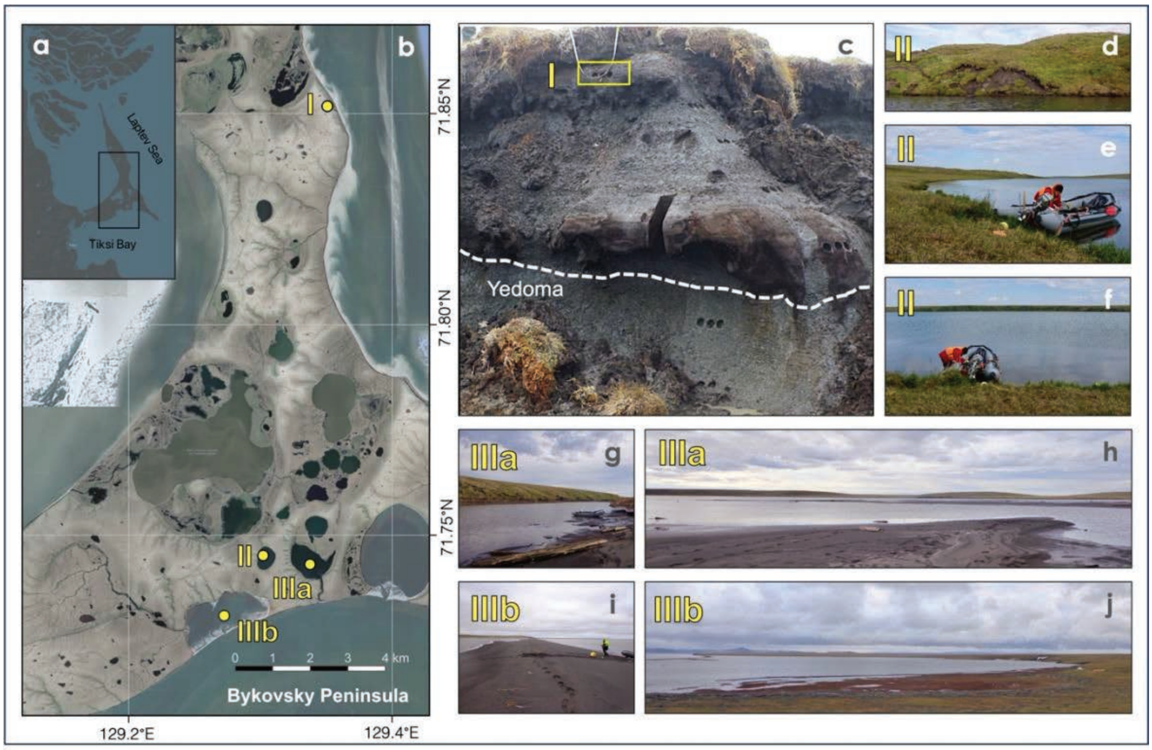

Figure 3.1. Study sites located on the Bykovsky Peninsula in Northeast Siberia, southeast of the Lena Delta (a). Close-up of central Bykovsky Peninsula, coring locations are marked by a dot (b) - I: Permafrost outcrop (TPF) located at an Upland on the West Coast, three replicate coring locations in thermokarst cover deposits overlying Yedoma marked by the yellow rectangle (c); II: Thermokarst Lake Goltsovoye (TKL) (d,e,f), drilling occurred about 60 m off the shore; IIIa: nearly-closed thermokarst lagoon Polar Fox (LAG1) temporarily connected to the sea in summer by a channel (g,h) and IIIb: semi-open lagoon Uomullyakh (LAG2) separated by a sand barrier (i,j) with a small inlet are located in close distance to each other on the southern coast of the peninsula. Imagery sources: a: ESRI base map; b: satellite map is a combination of Google Satellite Hybrid base map and a hillshade map derived from the stereophotogrammetric DEM 3epipolar based on WorldView imagery from 2015; c: Photo by G. Grosse in summer 2014; Photos d-j: by M. Angelopoulos in summer 2017.

The outcrop TPF (71.85175°N, 129.350883°E; Figure 3.1b, c) is located on the headwall of a retrogressive thaw slump eroding into a Yedoma upland on the northwestern coast of the peninsula. The exposure contains 2.9 m of nearly vertically exposed ice-rich terrestrial sediments. The lowest exposed portion consists of Yedoma with grey ice-rich silts with reticulated (vertical and horizontal ice veins) to ataxitic (suspended sediment) cryostructure and some fine grass rootlets. Above this, a horizon of 30-60 cm thickness contains brown sedge peat overlain by a cryoturbated paleosoil horizon, indicating initial thermokarst development on the original Yedoma upland (so-called Bylary, small thermokarst pits). The following organic-rich deposits all belong to this type of initial thermokarst development forming as cover deposits on Yedoma uplands. They include mixtures of brownish-grey ice-rich silt with reticulated cryostructure, small and large peat inclusions, small woody remains, and rootlets. Below the terrain surface another 20-30 cm organic-rich silt layer with peat inclusions was found, which was overlain by a cryoturbated brownish-grey mineral-rich layer and a ~8 cm thin layer of Sphagnum moss representing the soil surface organic layer. The active layer at this location was about 0.3 m thick. The uppermost samples from this exposure from 0.30-0.35 m depth serve as the terrestrial endmember for the three thermokarst settings (see Figure 3.1c).

The Thermokarst Lake Goltsovoye (TKL) (71.74515°N, 129.30217°E; Figure 3.1b, d, e, f)) is a Holocene freshwater lake that formed approximately 8,000 years ago and is located in between the two lagoons. At TKL, the sediments were coarse with pebbles at the bottom of the core (core length: 31.5 m) and became finer grained towards the top. Below 29.15 m measured from sediment surface, the sediments were frozen. The upper part of the TKL core consisted of unfrozen silty talik sediments. The core contained sediments with fresh pore water from top to bottom (EC_{max}: 1.3 mS/cm) (Jongejans et al., 2020).

The Polar Fox Lagoon (LAG1) (71.743056°N, 129.337778°E; Figure 3.1b, g, h), a nearly-closed lagoon located in a partially drained lake basin, is connected to Tiksi Bay by an approximately 800 m long and 50 m wide channel. The channel stays frozen for about 8 months of the year, resulting in the seasonal isolation of the lagoon from Tiksi Bay and thus increasing liquid water salinity beneath the ice cover during the freezing season (Angelopoulos et al., 2020b; Spangenberg et al., 2021). At LAG1, the grey to dark grey sediments gradually became finer upwards in the core with shell and plant remains in the uppermost layers (Jenrich et al., 2021). The upper part of LAG1 core (above 4.8m) was saline and unfrozen (Jenrich et al., 2021).

Uomullyakh Lagoon (LAG2) (71.730833°N, 129.2725°E; Figure 3.1b, i, j), a shallow semi-open lagoon, is well connected to Tiksi Bay via a narrow opening in the center of a flat sand spit. Similar to LAG1, this connection allows for warm freshwater discharge from the Lena River into the lagoon in summer months, leading to significant seasonal and interannual variations in temperature and salinity. However, at LAG2, storm surges can also flood the sand spit which further influences the lagoon's hydrodynamics. Perhaps the most significant difference between LAG1 and LAG2 is the water depth. In winter, LAG2 is ubiquitously covered by bedfast ice, resulting in a direct atmosphere-sediment thermal coupling. Thermistor data showed cold sub-zero (< -3 °C) sediment temperatures in the upper 30 m in April 2017. At LAG1, approximately 25 % of the lagoon still contained floating ice by the end of the winter (in 2017), resulting in a hypersaline and cryotic pool of liquid water beneath the ice cover. Thus, while the sediment temperatures beneath the center of LAG1 are cryotic, they are significantly warmer than the centre of LAG2 (Jenrich et al., 2021). The surface sediment of the LAG2 core was characterised as silty fine sand (Jenrich et al., 2021b). The LAG2 core revealed a complex structure with alternating frozen and thawed sections during field analysis. Temperature reconstructions described in Jenrich et al. (2021) revealed that the top 1 m of sediment was frozen because of bedfast ice. The core was saline from bottom to top (Jenrich et al., 2021).

Our reconstruction revealed that the sediment was frozen from the bottom up to 18.80 m, unfrozen thereafter and only the top 1 m was frozen again because of bedfast ice. The core was saline from bottom to top with a maximum electric conductivity of 108 mS/cm (hypersaline conditions) at the bottom part of the unfrozen segment (Jenrich et al., 2021).

3.3. Material and Methods

3.3.1. Fieldwork and Subsampling

The sample material was retrieved on the Bykovsky Peninsula, Siberia, during two German-Russian field expeditions focusing on carbon and nitrogen stocks (Fuchs et al., 2018; Jenrich et al., 2021b; Mishra et al., 2021), OM source and quality (Jongejans et al., 2020), methane dynamics (Spangenberg et al., 2021), microbiology (Yang et al., 2023) and the geophysical nature (Angelopoulos, 2022; Angelopoulos et al., 2021, 2020b, 2019; Arboleda-Zapata et al., 2022, Olenchenko et al., 2023) of the thermokarst affected peninsula and the nearshore subsea permafrost.

The permafrost outcrop TPF shown in Figure 3.1 was sampled during a field campaign in August 2014. Cylindrical samples (5 cm by 9 cm) in 3 replicates were drilled horizontally at seven depths with a hand-held electrical drill (Metabo, with HSS Bimetall hole saw) into Yedoma deposits, ancient thermokarst deposits, and the active layer soil. The sediment cores were stored in pre-combusted glass jars and transported in a frozen state to AWI Potsdam. The sample below the organic layer was chosen for the incubation (see Figure 3.1c and Table 3.2).

The drilling of TKL, LAG1 and LAG2 took place during a field campaign to the Bykovsky Peninsula in April of 2017 (Strauss et al., 2018). Detailed descriptions of sub-aquatic permafrost evolution, core retrieval, and sectioning were given by Jongejans et al. (2020), Angelopoulos et al. (2020b) and Jenrich et al. (2021) for TKL, LAG1, and LAG2, respectively. Briefly, sediment cores were taken from the center of the water bodies in TKL (core length: 31.5 m), LAG1 (core length: 27.7 m) and LAG2 (core length: 32.3 m) using a URB2-4T drilling rig (produced in Ozersk, Russia) mounted on a tracked vehicle, then sectioned and photographed. The cryolithology was described visually. The core sections were packed in core foil and transported frozen to AWI Potsdam.

For the incubation experiments, subsamples were taken from the surface (3-10 cm) of the cores and the outcrop. The 4 samples were kept frozen in pre-combusted glass jars until the start of the incubation experiments. Subsamples for hydrochemistry and geochemical analyses from the same depth were stored in WhirlPacks and weighed while frozen.

3.3.2. Laboratory Analyses

3.3.2.1. Hydrochemistry

For pre-incubation hydrochemical analysis, the pore water was extracted from thawed samples using Rhizon samplers (membrane pore size: 0.12-0.18 µm). Electrical conductivity (mS/cm), pH, dissolved organic carbon (DOC), and sulfate concentration were measured in the pore water.

To convert the measured electrical conductivity (referenced to 25 °C) to molality (mol/kg) and absolute salinity (g/kg), we used the MATLAB implementation of TEOS-10 (McDougall & Barker, 2011). This conversion package assumes that the pore water fluid is consistent with standard seawater composition (Millero et al., 2008).

To be able to test the GHG production in different sediments during the phases of landscape development (lake, lagoon, subsea), it is crucial to keep the seawater boundary conditions (fresh: c = 0g/L, brackish: c = 13g/L, marine: c = 36g/L) and the total water volume of 10.5 mL constant. For this purpose, we have calculated, based on the molarity of the pore water, how much of the highly concentrated artificial seawater solution (c = 182.55 g/L) needed to be added to the samples. The artificial seawater solution had a concentration higher than that of standard seawater, so a relatively lower volume of water could be added to the sediment pore water and be diluted. In terms of the relative proportions of its components, the artificial seawater contained NaCl (24.99 g/L), $MgCl_2 \times 6H_2O$ (4.14 g/L), Na_2SO_4 (0.79 g/L), $CaCl_2 \times 2H_2O$ (1.58 g/L), KCl (11.13 g/L) and $NaHCO_3$ (0.17 g/L) dissolved in ultrapure water and sterile filtered after. The pH and EC values were determined using a WTW Multilab 540 instrument, with an accuracy of ±0.01 for pH and ±1 mV for EC measurements. The DOC samples were treated with 50 µL of 30% HCl supra-pure, then stored at +4°C until analyzed using a Shimadzu Total Organic Carbon Analyzer (TOC-VCPH) with an accuracy of ±1.5%, following the method outlined by (Fritz et al., 2015).

Samples for measuring sulfate concentration were diluted (1:50) and subsequently analyzed in triplicates using the ion chromatograph Sykam S155 Compact IC-System with a detection limit of 0.1 mg/L. Integration of measured peaks in the chromatograms was done automatically by the ChromStar 7 software. The average of the triplicated was used for further evaluation.

3.3.2.2. Sedimentological and Biogeochemical Bulk Analyses

The sediment was weighed before and after freeze-drying (Zirbus Sublimator 15) and the absolute water content was determined based on weight difference between wet and dry sediment.

The samples for grain size analysis were treated with 35% H_2O_2 for 4-6 weeks to remove organic material. Subsequently, they were measured using a Malvern 316 Mastersizer 3000 with an attached Malvern Hydro LV wet-sample dispersion unit. The proportions of sand, silt, and clay fractions are provided as sums between 2 mm and 63 µm, 63 µm and 2 µm, and <2 µm, respectively. Grain-size parameters were calculated with the software Gradistat (Version 8.0; Blott and Pye, 2001).

Homogenized and milled bulk samples (using a planetary mill Fritsch Pulverisette 5) were analyzed for total carbon (TC) and total organic carbon (TOC) content (expressed in weight percent (wt%)) using a soliTOC cube, as well as the total nitrogen (TN) content using a rapid max N exceed (both Elementar Analysensysteme, Langenselbold, Germany; both with a device-specific accuracy of ± 0.1 wt% and a detection limit of 0.1 wt%).

On a separate aliquot for stable carbon isotope analysis (δ^{13}C-TOC), carbonates were removed from sediments with 1.3 molar hydrochloric acid (HCl) at 50 °C for five hours. Afterwards, chloride ions were washed out of the samples, and the samples were dried again. Stable carbon and nitrogen isotopes (δ^{15}N-TN) were then measured at AWI ISOLAB Facility Potsdam using a ThermoFisher Scientific Delta-V-Advantage gas mass spectrometer equipped with a FLASH 2000 elemental analyzer EA and a CONFLO IV with an accuracy of ± 0.01 ‰.

3.3.2.3. Incubation Experiment Set Up

To simulate the GHG production during the stages of coastal permafrost landscape development (lake formation - lagoon formation - subsea) under laboratory conditions (Table 3.1), we developed a systematic approach (Figure 3.2). We used terrestrial permafrost sediment from an outcrop close to the coast and incubated it with (1) sterilized tap water (fresh water conditions) to simulate a freshly formed lake, (2) with artificial brackish water to simulate a freshly formed lagoon, and (3) with artificial seawater to simulate subsea conditions after seawater inundation. Also, we incubated surface talik sediment of a thermokarst lake under the same three conditions. By maintaining freshwater conditions, we investigate the GHG production in an established lake. The incubation of the lake sediment under brackish conditions simulates a young lagoon, while incubating under marine conditions simulates either a highly saline lagoon or recently submerged sediment beneath the sea. The lagoon sediments contained salts initially so we omitted simulating the freshwater state. We used sediments from the two lagoons because they differ in age and connectivity with the sea and therefore represent two states of lagoon genesis. The younger and more isolated nearly-closed lagoon (LAG1) can be considered as an established lagoon, while the older more open LAG2 lagoon represents an old lagoon. Incubating the lagoon sediments under brackish conditions represents their mean annual salinity state because the incubated samples were close to the water/sediment interface. The mean annual salinity for Tiksi Bay is known to be brackish based on measurements of bottom water temperature and conductivity over the course of an entire year (Overduin et al., 2016). By incubating the lagoon sediments with marine water, the subsea stage is represented. We acknowledge that submerged sediments close to the coast of the Bykovsky Peninsula still experience brackish conditions, but for simplicity, we ignore the effects of river discharge for the subsea stage. In the further course, we use the term near natural conditions for the incubation conditions that are most similar to *in situ* conditions. In the case of permafrost and lake sediments, we use to near natural conditions when we refer to freshwater conditions, whereas for lagoon sediments, near natural conditions are brackish conditions.

Given the well-established anaerobic conditions in waterlogged soils *in situ*, we conducted the incubation anaerobically.

To be able to test the GHG production in different sediments during the phases of landscape development (lake, lagoon, subsea), it is crucial to keep the seawater boundary conditions (fresh: c = 0g/L, brackish: c = 13g/L, marine: c = 36g/L), the total water volume of 10.5 mL and the amount of soil (5 g of dry weight) constant. For this purpose, we have calculated, based on the molarity of the pore water, how much of the highly concentrated artificial seawater solution (c = 182.55 g/L) needed to be added to the samples. The artificial seawater solution had a concentration higher than that of standard seawater, so a relatively lower volume of water could be added to the sediment pore water and be diluted. In terms of the relative proportions of its components, the artificial seawater contained NaCl (24.99 g/L), $MgCl_2 \times 6H_2O$ (4.14 g/L), Na_2SO_4 (0.79 g/L), $CaCl_2 \times 2H_2O$ (1.58 g/L), KCl (11.13 g/L) and $NaHCO_3$ (0.17 g/L) dissolved in ultrapure water and sterile filtered after. Depending on the initial pore water content and salinity, different amounts of wet soil had to be weighed in and different volumes of artificial seawater added for the samples respectively to the treatment. More detail is given in supplementary Table S1.

Table 3.1. Applying the laboratory incubation approach to the landscape level. TPF is terrestrial permafrost sediment, TKL is thermokarst lake talik sediment and LAG1 and LAG2 are saline surface lagoon sediments of different age. Incubation conditions: anaerobic, 4°C, 1 year, freshwater (0 g/L), brackish (13 g/L), brackish (36 g/L). *considered as near-natural conditions

Sediment	Incubation condition freshwater	brackish	marine
TPF	young thermokarst lake* (low OM decomposition)	young lagoon (low OM decomposition)	young subsea (low OM decomposition)
TKL	old thermokarst lake* (high OM decomposition)	young lagoon (high OM decomposition)	high-saline lagoon or young subsea (high OM decomposition)
LAG1	—	established lagoon* (medium OM decomposition)	subsea (medium OM decomposition)
LAG2	—	old lagoon* (high OM decomposition)	subsea (high OM decomposition)

To ensure the exclusion of oxygen, which could adversely affect anaerobic microbial communities, we discarded the upper three centimeters of the sediment sample (given a maximum oxygen penetration depth of 25 mm (Crawshaw et al., 2019)) and maintained an oxygen-free atmosphere during sample preparation (overnight thawing and handling under a pure nitrogen atmosphere in a glovebox at 8 °C) and the incubation. In the glovebox, we homogenized the samples and filled them into pre-combusted 120 ml glass incubation vials. Three replicates were prepared for each treatment. Before starting the experiment, the headspace was flushed with pure nitrogen for 2 minutes. The oxygen concentration in the headspace of a test vial was measured at the beginning and regularly within the first 3 months of the experiment, remaining below 0.012%. The incubation temperature was set at 4 °C, approximately corresponding to the temperature of the water at the bottom of the water bodies in summer, and for comparability with other permafrost incubation studies (e.g. Jongejans et al., 2021; Tanski et al., 2019).

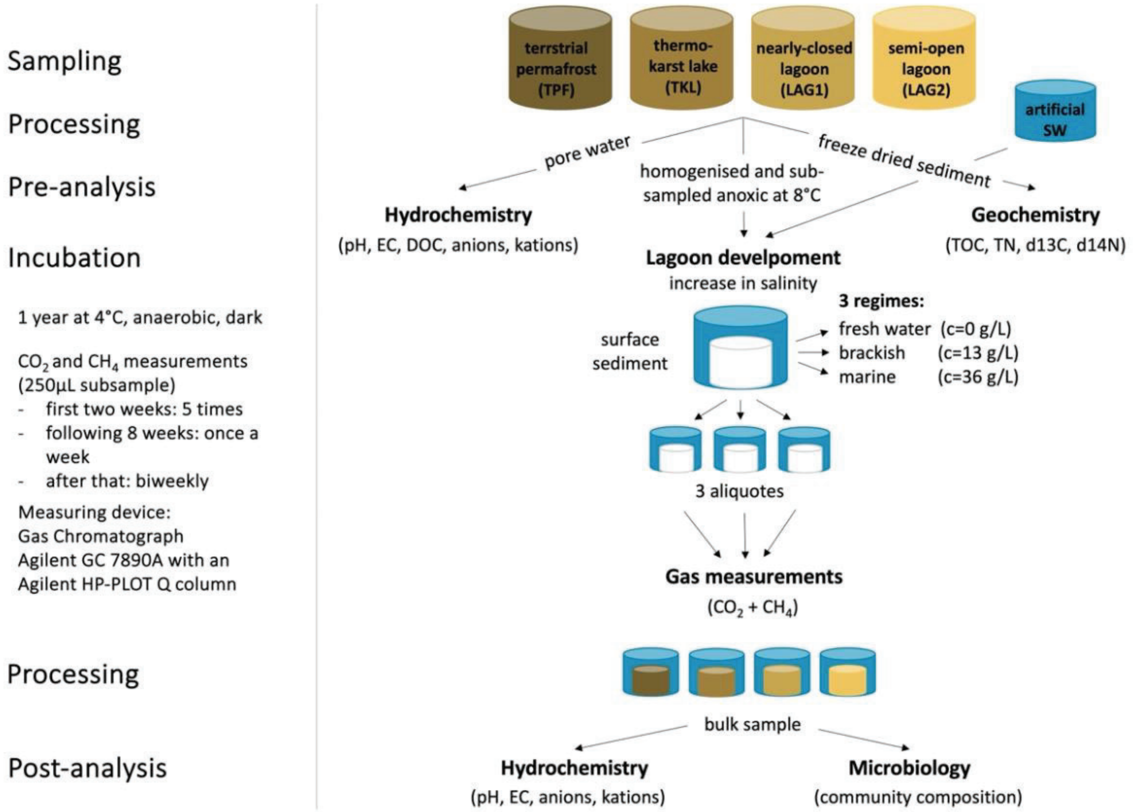

Figure 3.2 Design of the incubation experiment displaying the steps from sampling to post-analysis. In total 36 incubation vials (4 locations, 3 salinity treatments and 3 aliquots for each approach) were analyzed. Scheme modified after Tanski et al. (2019).

Concentrations of CO_2 and CH_4 were measured by gas chromatography (7890A Agilent, United States) equipped with a thermal conductivity detector and a flame ionization detector to measure CO_2 and CH_4 concentrations, respectively, with helium as the carrier gas and the oven furnace temperature of 100 °C. Before each measurement, the incubation vials were shaken to avoid zonation in sediment and water. Gas samples were drawn from the headspace of the vials with a gastight syringe and then immediately injected into the gas chromatograph. We carried out the measurements 5-times during the first two weeks, weekly for the following eight weeks and bimonthly thereafter. The amount of gas produced was calculated in parts per million (ppm) and normalized to sediment's dry weight (gdw^{-1}). Using the gas concentration, headspace volume, water volume, pH, temperature, and solubility - including carbonate and bicarbonate concentrations for CO_2 calculations (Millero et al., 2007a) - the total amount of CO_2 and CH_4 was determined in µmol using the ideal gas law (Knoblauch et al., 2018). By employing the molar mass (M) of C (12), the obtained amount of CO_2 and CH_4 in µmol was normalized to gdw^{-1} and recalculated into mg CO_2-C gdw^{-1} and CH_4-C gdw^{-1}. We further calculated the average for CO_2 and CH_4 production for the three replicates and normalized the results to $gSOC^{-1}$ using the TOC content. A detailed method description including calculation formulas can be found in supplement chapter 3.7.

3.3.3. Microbiology Analyses

3.3.3.1. DNA Extraction, PCR and, Sequencing

Total nucleic acids were extracted in duplicates using the PowerSoil-Kit (MO-Bio) according to the manufacturer's protocol. Amplicon libraries were prepared by using barcoded primer pair sets (Uni515-F[5'-GTGTGYCAGCMGCCGCGGTAA-3']/Uni806-R[5'-CCGGACTACNVGGGTWTCTAAT-3']), with duplicates for each sample. PCR reactions (50 µL) contained 10× Pol Buffer C (Roboklon GmbH, Berlin, Germany), 25 mM $MgCl_2$, 0.2 mM dNTP mix (ThermoFisher Scientific), 0.5 mM each primer (TIB Molbiol, Berlin, Germany) and 1.25 U of Opti Taq Polymerase (Roboklon, Germany). The PCR program included an initial denaturation step at 95 °C for 7 min, followed by 33 cycles at 95 °C for 15 s, annealing at 60 °C for 30 s, extension at 72 °C for 30 s and a final extension step at 72 °C for 5 min. After purification with the Agencourt AMPure XP kit (Beckman Coulter, Switzerland), the recovered PCR products were equilibrated into comparable equal amounts before pooling with positive and negative controls. For the positive controls, we utilized a commercially available mock community (ZymoBIOMICS Microbial Community DNA Standard II). As for the negative controls, they consisted of the DNA extraction buffer and the PCR buffer. Sequencing was run in paired-end mode (2 × 300 bp) on Illumina MiSeq platform by Eurofins Scientific (Konstanz, Germany).

3.3.4. Data Analyses

3.3.4.1. Microbiology

The raw data was processed by an in-house pipeline. Briefly, the demultiplexing was performed using cutadapt (Martin, 2011). The resulting sequences were further processed in DADA2, including steps of filtering, dereplication, chimera detection, sequence merging, and the identification of amplicon sequence variants (ASVs) (Callahan et al., 2016). The taxonomy was assigned against the SILVA138 database (Quast et al., 2013). The clustering dendrogram was generated on the Bray-Curtis dissimilarity using the 'hclust' function from the base package 'stats' embedded in R (v4.3.0) (R Core Team). The Bray-Curstis dissimilarity was calculated by using the 'vegdist' function from the R package vegan (v2.6-4) (Oksanen et al., 2022). The bubble plot at the taxonomic rank family was generated by the ggplot2 package (v3.4.2) (Wickham, 2016). The community data was collapsed at family level by package otuSummary (v0.1.1) (Yang et al., 2021).

3.3.4.2. Calculating Response Ratios

For investigating how GHG production changes depending on salinity increase we calculated response ratios by dividing the mean cumulative production per gram C for terrestrial sites (TPF and TKL) under freshwater conditions by that under brackish conditions (B_{terr}:F_{terr}), respectively with brackish and marine for the lagoons LAG 1 and LAG2 (M_{lag}:B_{lag}). Even though the sediment was homogenized before preparing the bottles and the replicates were treated equally, the GHG production differed. Therefore, we divided the value of each replicate of F and B by each replicate of B and M respectively. The data (n=18) was visualized as boxplots in Microsoft Excel Version 16.8.

3.4. Results

3.4.1. Environmental Parameters

Table 3.2 Overview of the environmental parameters of the surface sample at the four study sites. EC: pore water electric conductivity; salinity of the pore water; sulfate concentration; DOC: dissolved organic carbon; TOC: total organic carbon; TN: total nitrogen; TOC/TN: carbon-nitrogen ratio; d13C: stable carbon isotope composition of TOC.

	Site	Sytem	Name	Sample depth (cm)	Thermal state	Grain size descrip-tion	Mean grain size (µm)	Ice/water content (%)	pH	EC (mS/cm)	Salinity (g/L)	Sulfate (mg/L)	DOC (mg/L)	TOC (wt%)	TN (wt%)	TOC/TN	d13C (‰)
1	TPF	terrestrial permafrost	Byk14 outcrop	30-35	active layer	very poorly sorted medium silt	11.17	52.49	5.12	0.2	0.1	<0.1	158.70	9.06	0.54	16.87	-28.9
2	TKL	thermo-karst lake	Goltsovoye Lake	5-17	talik	very poorly sorted fine silt	7.48	58.53	5.93	0.2	0.1	<0.1	NA	4.03	0.31	13.21	-28.6
3a	LAG1	nearly-closed lagoon	Polar Fox Lagoon	3-10	talik	poorly sorted fine silt	5.90	51.34	7.67	40.5	26.1	75.84	126.20	4.03	0.26	15.38	-27.5
3b	LAG2	semi-open lagoon	Uomullyakh Lagoon	3-10	seasonally frozen	poorly sorted coarse silt	16.09	47.14	7.01	35.4	22.4	319.41	41.32	2.03	0.14	14.58	-26.6

The results of the environmental parameters show distinct patterns in various parameters across the studied locations, as displayed in Table 3.2, providing insights into the environmental conditions and sediment characteristics.

We found that the TPF outcrop shows consistently high values for Dissolved Organic Carbon (DOC; 158.70 mg/L), Total Organic Carbon (TOC; 9.06 wt%), and Total Nitrogen (TN; 0.54 wt%) and the highest depletion of $\delta^{13}C$ (-28.85 ‰).

Conversely, LAG2 stands out with the lowest values for most parameters, including DOC (41.32 mg/L), TOC (2.03 %), TN (0.14 %), and a higher $\delta^{13}C$ value (26.6 ‰). These findings suggest lower carbon and nitrogen content in the sediment and the pore water of LAG2, indicative of a potentially different environmental and depositional history. Remarkably, the DOC concentration at LAG1 is 3 times higher compared to LAG2.

Highest mean grain size was found at LAG2 (16.1 µm). This is attributed to the lagoon's openness, allowing the input of sandy marine depositions. Contrastingly, LAG1 exhibits the lowest mean grain size (5.9 µm), characterized by fine-grained lake deposits. There is low or no input of sandy marine sediment due to the long inlet channel.

The TKL stands out with the highest ice/water content (58.53 %). In contrast, LAG2 exhibits the lowest ice/water content at 47.14 %, suggesting a lower presence of frozen water in its sediment caused by the lower pore volume reflecting the coarser grain size in LAG2.

Hydrochemical measurements show that LAG1 had the highest pH (7.67) and EC (40.5 mS/cm) values, indicating alkaline and saline conditions. This is in stark contrast to TPF outcrop, which exhibits the lowest pH (5.12). The nearly-closed nature of Polar Fox Lagoon contributes to high salinity particularly due to brine formation below the lagoon ice in winter. Although LAG2 is shallower and hypersaline throughout many parts of its core, its total surface sediment salinity is similar to LAG1.

The terrestrial sites showed a similarly low electrical conductivity (0.2 mS/cm).

Sulfate concentrations at LAG2 were four times higher than those at LAG1, indicating a greater influence of the sea at LAG2. This can probably be mainly attributed by its closer proximity, but also by the shallow depth of LAG2. Hypersaline water beneath the lagoon ice cover can elevate sediment salinity (Jenrich et al., 2021b). Although this isn't apparent in the total salinity of the surface sample (representing all dissolved ions), hypersaline conditions are consistently observed throughout the LAG2 core over a 30 m depth range (Jenrich et al., 2021). As expected, there were no detectable sulfate concentrations at terrestrial freshwater sites (detection limit SO_4^{2-}: 0.1 mg/L).

The TPF outcrop exhibits the highest TOC/TN ratio (16.87). Conversely, TKL displays the lowest TOC/TN ratio (13.21).

3.4.2. Microbial Community Composition

The relative abundance analysis of archaea and bacteria shown in Figure 3.3 revealed that lagoons exhibited the highest microbial diversity, followed by the lake, while permafrost displayed the least diversity. The Bray-Curtis dissimilarity analysis (Figure 3.4) revealed that microbial communities tended to cluster based on landform. Lagoons notably formed a distinct cluster, and a larger group encompassed all inundated sites. In contrast, permafrost stood out as markedly different from other sites. Furthermore, the local signature of the microbial communities remained also at the end of the incubations.

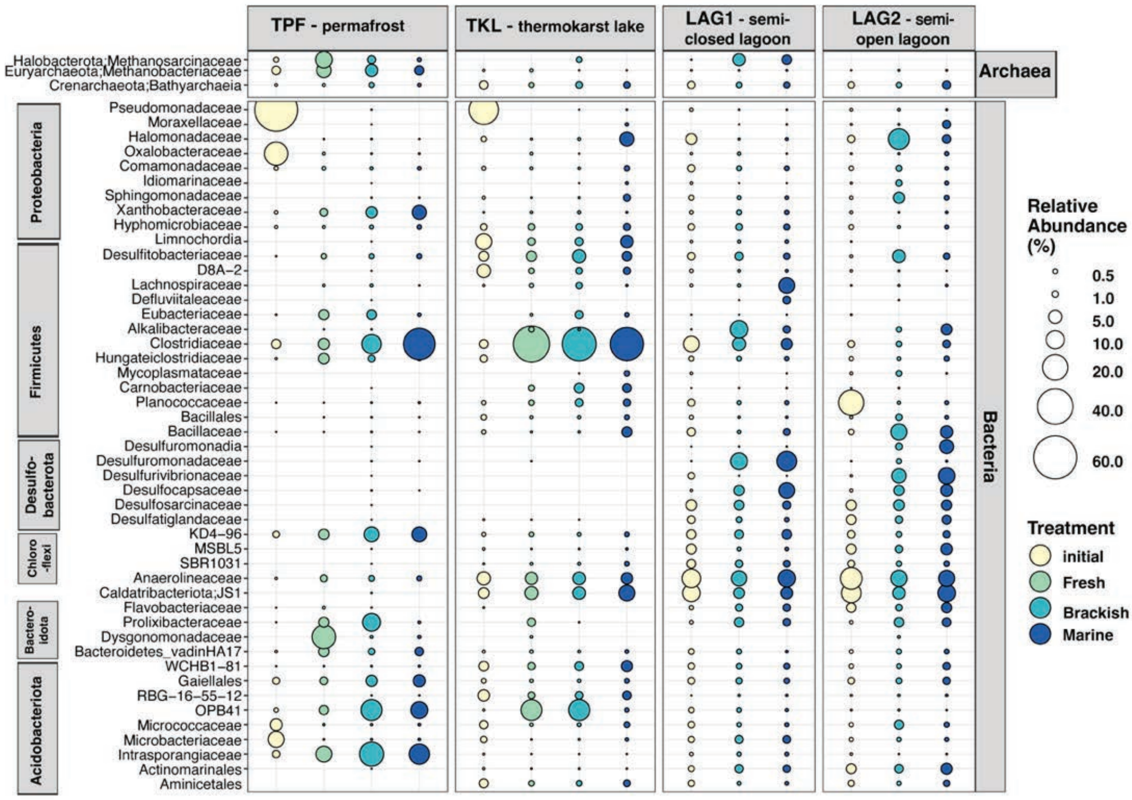

Figure 3.3 Bubble plot showing the relative abundance of archaea and bacteria before the incubation (initial, yellow) and after the incubation with freshwater (green), brackish water (turquoise) and marine water (blue) for the four study sites (TPF - permafrost outcrop, TKL - Goltsovoye Lake, LAG1 - Polar Fox Lagoon and LAG2 - Uomullyakh Lagoon). The bubble size denotes the relative abundance of different taxa. Bubbles decreasing in size from before to after incubation indicate that the treatment has a negative effect on the microorganisms present, while bubbles increasing in size indicate favorable conditions. The taxonomy was collapsed at family level. If an assignment to the family level was not possible the next higher assignable taxonomic level was used.

The most substantial shift in microbial composition over the one-year incubation period was observed for the permafrost. The microbial community was dominated initially by *Pseudomonadaceae*, known for aerobic chemoorganotrophic respiratory metabolism, and shifted towards anaerobic microorganisms during the incubation (Figure 3.3). In contrast, there was much less change observed for the lagoons.

A specific difference is that lineages that are able to reduce sulfate (*Desulphobacteria*) occur to a greater extent in the lagoon sediments than in the non-lagoon sediments.

Methanogenic Archaea, were abundant in permafrost sediments before the incubation (initial) and after the incubation, with highest relative abundance under freshwater conditions. Their relative abundance decreased with increasing salinity. In the lake and the lagoons, their presence was either minimal (< 0.5 %) or not detectable, but after one year of incubation, there was an increase in LAG1, correlating with substantial methane production in LAG1.

Clostridiaceae and *Acidobacteriota* are thriving in permafrost and lake environments (Figure 3.3). In lagoons, *Desulfuromonodaceae*, anaerobic sulfur reducers, dominated. Sulfur and sulfate reducers had already established in the lagoons and remained abundant in the salinity treatments, whereas in permafrost and the freshwater lake, they did not occur initially and also not at the end of the incubation. This coincided with the stronger development of CO_2 in the saline sites compared to the freshwater sites. *Halomonadaceae* were dominant in lagoon LAG2, especially under brackish conditions.

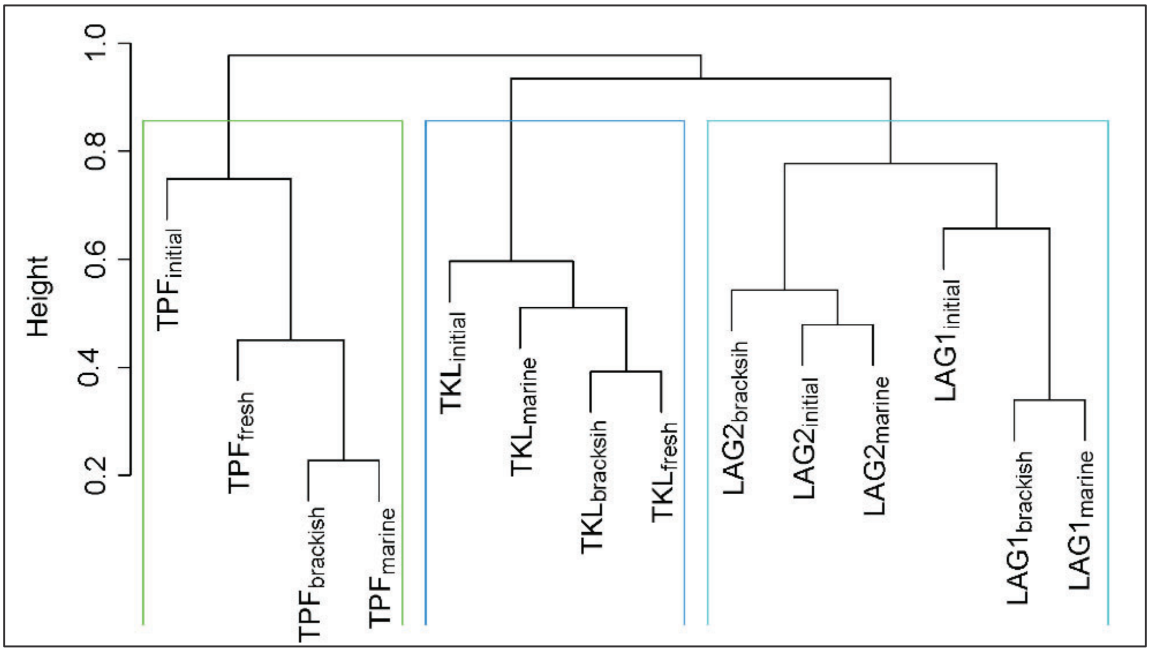

Figure 3.4 Clustering dendrogram based on Bray-Curtis dissimilarity shows that microbial communities group by landform (TPF - permafrost outcrop, TKL - Goltsovoye Lake, LAG1 - Polar Fox Lagoon and LAG2 - Uomullyakh Lagoon) rather than treatment (fresh - no addition of artificial seawater, brackish c=13 g/L, marine c=36 g/L).

3.4.3. Cumulative Anaerobic CO_2 and CH_4 production

The results on the cumulative anaerobic CO_2 and CH_4 production measured after 363 days are shown in Figure 3.5. The CO_2 production ranged from 0.001 +/- 0 mg CO_2-C gdw^{-1} for TKL-F to 0.91 +/- 0.03 mg CO_2-C gdw^{-1} for LAG1-B (Figure 3.5A). When normalized to soil organic carbon (SOC) content, both lagoons exhibited similar patterns in CO_2 production under brackish and marine conditions (22.7 +/- 0.8 and 22.1 +/- 3.1 mg CO_2-C $gSOC^{-1}$ for LAG1 and LAG2, respectively) (Figure 3.5B). At each location the highest CO_2 production occurred under near-natural conditions (freshwater for terrestrial permafrost and lake, brackish for lagoons). The CO_2 production decreases with increasing salinity under the laboratory conditions.

The methane production ranged from 5.4 x 10^{-6} mg CH_4-C gdw^{-1} for LAG2-M to 0.53 mg CH_4-C gdw^{-1} for TPF-F (Figure 3.5C), therefore methane production per gram of dry weight was highest in the permafrost sample incubated with freshwater (young lake). When normalized to SOC, LAG1 under brackish conditions exhibited higher CH_4 production (7.24 +/- 0.3 mg CH_4-C $gSOC^{-1}$) compared to the permafrost sample (TPF-F) (5.85 +/- 0.2 mg CH_4-C $gSOC^{-1}$). In contrast to LAG1-B, no methane was produced in LAG2 (Figure 3.5D).

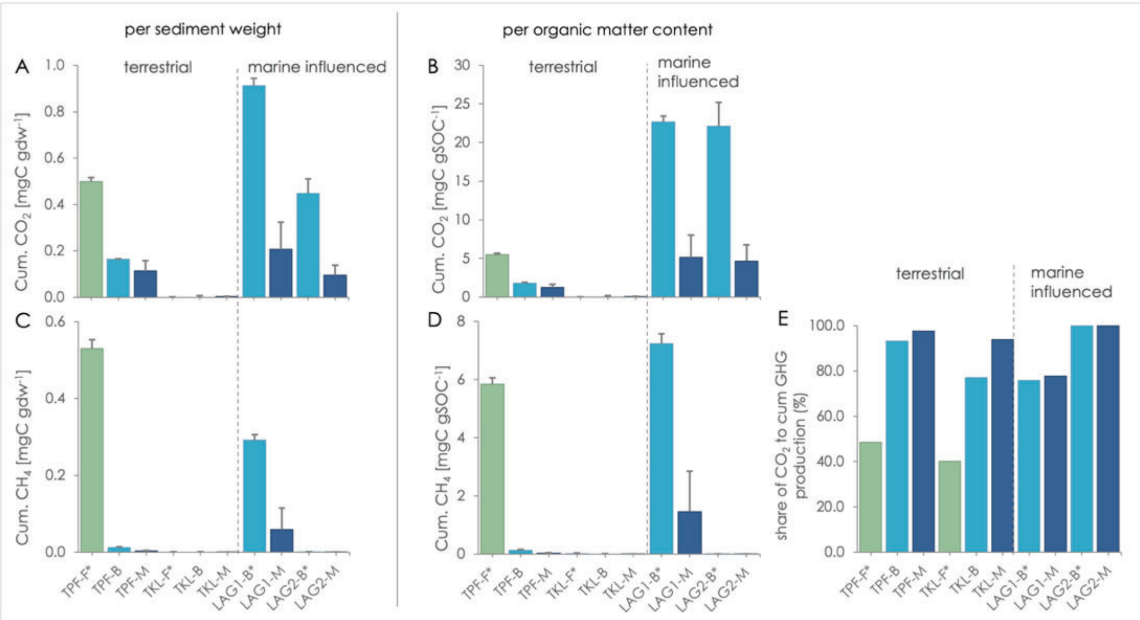

Figure 3.5 Cumulative anaerobic CO_2 and CH_4 production over the 363-day incubation at 4 °C for freshwater (green), brackish (turquoise) and marine (dark blue) conditions. A: cumulative CO_2 production in mg per gdw; B: cumulative CO_2 production in mg per gSOC; C: cumulative CH_4 production in mg per gdw; D: cumulative CH_4 production in mg per gSOC; E: percentage share of CO_2 to cumulative GHG production, the difference to 100 % is equivalent to the share of CH_4. TPF: terrestrial permafrost outcrop TPF; TKL: thermokarst lake Goltsovoye; LAG1: nearly-closed Polar Fox Lagoon; LAG2: semi-open Uomullyakh Lagoon; *near-natural conditions.

The thermokarst lake displayed the lowest CO_2 and CH_4 production overall (< 0.003 mg gdw^{-1}).

The contribution of CO_2 to cumulative GHG production after 362 days ranged from 40.1 % at TKL-F to 99.9 % at LAG2-B and LAG2-M (Figure 3.5E). There was equal CO_2 and CH_4

production for TPF under freshwater conditions. For brackish and marine conditions, CO_2 production dominated, with a share greater than 75.8 %.

During the one-year incubation period, we observed shifts in CO_2 and CH_4 headspace concentrations. In several samples (Figure S3.1a TPF-B and TPF-M, S1e TKL-F and TKL-B, S3.2a LAG1-B and LAG1-M), we noted a sharp increase in headspace CO_2 concentration in the initial weeks of the incubation, followed by a rapid decline within the first weeks.

Further, for LAG1-B we observed an exponential increase in both cumulative CH_4 production and daily CH_4 production rates from day 100 until approximately Day 220 (Figure S3.2b and d). After this period, daily rates of CH_4 production dropped, coupled with a stagnation in cumulative CH_4 production.

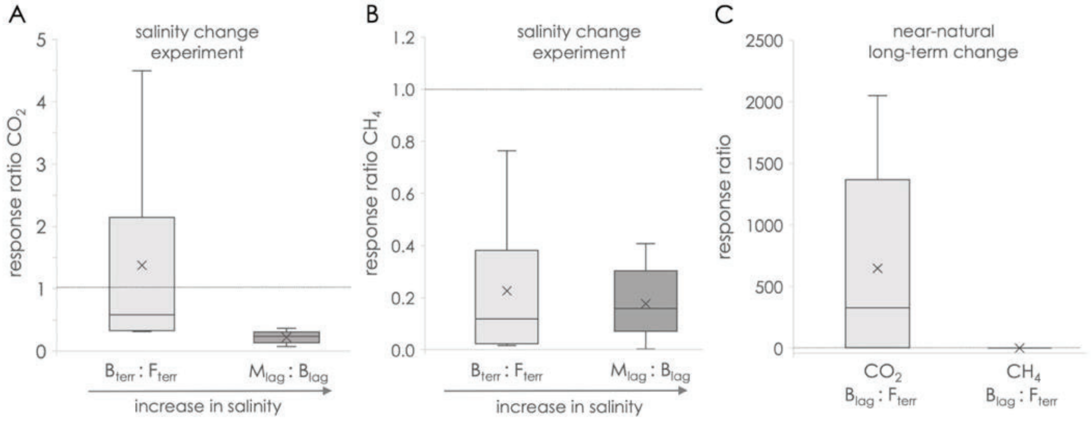

Figure 3.6. Ratio of cumulative A: CO_2 and B: CH_4 production per gram SOC from fresh to brackish conditions at the terrestrial sites (B_{terr}:F_{terr}) and from brackish to marine conditions for the lagoons (M_{lag}:B_{lag}). C: Ratio of cumulative CO_2 and CH_4 production per gram SOC for terrestrial samples vs. lagoon samples under near-natural conditions (B_{lag}:F_{terr}). Response ratio < 1 indicates a decrease in production, response ratio = 1 indicates no change and response ratio > 1 indicates increasing production. Box-whisker plots with outliers outside the lower and upper quartiles. Mean is symbolised by x.

By calculating the response ratios, we found that if terrestrial permafrost or talik sediment comes in contact with seawater (scenario $F_{terr} \rightarrow B_{terr}$ in Figure 3.6A and 3.6B), less CO_2 and CH_4 was produced in the incubation period. The decrease in methane production is slightly higher from fresh to brackish (median 0.12) than from brackish to marine conditions (median 0.16). However, the ratio of the cumulative CO_2 production for terrestrial samples vs. lagoon samples under near-natural conditions ($F_{terr} \rightarrow B_{lag}$ in Figure 3.6C) is greater 1 (median: 326.9), showing that CO_2 production increases significantly in the long-term, after lagoon formation. CH_4 production on the other hand decreases in the long term (median: 0.6).

3.4.4. Production Rates

Median CO_2 production rates ranged from 0.2 to 77.6 µg CO_2-C $gSOC^{-1}$ d^{-1}. Maximum CO_2 production rates were measured on the first day for all samples and ranged between 3.1 µg CO_2-C gdw^{-1} d^{-1} and 110.4 µg CO_2-C gdw^{-1} d^{-1} for TKL-B and LAG1 respectively (Figure 3.7A).

Median CH_4 production rates ranged from 0.001 - 4.4 µg CH_4-C $gSOC^{-1}$ d^{-1} and the maximum CH_4 production rates ranged between 0.002 µg CH_4-C gdw^{-1} d^{-1} for LAG2-M and 6.96 µg CH_4-C gdw^{-1} d^{-1} for TPF-F (Figure 3.7B). For those samples with neglectable CH_4 production (TKL and LAG2) the highest production rate was measured in the first days of incubation while for the others the maximum production rate was measured towards the end of the incubation period.

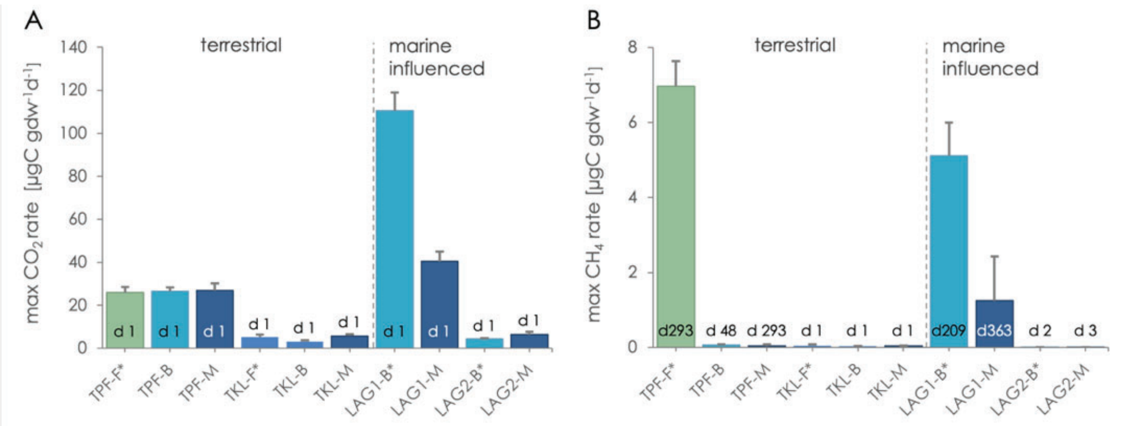

Figure 3.7. A: Maximum CO_2 production rates in µg gdw^{-1} d^{-1} and B: maximum CH_4 production rates in µg per gdw^{-1} d^{-1} for freshwater (green), brackish (turquoise) and marine (dark blue) conditions. The day of the maximum production rate is labelled at the base of the bars. TPF: terrestrial permafrost outcrop TPF; TKL: thermokarst lake Goltsovoye; LAG1: nearly-closed Polar Fox Lagoon; LAG2: semi-open Uomullyakh Lagoon; *near-natural conditions.

3.5. Discussion

3.5.1 Local short-term response to different incubation settings

3.5.1.1. Microbial composition and response to changing salinity

Microbial communities cluster based on landform, especially for lagoons, which show a unique cluster (Figure 3.4). In detail, a larger group encompassed all inundated sites, while terrestrial permafrost (TPF) stood out. It shows that microbial composition is highly shaped by the initial environmental conditions, with microbes in TPF being aerobic, in contrast to inundated sites, in which many are anaerobic. Additionally, there is an absence of sulfate for TPF and lake, whereas sulfate is present for the lagoons. Furthermore, the local signature of the microbial communities was still observed at the end of the incubations, suggesting that the time of incubation was too short for convergence of the communities according to treatments.

In our incubation experiment, a combination of stress factors likely caused the TPF to experience the most substantial shift in microbial composition between before the incubations (ice-bonded permafrost) and after the incubations (inundated). The shift from the dominating *Pseudomonadaceae*, known for aerobic chemoorganotrophic respiratory metabolism, towards a variety of anaerobic microorganisms (Figure 3.3), suggests that the lack of oxygen had a major impact on the microbial composition. Further, the abrupt thawing and the phase transition from ice to liquid water is one of the major stress factors for the biological system (Ernakovich et al., 2022) and leads to rapid changes in the structure of the permafrost microbiome (Barbato et al., 2022; Coolen et al., 2011; Coolen and Orsi, 2015; Mackelprang et al., 2011). There is also a difference in microbial composition between freshwater and brackish/marine incubations of the permafrost (TPF in Figure 3.3) but it is less pronounced, indicating that the changing salinity has a smaller impact than the thermal state and the availability of oxygen. Nevertheless, microbes have a salinity optimum for growth and a rapid shift in salinity might cause lower activity (Lyubetsky et al., 2020; Mitzscherling et al., 2019).

In contrast to the drastic microbial composition changes in the terrestrial permafrost following changing conditions, less changes were observed in the lake and the lagoon sample incubations, suggesting that the initial microbial communities were already adapted to thawed and inundated conditions. However, the microbial community in the lake differs considerably from that in the lagoons. Even after one year of incubating with sulfate-containing seawater, the proportion of SRB did not increase (Figure 3.3), indicating that the initial microbial community did not adapt to marine conditions in the short term and under the conditions of a closed system. In the permafrost and lake samples, the presence of spore-forming Clostridia suggests a response to disturbance, while the ability of Acidobacteria utilizing stable carbon sources proved advantageous at low substrate concentrations. New studies showed that some Acidobacteria, including OPB41, which were thriving in the terrestrial samples, use sulfate as electron acceptors (Khomyakova et al., 2022) and some Acidobacteria are able to switch between dissimilatory sulfate reduction and oxygen respiration (Dyksma and Pester, 2023), streamlining the multi-step mineralization of complex organic substances into CO_2 into a single process. The flexibility and adaptability of the Acidobacteria make them particularly successful in the terrestrial samples, where Desulfobacteriota (SRB) could not develop during the incubation time.

Recent research at the same study sites as ours by (Yang et al., 2023) explored how variations in geochemistry influenced the microbial methane-cycling community in two thermokarst lakes (Goltsovoye Lake, TKL and Northern Polar Fox Lake) and Polar Fox Lagoon. They observed that non-competitive methylotrophic methanogens dominated the methanogenic communities in both lakes and the lagoon, leading to elevated CH_4 concentrations in sulfate-poor sediments. In the nearly closed Polar Fox Lagoon (LAG1), we found that the abundance of both, *Methanosarcinaceae* and SRB increased during the incubation, demonstrating that even in the presence of sulfate and SRB methanogens may grow. The co-habitation of methanogens and sulfate reducers in marine environments was also noticed by other studies (Ozuolmez et al., 2015, 2020; Sela-Adler et al., 2017; Yang et al., 2023). We found that microbial communities were most diverse at brackish conditions, confirming previous findings showing that lagoons are unique microbial habitats (Yang et al., 2023).

Apart from this, the microbial composition in the lagoon samples remained similar before and after incubation, indicating that the microbial community was already adapted to saline conditions.

In contrast to nearly closed LAG1, the existence of methanogens is negligible at the more connected lagoon LAG2, which is likely due to the more distinct marine character pronounced by the four-time higher sulfate concentration. The adaptation to more sulfate-rich conditions is shown by the increase in SRB abundance with salinity.

3.5.1.2. Potential C production response

3.5.1.2.1. Variability in Carbon Dioxide Production

The elevated CO_2 production observed in near-natural conditions (freshwater for permafrost and lake, and brackish for the lagoons) compared to the lower levels in more saline treatments (Figure 3.5) suggests that the treatments induced disturbances rather than positive stimuli, which points towards a very strong microbial control. Even though electron acceptors in the form of sulfate were added to the permafrost and talik sample (TPF, TKL in Figure 3.2) in the brackish and marine treatment, CO_2 production did not increase, likely because of a lack of microbes (SRB) that can use them (Figure 3.7). Due to the closed system setting and the use of sterile artificial seawater, there was no external input of marine microbes and the existing community was not able to adapt to saline conditions in the incubation time.

Our median CO_2 production rates (0.2 - 77.6 µg CO_2-C $gSOC^{-1}$ d^{-1}) were slightly higher but in general agreement with other anaerobic incubations (median: 1.6 - 50 µg CO_2-C $gSOC^{-1}$ d^{-1}; Jongejans et al., 2021; Knoblauch et al., 2013; Zona et al., 2012). Other studies found higher cumulative CO_2 production but different conditions prevailed (e.g. Moore and Dalva, 1997; Schädel et al., 2016; Schuur et al., 2008; Tanski et al., 2019). Like other studies, we found a relationship with %C (Knoblauch et al., 2013; Treat et al., 2015), which is most pronounced in the CO_2 production in the lagoon sediments. When normalized to SOC, the same amount of CO_2 was produced in both lagoons (Figure 3.5 b), suggesting the sediment origin plays a secondary role. Previous findings by Jenrich et al. (2021) found that the surface sample at LAG2, low in TOC and TN, is very likely a mix of lacustrine and marine sediment, which was transported into the lagoon from the bay and therefore differs to the surface sediment of LAG1. The enclosed LAG1 on the other hand functions more as a sediment trap, capturing materials eroded from the Yedoma uplands and the shoreline, particularly OC-rich materials. LAG2 is more open and less of a trap so that OC can be exported into the ocean more easily. These sediment dynamics emphasize the importance of considering local variations in lagoon environments, especially when upscaling GHG production.

In the initial weeks of the incubation experiments, we observed a rapid decrease in headspace CO_2 concentration across several samples, regardless of the treatment (Figure S3.1a, e, S3.2a). Since this trend was consistent across all three replicates and the CH_4 concentration remained constant or increased, we can rule out the possibility of a leak. Similar patterns were observed in previous incubation experiments (Bischoff, 2024; Jenrich et al., 2024d; Jongejans et al., 2021). Bischoff (2024) suggested that higher CO_2 solubility in water under high pressure led to a decrease in headspace CO_2 concentration. However, after the initial drop, the CO_2 concentration increased, surpassing the pre-drop levels in most samples. This suggests that the pressure increased as well and therefore can not be the only reason for the declining concentration. Furthermore, we did not observe an extreme decline in pH during the incubations (Table S2), which would be expected for high CO_2 uptake in the water. Even for TKL, where CO_2 levels stayed low after the drop, the pH was higher at the end of the incubation.

Non-phototrophic CO_2 fixation, also known as dark CO_2 fixation, is a process by which soil bacteria can fix CO_2. Several soil types, including those found in Arctic tundra, have shown signs of this process (Akinyede et al., 2020; Šantrůčková et al., 2018). Using incubation experiments, they demonstrated that rates of dark CO_2 fixation increase with increasing headspace CO_2 concentrations (Beulig et al., 2016; Šantrůčková et al., 2018; Spohn et al., 2020). Although dark CO_2 fixation is low compared with respiration rates, it might be a more plausible explanation for the observed decline in CO_2 concentration in our incubation experiments. Further research is needed to support this.

3.5.1.2.2. Variability in Methane Production

In only two of our samples (TPF-F and LAG1-B), significant quantities of CH_4 were produced (Figure 3.5c). For these samples, the production rates correlated with the Archaea concentration (Figure 3.3). Furthermore, the start of CH_4 production was about 150 days after the incubations started (Figures S3.1b and S3.2b). Similar or even longer lag phases were reported by prior studies which concluded that the low initial colonisation of methanogens caused the delay (Jongejans et al., 2021; Knoblauch et al., 2013, 2018; Treat et al., 2014; Waldrop et al., 2010). Median CH_4 production rates (0.001 - 4.4 µg CH_4-C $gSOC^{-1}$ d^{-1}) were low but in the range of other anaerobic studies (0.02 - 135.1 µg CH_4-C $gSOC^{-1}$ d^{-1}; Heslop et al., 2015; Jongejans et al., 2021; Knoblauch et al., 2013; Lupascu et al., 2012; Zona et al., 2012).

The permafrost sample incubated with freshwater (young lake - Table 3.1) exhibited the highest methane production per sediment weight, highlighting the considerable methane release potential in freshly formed thermokarst ponds and lakes. Studies indicated faster CH_4 production from younger carbon compared to older carbon based on 14C ages in DOC in northern lakes (Douglas et al., 2020; Elder et al., 2018; Heslop et al., 2020). However, Walter Anthony et al. (2018) demonstrated that CH_4 emitted as gas bubbles, the dominant pathway of methane emissions from northern lakes, is older than dissolved CH_4 in the water column. In this study, under near-natural conditions, LAG1 showed higher CH_4 production normalized to SOC compared to the permafrost sample (Figure 3.5D), indicating differences in OM degradability. Notably, we detected methane production for LAG1 under marine conditions after a lag phase of about 300 days (Figure S3.2b), likely due to the abundance of non-competitive methanogens. These findings are consistent with Yang et al. (2023). In contrast, no methane was produced in LAG2, possibly due to the absence of an initial methanogenic community (Figure 3.3) and the more disturbed environmental setting compared to LAG1. The UWITEC core of LAG1 (Angelopoulos et al., 2020b) showed a diffusive salinity profile, indicative of gentle surface conditions. The upper 5 meters of sediment were identified as lacustrine (Jenrich et al., 2021). In contrast, the surface sediment of LAG2 was characterized by a mix of lacustrine and marine deposits. Also, initial sulfate concentrations in LAG1 are lower than in LAG2, which may pave the way for both CO_2 and CH_4 production at the same time. This again fits very well to the findings of Yang et al. (2023), who measured high methane concentrations in all sulfate-poor sediments. Further, the surface sediment of LAG2 freezes every winter due to the formation of bottom-fast ice opposed to LAG1 where the microbial community may persist year-round. In addition to the higher sulfate content, this significant microbial stressor may also be why LAG2 has a less established methanogenic community. Further, Holm et al. 2020 found that in thawing permafrost sediments, CH_4 production is influenced most by paleoenvironmental conditions during soil formation. They also highlighted the vulnerability of CH_4 production due to its restriction to a small group of archaea, contrasting with the various microbial groups contributing to anoxic CO_2 production.

Moreover, it can be assumed that the oxidation of CH_4 to CO_2, known as anaerobic oxidation of methane (AOM), plays a role in our incubation experiment. In their study of the same sites, Yang et al. (2023) demonstrated the presence of AOM-performing archaea in the sediments. In LAG1 (PFL in Yang et al., 2023), marine anaerobic methanotrophic archaea (ANME-2a/2b groups) were identified, while in TKL (LG in Yang et al., 2023), terrestrial AOMs were detected. The influence of AOM, visible in $\delta^{13}C$-CH_4 signatures and gas concentrations, was only observed in LAG1, suggesting that AOM primarily occurs in marine environments. It is therefore highly likely that more methane was produced in the lagoon sediments than is reflected in our results.

3.5.1.2.3. CO_2 Dominance under Increasing Saline Conditions

Our analysis revealed a pronounced dominance in CO_2 production, accounting for 76.0% to 99.9 % of the cumulative greenhouse gas production across all samples incubated under brackish and marine conditions (Figure 3.5E). This suggests that, during and after the transition from terrestrial to marine environments, CO_2 emerged as the primary produced GHG. The highest proportion of CO_2 in cumulative GHG production was observed in LAG2, situated closest to a marine environment and lacking a methanogenic community. Since LAG2 is older than LAG1, it is possible that LAG2 once had a methanogenic community in the past when the lagoon was presumably deeper and did not have the stressful agents it currently possesses, i.e., bottom-fast ice, hyper-salinity, turbidity etc.

In contrast, we measured similar CO_2 and CH_4 production for TPF under freshwater conditions (young lake). This aligns with the findings of Jongejans et al. (2021), who reported a similar CH_4:CO_2 production ratio in the surface sediment of an Alas Lake (81.3 µg/gdw CO_2 and 77.1 µg/gdw CH_4). In the surface sediment of the Yedoma Lake, they found a substantial difference, with CH_4 production surpassing CO_2 production (64.1 µg CO_2-C/gdw and 350.2 µg CH_4-C/gdw) which they explained by subsequent gradual population of methanogenic communities due to thaw front migration with talik formation. These observations emphasize the variability of GHG dynamics in different aquatic habitats and highlight the influence of local conditions on the cumulative CO_2 and CH_4 production.

3.5.1.2.4. Short- and Long-term CO_2 and CH_4 Dynamics

Our experiment indicates that if terrestrial permafrost or talik sediment is submerged with seawater (scenario F to B in left box of Figure 3.8), less CO_2 and CH_4 is produced in the short-term due to the lack of microbial communities adapted to the marine environment (see also Figure 3.6A, B ratios <1). However, in the long-term, after lagoon formation (scenario F in left box to B in right box of Figure 3.8) and an adaptation period in which SRB (Desulfobacteriota in Figure 3.3, panel LAG1 and LAG2) and likely marine anaerobic methanotrophic archaea performing AOM are established, CO_2 production increases (Figure 3.6C ratios >1) and even exceeds CO_2 production in terrestrial permafrost by 8 times (large CO_2 bubble in Figure 3.8). This suggests that we should expect much higher GHG production in the long-term after lagoon formation. A slightly stronger decrease in CH_4 production from fresh to brackish conditions compared to the decrease from brackish to marine conditions might suggest that the transition from a terrestrial to a saltwater-influenced ecosystem has a greater impact on CH_4 production than the increase in salinity within an established marine ecosystem.

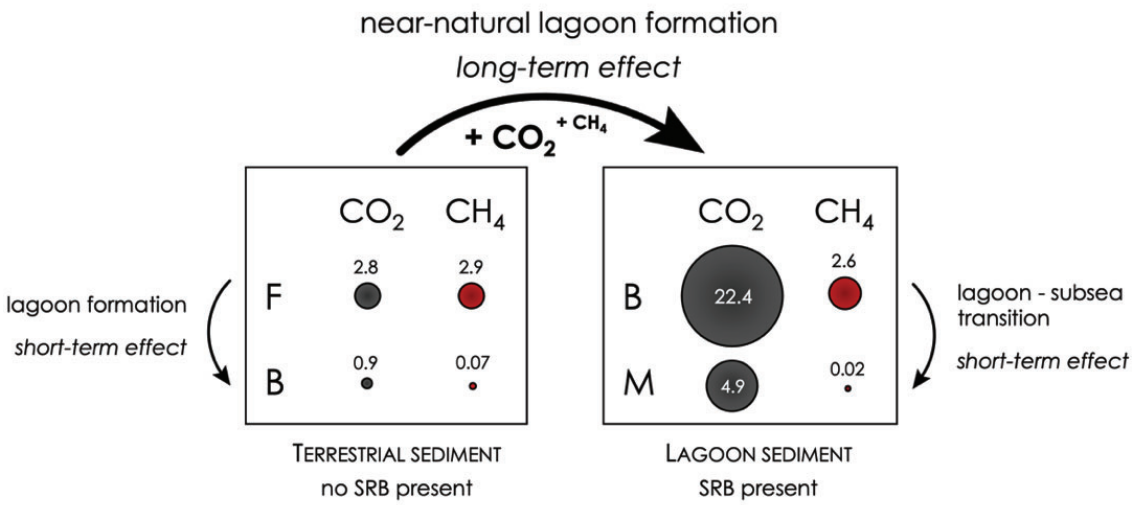

Figure 3.8. Significant increase in GHG production for lagoon formation under near-natural conditions in the long term by eight-fold from 2.8 to 22.4 mg C $gSOC^{-1}$. Short-term decrease in GHG production after artificial seawater inundation of terrestrial sediment (left box F→B) or the increase in salinity during the lagoon to subsea transition (right box B→M). The numbers are the mean cumulative CO_2 and CH_4 production (normalized to soil organic carbon content) in mg C $gSOC^{-1}$ under fresh (F) and brackish (B) conditions for terrestrial sites (left box) and brackish and marine (M) conditions for lagoons (right box) after one-year anaerobic incubation. The bubble size is proportional to the cumulative production.

3.5.1.3. High variability in thermokarst lake sediment production rates

Surprisingly, our observations revealed no substantial CH_4 and CO_2 production in the sediment of the thermokarst lake regardless of the treatment (with a maximum of 3.13 ± 0.99 µg CO_2-C/gdw measured for TKL-M and a maximum of 1.17 ± 0.16 µg CH_4-C/gdw for TKL-F). This is in contrast with the findings of Jongejans et al. (2021), who, under similar incubation conditions (1 year, 4°C, anaerobic), measured considerably higher cumulative greenhouse gas (GHG) production in surface samples from an Alas Lake and a Yedoma Lake in Central Yakutia (ranging from 64.1 to 81.3 µg CO_2-C/gdw and 77.1 to 350.3 µg CH_4-C/gdw). Furthermore, recent field studies have documented substantial GHG releases from thermokarst lakes in various regions (Schaefer et al., 2011; Schuur et al., 2008; Walter Anthony et al., 2018, 2016; Walter et al., 2007).

Several potential reasons could account for the observed low productivity in thermokarst Lake Goltsovoye (TKL):

Older Age of the Talik: The Goltsovoye Lake and its associated talik formed approximately 8000 years BP. Radiocarbon dating of the surface sediment revealed an age of 3600 BP as reported by Jongejans et al. (2020), which indicates that the sediment was unfrozen for a long time period. During this time, it is likely that the labile fraction of the OM was decomposed, leading to lower productivity now.

Lack of Substrate at the Time of Coring: A more convincing reason could be the potential lack of substrate at the time of coring at the end of winter. The long winter freezing period likely led to very limited primary production in the lake, resulting in no fresh substrate input from the water column. Microorganisms likely have metabolized easily accessible substrate sources during the winter. Since we did not add nutrients, only electron acceptors for brackish and marine conditions, the experiment started with a very low substrate level.

Low initial microbial colonization: According the qPCR data on gene copy numbers for Goltsovoye Lake (TKL) and Polar Fox Lagoon (LAG1) published by Yang et al. 2023 (Supplementary Figure S4), there are fewer bacteria and sulphate reducers in TKL, but methanogens (mcrA) are similar to those in LAG1. This again might explain the low CO_2 but not the low CH_4 production.

Acidic soil conditions: The low CH_4 production of TKL might be caused by low soil pH, ranging from 4.31 to 5.53 at the start of the incubation (Table S2). Previous studies have shown that extreme pH values negatively affect microbial biomass and activity (Aciego Pietri and Brookes, 2008) and can suppress methanogenesis by 71.7% for a pH of 5.5 or even up to 100% for a pH of 4 (Qiu et al., 2023). However, by the end of the incubation, pH values for TKL and TPF were similar, suggesting the low pH alone does not explain the difference in CH_4 production.

3.5.1.4. Limitations of incubation experiments

Laboratory incubations have several limitations. Microcosm incubations under lab conditions often fail to replicate complex environmental conditions, spatial heterogeneity, and microbial communities. Controlled settings are needed to examine the separate influences of specific parameters, such as salinity in our case, but they overlook dynamic natural changes, and microbial communities may shift during incubation. Abiotic interactions and the absence of plant-soil interactions are inadequately represented in microcosms. These factors lead to potential inaccuracies in predicting long-term, large-scale GHG emissions. However, laboratory incubations still provide valuable insights into the mechanisms of GHG production in permafrost.

3.5.2 Proposed microbial responses and GHG dynamics in changing coastal permafrost landscapes

Coastal permafrost landscapes are dynamic environments that undergo significant changes over time (Fritz et al., 2017; Irrgang et al., 2022; Lantuit et al., 2011, 2013; Nielsen et al., 2022; Overduin et al., 2014). Understanding the stages from thawing terrestrial permafrost over lake and lagoon formation towards the full submergence in the subsea stage is crucial for understanding the associated GHG production (Figure 3.9). In open systems, the input of nutrients and dissolved and particulate organic carbon promotes microbial growth. Further, the input of marine microorganisms through inundating seawater and transported sediment would promote initial colonization by, eg. sulfate-reducing bacteria and potentially anaerobic methane oxidizers, which will likely accelerate the shift from CH_4 to CO_2 production in land-sea transitioning systems. On the other hand, the export of organic carbon in the form of dissolved organic carbon (DOC) and particulate OC through leaching and erosion could result in a decrease in the availability of easily degradable organic matter especially in lagoons. Input of pollutants such as mercury, which tend to enrich in thermokarst features (Giest, 2024; Rydberg et al., 2010; Schuster et al., 2018) could inhibit microbial growth and thus lead to decreased CO_2 and CH_4 production. These are just a few examples of processes impacting GHG production in nature; however, it is not possible to integrate all of them in incubation experiments. While acknowledging the inherent limitations of small-scale laboratory experiments in replicating the complexity of the real world, these experiments can provide valuable insights into potential responses. Moreover, the comparison of II, IIIa, and IIIb (TKL, LAG1 and LAG2 respectively) is made possible by their close proximity and the similar genesis of the sites (Angelopoulos et al., 2020b; Jenrich et al., 2021b; Yang et al., 2023). Although more distant, Site I (TPF) serves as a valuable endmember.

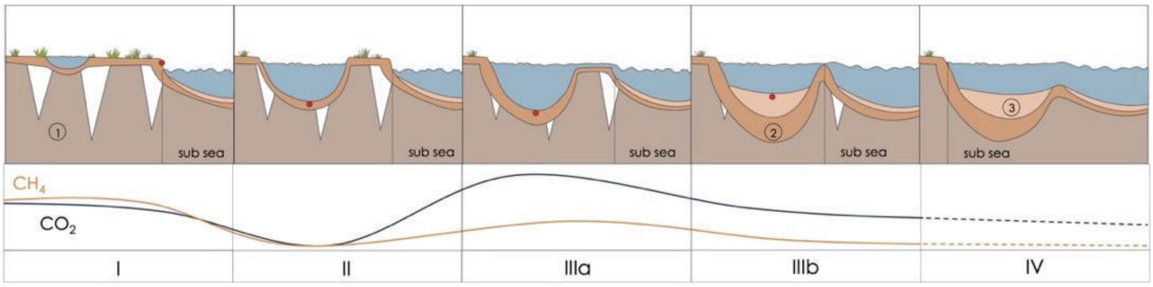

Figure 3.9 Generalised illustration of coastal landscape development in the study area and possible greenhouse gas production at each stage of development. I: thaw pond forming on terrestrial, ice-rich permafrost (outcrop TPF), II: advanced lake formation due to ongoing local permafrost thaw (old thermokarst lake Goltsovoye TKL), IIIa: first stage of lagoon formation - lake is connected to the sea via a channel with limited exchange (nearly closed lagoon Polar Fox LAG1), IIIb: older lagoon, more strongly connected to the sea (semi-open lagoon Uomullyakh LAG2) and IV: subsea after erosion of the land barrier. Red dots show sampling locations. ① frozen ground with ice wedges; ② active layer and talik; ③ marine sediment. CO_2 and CH_4 lines illustrate the production potential during that phase of landscape development based on cumulative production measured during the incubation experiment for the near natural conditions of the corresponding phase (freshwater for I and II, brackish for IIIa and IIIb, GHG production in subsea sediment IV is unknown, but the tendence is based on cumulative GHG production of LAG2 (IIIb) under marine conditions).

Thawing of ice-rich permafrost for the first time and the formation of a thaw pond or a young thermokarst lake triggers substantial GHG production (Figure 3.9 panel I). Our data suggest that both CO_2 and CH_4 are likely produced in equal amounts during this phase. After the long existence of thermokarst lakes, such as Goltsovoye TKL (panel II), a significant reduction in GHG production was observed in the surface sediment.

Following drainage, as the lake established a connection to the sea, nearly enclosed lagoons like Polar Fox LAG1 (panel IIIa) show very high CO_2 production along with substantial CH_4 production. Due to the limited connectivity, OC-rich materials eroded from the Yedoma uplands and the shoreline are captured. Rich substrate availability and moderate salinity facilitate high microbial diversity and the coexistence of methanogens and sulfate-reducing organisms.

With time and landward migration of the sea, the lagoon becomes more strongly connected (panel IIIb - semi-open lagoon Uomullyakh - LAG2). Increased marine sediment influx may lead to shallowing of the lagoon, resulting in seasonally frozen and increasingly saline ground. This environmental stressor triggers a decline in microbial abundance. Increased sulfate input induces a shift in microbial communities, favoring the growth of SRB (sulfate-reducing bacteria) and a significant increase in CO_2 production compared to CH_4. A recent study by Jones et al. (2023) suggests that the frequency of lake drainage events is rising due to changing hydrological patterns. This shift may result in a higher occurrence of nearly-closed lagoon formation along Arctic coasts, intensifying both CO_2 and CH_4 production. Rising sea level leading to complete submersion of the lagoon into subsea marks the final stage. Although CO_2 and CH_4 production was not measured directly in subsea sediments, trends can be derived from the cumulative greenhouse gas production in semi-open lagoon sediments (LAG2) under marine conditions showing a further decrease in GHG production.

Summing up, our data suggest that the dynamics of lagoon formation and its implications for CO_2 and CH_4 production unveil a nuanced relationship between microbial adaptation and greenhouse gas production. During the initial stages of permafrost sediment transitioning into a more marine environment through lagoon formation, new microbial communities have to evolve, leading to an initial reduction of CO_2 and CH_4 production. However, with an adaptation period marked by the establishment of SRB, CO_2 production undergoes a significant increase, surpassing levels observed in thawed terrestrial permafrost by about 8 times. Once SRB are established, methane production plays a secondary role.

Our marine lab experiments resulted in lower CO_2 production than other scenarios, indicating an incomplete adaptation of lagoon systems to marine conditions. This underscores the existence of a transition period during ecosystem shifts. Moreover, under near-natural conditions, where microbial organisms are likely optimally adapted, GHG production peaks at all sites.

Our results highlight that nearly closed thermokarst lagoons, partially connected to the sea and largely undisturbed by wave action, currents, and marine sediment influx, exhibit particularly high CO_2 production per gram of dry weight. Conversely, more open lagoons characterized by marine sediment influx demonstrate lower OC contents but appear to produce similar amounts of CO_2 if normalized to the organic matter content. These types of lagoons represent the first stages of the transition from lake to subsea. With an increase in lake drainage events and rising sea level, the distribution of thermokarst lagoons on Arctic coasts will escalate, resulting in further rising carbon mineralization and GHG release at the coast. This emphasizes the crucial role of microbial adaptation in shaping the carbon cycle and GHG emissions in permafrost-affected coastal environments.

3.6. Conclusion

Our incubation study of sediment samples from a depositional gradient – from terrestrial permafrost to freshwater thermokarst lakes to thermokarst lagoons – revealed that permafrost sediments inundated and thawed by seawater initially produce less CO_2 in the short term due to the delayed establishment of marine/salt-adapted microbial communities. Once sulfate-reducing bacteria adapt, CO_2 production increases, exceeding terrestrial permafrost levels by eightfold. Despite this, the marine scenario produces less CO_2 and CH_4

than the other scenarios, indicating that coastal systems are not fully adapted to marine conditions. This transition requires time for microbial adaptation, impacting biogeochemical cycling. We found GHG production to be highest in near-natural conditions, freshwater for terrestrial sites and brackish for lagoons, where microorganisms are best adapted. Our findings highlight the complex interplay of microbial processes and environmental transitions at the land-sea boundary in permafrost regions. While acknowledging the limitations of lab-scale experiments in fully capturing landscape and microbial processes, our approach enhances the understanding of climate change and carbon dynamics in permafrost coastal ecosystems.

3.7. Acknowledgements

We thank the Hydrobase Tiksi, Arctica GeoZentr, Stanislav Ostreldin and his drilling team, Waldemar Schneider, and Sergey Pravkin for their logistic contribution to the field expedition Bykovsky 2017. We thank Dirk Wagner (GFZ) for supporting the expedition. For their essential help in the laboratories, we thank the Alfred-Wegener Institute Helmholtz Centre for Polar and Marine Research (AWI) and Helmholtz-Zentrum Potsdam Deutsches GeoForschungsZentrum (GFZ) lab technicians (J. Lindemann, A. Eulenburg, O. Burckhardt, A. Saborowski, S. Okolski) in Potsdam for laboratory assistance. Thanks to S. Jansen for her assistance with the design of Figure 3.9.

3.8. Supplementary Material

3.8.1. Supplementary Methods

3.8.1.1. Preparing Incubation Vials

Table S1. Preparation of the incubation bottles using the same dry weight (5g), water content (10.5 mL) and salinity depending on the treatment. Treatments: F - fresh water c= 0 g/L, B - brackish c= 13 g/L, M - marine c= 36 g/L.

core name	sample	wet soil (g)	V (steril dest. water) (mL)	V (artificial seawater c=182.55 g/L) (µL)	V (steril tap water) (mL)
Byk14-1-A-04	TPF-F	10.5	--	--	5.30
	TPF -B	10.5	4.53	766.79	--
	TPF -M	10.5	3.19	2106.94	--
PG2412-1-1	TKL-F	12.1	--	--	4.70

	TKL-B	12.1	3.93	766.56	--
	TKL-M	12.1	2.59	2106.70	--
PG2411-1	LAG1-B	10.3	5.27	--	--
	LAG1-M	10.3	3.93	1339.97	--
PG2410-01	LAG2-B	9.5	5.88	211.25	--
	LAG2-M	9.5	4.54	1551.39	--

3.8.1.2. Calculating cumulative CO_2 and CH_4 Production

The CO_2 and CH_4 concentrations in the incubation vial headspace were calculated using measured gas concentrations, headspace volume, pH, salt concentration, incubation temperature, and pressure, following Henry's law (Equation 1) (Jongejans et al., 2021; Knoblauch et al., 2013; Walz et al., 2018).

$$V_g = \frac{m_{dw}}{S_d * w} * V_v \qquad \text{Equation 1}$$

V_g	[m³]	gas volume in the incubation vial
S_d	[g*cm⁻³]	substance density
V_v	[m³]	gas volume in the incubation vial
m_{dw}	[g]	weight of the dry sample material
w	[ml]	water content

Equation 2 provides a method to quantify mean CO_2 and CH_4 concentration in the incubation vial headspace, expressed as micromoles per gram of dry weight. The formula considers various physico-chemical parameters, with $C_{headspace}$ representing the gas amount (CO_2 and CH_4) in micromoles per gram of dry weight.

$$c_{headspace} = \frac{\rho * V_g * X}{R * T * m_{dw}} \qquad \text{Equation 2}$$

$c_{headspace}$	[µmol g_{dw}^{-1}]	concentration of CO_2 resp. CH_4 in the headspace gas produced
ρ	[Pa]	pressure inside the incubation vial
V_g	[m³]	gas volume in the incubation vial
X	[µmol mol⁻¹]	measured gas concentration (ppm)
R	[Pa*m³ mol⁻¹ K⁻¹]	gas constant of 8.3144 Pa*m³ mol⁻¹ K⁻¹
T	[K]	incubation temperature of 277.15 °K
m_{dw}	[g]	weight of the dry sample material

To account for dissolved CH_4, the CH_4 solubility in water is calculated using the Bunsen solubility coefficient of 0.0022 mol l^{-1} at 1 bar according to Yamamoto, Alcauskas and Crozier (1976).

Equation 3

$$\boldsymbol{Sb} = e^{-((-67.1962 + 99.1624 * (\frac{100}{T}) + 27.9015 * \ln(\frac{T}{100})) + S * (-0.072909 + 0.041674 * (\frac{T}{100}) - 0.0064603 * (\frac{T}{100})^{-2}))}$$

Utilizing the temperature-dependent solubility, we calculated the concentration of CH_4 in the sample pore water using Equation 4 (Jongejans et al., 2021; Knoblauch et al., 2013; Walz et al., 2018).

$$CH4_{aq} = \frac{S_{CH4} * \frac{m_{dw} * w}{1\,000 \frac{ml}{l}} * X_{CH4} * \frac{\rho}{100\,000 \frac{Pa}{bar}}}{m_d} \qquad \text{Equation 4}$$

CH_{4aq}	[µmol g_{dw}^{-1}]	concentration of CH_4 in the sample pore water
S_{CH4}	[mol l^{-1} at 1 bar]	Bunsen solubility coefficient of 0.0022 mol CH_4 l^{-1} at 1 bar for freshwater
m_{dw}	[g_{dw}]	weight of the dry sample material
w	[ml g_{ww}^{-1}]	water content
ρ	[Pa]	pressure in the incubation vial
X_{CH4}	[µmol mol^{-1}]	measured concentration in parts per million (ppm) or µmol/mol

Dissolved CO_2 concentrations are depending on temperature and pH. The CO_2 solubility equals 0.065 mol l^{-1} in water at 4 °C as defined by (Carroll et al., 1991). The calculation was adjusted to include pH-dependent dissociation constants (K1 and K2) according to Millero *et al.*, 2007.

The concentration of dissolved inorganic carbon (DIC) was then be determined based on Equation 5 (Jongejans et al., 2021; Knoblauch et al., 2013; Walz et al., 2018).

$$CO2_{DIC} = \frac{(S_{CO2} * \rho * X) * \left(1 + \left(\frac{K1}{10^{-pH}}\right)\right) + \left(\left(\frac{K1 * K2}{(10^{-pH})^2}\right)\right) * wc}{m_{dw}} \qquad \text{Equation 5}$$

$CO2_{DIC}$	[mol kg^{-1} bar^{-1}]	concentration of dissolved inorganic carbon (DIC)
S_{CO2}	[mol CO2 l^{-1} bar-1]	bei T (°K) (nach Carroll 1991)
K1	[mol kg^{-1} bar^{-1}] solutions	stoichiometric constants for the dissociation of carbonic acid in NaCl
K2	[mol kg^{-1} bar^{-1}] solutions	stoichiometric constants for the dissociation of carbonic acid in NaCl
m_{dw}	[g_{dw}]	weight of the dry sample material

To evaluate variations in salinity we measured the conductivity before and after the incubation. To convert the measured electrical conductivity (referenced to 25 °C) to molality (mol/kg) and absolute salinity (g/kg), we used the MATLAB implementation of TEOS-10 (McDougall and Barker, 2011). We utilized linear interpolation to determine NaCl concentration (Equation 6) at each measurement step and applied the same method for pH variations (Equation 7) during the incubation period.

$$S = Ss + (Se - Ss) * \frac{tn - tnmin}{t_{max} - tnmin} \qquad \text{Equation 6}$$

S_t	[mol]	NaCL concentration for each timestep
$S_{start/end}$	[mol]	NaCl concentration measured at the start/end
tn	[s]	normalized timestamp (from start (t_{min}) until end (t_{max}))

$$pH = pHs + (pHe - pHs) * \frac{tn - tnmin}{tnmax - tnmin} \qquad \text{Equation 7}$$

pH $_{(start/end)}$	pH from Measurements at the start and end of the incubation
tn	normalized timestamp from start (t_{min}) until end (t_{max}))

Further we calculated the amount of CO_2 and CH_4 in the sample for each measurement (Equation 8).

$$c_{sampling} = \frac{\frac{P * V_S}{Mv * X_{\frac{Co2}{CH4}}}}{m} \qquad \text{Equation 8}$$

$c_{sampling}$	[mol kg^{-1} bar^{-1}]	Amount of CO_2 or CH_4 taken out for measurement
Vs	[ml]	Volume sample (0,35ml)
K1	[mol kg^{-1} bar^{-1}]	stoichiometric constants for the dissociation of carbonic acid in NaCl solutions
K2	[mol kg^{-1} bar^{-1}]	stoichiometric constants for the dissociation of carbonic acid in NaCl solutions
m_{dw}	[g_{dw}]	weight of the dry sample material

The total amount of CO_2 and CH_4 produced in the incubation vials was further determined by applying Equation 9.

$$c = \left(c_{headspace} + c_{water} - Sum(c_{sampling)}\right) * M_C \qquad \text{Equation 9}$$

c	[µg g_{dw}^{-1}]	cumulative concentration of CO_2 or CH_4
$c_{headspace}$	[µmol g_{dw}^{-1}]	concentration of CO_2 or CH_4 inside the headspace
c_{water}	[µmol g_{dw}^{-1}]	concentration of CO_2 or CH_4 saluted in solution
M	[µg µmol^{-1}]	Molar mass of carbon of 12 µg/µmol

The mean CH_4 and CO_2 production for the three replicates were calculated based on concentrations and expressed in µg CH_4-C and CO_2-C per gram of dry weight and per gram of SOC. Rates were then determined using the measured time intervals. Cumulative values were obtained by subtracting the initial measurement from each subsequent one, allowing for the calculation of production rates.

3.8.2. Supplementary Results

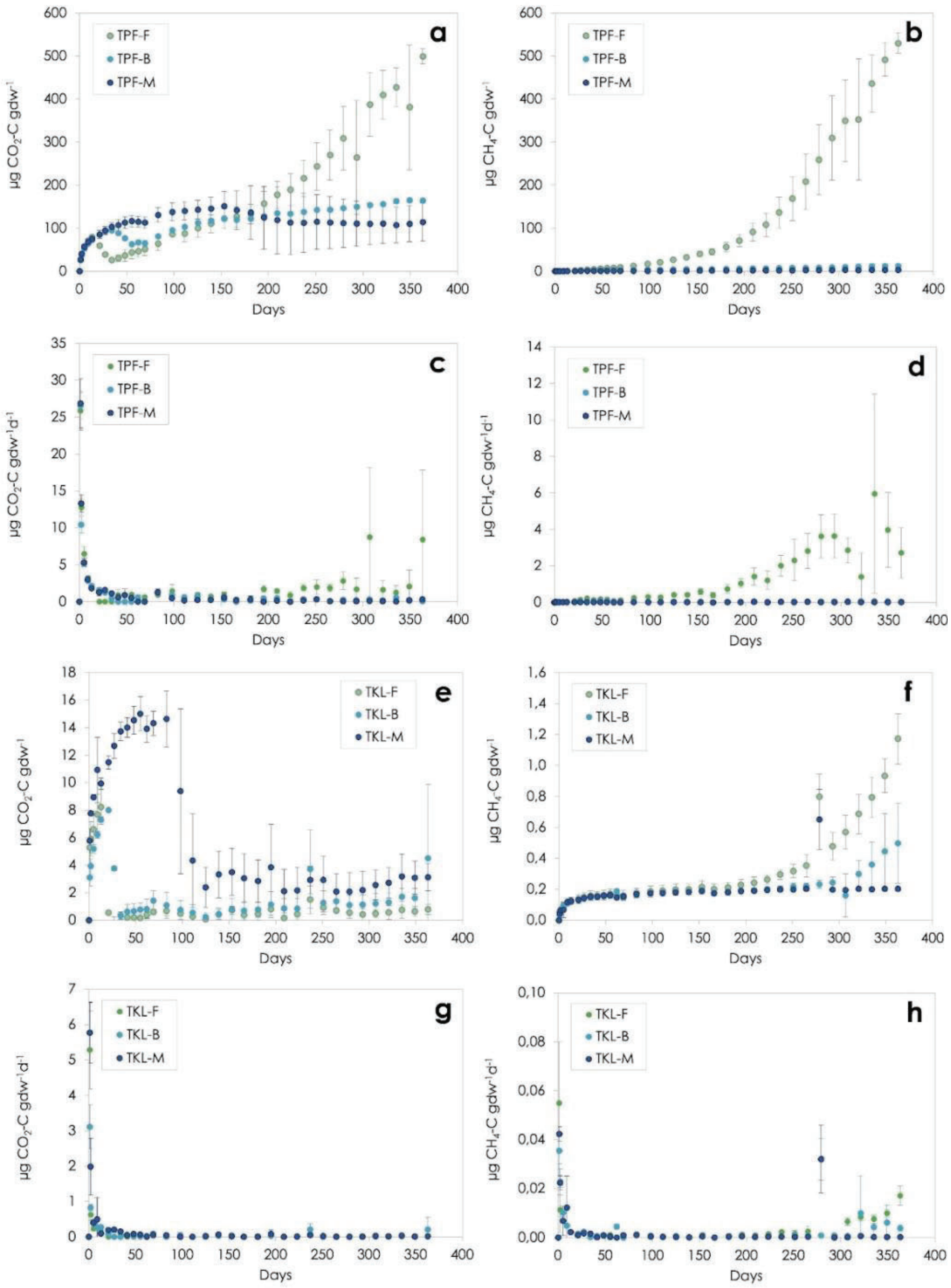

Figure S3.1 Cumulative anaerobic CO_2 (a, e) and CH_4 (b,f) production in µg per gdw and anaerobic CO_2 (c, g) and CH_4 (d,h) production rate in µg per gdw and day for the terrestrial sites during the 362 day incubation experiment at freshwater (green), brackish (turquoise) and marine (dark blue) conditions. TPF: terrestrial permafrost outcrop; TKL: thermokarst lake Goltsovoye. Error bars representing the standard deviation.

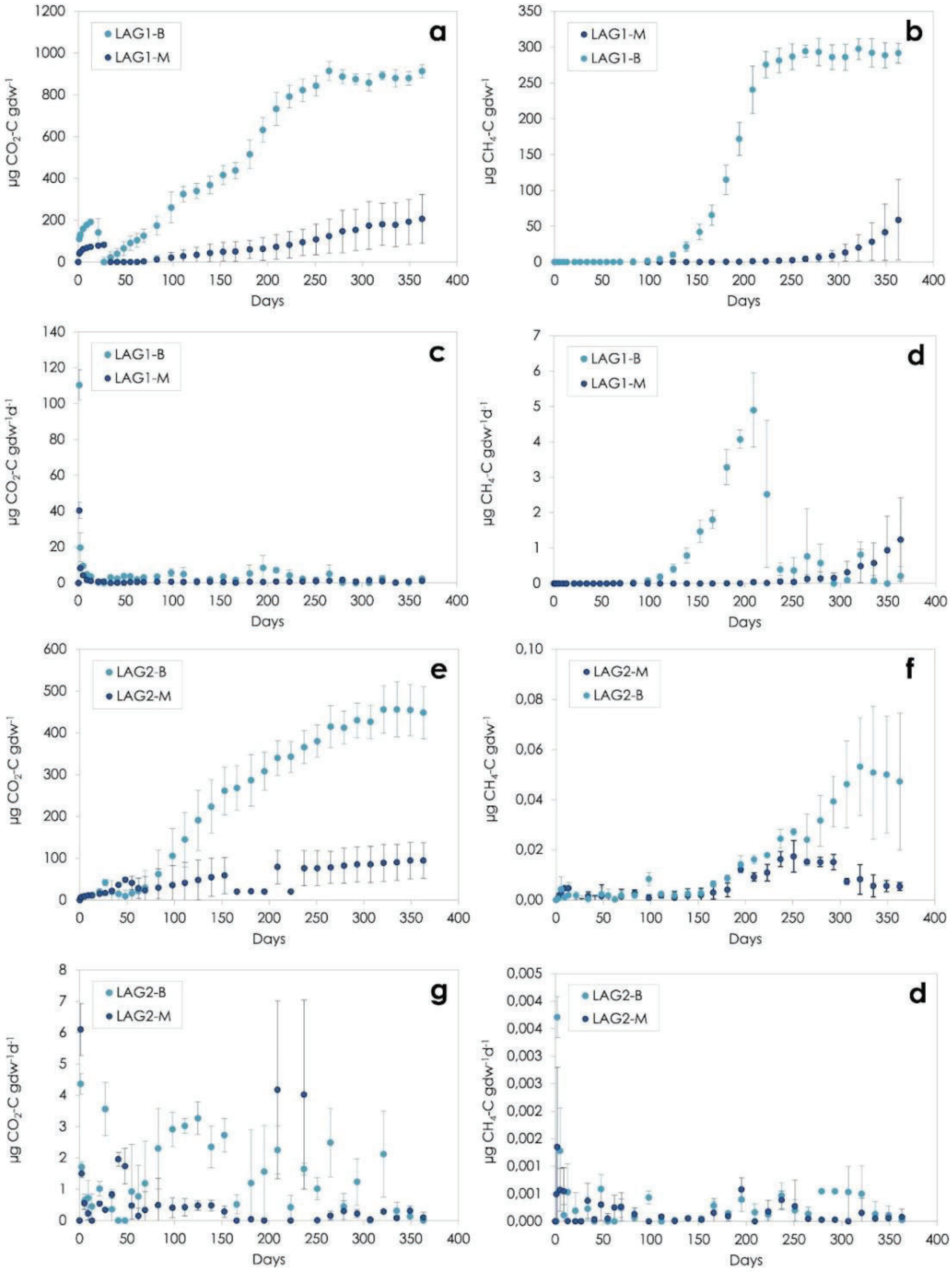

Figure S3.2 Cumulative anaerobic CO_2 (a, e) and CH_4 (b,f) production in µg per gdw and anaerobic CO_2 (c, g) and CH_4 (d,h) production rate in µg per gdw and day for the marine sites during the 362 day incubation experiment at freshwater (green), brackish (turquoise) and marine (dark blue) conditions. LAG1: nearly-closed Polar Fox Lagoon; LAG2: semi-open Uomullyakh Lagoon. Error bars representing the standard deviation.

Table S3.2 Change in pH from before (pre-inc) to after (post-inc) the one-year incubation with freshwater, brackish water and marine water for the four study sites (TPF - permafrost outcrop, TKL - Goltsovoye Lake, LAG1 - Polar Fox Lagoon and LAG2 - Uomullyakh Lagoon).

Treatment	TPF		TKL		LAG1		LAG2	
	pre-inc pH	post-inc pH	pre-inc pH	post-inc pH	pre-inc pH	post-inc pH	pre-inc pH	post-inc pH
non – original soil	5.12	-	5.93	-	7.67	-	7.01	-
fresh water	5.31	6.30	4.31	5.82	-	-	-	-
brackish water	5.58	5.66	5.09	5.58	8.03	7.62	7.26	6.56
marine water	5.94	5.54	5.53	5.46	7.94	7.03	7.00	6.21

4

Rising Arctic Seas and Thawing Permafrost: Uncovering the Carbon Cycle Impact in a Thermokarst Lagoon System in the outer Mackenzie Delta, Canada

Maren Jenrich[1,2], Juliane Wolter[1,3], Susanne Liebner[3,4], Christian Knoblauch[5,6], Guido Grosse[1,2], Fiona Giebler[1,2], Dustin Whalen[7] and Jens Strauss[1]

[1]Alfred Wegener Institute Helmholtz Centre for Polar and Marine Research, Permafrost Research Section, Potsdam, 14473, Germany

[2] University of Potsdam, Institute of Geosciences, Potsdam, 14469, Germany

[3] University of Potsdam, Institute of Biochemistry and Biology, Potsdam, 14469, Germany

[4] GFZ German Research Centre for Geosciences, Section Geomicrobiology, Potsdam, 14473, Germany

[5] Universität Hamburg, Institute of Soil Sciences, Faculty of Mathematics, Informatics and Natural Sciences, Hamburg, 20148, Germany

[6] Universität Hamburg, Center for Earth System Research and Sustainability, Hamburg, 20148, Germany

[7] Geological Survey of Canada Atlantic, Natural Resources Canada, Dartmouth, Nova Scotia, B2Y 4A2, Canada

This chapter is published as preprint and currently under review in: *EGU - Biogeosciences* DOI: https://doi.org/10.5194/egusphere-2024-2891, 2024.

Abstract Climate warming in the Arctic is directly connected to rising sea levels and increasing erosion of permafrost coasts, leading to inland-migrating coastlines and the transformation of coastal permafrost lakes into thermokarst lagoons. These lagoons represent transitional zones between terrestrial to sub-sea permafrost environments. So far, the effect of the transition on the carbon cycle is fairly unknown. In this study, we conducted long-term anoxic incubation experiments on surface samples from thermokarst lagoons with varying degrees of sea connectivity. We also included terrestrial permafrost and the active layer as endmembers to investigate variations in carbon dioxide (CO_2) and methane (CH_4) production within lagoon systems and along a land–sea transition transect on Reindeer Island, northeast Mackenzie Delta, Canada. Results show that CH_4 production peaks at 4.6 mg CH_4 g^{-1} C in younger, less connected lagoons with high-quality organic matter, leading to up to 18 times higher greenhouse gas (GHG) production (in CO_2 equivalents) compared to open lagoons. CO_2 production is higher under marine conditions (3.8–5.4 mg CO_2 g^{-1} C) than under brackish conditions (1.7–4.3 mg CO_2 g^{-1} C). Along a land–sea transect, CO_2 production increased with increasing marine influence. These findings suggest that the landward migration of the sea, resulting in the inundation of permafrost lowlands and thermokarst lakes, may lead to increased GHG emissions from Arctic coasts in the future.

4.1 Introduction

The Arctic region is experiencing unprecedented rates of temperature rise, nearly 4 times faster than the global average (Rantanen et al., 2022). The rapid warming has significant effects, particularly evident in the Arctic Ocean and its coastal areas, resulting in rising sea levels (Guimond et al., 2021; Nerem et al., 2018; Proshutinsky et al., 2001; Watson et al., 2015), extensive sea ice loss (Jahn et al., 2024; Kwok and Rothrock, 2009; Notz and Stroeve, 2016), and erosion of ice-rich permafrost coasts (Günther et al., 2013; Jones et al., 2018; Malenfant et al., 2022; Whalen et al., 2022).

With approximately 1 million people residing along the Arctic coastlines, they are directly impacted by the transformation of coastal permafrost landscapes and the migration of the sea inland (Ramage et al., 2021). The average rate of permafrost coastline change throughout the Arctic between 1950 and 2000 was -0.5 m yr^{-1}, with significant regional and intra-regional variations (Irrgang et al., 2022). The biggest rise in Arctic erosion rates, ranging from +80 % to +160 %, was observed along the permafrost coasts of the Alaska and Canadian Beaufort Sea (Jones et al., 2020). In the Mackenzie Delta area, shoreline retreat rates have been documented as high as -46 m yr^{-1}, leading to substantial land loss and inland migration of the coastline (Malenfant et al., 2022; Solomon, 2005).

As sea levels rise and coastal erosion progresses, previously isolated thermokarst lakes and basins with bottom elevations below sea level become connected to the ocean, forming thermokarst lagoons (Jenrich et al., 2021b; Schirrmeister et al., 2018). Along the Arctic coast, from the Taimyr Peninsula in Russia to the Tuktoyaktuk Peninsula in Canada, 520 thermokarst lagoons larger than 500 meters in diameter have been identified, covering a total area of nearly 3500 km^2 (Jenrich et al., 2024c). These lagoons, located at the interface between land and sea, form a critical transition zone from terrestrial to subsea permafrost environments. Electrical resistivity surveys revealed that permafrost degradation in former lagoon deposits occurs up to 170% faster than in submerged Yedoma permafrost (Angelopoulos et al., 2021), significantly accelerating carbon cycling in these areas.

Permafrost, which is ground that has been frozen for more than two consecutive years, lies beneath 13.9 × 106 km2 (ca. 15%) of the exposed land area (Obu, 2021) and about 407.680 km of arctic coasts (34% of the world coastline) are classified as permafrost coasts (Lantuit et al., 2012). Including also non-permafrost deposits the permafrost region stores ~1700 Pg organic carbon in active layer soils and deposits, frozen ground (Lindgren et al., 2018; Miner et al., 2022; Schuur et al., 2022), and lake taliks (Strauss et al., 2021; Walter Anthony et al., 2014), which is about 50% of the OC stored in all global soils (3350 Pg; Strauss et al., 2024). Additionally, model simulations estimate another ~2800 Pg OC in deep permafrost below the seafloor of Arctic shelves (Miesner et al., 2023), which cover an area of almost 2.5×10^6 km^2 (Overduin et al., 2019). Rising temperatures in a warming Arctic accelerate permafrost thaw, activating ancient microbes and leading to the decomposition of organic carbon into greenhouse gases (GHGs) such as carbon dioxide (CO_2) and methane (CH_4).

The transition from unsaturated, aerobic conditions in terrestrial permafrost to saturated, anaerobic conditions in inundated soils results in a shift in microbial composition and, consequently, greenhouse gas production (Bush et al., 2017; Jenrich et al., 2024b; Liu et al., 2022). Under laboratory conditions, carbon breakdown processes and the associated production of CO_2 and CH_4 during landscape changes can be replicated by incubation experiments (e.g. Laurent et al., 2023; Liu et al., 2022; Tanski et al., 2019). CO_2 production is dominant in unsaturated soils, while CH_4 production is happening in saturated, anoxic soils (Le Mer and Roger, 2001; Schädel et al., 2016). Marine sediments generally exhibit lower decomposition rates compared to terrestrial permafrost (Miesner et al., 2023). As terrestrial thermokarst lakes transition to marine environments, the hydrochemical and biogeochemical conditions of the sediment shift, affecting the microbial community composition (Jenrich et al., 2024b; Yang et al., 2023). In marine sediments, methanogens are found mostly in sediment layers below the sulfate reduction zone, as sulfate-reducing bacteria (SRB) outcompete methanogens for key substrates like acetate and hydrogen (Jørgensen, 2006; Oremland and Polcin, 1982). During this transition, as soils become inundated with seawater, CO_2-producing SRB grow (An et al., 2023). A few studies focusing on organic-rich sediments (Holmer and Kristensen, 1994; Jørgensen and Parkes, 2010), salt marshes (Oremland et al., 1982), coastal sediments (Maltby et al., 2018) as well as in the early stages of lagoon formation (Jenrich et al., 2024b; Yang et al., 2023) have reported the coexistence of methanogens and SRB, which is probably driven by noncompetitive substrates like methanol and methylated compounds. A recent study simulating greenhouse gas production during different transition stages in a coastal thermokarst landscape demonstrated that CO_2 production initially decreases following lagoon formation. However, in the long term, after SRB establish themselves, CO_2 production increases significantly, surpassing that in thawing terrestrial permafrost by a factor of eight (Jenrich et al., 2024b).

When highly degraded, lowland thermokarst landscapes are flooded by the sea, and thermokarst lagoons, lakes, and the sea become connected with each other, complex lagoon systems are formed. Consequently, a natural gradient of marine submergence age and connectivity emerges within the system with older, well-connected lagoons closer to the sea, and younger, less connected lagoons further inland. The individual basins of previous thermokarst lakes are often still identifiable by their characteristic round shape in the new lagoon system. These systems are widespread along all Arctic lowland coasts with ice-rich permafrost and abundant thermokarst lakes, such as the Laptev, East Siberian, Chukchi, and Beaufort seas. They serve as a natural study setting for investigating the impact of progressive marine inundation on permafrost and its organic matter pool. Different lagoon development stages found in the same region would represent a space-for-time gradient that could allow better understanding of the production of greenhouse gases in inundated permafrost soils under varying degrees of seawater influence. In Jenrich et al. (2024b), thermokarst lagoons are classified by openness and the degree of connectivity with the sea, both for single lagoons and lagoons within a lagoon system. They defined five connectivity classes from very high (5) for lagoons which are always open and in direct exchange with the sea to very low (1) for nearly-closed lagoons where the exchange is very limited due to long channels or for subsequent lagoons in lagoon systems with very limited exchange due to narrow inlets and great distances to the sea.

Despite the abundance of thermokarst lagoons and their potential interesting role in the Arctic carbon cycle, their GHG production dynamics during the transition from terrestrial permafrost to subsea permafrost remain poorly studied so far. In particular, knowledge gaps persist regarding the variation in carbon degradability and GHG production based on lagoon development stage as well as the evolution of GHG production with increasing seawater influence.

In this study, we address these gaps with answering the following questions:

1. How does greenhouse gas production differ within a lagoon system under near-natural conditions, considering different degrees of lagoon openness and distance to the sea?
2. How does greenhouse gas production differ with increasing seawater influence in the land-sea transition along a permafrost-lake-lagoon-transect?

This study is the first focusing on thermokarst lagoon development stages and the GHG production rates occurring during the transition of permafrost from a terrestrial to a marine setting to better understand the role of thermokarst lagoons in the Arctic carbon cycle and more broadly what happens when terrestrial permafrost becomes inundated by the sea.

4.2 Study Area

In this study, we collected and incubated surface samples of thermokarst lagoons of different transgression stages within a lagoon system as well as terrestrial samples from the active layer and permafrost on Reindeer Island, northeast Mackenzie Delta, Canada.

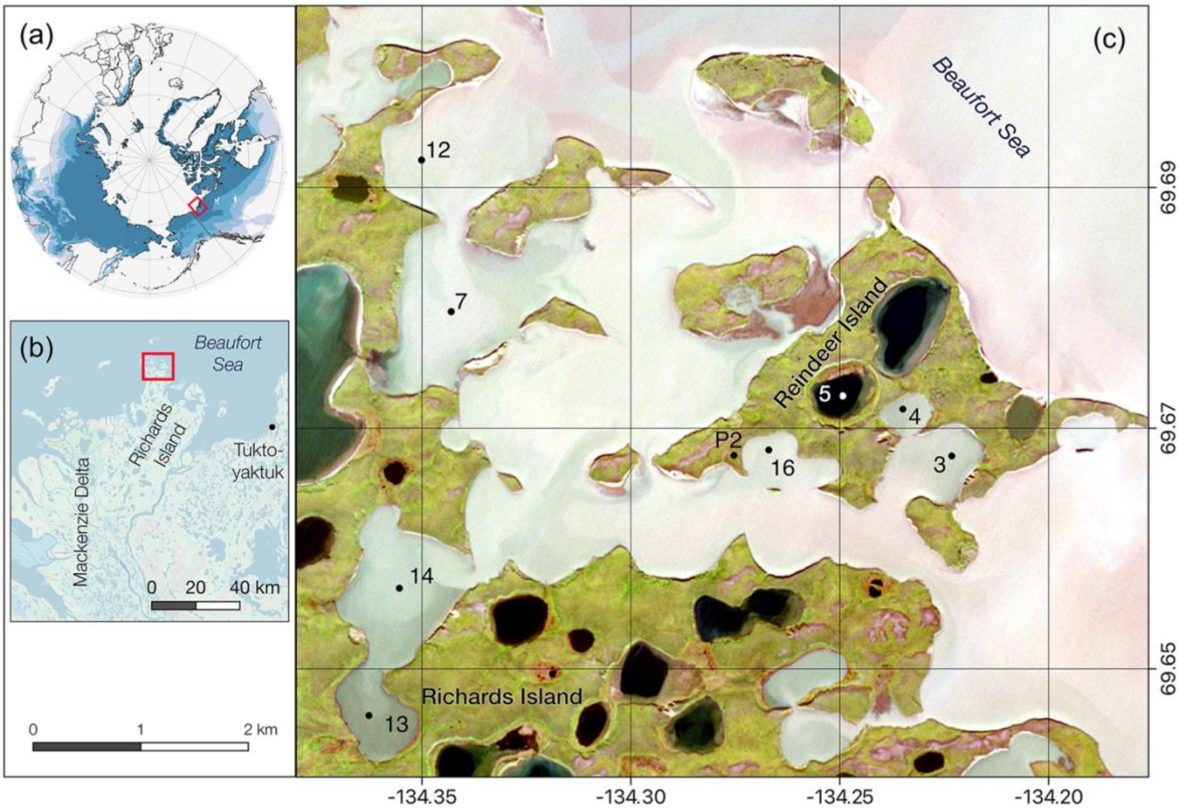

Figure 4.1 Study sites located on Reindeer Island and the surrounding lagoon system close to Richards Island, northern Mackenzie Delta, Canada (a, b). Coring sites are marked by a dot c): P2 soil pit - active layer and permafrost sampling; 5 - thermokarst lake; 3, 4, 7, 12-14, and 16 - thermokarst lagoons of varying connectivity. Imagery sources: a) Permafrost extent regions based on Brown et al. (1997); b) ESRI base map; c) Sentinel-2 satellite image band combination 4-3-2 from 2021-08-26. Note: different water colours are related to sediment load coming from the Mackenzie River plume and indicative of the different lagoon connectivity, with black colours being closed lake basins, darker grey colours limited-open or well-connected lagoon, and light grey waters in very open lagoons (similar the open sea)

Reindeer Island, formerly connected to the northern head of Richards Island, is situated in the northern region of the Mackenzie Delta, Northwest Territories, Canada (Figure 4.1). Richards Island is heavily influenced by thermokarst lake formation, covering 23.5% of its surface area (Burn, 2002). Seismic profiles revealed thaw depressions over 20 meters deep, half-filled with stratified sediments, while radiocarbon and ^{137}Cs data suggested sedimentation rates of 0.03±0.05 cm yr^{-1}, indicating lake formation over the past 10,000-15,000 years (Solomon et al., 2000). The permafrost on Richards Island is continuous, exceeding 500 m in thickness, contrasting sharply with the discontinuous permafrost of the Mackenzie Delta (Judge et al., 1987; Kohnert et al., 2017). The regional sedimentology is characterized by discontinuous unconsolidated till in an ice-rich permafrost environment. During the short open water (ice-free) season the area is exposed to high winds and increased wave action during coastal storms. Although the southside of Reindeer Island and most of the inner lagoon is protected from the forces of offshore waves during storms, it is still susceptible to thawing permafrost during increased air temperatures. There is a direct correlation to NW winds

(>50 km/hr) and air temperature to coastal erosion in this region (Berry et al., 2021; Lim et al., 2020). Richard Island has experienced moderate to rapid coastal erosion rates, Hynes et al. (2014) reported erosion rates for 1972-2000 to be up to 3.6 m yr^{-1}, with significant annual retreat occurring at North Head (the tip of the Richards Island) and the ocean side of Reindeer Island. The average erosion rate within the lagoon study area was reported to be 0.28 m yr^{-1} (Hynes et al., 2014), with increased rates (up to 1.1 m yr^{-1}) at some locations on the southside of Reindeer Island near samples sites 3, 4 and 16. Despite the regional and localized erosion it is clear that a significant portion of sediment are originating from the Mackenzie River's sediment plume (Solomon et al., 2000), which is supplying 128 Mt fluvial sediments on average per year (from 1974 to 1994; Carson et al., 1998). The Mackenzie River therefore is the largest supplier of fluvial sediments and the fourth-largest provider of freshwater to the Arctic Ocean (330 km^2 yr^{-1}) (Vonk et al., 2015a). 55% of the sedimentary OC is transported through the delta and deposited on the coastal shelf, suggesting that 45% are deposited mainly in lakes within the delta in the course of the spring ice break (Vonk et al., 2015a) and when lakes get more connected to the river system (Burn, 1995) but likely also in the thermokarst lagoons at the head of the delta.

To the east, Reindeer Island borders the Beaufort Sea, while to the south and west, flooded thermokarst lake basins form a lagoon system separating the island from Richards Island. This lagoon system, consisting of at least 14 individual former thermokarst lake basins, covers an area of 13.7 km^2 (Jenrich et al., 2024c) and was first investigated in 1993 (Solomon et al., 2000). Bathymetric investigations during these studies have revealed overall shallow water depths (< 2 m) around Reindeer Island, allowing for the formation of bottom fast ice during winter. ^{137}Cs data suggest that sedimentation rates in the lagoons ranged from 0.7 to 2 cm yr^{-1} of the past 50 years (Solomon et al., 2000). For this study we revisited five of the coring sites investigated by Solomon et al. (2000) (our site names: LAG 3, 4, 7, 12 and TKL 5) and added three more (LAG 13, 14, 16), all representing lagoons with varying connectivity with the sea and therefore varying influence of marine processes and fluvial inputs from the Mackenzie River. Based on the classification by Jenrich et al. (2024b), LAG7 and LAG12 are Class 5 lagoons with very high connectivity, which are always open. LAG3 and LAG16 are considered Class 4, which are defined as mostly open, spatially second-tier, lagoons which are very well connected to the primary lagoon. LAG4 and LAG14 are Class 3, semi-open second-tier lagoons which are well connected to the primary lagoon. LAG13 is a Class 2 second-tier lagoon, which is less connected to the primary lagoon due to the great distance to the sea and multiple narrow inlets reduce the exchange with the sea.

Further we sampled active layer and permafrost in a low land position (P2) on the island.

4.3 Methods

4.3.1 Fieldwork and Subsampling

Fieldwork was conducted at the Reindeer Island lagoon system in collaboration with Natural Resources Canada during August 2021. For this study we chose 7 distinct locations within the lagoon system as well as one thermokarst lake. Using a boat, we took surface water samples using a water sampler (UWITEC, Austria), collected Conductivity-Temperature-Depth (CTD) information by using a CastAway CTD device (SonTek, USA), and cored sediments using a gravity coring system (UWITEC Single Corer, Austria). A minimum of 2 cores were extracted from each site, with one core designated for microbiological analyses and subsequent incubation experiments. These cores were preserved within gas-proof bags filled with nitrogen gas to maintain anaerobic conditions and stored at a temperature of 4°C. A second core was reserved for sedimentological analyses and also stored at 4°C. The length of the cores varied from 10 cm to 49 cm.

Furthermore, active layer (AL) and permafrost samples were taken from a soil pit located on the lowland of Reindeer Island. The stratigraphy of the active layer was described and documented, with subsamples being selectively collected based on visual observations of distinct sediment layers. These subsamples were used for incubation experiments, including microbiological analyses and sediment analyses. Dimensions of the subsamples were recorded to calculate sample volumes for subsequent bulk density calculations. In addition, permafrost sampling was conducted using a Hilty hand drill, extracting uppermost permafrost samples extending to a depth of 12 cm. These permafrost samples were kept frozen in the field and transported to the Alfred Wegener Institute laboratories in Potsdam for further analysis.

Samples for incubation experiments were placed in precombusted glass jars, sealed and stored within nitrogen-filled gas proof bags. Biomarker samples were preserved in precombusted sterilized glass jars, and sediment samples for subsequent analyses were stored in sterile plastic bags (WhirlPack).

In the laboratory, the sediment cores were cut length-wise and the visual stratigraphy was described and documented. Subsamples were carefully extracted ranging from depths of 3 to 10 cm, intended for incubation and microbiological analyses. The edges of these subsamples were cleaned by scratching off the outermost material, and the sample material was deposited into pre-combusted glass jars. To minimize contact with oxygen, these jars were immediately flushed with nitrogen gas and subsequently stored in bags filled with nitrogen at a temperature of 4°C until the initiation of the planned experiments. Moreover, subsamples from one core half were taken every 5 cm for sedimentology and geochemistry analyses, while the other half was preserved in an archive freezer for future reference. The wet weight of all subsamples was recorded before further handling.

4.3.2 Hydrochemistry

Using Rhizon samplers (membrane pore size: 0.12-0.18 µm), pore water was collected from thawed samples for the hydrochemical pre-incubation analysis. The pH and electrical conductivity (EC in mS/cm) of the pore water were measured using a WTW Multilab 540, with an accuracy of ±0.01 for pH and ±1 mV for EC. After treating the DOC samples with 50 µL of 30% HCl supra-pure, they were stored at +4°C until analysis with a Shimadzu Total Organic Carbon Analyser (TOC-VCPH) following the protocol described by Fritz et al. (2015), with an accuracy of ±1.5%. Pore water for measuring sulfate concentration was diluted (1:50) and subjected to triplicate analysis using the Sykam S155 Compact IC-System ion chromatograph, which has a detection limit of 0.1 mg/L. The detected peaks in the chromatograms were automatically integrated using the ChromStar 7 program, and the triplicate average was used for further assessment.

Using the TEOS-10 MATLAB implementation, we were able to convert the measured electrical conductivity (with respect to 25 °C) to molality (mol/kg) and absolute salinity (g/kg) (McDougall and Barker, 2011). This conversion package assumes that the pore water fluid is consistent with standard seawater composition (Millero et al., 2008).

In order to be able to test GHG production in different sediments during the phases of landscape development (lake, lagoon, subsea), it is crucial to keep the boundary conditions (fresh: c = 0 g/L, brackish: c = 13 g/L, marine: c = 36 g/L) and the total water volume of 10.5 mL constant. For this purpose, we calculated based on the molarity of the pore water how much of the highly concentrated artificial seawater solution (c = 182.55 g/L) needed to be added to the samples. The artificial seawater solution had a higher concentration than that of standard seawater, so a relatively lower volume of water could be added to the sediment pore water and be diluted. The artificial seawater contained of NaCl (24.99 g/L), $MgCl_2 \times 6H2O$ (11.13 g/L), Na_2SO_4 (4.14 g/L), $CaCl_2 \times 2H_2O$ (1.58 g/L), KCl (0.79 g/L) and $NaHCO_3$ (0.17 g/L) dissolved in ultrapure water and sterile filtered after.

4.3.3 Sedimentological and biogeochemical bulk analyses

Prior to and following freeze-drying (using a Zirbus Sublimator 15), the sediment was weighed, and the weight difference between the wet and dry sediment was used to calculate the absolute water content.

Grain-size analyses were performed using a Malvern Mastersizer 3000 with a connected Malvern Hydro LV wet-sample dispersion machine on organic-free (processed with 35 percent H_2O_2) samples. The percentages of silt, clay, and sand are given as sums between 2 mm and 63 µm, 63 µm and 2 µm, and less than 2 µm, in that order. Grain-size parameters were computed using Gradistat (Blott and Pye, 2001; Version 8.0).

The total carbon (TC) and total organic carbon (TOC) content (expressed in weight percent, wt%) of homogenised and milled bulk samples (using a Fritsch Pulverisette 5 planetary mill) were analyzed using a soliTOC cube, and the total nitrogen (TN) content was determined using a rapid max N exceed (both Elementar Analysensysteme, Langenselbold, Germany); both instruments had a device-specific accuracy of ± 0.1 wt% and a detection limit of 0.1 wt%. Carbonates were removed from sediments using 1.3 molar hydrochloric acid (HCl) at 50 °C for five hours in order to perform stable carbon isotope analysis of organic carbon. The samples were then dried once more after being cleaned of chloride ions.

Next, at the AWI ISOLAB Facility Potsdam, stable carbon was analyzed with a ThermoFisher Scientific Delta-V-Advantage gas mass spectrometer fitted with a CONFLO IV and a FLASH 2000 elemental analyzer.

4.3.4 Incubation Experiment

To analyze how CO_2 and CH_4 production differs within a lagoon system (objective 1), given that well-connected lagoons (LAG7, LAG12, LAG14, LAG16) have been under seawater influence for a longer period and to a greater extent than poorly connected, younger lagoons (LAG4, LAG13), we incubated subsurface samples (3-10cm depth) of the lagoons anoxic under brackish (c=13 g/L) and marine (c=36 g/L) conditions using artificial seawater for 415 days. As oxygen has a negative impact on anaerobic microbial populations, we disposed of the first three cm of the sample and kept the environment oxygen-free for the duration of the incubation and sample processing (handling and overnight thawing at 8 °C in a glovebox under N_2 atmosphere).

To investigate the variation in CO_2 and CH_4 production with increasing seawater influence in a land-sea transect (objective 2) we incubated permafrost, lake, and lagoon samples, 4, 3, 16) under increasing saline conditions as described in (Jenrich et al., 2024b). In short, we incubated the terrestrial samples (P2-P, P2-AL, TKL5) with freshwater to simulate near-natural lake conditions, brackish to simulate freshly formed lagoons, and with marine water to simulate established lagoons. We used sediments from the three lagoons (LAG4, LAG3, LAG16) because they differ in age and connectivity with the sea and therefore represent different states of lagoon development. The lagoon samples were incubated under brackish and marine conditions to simulate near-natural conditions depending on their pore water salinity. Permafrost and active layer samples have been incubated for 244 days while lagoon samples have been incubated for 415 days. Accordingly, the cumulative CO_2 and CH_4 after 244 days is used to answer question 2 (GHG production along land-sea transect).

In order to ensure similar boundary conditions for the samples and their individual treatments, we used the same dry weight (5g) and the same water content (10.5 mL) in all bottles, as well as the same salinity for the brackish and marine treatment. Therefore, depending on the initial pore water content and salinity, different amounts of wet soil had to be weighed in and different volumes of artificial seawater added for the samples respectively to the treatment (fresh: c = 0 g/L, brackish: c = 13 g/L, 373 marine: c = 36 g/L). We acknowledge that submerged sediments close to the coast of the Mackenzie Delta still experience brackish conditions, but for simplicity, we ignore the effects of river discharge.

Given the well-established anaerobic conditions in waterlogged soils in situ, we conducted the incubation anaerobically.

The samples were homogenized before being put into 120 ml glass incubation vials that had been previously combusted. For every treatment, three replicates were incubated at 4 °C for comparability with previous permafrost incubation studies (e.g., Jongejans et al., 2021; Tanski et al., 2019) and to roughly match with the temperature of the water at the bottom of the water bodies in the summer.

CO_2 and CH_4 concentrations were measured using gas chromatography (7890A Agilent, United States) equipped with a thermal conductivity detector and a flame ionisation detector, respectively, with helium as the carrier gas and a 100 °C oven furnace temperature. To prevent zonation in sediment and water, the incubation vials were shaken before each measurement. Using a gastight syringe, gas samples were extracted from the vials' headspace and promptly fed into the gas chromatograph. The measurements were taken five times in the first two weeks, then every week for the next seven weeks, and then roughly every two weeks after that. Gas concentrations were normalized to the dry weight of the sediment (gdw^{-1}). The total amount of CO_2 and CH_4 was calculated in µmol using the ideal gas law (Knoblauch et al., 2018) employing the gas concentration, headspace volume, water volume, pH, temperature, and solubility, including carbonate and bicarbonate concentrations for CO_2 calculations (Millero et al., 2007). Further, the average of CO_2 and CH_4 for each of the three replicates was calculated, and we used the TOC content to normalize the data to $gSOC^{-1}$. Rates were then determined using the measured time intervals. Cumulative values were obtained by subtracting the initial measurement from each subsequent one, allowing for the calculation of production rates.

4.3.5 Statistics

All data analyses were conducted in R version 4.3.2 (R Core Team 2023). The Wilcoxon signed-rank test for paired samples was used to assess differences between brackish and marine treatments for all lagoons (n=7) and all transect sites (n=6), respectively. Principal component analyses (PCA) were performed on range transformed data using the base R function princompto explore which biogeochemical parameters correlate with CO_2 and CH_4 production in the different connectivity classes. The parameters tested included surface water EC, TOC, TN, and $\delta^{13}C$ under both brackish and marine conditions. The PCA results were visualized in a biplot using the 'ggbiplot' package (Vu and Friendly, 2023).

4.4 Results

4.4.1 Surface Water Hydrochemistry

Table 4.1 summarizes the surface water properties of the lake and the seven lagoons. Only two of the lagoons we examined (LAG3, LAG12) had a depth shallower than 2 m, while the others ranged between 2.3 m and 7.4 m in depth. Average EC over depth measured in the lagoons ranged from 5.8 to 17.5 mS/cm and is therefore much lower than the average surface water salinity of the Arctic Ocean (52.8 mS/cm, 33.8 psu; Hall et al., 2023).

During summer, stratification occurred in the deeper lagoons due to freshwater discharge from the Mackenzie River, particularly evident in LAG7 with a temperature difference of approximately 8°C and an EC difference of around 27mS/cm between surface and near-bottom layers. No stratification was observed in the lake and shallow lagoons LAG12 and LAG13, while in LAG16, there was no difference in temperature but a variation in salinity.

Table 4.1 Lake (TKL5) and Lagoon (LAG) surface water properties: Connectivity Class (2: low to 5: very high - open lagoons), water depth, temperature (T), electrical conductivity (EC), and pH have been measured in the field in August 2021. Dissolved organic carbon (DOC) and sulfate concentrations were measured in the laboratory. Min: minimal, max: maximal, av: avererage.

Site	Class	Latitude (decimal	Longitude degree)	Depth (m)	T_{min} (°C)	T_{max} (°C)	T_{av} (°C)	EC_{min} (mS/cm)	EC_{max} (mS/cm)	EC_{av} (mS/cm)	DOC (mg/L)	Sulfate (mg/L)	pH
TKL5		69.6723	-134.2493	12.9	10.0	10.9	10.4	0.3	0.4	0.3	3.7	2.9	8.5
LAG13	2	69.6457	-134.3627	2.3	9.7	9.7	9.7	10.6	11.5	11.1	5.0	671.0	8.2
LAG4	3	69.6714	-134.2341	4.6	4.6	8.3	6.6	11.6	17.5	14.0	5.5	656.0	7.9
LAG14	3	69.6563	-134.3555	6.4	6.4	9.8	8.9	10.3	16.3	12.9	5.0	660.0	8.2
LAG3	4	69.6673	-134.2214	1.1	5.6	8.6	7.1	10.5	17.8	13.2	4.9	NA	8.2
LAG16	4	69.6678	-134.2669	2.9	8.8	9.8	9.4	5.2	15.1	8.3	5.3	328.0	8.2
LAG7	5	69.6792	-134.3428	7.4	0.8	8.7	6.4	5.9	33.1	17.5	6.0	385.0	7.8
LAG12	5	69.6918	-134.3502	1.2	9.2	9.4	9.3	5.6	6.0	5.8	5.4	351.0	8.2

4.4.2 Bulk Sediment Biogeochemistry and Pore Water Hydrochemistry

Results on bulk sediment biogeochemistry and pore water hydrochemistry are presented in Table 4.2. The TOC content of the sediment was lowest in LAG3 (1.45 wt%) and highest in the active layer (26.31 wt%). Nitrogen content ranged from 0.17 % in

LAG3 and LAG12 to 1.53 % in the active layer, followed by permafrost and LAG13. The C/N ratio was lowest in LAG3 (8.53) and highest in permafrost (30.91). The average C/N ratio in the lagoons was approximately 14±3. Additionally, the $\delta^{13}C$ composition was relatively homogeneous, ranging from -27.65 ‰ in the AL to -25.86 ‰ in LAG3.

Regarding pore water, water content was lowest in the permafrost sample and highest in the AL. EC of the pore water varied significantly, with the lowest salinity recorded in the freshwater lake (EC: 0.59 mS/cm, 0.02 g/L) and the highest in LAG7 (EC: 50.7 mS/cm, 33.4 g/L). DOC concentrations showed marked differences, with the lowest levels detected in the lake, LAG 3 and LAG 13 and the highest in the permafrost samples.

In surface water, sulfate concentration exhibited diverse patterns. The lowest levels were recorded in the lake (3 mg/L), while the highest was observed in LAG13 (671 mg/L). Similar sulfate concentrations were detected for LAG7, 12, and 16, as well as for LAG4, 13, and 14.

Table 4.2 Bulk sediment and porewater biogeochemistry of permafrost (PF), active layer (AL), thermokarst lake (TKL05), and thermokarst lagoons (LAG): Total organic carbon (TOC) and nitrogen (N) content, carbon to nitrogen ratio, stable 13C isotopes, water content (WC), electrical conductivity (EC), salinity, pH, and dissolved organic carbon content (DOC).

Sample	Bulk sediment					Porewater				
	sample depth [cm]	TOC [%]	N [%]	C/N	d13C [‰] vs. PDB	WC [%]	EC [mS/cm]	Salinity [g/L]	pH	DOC [mg/L]
P2_PF	44.3	16.38	0.53	30.91	-27.45	9.81	1.64	0.02	6.55	216
P2_AL	3.5	26.31	1.53	17.20	-27.65	70.16	3.44	0.05	6.58	NA
TKL05	5.5	2.72	0.25	10.88	-27.15	52.74	0.59	0.29	7.05	5.03
LAG13	5.5	6.38	0.46	13.87	-26.64	56.84	20.75	12.46	7.08	7.08
LAG04	5.5	2.84	0.23	12.35	-25.99	57.43	48.10	31.49	7.17	20.14
LAG14	5.5	2.95	0.21	14.05	-26.34	46.82	29.06	18.02	7.27	18.06
LAG03	4.5	1.45	0.17	8.53	-25.86	27.84	16.44	9.67	7.32	7.76
LAG16	5.5	2.99	0.18	16.61	-26.34	40.92	36.60	23.23	7.16	26.65
LAG07	5.5	2.98	0.18	16.56	-26.45	48.23	50.70	33.40	7.40	16.95
LAG12	5.5	2.65	0.17	15.59	-26.35	33.59	33.40	21.00	7.40	23.90

4.4.3 Grain Size Distribution

The particle size distribution analysis shows significant differences between permafrost and the active layer (Figure S4.1). Permafrost exhibited a predominance of fine silt particles, with a mean grain size of 8.1 µm, whereas the active layer was characterized by sandy sediment, with a mean grain size of 97.3 µm. Lagoons LAG4 to LAG16 displayed a consistent pattern of fine silt composition, with mean grain sizes ranging from 3.75 to 7.41 µm. However, Lagoon LAG3 stood out due to its very poorly sorted medium to coarse silt with a mean grain size of 34.2µm. LAG3 also has a second peak in the sandy fraction, which is very similar to the sandy active layer. It is also notable that the permafrost has a unimodal (one peak) distribution, as do most of the lagoons within a similar range as the permafrost, while the lake and LAG3 exhibit a bimodal (two peaks) distribution. The active layer is unimodal but has its peak in a different range. This suggests that at least two main processes contribute to the depositional regimes.

4.4.4 Greenhouse Gas Production

CO_2 and CH_4 Production in Lagoon Sediments After 415 Days of Incubation

The results on the cumulative anaerobic CO_2 and CH_4 production measured after 415 days for the lagoons are shown in Figure 4.2.

CO_2 production ranged from 1.68 to 4.33 mgCO_2 $g^{-1}C$ under brackish and from 3.78 to 5.35 mgCO_2 $g^{-1}C$ under marine conditions and the CH_4 production ranged from 0.00 to 4.55 mgCH_4 $g^{-1}C$ under brackish and from 0.00 to 0.16 mgCH_4 $g^{-1}C$ under marine conditions (Figure 4.2a). CO_2 production was significantly lower under brackish, compared to marine conditions ($p=0.016$), while CH_4 production was significantly higher under brackish conditions ($p=0.023$) (Figure 4.2b). For six of the seven lagoons no CH_4 production was observed under marine conditions. The highest cumulative CH_4 production rate was observed at brackish conditions below the limited-open LAG13 (4.55 ± 1.12 mgCH_4 $g^{-1}C$). CH_4 production started after 150 to 200 days for the LAG13, 4 and 16 under brackish conditions and for LAG13 after 360 days under marine conditions (Figure S4.1). For Lagoons 14, 3, 7 and 12 no methane production was observed in the timeframe of the experiment.

LAG14 and LAG4, both categorized with medium connectivity (Class 3), exhibit very similar CO_2 productions under brackish conditions of 2.33 ± 0.32 mgCO_2 $g^{-1}C$ and 2.20 ± 0.17 mgCO_2 $g^{-1}C$, respectively, while under marine conditions LAG14 produced more CO_2.

Mostly open Class 4 lagoons, LAG3 and LAG16, both categorized with high connectivity to the sea, demonstrate different cumulative CO_2 productions under brackish conditions of 4.24 ± 0.46 mgCO_2 $g^{-1}C$ and 1.68 ± 0.05 mg mgCO_2 $g^{-1}C$, respectively but similar CO_2 production under marine conditions.

The very highly connected Class 5 lagoons, LAG7 and LAG12, both show high CO_2 production under brackish and marine conditions. Highest CO_2 production of all lagoons was observed in LAG12 with 5.35 ± 1.12 mgCO_2 $g^{-1}C$.

Relationships between biogeochemical parameters and gas production: Based on the principal component analysis (Figure S4.2, S4.3) of the parameters brackish and marine CO_2 and CH_4 production, TN, TOC, $\delta^{13}C$, and surface water EC, the sites are grouped by openness, with the most closed lagoon forming one group and the more open lagoons forming another. CO_2 production correlates with surface water EC but not clearly with substrate parameters, while CH_4 production correlates with substrate parameters in brackish and marine incubations.

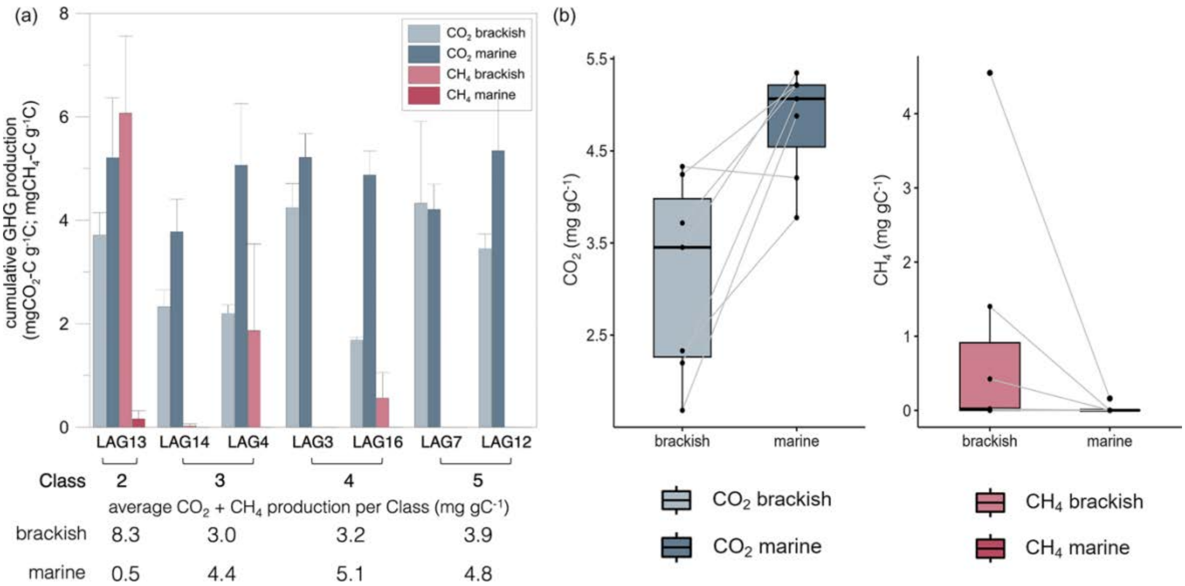

Figure 4.2 Cumulative CO_2 (mgCO_2 g^{-1}C) and CH_4 (mg mgCH_4 g^{-1}C) production of surface sediment from the seven lagoons of varying seawater connectivity under brackish (13 g/L) and marine (36 g/L) conditions after 415 days of anaerobic incubation. a: Grouped barplot with lagoons (LAG) ordered by connectivity class from low connectivity (Class 2) to very high connectivity (Class 5) to the sea. Error bars indicate standard deviation. b: Treatment comparison - paired box-whisker plots with connected data points (lines). The treatment has a significant effect on both CO_2 and CH_4 production (two-sided Wilcoxon test: p=0.031 and p=0.047, respectively).

4.4.4.1 CO_2 and CH_4 Production of Permafrost, Lake and Lagoon Sediments After 244 Days of Incubation

The incubation with fresh water, which represents natural conditions for the terrestrial sites showed that the thermokarst lake sample exhibited the highest cumulative CO_2 production of 2191 ± 136 µgCO_2 g^{-1}C, while the permafrost sample showed the lowest CO_2 production at 230.49 ± 16.95 µgCO_2 g^{-1}C (Figure 4.3A). The highest cumulative CH_4 production was measured in the active layer sample with 133.73 ± 13.53 µgCH_4 g^{-1}C (Figure 4.3B). In contrast, the thermokarst lake sample exhibited the lowest CH_4 production at 81.78 ± 17.14 µg CH_4g^{-1}C.

Under brackish conditions, the permafrost sample exhibited the lowest CO_2 production of 551.44 ± 25.38 µgCO_2 g^{-1}C. Even though brackish conditions are not natural for microbes in terrestrial settings, the active layer sample showed the highest cumulative CO_2 production (7997.90 ± 2349.58 µgCO_2 gC^{-1}), followed by the mostly open lagoon LAG3 (5495.74 ± 2631.84 µgCO_2 g^{-1}C) (Figure 4.3A). Regarding CH_4 production, the LAG4 sample displayed the highest cumulative production under brackish conditions with 198.10 ± 224.93 µgCH_4 g^{-1}C, while the active layer sample showed the lowest average CH_4 production at 0.2 ± 0.15 µgCH_4 g^{-1}C (Figure 4.3B).

Under marine water treatments, the most CO_2 was produced in the LAG3 sample (5874.11 ± 313.20 μgCO_2 g^{-1}C), while the lake sample showed the lowest CO_2 production (626.79 ± 1310.36 μgCO_2 g^{-1}C) (Figure 4.3A). Regarding CH_4 production, the permafrost sample displayed the highest cumulative production of 5.17 ± 1.36 μgCH_4 g^{-1}C, while the active layer sample showed the lowest CH_4 production at 0.07 ± 0.03 μgCH_4 g^{-1}C. However, CH_4 production under marine conditions was generally low for all samples (Figure 4.3B).

In Figure 4.3C, CO_2 and CH_4 production is compared by treatment. By testing the effect of the treatment on CO_2 and CH_4 production in a paired Wilcoxon test for the 6 transect settings, we found that CO_2 production does not differ significantly between brackish and marine treatments ($p=0.844$), but CH_4 production is significantly higher under brackish than marine conditions ($p=0.031$). If all 10 sites are considered, the difference is stronger (Wilcoxon test, paired, two-sided, $p=0.03711$).

Relationships between biogeochemical parameters and gas production: Based on the principal component analysis (Figures S4, S5) of the parameters brackish and marine CO_2 and CH_4 production, TOC, $\delta^{13}C$, and surface water EC, terrestrial and lagoon sites group separately. CO_2 production in brackish incubations shows no correlations, while in marine incubations, CO_2 production is positively correlated with $\delta^{13}C$ and surface water EC. CH_4 production in brackish incubations is positively correlated with $\delta^{13}C$ and surface water EC, and negatively correlated with TOC, but shows no clear correlations in marine incubations.

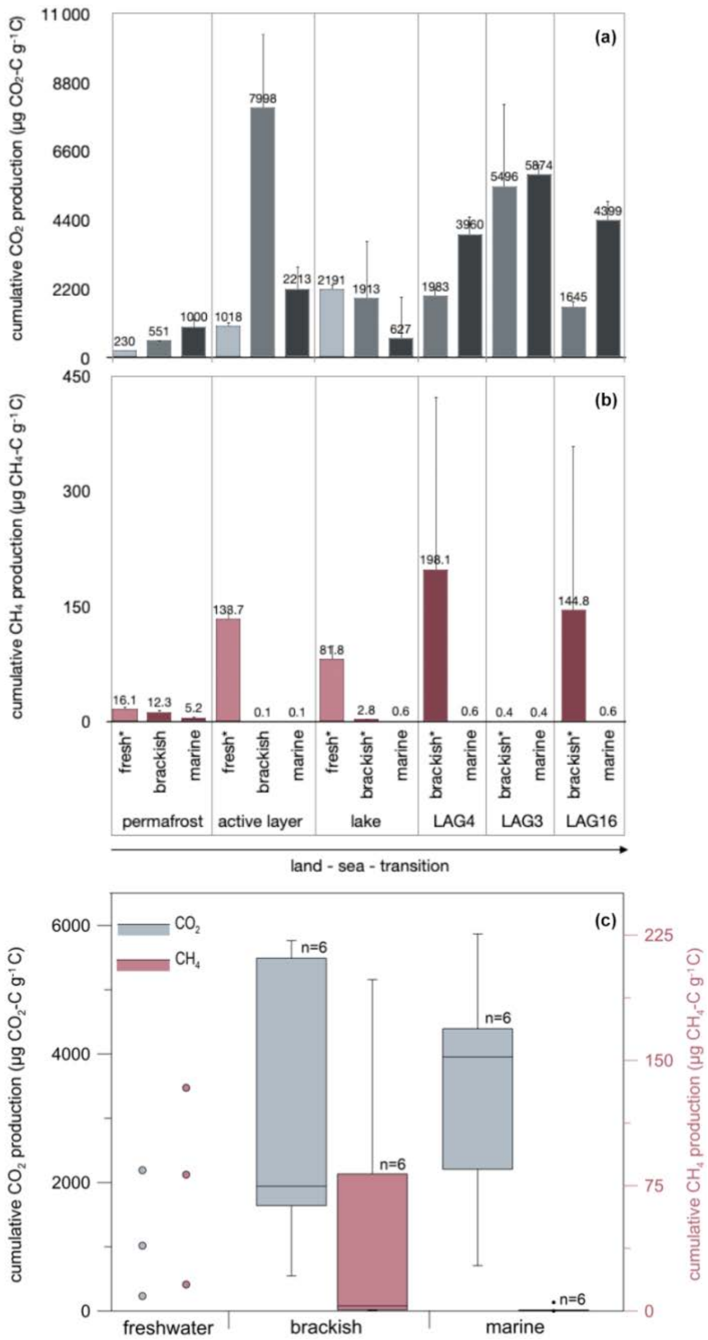

Figure 4.3 Cumulative A) CO_2 and B) CH_4 production after 244 days of anaerobic incubation at 4°C under an increasing seawater influence (treatment: fresh, brackish, marine conditions) and C) Box-whisker plots visualizing the effect of the treatment on CO_2 and CH_4 production. Note that CO_2 and CH_4 production are not at the same scale.

4.5 Discussion

The Reindeer Island lagoon system was first studied in 1994 to investigate the response of the Mackenzie Delta shoreline to changing hydrological influences (Solomon et al., 2000). Using seismic data to estimate the volume of flooded lake basins and sediment fill on Richards Island, along with estimates of sediment input from the Mackenzie River plume, they show that most of the sediment in the marine areas comes from tidal exchange with inner shelf water and storm surges. The study estimated that Richards Island's thaw lakes contain 250,000 tones of total organic carbon (Solomon et al., 2000). Almost 30 years later we revisited the study area to investigate the greenhouse gas production within the lagoon system and along a land-sea transition transect to get a better understanding on carbon dynamics in these transitional environments.

4.5.1 Variations of CO_2 and CH_4 Production within the Lagoons System

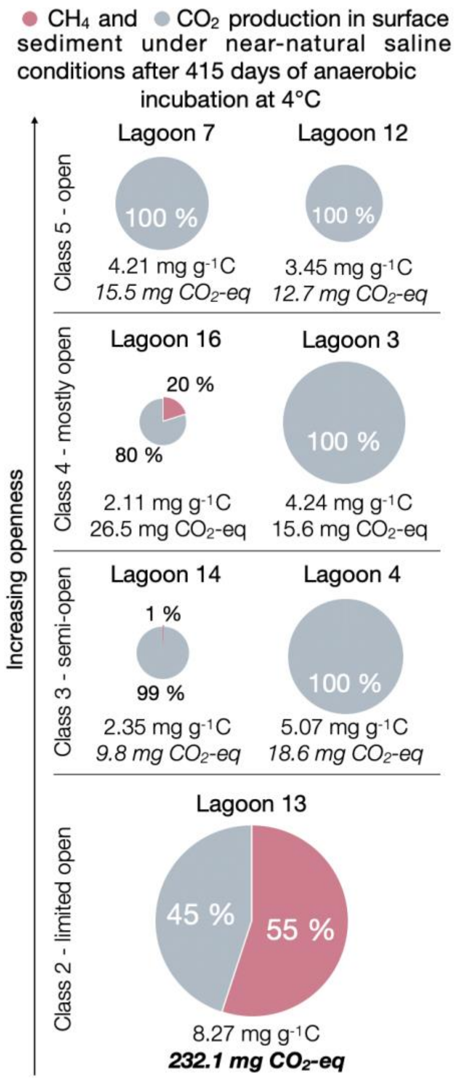

Figure 4.4 Cumulative CO_2 and CH_4 production in subsurface lagoon sediments after 415 days of anaerobic incubation under near-natural salinity conditions which are brackish conditions for Lagoons 12, 16, 3, 14 and 13 and under marine conditions for Lagoons 7 and 4. The size of the pie diagram is proportional to the total production of CO_2 and CH_4 in mg g^{-1}C (number below pie). The share of CH_4 (pink) and CO_2 (grey) for the total production of CO_2 and CH_4 (in mg g^{-1}C) is given in percent. The total in CO_2 equivalents is based on 36 gCO_2eq/gCH_4 for GWP100 (Balcombe et al., 2018). Map: true color sentinel 2 satellite image from 2021-08-26.

We found that the production of greenhouse gases within a lagoon system changes with increasing connection to the sea. In Figure 4.4, we show cumulative CO_2 and CH_4 production under near-natural saline conditions. Here, we define near-natural as brackish for pore water salinity of less than 24.5 g/L (mean of brackish (13 g/L) and marine (36 g/L) treatment), which was the case for LAG12, 16, 3, 14, and 13 and marine for pore water salinities greater than 24.5 g/L, LAG 7 and 4. In the youngest, less open LAG13 (Class 2), methane production was observed to be the highest (Figure 4.2). Observing CH_4 production in sulfate-containing environments is surprising, as the current understanding is that sulfate-reducing bacteria (SRB) outcompete methanogens for the major substrates hydrogen and acetate (Holmes et al., 2017; Kristjansson and Schönheit, 1983; Lovley et al., 1982; Olefeldt et al., 2013; Schönheit et al., 1982). Nevertheless, CH_4 production under brackish conditions in young lagoons has been observed before (Jenrich et al., 2024b; Yang et al., 2023). In these environments, which are in the early stages of transitioning from a terrestrial lake to a lagoon, terrestrial methanogens are still present. Under low sulfate levels, methanogens and SRB can coexist (Dar et al., 2008; Yang et al., 2023). LAG13 shows the highest TOC concentrations, which additionally was less depleted in ^{13}C. The higher availability of still high-quality organic matter for microbial decomposition is likely also driving this enhanced methane production. High CH_4 production is accompanied by high CO_2 production, indicating that in this initial stage of the land-sea transition, total GHG production reaches its peak. In terms of CO_2 equivalents, calculated based on 36 gCO_2eq/gCH_4 for a Global Warming Potential (GWP)100 (Balcombe et al., 2018), the CO_2-eq of LAG13 is significantly higher—up to 18 times—compared to the open lagoons (e.g. LAG12). This is in line with the results of Jenrich et al. (2024a), where the highest CO_2 and CH_4 production was also detected for the most closed lagoon (Class 1 after Jenrich et al., 2024a) under brackish conditions. Consequently, young lagoons with high OM content and quality exert the greatest climate impact among the studied lagoons (Figure S4.2). However, compared to current values, CO_2 production in the lagoons of this study area is lower than that of the studied lagoons on Bykovsky Peninsula, Siberia (Jenrich et al., 2024b). There, the maximum CO_2 production reached up to 23 $mgCO_2\ g^{-1}C$ for lagoon sediments (Class 1) under brackish conditions after one year of anaerobic incubation. Unlike the Reindeer Island lagoon system, the lagoons on the Bykovsky Peninsula are located in the Yedoma domain (Jenrich et al., 2021b; Strauss et al., 2021). Geographical differences and deposition mechanisms likely influence the colonization of microorganisms, which in turn could explain the variations in CO_2 production.

As the openness of the lagoon increases, signifying a longer exposure of the lake basin to marine conditions, methane production decreases drastically. In our Class 5 lagoons only CO_2 production was detected, which was similar to or even higher than that in LAG13. This indicates a shift in dominant biogeochemical processes with prolonged marine influence, evidenced by the enrichment in $\delta^{13}C$ values (from -26.64‰ to -26.34‰) and a decrease in TOC content (from 6.38 wt% to 2.65 wt%).

The porewater salinity of the studied lagoons exhibited considerable variation (Table 4.2) despite all having brackish surface water salinity during the summer (Table 4.1). This variation was also highlighted by Solomon et al. (2000) and can be attributed to differences in pore size and water depth among the lagoons. For example, LAG3, which is shallower (1.3 m depth) and has sandy sediment, shows a lower pore water salinity (16.44 mS/cm). In contrast, the neighboring LAG4, with a greater depth (4.6 m) and finer-grained sediment, exhibits a much higher pore water salinity (48.1 mS/cm). LAG3 tends to freeze to the bottom in winter due to its shallow depth, significantly impacting the salinity dynamics. During the formation of lagoon ice, high saline brines form at the lagoon bottom (Angelopoulos et al., 2020b; Jenrich et al., 2021b). These brines can infiltrate into the sediment, as high pore water salinities observed in LAG4 suggest. Bottom-fast ice can freeze the underlying sediment, potentially expelling salts further down, resulting in maximum salinities at greater depths (Jenrich et al., 2021b). In LAG4, which contains fine-grained sediments, the downward diffusion of salt is slower compared to lagoons with coarser-grained sediments, leading to higher salinities in the surface layers. The combination of these factors—ice formation, brine infiltration, sediment grain size, and water depth—creates complex salinity profiles within these thermokarst lagoons, influencing biogeochemical and microbial processes.

Greenhouse gas production varies between lagoons within the same class. LAG4 (Class 3), under near-natural (marine) conditions, produces more than twice as much CO_2 as the brackish LAG14 (Class 3) (Figure 4.4). However, when subjected to the same treatment, CO_2 production in both lagoons behaves similarly. The two lagoons differ in pore water salinity (31.5 vs. 18 g/L) and depth (4.6 m vs. 6.4 m), but they share similar biogeochemical and sedimentological parameters. Since the biogeochemical parameters in both lagoons are similar and the great water depth prevents bedfast ice formation, it is most likely that the composition of the microbial community is the reason for this difference, but no data is available to support this hypothesis. Despite their close proximity, Lagoons 3 and 16 differ in many parameters, which may cause the variation in GHG production. These differences include depth (1.1 m bedfast ice vs. 2.9 m floating ice), TOC (1.5% vs. 3%), C/N ratio (8.5 vs. 16.6), salinity (9.7 vs. 23.2 g/L), and DOC (7.8 vs. 26.7 mg/L). Under near-natural (brackish) conditions, Lagoon 3 produces 2.5 times more CO_2 than Lagoon 16, but no CH_4 production was detected within the experiment time frame. Many incubation studies have shown that methane production has a long lag time and can start much later than CO_2 production (Jenrich et al., 2024b; Jongejans et al., 2021; Knoblauch et al., 2013, 2018; Knorr and Blodau, 2009; Rivkina et al., 2007; Roy Chowdhury et al., 2015). Lagoon 3 is very shallow, and bedfast ice formation likely causes the upper sediment layers and the microbes within them to freeze. Freezing is a significant disturbance for microbes (Holm et al., 2020), especially for the slower-recovering and smaller methanogenic community. This is a possible reason why methane is produced in Lagoon 16 but not in the shallow Lagoon 3.

The observed differences in greenhouse gas production between lagoons within the same class highlight the potential influence of factors such as microbial community composition, salinity, and depth, while connectivity to the sea plays a crucial role in shaping the broader patterns of GHG production across different lagoon classes. Class 2 lagoons with low connectivity to the sea show the most dramatic difference between brackish and marine conditions, with significantly higher GHG production under brackish conditions, indicating that microbes are not yet adapted to higher salinities. Class 3 and 4 lagoons show a similar pattern, with a moderate GHG production under brackish conditions and a marked increase under marine conditions, indicating that microbes are already adapted to higher salinities at that stage of land-sea-transition.

Very open, Class 5 lagoons maintain relatively high GHG production under both brackish and marine conditions, with slightly higher production under marine conditions. Lagoons of this class exhibit the highest GHG production stability across both treatments, implying that microbes in very highly connected lagoons are less sensitive to changes in salinity compared to less open lagoons.

4.5.2 CO_2 and CH_4 Production along a Land-Sea Transition Gradient

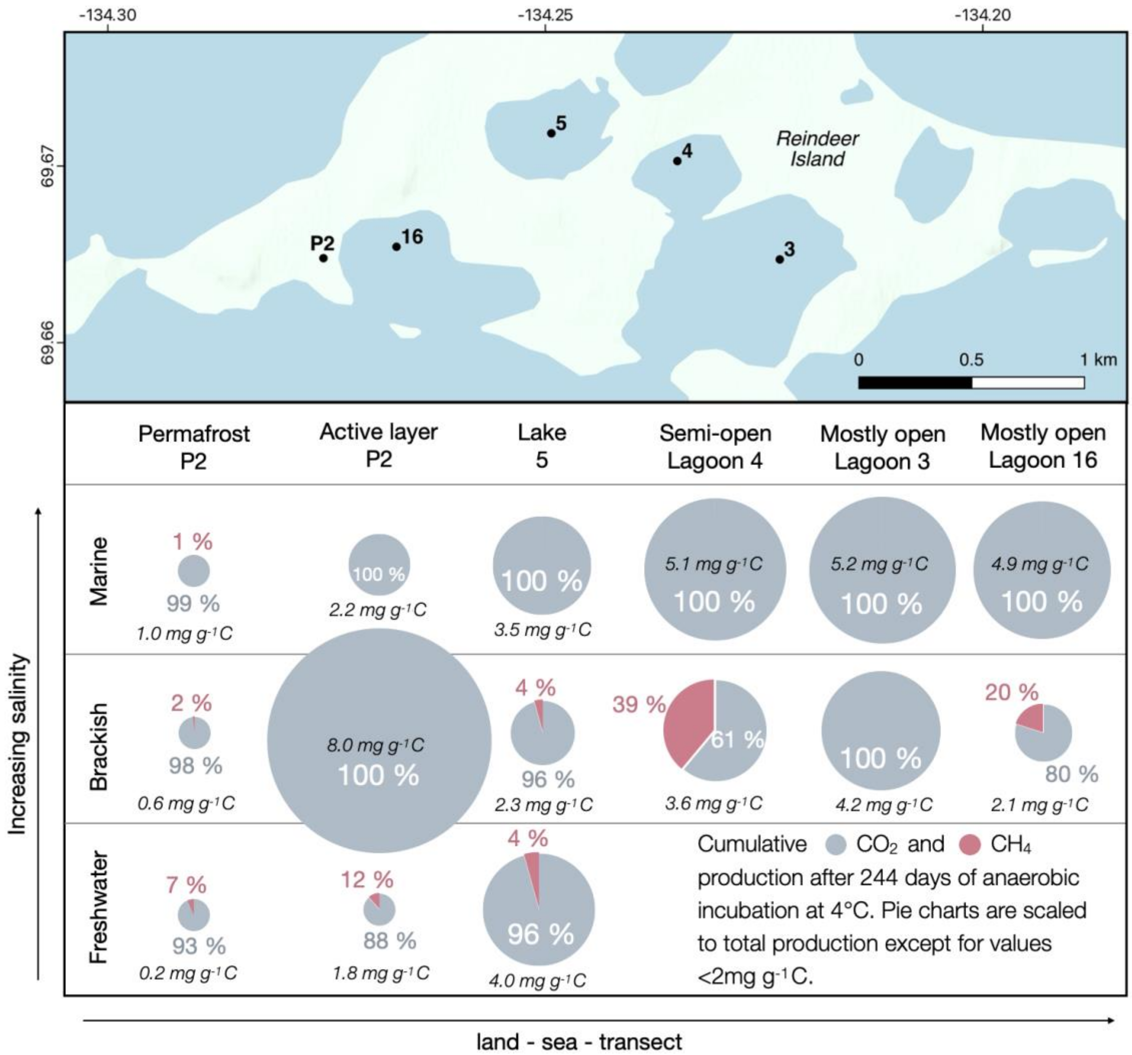

Figure 4.5 GHG production along a land - sea - transect. Cumulative CO_2 and CH_4 production after 244 days of anaerobic incubation under fresh, brackish and marine conditions for the terrestrial sites and under brackish and marine conditions for the lagoons. Total production normalized to gC. Map: basemap Esri.

The production of CO_2 and CH_4 varies significantly with increasing seawater (and thus salinity) influence along a land-sea transition gradient. Cumulative CO_2 and CH_4 production was measured after 244 days of anaerobic incubation under fresh, brackish, and marine conditions for terrestrial samples, and under brackish and marine conditions for the lagoons.

By incubating terrestrial permafrost, active layer, and lake sediment with freshwater, we simulated different stages of lake evolution reaching from a freshly formed pond after the first time of permafrost thaw to a young lake and an old lake respectively. The results demonstrated that the total GHG production increases as lakes evolve through these stages (Figure 4.5). CH_4 production in terrestrial samples is highest under freshwater conditions, where methanogens are best adapted (Wen et al., 2017), especially in the organic-rich active layer (Figure 4.3). In the active layer, the organic matter is less degraded than in the lake sediment. Further the sediment has thawed over many summers, so the microbial community is better adapted to current conditions than in the first-time thawed permafrost, which shows the lowest cumulative GHG production across all treatments. This suggests that microbial communities in these sediments need more time to establish than was allowed in this experiment. The long-term incubation study by Knoblauch et al. (2013) has revealed that the labile organic matter can be mineralized within the first 3 months but the turnover of stable carbon pools may take several thousands of years.

The incubation experiment revealed that methane production is highest in LAG4, the most closed along the transect, under brackish conditions (Figure 4.3). Compared to CO_2 production, CH_4 production starts after a long lag phase, assuming that sulfate concentrations were too high in the beginning of the experiment. In the end of the incubation sulfate was depleted in LAG4, conditions which promote methanogen activity and therefore CH_4 production (Dar et al., 2008). As marine conditions intensified, CO_2 production continued to rise, whereas CH_4 production stopped under marine conditions. The higher availability of sulfate as an electron acceptor is promoting SRB over methanogens under marine conditions (Kristjansson and Schönheit, 1983).

The observed increase in CO_2 production under marine conditions contrasts with findings from an incubation experiment using sediment from lagoons along the Bykovsky Peninsula coast in NE Siberia (Jenrich et al., 2024b), where higher salinities led to a decrease in CO_2 production. They suggested that microbes were better adapted to brackish, near-natural conditions than to marine conditions. Unlike the lagoons in this study, which are part of an interconnected system, the Bykovsky Peninsula lagoons are more isolated. It is possible that marine microorganisms are better distributed in a lagoon system, allowing them to colonize upper soil layers and adapt more effectively to marine conditions than in isolated lagoons. However, microbial analyses are needed to confirm this hypothesis. Further, the results of the PCA indicate that local conditions have the greatest impact on GHG production, therefore more studies are needed to get an understanding of the underlying mechanisms.

At Reindeer Island CO_2 production increased dramatically when the terrestrial active layer was inundated with brackish water for the first time, overshooting CO_2 production in lagoon sediments. This underlines that CO_2 production is highest in young, freshly formed lagoons or recently flooded coastal lowlands. In comparison, CO_2 production is much lower for active layer sediment incubated under marine conditions, showing that an extreme shift in salinity in a short timescale is not beneficial for microbial activity. The increase in CO_2 production from brackish to marine conditions in lagoon sediments demonstrates that once the former terrestrial microbial community has adapted to marine conditions during the slow process of seawater inundation, CO_2 production can pick up.

4.5.3 Incubation Experiments in the Context of Arctic Coastal Carbon Dynamics

Placing the greenhouse gas production rates we measured into the larger context of Arctic coastal carbon dynamics is challenging due to the limited number of comparable studies. Tanski et al. (2019) used a similar incubation setup to investigate carbon dioxide production from eroding coastal permafrost. Their CO_2 production values were higher; however, their setting is not directly comparable since they incubated under aerobic conditions where carbon turnover is known to be faster. Similar to our study, Tanski et al. (2019) found that CO_2 production is higher with seawater than without and concluded that CO_2 production is promoted along the coastal zones. Our investigation has shown that this effect occurs not only under aerobic conditions at the coast but also under anaerobic conditions in the sediment below the water column. The availability of sulfate as an alternative electron acceptor promotes SRB and leads to a shift from a balanced CH_4 and CO_2 production in young, less connected lagoons towards purely CO_2 production with ongoing marine impact.

Contrary to our findings, Lougheed et al. (2020) report higher in situ CO_2 concentrations in the water columns of freshwater systems (thermokarst ponds, lakes, and rivers) compared to saline and brackish systems (ocean, coastal lagoon, and brackish rivers) on the Arctic Coastal Plain in Alaska, USA. However, they did not survey thermokarst lagoons, which are distinct from coastal lagoons like the studied Elson Lagoon. Thermokarst lagoons originate from thermokarst lakes and therefore have a higher terrestrial signature than coastal lagoons. Elevated CO_2 concentrations in the nearshore waters of Elson Lagoon where the coastline is eroding highlights the role of terrestrial carbon and nutrient input (Tweedie et al., 2012). By studying the interface of sediment and the water column in Elson Lagoon, (Dunton et al., 2023) found a vertical gradient in CO_2 concentrations with high values at the lagoon bottom and a seasonal shift from net heterotrophic CO_2 release from sediments under ice to net autotrophic CO_2 uptake during break-up and open water. These findings underscore the complexity of carbon dynamics in Arctic coastal systems. So far we only know how much CO_2 and CH_4 is produced in thermokarst lagoon sediments under laboratory conditions. In-situ CO_2 concentration measurements of the water column would be needed to understand the carbon flux from the sediment to the atmosphere to predict their climate impact.

A total of 520 thermokarst lagoons exist along the coasts of the Laptev, East Siberian, Chukchi, and Beaufort shelf seas, including individual lagoons that are part of a larger lagoon system (Jenrich et al., 2024c). They are thus more than twice as abundant as the 216 identified coastal lagoons in the same region (Angelopoulos et al., 2021). More than half of the identified thermokarst lagoons are young, low connected lagoons (class 1 and 2) (Jenrich et al., 2024c). This study, along with the previous study by(Jenrich et al., 2024b), shows that these low connected lagoons, which are at the first stages of lake-to-sea transition, have the highest GHG production and therefore should be the focus of further research.

Laboratory incubations offer a controlled environment that provides valuable insights into how GHG production is influenced by specific factors, such as salinity. This approach allows us to isolate and understand the impact of single environmental parameters. However, while laboratory settings are excellent for focused investigations, they do not replicate the full complexity of natural environments, which involve a wide range of factors and interactions. In natural settings, various parameters, such as the duration of the open-water season, annual fluctuations in pH and water temperature, water depth, bathymetry, sediment and nutrient input from sources like the Mackenzie River, and plant-soil interactions, significantly affect GHG pathways in land-sea transitional areas. Due to the controlled nature of laboratory incubations, our study could not account for these additional variables. Despite this limitation, incubation experiments remain a valuable tool for studying GHG production and carbon dynamics in remote Arctic coastal environments. Future research should integrate laboratory experiments with field studies to encompass seasonal variations, water depth, and sediment interactions. This combined approach will provide a more comprehensive understanding of carbon fluxes and enhance predictions regarding how Arctic coastal systems will respond to environmental changes.

4.6 Conclusion

We found significant variations in GHG production along a gradient from terrestrial to marine settings in Arctic coastal regions. CH_4 production was high in terrestrial sediments under natural freshwater conditions due to methanogen adaptation. When Arctic permafrost lowlands are inundated with brackish water, CO_2 production accelerates. Young, less connected thermokarst lagoons, which comprise over 50% of the mapped pan-Arctic thermokarst lagoons, exhibited the highest CH_4 and CO_2 production. Their CO_2 equivalents can be up to 18 times higher than the open lagoons, attributed to high terrestrial organic carbon content and distinct microbial communities. As lagoons become more open, CH_4 production decreases or ceases, while CO_2 production rises with increased seawater influence. CO_2 production was significantly higher under marine conditions, whereas CH_4 production was significantly higher under brackish conditions.

Moreover, we found that pore water salinity in lagoon sediments was highly variable, but not directly related to the openness of the lagoon. Instead, water depth and the formation of bedfast ice, along with the associated brine exclusion, had the greatest impact on pore water salinity and thus likely on the lagoon GHG production potential.

In the context of climate change, thermokarst lagoons forming along Arctic permafrost coastlines with ice-rich permafrost and abundant thermokarst lakes and basins are a part of the overall permafrost-climate-feedback loop. Arctic warming, permafrost thaw, and accelerating permafrost coastal erosion likely will increase thermokarst lagoon formation, amplifying carbon release and contributing to further warming. Sea level rise further accelerates the transition from terrestrial to coastal environments in permafrost coastal lowlands, enhancing CO_2 production. Understanding these processes is crucial for predicting and mitigating the impacts of Arctic changes on global climate as well as capturing the full permafrost carbon picture in models.

4.7 Acknowledgements

We thank G. Tanski for helping organize field trip logistics. We further thank Jimmy Kalinek and Nya for boating us and for keeping us safe during fieldwork and remote camp life. We greatly thank our fieldwork assistant A. Flamand from Université du Québec à Rimouski for always having a helping hand and a bright mind. Thanks to A. Robertson for bringing a nitrogen bottle by helicopter which ensured keeping samples anoxic. For their essential help in the laboratories, we thank the Alfred-Wegener Institute Helmholtz Centre for Polar and Marine Research (AWI) and Helmholtz-Zentrum Potsdam Deutsches GeoForschungsZentrum (GFZ) lab technicians (J. Lindemann, A. Eulenburg, J. Serau, O. Burckhardt, S. Okolski).

4.8 Supplemental Material

4.8.1 Grain Size Distribution

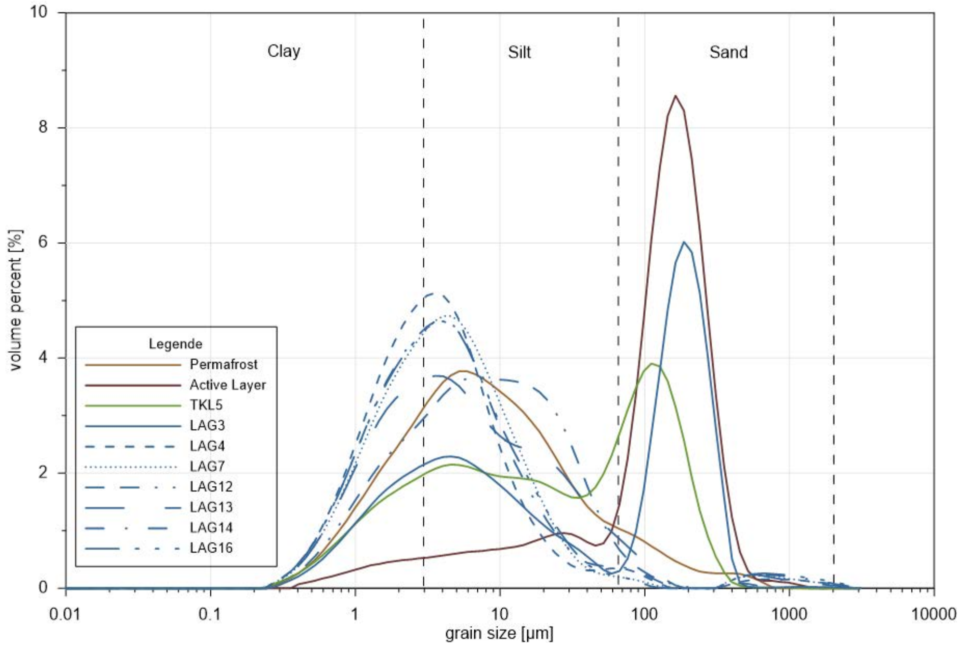

Figure S4.1 The particle size distribution of the surface sediment (mean of 0-10 cm subsamples) varies among different environments: permafrost and active layer (brown colours), thermokarst lake (green), and thermokarst lagoons (blue).

4.8.2 Principal Component Analysis (PCA)

4.8.2.1 Variations in CO_2 and CH_4 Production within a Lagoon System

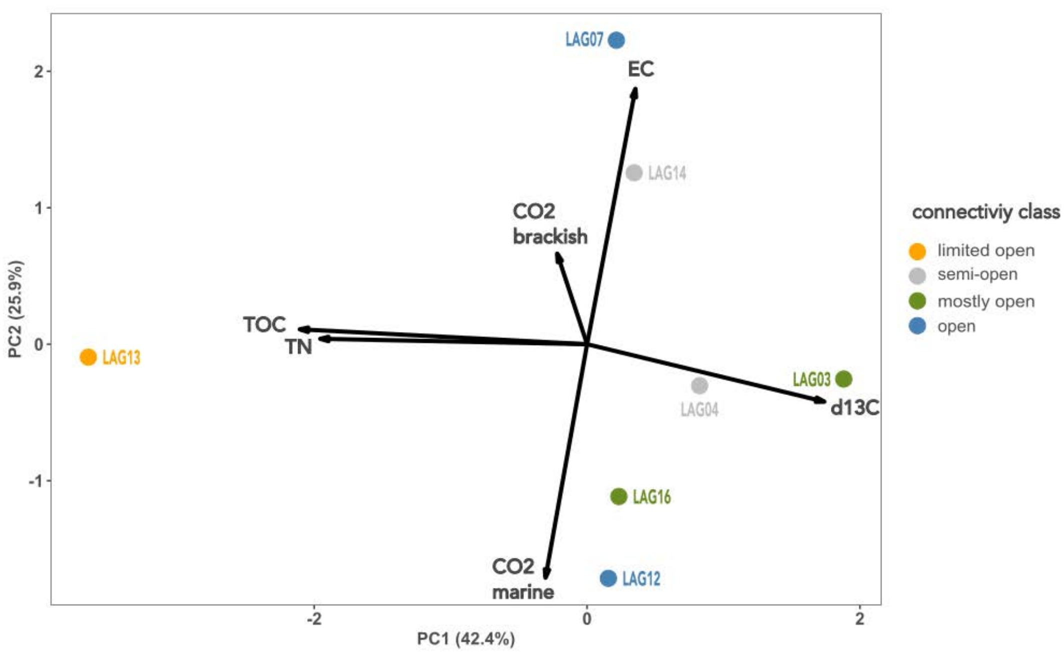

Figure S4.2. Principal component analysis of cumulative CO_2 production under brackish and marine conditions after 415 days, biogeochemical parameter (TN, TOC and $\delta^{13}C$) and hydrochemical parameter (surface water EC) for the 7 lagoons.

The PCA results for CO_2 production within the lagoon system show that the data clusters into two distinct groups: the young, most closed lagoon 13 is distinct to the more open lagoons. The main variance is explained by biogeochemical sediment properties, namely differences in TOC and TN content as well as $d^{13}C$, indicating that organic matter quality and quantity is the driving factor for CO_2 production in the lagoon system.

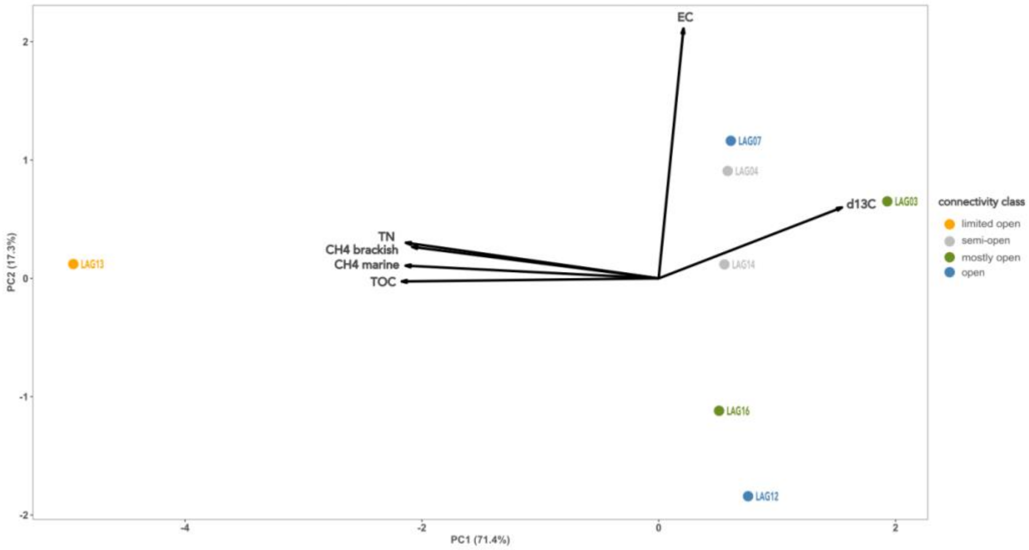

Figure S4.3 Principal component analysis of cumulative CH_4 production under brackish and marine conditions after 415 days, biogeochemical parameter (TN, TOC and $\delta^{13}C$) and hydrochemical parameter (surface water EC) for the 7 lagoons.

The PCA results for CH_4 production within the lagoon system show that the data clusters into two distinct groups: the young, most closed lagoon 13 is distinct to the more open lagoons. CH_4 production correlates with substrate parameters in brackish and marine incubations. Surface water EC does not seem to have an influence on CH_4 production.

4.8.2.2 Variations in CO_2 and CH_4 Production within a Lagoon System

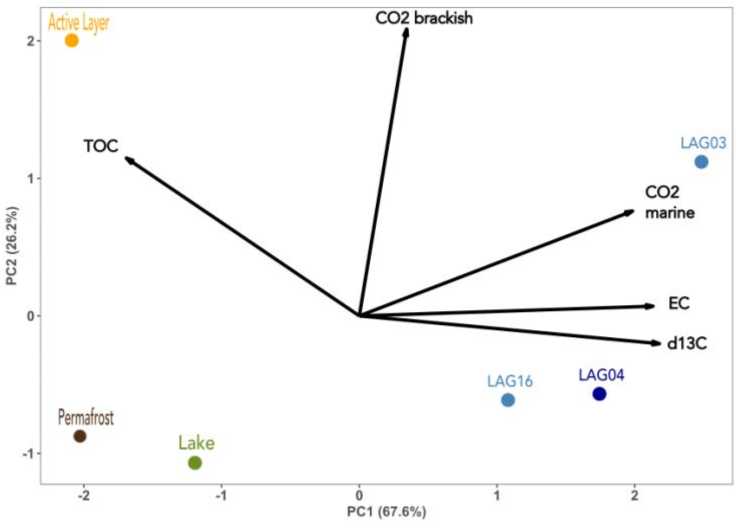

Figure S4.4 Principal component analysis of cumulative CO_2 production under brackish and marine conditions after 244 days, biogeochemical parameter (TOC and $\delta^{13}C$) and hydrochemical parameter (surface water EC) for the transect sites (PF, AL, TKL, LAG4, LAG3, LAG16).

The PCA results for CO_2 production show that the data clusters into two distinct groups: terrestrial sites and lagoons. Under brackish conditions, CO_2 production does not correlate with TOC, $\delta^{13}C$, or surface water EC. However, under marine conditions, a clear correlation emerges. Terrestrial sites, while high in TOC content, exhibit low CO_2 production under marine conditions, likely due to the microbial communities not yet being adapted to the higher salinities. This results in a misleading negative correlation between TOC and CO_2 production under marine conditions in the PCA.

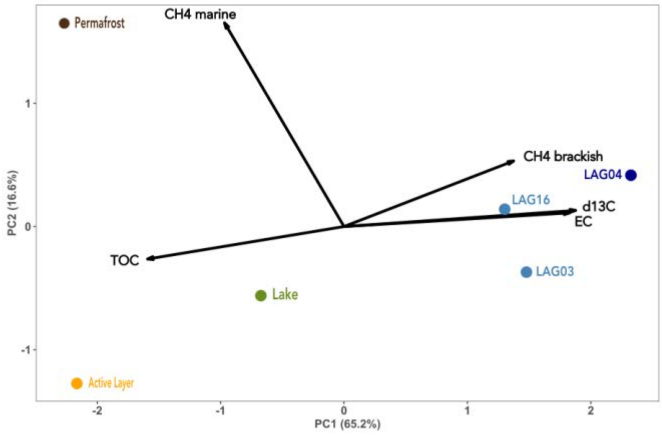

Figure S4.5 Principal component analysis of cumulative CO_2 production under brackish and marine conditions after 244 days, biogeochemical parameter (TOC and $\delta^{13}C$) and hydrochemical parameter (surface water EC) for the transect sites (PF, AL, TKL, LAG4, LAG3, LAG16).

The PCA results for CH_4 production show that the data clusters into four distinct groups: permafrost and active layer, lake, mostly-open lagoons, and semi-open lagoons. In brackish incubations, CH_4 production negatively correlates with TOC and positively correlates with $\delta^{13}C$ and surface water EC. Similar to Figure S4.4, the high TOC content of the terrestrial sites leads to a misleading negative correlation between TOC and CH_4 production. In marine incubations, CH_4 production does not show any significant correlation with TOC, $\delta^{13}C$, or surface water EC, indicating that other parameter, most likely microbial composition, are the driving factor for CH_4 production.

4.8.3 CO_2 and CH_4 Production over the Time of the Incubation

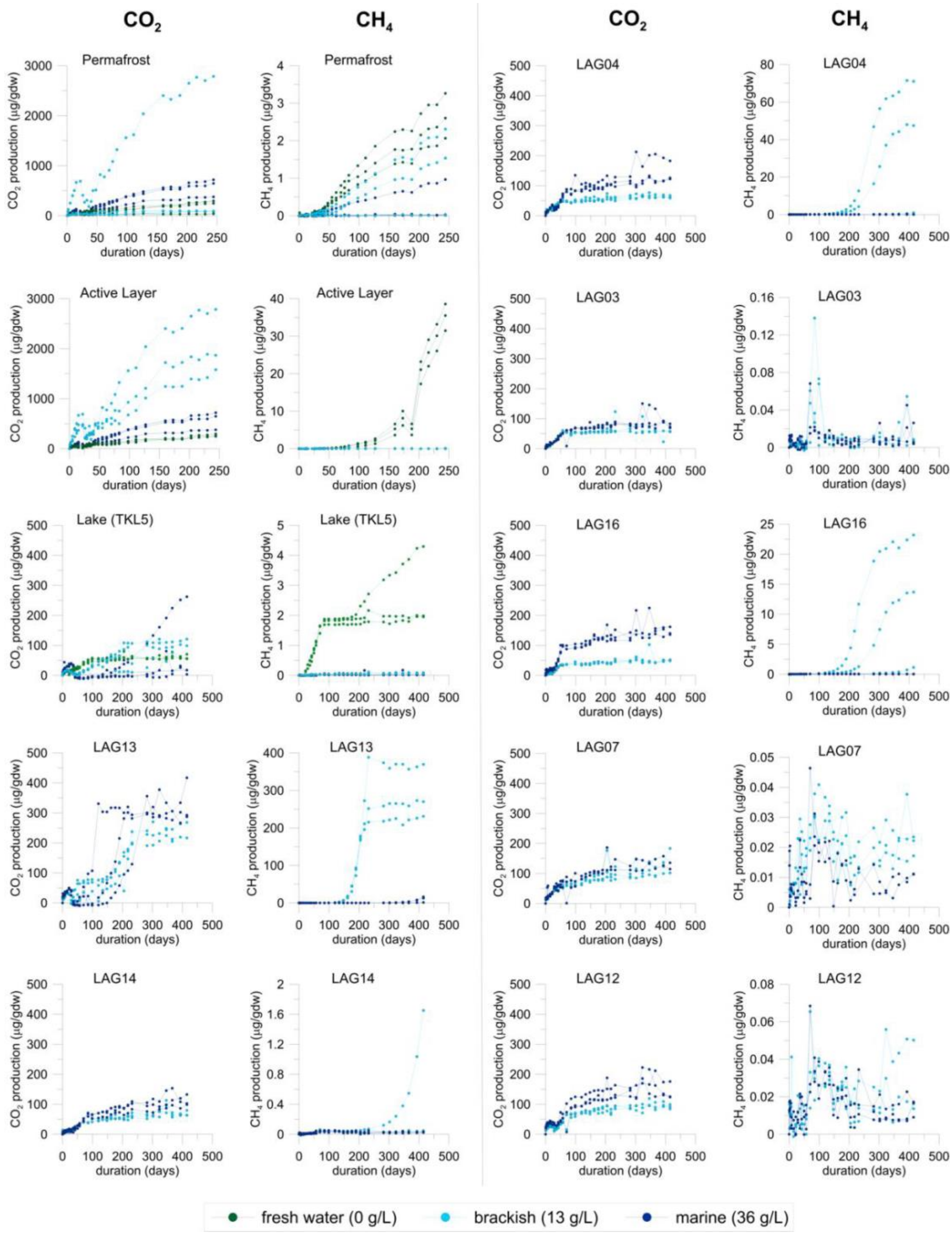

Figure S4.6 Cumulative anaerobic CO_2 and CH_4 production in µg per gdw for the terrestrial permafrost and active layer (a-d) during the 244-day incubation experiment and for lake and lagoons (e-t) during the 415-day incubation experiment at freshwater (green), brackish (turquoise) and marine (dark blue) conditions. Error bars representing the standard deviation.

5

Potential Future Greenhouse Gas Production in Deep Thawing Permafrost Sediments Under Saltwater Impact

5.1 Introduction

Terrestrial permafrost can reach thicknesses of up to 1600 m and holds a vast amount of organic carbon (~1460–1600 Pg (= 10^9 t = 10^{12} kg) on land, and in total more than 4300 Pg including organic carbon in subsea permafrost (Lindgren et al., 2018; Miesner et al., 2023; Miner et al., 2022; Schuur et al., 2022; Strauss et al., 2024). Once thawed, organic matter becomes partially available for microbes which is then decomposed into GHGs such as CO_2 and CH_4, further fueling climate warming.

The thaw of ice-rich permafrost causes land surface subsidence, forming thermokarst features like ponds, lakes, and lagoons. Thermokarst lagoons form when these features are breached by the sea due to coastal erosion (Günther et al., 2013; Jones et al., 2018; Nielsen et al., 2022) or sea-level rise (Guimond et al., 2021; Nerem et al., 2018; Proshutinsky et al., 2001; Watson et al., 2015). These lagoons combine traits of terrestrial and marine systems (Harris et al., 2017; Jenrich et al., 2021b; Kjerfve, 1994; Tagliapietra et al., 2009; Yang et al., 2023). The connectivity with the sea affects water and sediment exchange, influencing salinity, ionic composition, and nutrient levels (Tagliapietra et al., 2009).

Salt diffusion into sediments forms saline ground (Angelopoulos et al., 2020b, a; Jenrich et al., 2021b). Shallow lagoons (~<2m depth) can develop hypersalinity due to ice formation expelling salts into the sediment (Jenrich et al., 2021), creating environments where only halophiles survive. In marine environments, sulfate-reducing microorganisms use sulfate to produce sulfide (S2-) or oxidize CH_4. Sulfate-reducers outcompete methanogens in high sulfate concentrations, reducing CH_4 production (Holm et al., 2020; Kristjansson and Schönheit, 1983; Olefeldt et al., 2013; Schönheit et al., 1982). Seawater intrusion into lagoons introduces sulfate ions, altering CH_4 production and oxidation.

Understanding carbon cycling in these transitional coastal permafrost environments is limited. Building on the study by Jenrich et al. ((2024a); see Chapter 3), in which we observed CO_2 and CH_4 production and microbial changes in near-surface sediments during the transition from terrestrial to marine systems, we focus in this study on the potential future GHG production in deep sediments.

With incubation experiments, OM decomposition can be studied in controlled laboratory environments, and changing conditions can be simulated (Laurent et al., 2023; Tanski et al., 2019). Factors influencing OM decomposition include OC content (Knoblauch et al., 2013; Treat et al., 2015), OM quality (Jongejans et al., 2021), temperature (Schädel et al., 2016), salinity, and oxygen availability (Laurent et al., 2023; Schädel et al., 2016). Another study has shown that CO_2 production from permafrost OC remains high under both freshwater and marine conditions (Tanski et al., 2019). While many studies focus on GHG production in the upper layer of terrestrial permafrost and thermokarst landscapes (Galera et al., 2023; Heslop et al., 2015, 2019, 2020; Knoblauch et al., 2013, 2018; Kuhry et al., 2020; Lee et al., 2012), little is known about the potential GHG production in deep (>10 m) terrestrial permafrost sediments (Dutta et al., 2006; Jongejans et al., 2021; Lee et al., 2012). To our knowledge no studies have incubated deep seawater influenced permafrost and talik sediments.

Here, we studied GHG production and microbial composition in permafrost, lake talik and lagoon sediments in depth of up to 32 m under marine conditions in controlled one-year laboratory incubation experiments. With that, we aim to answer the question "what is the potential future GHG production in deep, thawed permafrost sediments after seawater inundation?"

5.2 Sampling Approach and Study Site

To answer the research question a deeper drilling approach was realized. Details are presented in Strauss et al. 2018. Drilling deep cores in remote Arctic locations is logistically challenging and samples are very rare, which makes this dataset very unique.

The Bykovsky Peninsula, southeast of the Lena Delta in northeastern Siberia (Figure 5.1a, b), features fine-grained late Pleistocene ice-rich Yedoma deposits and Holocene thermokarst lake and basin sediments (Schirrmeister et al., 2011, 2002; Sher et al., 2005). Thermokarst processes shape the landscape, with thermokarst lakes covering 15% and affected areas, including drained lake basins, making up over 50% of the peninsula (Grosse et al., 2005, 2008). The diverse topography includes Yedoma uplands, thermokarst depressions, and thermal erosional valleys.

We investigated a terrestrial permafrost (TPF) outcrop and three sediment cores from water bodies on the south coast of the peninsula. The TPF outcrop (71.85175°N, 129.350883°E) is a retrogressive thaw slump exposing 2.9 m of ice-rich terrestrial sediments (Figure 5.1 c). The lower section consists of Yedoma with ice-rich silts, topped by a brown sedge peat horizon, indicating initial thermokarst development. Above this are organic-rich deposits with peat and woody remains. The surface layer includes organic-rich silt and Sphagnum moss, with an active layer about 0.3 m thick. The topmost samples serve as the terrestrial endmember for thermokarst settings.

Thermokarst Lake Goltsovoye (TKL) (71.74515°N, 129.30217°E; Figure 5.1 d-f) formed about 8,000 years ago. The sediments transition from coarse with pebbles at the core bottom to finer grains towards the top. Below 29.15 m, sediments are frozen, while the upper part contains unfrozen silty talik sediments with fresh pore water (Jongejans et al., 2020).

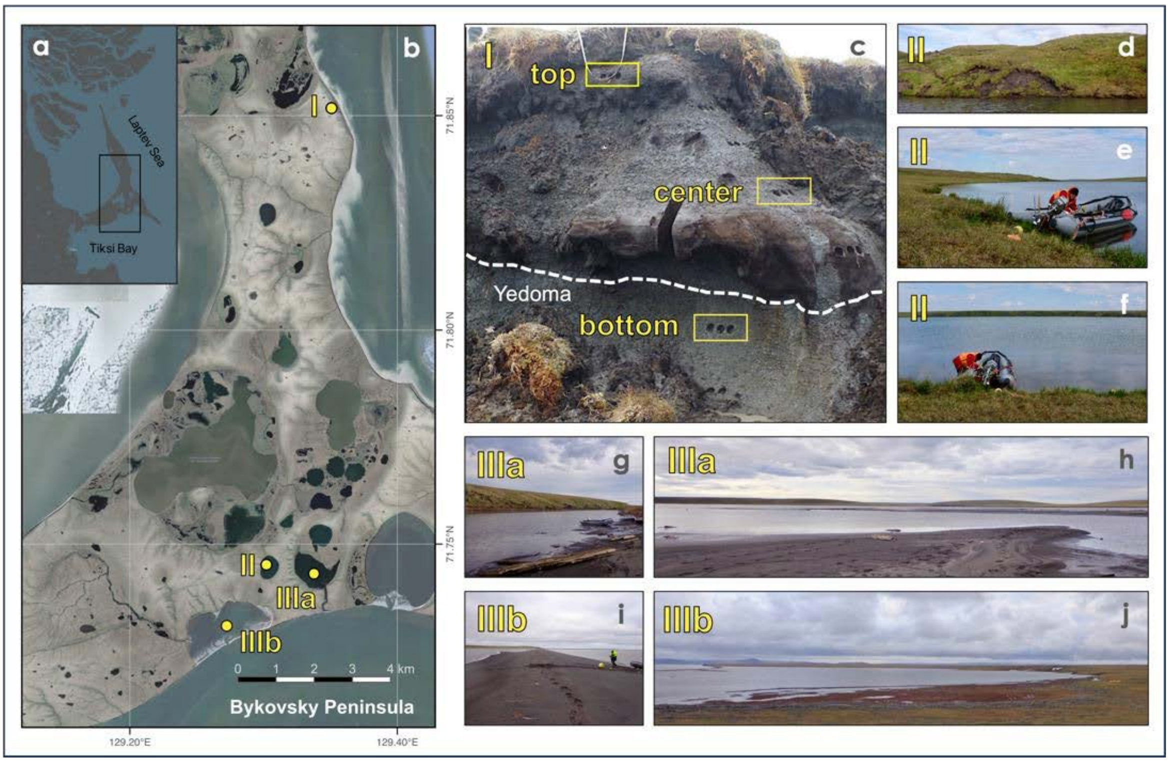

Figure 5.1 Study sites located on the Bykovsky Peninsula in Northeast Siberia, southeast of the Lena Delta (a). Close-up of central Bykovsky Peninsula, coring locations are marked by a dot (b) - I: Permafrost outcrop (TPF) located at an Upland on the West Coast, two coring locations in thermokarst cover deposits overlying Yedoma and one at the top of Yedoma marked by the yellow rectangles (c); II: Thermokarst Lake Goltsovoye (TKL) (d,e,f), drilling occurred about 60 m off the shore; IIIa: nearly-closed thermokarst lagoon Polar Fox (LAG1) temporarily connected to the sea in summer by a channel (g,h) and IIIb: semi-open lagoon Uomullyakh (LAG2) separated by a sand barrier (i,j) with a small inlet are located in close distance to each other on the southern coast of the peninsula. Imagery sources: a: ESRI base map; b: satellite map is a combination of Google Satellite Hybrid base map and a hillshade map derived from the stereophotogrammetric DEM 3 epipolar based on WorldView imagery from 2015; c: Photo by G. Grosse in summer 2014; Photos d-j: by M. Angelopoulos in summer 2017. Modified after Jenrich et al. (2024a)

Polar Fox Lagoon (LAG1) (71.743056°N, 129.337778°E; Figure 5.1 g,h) is a nearly-closed lagoon in a partially drained lake basin, connected to Tiksi Bay by an 800 m long channel. This connection, frozen for about 8 months annually, results in seasonal isolation and increased salinity beneath the ice cover (Angelopoulos et al., 2020b; Spangenberg et al., 2021). Sediments become finer upwards with shell and plant remains in the upper layers. The upper 4.8 m of the core is saline and unfrozen (Jenrich et al., 2021b).

Uomullyakh Lagoon (LAG2) (71.730833°N, 129.2725°E; Figure 5.1 i,j) is a shallow, semi-open lagoon connected to Tiksi Bay via a narrow opening. Warm freshwater discharge from the Lena River and storm surges influences its hydrodynamics, leading to temperature and salinity variations. LAG2 is covered by bedfast ice in winter, resulting in sub-zero sediment temperatures. Compared to LAG1, LAG2 experiences colder sediment temperatures and a complex structure with alternating frozen and thawed sections (Jenrich et al., 2021). The core is saline throughout (Jenrich et al., 2021).

5.3 Methods

Fieldwork, hydrochemistry, sediment- and biogeochemical and microbiology analyses were conducted as described in Chapter 3.3. only (Jenrich et al., 2024a). In this study the incubation experiment set up differs. Here, subsamples were taken at the surface, center and bottom of the three cores and the outcrop (Table 5.1).

Table 5.1. Sampling depth for incubation experiment. Depth is given in cm. * frozen; ** cryotic, measured and calculated borehole temperature was below 0°C but the core was received partly frozen or unfrozen.

	Permafrost Outcrop (TPF)	Thermokarst Lake (TKL)	Nearly-closed Lagoon (LAG1)	Semi-open Lagoon (LAG2)
sub-surface	45-50 cm*	5-17 cm	3-10 cm**	3-10 cm*
center	155-160 cm*	1505-1512 cm	1450-1460 cm	1400-1410 cm**
bottom	290-295 cm*	3050-3055 cm*	2428-2446 cm	3020-3030 cm*

To investigate future GHG production after seawater inundation we mixed 10 g of wet, homogenized, unfrozen sediment from three depths (surface (SI-1), center (SI-2) and bottom sediments (SI-3) (see Table 5.1) of all four sites with 20 mL artificial seawater (c=36 g/L). As for the relative proportions of its components, the artificial seawater contained NaCl (24.99 g/L), $MgCl_2 \times 6H_2O$ (4.14 g/L), Na_2SO_4 (0.79 g/L), $CaCl_2 \times 2H_2O$ (1.58 g/L), KCl (11.13 g/L) and $NaHCO_3$ (0.17 g/L), which were dissolved in ultrapure water and then sterile-filtered.

Subsequent to vial filling, rubber stoppers and aluminum caps were used for sealing the vial airtight, maintaining a constant water content throughout the entire incubation period. In total, 36 incubation vials (4 locations, 3 depth and 3 aliquots for each approach) were incubated at 4 °C under dark and anaerobic conditions for 1 year.

5.4 Results

When referring to surface layers, this includes the upper two samples of TPF and the top sample from the long cores of the aquatic sites (TKL, LAG, LAG2). Deep layers refer to the bottom Yedoma sample of TPF, as well as the center and bottom samples from the long cores of the aquatic sites.

5.4.1 Biogeochemistry

The pH for most samples was neutral to slightly alkaline and increased slightly over depth at all sites. Highest increase was observed for TPF from 6.13 below the

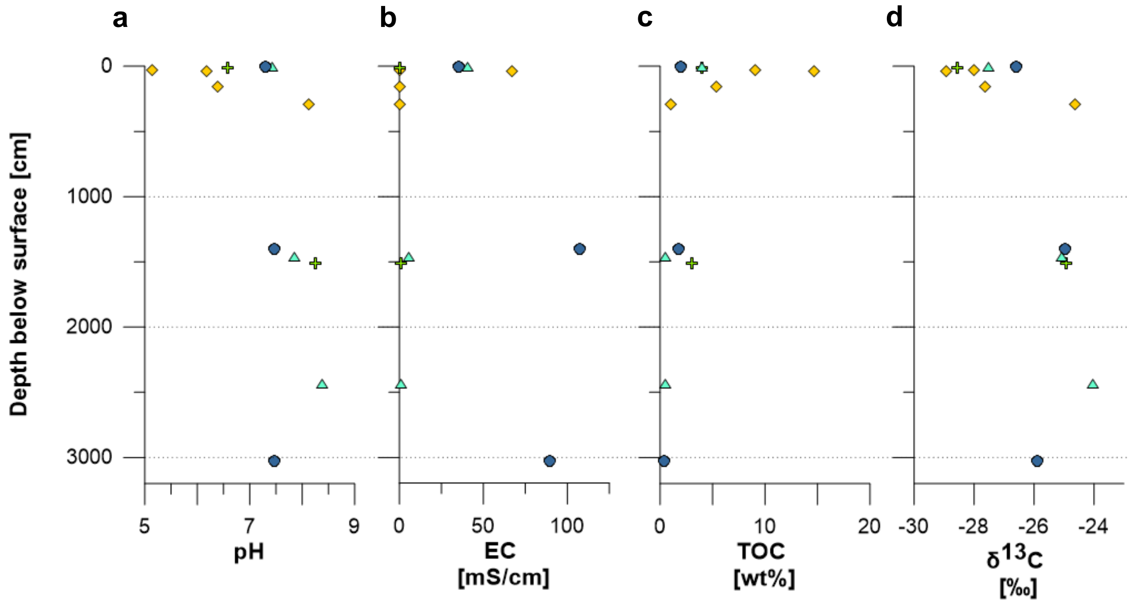

Figure 5.2 Biogeochemical parameters of the TPF (yellow diamond) and the sediment cores of TKL (green plus), LAG1 (turquoise triangle) and LAG2 (blue circle). a) pH, b) electric conductivity (EC), c) total organic carbon (TOC) content and d) ratio of stable carbon isotopes ($\delta^{13}C$) before the incubation.

active layer to 8.13 at the foot of the outcrop. Compared with the high length of the thermokarst cores, the change in pH was very low (Figure 5.2).

EC values are lowest for the freshwater thermokarst lake (0.2056 to 0.763 mS/cm). At TPF EC is high at the top of the permafrost (66.9 mS/cm) and decreases with depth. At the bottom we measured freshwater conditions (0.0593 mS/cm). At LAG1 (nearly-closed) EC starts moderately high at the surface (40.5 mS/cm) and then decreases with depth to 0.599 mS/cm at the bottom. At LAG2 EC values are highest, with a substantial increase from surface (35.4 mS/cm) to center (107.2 mS/cm) and a slight decrease at the bottom (89.4 mS/cm).

TOC is highest at the surface in all sites (mean: 6.02 wt%), except for the thermokarst lake where TOC is higher at the bottom. TOC content of the deep layers much lower (mean: 2.39 wt%). TOC is highest at TPF with a maximum of 14.66 wt% (mean: 7.02 wt%), slightly lower for TKL (mean: 5.52 wt%), while TOC much lower in the lagoon cores (mean LAG1: 1.69 wt%; LAG2: 1.39 wt%).

The surface δ13C values are relatively similar across all sites, ranging from -28.93‰ to -26.60‰. All sites show a trend of increasing δ13C values with depth. The terrestrial permafrost site shows the most pronounced change in δ13C values with depth, while the semi-open lagoon shows the least change.

5.4.2 Relative Abundance of Archaea and Bacteria

The analysis of microbial community composition, as illustrated in Figure 5.3, indicates a higher diversity in aquatic systems compared to the terrestrial permafrost outcrop. The Bray-Curtis dissimilarity analysis (Figure 5.4) shows distinct clustering based on sample depth: center and deep samples from the lake and lagoons (both pre- and post-incubation) form a green cluster, surface samples from these aquatic systems (before and after incubation) along with the incubated deep permafrost sample cluster together in blue, while permafrost samples form a unique ice-blue cluster.

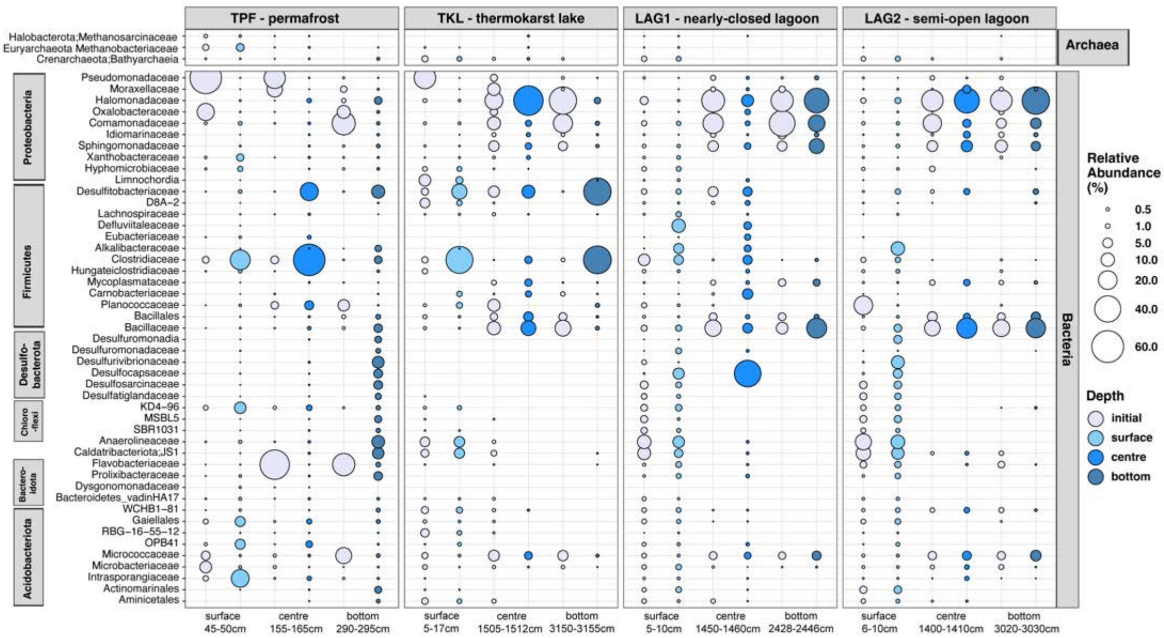

Figure 5.3: Bubble plot showing the relative abundance of archaea and bacteria initially before the incubation (for each depth - grey), after the incubation of surface samples (turquoise), centre samples (azure blue) and deep samples (dark blue) for the four sites (TPF - permafrost outcrop, TKL - Goltsovoye Lake, LAG1 - Polar Fox Lagoon and LAG2 - Uomullyakh Lagoon). Bubbles decreasing in size from before (initial) to after incubation indicate that the inundation with seawater has a negative effect on the microorganisms present, while bubbles increasing in size indicate favourable conditions. The taxonomy was collapsed at genus level. If an assignment to the genus level was not possible the next higher assignable taxonomic level was used.

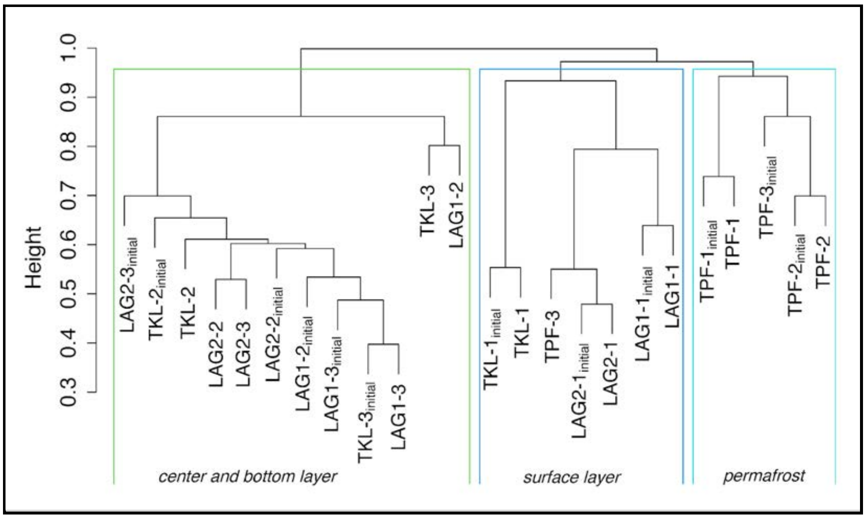

Figure 5.4 Clustering dendrogram based on Bray-Curtis dissimilarity shows that microbial communities group by sample depth for the aquatic sites (TKL - Goltsovoye Lake, LAG1 - Polar Fox Lagoon and LAG2 - Uomullyakh Lagoon), while the permafrost outcrop (TPF) is forming a distinct cluster.

For the long thermokarst lake and lagoon cores, the microbial composition of center and bottom layers was similar but differed substantially from that of the surface samples. Notably, there was a greater relative abundance of *Proteobacteriain* the deeper aquatic core samples, whereas *Desulfobacterota*, present in surface lagoon sediments, diminished with depth. Additionally, *Bacillales* were more prevalent in center and deep layers within aquatic systems.

The microbial community varied significantly between the terrestrial permafrost and aquatic environments. However, differences between surface, center, and bottom layers within aquatic sites were less pronounced. The TPF samples were closely spaced at 1-1.5 meters, whereas the long cores had sampling intervals of 10-15 meters. Variations in microbial community composition were most prominent between the surface and deep layers, highlighting the different ecological niches occupied within these environments.

Following a year-long anaerobic incubation, substantial shifts in microbial composition were observed in TPF, TKL, and the LAG1 center sample. The microbial signature of the bottom layer of TPF became more similar to that of surface layer from both lagoons, pronounced in declining abundancy of *Pseudomonadaceae, Comamonadaceae* (bottom TPF samples), and *Micrococcaceae* (in surface and bottom samples). Similarly, in TKL and in the center samples of both lagoon systems (LAG1 and LAG2), the abundance of *Proteobacteria* declined.

Certain microbial groups thrived under the marine conditions. *Desulfobacteraceae* increased in the center and deep TPF samples, and the bottom TKL sample, but remained stable in lagoons. *Clostridiaceae*, which were prominent in permafrost and TKL samples, also increased during the incubation. Methanogenic archaea remained present in TPF sediments during the incubation, with peak abundance in the upper layers. At the aquatic sites the abundance of methanogenic archaea was neglectable (< 0.5%) before and after the incubation.

5.4.3 GHG production

The results for cumulative anaerobic CO_2 and CH_4 production measured after 363 days are shown in Figure 5.5. CO_2 production per gram of dry weight is highest in LAG2, followed by LAG1, TPF, and TKL, ranging from 0.001 ± 0 mg CO_2-C gdw^{-1} for TPF-1 and TKL-1 to 0.15 ± 0.11 mg CO_2-C gdw^{-1} for LAG2-1 (Figure 5.5 a). CO_2 production shows a decreasing trend with depth in most sites, particularly in lagoon systems. When normalized SOC content (Figure 5.5 b), CO_2 production increases with depth in TPF (from 0.008 to 5.657 mg CO_2-C gC^{-1}), remains low in TKL (< 0.04 mg CO_2-C gC^{-1}), is higher in the surface and center layers than in the bottom layer for LAG1 (3.439 to 2.145 mg CO_2-C gC^{-1}), while in LAG2, CO_2 production remains high across depths (4.340 to 7.696 mg CO_2-C gC^{-1}). CO_2 production per gram of OC was highest in the sediment of the semi-open lagoon LAG2 (mean: 6.56 mg CO_2-C gC^{-1}), followed by the nearly-closed lagoon LAG1 (mean: 3.07 mg CO_2-C gC^{-1}), terrestrial permafrost TPF (mean: 2.18 mg CO_2-C gC^{-1}), and the thermokarst lake TKL (mean: 0.47 mg CO_2-C gC^{-1}). The contribution of CO_2 to cumulative GHG production after 362 days was over 90% for 11 of the 12 samples (Figure 5.5 c). Only in TPF-1 was there an equal production of CO_2 and CH_4, with CO_2 contributing 48% and CH_4 contributing 52% but here the measured CO_2 and CH_4 values are below the calibration limit.

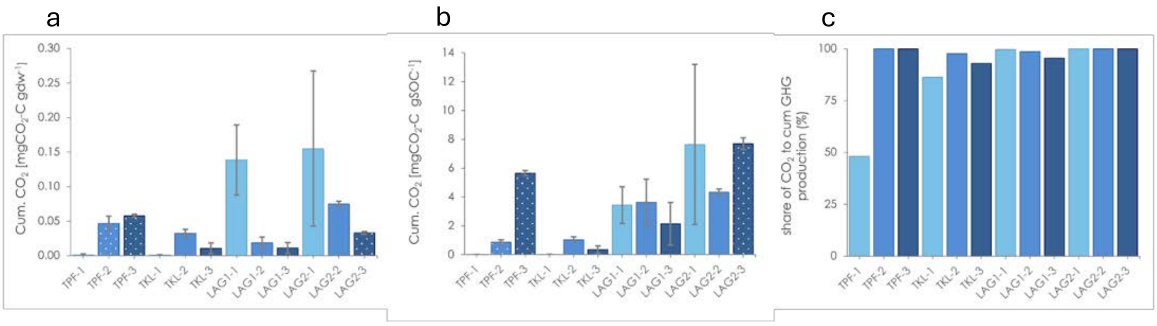

Figure 5.5: Cumulative anaerobic CO_2 production over the 363-day incubation at 4°C over depth (1: surface - light blue, 2: center - azure blue, 3: bottom - dark blue). a: cumulative CO_2 production in mg per gdw; b: cumulative CO_2 production in mg per gSOC; c: ratio of cumulative CH_4:CO_2. TPF: terrestrial permafrost outcrop; TKL: thermokarst lake Goltsovoye; LAG1: Polar Fox Lagoon; LAG2: Uomullyakh Lagoon. Patterned bars represent initially frozen conditions.

Cumulative CH_4 production is generally very low among all sites and depth reaching from 0.005 µg CH_4-C gdw^{-1} at LAG2-2 to 1.290 µg CH_4-C gdw^{-1} at TPF-1 and normalized to the SOC content from 8.6x10^{-5} mg CH_4-C gC^{-1} at LAG2-2 to 0.1 mg CH_4-C gC^{-1} for LAG1-3 (Figure S5.1). Highest mean CO_2 production rates were measured for all samples after 5 days of incubation. Max CO_2 production rates ranged between 8.5

µgCO_2-C gSOC-1 day-1 for TPF-1 and 677,9 µgCO_2-C gSOC-1 day-1 for LAG2-3 (Figure S5.3).

Highest CH_4-C production rate is 8.8 µgCH_4-C gSOC^{-1} day^{-1} on day 5 for LAG1-3 and lowest is TPF-2 with 0.02 µgCH_4-C gSOC^{-1} day^{-1} (Figure S5.3). Deep and center samples of LAG1 and TKL showed slightly higher rates than the rest of the samples.

5.4.4 Correlation of GHG Production and Biogeochemical Parameters

In Figure 5.6, the data distribution (scatter plot and histogram) and the non-parametric rank-based correlation among the parameters CO_2 production, sample depth, EC, TN, TOC, and $\delta^{13}C$ are presented. The data does not follow a normal distribution. CO_2 production shows a slight negative correlation with depth ($r = -0.42$) and a significant positive correlation with EC ($r = 0.57$, $p = 0.1$), suggesting that as depth increases, CO_2 production tends to decrease slightly, while higher electrical conductivity is associated with increased CO_2 production. TN and $\delta^{13}C$ are significantly correlated with depth ($r = -0.66$ and $r = 0.62$, respectively; $p = 0.05$), indicating that both TN decreases and $\delta^{13}C$ becomes more enriched with increasing depth. TOC and TN are strongly positively correlated ($r = 0.81$, $p = 0.001$). Conversely, TN and $\delta^{13}C$ are strongly negatively correlated ($r = -0.79$, $p = 0.001$). Additionally, TOC content is significantly negatively correlated with $\delta^{13}C$.

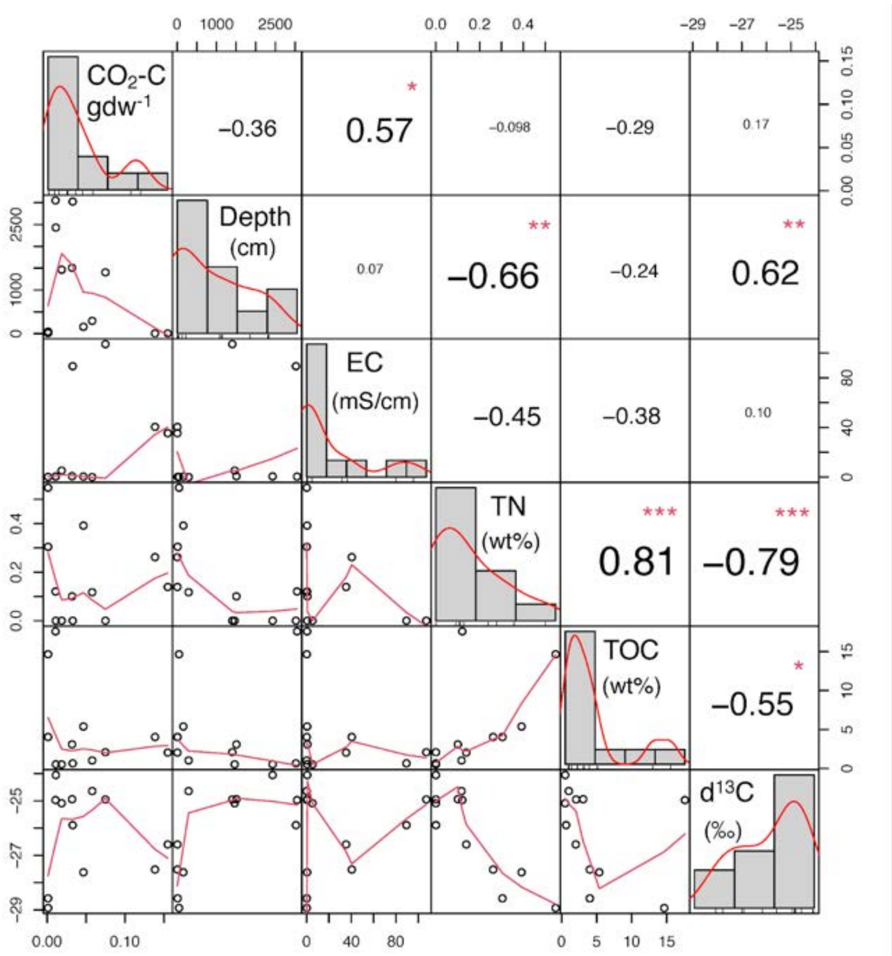

Figure 5.6 Combined scatter plot, histogram, and correlation matrix of the parameters cumulative CO_2 production (per g dry weight), sample depth, electrical conductivity (EC), total nitrogen content (TN), total organic carbon content (TOC) and stable carbon isotope composition ($d^{13}C$). The diagonal displays the distribution of each variable as histograms. Below the diagonal are bivariate scatter plots with fitted regression lines, illustrating relationships between pairs of variables. Above the diagonal, the correlation coefficients are shown, accompanied by significance levels indicated by stars: p-values (0.001, 0.05, 0.1) correspond to symbols (***, **, *.).

5.5 Discussion

5.5.1 Variations in Biogeochemical Parameters Over Depth

The semi-open lagoon (LAG2) exhibits the highest electrical conductivity (EC) values, with a peak at the center of the core. A study by Jenrich et al. (2021) reconstructing freezing conditions revealed that a hyper-saline talik formed due to subsurface groundwater inflow from Tiksi Bay, combined with seasonal salt injection during bedfast ice formation. In the deeper, more closed lagoon (LAG1), seawater inundation primarily affects the upper sediment layers, as a thin, partially frozen permafrost layer, beginning 160 cm below the surface, limits salt diffusion (Angelopoulos et al., 2020b; Jenrich et al., 2021b). Both the thermokarst lake and terrestrial permafrost show freshwater conditions from top to bottom, indicating that these locations are not influenced by the sea since deposition.

Increasing pH values with depth across are obvious at all sites except the semi-open lagoon, where it remains relatively stable. This trend suggests a shift toward more alkaline conditions in the deeper layers of terrestrial permafrost, the thermokarst lake, and nearly-closed lagoon environments.

Variations in carbon and nitrogen cycling are closely related to deposition history. Analyses reveal a decrease in TOC and TN and an increase (less negative) in $\delta^{13}C$ with depth at most sites. Whereby only TN and $\delta^{13}C$ are significantly correlated with depth ($r = -0.66$ and $r = 0.62$, respectively; $p = 0.05$). Nitrogen and organic carbon content and quality depend on various factors, such as environmental conditions (wet or dry), primary production at the time of deposition, the input and output of organic carbon, and its preservation, which depends on soil conditions and permafrost formation. The high carbon content at the bottom of the TKL core is attributed to early Weichselian fluvial deposition of highly degraded organic matter and driftwood from southern regions (Jongejans et al., 2020).). The terrestrial permafrost samples, which have not been subject to thaw since deposition, have the highest TOC content, especially in the top two layers above the Yedoma deposits. These layers are relatively young compared to the deep samples from the other three locations. From the center to the bottom sample of TPF, there is a shift in TOC, $\delta^{13}C$, and pH toward values similar to those in the deep samples of the other three locations, highlighting the distinct signature of Yedoma deposits. Estimations of Holocene thaw subsidence during lake formation suggest Yedoma surface subsidence of up to 25 meters for LAG2 and 27 meters for LAG1 (Jenrich et al., 2021), indicating that the sediment of the bottom sample of TPF could have been deposited during the same time as the center samples of the thermokarst sites.

5.5.2 Variations in microbial composition over depth and response to seawater inundation

Microbial communities cluster primarily by sample depth and landform (Figure 5.4). A significant cluster includes all deep layers (center and bottom samples) from the aquatic sites, which are distinct from the surface layers and permafrost, which form two smaller cluster. This pattern suggests that microbial composition is heavily influenced by the initial environmental conditions present when these layers were formed.

5.5.2.1 Change of initial microbial composition with depth

The initial microbial composition of the terrestrial permafrost is characterized by aerobic bacteria, indicating that these microbes thrived in oxygen-rich conditions when the permafrost was first established. Only the surface sample is inhabited by methanogens. A notable difference is observed in the bottom Yedoma sample compared to the top two layers. In the bottom layer, the family *Comamonadaceae* shows the highest relative abundance. This family is also prevalent in the deep samples of aquatic sites but is nearly absent in the upper layers of the terrestrial permafrost, where *Pseudomonadaceae* dominates. *Comamonadaceae* are typically associated with environments where they can metabolize simple organic compounds under low-oxygen conditions. The bottom layer, formed long ago and possibly exposed to different geochemical conditions, may have selected for these bacteria. In contrast, the top layers, more recently exposed to surface conditions, favor *Pseudomonadaceae*, which thrive in more aerobic environments.

The microbial composition in the deep layers of these aquatic sites is dominated by strictly aerobic families, such as *Halomonadaceae* and *Sphingomonadaceae*, along with *Comamonadaceae* and *Bacillaceae* families, which include mainly aerobic but also facultatively anaerobic species. These sediments were formed approximately 40,000 to 55,000 years ago (center layers) and more than 300,000 years ago (deepest layers) (Jenrich et al., 2021b; Jongejans et al., 2020). The predominance of aerobic species indicates that these microbes are ancient and have been preserved under frozen conditions since the sediments originally formed in aerobic environments.

The high similarity in microbial composition between the frozen bottom layer of LAG2 and the unfrozen bottom layers of TKL and LAG1, as well as the center layers of TKL, LAG1, and LAG2, suggests that talik deepening to these depths likely occurred only recently and has not significantly affected the microbial community.

The microbial community in the surface layer of the aquatic sites differs significantly from that in the deep samples. The surface layer shows greater diversity, reflecting the distinct environmental conditions of the lake and lagoons. For example, *Desulfobacterota*, which are sulfate reducers that oxidize acetate and other simple organic acids to carbon dioxide, highly adapted to marine conditions, are abundant only in lagoon samples. In contrast, *Pseudomonadaceae*, known for their aerobic chemoorganotrophic respiratory metabolism (Dodd, 2014), are highly abundant in the lake sediment.

5.5.2.2 Effects of Seawater Inundation

The shift in regimes from a terrestrial permafrost or freshwater lake system to a marine system has impacted the microbial composition, as seen in Figure 5.3. Before the incubation, *Pseudomonadaceae* were the dominant family of bacteria in the surface layers. After the incubation, they were almost non-existent. Instead, there was a shift towards a variety of anaerobic microorganisms, such as *Clostridiaceae, Acidobacteriota,* and *Chloroflexi* (Figure 5.3). For TKL and the surface and center samples of TPF, there was no or only minimal growth of SRB (*Desulfobacteriota*) detected. This suggests that the lack of oxygen in the anaerobic incubation was the major driver for the shift in microbial composition.

In contrast, in the Yedoma layer of TPF, a significant increase in a variety of SRB was observed after incubation. The microbial community of this sample clusters with the microbes of the surface layer of the aquatic sites (Figure 5.4). This supports the assumption that these are deposits of similar age that subsided during the formation of the thermokarst features.

No significant shift in microbial composition was observed in the surface and bottom layers of LAG2 and LAG1. However, in the center layer of LAG1, we detected a shift from aerobic *Proteobacteria* to bacteria with a wide range of metabolic capabilities, such as *Firmicutes* and SRB (*Desulfocapsaceae*). It is noteworthy that among all the deep samples from the aquatic sites, this is the only one where we observed growth in SRB, even though the electrical conductivity (EC) was much lower than at LAG2 (LAG1-2: 5 mS/cm vs. LAG2: 108 mS/cm), suggesting that seawater has not penetrated to the same depth. This lower salinity at LAG1, combined with the observed microbial shift, suggests that even slight increases in salinity can significantly alter microbial ecosystems in these environments. This has broader implications for understanding how climate change and rising sea levels could influence permafrost-associated ecosystems.

The lack of a significant change in the microbial community at LAG2 could be due to the microorganisms being well-adapted to the prevailing conditions. This stability might indicate that the existing microorganisms are highly adapted to and very competitive in cold and saline conditions, which may inhibit the establishment of new species. However, it could also be influenced by differences in ground temperature. While the temperature at LAG1 ranged from 0°C to -1°C, it was between -3°C and -5°C at LAG2. The colder environment at LAG2 might have further constrained microbial growth and community shifts due to the stress of thawing. The abrupt thawing and the phase transition from ice to liquid water are major stress factors for the biological system (Ernakovich et al., 2022), which can slow down the growth of new bacteria.

5.5.3 GHG Production in Deep and Surface Layers

Drilling deep boreholes of more than 10 meters in remote permafrost landscapes is logistically challenging. Consequently, there are few samples available. Even fewer studies focus on the potential GHG release, especially under anaerobic conditions that occur when deep permafrost layers thaw due to talik formation beneath thermokarst lakes and lagoons. To our knowledge this is the first study focusing on anaerobic GHG production under seawater influence in great depth. Therefore, it is hard to directly compare our results with other studies.

CH_4 production was very low (< 2 µg CH_4-C gdw^{-1}) for all samples, regardless of depth and setting. A previous incubation study focused on surface sediments from the same study areas found that CH_4 production decreases significantly under increasing marine conditions (Jenrich et al., 2024a), which likely explains the minimal CH_4 production observed in our experiment. Since CH_4 production is negligible, we focus in this discussion exclusively on CO_2 production.

Our study revealed distinct differences in CO_2 production across various landforms and depths. CO_2 production per gram of OC was highest in the sediment of the semi-open lagoon LAG2 (mean: 6.56 mg CO_2-C gC^{-1}), followed by the nearly-closed lagoon LAG1 (mean: 3.07 mg CO_2-C gC^{-1}), terrestrial permafrost TPF (mean: 2.18 mg CO_2-C gC^{-1}), and the thermokarst lake TKL (mean: 0.47 mg CO_2-C gC^{-1}). This reveals that environments that were in contact with seawater before produced more CO_2 than under terrestrial freshwater settings.

Jongejans et al. (2021) found a higher CO_2 production (30.5; 120.6 mg CO_2-C gC^{-1} for Alas and lake sediment respectively), but these samples were incubated without the addition of seawater, under natural conditions. Jenrich et al. (2024a, d; see Chapters 3 and 4) observed higher CO_2 production under natural conditions (freshwater for terrestrial sites) than with the addition of seawater. This indicates that seawater inundation is a disturbance and leads to lower production in the first phases of lagoon formation. Similar CO_2 production was measured for surface sediments of lagoons located at the Canadian Beaufort Sea (range: 0.2 - 8.0 mg CO_2-C gC^{-1}) (Jenrich et al., 2024d).

Interestingly, CO_2 production did not correlate with TOC and TN contents, or $\delta^{13}C$ values. Some previous incubation studies on permafrost sediments found a positive correlation between CO_2 production and TOC (Knoblauch et al., 2013; Lee et al., 2012; Walter Anthony et al., 2016) while others did not (Jongejans et al., 2021). Similar to Jongejans et al. (2021), our study compared sediments of great depth that have experienced different depositional conditions and thaw-freezing cycles. Additionally, we added another complexity by comparing terrestrial and marine settings, which may cause the lack of correlation between TOC, TN, $\delta^{13}C$, and CO_2 production in our findings.

CO_2 production per gram of dry weight shows no significant correlation with depth ($r = -0.36$) (Figure 5.6). Interestingly, CO_2 production was higher in the deep layers of LAG2, despite these layers being initially frozen or cryotic and highly saline (up to 108 mS/cm)—conditions that are typically stressful for microbes. Given the very similar microbial composition of the deep layers at both sites, one would expect lower CO_2 production from sediments stored under more extreme conditions, like those in LAG2. However, although TOC contents are similar, the harsh conditions in LAG2 may have better preserved the organic matter, possibly resulting in more labile carbon being available for microbial decomposition at the start of the experiment in LAG2. CO_2 production is significantly positive correlated with pore water EC ($r = 0.57$, $p = 0.1$), suggesting that microbial communities which were adapted to saline conditions before the incubation performed better.

When normalized to OC content, CO_2 production in deep layers is higher than in surface layers (mean: 3.55 and 2.40 mg CO_2-C gC^{-1} respectively) showing that even though the organic matter and the microbes in these layers are very old given that the feldspar in deep layers of the lagoons was dated to >300 ka using luminescence dating (Jenrich et al., 2021), the potential for GHG production is significant. In addition, their physical potential for mobilization is given due to deep disturbance processes like thermokarst formation or costal erosion. This is worth mentioning, especially in the context of accelerated deepening of taliks below lagoons due to the high freezing point depressions for saline and hypersaline layers. and acceleration erosion processes (Irrgang et al. 2022) So far it is unclear how long it takes for the produced GHG to diffuse up to the surface and how much is emitted to the atmosphere given that mineralization and transformation processes in the sediment and the water column might reduce the initially produced amount of gasses.

5.6 Conclusion

In conclusion we want to answer our research question on assessing the potential future GHG production in deep, thawed permafrost sediments after seawater inundation as following: Even though the overall CO_2 production per gram of dry weight decreases slightly with depth, the higher production potential normalized to OC content indicates that these layers could contribute substantially to GHG emissions once they are exposed to microbial activity due to climate change.

5.7 Supplements

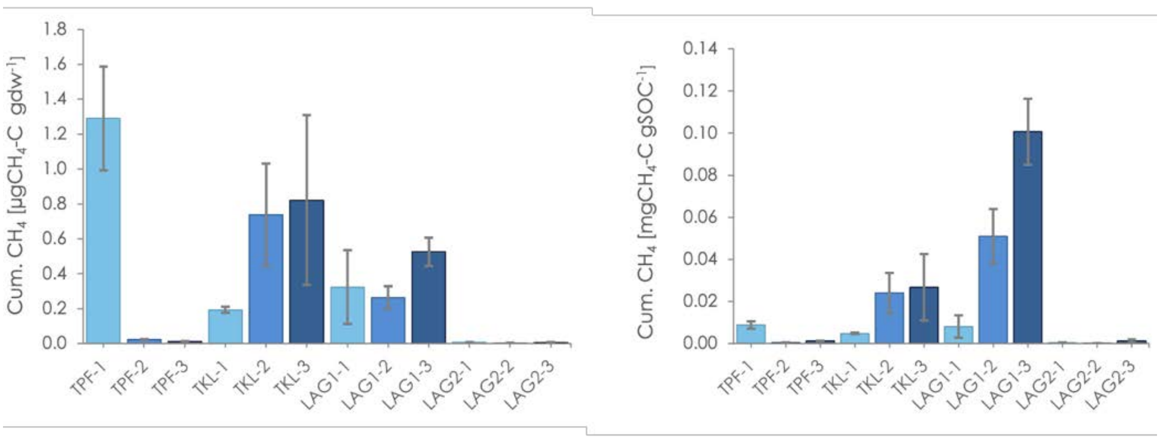

Figure S5.1 Cumulative anaerobic CH_4 production over the 363 day incubation at 4°C over depth (1: surface - light blue, 2: centre - azure blue, 3: bottom - dark blue). **a:** cumulative CH_4 production in mg per gdw; **b:** cumulative CH_4 production in mg per gSOC. TPF: terrestrial permafrost outcrop Byk14; TKL: thermokarst lake Goltsovoye; LAG1: Polar Fox Lagoon; LAG2: Uomullyakh Lagoon.

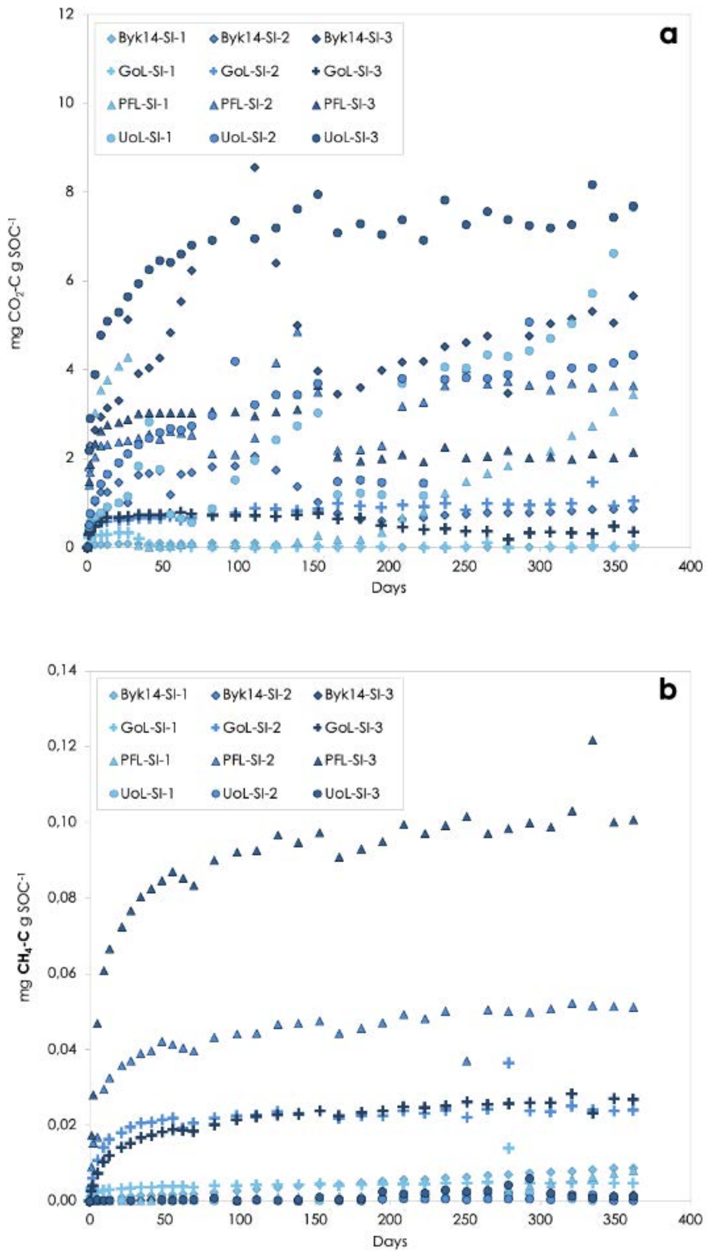

Figure S5.2 Cumulative anaerobic GHG production over depth (surface - light blue, centre - azure blue, bottom - dark blue) **a:** cumulative CO_2 production per gSOC - higher for deep sediments than surface sediments; **b:** cumulative CH_4 production per gSOC - generally very low but highest for bottom and centre samples of LAG1 (Polar Fox Lagoon) and TKL (Goltsovoye Lake).

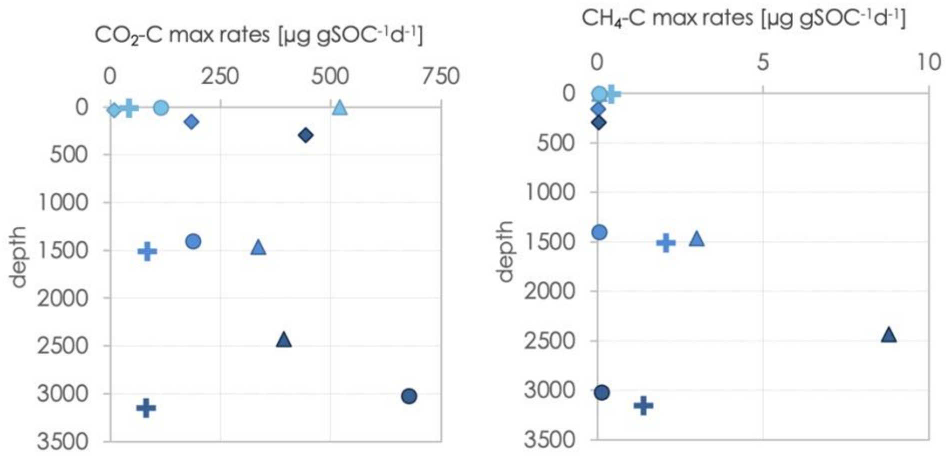

Figure S5.3 Maximum CO_2 (left) and CH_4 (right) production rates per gSOC for surface (light blue), centre (azure blue) and deep samples (dark blue) for TPF (diamond) and the sediment cores of TKL - Goltsovoye (plus), LAG1 - Polar Fox Lagoon (triangle) and LAG2 - Uomullyakh Lagoon (circle).

6

Simulated Inundation of a Coastal Plain: An Incubation Study of the Teshekpuk Coastal Region, Alaska

6.1 Introduction

Arctic permafrost coasts are sensitive to rising temperatures, which are observed especially in high latitudes (Rantanen et al., 2022). Warm air and seawater are leading to rapid ground-ice melt and permafrost thaw along the coast, leading to increasing erosion rates. Long-term sea level rise, combined with storm events, leads to the flooding of coastal permafrost lowlands. The inundation of permafrost with seawater is leading to intensified permafrost thaw and therefore the unlocking of formerly frozen soil organic carbon (SOC). Due to microbial decomposition, SOC is released as carbon dioxide and methane, leading to further heating. Land inward migrating coastlines cut thermokarst lakes and basins, turning them into lagoons. These lagoons are ideal to study the effect of seawater inundation on GHG production.

Using sediment samples from various locations along a land-sea transect in the Arctic coastal plain (ACP) of northern Alaska, we conducted incubation experiments under brackish and marine conditions to simulate GHG production following flooding of the coastal plain. This study goes along with the study by Giest et al. (in submission; see Appendix D) focusing in detail on carbon and sediment characteristics along the land-sea transect.

6.2 Study Area

The study area is located on ACP of northern Alaska, in the National Petroleum Reserve-Alaska (NPR-A). It is situated north of Teshekpuk Lake on the North Slope, a region defined by the Brooks Range to the south and the Beaufort Sea to the north. The region is underlain by a variety of geological deposits originating from the North American craton, including passive margin sediments, rift sediments, pelagic deposits, volcanoclastics, and foreland basin deposits (Jorgenson, 2011). The primary surficial deposits within the study area consist of glacio-marine silt, marine sand, and alluvial sand and silt from the Holocene and mid-Quaternary epochs (Jorgenson and Grunblatt, 2013).

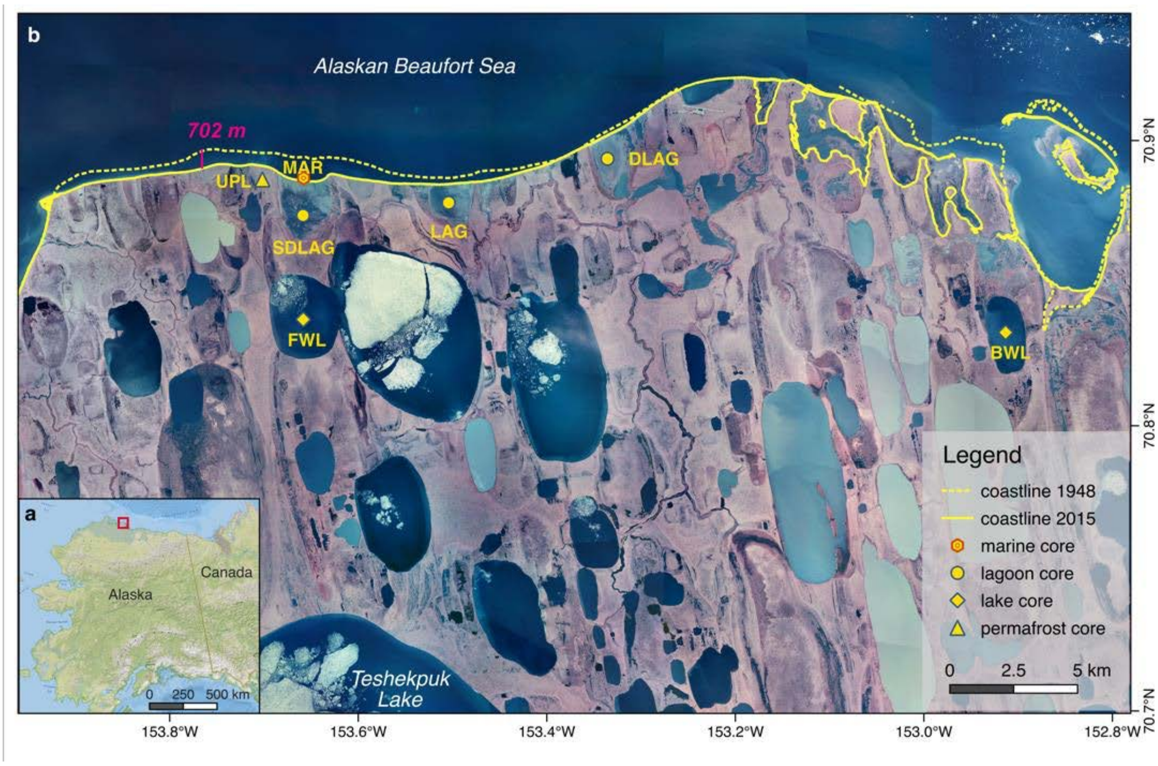

Figure 6.1 Coring locations at the (a) North Slope of Alaska north of the (b) Teshekpuk Lake. The inland migration of the sea led to the loss of up to 1km ice-rich coastal permafrost in 67 years. Abbreviations: UPL – upland permafrost; FWL – freshwater lake; BWL – brackish water lake; SDLAG – semi-drained lagoon; LAG – shallow lagoon; DLAG – drained lagoon; MAR – marine core. Source: (a) ESRI; (b) Color infrared ortho aerial image (U.S. Geological Survey, Earth Explorer, 2002)

The area is characterized by continuous permafrost, with thicknesses ranging from 320 to 400 meters near the Beaufort Sea (Parsekian et al., 2019). The active layer varies in thickness between 20 to 73 cm (Bockheim and Hinkel, 2007).

Due to thawing permafrost and melting ground ice, the landscape is continuously transformed, resulting in ground subsidence and the formation of thermokarst lakes and drained lake basins. Thermokarst lagoons and embayments are also forming rapidly along the coast due to accelerated coastal erosion (Arp et al., 2011; Jorgenson and Shur, 2007). Drained thermokarst lake basins cover approximately 62% of the ACP, while thermokarst lakes occupy more than 20% (Arp et al., 2011; Hinkel et al., 2012). The region also includes second-generation thermokarst lakes, typically oriented northwest, adding to the complexity of the landscape (Parsekian et al., 2019).

The study area represents a transition between two key geomorphological zones. The Outer Coastal Plain to the south, which is dominated by marine sands and the Younger Outer Coastal Plain to the north, characterized by marine silts (Hinkel et al., 2005; Jorgenson, 2011; Lenz et al., 2016). Distinct upland surfaces, covering approximately 7% of the study area, are characterized by high ice content, ice wedge polygons, and organic-rich Holocene cover deposits (Eisner et al., 2005). These uplands, which are elevated about 5 m above the surrounding flat terrain, represent higher-relief areas within the otherwise low-lying coastal plain.

The mean annual air temperature in the region is approximately −10°C (2004–2015) based on data from the Drew Point site (Urban and Clow, 2013). Precipitation is low, averaging around 200 mm/year (Jorgenson, 2011). The cold climate, combined with low precipitation, plays a significant role in maintaining the stability of the permafrost and shaping the hydrological and ecological processes in the area.

6.3 Methods

6.3.1 Fieldwork and Subsampling

Fieldwork was conducted at the coast north of Teshekpuk Lake in collaboration with University Fairbanks during April 2022. For this study we chose 7 distinct locations along a land-sea transect. One permafrost core from an upland site (UPL; 70.8851°N, 153.7062°W), serving as the endmember; two lake cores—one from a freshwater lake (FWL; 70.8362°N, 153.6628°W) and one from a brackish water lake (BWL; 70.8328°N, 152.9128°W); and cores from three nearly closed lagoons, which are separated from the sea by a sand barrier. One lagoon was semi-drained (SDLAG; 70.8727°N, 153.6643°W) with 43cm ice layer at the coring location, the following lagoon (LAG; 70.8776°N, 153.5088°W) was covered with 112cm ice overlaying a about 60cm unfrozen brine-sediment mixed layer and the third lagoon was fully drained at the time of coring (DLAG; 70.8934°N, 153.3390°W). Further, one marine core (MAR; 70.8857°N, 153.6643°W) was retrieved about 100m offshore from the recent margin of SDLAG. The shape of the former lake basin suggests that the location MAR is within the originally larger basin of SDLAG, which transitioned into a subsea state by now. The cores UPL, SDLAG, LAG and DLAG were frozen from top to bottom, whereas the cores TKL-F, TKL-B and MAR were unfrozen. The unfrozen sediment cores were sampled using a Push Corer [Ø 6 cm], the frozen sediment cores were sampled using a SIPRE Corer [Ø 7.6 cm]. The frozen sediment cores were kept frozen, while thawed samples were packed and cooled for transport to AWI Potsdam for further analysis.

6.3.2 Laboratory Analyses

6.3.2.1 Hydrochemistry and Bulk Sediment Analyses

Pore water from the thawed samples was extracted using Rhizon samplers (membrane pore size: 0.12–0.18 µm). The extracted pore water was then analyzed for pH, electrical conductivity (EC), and dissolved organic carbon (DOC) content as described in Chapter 3.3.2. The measured EC values were converted to molarity (see Chapter 3.3.2). Artificial seawater was prepared by dissolving NaCl (24.99 g/L), $MgCl_2 \times 6H_2O$ (11.13 g/L), Na_2SO4 (4.14 g/L), $CaCl2 \times 2H_2O$ (1.58 g/L), KCl (0.79 g/L), and $NaHCO_3$ (0.17 g/L) in ultrapure water, followed by sterile filtration.

The TN and TOC content was determined based on the method described in Chapter 3.3.3.

6.3.2.2 Anaerobic Incubation

To investigate greenhouse gas production under varying levels of seawater influence and simulating the flooding of an Arctic coastal plain, we incubated surface sediments from seven sites on a gradient of increasing seawater influence (UPL, FWL, BWL, SDLAG, LAG, DLAG and MAR). The sediments were incubated anaerobically at 4°C for 224 days (7.5 months) using artificial seawater at two concentrations: brackish (13 g/L) and marine (36 g/L), following the method described in Chapter 3.3.2.3, with one key difference. In this experiment, I either additionally or exclusively incubated the samples in their original condition—without adding water—when the pore water salinity closely matched the treatment conditions. This applied to the UPL, TKL-B, LAG1, and LAG3 samples. Based on their pore water salinity, UPL corresponded to freshwater conditions, TKL-B and LAG1 to brackish, and LAG3 to marine conditions. Due to limited sample availability, FWL and MAR were not incubated as original samples.

As in the previous two incubation experiments, freshwater conditions were used to simulate the lake stage, brackish conditions for young, less connected lagoons, and marine conditions to represent open lagoons and the subsea state.

6.4 Results

6.4.1 Environmental Parameters

Pore water salinity and EC vary greatly across the sites, with the UPL and FWL site showing very low salinities, while TKL-B, SDLAG and MAR show higher, brackish conditions and LAG and DLAG marine conditions (Table 6.1).

DOC in pore waters is highest at UPL (72.3 mg/L) and SDLAG (80.8 mg/L). In contrast, DOC is substantially lower in the MAR site (19.2 mg/L). LAG has no available pore water DOC data, but shows the highest surface water DOC (199 mg/L).

The grain size analyses revealed that MAR has the highest sand content (59%) compared to other locations, followed by UPL (27% sand), while other sites, particularly TKL-F, TKL-B, and LAG, are dominated by silty sediments.

Table 6.1. Environmental parameters measured at different sites along the Teshekpuk Lake coastal plain, Alaska. Data include sample depth, surface water DOC, pore water pH, electrical conductivity (EC), salinity, and DOC, as well as sediment composition (sand, silt, clay), $\delta^{13}C$, total organic carbon (TOC), and total nitrogen (TN) content. Sites sampled include Upland (UPL), Terrestrial Fresh Water Lake (TKL-F), Terrestrial Brackish Lake (TKL-B), Semi-Drained Lagoon (SDLAG), Lagoon (LAG), Drained Lagoon (DLAG), and Marine (MAR) locations.

Site	sample depth (cm)	Surface water depth (cm)	Surface water DOC (mg/L)	Pore water pH	Pore water EC (mS/cm)	Pore water Salinity (g/L)	Pore water DOC (mg/L)	Sediment Sand (%)	Sediment Silt (%)	Sediment Clay (%)	d13C (‰) vs. PDB	TOC (wt%)	TN (wt%)
UPL	3 - 11	0	NA	5.80	0.3	0.1	72.3	0.27	0.64	0.10	-28.84	2.56	0.17
TKL-F	3 - 9	217	12.7	5.71	0.8	0.4	NA	0.04	0.74	0.21	-28.21	5.22	0.34
TKL-B	1 - 7	163	53.4	6.42	26.7	16.4	48.1	0.05	0.76	0.19	NA	7.35	0.31
SDLAG	3.5 - 12	43	NA	7.64	39.0	24.9	80.8	0.05	0.78	0.17	-27.55	4.62	0.30
LAG	3 - 9	200	199	7.91	54.6	36.3	NA	0.03	0.82	0.15	-27.63	4.09	0.26
DLAG	2 - 10	0	NA	7.51	54.4	36.2	NA	0.04	0.8	0.16	NA	1.91	0.17
MAR	1 - 11.5	177	1.81	7.44	39.5	25.3	19.2	0.59	0.34	0.07	-26.21	1.30	< 0.10

Biogeochemical analyses revealed that TOC and TN contents are highest at the lakes (FWL, BWL), followed by the lagoons (SDLAG, LAG) and lower at the UPL and the drained lagoon and lowest at the Marine site (MAR).

$\delta^{13}C$ values increase along the terrestrial-marine gradient with UPL showing the most depleted value (-28.84 ‰) and MAR the less depleted value (-26.21 ‰).

6.4.2 CO_2 and CH_4 Production

Under brackish conditions, CO_2 production is highest at the LAG and SDLAG locations, with values of 7.77 ± 0.92 and 7.49 ± 0.53 mg CO_2-C $g^{-1}C$, respectively (Figure 6.2a). In contrast, the sites that have not been previously exposed to saltwater (UPL and FWL) exhibit the lowest CO_2 production, with values of 1.36 ± 0.37 and 0.89 ± 0.35 mg CO_2-C $g^{-1}C$, respectively. The highest overall CH_4 production was measured for LAG under brackish conditions (2.05 ± 0.42 mg CH_4 gC^{-1}).

In marine conditions, SDLAG (semi-drained lagoon) demonstrates the highest cumulative CO_2 production at 8.35 ± 2.30 mg CO_2-C $g^{-1}C$ (Figure 6.2b). CH_4 production remains close to zero across almost all locations, with detectable CH_4 production occurring only at BWL, where it is measured at 0.18 ± 0.03 mg CH_4 gC^{-1}.

Under near natural conditions (Figure 6.2c), the active layer of the upland produces the most CO_2 (6.78 ± 0.60 mg CO_2-C $g^{-1}C$). The BWL, SDLAG, and LAG locations show similar CO_2 production levels, ranging from 4.98 to 5.32 mg CO_2-C $g^{-1}C$. The lowest CO_2 production is observed at the DLAG, with a value of 1.46 ± 0.12 mg CO_2-C $g^{-1}C$. Notably, CH_4 production occurs only at BWL under natural conditions. Due to limited sample availability, FWL and MAR were not incubated in their original state.

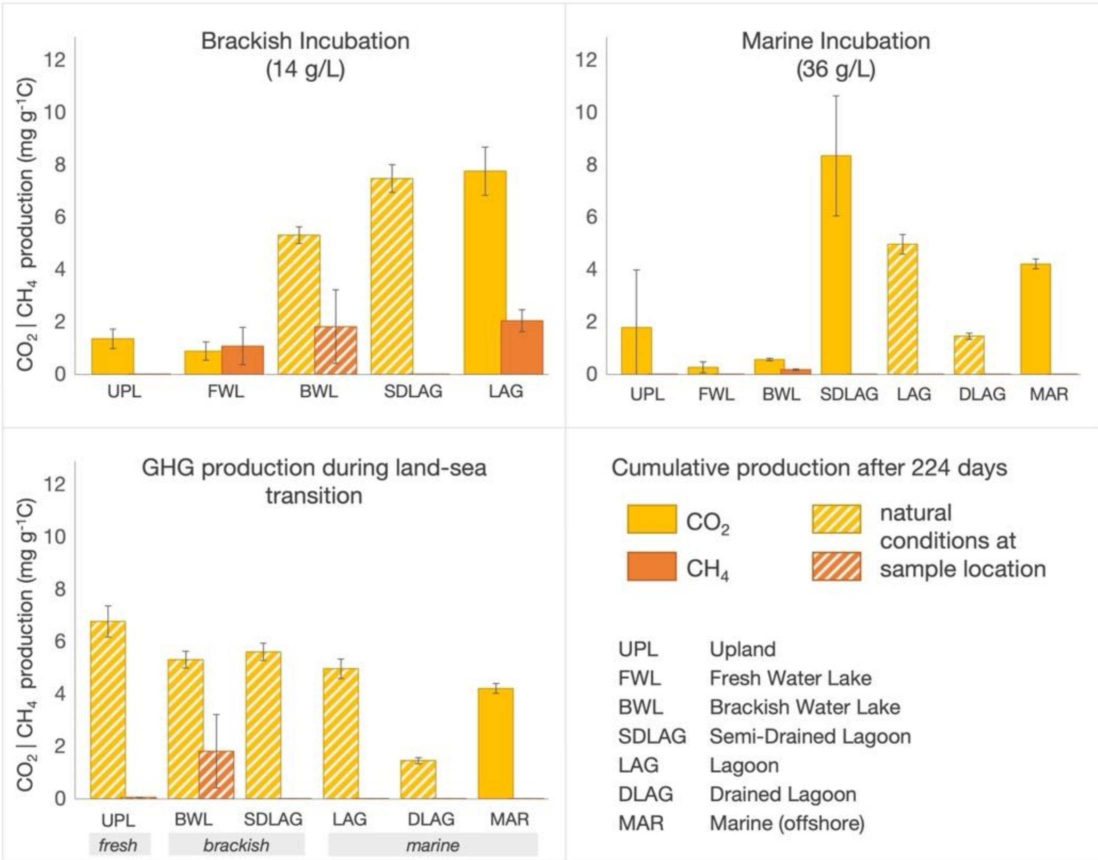

Figure 6.2 Cumulative GHG production measured over 224 days under brackish (14 g/L), marine (36 g/L) and near natural incubation conditions at 4°C for various Arctic coastal plain sites. CO_2 production (yellow) and CH_4 production (orange) reveal the influence of salinity on GHG emissions during simulated flooding of different landscape features: Upland (UPL), Fresh Water Lake (FWL), Brackish Water Lake (BWL), Semi-Drained Lagoon (SDLAG), Lagoon (LAG), Drained Lagoon (DLAG), and Marine (MAR).

6.5 Discussion

In the upland active layer significantly higher CO_2 production was observed under near-natural (here non-saline) conditions compared to brackish or marine conditions (natural: 6.78 ± 0.60 mg CO_2-C g^{-1}C; brackish: 1.36 ± 0.37 mg CO_2-C g^{-1}C; marine: 1.80 ± 2.21 mg CO_2-C g^{-1}C). This finding underscores the negative impact of abrupt environmental changes on microbial activity. Since the surface layer at the upland site had not previously been exposed to seawater, the microbial communities present are likely not adapted to saline conditions. The transformation to salt-tolerant communities requires time, which may explain the observed reduction in GHG production when salinity levels change. Notably, no methane production occurred even under freshwater conditions, which were intended to simulate a lake stage. Anaerobic lake sediments provide a favorable environment for methanogens (Heslop et al., 2015); however, the upper layers of the active layer had not been waterlogged at the time of coring, likely resulting in aerobic in-situ conditions. It is therefore likely that methanogens were absent in the incubated samples, and recolonization in a closed system, such as an incubation bottle, tends to be very slow if not entirely unfeasible. In natural ecosystems, seawater inundation facilitates the introduction of marine microbial communities, accelerating the establishment of new, salt-tolerant microbial communities.

In the terrestrial freshwater lake (FWL), overall GHG production under brackish conditions was low. However, the CO_2-to-CH_4 ratio of approximately 1:1, points to a relatively high level of CH_4 production. This ratio is similar to that observed in the young lagoon (LAG13) within the Reindeer Island lagoon system (Figure 4.4, Chapter 4.5.1). Since the FWL sample was not incubated under freshwater conditions, a direct comparison of GHG production between freshwater and brackish conditions .is not possible Nonetheless, previous findings shown in Figure 4.3 suggest that GHG production may decrease when transitioning from freshwater to brackish conditions, likely due to reduced microbial activity following environmental disturbance. In contrast, in the brackish lake (BWL), where microbial communities are already adapted to brackish conditions, GHG production is substantially higher. This observation implies that after a period of adaptation, GHG production in FWL sediment could increase following seawater inundation.

Salinity fluctuations have varying effects on GHG production across marine-influenced sites. In the BWL, increased salinity results in a reduction of GHG production, whereas in SDLAG, which is naturally brackish, CO_2 production rises when transitioning from brackish to marine conditions. It is likely that SDLAG sediment experienced higher salinities in the past, potentially due to brine injection beneath floating ice, leading to microbial communities that are better adapted to saline environments. Conversely, BWL is only sporadically exposed to seawater, primarily during flooding events or via lateral groundwater exchange, which makes it unlikely that salinity levels would reach significantly high concentrations. In turn, microbes are likely not yet adapted to saline conditions, resulting in the decrease in GHG production.

In the lagoon (LAG, Figure 6.1), where pore water is naturally marine, GHG production is higher under non-natural, brackish conditions. Here, the influence of salinity / sulfate on methane production is particularly evident: CH_4 is only produced under brackish conditions. This phenomenon aligns with previous observations of increased CH_4 production in brackish conditions in both Siberian and Canadian lagoons (Jenrich et al., 2024a, d; Yang et al., 2023; see Chapters 3, 4 and Appendix C). Studies have demonstrated that methanogens can coexist with SRB in low-sulfate environments, facilitating both CH_4 and CO_2 production under these conditions (Dar et al., 2008; Jenrich et al., 2024a; Yang et al., 2023). Such brackish environments are often characteristic of the early stages of transformation from terrestrial lakes to lagoons, allowing methanogens originally from terrestrial systems to persist.

Below the fully drained lagoon (DLAG), GHG production was lowest under natural marine conditions, comparable to that of UPL under marine conditions. The low water content of the DLAG sample suggests that at least the upper layers of DLAG were exposed to oxygen unlike the other lagoon and lake samples. Sequencing results shown in Figure 3.3 (Chapter 3) illustrate that the transition from aerobic to anaerobic conditions significantly impacts microbial composition. The shift from aerobic to anaerobic microbial communities is a gradual process, often leading to reduced microbial activity and consequently lower GHG production during the period of microbial adaptation.

The marine core was drilled within the former lagoon basin of SDLAG, in the section that is now fully submerged, representing the early subsea stage. CO_2 production is slightly lower compared to SDLAG, indicating that even in the early subsea stage significant amounts of CO_2 continue to be produced. Similar to SDLAG methane production is neglectable.

6.6 Conclusion

When Arctic coastal plains like those studied in Alaska are inundated with seawater, GHG production initially decreases until terrestrial microbial communities adapt to anaerobic and saline conditions. Methane production peaks under brackish conditions, while CO_2 production, generally much higher than CH_4, does not follow a clear pattern across treatments. Under near natural conditions, CO_2 production decreases slightly during the transition from terrestrial to marine environments. These findings underscore the complex interactions between microbial communities and salinity, suggesting that GHG emissions may vary considerably depending on the specific stage of lagoon development and prevailing salinity conditions.

7

Synthesis

When I began studying thermokarst lagoons in 2019, only few publications were focused on these unique Arctic water bodies, which form a transient frontier between land and ocean. These coastal ecosystems are important habitats for benthic organisms, fish, marine mammals and migratory birds, which rely on these sheltered transitional environments for feeding and breeding (Craig, 1984; Dunton et al., 2006, 2012). Besides ecological studies, existing research primarily examined the geology and evolution of thermokarst lagoons, particularly in the context of Holocene sea-level rise, with studies centered around the Mackenzie Delta region in Northwest Canada and the Bykovsky Peninsula in Northeast Siberia (Hequette et al., 1995; Hequette and Barnes, 1990; Hill, 1990; Hill and Solomon, 1999; Romanovskii et al., 2000; Schirrmeister et al., 2018). Until then, the number of thermokarst lagoons along circum-Arctic coasts, their total area, the carbon storage, and the impact of seawater inundation on permafrost thaw and carbon mobilization remained unknown.

The aim of my thesis was to address these knowledge gaps. Through multi-proxy analysis of deep sediment cores from two lagoons on the Bykovsky Peninsula, coupled with electrical resistivity surveys, my colleagues and I characterized thaw rates and the sediment history of these lagoons. I determined that approximately 5.7 Mt-C is stored in the upper 30 m of the sediment of the Bykovsky lagoons (Jenrich et al., 2021, see Appendix A), discovered pockets of hypersaline, unfrozen sediments, called cryopegs and found that permafrost beneath lagoons and inundated basins thaws 170% faster inundated Yedoma permafrost (Angelopoulos et al., 2021, see Appendix B). The analysis of lagoon sediments from the Teshekpuk coast revealed that carbon content is lower in lagoon sediments than in lakes sediments (see Chapter 6) and that organic matter is more highly degraded in saline deposits compared to deposits unaffected by saltwater (Giest et al., in submission; Appendix D).

The first mapping of Arctic lagoons between Taymyr Peninsula in North Siberia and Tuktoyaktuk Peninsula in NW Canada revealed that over half (54%) are thermokarst lagoons, originated from the flooding of former thermokarst lakes and drained basins. This widespread occurrence, combined with the knowledge that permafrost degradation is significantly accelerated in these areas, motivated me to investigate carbon mobilization during the flooding of permafrost coastal lowlands more closely. To achieve this, I measured CO_2 and CH_4 production in various sediments (permafrost, active layer, thermokarst lakes, and lagoons) from three distinct Arctic coastal regions under increasing seawater influence through four anaerobic long-term incubations (up to 415 days). During fieldwork and mapping, I recognized differences in lagoon connectivity to the sea and how this relates to various stages in the transition from a newly formed lagoon to full submergence. I developed a classification approach to categorize lagoons by their openness to better examine how GHG production evolves through the stages of land-to-sea transition (see Chapters 3, 4, and 6). The new classification highlighted the need for an updated mapping, as the initial mapping combined contiguous lagoons into single units, overlooking individual former lake basins that belong to different developmental stages and differ in GHG production (see Chapter 2). Based on the new mapping, the number of thermokarst lagoons in the study area increased from 253 (Angelopoulos et al., 2021; see Appendix B) to 520 (Jenrich et al., in review; see Chapter 2), altering the ratio of coastal to thermokarst lagoons to 30% and 70%, respectively.

The breakdown of stored organic material into CO_2 and CH_4 is carried out by microorganisms. Thus, carbon mobilization due to seawater inundation is closely linked to the response of microbial communities to changing conditions (mainly salinity and oxygen availability). This connection motivated me to analyze microbial communities in some of the incubated samples alongside GHG production. Together with colleagues, I found that young lagoons serve as transitional systems and offer suitable habitats for the establishment of new and mixed microbial communities. Lagoon environments, with high levels of organic carbon and non-competitive methanogenic substrates such as methylamines and methylated sulfur compounds, were found to support the coexistence of methanogens and other sulfate-reducing organisms (Jenrich et al., 2024a; Yang et al., 2023; see Chapter 3, 5 and Appendix C). This finding contrasts with previous assumptions that SRBs would dominate methanogens under seawater influence. The co-existence is reflected in the relatively high CH_4 production observed in low-connected lagoons. As these systems transition further towards marine environments, methanogens decline, and CO_2 becomes the dominant released GHG (Dolle et al., in review; Jenrich et al., 2024a, d; see Chapters 3, 4, 6 and Appendix E).

The thaw of ice-rich permafrost, as seen for the Bykovsky Peninsula Lagoons, leads not only to large surface subsidence but also to reworking of sediment. Based on optically stimulated luminescence analyses of feldspar, the sediment of both lagoons in depth of 25-30 m below sediment surface was deposited more than 300,000 years ago, while the analyzed carbon in these layers was younger than 50,000 years (Jenrich et al., 2021, see Appendix A). Cryoturbation (thawing and refreezing) processes can relocate young OM and the associated microorganisms into great depth. The incubation of these deep lagoon sediment samples revealed that the CO_2 production surpasses that of surface sediments under similar conditions relative to the carbon content. Therefore, substantial CO_2 production can occur in great depth after thawing and seawater infiltration, likely enhanced by the top-down movement of young OM and microbes.

In the following synthesis, I integrate the data gathered from the studies and explore potential drivers for GHG production during the early stages of the land-sea transition and in established lagoons using correlation analysis. Additionally, I examined variations in GHG production across different landscape features, regions, connectivity classes, and salinity treatments. The synthesis concludes with the first rough estimate for an upscaling of the potential carbon release from all mapped pan-Arctic lagoons.

7.1 Driving factors for GHG production

7.1.1 Early Stages of Lagoon Formation

Incubating terrestrial sediments with freshwater simulates thermokarst lakes, while brackish water mimics the early stages of lagoon formation, and marine water represents fully established lagoons. The correlation matrix in Figure 7.1, encompassing a range of biogeochemical and sediment parameters, providing indicators for potential drivers of GHG production throughout these transitions. CH_4 production shows a moderate, significant positive correlation with silt-rich deposits ($r = 0.46$, $p = 0.1$), which is positively correlated with the landscape features (1-permafrost, 2-active layer, 3-thermokarst lake), indicating higher CH_4 production in thermokarst lakes.

Additionally, increasing salinity has a significant negative impact on both CH_4 and CO_2 production for terrestrial sites, reinforcing the assumption from Chapter 3 that terrestrial microbes are not well adapted to saline conditions. This demonstrates that as ecosystems transition from freshwater to brackish and marine environments, microbial communities are under stress and need time to adapt.

The lack of strong, significant correlations between GHG production and many of the tested parameters suggests that key drivers may be missing from this analysis, and that the carbon cycle is more complex than these factors alone can explain. This analysis does not include microbial parameters due to limited data coverage, but findings from Chapters 3 and 5 suggest that the initial microbial composition is influencing the quantity and the ratio of CO_2 and CH_4 greatly. GHG production was higher when microbial communities were already adapted to the incubation conditions (anaerobic, near-natural salinity), and CH_4 was only produced when methanogens were already present in the sediment.

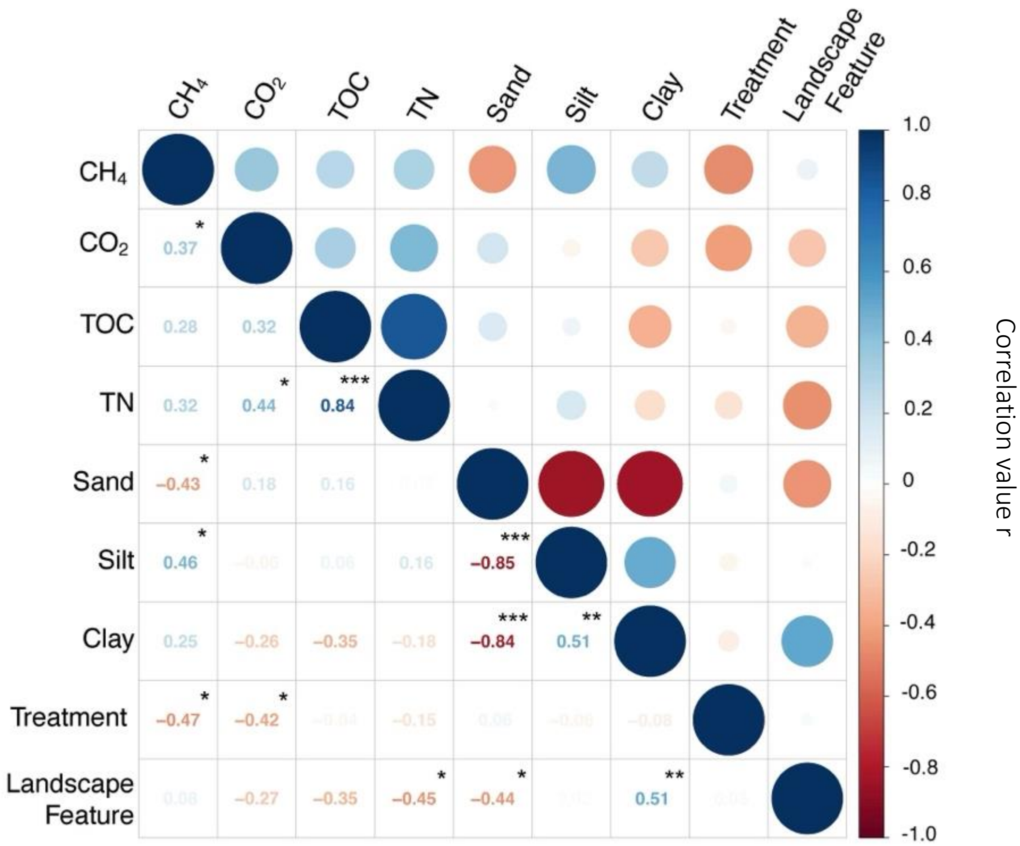

Figure 7.1 Correlation matrix illustrating the relationships between CH_4 and CO_2 production, total organic carbon (TOC), total nitrogen (TN), sedimentary parameters (sand, silt, clay) of terrestrial samples from different landscape features (1: permafrost, 2: active layer, 3: thermokarst lake) for three incubation treatments (1: freshwater, 2: brackish, 3: marine to simulate lagoon formation). Blue indicates positive and red negative correlations. Below the diagonal, the correlation coefficients are shown, accompanied by significance levels indicated by stars: p-values (0.001, 0.05, 0.1) correspond to symbols (***, **, *).

7.1.2 Established Lagoons

In contrast to terrestrial sediments, the analysis of lagoon sediments reveals stronger correlations. CO_2 production shows a significant positive correlation with both TOC ($r = 0.71$, $p = 0.001$) and TN ($r = 0.71$, $p = 0.001$), indicating that a high organic matter content leads to increased microbial respiration and, consequently, greater CO_2 production. Additionally, CO_2 production displays a clear negative correlation with $\delta^{13}C$ ($r = -0.69$, $p = 0.001$), suggesting that lighter organic carbon, typically associated with terrestrial sources (Kumar et al., 2016), is linked to higher CO_2 production. This is consistent with biomarker analyses, which reveal that terrestrial, non-salt-affected OM is less degraded compared to OM in salt-affected locations (Giest et al., in submission; see Appendix D). Less degraded OM can be decomposed more rapidly by microbes, explaining the elevated CO_2 production observed.

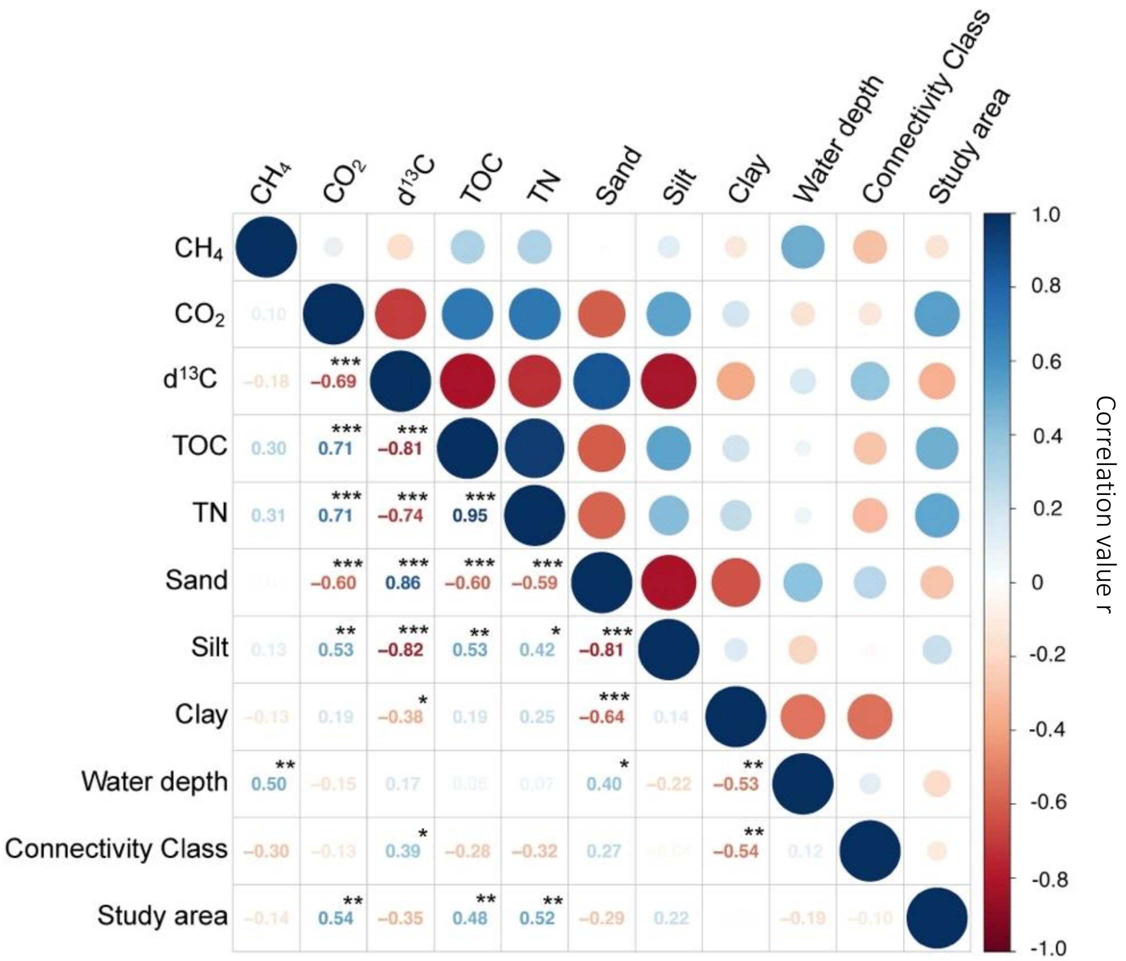

Figure 7.2 Correlation matrix illustrating the relationships between CH_4 and CO_2 production, total organic carbon (TOC), stable carbon isotopes ($\delta^{13}C$), total nitrogen (TN), sedimentary parameters (sand, silt, clay) and water depth for lagoons sites of different connectivity to the sea (1-low to 5-very high) and study areas (1: Bykovsky (Siberia); 2: Reindeer Island (Canada); 3: Teshekpuk (Alaska). Blue indicates positive and red negative correlations. Below the diagonal, the correlation coefficients are shown, accompanied by significance levels indicated by stars: p-values (0.001, 0.05, 0.1) correspond to symbols (***, **, *).

Grain size distribution, which reflects deposition patterns and transport mechanisms, is also associated with CO_2 production. As well as for the terrestrial sites (Chapter 7.1.1), CO_2 production is positively correlated with fine-grained, silty sediments ($r = 0.53$, $p = 0.001$), which are more common in sheltered, low-connected, and younger lagoons. In these environments, the accumulation of organic-rich, low degraded deposits is higher than in open lagoons, which are more connected to the sea and thus more influenced by currents resulting in higher sediment and organic matter export. Further, CO_2 production shows a moderate correlation with the study area ($r = 0.50$, $p = 0.01$), indicating that specific local environmental characteristics significantly influence the CO_2 production.

Unlike CO_2, CH_4 production does not exhibit strong correlations with TOC, TN, or $\delta^{13}C$, suggesting that methane production is less directly influenced by organic matter content or quality. Instead, CH_4 production likely depends more on microbial factors, particularly the presence of methanogens, which are essential for CH_4 production. As lagoons become more open and experience greater marine influence, the methanogens are outcompeted by SRB, resulting in decreasing CH_4 production (Holmes et al., 2017; Jenrich et al., 2024c; Kristjansson and Schönheit, 1983; Lovley et al., 1982; Yang et al., 2023; see Chapters 3, 4, and 6).

7.2 Variations in GHG Production During the Transition from Terrestrial to Marine Permafrost Environments

The synthesis-dataset encompasses the entirety of incubated sediments, from terrestrial permafrost to open lagoons under freshwater, brackish and marine condition (treatments) for all three study regions, thus reflecting GHG production across all stages of the land-sea transition. In Figure 7.3 the distribution of CO_2 and CH_4 production rates are shown for the different landscape features, regions, connectivity classes and treatments.

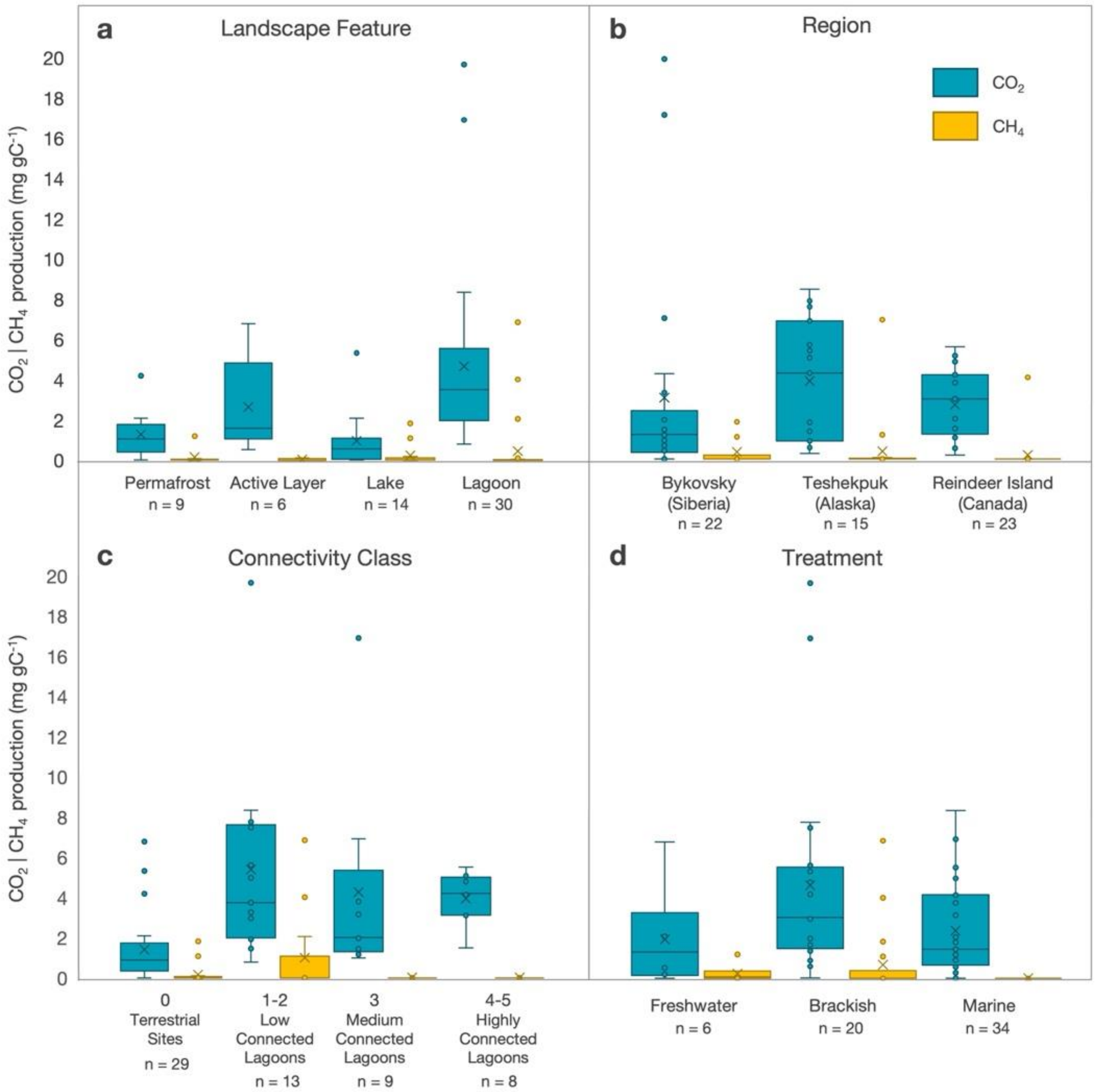

Figure 7.3 CO_2 and CH_4 production (mg C g^{-1}) after 223 days of anaerobic incubation for (a) different landscape features, (b) regions, (c) varying connectivity to the sea, whereby all terrestrial sites, including lakes are combined in class 0, and (d) salinity treatments. Box-whisker plots with outliers outside the lower and upper quartiles. Mean is symbolized by x.

7.2.1 Variations Across Landscape Features

Figure 7.3a illustrates the variations in GHG production during the transition from newly thawed terrestrial permafrost to seasonally thawed sediments, then to year-round thawed lake sediments, and finally to lagoon sediments, which were exposed to sulfate-containing seawater prior to the incubation experiment.

The overall results align well with the conclusions drawn from the individual incubation experiments discussed in Chapters 3, 4, and 5 (Jenrich et al., 2024a, d). Mean CH_4 production is low across all landscape features, though outliers suggest that certain lagoons exhibit relatively high CH_4 production. The top two outliers are the same as in Figures 7.3c and 7.3d, highlighting that young, low-connected lagoons experience the highest CH_4 production under brackish conditions.

CO_2 production is higher in the active layer compared to permafrost, likely because microbial communities require time to establish themselves (Knoblauch et al., 2013). **A key finding is that CO_2 and CH_4 production per gC is higher in lagoon sediments than in the sediment of the surrounding thermokarst lakes.** This is remarkable, as thermokarst lakes are known as GHG hotspots (Elder et al., 2021; Serikova et al., 2019; Walter Anthony et al., 2006, 2007, 2021). These studies measured *in situ* emissions, which includes more than gas production in the sediment, like also in the benthic zone and the water column, processes which are not reflected in the small-scale lab incubation experiments I conducted. However, there are no studies reporting *in situ* emissions from thermokarst lagoons. Nevertheless, the microbial analysis presented in Chapter 3.3.5, which shows that microbial diversity increases following seawater inundation and is highest in brackish thermokarst lagoons, underscores the unique nature of these habitats. Thermokarst lagoons act as ecotones, which are defined as transition zones between two distinct ecosystems (Risser, 1995), where both conditions are combined. In the lagoon system, high levels of organic carbon and non-competitive methanogenic substrates allow for the coexistence of methanogens and other sulfate-reducing organisms (Yang et al., 2023, see Appendix C), which may be the reason for the elevated GHG production in these sediments.

7.2.2 Variations Across Regions

While the study regions Teshekpuk Lake coast, Reindeer Island Lagoon System, and Bykovsky Peninsula share common characteristics — such as their location in the continuous permafrost zone, the strong influence of thermokarst processes, the presence of mostly shallow waterbodies (with water depths below 2.5 meters), and a wide range of pore water salinities (from freshwater to hypersaline) – they differ in terms of geological history, soil organic carbon content, and sediment and organic matter input pathways.

Microbial composition plays a key role in GHG production (Ernakovich et al., 2022; Jenrich et al., 2024a; Liebner et al., 2015; Mitzscherling et al., 2019). Although microbial analyses were not conducted for all sites, literature suggests that microbial communities can vary significantly even over small spatial scales (Li et al., 2019; Malard et al., 2021). Despite the unique characteristics of each region, the mean GHG production is relatively similar. Teshekpuk (Alaska) shows a slightly higher mean CO_2 production (3.8 mg gC^{-1}), followed by the Reindeer Island Lagoon System (Canada) (3.0 mg gC^{-1}) and the Bykovsky Peninsula (Siberia) (2.7 mg gC^{-1}). The high variability in CO_2 production within each location reflects the differences between landscape features, which are more pronounced than the regional differences. CH_4 production, on the other hand, shows less variability and remains consistently low across all regions, with means close to zero.

7.2.3 Variations Across Connectivity Stages

The connectivity of lagoons with the sea—essentially, their openness—reflects different stages of the lake-to-sea transition. Low-connected (Class 1-2), young lagoons exhibit the highest mean CO_2 and CH_4 production rates, as well as the greatest variability, and they also record the highest measured CO_2 production. These lagoons, which represent over 50% of pan-Arctic lagoons (Chapter 2), are unique environments that combine both lake and marine characteristics, possess higher carbon content than lagoons of other connectivity classes, and support diverse microbial communities, including both methanogens and SRB. Their sheltered nature fosters stable conditions for microbial activity. Since CH_4 has a greater global warming potential than CO_2, the GHG production in CO_2 equivalents can be up to 18 times higher than more open lagoons (Chapter 4).

In contrast, medium-connected lagoons (Class 3) and highly connected lagoons (classes 4-5) show similar mean CO_2 and CH_4 production rates, although the CO_2 production of class 3 lagoons shows greater variability. When comparing the medians, however, the differences between classes become less pronounced, which might indicate that local conditions (microbial composition and activity, organic matter characteristics, freezing processes) have the greatest influence on GHG production.

Terrestrial sites which include permafrost, active layer and lake deposits produce significantly less CO_2 and CH_4 than lagoon sites. This finding highlights the importance of lagoons, in contributing to GHG emissions in Arctic regions.

7.2.4 Variations by Salinity Level

The incubation under freshwater, brackish, and marine conditions allowed to simulate GHG production across different stages of coastal permafrost landscape development (lake formation, lagoon formation, and subsequent transition to subsea environments). As seen in Figure 7.3d, CO_2 and CH_4 production is highest under brackish conditions.

This suggests that intermediate salinity levels may promote the colonization of a greater variety of microbes, each capable of metabolizing different types of substrates, leading to overall higher carbon turnover. In contrast, extreme conditions—whether freshwater or saline—favor the growth of specialist microbial communities, which may occur in smaller numbers and may have lower metabolic rates. This could explain the lower GHG production observed under these conditions, and further highlight the special function of lagoons as transition environments.

7.3 Potential Carbon Release from pan-Arctic Lagoons

Carbon release from gradually and rapidly thawing terrestrial permafrost has been estimated in various studies (e.g. Matthews et al., 2020; Miner et al., 2022; Turetsky et al., 2020) and is now considered to be incorporated into global climate models. Although thermokarst lagoons currently cover only a small area, their significance is likely to increase as rising sea levels and intensified coastal erosion, such as that observed in the Mackenzie Delta/Tuktoyaktuk Area (see Chapter 4), lead to more flooding of coastal lowlands. As demonstrated in Chapters 3, 4, 6 and Appendix A and B saltwater inundation accelerates permafrost thaw and promotes long-term GHG production in surface layers. However, a specific estimation of carbon loss from thermokarst lagoons is still missing. Using GHG data from Chapters 3, 4, and 6, I estimated carbon loss for all mapped lagoons (see Chapter 2) as outlined in Section 1.3.5. Shallow parts of lagoons (<2 m water depth) may freeze to the bottom in winter, causing seasonal refreezing of surface sediments. Since there is no pan-Arctic dataset on the area and duration of bottom-fast ice formation in lagoons, I had to simplify the calculation by assuming the sediment does not refreeze seasonally, resulting in an estimate of maximum yearly carbon loss.

The highest total carbon loss is seen in brackish lagoons (Table 7.1). If the surface sediment of all mapped lagoons were brackish a maximum of 5 $TgCO_2eq$ per year could be released by 2100, which is comparable to the annual emissions from approximately 1.1 million gasoline-powered cars in the US (EPA, 2023). 2.3 $TgCO_2eq$ per year could be released from low connected, young lagoons (class 1 and 2). This estimation includes brackish and marine treatments accounting for the great diversity of sediment salinities. Carbon loss in CO_2 equivalents is much lower for more open lagoons with significant marine influence due to the absence of CH_4 production. On average, an estimated 3 Tg CO_2eq per year could be released from all mapped thermokarst lagoons by 2100 given the sediment remains unfrozen all year.

Table 7.1 Maximum carbon loss per year in form of CH_4 and CO_2 in CO_2-equivalents from thermokarst lagoons upscaled to the extent of the mapped lagoons. Calculated CO_2 equivalents are based on 36 gCO_2eq/gCH_4 for GWP100, which includes climate-carbon feedback and oxidation processes (IPCC, 2014).

Thermokarst Lagoons		**Area (km^2)**	**C loss in CH_4 ($Tg\ CO_2eq$)**	**C loss in CO_2 (Tg)**	**Total C loss ($Tg\ CO_2eq$)**
by Connectivity Class	1-2	1 450	1.897	0.461	2.358
	3	989	0.026	0.215	0.241
	4-5	1 018	0.019	0.333	0.352
by Treatment	Brackish	3 457	4.008	1.124	5.132
	Marine	3 457	0.055	0.759	0.814
Average		**3 457**	**1.928**	**1.091**	**3.019**

C release from thermokarst lakes (covering an area of 1.1×10^6 km^2) based on flux measurements was estimated at 14 to 18 Tg CH_4 per year, which corresponds to 108 days of thaw (Matthews et al., 2020). This equates to 174–223 Tg CO_2 equivalent (CO_2eq) when accounting for the higher global warming potential of CH_4. In terms of yearly emissions per unit area, thermokarst lagoons release an average of 0.87×10^{-3} Tg CO_2eq/km^2 for year-round thaw or 0.26×10^{-3} Tg CO_2eq/km^2 for 108 days of thaw. This exceeds emissions from thermokarst lakes, which emit $0.16–0.2 \times 10^{-3}$ Tg CO_2eq/km^2 for 108 days of thaw. These findings align well with results from my incubation studies, which showed that greenhouse gas production in surrounding thermokarst lake sediments was lower than in lagoon sediments (Figure 7.3a).

Carbon emissions from gradual and abrupt permafrost thaw (including features such as lakes and thaw slumps) result in releases of $0.034–0.045 \times 10^{-3}$ Tg CO_2eq/km^2 per year (613–802 Tg CO_2eq over 18×10^6 km^2) and 0.39×10^{-3} Tg CO_2eq/km^2 (624 Tg CO_2eq over 1.6×10^6 km^2), respectively (Turetsky et al., 2020). These estimates are based on aerobic incubation results used to model carbon pool turnover times at 5°C (Koven et al., 2015). Although these results are not directly comparable to my own estimates due to differences in methodology, both approaches yield values within the same order of magnitude, indicating a similar scale of carbon release.

Given the relatively higher potential C release per area and the expected increase in lagoon formation, thermokarst lagoons may play a more important role in the carbon budget of rapidly thawing Arctic landscapes than previously anticipated.

7.4 Conclusion and Outlook

CONCLUSION

The section addresses the research questions stated in Chapter 1.2 and provides an outlook on future research opportunities.

Concerning the first question on 'the spatial pan-Arctic extent of thermokarst lagoons, how are they distributed and how can they be classified according to their development stages', I mapped 520 thermokarst lagoons distributed along five Arctic shelf seas (Laptev, East Siberian, Chukchi, Alaskan Beaufort, and Canadian Beaufort seas) from the Taymyr Peninsula to the Tuktoyaktuk Peninsula. These lagoons cover an area of 3,457 km^2. They differ in size and distribution across the regions, with the majority found along the Canadian Beaufort Sea. I classified the lagoons based on their connectivity to the sea into five classes (high connected, always open lagoons to very low connected, nearly-closed lagoons), with 55% categorized as very low to low connected lagoons, which are in the early stage of lake to lagoon transition. From 2000 to 2021, lagoon area expanded across all regions, with the most significant growth occurring along the Alaskan Beaufort Sea coast, at a rate of 1.34%.

Concerning my second question on the effect of increasing seawater influence on GHG production and microbial community composition, I found an initial decrease in CO_2 production when freshwater permafrost sites are flooded with seawater. This reduction occurs due to the disruption of established microbial communities, which require time to adapt to increased salinity and anaerobic conditions. Over time, however, as salt-tolerant, anaerobic microbial communities establish, CO_2 and CH_4 production tends to increase, especially under brackish conditions in young lagoons where both terrestrial and marine microbes are present. This increase can be as much as eight times the CO_2 levels in terrestrial permafrost. Methane production is higher under brackish conditions than under either freshwater or marine conditions. This is due to the presence of both methanogenic archaea and SRB that can coexist in low-sulfate, brackish environments. Under fully marine conditions, SRB outcompete methanogens due to the higher sulfate concentrations. Therefore, methane emissions decline as the lagoon fully transitions to marine conditions, with CO_2 becoming the dominant greenhouse gas.

Finally, concerning my third question whether GHG production of inundated Arctic coastal lowlands differ between landscape features and regions. My clear answer is: Yes. CO_2 and CH_4 production are highest in lagoon sediments, followed by the active layer, permafrost, and then lake sediments. In lagoon sediments, which have been inundated prior to incubation, microbial communities are already adapted to saline conditions, unlike those in terrestrial features. This adaptation likely explains why GHG production is higher below lagoons.

Despite the unique environmental characteristics of each region, mean GHG production remains relatively consistent across Arctic coastal areas, with the Teshekpuk

Coast showing a slightly higher average CO_2 production than Reindeer Island and the Bykovsky Peninsula. As a result, the differences in GHG production are more pronounced on a local scale between distinct landscape features than across broader regional scales, where local variations tend to even out.

OUTLOOK

The incubation experiments I developed were useful for understanding the impact of changing salinities on microbial dynamics and GHG production in seawater-inundated terrestrial and lagoon sediments, as coastal permafrost landscapes transition to marine environments. The back-of-the-envelope upscaling of potential carbon loss from thermokarst lagoons, which revealed based on the incubation results a higher C production per area than the release for lakes and thawing permafrost, highlights the need for targeted research, especially as these lagoons continue to develop along Arctic coastlines.

To improve predictions of GHG release from inundated permafrost, it is essential to enhance *in situ* flux measurements, conduct more detailed characterizations of microbial communities, and improve our understanding of the environmental variables that influence carbon cycling. To my knowledge, there are currently no published *in situ* GHG flux data for thermokarst lagoons. Such measurements are crucial for accurately predicting GHG emissions from these lagoons, as they account for processes such as CH_4 oxidation, additional GHG production in the benthic zone and water column, seasonal changes, and other natural conditions that I was unable to capture in my laboratory experiments. Additionally, these measurements help validate lab-based incubation results and inform global climate models by capturing fluxes in real-time.

To build a more comprehensive dataset, a network of flux measurement sites across different lagoon types and regions should be established. Continuous measurements over extended periods would enhance our understanding of seasonal and long-term changes in GHG emissions.

Given that the decomposition of organic matter and the subsequent release of CO_2 and CH_4 is done by microbial communities, detailed characterization of these communities across various lowland coastal environments and lagoon types would be helpful. Different microbes respond distinctly to factors like temperature, salinity, and oxygen availability, which influence GHG production.

The organic carbon content and quality, along with the availability of nutrients, significantly impact GHG production. However, only a limited number of thermokarst lagoons have been analyzed so far. Establishing long-term monitoring sites would be beneficial for generating extensive datasets. This monitoring can be accomplished through a combination of remote sensing and ground-based measurements to track lagoon sediment and nutrient flow (e.g., using ocean color remote sensing techniques), lagoon ice thickness, and water and sediment characteristics. Furthermore, remote sensing could be used to predict likelihoods where and when new lagoons may be developed, and to monitor changes in lagoon size, data, which is needed for upscaling approaches.

The combined dataset would enable detailed simulations of future GHG release from inundated Arctic coastal lowlands under various climate warming.

BIBLIOGRAPHY

Aciego Pietri, J. C. and Brookes, P. C.: Relationships between soil pH and microbial properties in a UK arable soil, Soil Biology and Biochemistry, 40, 1856–1861, https://doi.org/10.1016/j.soilbio.2008.03.020, 2008.

Akinyede, R., Taubert, M., Schrumpf, M., Trumbore, S., and Küsel, K.: Rates of dark CO2 fixation are driven by microbial biomass in a temperate forest soil, Soil Biology and Biochemistry, 150, 107950, https://doi.org/10.1016/j.soilbio.2020.107950, 2020.

An, L., Yan, Y.-C., Tian, H.-L., Chi, C.-Q., Nie, Y., and Wu, X.-L.: Roles of sulfate-reducing bacteria in sustaining the diversity and stability of marine bacterial community, Front. Microbiol., 14, https://doi.org/10.3389/fmicb.2023.1218828, 2023.

Angelopoulos, M.: Mapping subsea permafrost with electrical resistivity surveys, Nat Rev Earth Environ, 3, 6–6, https://doi.org/10.1038/s43017-021-00258-5, 2022.

Angelopoulos, M., Westermann, S., Overduin, P., Faguet, A., Olenchenko, V., Grosse, G., and Grigoriev, M. N.: Heat and Salt Flow in Subsea Permafrost Modeled with CryoGRID2, Journal of Geophysical Research: Earth Surface, 124, 920–937, https://doi.org/10.1029/2018JF004823, 2019.

Angelopoulos, M., Overduin, P. P., Miesner, F., Grigoriev, M. N., and Vasiliev, A. A.: Recent advances in the study of Arctic submarine permafrost, Permafrost and Periglacial Processes, 31, 442–453, https://doi.org/10.1002/ppp.2061, 2020a.

Angelopoulos, M., Overduin, P. P., Westermann, S., Tronicke, J., Strauss, J., Schirrmeister, L., Biskaborn, B. K., Liebner, S., Maksimov, G., Grigoriev, M. N., and Grosse, G.: Thermokarst Lake to Lagoon Transitions in Eastern Siberia: Do Submerged Taliks Refreeze?, Journal of Geophysical Research: Earth Surface, 125, e2019JF005424, https://doi.org/10.1029/2019JF005424, 2020b.

Angelopoulos, M., Overduin, P. P., Jenrich, M., Nitze, I., Günther, F., Strauss, J., Westermann, S., Schirrmeister, L., Kholodov, A., Krautblatter, M., Grigoriev, M. N., and Grosse, G.: Onshore Thermokarst Primes Subsea Permafrost Degradation, Geophysical Research Letters, 48, e2021GL093881, https://doi.org/10.1029/2021GL093881, 2021.

Anon: LTER Core Research Areas, LTER, 2019.

Arboleda-Zapata, M., Angelopoulos, M., Overduin, P. P., Grosse, G., Jones, B. M., and Tronicke, J.: Exploring the capabilities of electrical resistivity tomography to study subsea permafrost, The Cryosphere, 16, 4423–4445, https://doi.org/10.5194/tc-16-4423-2022, 2022.

Arp, C. D., Jones, B. M., Urban, F. E., and Grosse, G.: Hydrogeomorphic processes of thermokarst lakes with grounded-ice and floating-ice regimes on the Arctic coastal plain, Alaska, Hydrological Processes, 25, 2422–2438, https://doi.org/10.1002/hyp.8019, 2011.

Balcombe, P., Speirs, J. F., Brandon, N. P., and Hawkes, A. D.: Methane emissions: choosing the right climate metric and time horizon, Environ. Sci.: Processes Impacts, 20, 1323–1339, https://doi.org/10.1039/C8EM00414E, 2018.

Barbato, R. A., Jones, R. M., Douglas, T. A., Doherty, S. J., Messan, K., Foley, K. L., Perkins, E. J., Thurston, A. K., and Garcia-Reyero, N.: Not all permafrost microbiomes are created equal: Influence of permafrost thaw on the soil microbiome in a laboratory incubation study, Soil Biology and Biochemistry, 167, 108605, https://doi.org/10.1016/j.soilbio.2022.108605, 2022.

Beamish, A., Raynolds, M. K., Epstein, H., Frost, G. V., Macander, M. J., Bergstedt, H., Bartsch, A., Kruse, S., Miles, V., Tanis, C. M., Heim, B., Fuchs, M., Chabrillat, S., Shevtsova, I., Verdonen, M., and Wagner, J.: Recent trends and remaining challenges for optical remote sensing of Arctic tundra vegetation: A review and outlook, Remote Sensing of Environment, 246, 111872, https://doi.org/10.1016/j.rse.2020.111872, 2020.

Berry, H. B., Whalen, D., and Lim, M.: Long-term ice-rich permafrost coast sensitivity to air temperatures and storm influence: lessons from Pullen Island, Northwest Territories, Canada, Arctic Science, 7, 723–745, https://doi.org/10.1139/as-2020-0003, 2021.

Beulig, F., Urich, T., Nowak, M., Trumbore, S. E., Gleixner, G., Gilfillan, G. D., Fjelland, K. E., and Küsel, K.: Altered carbon turnover processes and microbiomes in soils under long-term extremely high CO2 exposure, Nat Microbiol, 1, 1–10, https://doi.org/10.1038/nmicrobiol.2015.25, 2016.

Bischoff, V.: Carbon Degradation and Potential Greenhouse Gas Production in a Changing Arctic Thermokarst Landscape—A Case Study From Drained Lake Basins on the Yukon Coastal Plain, Canada, RWTH Aachen University, Germany, 2024.

Blott, S. J. and Pye, K.: GRADISTAT: a grain size distribution and statistics package for the analysis of unconsolidated sediments, Earth Surf Processes Landf, 26, 1237–1248, https://doi.org/10.1002/esp.261, 2001.

Bockheim, J. G. and Hinkel, K. M.: The Importance of "Deep" Organic Carbon in Permafrost-Affected Soils of Arctic Alaska, Soil Science Society of America Journal, 71, 1889–1892, https://doi.org/10.2136/sssaj2007.0070N, 2007.

Brown, J., Jr, O. J. F., Heginbottom, J. A., and Melnikov, E. S.: Circum-Arctic map of permafrost and ground-ice conditions, Circum-Pacific Map, U.S. Geological Survey, https://doi.org/10.3133/cp45, 1997.

Burn, C. R.: The hydrologic regime of Mackenzie River and connection of "no-closure" lakes to distributary channels in the Mackenzie Delta, Northwest Territories, Can. J. Earth Sci., 32, 926–937, https://doi.org/10.1139/e95-078, 1995.

Burn, C. R.: Tundra lakes and permafrost, Richards Island, western Arctic coast, Canada, Can. J. Earth Sci., 39, 1281–1298, https://doi.org/10.1139/e02-035, 2002.

Bush, T., Diao, M., Allen, R. J., Sinnige, R., Muyzer, G., and Huisman, J.: Oxic-anoxic regime shifts mediated by feedbacks between biogeochemical processes and microbial community dynamics, Nat Commun, 8, 789, https://doi.org/10.1038/s41467-017-00912-x, 2017.

Callahan, B. J., McMurdie, P. J., Rosen, M. J., Han, A. W., Johnson, A. J. A., and Holmes, S. P.: DADA2: High-resolution sample inference from Illumina amplicon data, Nat Methods, 13, 581–583, https://doi.org/10.1038/nmeth.3869, 2016.

Carroll, J. J., Slupsky, J. D., and Mather, A. E.: The Solubility of Carbon Dioxide in Water at Low Pressure, Journal of Physical and Chemical Reference Data, 20, 1201–1209, https://doi.org/10.1063/1.555900, 1991.

Carson, M. A., Jasper, J. N., and Conly, F. M.: Magnitude and Sources of Sediment Input to the Mackenzie Delta, Northwest Territories, 1974–94, Arctic, 51, 116–124, 1998.

Chalov, S., Prokopeva, K., Magritsky, D., Grigoriev, V., Fingert, E., Habel, M., Juhls, B., Morgenstern, A., Overduin, P. P., and Kasimov, N.: Climate change impacts on streamflow, sediment load and carbon fluxes in the Lena River delta, Ecological Indicators, 157, 111252, https://doi.org/10.1016/j.ecolind.2023.111252, 2023.

Chan, N.-H., Langer, M., Juhls, B., Rettelbach, T., Overduin, P., Huppert, K., and Braun, J.: An Arctic delta reduced-complexity model and its reproduction of key geomorphological structures, Earth Surface Dynamics, 11, 259–285, https://doi.org/10.5194/esurf-11-259-2023, 2023.

Cohen, J., Zhang, X., Francis, J., Jung, T., Kwok, R., Overland, J., Ballinger, T. J., Bhatt, U. S., Chen, H. W., Coumou, D., Feldstein, S., Gu, H., Handorf, D., Henderson, G., Ionita, M., Kretschmer, M., Laliberte, F., Lee, S., Linderholm, H. W., Maslowski, W., Peings, Y., Pfeiffer, K., Rigor, I., Semmler, T., Stroeve, J., Taylor, P. C., Vavrus, S., Vihma, T., Wang, S., Wendisch, M., Wu, Y., and Yoon, J.: Divergent consensuses on Arctic amplification influence on midlatitude severe winter weather, Nat. Clim. Chang., 10, 20–29, https://doi.org/10.1038/s41558-019-0662-y, 2020.

Coolen, M. J. L. and Orsi, W. D.: The transcriptional response of microbial communities in thawing Alaskan permafrost soils, Frontiers in Microbiology, 6, 2015.

Coolen, M. J. L., van de Giessen, J., Zhu, E. Y., and Wuchter, C.: Bioavailability of soil organic matter and microbial community dynamics upon permafrost thaw, Environmental Microbiology, 13, 2299–2314, https://doi.org/10.1111/j.1462-2920.2011.02489.x, 2011.

Copernicus Sentinel: Copernicus Data Space Ecosystem Browser, 2024.

Craig, P. C.: Fish Use of Coastal Waters of the Alaskan Beaufort Sea: A Review, Transactions of the American Fisheries Society, 113, 265–282, https://doi.org/10.1577/1548-8659(1984)113<265:FUOCWO>2.0.CO;2, 1984.

Crawshaw, J. A., Schallenberg, M., and Savage, C.: Physical and biological drivers of sediment oxygenation and denitrification in a New Zealand intermittently closed and open lake lagoon, New Zealand Journal of Marine and Freshwater Research, 53, 33–59, https://doi.org/10.1080/00288330.2018.1476388, 2019.

Creel, R., Guimond, J., Jones, B. M., Nielsen, D. M., Bristol, E., Tweedie, C. E., and Overduin, P. P.: Permafrost thaw subsidence, sea-level rise, and erosion are transforming Alaska's Arctic coastal zone, Proceedings of the National Academy of Sciences, 121, e2409411121, https://doi.org/10.1073/pnas.2409411121, 2024.

Dar, S. A., Kleerebezem, R., Stams, A. J. M., Kuenen, J. G., and Muyzer, G.: Competition and coexistence of sulfate-reducing bacteria, acetogens and methanogens in a lab-scale anaerobic bioreactor as affected by changing substrate to sulfate ratio, Appl Microbiol Biotechnol, 78, 1045–1055, https://doi.org/10.1007/s00253-008-1391-8, 2008.

Dodd, C. E. R.: PSEUDOMONAS | Introduction, in: Encyclopedia of Food Microbiology (Second Edition), edited by: Batt, C. A. and Tortorello, M. L., Academic Press, Oxford, 244–247, https://doi.org/10.1016/B978-0-12-384730-0.00282-2, 2014.

Dolle, M. L., Laurent, M., Schaller, J., Seemann, F., Jenrich, M., Strauss, J., and Treat, C.: Effect of Sea Water Inundation on CO2 and CH4 Production of Thawing Coastal Permafrost near Utqiaġvik, Alaska, in review.

Douglas, P. M. J., Gonzalez Moguel, R., Walter Anthony, K. M., Wik, M., Crill, P. M., Dawson, K. S., Smith, D. A., Yanay, E., Lloyd, M. K., Stolper, D. A., Eiler, J. M., and Sessions, A. L.: Clumped Isotopes Link Older Carbon Substrates With Slower Rates of Methanogenesis in Northern Lakes, Geophysical Research Letters, 47, e2019GL086756, https://doi.org/10.1029/2019GL086756, 2020.

Dunton, K. H., Weingartner, T., and Carmack, E. C.: The nearshore western Beaufort Sea ecosystem: Circulation and importance of terrestrial carbon in arctic coastal food webs, Progress in Oceanography, 71, 362–378, https://doi.org/10.1016/j.pocean.2006.09.011, 2006.

Dunton, K. H., Schonberg, S. V., and Cooper, L. W.: Food Web Structure of the Alaskan Nearshore Shelf and Estuarine Lagoons of the Beaufort Sea, Estuaries and Coasts, 35, 416–435, https://doi.org/10.1007/s12237-012-9475-1, 2012.

Dunton, K. H., Whiteaker, T., and McMeans, B.: LTER: Seasonal Controls and Emergent Effects of Changing Land-Ice-Ocean Interactions on Arctic Coastal Ecosystems (BLE II), UNIVERSITY OF TEXAS AT AUSTIN, 2023.

Dutta, K., Schuur, E. a. G., Neff, J. C., and Zimov, S. A.: Potential carbon release from permafrost soils of Northeastern Siberia, Global Change Biology, 12, 2336–2351, https://doi.org/10.1111/j.1365-2486.2006.01259.x, 2006.

Dyksma, S. and Pester, M.: Oxygen respiration and polysaccharide degradation by a sulfate-reducing acidobacterium, Nat Commun, 14, 6337, https://doi.org/10.1038/s41467-023-42074-z, 2023.

Eisner, W. R., Bockheim, J. G., Hinkel, K. M., Brown, T. A., Nelson, F. E., Peterson, K. M., and Jones, B. M.: Paleoenvironmental analyses of an organic deposit from an erosional landscape remnant, Arctic Coastal Plain of Alaska, Palaeogeography, Palaeoclimatology, Palaeoecology, 217, 187–204, https://doi.org/10.1016/j.palaeo.2004.11.025, 2005.

Elder, C. D., Xu, X., Walker, J., Schnell, J. L., Hinkel, K. M., Townsend-Small, A., Arp, C. D., Pohlman, J. W., Gaglioti, B. V., and Czimczik, C. I.: Greenhouse gas emissions from diverse Arctic Alaskan lakes are dominated by young carbon, Nature Clim Change, 8, 166–171, https://doi.org/10.1038/s41558-017-0066-9, 2018.

Elder, C. D., Schweiger, M., Lam, B., Crook, E. D., Xu, X., Walker, J., Walter Anthony, K. M., and Czimczik, C. I.: Seasonal Sources of Whole-Lake CH4 and CO2 Emissions From Interior Alaskan Thermokarst Lakes, Journal of Geophysical Research: Biogeosciences, 124, 1209–1229, https://doi.org/10.1029/2018JG004735, 2019.

Elder, C. D., Thompson, D. R., Thorpe, A. K., Chandanpurkar, H. A., Hanke, P. J., Hasson, N., James, S. R., Minsley, B. J., Pastick, N. J., Olefeldt, D., Walter Anthony, K. M., and Miller, C. E.: Characterizing Methane Emission Hotspots From Thawing Permafrost, Global Biogeochemical Cycles, 35, e2020GB006922, https://doi.org/10.1029/2020GB006922, 2021.

EPA: Tailpipe Greenhouse Gas Emissions from a Typical Passenger Vehicle, U.S. Environmental Protection Agency, Office of Transportation and Air Quality, 2000 Traverwood Drive Ann Arbor, MI 48105, USA, 2023.

Ernakovich, J. G., Barbato, R. A., Rich, V. I., Schädel, C., Hewitt, R. E., Doherty, S. J., Whalen, E. D., Abbott, B. W., Barta, J., Biasi, C., Chabot, C. L., Hultman, J., Knoblauch, C., Vetter, M. C. Y. L., Leewis, M.-C., Liebner, S., Mackelprang, R., Onstott, T. C., Richter, A., Schütte, U. M. E., Siljanen, H. M. P., Taş, N., Timling, I., Vishnivetskaya, T. A., Waldrop, M. P., and Winkel, M.: Microbiome assembly in thawing permafrost and its feedbacks to climate, Global Change Biology, 28, 5007–5026, https://doi.org/10.1111/gcb.16231, 2022.

Fenchel, T., King, G. M., and Blackburn, T. H.: Chapter 1 - Bacterial Metabolism, in: Bacterial Biogeochemistry (Third Edition), edited by: Fenchel, T., King, G. M., and Blackburn, T. H., Academic Press, Boston, 1–34, https://doi.org/10.1016/B978-0-12-415836-8.00001-3, 2012.

Fortier, D., Allard, M., and Shur, Y.: Observation of rapid drainage system development by thermal erosion of ice wedges on Bylot Island, Canadian Arctic Archipelago, Permafrost and Periglacial Processes, 18, 229–243, https://doi.org/10.1002/ppp.595, 2007.

Fraley, K. M., Robards, M. D., Rogers, M. C., Vollenweider, J., Smith, B., Whiting, A., and Jones, T.: Freshwater input and ocean connectivity affect habitats and trophic ecology of fishes in Arctic coastal lagoons, Polar Biol, 44, 1401–1414, https://doi.org/10.1007/s00300-021-02895-4, 2021.

Fraley, K. M., Jones, T., Robards, M. D., Smith, B., Tibbles, M., and Whiting, A.: The Forgotten Coast: A Synthesis of Current Knowledge of Southern Chukchi Sea Lagoon Ecosystems, ARCTIC, 75, 300–319, https://doi.org/10.14430/arctic75608, 2022.

Fritz, M., Opel, T., Tanski, G., Herzschuh, U., Meyer, H., Eulenburg, A., and Lantuit, H.: Dissolved organic carbon (DOC) in Arctic ground ice, The Cryosphere, 9, 737–752, https://doi.org/10.5194/tc-9-737-2015, 2015.

Fritz, M., Vonk, J. E., and Lantuit, H.: Collapsing Arctic coastlines, Nature Clim Change, 7, 6–7, https://doi.org/10.1038/nclimate3188, 2017.

Fuchs, M., Grosse, G., Strauss, J., Günther, F., Grigoriev, M., Maximov, G. M., and Hugelius, G.: Carbon and nitrogen pools in thermokarst-affected permafrost landscapes in Arctic Siberia, Biogeosciences, 15, 953–971, https://doi.org/10.5194/bg-15-953-2018, 2018.

Galera, L. de A., Eckhardt, T., Beer, C., Pfeiffer, E.-M., and Knoblauch, C.: Ratio of In Situ CO2 to CH4 Production and Its Environmental Controls in Polygonal Tundra Soils of Samoylov Island, Northeastern Siberia, Journal of Geophysical Research: Biogeosciences, 128, e2022JG006956, https://doi.org/10.1029/2022JG006956, 2023.

Giest, F. P.: Carbon Storage, Carbon Degradation and Sediment Transport Mechanisms in a Changing Coastal Thermokarst Landscape—Case Study for a Land—Near Shore Transect in the Teshekpuk Lake Region, Alaska, USA, University of Potsdam, Germany, 2024.

Giest, F. P., Jenrich, M., Grosse, G., Jones, B. M., Mangelsdorf, K., Windirsch, T., and Strauss, J.: Organic Carbon, Mercury, and Sediment Characteristics along a land – shore transect in Arctic Alaska, submitted to Biogeosciences, n.d.

Gordeev, V. V.: Fluvial sediment flux to the Arctic Ocean, Geomorphology, 80, 94–104, https://doi.org/10.1016/j.geomorph.2005.09.008, 2006.

Gorelick, N., Hancher, M., Dixon, M., Ilyushchenko, S., Thau, D., and Moore, R.: Google Earth Engine: Planetary-scale geospatial analysis for everyone, Remote Sensing of Environment, 202, 18–27, https://doi.org/10.1016/j.rse.2017.06.031, 2017.

Grasby, S. E., Rod Smith, I., Bell, T., and Forbes, D. L.: Cryogenic formation of brine and sedimentary mirabilite in submergent coastal lake basins, Canadian Arctic, Geochimica et Cosmochimica Acta, 110, 13–28, https://doi.org/10.1016/j.gca.2013.02.014, 2013.

Greene, S., Walter Anthony, K. M., Archer, D., Sepulveda-Jauregui, A., and Martinez-Cruz, K.: Modeling the impediment of methane ebullition bubbles by seasonal lake ice, Biogeosciences, 11, 6791–6811, https://doi.org/10.5194/bg-11-6791-2014, 2014.

Grosse, G., Schirrmeister, L., Kunitsky, V. V., and Hubberten, H.-W.: The use of CORONA images in remote sensing of periglacial geomorphology: an illustration from the NE Siberian coast, Permafrost and Periglacial Processes, 16, 163–172, https://doi.org/10.1002/ppp.509, 2005.

Grosse, G., Morgenstern, A., and Lantuit, H.: Distribution of Thermokarst Lakes and Ponds at Three Yedoma Sites in Siberia, NINTH INTERNATIONAL CONFERENCE ON PERMAFROST, 2008.

Grosse, G., Jones, B., and Arp, C.: 8.21 Thermokarst Lakes, Drainage, and Drained Basins, in: Treatise on Geomorphology, edited by: Shroder, J. F., Academic Press, San Diego, 325–353, https://doi.org/10.1016/B978-0-12-374739-6.00216-5, 2013.

Guimond, J. A., Mohammed, A. A., Walvoord, M. A., Bense, V. F., and Kurylyk, B. L.: Saltwater Intrusion Intensifies Coastal Permafrost Thaw, Geophysical Research Letters, 48, e2021GL094776, https://doi.org/10.1029/2021GL094776, 2021.

Günther, F., Overduin, P. P., Sandakov, A. V., Grosse, G., and Grigoriev, M. N.: Short- and long-term thermo-erosion of ice-rich permafrost coasts in the Laptev Sea region, Biogeosciences, 10, 4297–4318, https://doi.org/10.5194/bg-10-4297-2013, 2013.

Günther, F., Overduin, P. P., Yakshina, I. A., Opel, T., Baranskaya, A. V., and Grigoriev, M. N.: Observing Muostakh disappear: permafrost thaw subsidence and erosion of a ground-ice-rich island in response to arctic summer warming and sea ice reduction, The Cryosphere, 9, 151–178, https://doi.org/10.5194/tc-9-151-2015, 2015.

Gutekunst, C. N., Liebner, S., Jenner, A.-K., Knorr, K.-H., Unger, V., Koebsch, F., Racasa, E. D., Yang, S., Böttcher, M. E., Janssen, M., Kallmeyer, J., Otto, D., Schmiedinger, I., Winski, L., and Jurasinski, G.: Effects of brackish water inflow on methane-cycling microbial communities in a freshwater rewetted coastal fen, Biogeosciences, 19, 3625–3648, https://doi.org/10.5194/bg-19-3625-2022, 2022.

Hagen, D.: Coastal storm flooding hits Kotzebue-area communities, Alaska Public Media, 2024.

Hall, S. B., Subrahmanyam, B., and Steele, M.: The Role of the Russian Shelf in Seasonal and Interannual Variability of Arctic Sea Surface Salinity and Freshwater Content, Journal of Geophysical Research: Oceans, 128, e2022JC019247, https://doi.org/10.1029/2022JC019247, 2023.

Harris, C. M., McClelland, J. W., Connelly, T. L., Crump, B. C., and Dunton, K. H.: Salinity and Temperature Regimes in Eastern Alaskan Beaufort Sea Lagoons in Relation to Source Water Contributions, Estuaries and Coasts, 40, 50–62, https://doi.org/10.1007/s12237-016-0123-z, 2017.

Harris, P. T., Macmillan-Lawler, M., Rupp, J., and Baker, E. K.: Geomorphology of the oceans, Marine Geology, 352, 4–24, https://doi.org/10.1016/j.margeo.2014.01.011, 2014.

Hequette, A. and Barnes, P. W.: Coastal retreat and shoreface profile variations in the Canadian Beaufort Sea, Marine Geology, 91, 113–132, https://doi.org/10.1016/0025-3227(90)90136-8, 1990.

Hequette, A., Ruz, M.-H., and Hill, P. R.: The effects of the Holocene sea level rise on the evolution of the southeastern coast of the Canadian Beaufort Sea, Journal of Coastal Research, 494–507, 1995.

Hequette, A., Desrosiers, M., Hill, P. R., and Forbes, D. L.: The Influence of Coastal Morphology on Shoreface Sediment Transport under Storm Combined Flows, Canadian Beaufort Sea, Journal of Coastal Research, 17, 2001.

Heslop, J. K., Walter Anthony, K. M., Sepulveda-Jauregui, A., Martinez-Cruz, K., Bondurant, A., Grosse, G., and Jones, M. C.: Thermokarst lake methanogenesis along a complete talik profile, Biogeosciences, 12, 4317–4331, https://doi.org/10.5194/bg-12-4317-2015, 2015.

Heslop, J. k., Winkel, M., Walter Anthony, K. m., Spencer, R. g. m., Podgorski, D. c., Zito, P., Kholodov, A., Zhang, M., and Liebner, S.: Increasing Organic Carbon Biolability With Depth in Yedoma Permafrost: Ramifications for Future Climate Change, Journal of Geophysical Research: Biogeosciences, 124, 2021–2038, https://doi.org/10.1029/2018JG004712, 2019.

Heslop, J. K., Walter Anthony, K. M., Winkel, M., Sepulveda-Jauregui, A., Martinez-Cruz, K., Bondurant, A., Grosse, G., and Liebner, S.: A synthesis of methane dynamics in thermokarst lake environments, Earth-Science Reviews, 210, 103365, https://doi.org/10.1016/j.earscirev.2020.103365, 2020.

Hill, P. R.: Coastal geology of the King Point area, Yukon Territory, Canada, Marine Geology, 91, 93–111, https://doi.org/10.1016/0025-3227(90)90135-7, 1990.

Hill, P. R. and Solomon, S.: Geomorphologic and Sedimentary Evolution of a Transgressive Thermokarst Coast, Mackenzie Delta Region, Canadian Beaufort Sea, Journal of Coastal Research, 15, 1999.

Hinkel, K. M., Frohn, R. C., Nelson, F. E., Eisner, W. R., and Beck, R. A.: Morphometric and spatial analysis of thaw lakes and drained thaw lake basins in the western Arctic Coastal Plain, Alaska, Permafrost and Periglacial Processes, 16, 327–341, https://doi.org/10.1002/ppp.532, 2005.

Hinkel, K. M., Jones, B. M., Eisner, W. R., Cuomo, C. J., Beck, R. A., and Frohn, R.: Methods to assess natural and anthropogenic thaw lake drainage on the western Arctic coastal plain of northern Alaska, Journal of Geophysical Research: Earth Surface, 112, https://doi.org/10.1029/2006JF000584, 2007.

Hinkel, K. M., Lenters, J. D., Sheng, Y., Lyons, E. A., Beck, R. A., Eisner, W. R., Maurer, E. F., Wang, J., and Potter, B. L.: Thermokarst Lakes on the Arctic Coastal Plain of Alaska: Spatial and Temporal Variability in Summer Water Temperature, Permafrost and Periglacial Processes, 23, 207–217, https://doi.org/10.1002/ppp.1743, 2012.

Holm, S., Walz, J., Horn, F., Yang, S., Grigoriev, M. N., Wagner, D., Knoblauch, C., and Liebner, S.: Methanogenic response to long-term permafrost thaw is determined by paleoenvironment, FEMS Microbiology Ecology, 96, fiaa021, https://doi.org/10.1093/femsec/fiaa021, 2020.

Holmer, M. and Kristensen, E.: Coexistence of sulfate reduction and methane production in an organic-rich sediment, Mar. Ecol. Prog. Ser., 107, 177–184, https://doi.org/10.3354/meps107177, 1994.

Holmes, D. E., Shrestha, P. M., Walker, D. J. F., Dang, Y., Nevin, K. P., Woodard, T. L., and Lovley, D. R.: Metatranscriptomic Evidence for Direct Interspecies Electron Transfer between Geobacter and Methanothrix Species in Methanogenic Rice Paddy Soils, Appl Environ Microbiol, 83, e00223-17, https://doi.org/10.1128/AEM.00223-17, 2017.

Hugelius, G., Strauss, J., Zubrzycki, S., Harden, J. W., Schuur, E. a. G., Ping, C.-L., Schirrmeister, L., Grosse, G., Michaelson, G. J., Koven, C. D., O'Donnell, J. A., Elberling, B., Mishra, U., Camill, P., Yu, Z., Palmtag, J., and Kuhry, P.: Estimated stocks of circumpolar permafrost carbon with quantified uncertainty ranges and identified data gaps, Biogeosciences, 11, 6573–6593, https://doi.org/10.5194/bg-11-6573-2014, 2014.

Hynes, S., Solomon, S. M., and Whalen, D.: GIS compilation of coastline variability spanning 60 years in the Mackenzie Delta and Tuktoyaktuk in the Beaufort Sea, https://doi.org/10.4095/295579, 2014.

IPCC: Climate Change 2014: Synthesis Report. Contribution of Working Groups I, II and III to the Fifth Assessment Report of the Intergovernmental Panel on Climate Change, IPCC, Geneva, Switzerland, 2014.

IPCC: Climate Change 2022 – Impacts, Adaptation and Vulnerability: Working Group II Contribution to the Sixth Assessment Report of the Intergovernmental Panel on Climate Change, Cambridge University Press, Cambridge, https://doi.org/10.1017/9781009325844, 2023.

Irrgang, A. M., Lantuit, H., Manson, G. K., Günther, F., Grosse, G., and Overduin, P. P.: Variability in Rates of Coastal Change Along the Yukon Coast, 1951 to 2015, Journal of Geophysical Research: Earth Surface, 123, 779–800, https://doi.org/10.1002/2017JF004326, 2018.

Irrgang, A. M., Bendixen, M., Farquharson, L. M., Baranskaya, A. V., Erikson, L. H., Gibbs, A. E., Ogorodov, S. A., Overduin, P. P., Lantuit, H., Grigoriev, M. N., and Jones, B. M.: Drivers, dynamics and impacts of changing Arctic coasts, Nat Rev Earth Environ, 3, 39–54, https://doi.org/10.1038/s43017-021-00232-1, 2022.

Jahn, A., Holland, M. M., and Kay, J. E.: Projections of an ice-free Arctic Ocean, Nat Rev Earth Environ, 5, 164–176, https://doi.org/10.1038/s43017-023-00515-9, 2024.

Jansson, J. K. and Hofmockel, K. S.: The soil microbiome—from metagenomics to metaphenomics, Current Opinion in Microbiology, 43, 162–168, https://doi.org/10.1016/j.mib.2018.01.013, 2018.

Jenrich, M.: Thermokarst Lagoons - Carbon Pools and Panarctic Distribution, Alfred Wegener Institute, University of Potsdam, Potsdam, 2020.

Jenrich, M., Angelopoulos, M., Overduin, P. P., Nitze, I., Günther, F., Strauss, J., Westermann, S., Schirrmeister, L., Kholodov, A. L., Krautblatter, M., Grigoriev, M. N., and Grosse, G.: Distribution of lagoons along the Arctic coast from the Taimyr Peninsula in Russia to the Tuktoyaktuk Peninsula in Canada, https://doi.org/10.1594/PANGAEA.934158, 2021a.

Jenrich, M., Angelopoulos, M., Grosse, G., Overduin, P. P., Schirrmeister, L., Nitze, I., Biskaborn, B. K., Liebner, S., Grigoriev, M., Murray, A., Jongejans, L. L., and Strauss, J.: Thermokarst Lagoons: A Core-Based Assessment of Depositional Characteristics and an Estimate of Carbon Pools on the Bykovsky Peninsula, Front. Earth Sci., 9, 637899, https://doi.org/10.3389/feart.2021.637899, 2021b.

Jenrich, M., Nitze, I., Laboor, S., Angelopoulos, M., Grosse, G., and Strauss, J.: Spatial extent of thermokarst lagoons along pan-Arctic coasts - an upscaling approach, https://doi.org/10.1594/PANGAEA.948267, 2023.

Jenrich, M., Angelopoulos, M., Liebner, S., Treat, C., Knoblauch, C., Yang, S., Grosse, G., Giebeler, F., Jongejans, L. L., Grigoriev, M., and Strauss, J.: Greenhouse Gas Production and Microbial Response During the Transition From Terrestrial Permafrost to a Marine Environment, Permafrost and Periglacial Processes, 0, 1–20, https://doi.org/10.1002/ppp.2251, 2024a.

Jenrich, M., Angelopoulos, M., Liebner, S., Treat, C., Yang, S., Grosse, G., Giebeler, F., Jongejans, L. L., and Strauss, J.: Greenhouse gas production and microbial response during the transition from terrestrial permafrost to a marine environment, Permafrost and Periglacial Processes, 2024b.

Jenrich, M., Prodinger, M., Nitze, I., Grosse, G., and Strauss, J.: Pan-Arctic thermokarst lagoon distribution, area and classification, https://doi.org/10.1594/PANGAEA.968886, 2024c.

Jenrich, M., Wolter, J., Liebner, S., Knoblauch, C., Grosse, G., Giebeler, F., Whalen, D., and Strauss, J.: Rising Arctic Seas and Thawing Permafrost: Uncovering the Carbon Cycle Impact in a Thermokarst Lagoon System in the outer Mackenzie Delta, Canada, Biogeosciences, 1–30, https://doi.org/10.5194/egusphere-2024-2891, 2024d.

Jenrich, M., Prodinger, M., Nitze, I., Grosse, G., and Strauss, J.: Thermokarst Lagoons: Distribution, Classification, and Dynamics in Permafrost-to-Marine Transitions, Permafrost and Periglacial Processes, in review.

Jin, Y., Chen, M., Yan, H., Wang, T., and Yang, J.: Sea level variation in the Arctic Ocean since 1979 based on ORAS5 data, Front. Mar. Sci., 10, https://doi.org/10.3389/fmars.2023.1197456, 2023.

Jones, B. M. and Arp, C. D.: Observing a Catastrophic Thermokarst Lake Drainage in Northern Alaska, Permafrost and Periglacial Processes, 26, 119–128, https://doi.org/10.1002/ppp.1842, 2015.

Jones, B. M., Farquharson, L. M., Baughman, C. A., Buzard, R. M., Arp, C. D., Grosse, G., Bull, D. L., Günther, F., Nitze, I., Urban, F., Kasper, J. L., Frederick, J. M., Thomas, M., Jones, C., Mota, A., Dallimore, S., Tweedie, C., Maio, C., Mann, D. H., Richmond, B., Gibbs, A., Xiao, M., Sachs, T., Iwahana, G., Kanevskiy, M., and Romanovsky, V. E.: A decade of remotely sensed observations highlight complex processes linked to coastal permafrost bluff erosion in the Arctic, Environ. Res. Lett., 13, 115001, https://doi.org/10.1088/1748-9326/aae471, 2018.

Jones, B. M., Irrgang, A. M., Farquharson, L. M., Lantuit, H., Whalen, D., Ogorodov, S., Grigoriev, M., Tweedie, C., Gibbs, A. E., Strzelecki, M. C., Baranskaya, A., Belova, N., Sinitsyn, A., Kroon, A., Maslakov, A., Vieira, G., Grosse, G., Overduin, P., Nitze, I., Maio, C., Overbeck, J., Bendixen, M., Zagórski, P., and Romanovsky, V. E.: Arctic Report Card 2020: Coastal Permafrost Erosion, https://doi.org/10.25923/E47W-DW52, 2020.

Jones, B. M., Grosse, G., Farquharson, L. M., Roy-Léveillée, P., Veremeeva, A., Kanevskiy, M. Z., Gaglioti, B. V., Breen, A. L., Parsekian, A. D., Ulrich, M., and Hinkel, K. M.: Lake and drained lake basin systems in lowland permafrost regions, Nat Rev Earth Environ, 3, 85–98, https://doi.org/10.1038/s43017-021-00238-9, 2022.

Jones, M. C., Grosse, G., Treat, C., Turetsky, M., Anthony, K. W., and Brosius, L.: Past permafrost dynamics can inform future permafrost carbon-climate feedbacks, Commun Earth Environ, 4, 272, https://doi.org/10.1038/s43247-023-00886-3, 2023.

Jongejans, L. L., Mangelsdorf, K., Schirrmeister, L., Grigoriev, M. N., Maksimov, G. M., Biskaborn, B. K., Grosse, G., and Strauss, J.: n-Alkane Characteristics of Thawed Permafrost Deposits Below a Thermokarst Lake on Bykovsky Peninsula, Northeastern Siberia, Front. Environ. Sci., 8, 118, https://doi.org/10.3389/fenvs.2020.00118, 2020.

Jongejans, L. L., Liebner, S., Knoblauch, C., Mangelsdorf, K., Ulrich, M., Grosse, G., Tanski, G., Fedorov, A. N., Konstantinov, P. Ya., Windirsch, T., Wiedmann, J., and Strauss, J.: Greenhouse gas production and lipid biomarker distribution in Yedoma and Alas thermokarst lake sediments in Eastern Siberia, Global Change Biology, 27, 2822–2839, https://doi.org/10.1111/gcb.15566, 2021.

Jørgensen, B. B.: Bacteria and Marine Biogeochemistry, in: Marine Geochemistry, edited by: Schulz, H. D. and Zabel, M., Springer, Berlin, Heidelberg, 169–206, https://doi.org/10.1007/3-540-32144-6_5, 2006.

Jørgensen, B. B. and Parkes, R. J.: Role of sulfate reduction and methane production by organic carbon degradation in eutrophic fjord sediments (Limfjorden, Denmark), Limnology and Oceanography, 55, 1338–1352, https://doi.org/10.4319/lo.2010.55.3.1338, 2010.

Jorgenson, M. T.: Coastal region of northern Alaska, Guidebook to permafrost and related features, Alaska Division of Geological & Geophysical Surveys, https://doi.org/10.14509/22762, 2011.

Jorgenson, M. T. and Grunblatt, J.: Landscapelevel ecological mapping of Northern Alaska and field site photograph, Final Report for the Arctic Landscape Conservation Cooperative, 2013.

Jorgenson, M. T. and Shur, Y.: Evolution of lakes and basins in northern Alaska and discussion of the thaw lake cycle, Journal of Geophysical Research: Earth Surface, 112, https://doi.org/10.1029/2006JF000531, 2007.

Judge, A. S., Pelletier, B. R., and Norquay, I.: Metadata - Permafrost Base and Distribution of Gas Hydrates, Geological Survey of Canada, 1987.

Jung, J., Lee, Y., Cho, K.-H., Yang, E. J., and Kang, S.-H.: Spatial Distributions of Riverine and Marine Dissolved Organic Carbon in the Western Arctic Ocean: Results From the 2018 Korean Expedition, Journal of Geophysical Research: Oceans, 127, e2021JC017718, https://doi.org/10.1029/2021JC017718, 2022.

Kanevskiy, M., Shur, Y., Fortier, D., Jorgenson, M. T., and Stephani, E.: Cryostratigraphy of late Pleistocene syngenetic permafrost (yedoma) in northern Alaska, Itkillik River exposure, Quaternary Research, 75, 584–596, https://doi.org/10.1016/j.yqres.2010.12.003, 2011.

Khomyakova, M. A., Zavarzina, D. G., Merkel, A. Y., Klyukina, A. A., Pikhtereva, V. A., Gavrilov, S. N., and Slobodkin, A. I.: The first cultivated representatives of the actinobacterial lineage OPB41 isolated from subsurface environments constitute a novel order Anaerosomatales, Front. Microbiol., 13, 1047580, https://doi.org/10.3389/fmicb.2022.1047580, 2022.

Kim, J., Murphy, E., Nistor, I., Ferguson, S., and Provan, M.: Numerical Analysis of Storm Surges on Canada's Western Arctic Coastline, Journal of Marine Science and Engineering, 9, 326, https://doi.org/10.3390/jmse9030326, 2021.

Kjerfve, B.: Chapter 1 Coastal Lagoons, in: Elsevier Oceanography Series, vol. 60, edited by: Kjerfve, B., Elsevier, 1–8, https://doi.org/10.1016/S0422-9894(08)70006-0, 1994.

Knoblauch, C., Beer, C., Sosnin, A., Wagner, D., and Pfeiffer, E.-M.: Predicting long-term carbon mineralization and trace gas production from thawing permafrost of Northeast Siberia, Global Change Biology, 19, 1160–1172, https://doi.org/10.1111/gcb.12116, 2013.

Knoblauch, C., Beer, C., Liebner, S., Grigoriev, M. N., and Pfeiffer, E.-M.: Methane production as key to the greenhouse gas budget of thawing permafrost, Nature Clim Change, 8, 309–312, https://doi.org/10.1038/s41558-018-0095-z, 2018.

Knorr, K.-H. and Blodau, C.: Impact of experimental drought and rewetting on redox transformations and methanogenesis in mesocosms of a northern fen soil, Soil Biology and Biochemistry, 41, 1187–1198, https://doi.org/10.1016/j.soilbio.2009.02.030, 2009.

Kohnert, K., Serafimovich, A., Metzger, S., Hartmann, J., and Sachs, T.: Strong geologic methane emissions from discontinuous terrestrial permafrost in the Mackenzie Delta, Canada, Sci Rep, 7, 5828, https://doi.org/10.1038/s41598-017-05783-2, 2017.

Koven, C. D., Schuur, E. a. G., Schädel, C., Bohn, T. J., Burke, E. J., Chen, G., Chen, X., Ciais, P., Grosse, G., Harden, J. W., Hayes, D. J., Hugelius, G., Jafarov, E. E., Krinner, G., Kuhry, P., Lawrence, D. M., MacDougall, A. H., Marchenko, S. S., McGuire, A. D., Natali, S. M., Nicolsky, D. J., Olefeldt, D., Peng, S., Romanovsky, V. E., Schaefer, K. M., Strauss, J., Treat, C. C., and Turetsky, M.: A simplified, data-constrained approach to estimate the permafrost carbon–climate feedback, Philosophical Transactions of the Royal Society A: Mathematical, Physical and Engineering Sciences, 373, 20140423, https://doi.org/10.1098/rsta.2014.0423, 2015.

Kristjansson, J. K. and Schönheit, P.: Why Do Sulfate-Reducing Bacteria Outcompete Methanogenic Bacteria for Substrates?, Oecologia, 60, 264–266, 1983.

Kuhry, P., Bárta, J., Blok, D., Elberling, B., Faucherre, S., Hugelius, G., Jørgensen, C. J., Richter, A., Šantrůčková, H., and Weiss, N.: Lability classification of soil organic matter in the northern permafrost region, Biogeosciences, 17, 361–379, https://doi.org/10.5194/bg-17-361-2020, 2020.

Kumar, V., Tiwari, M., Nagoji, S., and Tripathi, S.: Evidence of Anomalously Low δ13C of Marine Organic Matter in an Arctic Fjord, Sci Rep, 6, 36192, https://doi.org/10.1038/srep36192, 2016.

Kwok, R. and Rothrock, D. A.: Decline in Arctic sea ice thickness from submarine and ICESat records: 1958–2008, Geophysical Research Letters, 36, https://doi.org/10.1029/2009GL039035, 2009.

Lantuit, H., Atkinson, D., Overduin, P. P., Grigoriev, M., Rachold, V., Grosse, G., and Hubberten, H.-W.: Coastal erosion dynamics on the permafrost-dominated Bykovsky Peninsula, north Siberia, 1951-2006, Polar Research, https://doi.org/10.3402/polar.v30i0.7341, 2011.

Lantuit, H., Overduin, P. P., Couture, N., Wetterich, S., Aré, F., Atkinson, D., Brown, J., Cherkashov, G., Drozdov, D., Forbes, D. L., Graves-Gaylord, A., Grigoriev, M., Hubberten, H.-W., Jordan, J., Jorgenson, T., Ødegård, R. S., Ogorodov, S., Pollard, W. H., Rachold, V., Sedenko, S., Solomon, S., Steenhuisen, F., Streletskaya, I., and Vasiliev, A.: The Arctic Coastal Dynamics Database: A New Classification Scheme and Statistics on Arctic Permafrost Coastlines, Estuaries and Coasts, 35, 383–400, https://doi.org/10.1007/s12237-010-9362-6, 2012.

Lantuit, H., Overduin, P. P., and Wetterich, S.: Recent Progress Regarding Permafrost Coasts, Permafrost and Periglacial Processes, 24, 120–130, https://doi.org/10.1002/ppp.1777, 2013.

Lantuit, H., Overduin, P. P., Couture, N., Wetterich, S., Are, F., Atkinson, D., Brown, J., Cherkashov, G. A., Drozdov, D. S., Forbes, D. L., Graves-Gaylord, A., Grigoriev, M. N., Hubberten, H.-W., Jordan, J., Jorgenson, M. T., Ødegård, R. S., Ogorodov, S., Pollard, W. H., Rachold, V., Sedenko, S., Solomon, S., Steenhuisen, F., Streletskaya, I., and Vasiliev, A.: The ACD Classification of Arctic Coasts, https://doi.org/10.1594/PANGAEA.919573, 2020.

Laske, S. M., von Biela, V. R., Stanek, A. E., and Dunton, K. H.: Local environmental conditions structured discrete fish assemblages in Arctic lagoons, Polar Biol, 47, 551–568, https://doi.org/10.1007/s00300-024-03239-8, 2024.

Laurent, M., Fuchs, M., Herbst, T., Runge, A., Liebner, S., and Treat, C. C.: Relationships between greenhouse gas production and landscape position during short-term permafrost thaw under anaerobic conditions in the Lena Delta, Biogeosciences, 20, 2049–2064, https://doi.org/10.5194/bg-20-2049-2023, 2023.

Le Mer, J. and Roger, P.: Production, oxidation, emission and consumption of methane by soils: A review, European Journal of Soil Biology, 37, 25–50, https://doi.org/10.1016/S1164-5563(01)01067-6, 2001.

Lee, H., Schuur, E. A. G., Inglett, K. S., Lavoie, M., and Chanton, J. P.: The rate of permafrost carbon release under aerobic and anaerobic conditions and its potential effects on climate, Global Change Biology, 18, 515–527, https://doi.org/10.1111/j.1365-2486.2011.02519.x, 2012.

Lehner, B. and Döll, P.: Development and validation of a global database of lakes, reservoirs and wetlands, Journal of Hydrology, 296, 1–22, https://doi.org/10.1016/j.jhydrol.2004.03.028, 2004.

Lenz, J., Jones, B. M., Wetterich, S., Tjallingii, R., Fritz, M., Arp, C. D., Rudaya, N., and Grosse, G.: Impacts of shore expansion and catchment characteristics on lacustrine thermokarst records in permafrost lowlands, Alaska Arctic Coastal Plain, Arktos, 2, 25, https://doi.org/10.1007/s41063-016-0025-0, 2016.

Li, Q., Feng, J., Wu, J., Jia, W., Zhang, Q., Chen, Q., Zhang, D., and Cheng, X.: Spatial variation in soil microbial community structure and its relation to plant distribution and local environments following afforestation in central China, Soil and Tillage Research, 193, 8–16, https://doi.org/10.1016/j.still.2019.05.015, 2019.

Liebner, S., Ganzert, L., Kiss, A., Yang, S., Wagner, D., and Svenning, M. M.: Shifts in methanogenic community composition and methane fluxes along the degradation of discontinuous permafrost, Frontiers in Microbiology, 6, 2015.

Lim, M., Whalen, D., J. Mann, P., Fraser, P., Berry, H. B., Irish, C., Cockney, K., and Woodward, J.: Effective Monitoring of Permafrost Coast Erosion: Wide-scale Storm Impacts on Outer Islands in the Mackenzie Delta Area, Front. Earth Sci., 8, https://doi.org/10.3389/feart.2020.561322, 2020.

Lindgren, A., Hugelius, G., and Kuhry, P.: Extensive loss of past permafrost carbon but a net accumulation into present-day soils, Nature, 560, 219–222, https://doi.org/10.1038/s41586-018-0371-0, 2018.

Liu, L., Chen, H., and Tian, J.: Varied response of carbon dioxide emissions to warming in oxic, anoxic and transitional soil layers in a drained peatland, Commun Earth Environ, 3, 1–12, https://doi.org/10.1038/s43247-022-00651-y, 2022.

Lougheed, V. L., Tweedie, C. E., Andresen, C. G., Armendariz, A. M., Escarzaga, S. M., and Tarin, G.: Patterns and Drivers of Carbon Dioxide Concentrations in Aquatic Ecosystems of the Arctic Coastal Tundra, Global Biogeochemical Cycles, 34, e2020GB006552, https://doi.org/10.1029/2020GB006552, 2020.

Loveland, T. R. and Irons, J. R.: Landsat 8: The plans, the reality, and the legacy, Remote Sensing of Environment, 185, 1–6, https://doi.org/10.1016/j.rse.2016.07.033, 2016.

Lovley, D. R., Dwyer, D. F., and Klug, M. J.: Kinetic analysis of competition between sulfate reducers and methanogens for hydrogen in sediments, Appl Environ Microbiol, 43, 1373–1379, https://doi.org/10.1128/aem.43.6.1373-1379.1982, 1982.

Lupascu, M., Wadham, J. L., Hornibrook, E. R. C., and Pancost, R. D.: Temperature Sensitivity of Methane Production in the Permafrost Active Layer at Stordalen, Sweden: A Comparison with Non-permafrost Northern Wetlands, Arctic, Antarctic, and Alpine Research, 44, 469–482, https://doi.org/10.1657/1938-4246-44.4.469, 2012.

Lyubetsky, V. A., Zverkov, O. A., Rubanov, L. I., and Seliverstov, A. V.: Optimal Growth Temperature and Intergenic Distances in Bacteria, Archaea, and Plastids of Rhodophytic Branch, Biomed Res Int, 2020, 3465380, https://doi.org/10.1155/2020/3465380, 2020.

Mackelprang, R., Waldrop, M. P., DeAngelis, K. M., David, M. M., Chavarria, K. L., Blazewicz, S. J., Rubin, E. M., and Jansson, J. K.: Metagenomic analysis of a permafrost microbial community reveals a rapid response to thaw, Nature, 480, 368–371, https://doi.org/10.1038/nature10576, 2011.

Malard, L. A., Anwar, M. Z., Jacobsen, C. S., and Pearce, D. A.: Influence of Spatial Scale on Structure of Soil Bacterial Communities across an Arctic Landscape, Applied and Environmental Microbiology, 87, e02220, https://doi.org/10.1128/AEM.02220-20, 2021.

Malenfant, F., Whalen, D., Fraser, P., and van Proosdij, D.: Rapid coastal erosion of ice-bonded deposits on Pelly Island, southeastern Beaufort Sea, Inuvialuit Settlement Region, western Canadian Arctic, Can. J. Earth Sci., 59, 961–972, https://doi.org/10.1139/cjes-2021-0118, 2022.

Malito, J., Eidam, E., and Nienhuis, J.: Increasing Wave Energy Moves Arctic Continental Shelves Toward a New Future, JGR Oceans, 127, e2021JC018374, https://doi.org/10.1029/2021JC018374, 2022.

Maltby, J., Steinle, L., Löscher, C. R., Bange, H. W., Fischer, M. A., Schmidt, M., and Treude, T.: Microbial methanogenesis in the sulfate-reducing zone of sediments in the Eckernförde Bay, SW Baltic Sea, Biogeosciences, 15, 137–157, https://doi.org/10.5194/bg-15-137-2018, 2018.

Marsh, P., Russell, M., Pohl, S., Haywood, H., and Onclin, C.: Changes in thaw lake drainage in the Western Canadian Arctic from 1950 to 2000, Hydrological Processes, 23, 145–158, https://doi.org/10.1002/hyp.7179, 2009.

Martin, M.: Cutadapt removes adapter sequences from high-throughput sequencing reads, EMBnet.journal, 17, 10–12, https://doi.org/10.14806/ej.17.1.200, 2011.

Martinez-Cruz, K., Sepulveda-Jauregui, A., Walter Anthony, K., and Thalasso, F.: Geographic and seasonal variation of dissolved methane and aerobic methane oxidation in Alaskan lakes, Biogeosciences, 12, 4595–4606, https://doi.org/10.5194/bg-12-4595-2015, 2015.

Matthews, E., Johnson, M. S., Genovese, V., Du, J., and Bastviken, D.: Methane emission from high latitude lakes: methane-centric lake classification and satellite-driven annual cycle of emissions, Sci Rep, 10, 12465, https://doi.org/10.1038/s41598-020-68246-1, 2020.

McClelland, J. W., Holmes, R. M., Dunton, K. H., and Macdonald, R. W.: The Arctic Ocean Estuary, Estuaries and Coasts, 35, 353–368, https://doi.org/10.1007/s12237-010-9357-3, 2012.

McDougall, T. J. and Barker, P. M.: Getting started with TEOS-10 and the Gibbs Seawater (GSW) Oceanographic Toolbox, 2011.

McMahon, K. W., Ambrose, W. G., Reynolds, M. J., Johnson, B. J., Whiting, A., and Clough, L. M.: Arctic lagoon and nearshore food webs: Relative contributions of terrestrial organic matter, phytoplankton, and phytobenthos vary with consumer foraging dynamics, Estuarine, Coastal and Shelf Science, 257, 107388, https://doi.org/10.1016/j.ecss.2021.107388, 2021.

Miesner, F., Overduin, P. P., Grosse, G., Strauss, J., Langer, M., Westermann, S., Schneider Von Deimling, T., Brovkin, V., and Arndt, S.: Subsea permafrost organic carbon stocks are large and of dominantly low reactivity, Sci Rep, 13, 9425, https://doi.org/10.1038/s41598-023-36471-z, 2023.

Millero, F., Huang, F., Graham, T., and Pierrot, D.: The dissociation of carbonic acid in NaCl solutions as a function of concentration and temperature, Geochimica et Cosmochimica Acta, 71, 46–55, https://doi.org/10.1016/j.gca.2006.08.041, 2007a.

Millero, F., Huang, F., Graham, T., and Pierrot, D.: The dissociation of carbonic acid in NaCl solutions as a function of concentration and temperature, Geochimica et Cosmochimica Acta, 71, 46–55, https://doi.org/10.1016/j.gca.2006.08.041, 2007b.

Millero, F. J., Feistel, R., Wright, D. G., and McDougall, T. J.: The composition of Standard Seawater and the definition of the Reference-Composition Salinity Scale, Deep Sea Research Part I: Oceanographic Research Papers, 55, 50–72, https://doi.org/10.1016/j.dsr.2007.10.001, 2008.

Miner, K. R., Turetsky, M. R., Malina, E., Bartsch, A., Tamminen, J., McGuire, A. D., Fix, A., Sweeney, C., Elder, C. D., and Miller, C. E.: Permafrost carbon emissions in a changing Arctic, Nat Rev Earth Environ, 3, 55–67, https://doi.org/10.1038/s43017-021-00230-3, 2022.

Mishra, U., Hugelius, G., Shelef, E., Yang, Y., Strauss, J., Lupachev, A., Harden, J. W., Jastrow, J. D., Ping, C.-L., Riley, W. J., Schuur, E. A. G., Matamala, R., Siewert, M., Nave, L. E., Koven, C. D., Fuchs, M., Palmtag, J., Kuhry, P., Treat, C. C., Zubrzycki, S., Hoffman, F. M., Elberling, B., Camill, P., Veremeeva, A., and Orr, A.: Spatial heterogeneity and environmental predictors of permafrost region soil organic carbon stocks, Science Advances, 7, eaaz5236, https://doi.org/10.1126/sciadv.aaz5236, 2021.

Mitzscherling, J., Horn, F., Winterfeld, M., Mahler, L., Kallmeyer, J., Overduin, P. P., Schirrmeister, L., Winkel, M., Grigoriev, M. N., Wagner, D., and Liebner, S.: Microbial community composition and abundance after millennia of submarine permafrost warming, Biogeosciences, 16, 3941–3958, https://doi.org/10.5194/bg-16-3941-2019, 2019.

Moore, T. R. and Dalva, M.: Methane and carbon dioxide exchange potentials of peat soils in aerobic and anaerobic laboratory incubations, Soil Biology and Biochemistry, 29, 1157–1164, https://doi.org/10.1016/S0038-0717(97)00037-0, 1997.

Natali, S. M., Watts, J. D., Rogers, B. M., Potter, S., Ludwig, S. M., Selbmann, A.-K., Sullivan, P. F., Abbott, B. W., Arndt, K. A., Birch, L., Björkman, M. P., Bloom, A. A., Celis, G., Christensen, T. R., Christiansen, C. T., Commane, R., Cooper, E. J., Crill, P., Czimczik, C., Davydov, S., Du, J., Egan, J. E., Elberling, B., Euskirchen, E. S., Friborg, T., Genet, H., Göckede, M., Goodrich, J. P., Grogan, P., Helbig, M., Jafarov, E. E., Jastrow, J. D., Kalhori, A. A. M., Kim, Y., Kimball, J. S., Kutzbach, L., Lara, M. J., Larsen, K. S., Lee, B.-Y., Liu, Z., Loranty, M. M., Lund, M., Lupascu, M., Madani, N., Malhotra, A., Matamala, R., McFarland, J., McGuire, A. D., Michelsen, A., Minions, C., Oechel, W. C., Olefeldt, D., Parmentier, F.-J. W., Pirk, N., Poulter, B., Quinton, W., Rezanezhad, F., Risk, D., Sachs, T., Schaefer, K., Schmidt, N. M., Schuur, E. A. G., Semenchuk, P. R., Shaver, G., Sonnentag, O., Starr, G., Treat, C. C., Waldrop, M. P., Wang, Y., Welker, J., Wille, C., Xu, X., Zhang, Z., Zhuang, Q., and Zona, D.: Large loss of CO2 in winter observed across the northern permafrost region, Nat. Clim. Chang., 9, 852–857, https://doi.org/10.1038/s41558-019-0592-8, 2019.

Nerem, R. S., Beckley, B. D., Fasullo, J. T., Hamlington, B. D., Masters, D., and Mitchum, G. T.: Climate-change-driven accelerated sea-level rise detected in the altimeter era, Proc Natl Acad Sci U S A, 115, 2022–2025, https://doi.org/10.1073/pnas.1717312115, 2018.

Nicu, I. C., Tanyas, H., Rubensdotter, L., and Lombardo, L.: A glimpse into the northernmost thermo-erosion gullies in Svalbard archipelago and their implications for Arctic cultural heritage, CATENA, 212, 106105, https://doi.org/10.1016/j.catena.2022.106105, 2022.

Nielsen, D. M., Pieper, P., Barkhordarian, A., Overduin, P., Ilyina, T., Brovkin, V., Baehr, J., and Dobrynin, M.: Increase in Arctic coastal erosion and its sensitivity to warming in the twenty-first century, Nat. Clim. Chang., 12, 263–270, https://doi.org/10.1038/s41558-022-01281-0, 2022.

Nitzbon, J., Westermann, S., Langer, M., Martin, L. C. P., Strauss, J., Laboor, S., and Boike, J.: Fast response of cold ice-rich permafrost in northeast Siberia to a warming climate, Nat Commun, 11, 2201, https://doi.org/10.1038/s41467-020-15725-8, 2020.

Nitze, I., Grosse, G., Jones, B., Arp, C., Ulrich, M., Fedorov, A., and Veremeeva, A.: Landsat-Based Trend Analysis of Lake Dynamics across Northern Permafrost Regions, Remote Sensing, 9, 640, https://doi.org/10.3390/rs9070640, 2017.

Notz, D. and Stroeve, J.: Observed Arctic sea-ice loss directly follows anthropogenic CO2 emission, Science, 354, 747–750, https://doi.org/10.1126/science.aag2345, 2016.

Obu, J.: How Much of the Earth's Surface is Underlain by Permafrost?, Journal of Geophysical Research: Earth Surface, 126, e2021JF006123, https://doi.org/10.1029/2021JF006123, 2021.

Obu, J., Westermann, S., Bartsch, A., Berdnikov, N., Christiansen, H. H., Dashtseren, A., Delaloye, R., Elberling, B., Etzelmüller, B., Kholodov, A., Khomutov, A., Kääb, A., Leibman, M. O., Lewkowicz, A. G., Panda, S. K., Romanovsky, V., Way, R. G., Westergaard-Nielsen, A., Wu, T., Yamkhin, J., and Zou, D.: Northern Hemisphere permafrost map based on TTOP modelling for 2000–2016 at 1 km2 scale, Earth-Science Reviews, 193, 299–316, https://doi.org/10.1016/j.earscirev.2019.04.023, 2019.

Oksanen, J., Simpson, G., Blanchet, F. G., Kindt, R., Legendre, P., Minchin, P., hara, R., Solymos, P., STEVENS, H., Szöcs, E., Wagner, H., Barbour, M., Bedward, M., Bolker, B., Borcard, D., Carvalho, G., Chirico, M., De Cáceres, M., Durand, S., and Weedon, J.: vegan community ecology package version 2.6-2 April 2022, 2022.

Olefeldt, D., Turetsky, M. R., Crill, P. M., and McGuire, A. D.: Environmental and physical controls on northern terrestrial methane emissions across permafrost zones, Global Change Biology, 19, 589–603, https://doi.org/10.1111/gcb.12071, 2013.

Olefeldt, D., Goswami, S., Grosse, G., Hayes, D., Hugelius, G., Kuhry, P., McGuire, A. D., Romanovsky, V. E., Sannel, A. B. K., Schuur, E. A. G., and Turetsky, M. R.: Circumpolar distribution and carbon storage of thermokarst landscapes, Nat Commun, 7, 13043, https://doi.org/10.1038/ncomms13043, 2016.

Oremland, R. S. and Polcin, S.: Methanogenesis and sulfate reduction: competitive and noncompetitive substrates in estuarine sediments, Appl Environ Microbiol, 44, 1270–1276, https://doi.org/10.1128/aem.44.6.1270-1276.1982, 1982.

Oremland, R. S., Marsh, L. M., and Polcin, S.: Methane production and simultaneous sulphate reduction in anoxic, salt marsh sediments, Nature, 296, 143–145, https://doi.org/10.1038/296143a0, 1982.

Overduin, P. P., Strzelecki, M. C., Grigoriev, M. N., Couture, N., Lantuit, H., St-Hilaire-Gravel, D., Günther, F., and Wetterich, S.: Coastal changes in the Arctic, Geological Society, London, Special Publications, 388, 103–129, https://doi.org/10.1144/SP388.13, 2014.

Overduin, P. P., Wetterich, S., Günther, F., Grigoriev, M. N., Grosse, G., Schirrmeister, L., Hubberten, H.-W., and Makarov, A.: Coastal dynamics and submarine permafrost in shallow water of the central Laptev Sea, East Siberia, The Cryosphere, 10, 1449–1462, https://doi.org/10.5194/tc-10-1449-2016, 2016.

Overduin, P. P., Schneider von Deimling, T., Miesner, F., Grigoriev, M. N., Ruppel, C., Vasiliev, A., Lantuit, H., Juhls, B., and Westermann, S.: Submarine Permafrost Map in the Arctic Modeled Using 1-D Transient Heat Flux (SuPerMAP), Journal of Geophysical Research: Oceans, 124, 3490–3507, https://doi.org/10.1029/2018JC014675, 2019.

Ozuolmez, D., Na, H., Lever, M., Kjeldsen, K., Jørgensen, B., and Plugge, C.: Methanogenic archaea and sulfate reducing bacteria co-cultured on acetate: teamwork or coexistence?, Frontiers in Microbiology, 6, 2015.

Ozuolmez, D., Moore, E. K., Hopmans, E. C., Sinninghe Damsté, J. S., Stams, A. J. M., and Plugge, C. M.: Butyrate Conversion by Sulfate-Reducing and Methanogenic Communities from Anoxic Sediments of Aarhus Bay, Denmark, Microorganisms, 8, 606, https://doi.org/10.3390/microorganisms8040606, 2020.

Parsekian, A. D., Creighton, A. L., Jones, B. M., and Arp, C. D.: Surface nuclear magnetic resonance observations of permafrost thaw below floating, bedfast, and transitional ice lakes, GEOPHYSICS, 84, EN33–EN45, https://doi.org/10.1190/geo2018-0563.1, 2019.

Pekel, J.-F., Cottam, A., Gorelick, N., and Belward, A. S.: High-resolution mapping of global surface water and its long-term changes, Nature, 540, 418–422, https://doi.org/10.1038/nature20584, 2016.

Piliouras, A. and Rowland, J. C.: Arctic River Delta Morphologic Variability and Implications for Riverine Fluxes to the Coast, Journal of Geophysical Research: Earth Surface, 125, e2019JF005250, https://doi.org/10.1029/2019JF005250, 2020.

Porter, C., Morin, P., Howat, I., Noh, M.-J., Bates, B., Peterman, K., Keesey, S., Schlenk, M., Gardiner, J., Tomko, K., Willis, M., Kelleher, C., Cloutier, M., Husby, E., Foga, S., Nakamura, H., Platson, M., Wethington, M., Jr., Williamson, C., Bauer, G., Enos, J., Arnold, G., Kramer, W., Becker, P., Doshi, A., D'Souza, C., Cummens, P., Laurier, F., and Bojesen, M.: ArcticDEM, Version 3, https://doi.org/10.7910/DVN/OHHUKH, 2018.

Proshutinsky, A., Pavlov, V., and Bourke, R. H.: Sea level rise in the Arctic Ocean, Geophysical Research Letters, 28, 2237–2240, https://doi.org/10.1029/2000GL012760, 2001.

Qiu, S., Zhang, X., Xia, W., Li, Z., Wang, L., Chen, Z., and Ge, S.: Effect of extreme pH conditions on methanogenesis: Methanogen metabolism and community structure, Science of The Total Environment, 877, 162702, https://doi.org/10.1016/j.scitotenv.2023.162702, 2023.

Quast, C., Pruesse, E., Yilmaz, P., Gerken, J., Schweer, T., Yarza, P., Peplies, J., and Glöckner, F. O.: The SILVA ribosomal RNA gene database project: improved data processing and web-based tools, Nucleic Acids Res, 41, D590–D596, https://doi.org/10.1093/nar/gks1219, 2013.

Ramage, J., Jungsberg, L., Wang, S., Westermann, S., Lantuit, H., and Heleniak, T.: Population living on permafrost in the Arctic, Popul Environ, 43, 22–38, https://doi.org/10.1007/s11111-020-00370-6, 2021.

Rantanen, M., Karpechko, A. Yu., Lipponen, A., Nordling, K., Hyvärinen, O., Ruosteenoja, K., Vihma, T., and Laaksonen, A.: The Arctic has warmed nearly four times faster than the globe since 1979, Commun Earth Environ, 3, 168, https://doi.org/10.1038/s43247-022-00498-3, 2022.

Richter-Menge, J., Overland, J. E., Mathis, J. T., Osborne, E., and Eds: Arctic Report Card 2017: Arctic shows no sign of returning to reliably frozen region of recent past decades, 2017.

Risser, P. G.: The Status of the Science Examining Ecotones: A dynamic aspect of landscape is the area of steep gradients between more homogeneous vegetation associations, BioScience, 45, 318–325, https://doi.org/10.2307/1312492, 1995.

Rivkina, E., Shcherbakova, V., Laurinavichius, K., Petrovskaya, L., Krivushin, K., Kraev, G., Pecheritsina, S., and Gilichinsky, D.: Biogeochemistry of methane and methanogenic archaea in permafrost, FEMS Microbiology Ecology, 61, 1–15, https://doi.org/10.1111/j.1574-6941.2007.00315.x, 2007.

Romanovskii, N. N., Hubberten, H.-W., Gavrilov, A. V., Tumskoy, V. E., Tipenko, G. S., Grigoriev, M. N., and Siegert, C.: Thermokarst and land–ocean interactions, Laptev sea region, Russia, Permafrost and Periglacial Processes, 11, 137–152, https://doi.org/10.1002/1099-1530(200004/06)11:2<137::AID-PPP345>3.0.CO;2-L, 2000.

Roy Chowdhury, T., Herndon, E. M., Phelps, T. J., Elias, D. A., Gu, B., Liang, L., Wullschleger, S. D., and Graham, D. E.: Stoichiometry and temperature sensitivity of methanogenesis and CO2 production from saturated polygonal tundra in Barrow, Alaska, Global Change Biology, 21, 722–737, https://doi.org/10.1111/gcb.12762, 2015.

Ruz, M.-H., Héquette, A., and Hill, P. R.: A model of coastal evolution in a transgressed thermokarst topography, Canadian Beaufort Sea, Marine Geology, 106, 251–278, https://doi.org/10.1016/0025-3227(92)90133-3, 1992.

Rydberg, J., Klaminder, J., Rosén, P., and Bindler, R.: Climate driven release of carbon and mercury from permafrost mires increases mercury loading to sub-arctic lakes, Science of The Total Environment, 408, 4778–4783, https://doi.org/10.1016/j.scitotenv.2010.06.056, 2010.

Šantrůčková, H., Kotas, P., Bárta, J., Urich, T., Čapek, P., Palmtag, J., Eloy Alves, R. J., Biasi, C., Diáková, K., Gentsch, N., Gittel, A., Guggenberger, G., Hugelius, G., Lashchinsky, N., Martikainen, P. J., Mikutta, R., Schleper, C., Schnecker, J., Schwab, C., Shibistova, O., Wild, B., and Richter, A.: Significance of dark CO2 fixation in arctic soils, Soil Biology and Biochemistry, 119, 11–21, https://doi.org/10.1016/j.soilbio.2017.12.021, 2018.

Schädel, C., Bader, M. K.-F., Schuur, E. A. G., Biasi, C., Bracho, R., Čapek, P., De Baets, S., Diáková, K., Ernakovich, J., Estop-Aragones, C., Graham, D. E., Hartley, I. P., Iversen, C. M., Kane, E., Knoblauch, C., Lupascu, M., Martikainen, P. J., Natali, S. M., Norby, R. J., O'Donnell, J. A., Chowdhury, T. R., Šantrůčková, H., Shaver, G., Sloan, V. L., Treat, C. C., Turetsky, M. R., Waldrop, M. P., and Wickland, K. P.: Potential carbon emissions dominated by carbon dioxide from thawed permafrost soils, Nature Clim Change, 6, 950–953, https://doi.org/10.1038/nclimate3054, 2016.

Schaefer, K., Zhang, T., Bruhwiler, L., and Barrett, A. P.: Amount and timing of permafrost carbon release in response to climate warming, Tellus B: Chemical and Physical Meteorology, 63, 168–180, https://doi.org/10.1111/j.1600-0889.2010.00527.x, 2011.

Schirrmeister, L., Siegert, C., Kuznetsova, T., Kuzmina, S., Andreev, A., Kienast, F., Meyer, H., and Bobrov, A.: Paleoenvironmental and paleoclimatic records from permafrost deposits in the Arctic region of Northern Siberia, Quaternary International, 89, 97–118, https://doi.org/10.1016/S1040-6182(01)00083-0, 2002.

Schirrmeister, L., Grosse, G., Wetterich, S., Overduin, P. P., Strauss, J., Schuur, E. A. G., and Hubberten, H.-W.: Fossil organic matter characteristics in permafrost deposits of the northeast Siberian Arctic, Journal of Geophysical Research: Biogeosciences, 116, https://doi.org/10.1029/2011JG001647, 2011.

Schirrmeister, L., Grigoriev, M. N., Strauss, J., Grosse, G., Overduin, P. P., Kholodov, A., Guenther, F., and Hubberten, H.-W.: Sediment characteristics of a thermokarst lagoon in the northeastern Siberian Arctic (Ivashkina Lagoon, Bykovsky Peninsula), Arktos, 4, 1–16, https://doi.org/10.1007/s41063-018-0049-8, 2018.

Schneider von Deimling, T., Meinshausen, M., Levermann, A., Huber, V., Frieler, K., Lawrence, D. M., and Brovkin, V.: Estimating the near-surface permafrost-carbon feedback on global warming, Biogeosciences, 9, 649–665, https://doi.org/10.5194/bg-9-649-2012, 2012.

Schönheit, P., Kristjansson, J. K., and Thauer, R. K.: Kinetic mechanism for the ability of sulfate reducers to out-compete methanogens for acetate, Arch. Microbiol., 132, 285–288, https://doi.org/10.1007/BF00407967, 1982.

Schuster, P. F., Schaefer, K. M., Aiken, G. R., Antweiler, R. C., Dewild, J. F., Gryziec, J. D., Gusmeroli, A., Hugelius, G., Jafarov, E., Krabbenhoft, D. P., Liu, L., Herman-Mercer, N., Mu, C., Roth, D. A., Schaefer, T., Striegl, R. G., Wickland, K. P., and Zhang, T.: Permafrost Stores a Globally Significant Amount of Mercury, Geophysical Research Letters, 45, 1463–1471, https://doi.org/10.1002/2017GL075571, 2018.

Schuur, E. A. G., Bockheim, J., Canadell, J. G., Euskirchen, E., Field, C. B., Goryachkin, S. V., Hagemann, S., Kuhry, P., Lafleur, P. M., Lee, H., Mazhitova, G., Nelson, F. E., Rinke, A., Romanovsky, V. E., Shiklomanov, N., Tarnocai, C., Venevsky, S., Vogel, J. G., and Zimov, S. A.: Vulnerability of Permafrost Carbon to Climate Change: Implications for the Global Carbon Cycle, BioScience, 58, 701–714, https://doi.org/10.1641/B580807, 2008.

Schuur, E. A. G., Vogel, J. G., Crummer, K. G., Lee, H., Sickman, J. O., and Osterkamp, T. E.: The effect of permafrost thaw on old carbon release and net carbon exchange from tundra, Nature, 459, 556–559, https://doi.org/10.1038/nature08031, 2009.

Schuur, E. A. G., Abbott, B. W., Commane, R., Ernakovich, J., Euskirchen, E., Hugelius, G., Grosse, G., Jones, M., Koven, C., Leshyk, V., Lawrence, D., Loranty, M. M., Mauritz, M., Olefeldt, D., Natali, S., Rodenhizer, H., Salmon, V., Schädel, C., Strauss, J., Treat, C., and Turetsky, M.: Permafrost and Climate Change: Carbon Cycle Feedbacks From the Warming Arctic, Annual Review of Environment and Resources, 47, 343–371, https://doi.org/10.1146/annurev-environ-012220-011847, 2022.

Permafrost and Climate Change: Carbon Cycle Feedbacks From the Warming Arctic:

Sela-Adler, M., Ronen, Z., Herut, B., Antler, G., Vigderovich, H., Eckert, W., and Sivan, O.: Co-existence of Methanogenesis and Sulfate Reduction with Common Substrates in Sulfate-Rich Estuarine Sediments, Frontiers in Microbiology, 8, 2017.

Serikova, S., Pokrovsky, O. S., Laudon, H., Krickov, I. V., Lim, A. G., Manasypov, R. M., and Karlsson, J.: High carbon emissions from thermokarst lakes of Western Siberia, Nat Commun, 10, 1552, https://doi.org/10.1038/s41467-019-09592-1, 2019.

Solomon, S., Mudie, P. J., Cranston, R., Hamilton, T., Thibaudeau, S. A., and Collins, E. S.: Characterisation of marine and lacustrine sediments in a drowned thermokarst embayment, Richards Island, Beaufort Sea, Canada, International Journal of Earth Sciences, 89, 503–521, https://doi.org/10.1007/s005310000126, 2000.

Solomon, S. M.: Spatial and temporal variability of shoreline change in the Beaufort-Mackenzie region, northwest territories, Canada, Geo-Mar Lett, 25, 127–137, https://doi.org/10.1007/s00367-004-0194-x, 2005.

Spangenberg, I., Overduin, P. P., Damm, E., Bussmann, I., Meyer, H., Liebner, S., Angelopoulos, M., Biskaborn, B. K., Grigoriev, M. N., and Grosse, G.: Methane pathways in winter ice of a thermokarst lake–lagoon–coastal water transect in north Siberia, The Cryosphere, 15, 1607–1625, https://doi.org/10.5194/tc-15-1607-2021, 2021.

Speetjens, N. J., Hugelius, G., Gumbricht, T., Lantuit, H., Berghuijs, W. R., Pika, P. A., Poste, A., and Vonk, J. E.: The pan-Arctic catchment database (ARCADE), Earth System Science Data, 15, 541–554, https://doi.org/10.5194/essd-15-541-2023, 2023.

Spohn, M., Müller, K., Höschen, C., Mueller, C. W., and Marhan, S.: Dark microbial CO2 fixation in temperate forest soils increases with CO2 concentration, Global Change Biology, 26, 1926–1935, https://doi.org/10.1111/gcb.14937, 2020.

Stanek, A. E., von Biela, V. R., Laske, S. M., Taylor, R. L., and Dunton, K. H.: Barrier islands influence the assimilation of terrestrial energy in nearshore fishes, Estuarine, Coastal and Shelf Science, 278, 108094, https://doi.org/10.1016/j.ecss.2022.108094, 2022.

Strauss, J., Schirrmeister, L., Grosse, G., Fortier, D., Hugelius, G., Knoblauch, C., Romanovsky, V., Schädel, C., Schneider von Deimling, T., Schuur, E. A. G., Shmelev, D., Ulrich, M., and Veremeeva, A.: Deep Yedoma permafrost: A synthesis of depositional characteristics and carbon vulnerability, Earth-Science Reviews, 172, 75–86, https://doi.org/10.1016/j.earscirev.2017.07.007, 2017.

Strauss, J., Boike, J., Bolshiyanov, D. Y., Grigoriev, M. N., El-Hajj, H., Morgenstern, A., Overduin, P. P., and Udke, A.: Russian-German Cooperation: Expeditions to Siberia in 2017, Berichte zur Polar- und Meeresforschung = Reports on Polar and Marine Research, Alfred-Wegener-Institut, Helmholtz-Zentrum für Polar- und Meeresforschung, https://doi.org/10.2312/BZPM_0725_2018, 2018.

Strauss, J., Laboor, S., Schirrmeister, L., Fedorov, A. N., Fortier, D., Froese, D., Fuchs, M., Günther, F., Grigoriev, M., Harden, J., Hugelius, G., Jongejans, L. L., Kanevskiy, M., Kholodov, A., Kunitsky, V., Kraev, G., Lozhkin, A., Rivkina, E., Shur, Y., Siegert, C., Spektor, V., Streletskaya, I., Ulrich, M., Vartanyan, S., Veremeeva, A., Anthony, K. W., Wetterich, S., Zimov, N., and Grosse, G.: Circum-Arctic Map of the Yedoma Permafrost Domain, Front. Earth Sci., 9, 758360, https://doi.org/10.3389/feart.2021.758360, 2021.

Strauss, J., Laboor, S., Schirrmeister, L., Fedorov, A. N., Fortier, D., Froese, D. G., Fuchs, M., Günther, F., Grigoriev, M. N., Harden, J. W., Hugelius, G., Jongejans, L. L., Kanevskiy, M. Z., Kholodov, A. L., Kunitsky, V., Kraev, G., Lozhkin, A. V., Rivkina, E., Shur, Y., Siegert, C., Spektor, V., Streletskaya, I., Ulrich, M., Vartanyan, S. L., Veremeeva, A., Walter Anthony, K. M., Wetterich, S., Zimov, N. S., and Grosse, G.: Database of Ice-Rich Yedoma Permafrost Version 2 (IRYP v2), https://doi.org/10.1594/PANGAEA.940078, 2022.

Strauss, J., Fuchs, M., Hugelius, G., Miesner, F., Nitze, I., Opfergelt, S., Schuur, E., Treat, C., Turetsky, M., Yang, Y., and Grosse, G.: Organic matter storage and vulnerability in the permafrost domain, in: Encyclopedia of Quaternary Science: Reference Module in Earth Systems and Environmental Sciences, Elsevier, https://doi.org/10.1016/B978-0-323-99931-1.00164-1, 2024.

Strauss, J., Fuchs, M., Hugelius, G., Miesner, F., Nitze, I., Opfergelt, S., Schuur, E., Treat, C., Turetsky, M., Yang, Y., and Grosse, G.: Organic matter storage and vulnerability in the permafrost domain, in: Encyclopedia of Quaternary Science (Third edition), edited by: Elias, S., Elsevier, Oxford, 399–410, https://doi.org/10.1016/B978-0-323-99931-1.00164-1, 2025.

Tagliapietra, D., Sigovini, M., and Volpi Ghirardini, A.: A review of terms and definitions to categorise estuaries, lagoons and associated environments, MARINE AND FRESHWATER RESEARCH, 60, 497–509, https://doi.org/10.1071/MF08088, 2009.

Tank, S. E., Manizza, M., Holmes, R. M., McClelland, J. W., and Peterson, B. J.: The Processing and Impact of Dissolved Riverine Nitrogen in the Arctic Ocean, Estuaries and Coasts, 35, 401–415, https://doi.org/10.1007/s12237-011-9417-3, 2012.

Tanski, G., Wagner, D., Knoblauch, C., Fritz, M., Sachs, T., and Lantuit, H.: Rapid CO $_2$ Release From Eroding Permafrost in Seawater, Geophysical Research Letters, 46, 11244–11252, https://doi.org/10.1029/2019GL084303, 2019.

Townsend-Small, A., Disbennett, D., Fernandez, J. M., Ransohoff, R. W., Mackay, R., and Bourbonniere, R. A.: Quantifying emissions of methane derived from anaerobic organic matter respiration and natural gas extraction in Lake Erie, Limnology and Oceanography, 61, S356–S366, https://doi.org/10.1002/lno.10273, 2016.

Treat, C. C., Wollheim, W. M., Varner, R. K., Grandy, A. S., Talbot, J., and Frolking, S.: Temperature and peat type control CO2 and CH4 production in Alaskan permafrost peats, Global Change Biology, 20, 2674–2686, https://doi.org/10.1111/gcb.12572, 2014.

Treat, C. C., Natali, S. M., Ernakovich, J., Iversen, C. M., Lupascu, M., McGuire, A. D., Norby, R. J., Roy Chowdhury, T., Richter, A., Šantrůčková, H., Schädel, C., Schuur, E. A. G., Sloan, V. L., Turetsky, M. R., and Waldrop, M. P.: A pan-Arctic synthesis of CH_4 and CO_2 production from anoxic soil incubations, Global Change Biology, 21, 2787–2803, https://doi.org/10.1111/gcb.12875, 2015.

Turetsky, M. R., Abbott, B. W., Jones, M. C., Anthony, K. W., Olefeldt, D., Schuur, E. A. G., Grosse, G., Kuhry, P., Hugelius, G., Koven, C., Lawrence, D. M., Gibson, C., Sannel, A. B. K., and McGuire, A. D.: Carbon release through abrupt permafrost thaw, Nat. Geosci., 13, 138–143, https://doi.org/10.1038/s41561-019-0526-0, 2020.

Tweedie, C. E., Aguirre, A., Cody, R., Vargas, S., and Brown, J.: Spatial and Temporal Dynamics of Erosion Along the Elson Lagoon Coastline near Barrow, Alaska (2002-2011), in: Proceedings of the 10th International Conference on Permafrost, 2012.

Ulrich, M., Morgenstern, A., Günther, F., Reiss, D., Bauch, K. E., Hauber, E., Rössler, S., and Schirrmeister, L.: Thermokarst in Siberian ice-rich permafrost: Comparison to asymmetric scalloped depressions on Mars, Journal of Geophysical Research: Planets, 115, https://doi.org/10.1029/2010JE003640, 2010.

Urban, F. E. and Clow, G. D.: USGS Open-File Report 2013–1063: Air Temperature, Wind Speed, and Wind Direction in the National Petroleum Reserve–Alaska and the Arctic National Wildlife Refuge, 1998–2011, 2013.

Vincent, S. G. T., Jennerjahn, T., and Ramasamy, K.: Chapter 3 - Environmental variables and factors regulating microbial structure and functions, in: Microbial Communities in Coastal Sediments, edited by: Vincent, S. G. T., Jennerjahn, T., and Ramasamy, K., Elsevier, 79–117, https://doi.org/10.1016/B978-0-12-815165-5.00003-0, 2021.

Vonk, J. E., Sánchez-García, L., van Dongen, B. E., Alling, V., Kosmach, D., Charkin, A., Semiletov, I. P., Dudarev, O. V., Shakhova, N., Roos, P., Eglinton, T. I., Andersson, A., and Gustafsson, Ö.: Activation of old carbon by erosion of coastal and subsea permafrost in Arctic Siberia, Nature, 489, 137–140, https://doi.org/10.1038/nature11392, 2012.

Vonk, J. E., Tank, S. E., Bowden, W. B., Laurion, I., Vincent, W. F., Alekseychik, P., Amyot, M., Billet, M. F., Canário, J., Cory, R. M., Deshpande, B. N., Helbig, M., Jammet, M., Karlsson, J., Larouche, J., MacMillan, G., Rautio, M., Walter Anthony, K. M., and Wickland, K. P.: Reviews and syntheses: Effects of permafrost thaw on Arctic aquatic ecosystems, Biogeosciences, 12, 7129–7167, https://doi.org/10.5194/bg-12-7129-2015, 2015a.

Vonk, J. E., Giosan, L., Blusztajn, J., Montlucon, D., Graf Pannatier, E., McIntyre, C., Wacker, L., Macdonald, R. W., Yunker, M. B., and Eglinton, T. I.: Spatial variations in geochemical characteristics of the modern Mackenzie Delta sedimentary system, Geochimica et Cosmochimica Acta, 171, 100–120, https://doi.org/10.1016/j.gca.2015.08.005, 2015b.

Vonk, J. E., Dickens, A. F., Giosan, L., Hussain, Z. A., Kim, B., Zipper, S. C., Holmes, R. M., Montlucon, D. B., Galy, V., and Eglinton, T. I.: Arctic Deltaic Lake Sediments As Recorders of Fluvial Organic Matter Deposition, Front. Earth Sci., 4, https://doi.org/10.3389/feart.2016.00077, 2016.

Vu, V. Q. and Friendly, M.: ggbiplot: A Grammar of Graphics Implementation of Biplots, https://doi.org/10.32614/CRAN.package.ggbiplot, 2023.

Waldrop, M. P., Wickland, K. P., White Iii, R., Berhe, A. A., Harden, J. W., and Romanovsky, V. E.: Molecular investigations into a globally important carbon pool: permafrost-protected carbon in Alaskan soils, Global Change Biology, 16, 2543–2554, https://doi.org/10.1111/j.1365-2486.2009.02141.x, 2010.

Walter Anthony, K., Daanen, R., Anthony, P., Schneider von Deimling, T., Ping, C.-L., Chanton, J. P., and Grosse, G.: Methane emissions proportional to permafrost carbon thawed in Arctic lakes since the 1950s, Nature Geosci, 9, 679–682, https://doi.org/10.1038/ngeo2795, 2016.

Walter Anthony, K., Schneider von Deimling, T., Nitze, I., Frolking, S., Emond, A., Daanen, R., Anthony, P., Lindgren, P., Jones, B., and Grosse, G.: 21st-century modeled permafrost carbon emissions accelerated by abrupt thaw beneath lakes, Nat Commun, 9, 3262, https://doi.org/10.1038/s41467-018-05738-9, 2018.

Walter Anthony, K. M., Zimov, S. A., Chanton, J. P., Verbyla, D., and Chapin, F. S.: Methane bubbling from Siberian thaw lakes as a positive feedback to climate warming, Nature, 443, 71–75, https://doi.org/10.1038/nature05040, 2006.

Walter Anthony, K. M., Edwards, M. E., Grosse, G., Zimov, S. A., and Chapin, F. S.: Thermokarst Lakes as a Source of Atmospheric CH4 During the Last Deglaciation, Science, 318, 633–636, https://doi.org/10.1126/science.1142924, 2007.

Walter Anthony, K. M., Zimov, S. A., Grosse, G., Jones, M. C., Anthony, P. M., Iii, F. S. C., Finlay, J. C., Mack, M. C., Davydov, S., Frenzel, P., and Frolking, S.: A shift of thermokarst lakes from carbon sources to sinks during the Holocene epoch, Nature, 511, 452–456, https://doi.org/10.1038/nature13560, 2014.

Walter Anthony, K. M., Lindgren, P., Hanke, P., Engram, M., Anthony, P., Daanen, R. P., Bondurant, A., Liljedahl, A. K., Lenz, J., Grosse, G., Jones, B. M., Brosius, L., James, S. R., Minsley, B. J., Pastick, N. J., Munk, J., Chanton, J. P., Miller, C. E., and Meyer, F. J.: Decadal-scale hotspot methane ebullition within lakes following abrupt permafrost thaw, Environ. Res. Lett., 16, 035010, https://doi.org/10.1088/1748-9326/abc848, 2021.

Walz, J., Knoblauch, C., Tigges, R., Opel, T., Schirrmeister, L., and Pfeiffer, E.-M.: Greenhouse gas production in degrading ice-rich permafrost deposits in northeastern Siberia, Biogeosciences, 15, 5423–5436, https://doi.org/10.5194/bg-15-5423-2018, 2018.

Watson, C. S., White, N. J., Church, J. A., King, M. A., Burgette, R. J., and Legresy, B.: Unabated global mean sea-level rise over the satellite altimeter era, Nature Clim Change, 5, 565–568, https://doi.org/10.1038/nclimate2635, 2015.

Wen, X., Yang, S., Horn, F., Winkel, M., Wagner, D., and Liebner, S.: Global Biogeographic Analysis of Methanogenic Archaea Identifies Community-Shaping Environmental Factors of Natural Environments, Front. Microbiol., 8, https://doi.org/10.3389/fmicb.2017.01339, 2017.

Whalen, D., Forbes, D. L., Kostylev, V., Lim, M., Fraser, P., Nedimović, M. R., and Stuckey, S.: Mechanisms, volumetric assessment, and prognosis for rapid coastal erosion of Tuktoyaktuk Island, an important natural barrier for the harbour and community, Can. J. Earth Sci., 59, 945–960, https://doi.org/10.1139/cjes-2021-0101, 2022.

Wickham, H.: ggplot2, Springer International Publishing, Cham, https://doi.org/10.1007/978-3-319-24277-4, 2016.

Wilkenskjeld, S., Miesner, F., Overduin, P. P., Puglini, M., and Brovkin, V.: Strong increase in thawing of subsea permafrost in the 22nd century caused by anthropogenic climate change, The Cryosphere, 16, 1057–1069, https://doi.org/10.5194/tc-16-1057-2022, 2022.

Winkel, M., Sepulveda-Jauregui, A., Martinez-Cruz, K., Heslop, J. K., Rijkers, R., Horn, F., Liebner, S., and Anthony, K. M. W.: First evidence for cold-adapted anaerobic oxidation of methane in deep sediments of thermokarst lakes, Environ. Res. Commun., 1, 021002, https://doi.org/10.1088/2515-7620/ab1042, 2019.

Wulder, M. A., Loveland, T. R., Roy, D. P., Crawford, C. J., Masek, J. G., Woodcock, C. E., Allen, R. G., Anderson, M. C., Belward, A. S., Cohen, W. B., Dwyer, J., Erb, A., Gao, F., Griffiths, P., Helder, D., Hermosilla, T., Hipple, J. D., Hostert, P., Hughes, M. J., Huntington, J., Johnson, D. M., Kennedy, R., Kilic, A., Li, Z., Lymburner, L., McCorkel, J., Pahlevan, N., Scambos, T. A., Schaaf, C., Schott, J. R., Sheng, Y., Storey, J., Vermote, E., Vogelmann, J., White, J. C., Wynne, R. H., and Zhu, Z.: Current status of Landsat program, science, and applications, Remote Sensing of Environment, 225, 127–147, https://doi.org/10.1016/j.rse.2019.02.015, 2019.

Yamamoto, S., Alcauskas, J. B., and Crozier, T. E.: Solubility of methane in distilled water and seawater, J. Chem. Eng. Data, 21, 78–80, https://doi.org/10.1021/je60068a029, 1976.

Yang, S., Liebner, S., Walz, J., Knoblauch, C., Bornemann, T. L. V., Probst, A. J., Wagner, D., Jetten, M. S. M., and in 't Zandt, M. H.: Effects of a long-term anoxic warming scenario on microbial community structure and functional potential of permafrost-affected soil, Permafrost and Periglacial Processes, 32, 641–656, https://doi.org/10.1002/ppp.2131, 2021.

Yang, S., Anthony, S. E., Jenrich, M., in 't Zandt, M. H., Strauss, J., Overduin, P. P., Grosse, G., Angelopoulos, M., Biskaborn, B. K., Grigoriev, M. N., Wagner, D., Knoblauch, C., Jaeschke, A., Rethemeyer, J., Kallmeyer, J., and Liebner, S.: Microbial methane cycling in sediments of Arctic thermokarst lagoons, Global Change Biology, 29, 2714–2731, https://doi.org/10.1111/gcb.16649, 2023.

Young, M., Feyrer, F., Fong, D., Johnson, R., Kraus, T., Larwood, V., Stumpner, E., and Young, M.: Ocean connectivity drives trophic support for consumers in an intermittently closed coastal lagoon, Estuarine, Coastal and Shelf Science, 264, 107665, https://doi.org/10.1016/j.ecss.2021.107665, 2022.

Zhang, Y., Yamamoto-Kawai, M., Watanabe, E., and Park, H.: How Much Can Riverine Biogeochemical Fluxes Affect the Arctic Ocean Acidification?, Journal of Geophysical Research: Oceans, 129, e2023JC020404, https://doi.org/10.1029/2023JC020404, 2024.

Zona, D., Lipson, D. A., Paw U, K. T., Oberbauer, S. F., Olivas, P., Gioli, B., and Oechel, W. C.: Increased CO2 loss from vegetated drained lake tundra ecosystems due to flooding, Global Biogeochemical Cycles, 26, https://doi.org/10.1029/2011GB004037, 2012.

APPENDIX

A

Thermokarst Lagoons: A Core-Based Assessment of Depositional Characteristics and an Estimate of Carbon Pools on the Bykovsky Peninsula

Maren Jenrich[1,2*], Michael Angelopoulos[1,2], Guido Grosse[1,2], Pier Paul Overduin[1], Lutz Schirrmeister[1], Ingmar Nitze[1], Boris K. Biskaborn[3], Susanne Liebner[4,5], Mikhail Grigoriev[6], Andrew Murray[7], Loeka L. Jongejans[1,2] and Jens Strauss[1]

[1]Alfred Wegener Institute, Helmholtz Centre for Polar and Marine Research, Section of Permafrost Research, Potsdam, Germany,

[2]University of Potsdam, Institute of Geosciences, Potsdam, Germany,

[3]Alfred Wegener Institute, Helmholtz Centre for Polar and Marine Research, Section of Polar Terrestrial Environmental Systems, Potsdam, Germany,

[4] GFZ German Research Centre for Geosciences, Section Geomicrobiology, Potsdam, Germany, [5]Institute of Biochemistry and Biology, University of Potsdam, Potsdam, Germany,

[6]Melnikov Permafrost Institute, Russian Academy of Sciences, Siberian Branch, Yakutsk, Russia,

[7]Nordic Laboratory for Luminescence Dating, Department of Geoscience, Aarhus University and DTU Physics, Risø Campus, Roskilde, Denmark

[*]*correspondence to: Maren Jenrich*

This chapter is published in:

Frontiers in Earth Science: Biogeoscience - DOI: 10.3389/feart.2021.637899, 2021

AUTHOR CONTRIBUTIONS

M. Jenrich and J. Strauss designed this study. M. Jenrich led the writing of the first draft of the manuscript. J. Strauss, G. Grosse, and M. Grigoriev developed the overall coring plans for the Bykovsky Peninsula field campaign. J. Strauss, M. Grigoriev, L. Schirrmeister, B. Biskaborn, P. Overduin, M. Angelopoulos, S. Liebner, and G. Grosse conducted the field work. M. Angelopoulos and P. Overduin did the subsampling for the Polar Fox sediment core and M. Jenrich for the Uomullyakh core. M. Jenrich and P. Overduin performed laboratory analyses. M. Jenrich led the data interpretation for both cores. M. Jenrich and I. Nitze conducted the spatial analysis and mapping of the lagoons. A. Murray performed optical luminescence analyses and data interpretation. All co-authors contributed within their specific expertise to data interpretation.

frontiers in Earth Science

ORIGINAL RESEARCH
published: 23 July 2021
doi: 10.3389/feart.2021.637899

Thermokarst Lagoons: A Core-Based Assessment of Depositional Characteristics and an Estimate of Carbon Pools on the Bykovsky Peninsula

Maren Jenrich[1,2], Michael Angelopoulos[1,2], Guido Grosse[1,2], Pier Paul Overduin[1], Lutz Schirrmeister[1], Ingmar Nitze[1], Boris K. Biskaborn[3], Susanne Liebner[4,5], Mikhail Grigoriev[6], Andrew Murray[7], Loeka L. Jongejans[1,2] and Jens Strauss[1]*

[1]Alfred Wegener Institute, Helmholtz Centre for Polar and Marine Research, Section of Permafrost Research, Potsdam, Germany, [2]University of Potsdam, Institute of Geosciences, Potsdam, Germany, [3]Alfred Wegener Institute, Helmholtz Centre for Polar and Marine Research, Section of Polar Terrestrial Environmental Systems, Potsdam, Germany, [4]GFZ German Research Centre for Geosciences, Section Geomicrobiology, Potsdam, Germany, [5]Institute of Biochemistry and Biology, University of Potsdam, Potsdam, Germany, [6]Melnikov Permafrost Institute, Russian Academy of Sciences, Siberian Branch, Yakutsk, Russia, [7]Nordic Laboratory for Luminescence Dating, Department of Geoscience, Aarhus University and DTU Physics, Risø Campus, Roskilde, Denmark

OPEN ACCESS

Edited by:
Alexandra V Turchyn, University of Cambridge, United Kingdom

Reviewed by:
Brendan O'Neill, Geological Survey of Canada, Canada
Edward A. Johnson, University of Calgary, Canada

***Correspondence:**
Maren Jenrich
maren.jenrich@awi.de

Specialty section:
This article was submitted to Biogeoscience, a section of the journal Frontiers in Earth Science

Received: *05 March 2021*
Accepted: *15 June 2021*
Published: *23 July 2021*

Citation:
Jenrich M, Angelopoulos M, Grosse G, Overduin PP, Schirrmeister L, Nitze I, Biskaborn BK, Liebner S, Grigoriev M, Murray A, Jongejans LL and Strauss J (2021) Thermokarst Lagoons: A Core-Based Assessment of Depositional Characteristics and an Estimate of Carbon Pools on the Bykovsky Peninsula. Front. Earth Sci. 9:637899. doi: 10.3389/feart.2021.637899

Permafrost region subsurface organic carbon (OC) pools are a major component of the terrestrial carbon cycle and vulnerable to a warming climate. Thermokarst lagoons are an important transition stage with complex depositional histories during which permafrost and lacustrine carbon pools are transformed along eroding Arctic coasts. The effects of temperature and salinity changes during thermokarst lake to lagoon transitions on thaw history and lagoon deposits are understudied. We analyzed two 30-m-long sediment cores from two thermokarst lagoons on the Bykovsky Peninsula, Northeast Siberia, using sedimentological, geochronological, hydrochemical, and biogeochemical techniques. Using remote sensing we distinguished between a semi-closed and a nearly closed lagoon. We (1) characterized the depositional history, (2) studied the impact of marine inundation on ice-bearing permafrost and taliks, and (3) quantified the OC pools for different stages of thermokarst lagoons. Fluvial and former Yedoma deposits were found at depth between 30 and 8.5 m, while lake and lagoon deposits formed the upper layers. The electrical conductivity of the pore water indicated hypersaline conditions for the semi-closed lagoon (max: 108 mS/cm), while fresh to brackish conditions were observed beneath a 5 m-thick surface saline layer at the nearly closed lagoon. The deposits had a mean OC content of 15 ± 2 kg/m^3, with higher values in the semi-closed lagoon. Based on the cores we estimated a total OC pool of 5.7 Mt-C for the first 30 m of sediment below five mapped lagoons on the Bykovsky Peninsula. Our results suggest that paleo river branches shaped the middle Pleistocene landscape followed by late Pleistocene Yedoma permafrost accumulation and early Holocene lake development. Afterward, lake drainage, marine flooding, and bedfast ice formation caused the saline enrichment of pore water, which led to cryotic talik development. We find that the OC-pool of Arctic lagoons may comprise a substantial inventory of partially thawed and partially refrozen OC, which is available for microbial degradation processes at the Arctic terrestrial-marine interface. Climate change in the Arctic leading to sea level rise, permafrost thaw, coastal erosion, and sea ice loss may increase the rate of thermokarst lagoon formation and thus increase the importance of lagoons as biogeochemical processors of former permafrost OC.

Keywords: talik, Arctic Siberia, Yedoma, inundation, permafrost carbon, OSL (optically stimulated luminescence), coastal erosion

INTRODUCTION

Over the last 2 decades, the Arctic has been warming more than twice as fast as the global average (Johannessen et al., 2004; Berner et al., 2005; Notz and Stroeve 2016). This amplified warming has led to rapid surface warming in Siberia with modeled temperature rise of up to 4°C over the last 5 decades (Romanovsky et al., 2010; Biskaborn et al., 2019; Lenssen et al., 2019; GISTEMP Team, 2020). As a consequence, permafrost is thawing in many regions, mobilizing large amounts of sediments including organic carbon and allowing microbial decomposition of previously frozen organic matter (Strauss et al., 2013; Strauss et al. 2021; Schuur et al., 2015). Arctic coastal systems are especially affected by rapid permafrost thaw and mobilization of organic matter by erosion and marine inundation (Fritz et al., 2017). Lagoons, a frontier environment between land and ocean, are transitional and dynamic coastal landforms combining characteristics of both terrestrial and marine systems (Kjerfve, 1994; Tagliapietra et al., 2009; Harris et al., 2017). Globally, coastal lagoons are defined as shallow coastal water bodies separated from the sea by a barrier, connected at least intermittently to the ocean by one or more restricted inlets, and usually have a shore-parallel orientation (Kjerfve, 1994). As lagoons are complex and diverse systems, there are many different approaches to classify them, for example based on geomorphological and geological origin, their morphological properties such as size and water depth (Kosyan, 2016), the degree of isolation from the sea (Kjerfve, 1994), their physicochemical state (for example, salinity, ionic composition, temperature, turbidity, nutrients) (Tagliapietra et al., 2009), or the degree of influence by living organisms such as corals and humans (Brovko 1990).

Permafrost thaw results in landscape change as melting excess ground ice causes surface subsidence, eventually forming thermokarst lakes (Osterkamp et al., 2009; Jones et al., 2011; Lenz et al., 2016). Along eroding sections of Arctic coasts, lowered thermokarst terrain is affected by flooding of nearshore thermokarst lakes and basins with seawater, transforming them into thermokarst lagoons (Ruz et al., 1992; Romanovskii et al., 2000). Thermokarst lagoons are also formed by natural thermokarst lake dynamics in the course of lake drainage at coasts (Arp et al., 2010). However, rates of formation are expected to intensify as a result of ongoing climate change in the Arctic. Increasing coastal erosion (Günther et al., 2015; Jones et al., 2018), sea-level rise (Proshutinsky et al., 2001; Watson et al., 2015; Nerem et al., 2018), and higher sea water temperatures (Bindoff et al., 2007) are likely to result in an acceleration of erosion of permafrost coasts and in particular lagoon formation. Incubation experiments performed by Tanski et al. (2019) indicate that along eroding permafrost coastlines, large amounts of carbon dioxide can be produced. Therefore, thermokarst lagoon formation is an important process affecting permafrost carbon pools along rapidly changing permafrost coasts. In addition, marine inundation affects the temperature and salinity of taliks formerly beneath thermokarst lakes during their transition to the marine environment (Angelopoulos et al., 2020a). The formation of hypersaline, unfrozen ground beneath thermokarst lagoons may preserve existing thermokarst lake taliks, forming migration pathways for methane (Shakhova et al., 2019; Angelopoulos et al., 2020a). However, lagoon formation can also cause taliks to partially refreeze, provided that heat loss is faster than salt diffusion (Angelopoulos et al., 2020a). Ascending gas can get trapped below low-permeability sediment layers (Ruppel and Kessler, 2017) and be released when conditions warm up. These pathways, which may contain low-permeability ice-saturated zones, become part of the offshore environment with sufficient coastal erosion and so become potential sources of gas release in subsea permafrost areas (Frederick and Buffett, 2014; Shakhova et al., 2017).

Although thermokarst lagoons are widespread along the pan-Arctic coast (Jenrich, 2020), there is still no qualitative or quantitative assessment of their distribution or of the size of the total carbon reservoir they represent. Until now, Arctic thermokarst lagoon research has concentrated on the Mackenzie Delta region in Northwest Canada (Hill, 1990; Ruz et al., 1992; Héquette et al., 1995; Campeau et al., 2000; Solomon et al., 2000) and the Bykovsky Peninsula in Northeast Siberia. On the Bykovsky Peninsula, several lagoons have evolved from thermokarst lake basins in ice-rich Yedoma Ice Complex permafrost, and these are now actively developing in different stages (Romanovskii et al., 2000; Romanovskii et al., 2004; Ulyantsev et al., 2017; Schirrmeister et al., 2018). Still, little is known of the sedimentary history of thermokarst lagoons, the impact of marine inundation, and the amount and quality of carbon stored in greater depths.

To address these research gaps, we applied a multidisciplinary approach to characterize the sedimentological, geochronological, hydrochemical, and biogeochemical properties of two approximately 30 m deep (below lagoon ice surface level in spring) sediment cores from two typical thermokarst lagoons on the Bykovsky Peninsula (**Figure 1**). We paired this with remote sensing observations to identify, map, and characterize thermokarst lagoons in a regional context along the coast of the

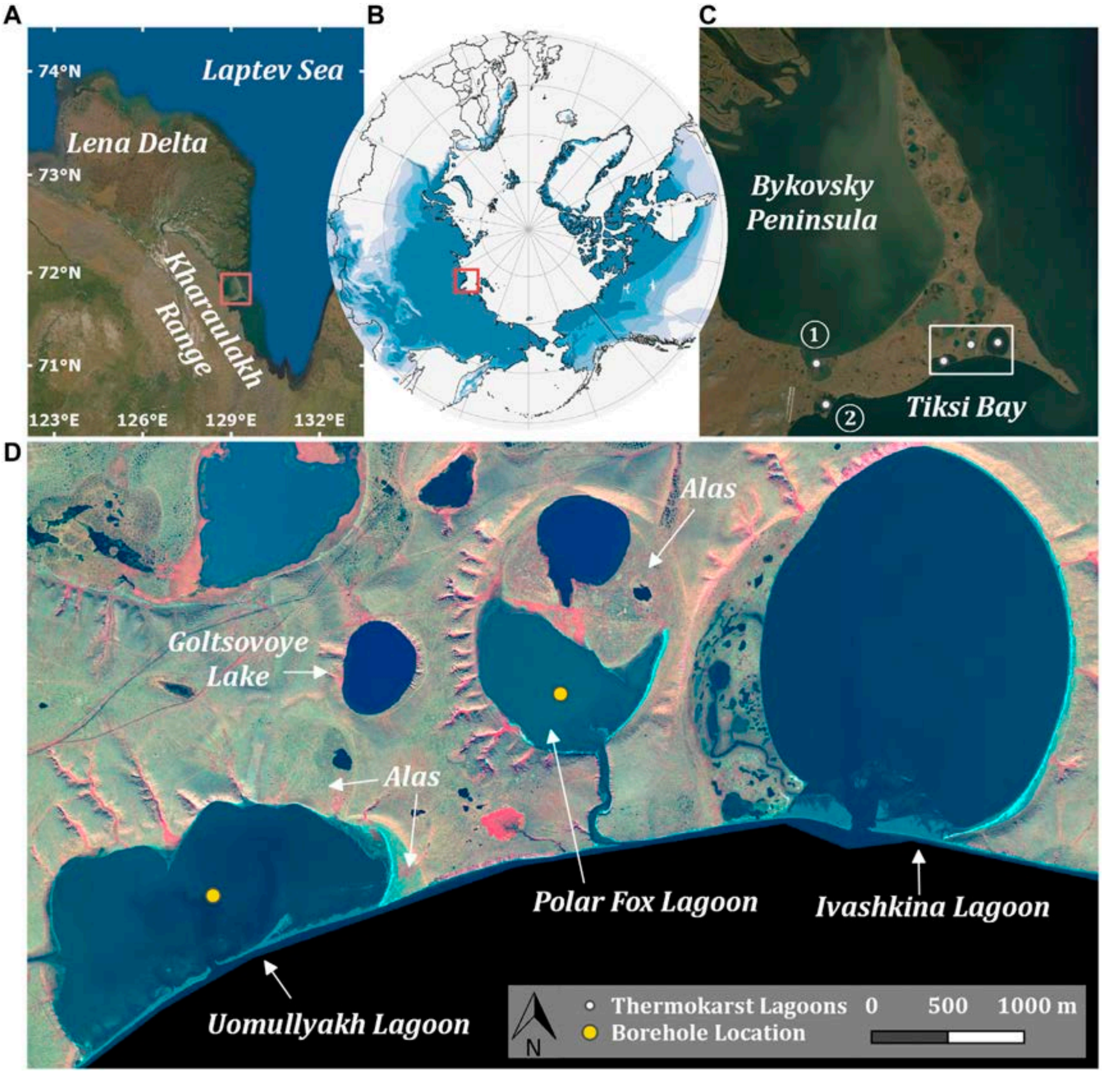

FIGURE 1 | Bykovsky Peninsula in Northeast Siberia, south of Lena Delta **(A, B)**. Both the Stepanenko ① and Safroneeva ② lagoons **(C)** as well as the Uomullyakh, Polar Fox, and Ivashkina lagoons are located at the southern coast of the Bykovsky Peninsula **(D)**. The drilling locations in the lagoon centers of Uomullyakh and Polar Fox lagoons are indicated by yellow dots **(D)**. Source imagery: **(A, C)**: ESRI Satellite World Imagery b: Permafrost extent regions based on Brown et al. (1997) **(D)** WorldView3 false colour satellite image (8-5-3), acquired 2016-09-02.

Bykovsky Peninsula. The specific aims of this paper are to characterize (1) the sediments and (2) pore water below the lagoons and (3) to quantify the regional carbon inventory based on spatially explicit lagoon areas in the region.

Study Area

The lagoons investigated here are the semi-closed Uomullyakh Lagoon (UoL) and the nearly closed Polar Fox Lagoon (PFL) (**Table 1**), located on the southern coast of the Bykovsky Peninsula (71°51′ N, 129°19′ E) (Strauss et al., 2018, **Figure 1D**). The peninsula is located in Northeast Siberia (**Figure 1B**), at the mouth of the Bykovskaya Channel, one of the main outflow channels of the Lena River Delta (**Figure 1A**). The hinterland of the Bykovsky Peninsula is the Kharaulakh Range with elevations up to 500 m above sea level (asl), which is part of the northern foothills of the Verkhoyansk Mountains. The peninsula consists of the remains of a former late Pleistocene sediment accumulation plain with elevations of up to 45 m asl (Schirrmeister et al., 2002; Schirrmeister et al., 2018). It lies within the continuous permafrost zone and is characterized by thick, ice-rich Yedoma Ice Complex deposits (Grosse et al., 2007). Postglacial sea level rise during the Lateglacial interstadial and the early Holocene inundated the shallow Laptev Sea shelf and transformed terrestrial permafrost into subsea permafrost (Romanovskii et al., 1998; Lantuit et al., 2011). Cliffs and thermokarst basins are the typical backshore coastal

TABLE 1 | Classification of lagoons into "open", "semi-closed" and "nearly closed" lagoon systems which occur along a gradient of coastal erosion.

Lagoon class	Connectivity with the sea	Impact of coastal erosion	Examples
Open	Full and broad exchange with the sea	Fully affected and far ahead in the transition to an open marine system	Stepanenko and Safroneeva lagoons (**Figure 1**), many in the northern Lena Delta, and on the Cape Halkett coast of Beaufort Sea
Semi-closed	Barrier islands or sand spits partially block exchange with the sea either temporally or spatially	Moderately to substantially affected	Uomullyakh Lagoon (**Figure 1**), many on Tuktoyaktuk Peninsula, eastern Alaskan Beaufort Sea (Harris et al., 2017)
Nearly closed	Narrow outlet/inlet channel connecting lagoon and sea, with the possibility of having lake character temporarily	Not yet affected	Polar Fox Lagoon (**Figure 1**), and other lagoons connected through small channels

landforms. Sixteen large thermokarst depressions are found on the peninsula (Grosse et al., 2005; Fuchs et al., 2018). In total, more than 50% of the Bykovsky Peninsula is strongly influenced by thermokarst and thermo-erosion landforms (Grosse et al., 2005; Lantuit et al., 2011).

According to the Köppen–Geiger world climate classification (Peel et al., 2007), the peninsula is located in the polar tundra climate zone (ET). Despite the coastal location, the climate is strongly continental with long, cold winters (September–May) and short, cool summers. In January, the mean air temperature is −30.0°C and rises to +8.5°C in July (1987–2016). The mean annual precipitation does not exceed 350 mm (Tiksi Hydrometeorological Observatory, WMO 218240). The open-water season in the southern Laptev Sea starts on average in mid-June and extends to mid-October (Lantuit et al., 2011).

During drilling campaigns within the Russian-German science cooperation Lena Expedition in 2017, deep sediment cores from two thermokarst lagoons (UoL and PFL) and one thermokarst lake (Goltsovoye Lake (GoL)) were drilled on the Bykovsky Peninsula (**Figure 1D**). Furthermore, sediment characteristics of a 6.2 m deep core from the Ivashkina Lagoon (IvL) drilled in 1999 were published by Schirrmeister et al. (2018). The results showed several stages of landscape development from the initial Yedoma Ice Complex through thaw-induced lake development and eventually lagoon formation. In this study, we report on results from the approximately 30 m deep cores from Polar Fox and Uomullyakh lagoons.

The Uomullyakh Lagoon (71°43′51″N, 129°16′21″E, **Figure 1D**) is a 2.1 km^2 large, shallow lagoon (water depth 0.8 m at the borehole location) with underlying former Yedoma and Alas permafrost (Strauss et al., 2018). The lagoon is well connected with the Tiksi Bay via a 90 m wide opening in the center of the narrow and flat sand spit, which can be flooded by storm surges. In April 2017, test hole drilling (17 locations) with a Kovacs 5 cm diameter ice auger revealed bedfast ice at all locations. However, bathymetry surveys in summer 2017 (Strauss et al., 2018) suggest that small isolated water pockets might have existed in April 2017. We recorded 40 cm of compacted snow on top of 80 cm ice, which was overlying the frozen lagoon bed at the drilling location (71°43′51″N, 129°16′29″E). In the west, the lagoon is connected to two drained thermokarst lakes basins by a former drainage channel.

The Polar Fox Lagoon (71°44′35″N, 129°20′16″E; **Figure 1D**) is a smaller sized (0.6 km^2), brackish to salty water body (water depth 3.30 m in the lagoon center) formed after partial lake drainage. This nearly closed lagoon is located in a partially drained thermokarst basin (Alas in **Figure 1D**) and is connected to the sea only during the open water season via an 800 m long and roughly 50 m wide outlet channel. The water level in the lagoon is at about sea level and water flow occurs in both directions depending on wind, wave, and tide conditions. Ice thickness measurements from April 2017 and bathymetry from July 2017 suggest that the lagoon was 75% covered with bedfast ice (Angelopoulos et al., 2020a). In the center of the lagoon, at the borehole location (71°44′58″N, 129°20′30″E), a 175 cm salty water layer was present underneath the 155 cm thick seasonal ice layer in April 2017 (Strauss et al., 2018).

Both lagoons are strongly impacted by warm freshwater discharge from the Lena River into the Buor Khaya and Tiksi bays (Juhls et al., 2019). This discharge causes large seasonal and interannual variations in temperature and salinity (**Supplementary Table S1**). For example, Polar Fox Lagoon had a salinity of 13 psu (practical salinity unit) and 44 psu below the ice cover in April 2017 and April 2019, respectively. In July 2017, the salinity dropped to less than 1 psu.

METHODS

Field Work

Fieldwork on the Bykovsky Peninsula was carried out in April 2017 (Strauss et al., 2018). Over eight days, a 33.5 m deep borehole was drilled from the ice surface on UoL (core number PG2410) and a 31 m deep borehole was drilled from the ice surface of neighboring PFL (PG2411) (**Figure 1**) using a URB2-4T drilling rig mounted on a tracked vehicle. The sediment core retrieved at UoL was 32.3 m long and at PFL 27.7 m long. Immediately after recovery, the cryolithology of the sediment cores was visually described and the cores were packed and transported frozen to AWI Potsdam. GeoPrecision temperature chains were installed in both boreholes, each with an accuracy of ± 0.1°C at 0°C and a resolution of 0.01°C. The thermistors had been calibrated in a MilliQ water-ice bath to measure their offset from 0°C prior to deployment. The chains remained in the boreholes for 5 days at Polar Fox Lagoon and 11 days at Uomullyakh Lagoon. To account for drilling heat effects, the observed temperature drift for each thermistor was analyzed following Lachenbruch et al. (1982) to estimate the undisturbed temperature. Both sediment cores were mostly unfrozen but had some partially frozen layers. The heat generated during the drilling of the cores caused the cores to partially thaw, so that the on-site haptic observation of the frozen state included some uncertainty. The PFL raw temperature data is available from Angelopoulos et al. (2020a) and the UoL temperature data and processing are described in the supporting information (**Supplementary Figure A4**).

Laboratory Analyses

In the cold lab (−9°C), the sediment cores were opened, cleaned and split, and the cryolithology was described in more detail. Furthermore, the core halves were photographed and subsamples were taken approximately every 50 cm for laboratory analyses. For the Polar Fox core, a higher sampling resolution of about every 10 cm was used for pore water extraction.

Hydrochemical Analyses

Pore water was extracted from thawed samples using Rhizons™ with a membrane pore size of 0.15 µm and analyzed for pH, electrical conductivity (EC, mS/cm), DOC (mg/L) and stable water isotopes (δD, $\delta^{18}O$ (‰ vs. VSMOW)). The pH and EC values were measured with a WTW Multilab 540 (accuracy: ± 0.01/± 1 mV). DOC samples were acidified with 50 µL of 30% HCl supra-pure and stored at + 4°C until measured with a Shimadzu Total Organic Carbon Analyzer (TOC-VCPH) (accuracy: ± 1.5%) following Fritz et al. (2015). For analyzing the ratios of δD and $\delta^{18}O$, water and ice samples were processed following Meyer et al. (2000) and measured with a Finnigan MAT Delta-S mass spectrometer.

Sedimentology Analyses

Grain size measurements were conducted to gain information about the transportation medium and the level of sediment accumulation at the study areas. Mass specific magnetic susceptibility, describing the ability of a material to be magnetized, gives an indication of the amount of ferri- and ferromagnetic minerals in a sample. Differences in mineral composition between samples usually indicate sediment sources and changes in stratification (Liu et al., 2010). For both measurements the samples were pre-weighed and freeze-dried. The absolute ice or water content was determined based on the difference in weight before thawing and after freeze drying related to the wet weight (Phillips et al., 2015). The bulk density (BD in kg/m^3) was calculated from the ice content according to Strauss et al. (2012). The grain size distributions of 74 samples from both cores were measured with a Malvern Mastersizer 3000 laser particle size analyser with a measuring range of 0.01–1000 µm. Additional details on BD calculation and grain size measurement can be found in the supplementary material. Mass-specific magnetic susceptibility (MS in $10^{-8}\,m^3/kg$) was measured with a Magnetic Susceptibility Meter (Model MS2, Sensor Type MS 2B, Bartington Instruments) on the freeze-dried, but not homogenized samples at a frequency of 0.465 kHz (low frequency).

Bulk Biogeochemistry

To gain information about changes in the nutrient cycle during the transformation of terrestrial permafrost into sub-aquatic permafrost, the biogeochemical parameters total nitrogen (TN), total carbon (TC) and total organic carbon content (TOC), and their stable isotopes ($\delta^{13}C$ and $\delta^{15}N$) were measured and the TOC/TN ratio determined. The parameters TOC/TN and $\delta^{13}C$ are widely used as a broad indicator for the degree of decomposition and source of organic matter (OM) (e.g. Mary et al., 1992; Meyers 1994; Meyers, 1997; Gundelwein et al., 2007; Andersson et al., 2012; Strauss et al., 2015). Generally, a lower TOC/TN ratio and higher $\delta^{13}C$ indicate more decomposed organic material (Schirrmeister et al., 2011; Strauss et al., 2015). Since microorganisms prefer easily accessible carbon compounds, the organic carbon quality decreases with increasing organic matter decomposition (Schowalter, 2016). Using $\delta^{13}C$ and TOC/TN, it is possible to distinguish between land plants and marine, brackish and freshwater algae (decreasing $\delta^{13}C$ is associated with decreasingly saline environment) (Meyers et al., 1994) (**Supplementary Table S2**).

To determine TC and TN content, the homogenized, freeze dried and ground samples were measured with a carbon–nitrogen–sulfur analyzer (Vario EL III, Elementar). TOC was measured with a TOC analyser (Vario Max C, Elementar). We measured two replicates of each sample and accepted only <5% deviation for the replicates. The TOC/TN ratio is expressed as atomic TOC/TN value to ensure comparability between studies. The atomic TOC/TN value was calculated following Meyers et al. (1994) by multiplying the weight ratio with 1.167, which is the ratio of the atomic weights of nitrogen (14.007 amu, atomic mass unit) and carbon (12.001 amu). The rate of mineralization was considered high at TOC/TN < 12, moderate between 12 and 25, and low at values >25 (Walhert et al., 2004).

The volumetric TOC content (carbon density, kg TOC/m^3) was calculated following Strauss et al. (2013) according to **Eq. 1**:

$$organic\ carbon\ content = V_{ref} \cdot BD \cdot \frac{TOC_{wt\%}}{100}, \qquad (1)$$

where V_{ref} is the reference volume of 1 m^3, BD in kg/m^3 and TOC in wt%.

The stable carbon and nitrogen isotopic composition was measured for all samples with TOC or TN values above the detection limit (0.1 wt%) with a ThermoFisher Scientific Delta-V-Advantage gas mass spectrometer equipped with an organic elemental analyser Carlo-Erba NC2500 (accuracy: < 0.2‰). Measured $\delta^{13}C$ and $\delta^{15}N$ was compared to the standardized Vienna Pee Dee Belemnite (VPDB) and expressed in per mille (‰ vs. VPDB). TOC and TN values below the detection limit were neglected in further calculations.

Geochronology

For radiocarbon dating, we chose samples about every 3 m ($n = 19$ for both cores). When present, macroplant remains were hand-picked under a stereomicroscope, otherwise bulk sediment was selected and dated using Accelerator Mass Spectrometry in the AWI MICADAS (MIni radioCArbon DAting System) Laboratory in Bremerhaven. Radiocarbon dates were calibrated using Calib 7.04 software after (Reimer et al., 2013) and the IntCal13 calibration curve (Stuiver et al., 2020) to calculate calibrated years before present (cal. years BP).

For optically stimulated luminescence (OSL) dating, three core segments were selected in the field from the Uomullyakh core, and two from the Polar Fox core. The core segments were frozen in their original state, wrapped in black foil, and delivered frozen to Aarhus University's Nordic Laboratory for Luminescence Dating (Roskilde, Denmark). The core segments were then thawed in a controlled-light environment and the outer ~5 mm removed to minimize the effects of smearing, and to ensure that the material used for OSL measurements had not been exposed to daylight during or after retrieval. Luminescence measurements were made using a Risø TL/OSL reader, model TLDA 20. A standard SAR protocol based on Murray and Wintle (2000; 2003) was used for quartz dose estimation, and a comparison with feldspar data was used to investigate the degree of bleaching at deposition (e.g. Möller and Murray, 2015). Radionuclide concentrations were measured using high resolution gamma spectrometry (Murray et al., 1987; Murray et al., 2018), calibrated using Certified Reference Materials produced by Natural Resources Canada (NRCAN). For detailed information see supplementary material.

Borehole Temperature Measurements and Calculation of Freezing Conditions

Ground temperature was recorded for 11 days in the Uomullyakh borehole and for 5 days in the Polar Fox borehole in April 2017. The freezing point depression ΔT_f of the sediment was calculated from the molality of dissolved ions estimated from the measured pore water electrical conductivity according to **Eq. 2** (Atkins, 2018) and then compared with the measured borehole temperatures.

$$\Delta T_f = \frac{R\left(T_{m,fw}\right)^2}{L_f} c \tag{2}$$

This equation describes the lowering of the freezing point of free water with the salt content c (mol/kg). R is the universal gas constant 8.314 J/(K mol), $T_{m,fw}$ is the freezing point of free water (273.15 K) and L_f is the latent heat of fusion of water (334,000 J/kg). For the conversion of the measured EC to molality (mol/kg) the MATLAB implementation of TEOS-10 (McDougall and Barker 2011) was used. It has been demonstrated that TEOS-10 also performs well for hypersaline solutions (Pawlowicz, 2012). Further details can be found in the supplementary material.

Lagoon Mapping

Along the coast of the Bykovsky Peninsula six lagoons exist, five of them originated from thermokarst basins (Jenrich, 2020). All of them are located in the southern part of the peninsula (**Figure 1**). We used a simple geomorphological approach to further differentiate them based on their connectivity with the ocean into open, semi-closed and nearly closed thermokarst lagoons (**Table 1**).

The extent of each of the five lagoons was determined using the Global Surface Water dataset which is based on Landsat-5, -7, and -8 satellite images from 1984 to 2018 at 30 m resolution (Pekel et al., 2016). Water bodies were defined by a water occurrence threshold of >75% over this time period. The raster dataset was vectorized and smaller geometric errors, which occurred during vectorization, were solved with the Fix Geometry function in QGIS3.6. The five Bykovsky Peninsula lagoon polygons were selected manually and these water bodies were split from the ocean by using the function "split by line". The resulting lagoon polygons were re-projected in UTM Zone 52N (EPSG:32652) to calculate the polygon area in km^2.

Upscaling Carbon Pools

The organic carbon pools of Uomullyakh and Polar Fox lagoons were estimated after Jongejans et al. (2018) using **Equation 3**, based on a deposit thickness of 30 m, the lagoon size, bulk density, and TOC content. We assume that there is no form of massive ice in the thermokarst lagoon sediments, so that the TOC pool can be calculated as:

$$TOC_{pool}\,(Mt) = \frac{thickness \cdot coverage \cdot BD \cdot \frac{TOC}{100}}{10^6} \tag{3}$$

with thickness and coverage in m, BD in kg/m^3 and TOC in wt%. For further calculations, we assumed a TOC of 0.05 wt% for the samples with TOC below the detection limit (n = 21). To compensate for data gaps caused by core loss or larger sampling distances, the BD and TOC values were first multiplied, and the depth interval given as the difference of two adjoining depths was calculated. For core loss sections, this interval was accordingly higher. The product of BD and TOC was weighted and replicated for each depth interval. To interpolate the carbon content of point measurements to greater areas, the data was resampled using the bootstrapping method after Jongejans and Strauss (2020). Assuming that the deposition of organic material in the study area did not show significant differences, the calculated C-budgets of UoL and PFL were averaged and upscaled on the three further lagoons on the peninsula. Therefore, the size of each lagoon was multiplied with the mean of the TOC pool of UoL and PFL, and divided by the mean size of UoL and PFL.

Statistics

We used the R environment to perform various statistical analyses on 10 parameters (R Core Team (2016); R version 3.6.3). In order to compare the differently scaled parameters, the data was normalized with the function "normalize". To subdivide the cores into stratigraphic zones, the stratigraphically constrained, incremental sum of squares cluster analysis (CONISS) was applied. Thereby, only stratigraphically adjacent clusters are considered for merging. The CONISS clustering was performed in R with the 'chclust' function from the package 'rioja'. The used dissimilarity index was 'bray'. In order to compare the properties at the time of sediment deposition, only sedimentological and biogeochemical parameters were included in the calculation. In total 10 parameters: mean depth, grain size (mean, volumetric proportion of clay, silt and sand), mass specific magnetic susceptibility, TOC, TN, TOC/TN and $\delta^{13}C$. Hydrochemical parameters were not used as pore water in

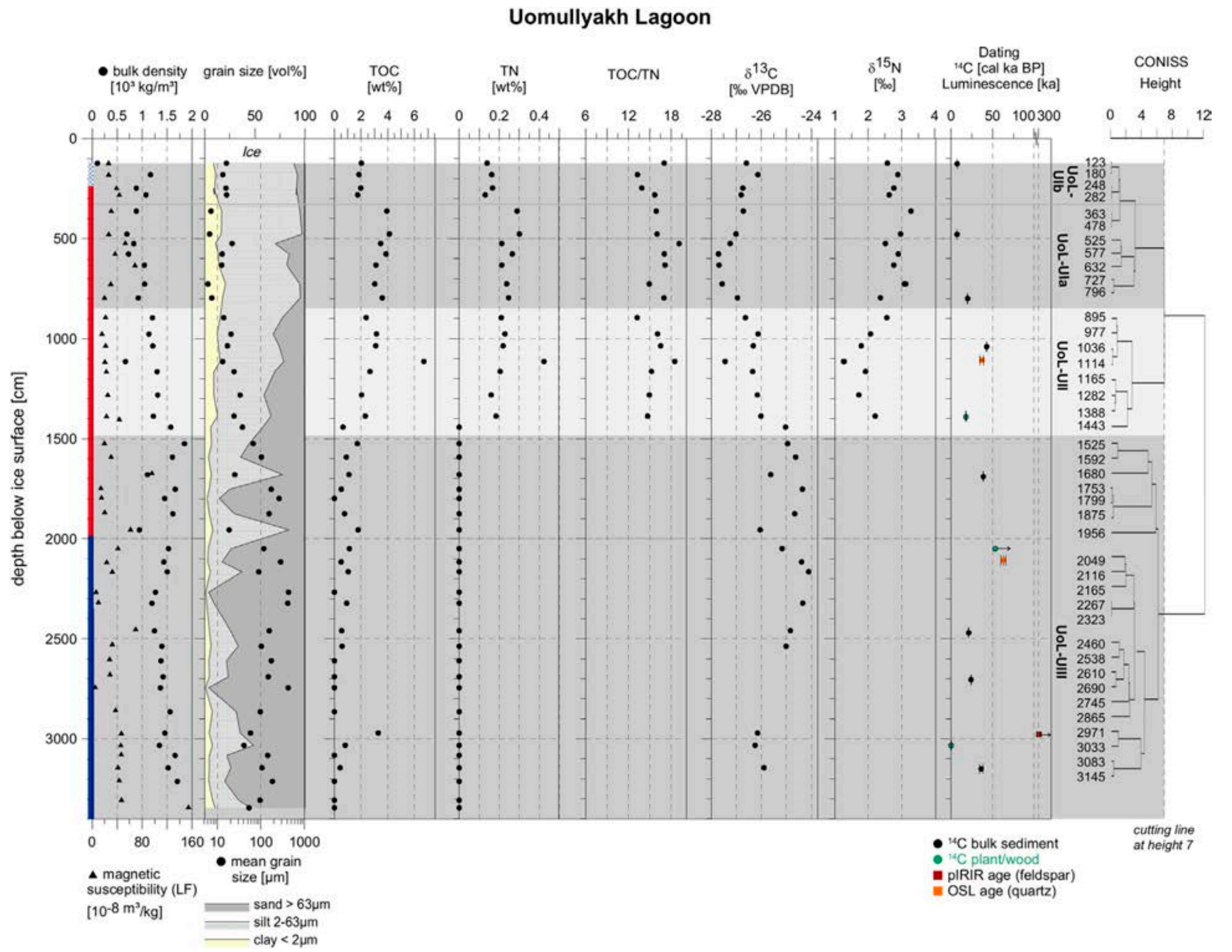

FIGURE 2 | Summary of sedimentological, geochronological and biogeochemical parameters for the Uomullyakh Lagoon core: bulk density (upper axis), mass specific magnetic susceptibility (lower axis), grain size (upper axis: volumetric proportions, lower axis: mean grain size), total organic carbon content (TOC), total nitrogen content (TN), organic carbon and nitrogen ratio (TOC/TN), stable carbon and nitrogen isotope composition ($\delta^{13}C$, $\delta^{15}N$), radiocarbon dating (^{14}C) and luminescence dating (pIRIR, OSL). The top 120 cm is the overlying ice cover. The core was divided into three stratigraphic units based on a CONISS analysis. Color bar at the *y*-axis indicates frozen (blue), unfrozen (red) and partially frozen (shaded) core segments. Note that "frozen" includes visibly frozen core sections and re-constructed frozen conditions. Arrows indicate non-finite ages.

unfrozen soil is flowing and mixing constantly and so does not represent the hydrochemical composition at the time of sediment deposition. The results were visualized in a dendrogram. The cutting point was selected based on visual validation and dating results.

A principal component analysis (PCA) was performed on the same parameters to reduce this high-dimensional data set to fewer dimensions and to detect patterns in the distribution of sedimentological and biogeochemical parameters over depth. The results were visualized in a biplot. The arrows show the loading on each variable, with the length approximating the variance and the angle between the arrows their correlation. Points close together correspond to depth that have similar scores on the PCA components. PCA was performed using the 'prcomp' function from the Package 'stats'.

RESULTS

The cores are described according to the depositional record from bottom to top. All depth specifications refer to the top of the ice cover (contains a compacted snow layer on top of lagoon ice) unless they are specifically stated as sediment depth, in which case we refer to the depth from the top of sediment. The units were separated according to a vertical cut in the dissimilarity dendrogram at height 7 for the Uomullyakh sediment core (**Figure 2**) and at height 4 for the Polar Fox sediment core (**Figure 3**). Therefore, the Uomullyakh core (PG2410, core recovery of 85%) was divided into three units, whereby Unit I was divided into two subunits: UoL-UIII ranges from 3350 to 1480 cm, UoL-UII from 1480 to 820 cm, UoL-UIa from 820 to 320 cm and UoL-UIb from 320 to 120 cm depth. The Polar Fox

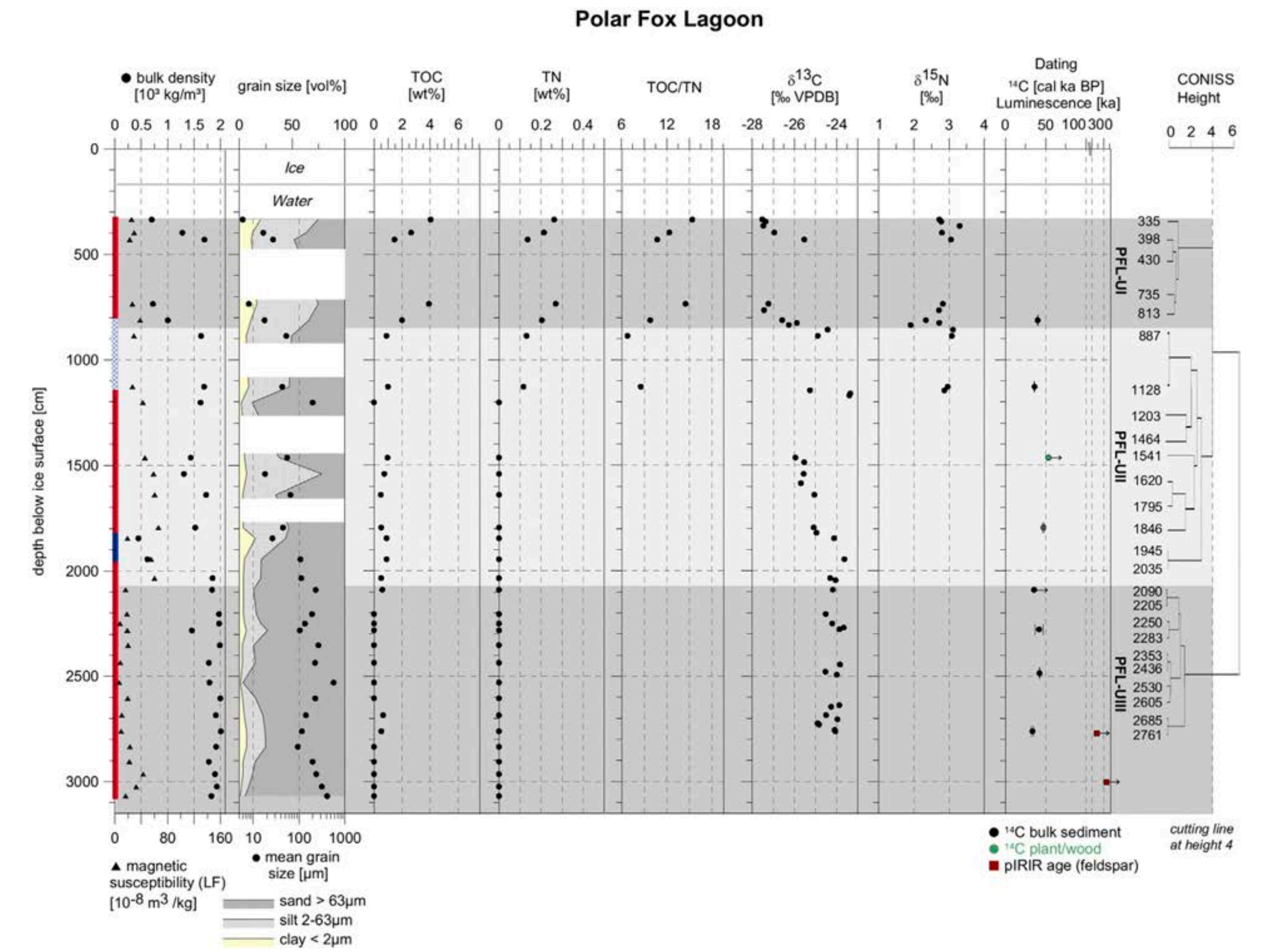

FIGURE 3 | Summary of sedimentological, geochronological and biogeochemical parameters for Polar Fox Lagoon core: bulk density (upper axis), mass specific magnetic susceptibility (lower axis), grain size (upper axis: volumetric proportions, lower axis: mean grain size), total organic carbon content (TOC), total nitrogen content (TN), organic carbon and nitrogen ratio (TOC/TN), stable carbon and nitrogen isotope composition ($\delta^{13}C$, $\delta^{15}N$), radiocarbon dating (^{14}C) and luminescence dating (pIRIR). The top 330 cm is the overlaying ice and water layer. The core is divided into three stratigraphic units based on a CONISS analysis. Color bar at the *y*-axis indicates frozen (blue), unfrozen (red) and partially frozen (shaded) core segments. Arrows indicate non-finite ages.

sediment core (PG2411, core recovery of 70%) was also divided into three units: PFL-UIII from 3070 to 2080 cm, PFL-UII from 2080 to 860 cm and PFL-UI ranges from 860 to 330 cm depth.

Core Description

At UoL, from core bottom up to 1480 cm depth (UoL-UIII), the grain-size of the sediments alternated several times from silty fine sand to coarse-grained sand. Rounded pebbles up to 2 cm in diameter were found up to 1030 cm depth. In UoL-UII, layers of silty fine sand became thicker and coarse-grained layers thinner. From 820 cm to the top (UoL-UI), the sediment consisted of black to dark grey clayish to silty fine sand with parallel sediment structures. UoL-UIb was partially frozen. From 2100 cm downwards the sediment was rich in structureless ground-ice. Between the frozen parts the core was thawed. Several organic-bearing layers were encountered along the core. At 1530 cm, a layer of large wood pieces (up to 5 cm in size) was observed.

At PFL, the sediment gradually became finer upwards in the core. From core end up to 860 cm (PFL-UIII & II), the sediment was sandy with fine, medium and coarse sand alternating frequently. Rounded pebbles up to 3 cm in diameter were found up to 1120 cm depth. Above 860 cm in PFL-Unit I, the sediment was dark grey and increasingly silty. From 630 cm onwards, shell and plant remains were encountered. Between 2245 cm and 2100 cm two 5–10 cm thick macro organic containing layers were observed. At 1810 cm, a 5 cm layer of large wood pieces (up to 8 cm in size) similar to UoL was found. The upper 1500 cm of sediment contained only sparse organic remains. The core was mostly thawed and had only small frozen sections (1815–1855 cm, 2040–2050 cm and 2970–2985 cm, and ground ice structures between 810 and 1160 cm).

Geochronology

Radiocarbon dates for the Uomullyakh Lagoon core ranged from >53.2 cal ka BP to 2.6 cal ka BP (**Figure 2**, **Supplementary Table S3**) and showed several age inversions from 1036 cm depth downwards. The upper two samples until 478 cm depth were of early Holocene age. Both the oldest sample (>53 cal ka BP) at a depth of 2049 cm, and the (even deeper) youngest sample (2.6 cal ka BP) at 3033 cm, were from plant macrofossils. Bulk organic samples also showed inversions although not so extreme, and varied between 18 and 34 cal ka BP. The luminescence ages of quartz (OSL) and feldspar (pIRIR) (**Supplementary Table S4**) were similar in range to the radiocarbon dates at 1107 cm [37 ± 2 ka (OSL), 29.9 ± 1.6 ka (pIRIR) and 43.0 ± 0.6 ka cal BP (radiocarbon)] and 2108 cm depth [63 ± 3 ka (OSL), 59 ± 4 ka (pIRIR) and >53.2 ka cal BP (radiocarbon)]. Since quartz dose recovery was satisfactory for these samples from UoL, the OSL ages are considered more reliable for these samples than the feldspar and radiocarbon ages. The lowermost luminescence age at 2978 cm was non-finite for both quartz (>100 ka) and feldspar (>300 ka). Since feldspar provided the more limiting constraint, the minimum feldspar age is shown in **Figure 2**.

Radiocarbon dates for Polar Fox Lagoon ranged from > 53.3 cal ka BP to 33.5 cal ka BP (**Figure 3**, **Supplementary Table S3**). For the uppermost sample, the radiocarbon dating failed due to insufficient organic carbon content, so that available dates started at 480 cm sediment depth (corresponding to depth of 813 cm measured from ice surface). As seen at UoL, the age dating revealed no linear trend over depth. The youngest age was found in the greatest depth (2761 cm), while the oldest sample was found at 1130 cm sediment depth. The luminescence ages included only non-finite ages for quartz and feldspar of >100 ka and >300 ka at 2771 cm and of >100 ka and >320 ka at 3002 cm depth (**Supplementary Figure S1, Table S4**). Therefore, the feldspar pIRIR ages were used for interpretation of the lowest core ages, as with UoL.

The radiocarbon ages of the lowest unit UIII of both cores were not used in the discussion because of low carbon content and high risk of contamination. The results of the luminescence dating, aiming at a depositional age of mineral grains, were considered more reliable. The two samples with quartz OSL ages from the Uomullyakh Lagoon core had ages well within the range of the method and they were in stratigraphic order.

We acknowledge the fact that shore erosion and sediment mixing in such permafrost thaw-affected aquatic environments may easily result in radiocarbon age inversions and thus challenge chronological interpretation.

Detailed dose rate results and luminescence ages are summarized in **Supplementary Table S4**. Information on radionuclide concentrations are shown in **Supplementary Table S5**.

Sediment Characteristics

Uomullyakh Lagoon

The sediments of UoL-UIII (**Figure 2**) were very poorly sorted. Up to 2000 cm depth, sand dominated with a share of up to 96 wt%, mainly fine to medium sand (measured mean grain size of the < 1 mm fraction: 161 μm) and visually observed rounded pebbles up to 2 cm in size. The upper part of UoL-UIII was also characterized by an alternation of coarser deposits (mean grain size: 193 μm) with low MS of 20 × 10^{-8} m^3/kg and fine deposits (mean grain size: 37 μm) with high MS values of 59 × 10^{-8} m^3/kg. At the lower end of UoL-UII, the TN content decreased below the detection limit of 0.1 wt%. In UoL-UII, coarse sand layers with pebbles and silty fine sand layers alternated. The sand fraction decreased (mean grain size: 24.3 μm). At 1110 cm, TOC (6.7 wt%) and TN (0.4 wt%) values were at a maximum and were associated with low $\delta^{13}C$ (−27.5‰ VPDB) and low $\delta^{15}N$ (1.3‰) values (**Supplementary Table S3**). In Unit Ia of UoL, poorly sorted clay and silt deposits were predominant with a share of 16 and 73% respectively (mean grain size: 12.5 μm) (**Figure 2**). The TOC content ranged between 3.2 and 4.5 wt% and the TN content between 0.2 and 0.3 wt%. UoL-UIb, containing the upper 200 cm, was distinguished from the lower unit UoL-UIa by coarser grain size and lower TOC and TN content (1.9 wt% and 0.15 wt%, respectively). In samples with a mean grain size below 63 μm (mainly Units I and II), the $\delta^{13}C$ values were mostly below −26‰ VPDB, whereas they were higher in coarse-grained samples. The bulk density decreased from the core bottom to the top (1600–100 kg/m^3, mean 1200 kg/m^3). For further details of the biogeochemical results see **Supplementary Table S6**. The MS ranged from 5 to 154 × 10^{-8} m^3/kg, with variations mainly in areas of abrupt changes in grain size. Fine deposits corresponded with high TOC content over the core length.

Polar Fox Lagoon

The lowermost Unit III (PFL-UIII) stretching up to 2080 cm depth was characterized by a large proportion of coarse material (sand and gravel, measured mean grain size of the <1 mm fraction: 230 μm) and a very low organic carbon content of 0.1 wt%. The sediment of this unit was mostly moderately well sorted.

In the overlying PFL-UII the sorting was poor. Silty fine sand and medium sand layers alternated (mean grain size: 72.3 μm) along with MS changes. Changes in MS correspond to rapid increases in grain size (at 630 and 530 cm depth). MS ranged between 6 and 66 × 10^{-8} m^3/kg, with particularly strong variation in the small frozen core sections. Overall, the Polar Fox Lagoon core had coarser material composition of the < 1 mm fraction than the Uomullyakh Lagoon core. The TOC content was low (0.7 wt%) and the TN content decreased to below the detection limit at 1200 cm depth.

The uppermost Unit I (PFL-UI) comprised approximately the uppermost 5 m of sediment (corresponding to a depth of 860 cm) and was characterized by clay, silt and fine sand (mean grain size: 15.1 μm). Samples of the upper and the lower half of this unit show the same pattern of decreasing grain size, associated with increasing TOC and TN contents, as well as an increase in TOC/TN ratio and a depletion in $\delta^{13}C$. In contrast to UoL-UI, TOC, maximal at 4 wt%, was highest in the uppermost sample (**Supplementary Table S7**). TN ranged between 0.14 and 0.27 wt%. Changes in MS corresponded to rapid increases

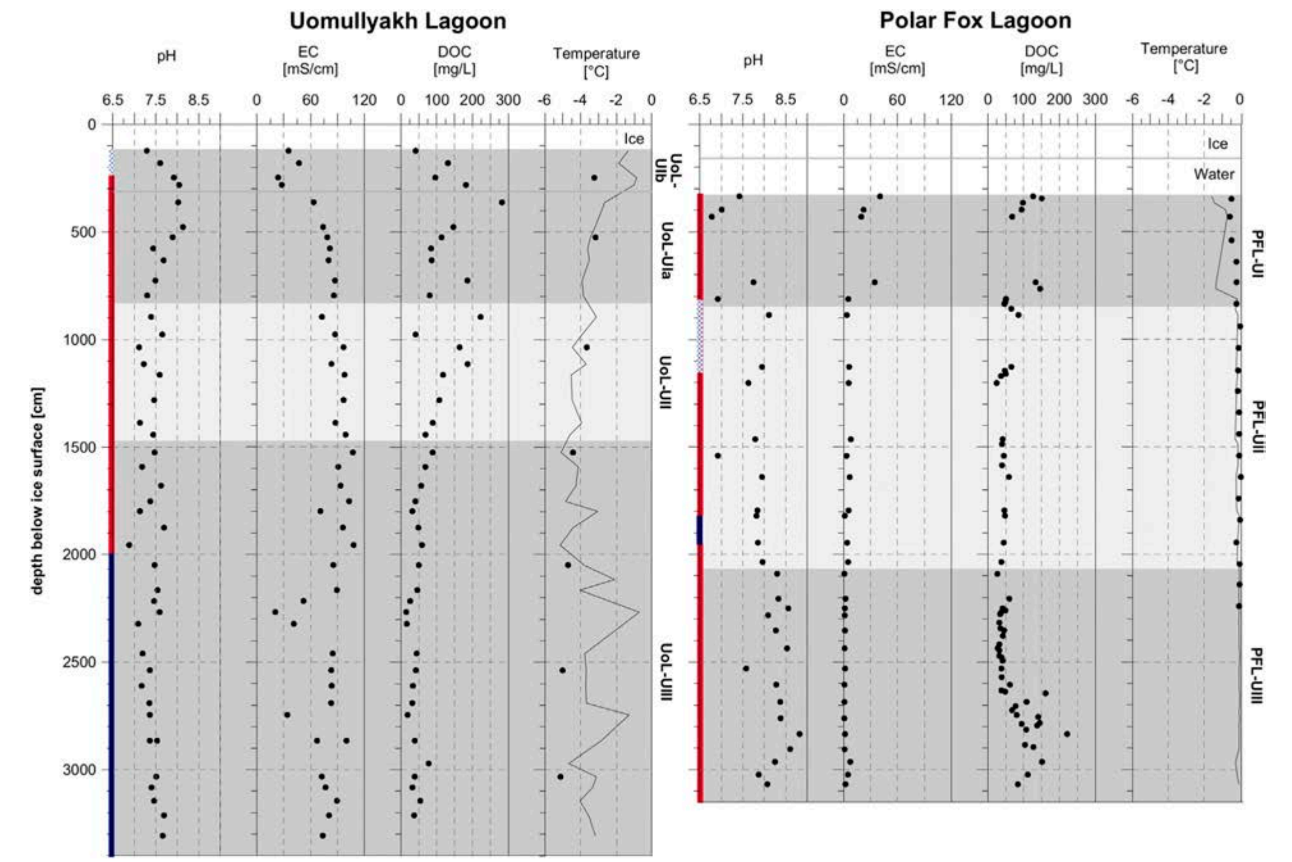

FIGURE 4 | Hydrochemical parameters of the pore water and borehole temperature of the Uomullyakh Lagoon **(left)** and the Polar Fox Lagoon cores **(right)**: pH, electrical conductivity (EC), dissolved organic carbon concentration (DOC), measured borehole temperature (point) and freezing point (line) estimated from pore water salinity. Color bar at the *y*-axis indicates frozen (blue), unfrozen (red) and partially frozen (shaded) core segments. Note that at UoL "frozen" includes visibly frozen core sections and re-constructed frozen conditions.

in grain size (at 630 and 530 cm). MS ranged between 6 and 66 × 10^{-8} m^3/kg, with particularly strong variation in the small frozen core sections.

Hydrochemistry and Reconstructed Freezing Conditions

Results of the hydrochemical analyses of pore water are shown in **Figure 4** and also in **Supplementary Table S8**. The pore water pH of both lagoons was neutral to slightly alkaline with a median of 7.5 for UoL and 8.0 for PFL. The EC was much higher in the pore water of the UoL-core with a maximum of 108 mS/cm at 1955 cm depth (median: 83.1 mS/cm) and showed higher variations over depth. Relatively low EC values at 2267 and 2745 cm depth were correlated with heavy stable water isotopes (**Supplementary Figure S2A**). The EC of the Polar Fox core pore water was highest in the upper sediment layer (max: 41 mS/cm) and showed freshwater to brackish conditions from 800 cm depth downwards (median: 3.3 mS/cm). The DOC distribution differed between the two lagoons, while the median value was similar (UoL: 58 mg/L, PFL: 50 mg/L). In UoL, the DOC concentration varied most in the uppermost unit and was highest at 360 cm depth (282 mg/L), while in PFL the greatest variation was found in the lower 5 m with the highest DOC concentration measured at 2835 cm depth (221 mg/L; **Figure 4** and **Supplementary Table S8**).

The stable water isotope composition was generally heavier in the pore water of the semi-closed Uomullyakh Lagoon (mean $\delta^{18}O/\delta D$: −20.9‰/−163.4‰) (**Supplementary Figure S2A**) than in the nearly closed Polar Fox Lagoon (mean $\delta^{18}O/\delta D$: −17.7‰/−133.7‰) (**Supplementary Figure S3A**). In the UoL core, the pore water of the upper sample had the lightest isotope composition with $\delta^{18}O$ of −19.8‰, which is comparable to the upper 5 m of PFL core pore water where its isotope composition was heaviest. There was no significant difference in isotopic composition between frozen and unfrozen samples (**Supplementary Figure S2B, S3B**). For UoL, we found a depletion of $\delta^{18}O$ with increased salinity. This was not found in the mainly freshwater to brackish dominated PFL core.

High freezing point depressions were observed for hypersaline samples (**Figure 4**) (e.g. for Uomullyakh at a depth of 1955 cm). For UoL, the borehole temperature was below the calculated

TABLE 2 | Calculated carbon pools for the upper 3 m and 30 m deposits below Uomullyakh and Polar Fox lagoons and estimated carbon pools below the three additional thermokarst lagoons of the southern Bykovsky Peninsula. Calculation is based on the bootstrapping method. The C-density of Stepanenko, Ivashkina and Safroneeva lagoons is the mean of the C-density calculated for Uomullyakh and Polar Fox lagoons.

Lagoon	Lagoon size (km^2)	C-budget (Mt)			C-density (kg/m^3)		
		3 m	30 m	Yedoma deposits	3 m	30 m	Yedoma deposits
Uomullyakh	2.10	0.15 ± 0.01	1.14 ± 0.20	0.42 ± 0.03	24.37 ± 2.09	18.03 ± 3.12	30.86 ± 1.91
Polar fox	0.64	0.05 ± 0.001	0.24 ± 0.04	0.13 ± 0.02	26.50 ± 0.57	12.55 ± 0.04	18.58 ± 2.95
Stepanenko	2.88	0.22	1.45	0.58			
Ivashkina	3.87	0.29	1.95	0.78	25.44	15.29	24.72
Safroneeva	1.89	0.14	0.95	0.38			
Total	11.39	0.85 ± 0.09	5.72 ± 0.63	2.29 ± 0.24	25.44 ± 0.75	15.29 ± 1.94	24.72 ± 4.34

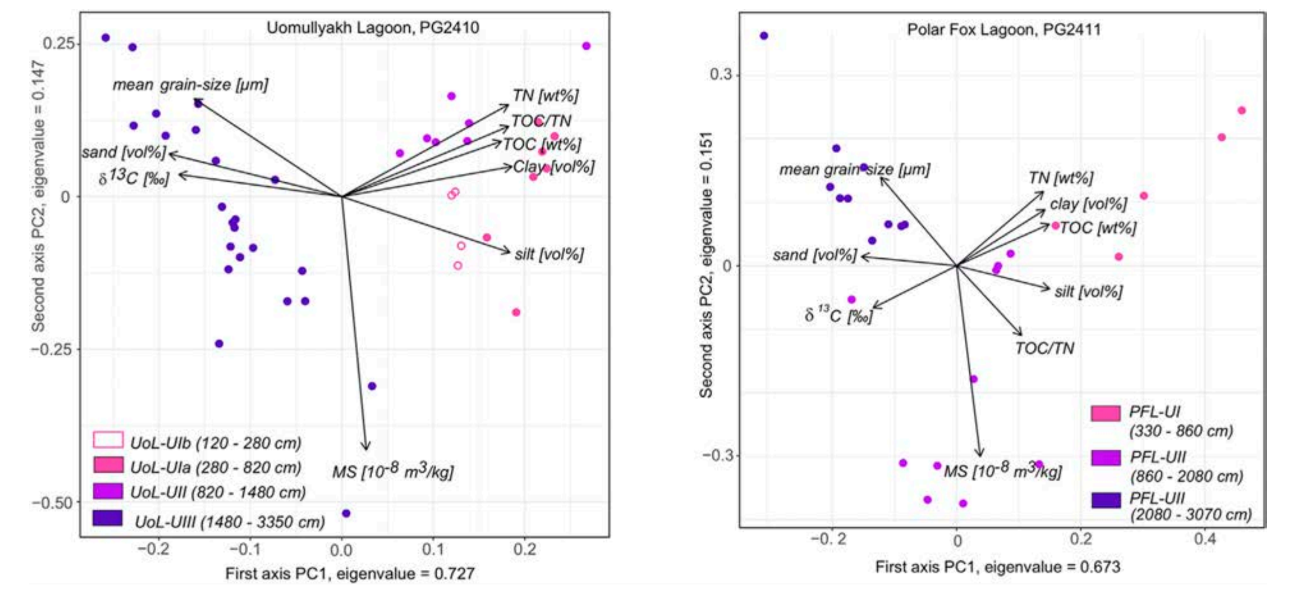

FIGURE 5 | Principal component analysis of biogeochemical parameter (TN, TOC/TN, TOC and $\delta^{13}C$) and sedimentological parameter (volumetric and mean grain size, MS) for Uomullyakh Lagoon **(left)** and Polar Fox Lagoon **(right)**. Main variance in the data is explained by differences in grain size and organic matter content and composition along the core.

freezing points in the lower core (1880 cm sediment depth and deeper) and thus the sediment could have been frozen at the time of drilling. In comparison to Uomullyakh, the Polar Fox borehole temperatures were significantly warmer (up to 5.2°C warmer) and significantly exceeded the calculated freezing point in the upper 480 cm of sediment above the partially frozen layer. Within Unit II and III of PFL, the calculated freezing point was very close to the observed temperature, suggesting that the system was close to equilibrium. This confirms the observations made in the field on the mostly thawed state of the core.

Carbon Pool Calculation

The surface areas for the Uomullyakh, Polar Fox, Ivashkina, Stepanenko, and Safroneeva lagoons were determined with remote sensing to be 2.10, 0.64, 3.87, 2.88, and 1.89 km^2, respectively. The total thermokarst lagoon area is 11.4 km^2. **Table 2** presents C-budgets and C-density calculated for the upper 3 m and 30 m of the sediment deposited in the Uomullyakh and Polar Fox lagoons. Results were extrapolated for the deposits below the other three thermokarst lagoons on the southern Bykovsky Peninsula using mean values for C-budget and C-density of Uomullyakh and Polar Fox lagoons. Below UoL, a carbon stock of 0.15 ± 0.01 Mt with a carbon density of 24.37 ± 2.09 kg/m^3 for the upper 3 m and 1.14 ± 0.2 Mt with a carbon density of 18.03 ± 3.12 kg/m^3 for 30 m thick deposits was calculated. The upper 3 m of PFL stored 0.05 ± 0.001 Mt organic carbon with a density of 26.50 ± 0.57 kg/m^3. The carbon stock amounts to 0.24 ± 0.04 Mt with a carbon density of 12.55 ± 0.04 kg/m^3 for 30 m thick deposits. The total carbon pool of the thermokarst lagoons on the southern Bykovsky Peninsula is 5.72 ± 0.63 Mt with an average carbon density of 15.29 ± 1.94 kg/m^3 for the upper 30 m (for the upper 3 m: 0.85 ± 0.09 Mt, 25.44 ± 0.75 kg/m^3).

PCA

The first two PCA axes explained 88% of the variation in the data for the Uomullyakh Lagoon core and 82% for PF Lagoon core (**Figure 5**). Though the variance is small, two groups were distinguished for both lagoon cores. Shallow depth correlated

TABLE 3 | Summary of stratigraphy, geochrononoly, sedimentology, biogeochemistry, facies, temperature, and pore water hydrochemistry deduced from multiproxy records.

Stratigraphy	Properties	UoL-core	PFL-core
Holocene lagoon deposition		**Unit Ib 320–120 cm**	
	Age	7.4 cal ka BP (radiocarbon)	
	Sediment	Dark gray clayish silt, fine sand layers → marine deposition	
	Carbon	Low OC content, moderately mineralized	
	Pore water	Lower salinity than UoL-UIa due to brine rejection from seasonal freezing, high decrease in DOC content	
	Temperature	−3.2°C, frozen due to bedfast ice	
Holocene thermokarst lake deposition		**Unit Ia 820–320 cm**	**Unit I 860–330 cm**
	Age	10.5 cal ka BP (radiocarbon)	No clear radiocarbon data
	Sediment	Mostly clayish silt (grayish-black), two sandy layers → lake deposition and external sediment input	Overall sandy silt (dark grey), plant and shell remains, slightly layered, two patterns of decreasing grain size → lake deposition, two phases of lake drainage or expansion
	Carbon	High OC content, moderately mineralized	Increasing OC content and quality with deposition of fine grained sediment
	Pore water	Hypersaline, ongoing depletion of stable water isotopes → increasingly heavy isotope signature with increasing depth suggest downward transport	Brackish to hypersaline conditions → less advanced salt intrusion than UoL
	Temperature	−3.2°C, unfrozen	0 to −0.6°C, unfrozen
Late Weichelian (MIS 2) fluvial and Yedoma deposition		**Unit II 1480–820 cm**	**Unit II 1200 cm–860 cm**
	Age	37 ± 2 ka (OSL) 43 ± 0.6–18.4 ± 0.3 ka cal BP (radiocarbon)	36.1 ka cal BP (radiocarbon)
	Sediment	Alternating, increasing thickness of silty layers (21–42% sand) → change in river discharge or orientation	Medium to coarse sand with pebbles overlaid by sandy silt (14–56% sand) → change in river orientation or dry up
	Carbon	Increasing OC content and quality	Low OC content, highly degraded
	Pore water	Hypersaline, depletion of stable water isotopes	Brackish conditions
	Temperature	−3.7 to −4.4°C, unfrozen → high freezing point depression due to high salinity	−0.1°C, partly frozen
(Middle)/Late Pleistocene fluvial deposition		**Unit III 3350–1480 cm**	**Unit III & II 3070–1200 cm**
	Age	>300 ka (pIRIR) – 63 ± 3 ka (OSL)	>360 ka – > 320 ka (pIRIR)
	Sediment	Alternating coarse and fine grained layers with pebbles (51–96% sand) → changing current conditions	More continuous and coarser grained sediment with larger pebbles (67–96% sand) → fluvial current conditions
	Carbon	Generally low OC content, highly degraded	Very low OC content, highly degraded
	Pore water	Hypersaline up to core end → was once completely thawed, isotopic composition similar to Tiksi Bay water	Fresh water conditions, light isotopic composition in comparison to UoL-UIII → different water sources of both lagoons
	Temperature	Alternating between −4.4 and −5.1°C → still partly unfrozen, refrozen talik from bottom of core up to 2000 cm depth	Uniform between −0.2 and 0.1°C → sediment completely thawed

with fine deposits and high organic matter content and quality, while in the deeper core, the variables sand content and $\delta^{13}C$ were decisive. The main variance in the data was explained by differences in grain size and organic matter contents and composition along the core.

DISCUSSION

Depositional History and Sediment Facies

At both lagoons, we identified four phases of landscape development based on sedimentological and biogeochemical parameters. These are: 1. Middle/Late Pleistocene fluvial deposition, 2. Late Weichelian (MIS 2) Yedoma deposition, 3. Holocene thermokarst lake formation and 4. Holocene lagoon formation.

The grain size distribution of sediments beneath Uomullyakh Lagoon and Polar Fox Lagoon indicates a changing depositional environment over time. In both lagoons, the sediments represent accumulation over the last glacial and interglacial cycles (**Table 3**). It is very likely that only the top few meters were accumulated since the previous interglacial. Based on stratigraphically constrained cluster analysis (CONISS) and visual observation, we distinguished four main stages of the late Quaternary history of the study area. The horizontal axis of the dendrogram (heights) represents the distance and therefore dissimilarity between clusters. The CONISS analysis of the 10 sedimentological and biogeochemical parameters at UoL showed a greater dissimilarity between clusters as for PFL. That hints to a more diverse depositional history for UoL. The cut of the dendrogram at height 7 for UoL (**Figure 2**) and height 4 for PFL (**Figure 3**), divided the cores into three main units, which is supported by the results of the PCA (**Figure 5**).

Radiocarbon ages out of stratigraphic order due to reworking of sediment as part of thawing and re-freezing processes are common for sedimentary deposits in thermokarst landscapes (Wetterich et al., 2009; Biskaborn et al., 2013; Schirrmeister et al., 2017, 2018; Jongejans et al., 2018). In the case of UoL, radiocarbon age reversals occur in Unit II (11–17 m) and Unit III (below 17 m). Possible reasons for unexpected high radiocarbon concentrations include processes associated with the melt of large ice wedges and subsequent mixing, which transport younger material into older layers. Also, possible contamination by younger material during the drilling process and sample preparation have a larger effect when sample TOC contents are very low and available material is limited and can lead to dating bias (Oswald et al., 2005; Vyse et al., 2020). Unit II is characterized by thawed Yedoma Ice Complex deposits (see chapter 5.1.2). Existing intact Yedoma deposits, in north-east Siberian Arctic lowlands consist of massive syngenetic ice wedges several tens meters in height (Schirrmeister et al., 2002, 2011, 2013; Wetterich et al., 2014; Strauss et al., 2017; Möller et al., 2019; Fuchs et al., 2020). On the Bykovsky Peninsula only 10 km northeast of the lagoons, the Mamontovy Khayata Yedoma exposure is an example with syngenetic ice wedges up to 40 m high and 5–6 m wide (Schirrmeister et al., 2002). Likely, the same deposits were present at our drilling sites before thermokarst degradation. To estimate total thaw subsidence for the sites we measured the elevation difference of lagoon bottoms and the surrounding Yedoma upland based on height information of the ArcticDEM (Porter et al., 2018). The results suggest that Holocene permafrost degradation subsided the Yedoma surface by up to 25 m for UoL and 27 m for PFL, potentially causing mass flux of sediment and its organic carbon. At many locations across the landscape, large ice wedges thawed and the surface subsided, leaving ice wedge casts and water bodies, both of which infilled with local sediment. Where young near-surface organic matter slumped, and mixed into lower, older layers, age inversions as seen at UoL would have been created.

Though sediment mixing in such thaw-affected aquatic environments challenges chronological interpretation, comparison with deposits at other sites on the peninsula are consistent with our interpretation of the landscape development. In general, the radiocarbon age ranges of both cores correspond to previous dating from Yedoma sequences of Mamontovy Khayata (58.4–12 ka BP), about 10 km northeast (Schirrmeister et al., 2002), of Cape Razdelny (core 103/81: 40.8–21.63 ka BP) about 10 km southwest (Slagoda, 1993; Grosse et al., 2016) and of the Goltsovoye Lake (47.5–21.39 cal ka BP) less than 500 m north (Jongejans et al., 2020). Furthermore, the luminescence dating at 1107 cm and 2106 cm depth is consistent with the corresponding radiocarbon ages, showing an overall chronological succession. This sequence comprises Pleistocene ages in deep fluvial deposits, followed by late Weichelian ages in overlying Yedoma deposits. Therefore, the age range for the upper sections (UII, UI) appear reasonable. We correlate stratigraphic units between cores to assign the late Pleistocene ages of UoL-UII to the upper part of PFL-UII.

For deeper layers, especially Unit III of both cores, the results of the luminescence dating were used. The dose recovery ratios are satisfactory, and the comparison with the more-difficult-to-bleach feldspar IR_{50} and post-IRIR signals indicates that it is very likely that the quartz was well bleached at deposition (see **Supplementary Material Chapter 1.3** for a more detailed technical discussion of these issues).

Unfortunately, the quartz luminescence signals from the bottom Uomullyakh Lagoon sample, and both samples from the Polar Fox Lagoon, are saturated, and so all give minimum quartz age estimates of >100 ka. Interestingly, the feldspar pIRIR signals are also saturated, and since the dose range of the feldspar signal is considerably larger than that for the quartz OSL signal, the implied minimum age is > 300 ka. At least for the two lagoons located in a similar morphological setting and with similar sedimentology (see below) it is reasonable to assume that the bleaching history of the sediment entering the two water bodies is also similar. Luminescence dating from the adjoining Goltsovoye Lake supports this assumption (**Supplementary Table S4**). The quartz and feldspar signals of the bottom sample (fluvial deposits at 3513 cm depth) are also saturated and in the same age range as for UoL and PFL (quartz age: >90 ka, feldspar age: >280 ka). The implication of the broad agreement between the pIRIR and OSL signals in the top two Uomullyakh samples is that both were well bleached before deposition. If we extrapolate this observation to the bottom-most Uomullyakh sample and the two Polar Fox samples, we may assume that the pIRIR minimum ages should also be reliable, and since they are the most constraining, they are used in further discussion.

Middle/Late Pleistocene Fluvial Deposition – UoL-UIII (3350–1480 cm) and PFL-UIII + II (3070–1460 cm)

The first phase of landscape history at the study area is mainly characterized by fluvial deposits. Under the Polar Fox Lagoon, they range in age from >360 to >320 ka (pIRIR) and include the units PFL-UIII and the lower part of PFL-UII (in total 1590 cm). Below Uomullakh Lagoon, these deposits (Uol-UIII) have an age between >300 ka (pIRIR) to 63 ± 2 ka (OSL). This long time period is represented by only about 9 m of sediment, indicating an overall low accumulation rate under a dynamic fluvial regime with frequently alternating phases of accumulation and erosion in Unit III.

The presence of coarse sediments, rounded gravel and pebbles up to 2 cm, as well as driftwood indicates fluvial transportation and deposition (**Supplementary Figure S4**). Several studies also found fluvial sediments in similar depth underneath the neighboring Ivashkina Lagoon (Romankevich et al., 2017; Schirrmeister et al., 2018) and underlying Yedoma deposits on the Bykovsky Peninsula (Slagoda 1993; Slagoda, 2004; Siegert et al., 2002; Grosse et al., 2007; Jongejans et al., 2020). Kunitsky (1989) and Wetterich et al. (2008) assumed that the paleo-Lena River crossed the present Bykovsky Peninsula in an early Weichselian period (MIS 4 and maybe older). Our luminescence ages suggest that river transport existed over a long period from >360 ka (pIRIR) to 63 ± 2 ka (OSL).

While in UoL-UIII, discontinuous grain sizes, very poor sorting and higher organic matter content reflect frequently varying water runoff in a shallow river branch or near-shore area, PFL-UIII is distinguished by very little organic material, more continuous and coarser grain sizes, and a higher degree of sorting. Such properties reflect stable fluvial current conditions (Wetterich et al., 2008). This could suggest that UoL core was located in the near-shore area and PFL core closer to the center of a paleo river. However, the large distance between both cores

(2.5 km) and the deposition of fine grained sediment underneath the Goltsovoye Lake, located in the middle of both lagoons, makes this scenario improbable. It is more likely that two neighboring river branches, part of a braided river system or delta run through the location of today's lagoons. This assumption is encouraged by finds of fluvial deposits across the peninsula. Alternation of fine and coarse grained layers at UoL-UIII indicate ongoing changes in river morphology. In PFL-UII until 1200 cm depth, organic containing fine sand layers were interbedded with coarser sand and gravel layers similar to the upper part of UoL-UIII also indicating varying water runoff or change in river course.

A layer of large driftwood pieces of similar shape and size found in UoL-UIII (at 1530 cm), PFL-UII (at 1810 cm) as well as GoL (at 2045 cm) (Unit II in Jongejans et al., 2020) are presumably deposited at the same flood event. In comparison to PFL and GoL, UoL core showed coarser grained fluvial deposits after the flood event which go along with increased erosion of overlying sediment explaining the higher elevation of the driftwood layer at UoL. Based on biomarker analyses carried out for the Goltsovoye Lake core, Jongejans et al. (2020) concluded that the area at time of flooding was a wetland, dominated by low-centered polygons formed during the Kargin Interstadial (MIS 3).

Late Weichelian (MIS 2) Yedoma Deposition – UoL-UII (1480–820 cm) and PFL-UII (1200–860 cm)

In the second phase of the landscape development an increase in silt deposition and organic matter content, as well as a depletion of $\delta^{13}C$ point to changing environmental conditions away from high energy fluvial processes toward lower energy alluvial and other transport processes. Luminescence dating for UoL at 1107 cm to 37 ± 2 ka (OSL) revealed a late Pleistocene age (beginning of late Weichelian stadial). Radiocarbon dates from sediments of similar depth for both UoL (43 ± 0.56 cal ka BP at 1063 cm) and PFL (36.1 ± 0.39 cal ka BP at 1128 cm) are in a similar time range. Paleo-ecological data from the nearby Mamontovy Khayata Yedoma cliff (Andreev et al., 2002; Schirrmeister et al., 2002) and biomarker analyses from GoL (Jongejans et al., 2020) revealed that the climate was drier and colder, transforming the former wetland into a steppe-like tundra, which probably caused decreasing river run off and changing river morphology.

When comparing the data with those of the Yedoma Ice Complex of Mamontovy Khayata, they appear to resemble mostly the fine-grained layer of the units Uo-UII and PFL-UII. Thus, it can be deduced that ice-rich Yedoma Ice Complex deposits started accumulating when either the previously existing river fell dry or changed its course.

Holocene Thermokarst Lake Formation – UoL-UIa (820–320 cm) and PFL-UI (860–330 cm)

The third phase involves the formation of a thermokarst lake, which is a prerequisite for a thermokarst lagoon. High proportions of clay and silt as well as high TOC and TN content and shell remains (PFL at 400–440 cm) indicate that Unit I of both cores represent the lake stage. Based on the results of the CONISS analysis, we discovered ~5.5 m thick lake sediments for both lagoons, which are likely mixed with Yedoma deposits from the lake shore.

In northeast Siberia, thermokarst lake formation began with rapid warming and wetting between 14 and 11.7 ka (Kaplina and Lozhkin, 1979; Kaplina, 2009; Anthony et al., 2014; Subetto et al., 2017). Grosse et al. (2007) estimated that major lakes and basins on the Bykovsky Peninsula were formed in the early Holocene, probably starting between 12.5 and 9.4 cal ka BP when a sedimentation gap on top of local Yedoma deposits suggests widespread reorganization of the landscape. This is in agreement with a radiocarbon date of 10.5 ka cal BP at 480 cm for UoL-UIa which we interpret as lacustrine deposits.

The gravimetric ice content of Yedoma deposited at Mamontovy Khayata is between 60 and 180% (Schirrmeister et al., 2002). Assuming that the Yedoma deposits were similarly ice-rich underneath the lagoons, thawing of these ice-rich sediments explains the large surface subsidence discussed before and suggests a substantial deposit compaction during lake stage.

The size of the drained thermokarst lake basins, shown in the landform classification map of Fuchs et al. (2018) (**Supplementary Figure S5**), indicates that Uomullyakh and Polar Fox basins were once significantly larger than the current water bodies and that drainage events occurred in the past. Lake drainages are common for thermokarst landscapes and are often rapid events with formation of drainage channels cutting deep into ice-rich permafrost (Grosse et al., 2013).

In UoL-UIa, a rapid increase in grain size at 630 and 530 cm depth corresponds to erratic changes in mass specific magnetic susceptibility indicating an external input of sediment at least twice. Upstream, south-west and north-west of UoL, two drained lake basins (**Supplementary Figure S5**) are located. Drainage channels connecting the basins with UoL, still visible at satellite images, suggest that UoL has been flooded while these lakes drained. As lake drainage may cause sediment erosion and downstream deposition, it is possibly the reason for the external sediment and organic matter input found in the UoL core.

In PFL-UI, two repetitive patterns of decreasing grain size associated with increasing TOC and TN content and organic matter quality are visible and might indicate drainage events. Therefore, Polar Fox Lagoon may have drained twice during the lake phase. The first drainage could have been northwards toward the adjoining lake basin (**Supplementary Figure S5**) and the second drainage southwards to the sea leading to lagoon formation.

A wider TOC/TN ratio and lighter $\delta^{13}C$ composition of the sediment beneath UoL indicates that the organic matter was less mineralized than beneath PFL. That is likely because the UoL-UIb horizon is frozen in winter due to bedfast ice formation and subsequent lagoon bottom freezing, while PFL-UI is mostly thawed throughout the year, allowing more time for microbial degradation of organic matter. Seasonal freezing under floating ice conditions at PFL is also

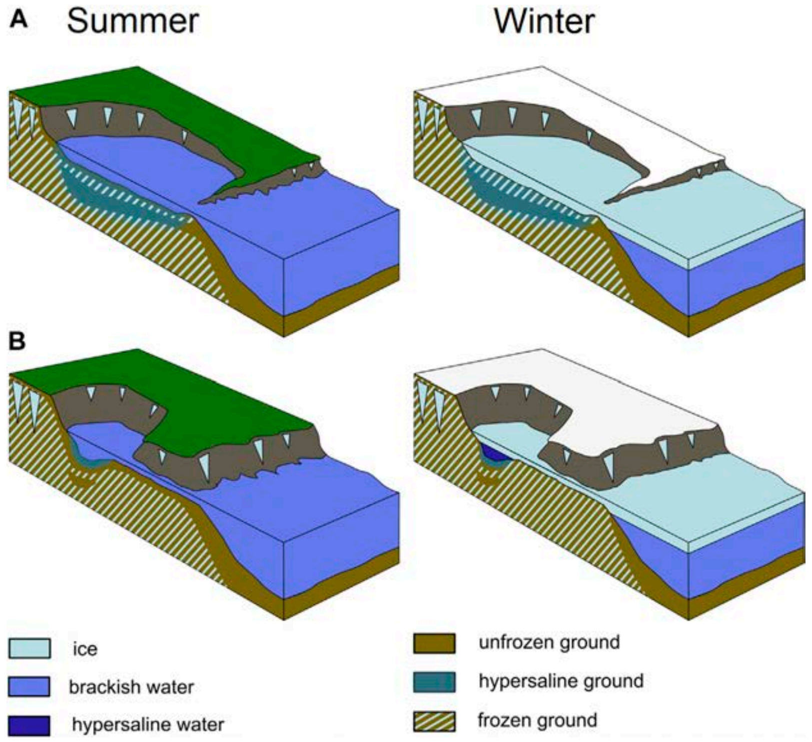

FIGURE 6 | Schematic diagram showing two types of lagoon systems in summer and winter. **(A)** semi-closed lagoon system (similar to Uomullyakh Lagoon). Bedfast ice in winter leads to salt enrichment of the pore water up to great depth. **(B)** nearly closed lagoon system (similar to Polar Fox Lagoon) which is connected during the open-water season only. The long and shallow channel mitigates sediment exchange. Floating ice that thickens in winter leads to salt enrichment of free water and upper sediment. Modified after Angelopoulos et al. (2020a).

possible but would likely only result in partial sediment freezing and a thinner seasonally frozen layer compared to UoL (Angelopoulos et al., 2020a).

Holocene Lagoon Formation – UoL-UIb (320–120 cm)

Indications for the fourth phase of landscape development, the formation of a thermokarst lagoon, were found at the boundary between UoL-UIb and UoL-UIa (between 360 and 280 cm). The increase in mass specific magnetic susceptibility and grain size, the decrease in TOC and TN content, as well as a slight decrease in TOC/TN ratio indicate a system change. In our interpretation, this shift is caused by marine inundation and marks the beginning of the third stage, the lagoon formation. Postglacial rising sea levels caused by melting of continental ice sheets led to the inundation of former terrestrial permafrost on the Laptev Sea shelf until about 5 ka (Bauch et al., 2001) when sea levels stabilized and coastal erosion of ice-rich permafrost started to dominate the coastline (Romanovskii et al., 2000; Romanovskii et al., 2004). Likely, the Uomullyakh thermokarst lake was breached by the transgressing sea and coastal erosion in the early to mid-Holocene. A similar breaching and submergence of thermokarst lakes and drained lake basins has been observed in thermokarst-affected coastal lowlands on the Alaska North Slope (Arp et al., 2010), in the Mackenzie Delta region (e.g. Ruz et al., 1992), and on Banks Island (Grasby et al., 2013).

Satellite images (e.g. **Figure 1**) indicate that the Uomullyakh Lagoon is characterized by stronger turbidity due to lack of topographical wind shadow (compared to the Yedoma upland surrounded PFL) and its connection to the sea, which enables waves to enter. High connectivity to the sea likely leads to an increased input of marine sediment (Grotheer et al., 2020). This is in agreement with sediment analyses indicating marine deposition in Uomullyakh Lagoon for the upper 2 m mixed with lacustrine deposits.

At Polar Fox Lagoon, this distinction could not be made. This is very likely caused by the different morphology of both lagoons. The Polar Fox Lagoon was formed as a result of thermokarst lake drainage, which led to the formation of a shallow and winding channel connecting lake and sea (Angelopoulos et al., 2020a). The connection to the Tiksi Bay is cut off during winter when ice formation reaches the channel bed, restricting water and sediment exchange (Spangenberg et al., 2021).

Impact of Marine Inundation

Our data suggests that deep (~20 m) hypersaline taliks (UoL) preserve organic carbon better than taliks that contain mostly

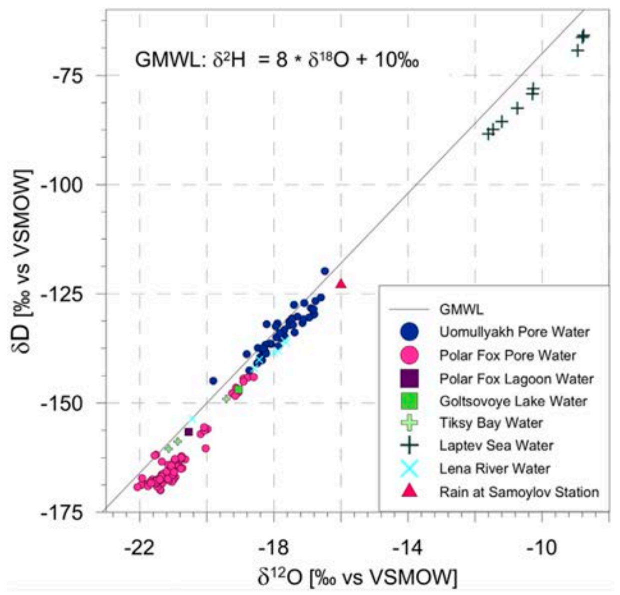

FIGURE 7 | Comparison of the stable water isotope composition of lagoon core pore water and surface water of different possible endmember; sediment pore water from April 2017 (this study); water of Polar Fox Lagoon, Goltsovoye Lake, and Tiksi Bay were sampled in July 2017 (P. Overduin, unpublished data); Laptev Sea water was sampled during expedition with the research vessel Pavel Bashmakov at the end of August 2002 (H. Meyer, unpublished data); Lena River water from summer 2005–2016 (clustered points) and one sample from April 2013 (isolated point) (H. Meyer, unpublished data). Stable water isotopes δD and δ^{18}O relative to Vienna Standard Mean Ocean Water (VSMOW).

freshwater below a thin saline layer (PFL). Drawing on microbial subsea permafrost research (Mitzscherling et al., 2017), hypersaline cryotic taliks can stress microbes and slow the decay of organic matter.

Once a connection from the lake to the sea is established, salts from seawater can diffuse into the sediment (Angelopoulos et al., 2020a) or transport into the sediment more rapidly via convection (Shakhova et al., 2017). Therefore, the frozen/thawed state of the sediment is largely a reflection of recent marine sediment deposition and salt transport. In the Uomullyakh Lagoon core, the EC of pore water generally increased with depth, from 30 mS/cm just below the seasonally frozen layer (240 cm below ice) to 108 mS/cm at 1525 cm depth below ice (mean 77 mS/cm for the entire core). The salinities were significantly higher than the Tiksi Bay water (3.8 mS/cm) (**Supplementary Table S1**) for the same time of the year. At the Polar Fox Lagoon core, the maximum EC (41 mS/cm) was measured in the uppermost sample just below the sediment surface. The relatively high EC in both lagoons suggests that brine rejection from lagoon ice formation and the seasonal isolation of the water bodies from Tiksi Bay are key processes affecting the pore water salinity.

Uomullyakh is a semi-closed lagoon, especially during the open water season when it may experience flooding and enhanced marine sediment deposition from storm surges (e.g. Nazarova et al., 2017) (**Figure 6A**). Polar Fox Lagoon, on the other hand, is a nearly closed lagoon (**Figure 6B**). It is isolated from the sea once bedfast ice forms at the shallow inlet (~0.5 m) of the connecting channel (Spangenberg et al., 2021).

At Uomullyakh Lagoon, all 17 ice-auger measurements in April 2017 revealed bedfast ice, suggesting that there was nearly no surface water exchange with Tiksi Bay. Despite a seasonally closed system for the surface water, lateral groundwater exchange in the sediment can still occur if the sub-lagoon and subsea permafrost taliks are connected. This talik connection is possible, because the sediment just offshore of the spit is also characteristic of the lagoon talik when the spit was located further south. Furthermore, permafrost aggradation beneath the spit is controlled by limited sub-aerial exposure time as the spit retreats further north with coastal erosion. The large difference in isotopic composition of the pore water between the lagoons confirms that the Uomullyakh Lagoon sediment had a larger source water contribution from Tiksi Bay (**Figure 7**). Tiksi Bay as a heavy endmember likely caused the enrichment in heavier water isotopes of the Uomullyakh Lagoon pore water. Pedrazas et al. (2020) used electrical resistivity surveys to map continuous unfrozen sediment from an onshore cryopeg to a sub-lagoon talik down to a depth of 20 m in northern Alaska, and suggested it could be a conduit for groundwater and nutrient exchange. The isotopic composition of the pore water, along with the near vertical profile of salinity with depth (5–20 m and 25–33 m; **Supplementary Figure S3**) suggests that convective processes influenced the salt distribution (Harrison and Osterkamp, 1982). In addition, there was a likely high salt content injection into the sediment following bedfast ice formation. The seasonally frozen layer can still have been permeable and susceptible to brine flow (Osterkamp et al., 1989). Although temperatures were as low as −4.4°C (at 1540 cm), the freezing point of the hypersaline sediment was calculated to have been as low as −5.1°C (at 1520 cm), resulting in a cryotic talik. At a depth of 2040 cm, the observed temperature (−4.7°C) was below the freezing point (−3.82°C), indicating the approximate depth to ice-bearing permafrost. It is unclear how the ice-bearing permafrost table evolved, but the decreasing temperature trend with depth suggests the lagoon sediment column might be warming. Therefore, it is plausible that hypersaline sediment partially froze once sufficient sediment deposition in the lagoon created a mostly bedfast ice regime with some small isolated water pockets. Now, the ice-bearing permafrost table may be degrading under warmer, but still cryotic bedfast ice conditions. This is similar to terrestrial cryopeg expansion under warming subaerial conditions (Streletskaya, 1998).

At Polar Fox Lagoon, the contemporary distribution of ice-bearing permafrost and taliks is somewhat different. Polar Fox Lagoon is presumably younger than Uomullyakh Lagoon and still contains a floating ice area with a maximum water depth of 340 cm. In the floating ice area, coupled heat and salt diffusion models suggest that the thin partially frozen permafrost layer (830 to 480 cm below the sediment surface) developed sub-aquatically after the lake to lagoon transition. The partially frozen layer depth and thickness are transient, as the top-down chemical

TABLE 4 | Comparison of biogeochemistry characteristics with different lagoons, Yedoma sites and a thermokarst lake: total organic carbon content (TOC), total nitrogen (TN), atomic carbon nitrogen ratio, stable carbon isotope composition ($\delta^{13}C$). Note that given depth are measured from the sediment surface for better comparability of the sites.

Site	Sediment	TOC range (mean) (wt%)	TN range (mean) (wt%)	Atomic TOC/TN range (mean)	$\delta^{13}C$ range (mean) (‰ VPDB)	Citation
Uomullyakh Lagoon (Bykovsky) core length: 32.3 m	Marine 0–2 m	1.7–2.0 (1.9)	0.13–0.17 (0.15)	13–17 (15)	−26.8 to −26.1 (−26.6)	This study
	Lacustrine 2–7 m	2.0–4.1 (3.4)	0.17–0.30 (0.24)	14–19 (16)	−27.7 to −26.7 (−27.3)	
	Former terrestrial Yedoma 7–15 m	0.6–6.7 (2.5)	<0.1–0.14 (0.05)	13–18 (16)	−27.5 to −25.0 (−26.0)	
	Fluvial deposits 15–32.3 m	<0.1–3.3 (0.6)	<0.1	—	−26.3 to −24.1 (−25.1)	
Polar Fox Lagoon (Bykovsky) core length: 27.7 m	Lacustrine 0–5.3 m	1.5–4.0 (2.8)	0.14–0.27 (0.22)	11–18 (15)	−27.5 to −25.5 (−26.8)	This study
	Former terrestrial Yedoma 5.3–9 m	0.5–1.0 (0.8)	<0.1–0.14 (0.05) (0.12 for upper 2 samples)	8–10 (9) $n = 2$	−25.6 to −24.1 (−25.0)	
	Fluvial deposits 12–31.5 m	<0.1–1.0 (0.2)	<0.1	—	−24.9 to −23.4 (−24.2)	
Goltsovoye Lake (Bykovsky) core length: 31.5 m	Lacustrine 0–5 m	1.0–4.3 (3.0)	0.14–0.33 (0.25)	8–16 (13)	−28.6 to −24.8 (−27.0)	Jongejans et al. (2020)
	Former Yedoma 5–28 m	<0.1–3.1 (0.7)	<0.1–0.22 (0.05)	0–36 (4)	−26.6 to −23.8 (−24.8)	
	Fluvial deposits 28–31.5 m	<0.1–17.8 (3.1)	<0.1–0.46 (0.08)	0–171 (20)	−23.6 to −24.5 (−25.7)	
Ivashkina Lagoon (Bykovsky) core length: 6.15 m	Marine 0–0.24 m	2.0–2.5 (2.2)	0.19–0.24 (0.21)	9–12 (11)	−26.4 to −26.2 (−26.3)	Schirrmeister et al. (2018)
	Lacustrine 0.24–2.51 m	1.7–2.8 (2.6)	0.14–0.26 (0.20)	10–14 (12)	−27.2 to −25.5 (−26.6)	
	Former terrestrial Yedoma 2.53–6.15 m	0.9–5.6 (2.7)	0.10–0.84 (0.26)	3–18 (13)	−27.8 to −23.9 (−26.4)	
Mamontovy Khayata (Yedoma on Bykovsky) profile length: ca. 38 m	Terrestrial 14–34 m	1.3–27.0 (4.8)	0.17–1.38 (0.40)	8–34 (20)	−28.7 to −23.9 (−26.1)	Schirrmeister et al. (2002), Schirrmeister et al. (2011)

degradation of newly formed frozen sediment lags behind the talik refreezing (Angelopoulos et al., 2020a). In bedfast ice zones (approximately 75% of Polar Fox Lagoon), electrical resistivity surveys showed that the thickness of the frozen layer and that of the overlying saline layer increased and decreased toward the shoreline, respectively.

The transient nature of frozen sediment and taliks beneath may affect CO_2 and CH_4 fluxes in the sediment column, because partially frozen sediment with an ice saturation exceeding 60% has proven to be an effective barrier to gas flow (Chuvilin et al., 2016). In the case of a shallow lagoon with bedfast ice, the frozen sediment can be saline and have a lower freezing point compared to frozen sediment without salt. Therefore, lagoons may precondition the frozen sediment for rapid thawing (compared to Yedoma permafrost) once it is exposed to warmer coastal waters in the subsea permafrost environment. This, in turn, could contribute to the development of offshore gas migration pathways for greenhouse gas released from thawing subsea permafrost (Shakhova et al., 2019). Any released gas might not reach the atmosphere, as it has to bypass numerous sinks, including anaerobic oxidation in the sediment column (Overduin et al., 2015), dissolution in the pore water and surface water, low-permeability layers, and lagoon ice. Angelopoulos et al. (2020b) provide a review of subsea permafrost within the context of global climate change, and Ruppel and Kessler (2017) provide a review specific to climate change interactions with gas hydrates.

Carbon Pool Upscaling

Permafrost thaw beneath thermokarst lakes is more rapid than gradual thaw of near-surface permafrost and could double permafrost carbon emissions this century (Walter Anthony et al., 2018; Turetsky et al., 2020). Field-based observations on carbon turnover and greenhouse gas production in thermokarst lake sediments are scarce (Heslop et al., 2015; Heslop et al., 2019a; Heslop et al., 2019b) and completely missing for thermokarst lagoons. In order to estimate potential future greenhouse gas release from emerging thermokarst lagoons, we assessed the size of the lagoon C-pool by extrapolating our TOC and BD of the two analyzed lagoons to the other three thermokarst lagoons on the Bykovsky Peninsula.

The calculations of the carbon budgets show that the carbon density differs between the neighboring lagoons, especially for greater depths (upper 3 m: 22.5 kg/m^3 (Uo) vs. 26.5 kg/m^3 (PFL); upper 30 m: 17.4 kg/m^3 (UoL) vs. 10.2 kg/m^3 (PFL), which demonstrates the small scale spatial variability of the carbon deposits. The input and output of organic matter are strongly dependent on environmental conditions and lake drainage events. Schirrmeister et al. (2018) estimated the carbon density for the upper 6 m of the thermokarst lagoons on the Bykovsky Peninsula at 25 ± 5 kg/m^3, which is in the same range as the carbon density we calculated for the upper 3 m (24.5 ± 1.4 kg/m^3), but 45% higher than the mean carbon density of the 30 m-long sediment cores (13.8 ± 3 kg/m^3). We explain this with the higher TOC values we measured in the lake influenced sediments (UoL-UIa, PFL-UI), which were the stratigraphic class dominating the Schirrmeister et al. (2018) dataset.

A similar carbon storage was estimated for thermokarst lagoons on northern Richards Island, Mackenzie Delta, Canada. Based on an average carbon content of 2.75–3% for marine and lacustrine deposits, Solomon et al. (2000) estimated a carbon deposition of ca. 25×10^4 t in the investigated embayment area (10.3 km^2) since thermokarst lake development. This corresponds to a carbon density of 25 kg/m^3 for the upper 10 m, which is similar to the carbon density of the lacustrine sediments of the Bykovsky lagoons. Comparing the carbon stored in undisturbed, previously unthawed ice-rich Yedoma deposits of Mamotovy Khayata (Schirrmeister et al., 2011) with the TOC of Yedoma thawed under thermokarst lake and lagoon conditions (**Table 4**), we would expect to find a gradient of C loss in thawed Yedoma underneath thermokarst landforms that is linked to thaw histories. Using a simple mass balance approach, the difference in mean TOC content between the Mamotovy Khayata Yedoma and the thawed Yedoma beneath thermokarst sites (**Table 4**) can be expressed as percentage carbon loss. This approach suggests a C loss of 85% for thawed Yedoma under Goltsovoye Lake, 83% C loss for PFL, 48% C loss for UoL, and 44% C loss for IvL due to subaquatic permafrost thaw. These estimations imply that less organic carbon is lost in the more open UoL and IvL compared to the younger, nearly closed PFL and the freshwater GoL. If our assumptions are valid, this would signify that a freshwater dominated lake and the floating ice areas of nearly closed lagoon systems like PFL result in strong organic carbon loss upon thaw while seawater dominated systems seem to better preserve organic carbon. In addition, higher TOC/TN and lower $\delta^{13}C$ values for thawed Yedoma underneath UoL and IvL indicate lower organic matter degradation both more open lagoons, further supporting this hypothesis. Since approximately 75% of PFL was characterized by bedfast ice in April 2017 (Angelopoulos et al., 2020a), additional C is likely preserved in areas with thick frozen sediment. At UoL, the hypersalinity of the cryotic talik can stress microbial communities, leading to reduced population, diversity, and decay of organic matter (Mitzscherling et al., 2017). Although bacterial communities can adapt to increasingly saline conditions, past refreezing events in the upper 20 m of the sediment core (refer to "Impact of Marine Inundation" Section 5.2), can also preserve C at UoL.

The calculated average C-density of the core section referred to Yedoma deposits of the five thermokarst lagoons on Bykovsky Peninsula is 24.72 ± 4 kg/m^3 and therefore in the upper range of the C-density estimated for the 0.41×10^6 km^2 large Yedoma region (19 + 13/-11 kg/m^3) (Strauss et al., 2013) and in the lower range of terrestrial thermokarst deposits of the Yedoma region (33 + 25/-19 kg/m^3) (Schirrmeister et al., 2011; Strauss et al., 2013).

Using the lagoon C-density mean, we calculated 5.7 Mt C in the first 30 m of lagoon sediments covering an area of 11.4 km^2. This is a substantial inventory of formerly frozen C, which is now largely unfrozen and thus available for microbial degradation processes. $\delta^{13}C$ and TOC/TN values indicate that the degradation of the primarily terrestrial plant material is advanced. Highest organic matter degradation was indicated for the fluvial deposits possibly because the alluvial material was already strongly degraded at the time of deposition.

The comparison of different sites shows that the biogeochemical parameters differ between sediment types rather than between the sites (**Table 4**). For example, the lacustrine sediments at all four sites (PFL, UoL, GoL and IvL) have very similar TOC and TN contents as well as similar TOC/TN ratios and $\delta^{13}C$ signals, but they differ from the over- or underlying sediment facies (Schirrmeister et al., 2018; Jongejans et al., 2020). The lacustrine sediments in the deep sediment cores of UoL, PFL and GoL are richer in TOC and TN than the underlying former terrestrial or overlying marine sediments. High carbon accumulation in thermokarst lake sediments can be caused by shore erosion and deposition of terrestrial organic matter, high aquatic productivity, and unique preservation conditions (Anthony et al., 2014). In contrast, the biogeochemical parameters of lacustrine and underlying Yedoma deposits of the Ivashkina Lagoon differ only slightly (Schirrmeister et al., 2018). This is not surprising, as the upper part of the Yedoma deposits (IvL core reaches only to 6.15 m depth) tend to have higher carbon and nitrogen contents and lower degradation rate than the deeper deposits. An exception are the deep fluvial deposits under the GoL, where allochthonous organic material leads to very high TOC and TN contents (Jongejans et al., 2020). The TOC content of thawed talik sediments (former Yedoma deposits) is highest for the UoL, with similar values found in Taberites (2.7 ± 1.4 wt%) and late Weichelian (MIS 2) Ice Complex deposits (2.2 ± 0.9 wt %) of the Siberian permafrost region (Schirrmeister et al., 2011). The organic matter mineralization is highest for former Yedoma deposits below GoL (TOC/TN = 4) and lowest for Yedoma deposits at Mamontovy Khayata (TOC/TN = 20). The high mean TOC/TN ratio of fluvial deposits below GoL is based on five samples with very high TOC/TN ratios. The median TOC/TN ratio of 0 shows that the carbon mineralization is high for most samples of the fluvial deposits below GoL. In general, the carbon mineralization is mostly high (TOC/TN < 12) or in the lower moderate range (TOC/TN 12–25) for thermokarst affected sites. This is a common phenomenon in the warming Arctic, as rising permafrost temperatures result in increasing thermokarst development which favors the microbial decomposition of thawing organic matter (Strauss et al., 2017).

Greenhouse gas production in thermokarst lagoons connected to the marine environment is expected to differ substantially from that in thermokarst lakes: the supply of electron acceptors, specifically of sulfate, will promote sulfate reduction and anaerobic methane oxidation thus favoring the release of CO_2 relative to that of methane (Segers and Kengen, 1998). In line with this, substantial CO_2 release was recently reported for a laboratory study that incubated permafrost with seawater (Tanski et al., 2019). In addition, anaerobic methane oxidation was observed in thawing seawater-affected permafrost (Winkel et al., 2018) and thermokarst lake sediments with temperatures close to 0°C (Winkel et al., 2019). Given both our first estimate of thermokarst lagoon carbon budgets, and the expectation that the rate of formation of such lagoons will increase due to coastal erosion, thermokarst lagoons are considered important biogeochemical processors of former permafrost carbon and a critical component of the future Arctic greenhouse gas system.

CONCLUSION

This study shows that thermokarst lagoons are highly dynamic landforms at the boundary between terrestrial permafrost and marine systems. Based on two ~30 m long sediment cores from two contrasting thermokarst lagoon systems, we examined the depositional history, the impact of marine inundation and the amount of stored organic carbon for different stages of thermokarst lagoons. We identified several different phases of sediment deposition in the semi-closed Uomullyakh Lagoon and the nearly closed Polar Fox Lagoon. The sedimentological analysis of both lagoon cores shows that fluvial deposition from a paleo-river system dominated at the sites from >360 ka to the late Pleistocene, when silty to sandy ice-rich Yedoma deposits started to accumulate in this region. These former Yedoma deposits are now present as thawed talik sediments. With the beginning of the warmer Late Glacial to Holocene period, the formation of thermokarst lakes began and resulted in lacustrine sediment deposition at both lagoons. At the more open Uomullyakh Lagoon, marine sediments overlying lacustrine deposits indicate the onset of the lagoon phase starting in the early to mid-Holocene. Inundation with seawater and formation of seasonal bedfast ice caused the saline enrichment of the pore water, which led to cryotic talik formation.

Our case study from the Bykovsky Peninsula provides a first estimate of organic carbon quantity and quality based on deep sediment cores below thermokarst lagoons. We have identified large organic carbon stocks in these special Arctic lagoon systems. We measured a mean C-density of 15.3 ± 2 kg/m^3 for the 30 m thick deposits below the lagoons, with higher values found below the semi-closed lagoon. The measured carbon density for the Yedoma deposits (24.72 ± 4 kg/m^3) is in the upper range of the estimate of terrestrial Yedoma (19 + 13/-11 kg/m^3), but lower range of terrestrial thermokarst deposits (33 + 25/-19 kg/m^3) in the Yedoma region. Based on the mean C-density and the remote sensing-based spatial extent of thermokarst lagoons, we calculate a total C storage of 5.7 Mt C in the upper 30 m of sediment in five thermokarst lagoons on the southern Bykovsky Peninsula.

Our data indicate that open thermokarst lagoons under high seawater influence seem to better preserve organic carbon more then freshwater dominated systems. This shows the potential importance of the role and contribution of thermokarst lagoons in the transformation of terrestrial permafrost carbon under increasingly marine influence.

DATA AVAILABILITY STATEMENT

The datasets presented in this study can be found in online repositories. The names of the repository/repositories and accession number(s) can be found below: https://doi.pangaea.de/10.1594/PANGAEA.922169.

AUTHOR CONTRIBUTIONS

MJ and JS designed this study. MJ led the writing of the first draft of the manuscript. JS, GG, and MG developed the overall coring plans for the Bykovsky Peninsula field campaign. JS, MG, LS, BB, PO, MA, SL, and GG conducted the field work. MA and PO did the subsampling for the Polar Fox sediment core and MJ for the Uomullyakh core. MJ and PO performed laboratory analyses. MJ led the data interpretation for both cores. MJ and IN conducted the spatial analysis and mapping of the lagoons. AM performed optical luminescence analyses and data interpretation. All co-authors contributed within their specific expertise to data interpretation.

FUNDING

This study was carried out within the NERC-BMBF project CACOON (Changing Arctic Carbon cycle in the cOastal Ocean Near-shore, grant no. 03F0806A), the ERC Project PETA-CARB (#338335), and the BMBF project KoPF (03F0764B, 03F0764F). The Alfred Wegener Institute Helmholtz Centre for Polar and Marine Research (AWI) provided baseline funding and together with the Germany Research Centre for Geosciences (GFZ) AWI provided funding for the expedition.

ACKNOWLEDGMENTS

We thank the Hydrobase Tiksi, Arctica GeoZentr, Stanislav Ostreldin, Waldemar Schneider, Dmitri Bolshiyanov, and Sergey Pravkin for their logistic contributions to the field expedition Bykovsky 2017. We thank the MICADAS Team at AWI Bremerhaven for dating the radiocarbon samples and Hanno Meyer for discussing the isotope results. Torben Windirsch is acknowledged for his support during subsampling the Uomullyakh core as well as Antje Eulenburg, Dyke Scheidemann, Jonas Sernau and Angélique Opitz for their support and assistance in the lab. We also thank Frederieke Miesner for her help on modifying **Figure 6**. We acknowledge the support by the Open Access Publication Funds of Alfred-Wegener-Institut Helmholtz Zentrum für Polar- und Meeresforschung.

SUPPLEMENTARY MATERIAL

The Supplementary Material for this article can be found online at: https://www.frontiersin.org/articles/10.3389/feart.2021.637899/full#supplementary-material

REFERENCES

Andersson, R. A., Meyers, P., Hornibrook, E., Kuhry, P., and Mörth, C.-M. (2012). Elemental and Isotopic Carbon and Nitrogen Records of Organic Matter Accumulation in a Holocene Permafrost Peat Sequence in the East European Russian Arctic. *J. Quat. Sci.* 27 (6), 545–552. doi:10.1002/jqs.2541

Andreev, A. A., Schirrmeister, L., Siegert, C., Bobrov, A. A., Demske, D., Seiffert, M., et al. (2002). Paleoenvironmental Changes in Northeastern Siberia during the Late Quaternary - Evidence from Pollen Records of the Bykovsky Peninsula'. *Polarforschung* 70, 13–25. doi:10.2312/polarforschung.70.13

Angelopoulos, M., Overduin, P. P., Miesner, F., Grigoriev, M. N., and Vasiliev, A. A. (2020b). Recent Advances in the Study of Arctic Submarine Permafrost. *Permafrost and Periglac Process* 31 (3), 442–453. doi:10.1002/ppp.2061

Angelopoulos, M., Overduin, P. P., Westermann, S., Tronicke, J., Strauss, J., Schirrmeister, L., et al. (2020a). Thermokarst lake to Lagoon Transitions in Eastern Siberia: Do Submerged Taliks Refreeze? *J. Geophys. Res. Earth Surf.* 125. doi:10.1029/2019JF005424

Anthony, K. M. W., Zimov, S. A., Grosse, G., Jones, M. C., Anthony, P. M., Iii, F. S. C., Iii, et al. (2014). A Shift of Thermokarst Lakes from Carbon Sources to Sinks during the Holocene Epoch. *Nature* 511 (7510), 452–456. doi:10.1038/nature13560

Arp, C. D., Jones, B. M., Whitman, M., Larsen, A., and Urban, F. E. (2010). Lake Temperature and Ice Cover Regimes in the Alaskan Subarctic and Arctic: Integrated Monitoring, Remote Sensing, and Modeling1. *JAWRA J. Am. Water Resour. Assoc.* 46 (4), 777–791. doi:10.1111/j.1752-1688.2010.00451.x

Bauch, H. A., Mueller-Lupp, T., Taldenkova, E., Spielhagen, R. F., Kassens, H., Grootes, P. M., et al. (2001). Chronology of the Holocene Transgression at the North Siberian Margin. *Glob. Planet. Change* 31 (1-4), 125–139. doi:10.1016/S0921-8181(01)00116-3

Berner, J., Symon, C., Arris, L., and Heal, O. W. (2005). *Arctic Climate Impact Assessment, National Science Foundation (U.S.), United States, and National Oceanic and Atmospheric Administration*. New York, N.Y.: Cambridge University Press.

Bindoff, N. L., Willebrand, J., Artale, V., Cazenave, A., Gregory, J., Gulev, S., et al. (2007). "Observations: Oceanic Climate Change and Sea Level," in *Climate Change 2007: The Physical Science Basis. Contribution of Working Group I to the Fourth Assessment Report of the Intergovernmental Panel on Climate Change*. Editors S. Solomon, D. Qin, M. Manning, Z. Chen, M. Marquis, K.B. Averyt, et al. (Cambridge, United Kingdom and New York, NY, USA: Cambridge University Press).

Biskaborn, B. K., Herzschuh, U., Bolshiyanov, D. Y., Schwamborn, G., and Diekmann, B. (2013). Thermokarst Processes and Depositional Events in a Tundra Lake, Northeastern Siberia: Thermokarst Processes in a Siberian Tundra Lake. *Permafrost Periglacial Process.* 24 (3), 160–174. doi:10.1002/ppp.1769

Biskaborn, B. K., Smith, S. L., Noetzli, J., Matthes, H., Vieira, G., Streletskiy, D. A., et al. (2019). Permafrost Is Warming at a Global Scale. *Nat. Commun.* 10 (1), 264. doi:10.1038/s41467-018-08240-4

Brovko, P. (1990). *Development of Coastal Lagoons*. Vladivostok (Russia): Publishing house of the Far East University press.

Brown, J., Ferrians, O. J., Jr, Heginbottom, J. A., and Melnikov, E. S. (1997). Circum-Arctic Map of Permafrost and Ground-Ice Conditions. *Circum-Pacific Map*. doi:10.3133/cp45

Campeau, S., Héquette, A., and Pienitz, R. (2000). Late Holocene Diatom Biostratigraphy and Sea-Level Changes in the southeastern Beaufort Sea. *Can. J. Earth Sci.* 37 (1), 63–80. doi:10.1139/e99-107

Chuvilin, E. M., Grebenkin, S. I., and Sacleux, M. (2016). Influence of Moisture Content on Permeability of Frozen and Unfrozen Soils. *Kriosfera Zemli* 20 (3), 66–72. doi:10.21782/EC2541-9994-2018-1(41-45)

Frederick, J. M., and Buffett, B. A. (2014). Taliks in Relict Submarine Permafrost and Methane Hydrate Deposits: Pathways for Gas Escape under Present and Future Conditions. *J. Geophys. Res. Earth Surf.* 119 (2), 106–122. doi:10.1002/2013JF002987

Fritz, M., Opel, T., Tanski, G., Herzschuh, U., Meyer, H., Eulenburg, A., et al. (2015). Dissolved Organic Carbon (DOC) in Arctic Ground Ice. *The Cryosphere* 9 (2), 737–752. doi:10.5194/tc-9-737-2015

Fritz, M., Vonk, J. E., and Lantuit, H. (2017). Collapsing Arctic Coastlines. *Nat. Clim. Change* 7 (1), 6–7. doi:10.1038/nclimate3188

Fuchs, M., Grosse, G., Strauss, J., Günther, F., Grigoriev, M., Maximov, G. M., et al. (2018). Carbon and Nitrogen Pools in Thermokarst-Affected Permafrost Landscapes in Arctic Siberia. *Biogeosciences* 15 (3), 953–971. doi:10.5194/bg-15-953-2018

Fuchs, M., Nitze, I., Strauss, J., Günther, F., Wetterich, S., Kizyakov, A., et al. (2020). Rapid Fluvio-Thermal Erosion of a Yedoma Permafrost Cliff in the Lena River Delta. *Front. Earth Sci.* 8. doi:10.3389/feart.2020.00336

GISTEMP Team (2020). GISS Surface Temperature Analysis (GISTEMP). version 4. NASA Goddard Institute for Space Studies. Dataset accessed 2020-22-26 at: data.giss.nasa.gov/gistemp/.

Grasby, S. E., Rod Smith, I., Bell, T., and Forbes, D. L. (2013). Cryogenic Formation of Brine and Sedimentary Mirabilite in Submergent Coastal lake Basins, Canadian Arctic. *Geochimica et Cosmochimica Acta* 110(0): 13–28. doi:10.1016/j.gca.2013.02.014

Grosse, G., Goetz, S., McGuire, A. D., Romanovsky, V. E., and Schuur, E. A. G. (2016). Changing Permafrost in a Warming World and Feedbacks to the Earth System. *Environ. Res. Lett.* 11 (4), 040201. doi:10.1088/1748-9326/11/4/040201

Grosse, G., Jones, B., and Arp, C. (2013). 8.21 Thermokarst Lakes, Drainage, and Drained Basins. *Treatise on Geomorphology*. Fairbanks: Elsevier, 325–353. doi:10.1016/B978-0-12-374739-6.00216-5

Grosse, G., Schirrmeister, L., Kunitsky, V. V., and Hubberten, H.-W. (2005). The Use of CORONA Images in Remote Sensing of Periglacial Geomorphology: An Illustration from the NE Siberian Coast. *Permafrost Periglac. Process.* 16 (2), 163–172. doi:10.1002/ppp.509

Grosse, G., Schirrmeister, L., Siegert, C., Kunitsky, V. V., Slagoda, E. A., Andreev, A. A., et al. (2007). Geological and Geomorphological Evolution of a Sedimentary Periglacial Landscape in Northeast Siberia during the Late Quaternary. *Geomorphology* 86 (1–2), 25–51. doi:10.1016/j.geomorph.2006.08.005

Grotheer, H., Meyer, V., Riedel, T., Pfalz, G., Mathieu, L., Hefter, J., et al. (2020). Burial and Origin of Permafrost-Derived Carbon in the Nearshore Zone of the Southern Canadian Beaufort Sea. *Geophys. Res. Lett.* 47 (3), e2019GL085897. doi:10.1029/2019GL085897

Gundelwein, A., Müller-Lupp, T., Sommerkorn, M., Haupt, E. T. K., Pfeiffer, E.-M., and Wiechmann, H. (2007). Carbon in Tundra Soils in the Lake Labaz Region of Arctic Siberia. *Eur. J. Soil Sci.* 58 (5), 1164–1174. doi:10.1111/j.1365-2389.2007.00908.x

Günther, F., Overduin, P. P., Yakshina, I. A., Opel, T., Baranskaya, A. V., and Grigoriev, M. N. (2015). Observing Muostakh Disappear: Permafrost Thaw Subsidence and Erosion of a Ground-Ice-Rich Island in Response to Arctic Summer Warming and Sea Ice Reduction. *The Cryosphere* 9 (1), 151–178. doi:10.5194/tc-9-151-2015

Harris, C. M., McClelland, J. W., Connelly, T. L., Crump, B. C., and Dunton, K. H. (2017). Salinity and Temperature Regimes in Eastern Alaskan Beaufort Sea Lagoons in Relation to Source Water Contributions. *Estuaries and Coasts* 40 (1), 50–62. doi:10.1007/s12237-016-0123-z

Harrison, W. D., and Osterkamp, T. E. (1982). Measurements of the Electrical Conductivity of Interstitial Water in Subsea Permafrost. Proceedings of the Fourth Canadian Permafrost Conference, Ottawa, Canada: National Research Council of Canada, 229–237.

Héquette, A., Ruz, M.-H., and Hill, P. R. (1995). The Effects of the Holocene Sea Level Rise on the Evolution of the Southeastern Coast of the Canadian Beaufort Sea. *J. Coastal Res.* 11 (2), 494–507.

Heslop, J. K., Walter Anthony, K. M., Grosse, G., Liebner, S., and Winkel, M. (2019b). Century-scale Time since Permafrost Thaw Affects Temperature Sensitivity of Net Methane Production in Thermokarst-Lake and Talik Sediments. *Sci. Total Environ.* 691 (November), 124–134. doi:10.1016/j.scitotenv.2019.06.402

Heslop, J. K., Walter Anthony, K. M., Sepulveda-Jauregui, A., Martinez-Cruz, K., Bondurant, A., Grosse, G., et al. (2015). Thermokarst Lake Methanogenesis along a Complete Talik Profile. *Biogeosciences* 12 (14), 4317–4331. doi:10.5194/bg-12-4317-2015

Heslop, J. K., Winkel, M., Walter Anthony, K. M., Spencer, R. G. M., Podgorski, D. C., Zito, P., et al. (2019a). Increasing Organic Carbon Biolability with Depth in Yedoma Permafrost: Ramifications for Future Climate Change. *J. Geophys. Res. Biogeosci.* 124 (7), 2021–2038. doi:10.1029/2018JG004712

Hill, P. R. (1990). Coastal Geology of the King Point Area, Yukon Territory, Canada. *Mar. Geology* 91 (1), 93–111. doi:10.1016/0025-3227(90)90135-7

Jenrich, M. (2020). "Thermokarst Lagoons – Carbon Pools and Panarctic Distribution," (Germany: University of Potsdam). Master Thesis. Avilable at: https://epic.awi.de/id/eprint/51597/.

Johannessen, O. M., Bengtsson, L., Miles, M. W., Kuzmina, S. I., Semenov, V. A., Alekseev, G. V., et al. (2004). Arctic Climate Change: Observed and Modelled Temperature and Sea-Ice Variability. *Tellus A: Dynamic Meteorology and Oceanography* 56 (4), 328–341. doi:10.3402/tellusa.v56i4.14418

Jones, B. M., Farquharson, L. M., Baughman, C. A., Buzard, R. M., Arp, C. D., Grosse, G., et al. (2018). A Decade of Remotely Sensed Observations Highlight Complex Processes Linked to Coastal Permafrost bluff Erosion in the Arctic. *Environ. Res. Lett.* 13 (11), 115001. doi:10.1088/1748-9326/aae471

Jones, B. M., Grosse, G., Arp, C. D., Jones, M. C., Walter Anthony, K. M., and Romanovsky, V. E. (2011). Modern Thermokarst Lake Dynamics in the Continuous Permafrost Zone, Northern Seward Peninsula, Alaska. *J. Geophys. Res.* 116 (G2). doi:10.1029/2011JG001666

Jongejans, L. L., Mangelsdorf, K., Schirrmeister, L., Grigoriev, M. N., Maksimov, G. M., Biskaborn, B. K., et al. (2020). *n*-Alkane Characteristics of Thawed Permafrost Deposits below a Thermokarst Lake on Bykovsky Peninsula, Northeastern Siberia. *Front. Environ. Sci.* 8. doi:10.3389/fenvs.2020.00118

Jongejans, L. L., and Strauss, J. (2020). Bootstrapping Approach for Permafrost Organic Carbon Pool Estimation. *Zenodo*. doi:10.5281/zenodo.3734247

Jongejans, L. L., Strauss, J., Lenz, J., Peterse, F., Mangelsdorf, K., Fuchs, M., et al. (2018). Organic Matter Characteristics in Yedoma and Thermokarst Deposits on Baldwin Peninsula, West Alaska. *Biogeosciences* 15 (20), 6033–6048. doi:10.5194/bg-15-6033-2018

Juhls, B., Overduin, P. P., Hölemann, J., Hieronymi, M., Matsuoka, A., Heim, B., et al. (2019). Dissolved Organic Matter at the Fluvial-marine Transition in the Laptev Sea Using *In Situ* Data and Ocean Colour Remote Sensing. *Biogeosciences* 16 (13), 2693–2713. doi:10.5194/bg-16-2693-2019

Kaplina, T. N. (2009). Alas Complexes of Northern Yakutia. *Earth's Cryosphere* 12, 3–17. (in Russian).

Kaplina, T. N., and Lozhkin, A. V. (1979). Age of Alas Deposits of the Coastal plain of Yakutia (Radiocarbon Substantiation). *Izv. SSSR. Ser. Geol.* 2, 69–76. (in Russian).

Kjerfve, B. (1994). Coastal Lagoons. *Coastal Lagoon Processes, 8. Elsevier Oceanography Series 60*. Elsevier Science Publisher B.V.

Kosyan, R. (2016). *The Diversity of Russian Estuaries and Lagoons Exposed to Human Influence*. New York, NY: Springer Berlin Heidelberg.

Kunitsky, V. V. (1989). *Kriolitologiya Nizo'ev Leny (Cryolithology of the Lower LENA)*. Yakutsk: Permafrost Institute Press.

Lachenbruch, A. H., Sass, J. H., Marshall, B. V., and Moses, T. H. (1982). Permafrost, Heat Flow, and the Geothermal Regime at Prudhoe Bay, Alaska. *J. Geophys. Res.* 87 (B11), 9301–9316. doi:10.1029/JB087iB11p09301

Lantuit, H., Atkinson, D., Paul Overduin, P., Grigoriev, M., Rachold, V., Grosse, G., et al. (2011). Coastal Erosion Dynamics on the Permafrost-Dominated Bykovsky Peninsula, north Siberia, 1951-2006. *Polar Res.* 30 (1), 7341. doi:10.3402/polar.v30i0.7341

Lenssen, N. J. L., Schmidt, G. A., Hansen, J. E., Menne, M. J., Persin, A., Ruedy, R., et al. (2019). Improvements in the GISTEMP Uncertainty Model. *J. Geophys. Res. Atmos.* 124 (12), 6307–6326. doi:10.1029/2018JD029522

Lenz, J., Wetterich, S., Jones, B. M., Meyer, H., Bobrov, A., and Grosse, G. (2016). Evidence of Multiple Thermokarst lake Generations from an 11 800-year-old Permafrost Core on the Northern S Eward P Eninsula, A Laska. *Boreas* 45 (4), 584–603. doi:10.1111/bor.12186

Liu, J., Chen, Z., Chen, M., Yan, W., Xiang, R., and Tang, X. (2010). Magnetic Susceptibility Variations and Provenance of Surface Sediments in the South China Sea. *Sediment. Geology* 230 (1), 77–85. doi:10.1016/j.sedgeo.2010.07.001

Mary, B., Mariotti, A., and Morel, J. L. (1992). Use Ofr 13C Variations at Natural Abundance for Studying the Biodegradation of Root Mucilage, Roots and Glucose in Soil. *Soil Biol. Biochem.* 24 (10), 1065–1072. doi:10.1016/0038-0717(92)90037-X

McDougall, T. J., and Barker, P. M. (2011). Getting Started with TEOS-10 and the Gibbs Seawater (GSW) Oceanographic Toolbox. *SCOR/IAPSO WG* 127, 1–28.

Meyer, H., Schönicke, L., Wand, U., Hubberten, H. W., and Friedrichsen, H. (2000). Isotope Studies of Hydrogen and Oxygen in Ground Ice - Experiences with the Equilibration Technique. *Isotopes Environ. Health Stud.* 36 (2), 133–149. doi:10.1080/10256010008032939

Meyers, P. A. (1997). Organic Geochemical Proxies of Paleoceanographic, Paleolimnologic, and Paleoclimatic Processes. *Org. Geochem.* 27 (5), 213–250. doi:10.1016/S0146-6380(97)00049-1

Meyers, P. A. (1994). Preservation of Elemental and Isotopic Source Identification of Sedimentary Organic Matter. *Chem. Geology* 114 (3–4), 289–302. doi:10.1016/0009-2541(94)90059-0

Mitzscherling, J., Winkel, M., Winterfeld, M., Horn, F., Yang, S., Grigoriev, M. N., et al. (2017). The Development of Permafrost Bacterial Communities under Submarine Conditions. *J. Geophys. Res. Biogeosci.* 122 (7), 1689–1704. doi:10.1002/2017JG003859

Möller, P., Benediktsson, Í. Ö., Anjar, J., Bennike, O., Bernhardson, M., Funder, S., et al. (2019). Data Set on Sedimentology, Palaeoecology and Chronology of Middle to Late Pleistocene Deposits on the Taimyr Peninsula, Arctic Russia. *Data in Brief* 25, 104267. doi:10.1016/j.dib.2019.104267

Möller, P., and Murray, A. S. (2015). Drumlinised Glaciofluvial and Glaciolacustrine Sediments on the Småland Peneplain, South Sweden - New Information on the Growth and Decay History of the Fennoscandian Ice Sheets during MIS 3. *Quat. Sci. Rev.* 122 (August), 1–29. doi:10.1016/j.quascirev.2015.04.025

Murray, A. S., Helsted, L. M., Autzen, M., Jain, M., and Buylaert, J. P. (2018). Measurement of Natural Radioactivity: Calibration and Performance of a High-Resolution Gamma Spectrometry Facility. *Radiat. Measurements* 120, 215–220. doi:10.1016/j.radmeas.2018.04.006

Murray, A. S., Marten, R., Johnston, A., and Martin, P. (1987). Analysis for Naturally Occuring Radionuclides at Environmental Concentrations by Gamma Spectrometry. *J. Radioanal. Nucl. Chem. Articles* 115, 263–288. doi:10.1007/bf02037443

Murray, A. S., and Wintle, A. G. (2000). Luminescence Dating of Quartz Using an Improved Single-Aliquot Regenerative-Dose Protocol. *Radiat. Measurements* 32, 57–73. doi:10.1016/S1350-4487(99)00253-X

Murray, A. S., and Wintle, A. G. (2003). The Single Aliquot Regenerative Dose Protocol: Potential for Improvements in Reliability. *Radiat. Measurements* 37, 377–381. doi:10.1016/S1350-4487(03)00053-2

Nazarova, L., Grebennikova, T. A., Razjigaeva, N. G., Ganzey, L. A., Belyanina, N. I., Arslanov, K. A., et al. (2017). Reconstruction of Holocene Environmental Changes in Southern Kurils (North-Western Pacific) Based on Palaeolake Sediment Proxies from Shikotan Island. *Glob. Planet. Change* 159 (December), 25–36. doi:10.1016/j.gloplacha.2017.10.005

Nerem, R. S., Beckley, B. D., Fasullo, J. T., Hamlington, B. D., Masters, D., and Mitchum, G. T. (2018). Climate-change-driven Accelerated Sea-Level Rise Detected in the Altimeter Era. *Proc. Natl. Acad. Sci. USA* 115 (9), 2022–2025. doi:10.1073/pnas.1717312115

Notz, D., and Stroeve, J. (2016). Observed Arctic Sea-Ice Loss Directly Follows Anthropogenic CO2emission. *Science* 354 (6313), 747–750. doi:10.1126/science.aag2345

Osterkamp, T. E., Baker, G. C., Harrison, W. D., and Matava, T. (1989). Characteristics of the Active Layer and Shallow Subsea Permafrost. *J. Geophys. Res.* 94 (C11), 16227–16236. doi:10.1029/JC094iC11p16227

Osterkamp, T. E., Jorgenson, M. T., Schuur, E. a. G., Shur, Y. L., Kanevskiy, M. Z., Vogel, J. G., et al. (2009). Physical and Ecological Changes Associated with Warming Permafrost and Thermokarst in Interior Alaska. *Permafrost Periglac. Process.* 20 (3), 235–256. doi:10.1002/ppp.656

Oswald, W. W., Anderson, P. M., Brown, T. A., Brubaker, L. B., Hu, F. S., Lozhkin, A. V., et al. (2005). Effects of Sample Mass and Macrofossil Type on Radiocarbon Dating of Arctic and Boreal lake Sediments. *The Holocene* 15, 758–767. doi:10.1191/0959683605hl849rr

Overduin, P. P., Liebner, S., Knoblauch, C., Günther, F., Wetterich, S., Schirrmeister, L., et al. (2015). Methane Oxidation Following Submarine Permafrost Degradation: Measurements from a Central Laptev Sea Shelf Borehole. *J. Geophys. Res. Biogeosci.* 120 (5), 965–978. doi:10.1002/2014JG002862

Pawlowicz, R. (2012). The Electrical Conductivity of Seawater at High Temperatures and Salinities. *Desalination* 300, 32–39. doi:10.1016/j.desal.2012.06.001

Pedrazas, M. N., Cardenas, M. B., Demir, C., Watson, J. A., Connolly, C. T., and McClelland, J. W. (2020). Absence of Ice-Bonded Permafrost beneath an Arctic Lagoon Revealed by Electrical Geophysics. *Sci. Adv.* 6 (43), eabb5083. doi:10.1126/sciadv.abb5083

Peel, M. C., Finlayson, B. L., and Mcmahon, T. A. (2007). Updated World Map of the Köppen-Geiger Climate Classification. *Hydrol. Earth Syst. Sci.* 11, 1633–1644. doi:10.5194/hess-11-1633-2007

Pekel, J.-F., Cottam, A., Gorelick, N., and Belward, A. S. (2016). High-Resolution Mapping of Global Surface Water and its Long-Term Changes. *Nature* 540 (7633), 418–422. doi:10.1038/nature20584

Phillips, M. R., Burn, C. R., Wolfe, S. A., Morse, P. D., Gaanderse, A. J., 'Neill, H. B. O., et al. (2015). *Improving Water Content Description of Ice-Rich Permafrost Soils*, 7th Canadian Permafrost Conference. Available at: http://works.bepress.com/dan-shugar/9/.

Porter, C., Morin, P., Howat, I., Noh, M. J., Bates, B., Peterman, B., et al. (2018). ArcticDEM. doi:10.7910/DVN/OHHUKH

Proshutinsky, A., Pavlov, V., and Bourke, R. H. (2001). Sea Level Rise in the Arctic Ocean. *Geophys. Res. Lett.* 28 (11), 2237–2240. doi:10.1029/2000GL012760

R Core Team (2016). *R: A Language and Environment for Statistical Computing*. Vienna, Austria: R Foundation for Statistical Computing.

Reimer, P. J., Bard, E., Bayliss, A., Beck, J. W., Blackwell, P. G., Ramsey, C. B., et al. (2013). IntCal13 and Marine13 Radiocarbon Age Calibration Curves 0-50,000 Years Cal BP. *Radiocarbon* 55 (4), 1869–1887. doi:10.2458/azu_js_rc.55.16947

Romankevich, E. A., Vetrov, A. A., Belyaev, N. A., Sergienko, V. I., Semiletov, I. P., Sukhoverkhov, S. V., et al. (2017). Alkanes in Quaternary Deposits of the Laptev Sea. *Dokl. Earth Sc.* 472 (1), 36–39. doi:10.1134/S1028334X17010093

Romanovskii, N., Hubberten, H.-W., Gavrilov, A. V., Tumskoy, V. E., and Kholodov, A. L. (2004). Permafrost of the East Siberian Arctic Shelf and Coastal Lowlands. *Quat. Sci. Rev.* 23 (11), 1359–1369. doi:10.1016/j.quascirev.2003.12.014

Romanovskii, N. N., Gavrilov, A. V., Kholodov, A. L., Pustovoit, G. P., Hubberten, H. W., Niessen, F., et al. (1998). Map of Predicted Offshore Permafrost Distribution on the Laptev Sea Shelf. *Nordicana*, 55. Yellowknife, Canada, 6.

Romanovskii, N. N., Hubberten, H.-W., Gavrilov, A. V., Tumskoy, V. E., Tipenko, G. S., Grigoriev, M. N., et al. (2000). Thermokarst and Land-Ocean Interactions, Laptev Sea Region, Russia. *Permafrost Periglac. Process.* 11 (2), 137–152. doi:10.1002/1099-1530(200004/06)11:2<137::aid-ppp345>3.0.co;2-l

Romanovsky, V. E., Drozdov, D. S., Oberman, N. G., Malkova, G. V., Kholodov, A. L., Marchenko, S. S., et al. (2010). Thermal State of Permafrost in Russia. *Permafrost Periglac. Process.* 21 (2), 136–155. doi:10.1002/ppp.683

Ruppel, C. D., and Kessler, J. D. (2017). The Interaction of Climate Change and Methane Hydrates. *Rev. Geophys.* 55 (1), 126–168. doi:10.1002/2016RG000534

Ruz, M.-H., Héquette, A., and Hill, P. R. (1992). A Model of Coastal Evolution in a Transgressed Thermokarst Topography, Canadian Beaufort Sea. *Mar. Geology* 106, 251–278. doi:10.1016/0025-3227(92)90133-3

Schirrmeister, L., Froese, D., Tumskoy, V., Grosse, G., and Wetterich, S. (2013). "PERMAFROST and PERIGLACIAL FEATURES | Yedoma: Late Pleistocene Ice-Rich Syngenetic Permafrost of Beringia," in *Encyclopedia of Quaternary Science.* Editors S A. Elias and C J. Mock Second Edition (Amsterdam: Elsevier), 542–552. doi:10.1016/B978-0-444-53643-3.00106-0

Schirrmeister, L., Grigoriev, M. N., Strauss, J., Grosse, G., Overduin, P. P., Kholodov, A., et al. (2018). Sediment Characteristics of a Thermokarst Lagoon in the Northeastern Siberian Arctic (Ivashkina Lagoon, Bykovsky Peninsula). *Arktos* 4 (1), 13. doi:10.1007/s41063-018-0049-8

Schirrmeister, L., Kunitsky, V., Grosse, G., Wetterich, S., Meyer, H., Schwamborn, G., et al. (2011). Sedimentary Characteristics and Origin of the Late Pleistocene Ice Complex on north-east Siberian Arctic Coastal Lowlands and Islands - A Review. *Quat. Int.* 241 (1–2), 3–25. doi:10.1016/j.quaint.2010.04.004

Schirrmeister, L., Schwamborn, G., Overduin, P. P., Strauss, J., Fuchs, M. C., Grigoriev, M., et al. (2017). Yedoma Ice Complex of the Buor Khaya Peninsula (Southern Laptev Sea). *Biogeosciences* 14, 1261–1283. doi:10.5194/bg-14-1261-2017

Schirrmeister, L., Siegert, C., Kunitzky, V. V., Grootes, P. M., and Erlenkeuser, H. (2002). Late Quaternary Ice-Rich Permafrost Sequences as a Paleoenvironmental Archive for the Laptev Sea Region in Northern Siberia. *Int. J. Earth Sci.* 91 (1), 154–167. doi:10.1007/s005310100205

Schowalter, T. D. (2016). Chapter 14 - Decomposition and Pedogenesis. *Insect Ecol.*, 4, 477–510. doi:10.1016/b978-0-12-803033-2.00014-5

Schuur, E. A. G., McGuire, A. D., Schädel, C., Grosse, G., Harden, J. W., Hayes, D. J., et al. (2015). Climate Change and the Permafrost Carbon Feedback. *Nature* 520 (7546), 171–179. doi:10.1038/nature14338

Segers, R., and Kengen, S. W. M. (1998). Methane Production as a Function of Anaerobic Carbon Mineralization: A Process Model. *Soil Biol. Biochem.* 30 (8), 1107–1117. doi:10.1016/S0038-0717(97)00198-3

Shakhova, N., Semiletov, I., and Chuvilin, E. (2019). Understanding the Permafrost-Hydrate System and Associated Methane Releases in the East Siberian Arctic Shelf. *Geosciences* 9 (6), 251. doi:10.3390/geosciences9060251

Shakhova, N., Semiletov, I., Gustafsson, O., Sergienko, V., Lobkovsky, L., Dudarev, O., et al. (2017). Current Rates and Mechanisms of Subsea Permafrost Degradation in the East Siberian Arctic Shelf. *Nat. Commun.* 8 (1), 15872. doi:10.1038/ncomms15872

Siegert, C., Schirrmeister, L., and Babiy, O. (2002). The Sedimentologieal, Mineralogieal and Geoehemieal Composition of Late Pleistoeene Deposits from the Lee Complex on the Bykovsky Peninsula, Northern Siberia. *Permafrostforschung* 70, 9., no.

Slagoda, E. A. (1993). "Genesis I Mikrostroenie Kriolitogennykh Otlozhenii Bykovskogo Polyostrova I Ostrova Muoastakh [Genesis and Microstructure of Cryolithogenic Deposits at the Bykovsky Peninsula and the Muostakh Island]," (Yakutsk: Permafrost Institute Yakutsk, 1993). Ph.D. thesis.

Slagoda, E. A. (2004). *Kriogennye otlozheniya Primorskoi ravniny morya Laptebykh: litologiya i mikromorfologiya* [Cryolithogenic Deposits of the Laptev Sea Coastal Plain: Lithology and Micromorphology]. Tyumen: Express, (in Russian).

Solomon, S., Mudie, P. J., Cranston, R., Hamilton, T., Thibaudeau, S. A., and Collins, E. S. (2000). Characterisation of marine and Lacustrine Sediments in a Drowned Thermokarst Embayment, Richards Island, Beaufort Sea, Canada. *Int. J. Earth Sci.* 89 (3), 503–521. doi:10.1007/s005310000126

Spangenberg, I., Overduin, P. P., Damm, E., Bussmann, I., Meyer, H., Liebner, S., et al. (2021). Methane Pathways in Winter Ice of a Thermokarst Lake–Lagoon–Coastal Water Transect in North Siberia. *Cryosphere* 15 (3), 1607–1625. doi:10.5194/tc-15-1607-2021

Strauss, J., Abbott, B. W., Hugelius, G., Schuur, E., Treat, C., Fuchs, M., et al. (2021). "Permafrost," in *Recarbonizing global soils: A technical manual of best management practices, Volume 2. Hot spots and bright spots of soil organic carbon* (Rome, Italy: Food and agriculture Organization of the United Nations).

Strauss, J., Boike, J., Bolshiyanov, D. Y., Grigoriev, M. N., El-Hajj, H., Morgenstern, A., et al. (2018). Russian-German Cooperation: Expeditions to Siberia in 2017, Berichte zur Polar- und Meeresforschung = Reports on polar and marine research. *Bremerhaven, Alfred Wegener Inst. Polar Mar. Res.* 725, 296, 2018 . EPIC. doi:10.2312/BzPM_0725_2018

Strauss, J., Schirrmeister, L., Grosse, G., Fortier, D., Hugelius, G., Knoblauch, C., et al. (2017). Deep Yedoma Permafrost: A Synthesis of Depositional Characteristics and Carbon Vulnerability. *Earth-Science Rev.* 172 (September), 75–86. doi:10.1016/j.earscirev.2017.07.007

Strauss, J., Schirrmeister, L., Grosse, G., Wetterich, S., Ulrich, M., Herzschuh, U., et al. (2013). The Deep Permafrost Carbon Pool of the Yedoma Region in Siberia and Alaska. *Geophys. Res. Lett.* 40 (23), 6165–6170. doi:10.1002/2013GL058088

Strauss, J., Schirrmeister, L., Mangelsdorf, K., Eichhorn, L., Wetterich, S., and Herzschuh, U. (2015). Organic-matter Quality of Deep Permafrost Carbon - a Study from Arctic Siberia. *Biogeosciences* 12, 2227–2245. doi:10.5194/bg-12-2227-2015

Strauss, J., Schirrmeister, L., Wetterich, S., Borchers, A., Davydov, S. P., and Davydov, S. P. (2012). Grain-size properties and organic-carbon stock of Yedoma Ice Complex permafrost from the Kolyma lowland, northeastern Siberia. *Global Biogeochem. Cycles* 26 (23). doi:10.1029/2011GB004104

Streletskaya, I. D. (1998). Yellowknife, Canada.Cryopeg Responses to Periodic Climate Fluctuations. Permafrost. Proceedings of the Seventh International Conference, Yellowknife, Canada, June 23–27, 1998.

Stuiver, M., Reimer, P. J., and Reimer, R. W. (2020). CALIB 7.1 [WWW Program]. http://calib.org (Accessed 02 12, 2020).

Subetto, D. A., Nazarova, L. B., Pestryakova, L. A., Syrykh, L. S., Andronikov, A. V., Biskaborn, B., et al. (2017). Paleolimnological Studies in Russian Northern Eurasia: A Review. *Contemp. Probl. Ecol.* 10 (4), 327–335. doi:10.1134/S1995425517040102

Tagliapietra, D., Sigovini, M., and Ghirardini, A. V. (2009). A Review of Terms and Definitions to Categorise Estuaries, Lagoons and Associated Environments. *Mar. Freshw. Res.* 60 (6), 497. doi:10.1071/MF08088

Tanski, G., Wagner, D., Knoblauch, C., Fritz, M., Sachs, T., and Lantuit, H. (2019). Rapid CO 2 Release from Eroding Permafrost in Seawater. *Geophys. Res. Lett.* 46 (20), 11244–11252. doi:10.1029/2019GL084303

Turetsky, M. R., Abbott, B. W., Jones, M. C., Anthony, K. W., Olefeldt, D., Schuur, E. A. G., et al. (2020). Carbon Release through Abrupt Permafrost Thaw. *Nat. Geosci.* 13 (2), 138–143. doi:10.1038/s41561-019-0526-0

Ulyantsev, A. S., Romankevich, E. A., Bratskaya, S. Y., Semiletov, I. P., and Avramenko, V. A. (2017). Organic and Carbonate Carbon in Permafrost and Thawed Deposits from Buor-Khaya Bay (Laptev Sea). *Dokl. Earth Sc.* 473 (2), 467–471. doi:10.1134/s1028334x17040237

Vyse, S. A., Herzschuh, U., Andreev, A. A., Pestryakova, L. A., Diekmann, B., Armitage, S. J., et al. (2020). Geochemical and Sedimentological Responses of Arctic Glacial Lake Ilirney, Chukotka (Far East Russia) to Palaeoenvironmental Change since ~51.8 Ka BP. *Quat. Sci. Rev.* 247, 106607. doi:10.1016/j.quascirev.2020.106607

Walhert, L., Zimmermann, S., Blaser, P., Luster, J., and Lüscher, P. (2004). Waldböden der Schweiz 1: Grundlagen und Region Jura. *(in German) [Forrest Soils of Swizerland, Chapter 1: Principles and the Jura Region]*. Bern: hep verlag.

Walter Anthony, K., Schneider von Deimling, T., Nitze, I., Frolking, S., Emond, A., Daanen, R., et al. (2018). 21st-Century Modeled Permafrost Carbon Emissions Accelerated by Abrupt Thaw beneath Lakes. *Nat. Commun.* 9 (1), 3262. doi:10.1038/s41467-018-05738-9

Watson, C. S., White, N. J., Church, J. A., King, M. A., Burgette, R. J., and Legresy, B. (2015). Unabated Global Mean Sea-Level Rise over the Satellite Altimeter Era. *Nat. Clim. Change* 5 (6), 565–568. doi:10.1038/nclimate2635

Wetterich, S., Kuzmina, S., Andreev, A. A., Kienast, F., Meyer, H., Schirrmeister, L., et al. (2008). Palaeoenvironmental Dynamics Inferred from Late Quaternary Permafrost Deposits on Kurungnakh Island, Lena Delta, Northeast Siberia, Russia. *Quat. Sci. Rev.* 27, 1523–1540. doi:10.1016/j.quascirev.2008.04.007

Wetterich, S., Schirrmeister, L., Andreev, A. A., Pudenz, M., Plessen, B., Meyer, H., et al. (2009). Eemian and Late Glacial/Holocene Palaeoenvironmental Records from Permafrost Sequences at the Dmitry Laptev Strait (NE Siberia, Russia). *Palaeogeogr. Palaeoclimatol. Palaeoecol.* 279 (1), 73–95. doi:10.1016/j.palaeo.2009.05.002

Wetterich, S., Tumskoy, V., Rudaya, N., Andreev, A. A., Opel, T., Meyer, H., et al. (2014). Ice Complex Formation in Arctic East Siberia during the MIS3 Interstadial. *Quat. Sci. Rev.* 84, 39–55. doi:10.1016/j.quascirev.2013.11.009

Winkel, M., Mitzscherling, J., Overduin, P. P., Horn, F., Winterfeld, M., Rijkers, R., et al. (2018). Anaerobic Methanotrophic Communities Thrive in Deep Submarine Permafrost. *Sci. Rep.* 8 (1), 1291. doi:10.1038/s41598-018-19505-9

Winkel, M., Sepulveda-Jauregui, A., Martinez-Cruz, K., Heslop, J. K., Rijkers, R., Horn, F., et al. (2019). First Evidence for Cold-Adapted Anaerobic Oxidation of Methane in Deep Sediments of Thermokarst Lakes. *Environ. Res. Commun.* 1 (2), 021002. doi:10.1088/2515-7620/ab1042

Conflict of Interest: The authors declare that the research was conducted in the absence of any commercial or financial relationships that could be construed as a potential conflict of interest.

Publisher's Note: All claims expressed in this article are solely those of the authors and do not necessarily represent those of their affiliated organizations, or those of the publisher, the editors and the reviewers. Any product that may be evaluated in this article, or claim that may be made by its manufacturer, is not guaranteed or endorsed by the publisher.

B

Onshore Thermokarst Primes Subsea Permafrost Degradation

Michael Angelopoulos[1,2], Pier P. Overduin[1], Maren Jenrich[1,2], Ingmar Nitze[1], Frank Günther[2], Jens Strauss[1], Sebastian Westermann[3], Lutz Schirrmeister[1], Alexander Kholodov[4,5], Michael Krautblatter[6], Mikhail N. Grigoriev[7], and Guido Grosse[1,2]

[1]Permafrost Research Section, Alfred Wegener Institute Helmholtz Centre for Polar and Marine Research, Potsdam, Germany

[2]Institute of Geosciences, University of Potsdam, Potsdam, Germany

[3]Department of Geosciences, University of Oslo, Oslo, Norway

[4]Geophysical Institute, University of Alaska Fairbanks, Fairbanks, AK, USA

[5]Institute of Physical-Chemical and Biological Problems of Soil Science, Russian Academy of Sciences, Pushchino, Russia

[6]Department of Civil, Geo, and Environmental Engineering, Technical University of Munich, Munich, Germany

[7]Melnikov Permafrost Institute, Siberian Branch of the Russian Academy of Sciences, Yakutsk, Russia

This chapter is published in:

Geophysical Research Letters - DOI: 10.1029/2021GL093881, 2021

AUTHOR CONTRIBUTIONS

To highlight the importance of lagoons on a circum-Arctic scale, M. Jenrich identified and classified all the lagoons (>= 500 m wide) along the American, Canadian, and Siberian Arctic coasts. Her expertise contributed to the first Arctic-wide assessment and quantification of lagoons initiated by thermokarst processes. M. Jenrich led this entire component of the manuscript, from conceptualization, data analysis and interpretation, as well as writing and editing. Overall, her contribution helped elevate a site-specific permafrost geophysics study to a higher impact paper worthy of publication in GRL.

Geophysical Research Letters

RESEARCH LETTER
10.1029/2021GL093881

Special Section:
The Arctic: An AGU Joint Special Collection

Key Points:

- Subsea permafrost degradation was up to 170% faster below submerged thermokarst basins compared to submerged Yedoma remnants nearshore
- Re-worked permafrost beneath thermokarst basins adjacent to lagoons induces rapid offshore thaw
- Along the assessed Arctic coastline, 54% of lagoons originated in thermokarst basins

Supporting Information:

Supporting Information may be found in the online version of this article.

Correspondence to:
M. Angelopoulos,
michael.angelopoulos@awi.de

Citation:
Angelopoulos, M., Overduin, P. P., Jenrich, M., Nitze, I., Günther, F., Strauss, J., et al. (2021). Onshore thermokarst primes subsea permafrost degradation. *Geophysical Research Letters*, *48*, e2021GL093881. https://doi.org/10.1029/2021GL093881

Received 24 APR 2021
Accepted 16 JUL 2021

Onshore Thermokarst Primes Subsea Permafrost Degradation

Michael Angelopoulos[1,2], Pier P. Overduin[1], Maren Jenrich[1,2], Ingmar Nitze[1], Frank Günther[2], Jens Strauss[1], Sebastian Westermann[3], Lutz Schirrmeister[1], Alexander Kholodov[4,5], Michael Krautblatter[6], Mikhail N. Grigoriev[7], and Guido Grosse[1,2]

[1]Permafrost Research Section, Alfred Wegener Institute Helmholtz Centre for Polar and Marine Research, Potsdam, Germany, [2]Institute of Geosciences, University of Potsdam, Potsdam, Germany, [3]Department of Geosciences, University of Oslo, Oslo, Norway, [4]Geophysical Institute, University of Alaska Fairbanks, Fairbanks, AK, USA, [5]Institute of Physical-Chemical and Biological Problems of Soil Science, Russian Academy of Sciences, Pushchino, Russia, [6]Department of Civil, Geo, and Environmental Engineering, Technical University of Munich, Munich, Germany, [7]Melnikov Permafrost Institute, Siberian Branch of the Russian Academy of Sciences, Yakutsk, Russia

Abstract The response of permafrost to marine submergence can vary between ice-rich late Pleistocene deposits and the thermokarst basins that thawed out during the Holocene. We hypothesize that inundated Alases offshore thaw faster than submerged Yedoma. To test this hypothesis, we estimated depths to the top of ice-bearing permafrost offshore of the Bykovsky Peninsula in northeastern Siberia using electrical resistivity surveys. The surveys traversed submerged lagoon deposits, drained and refrozen Alas deposits, and undisturbed Yedoma from the coastline to 373 m offshore. While the permafrost degradation rates of the submerged Yedoma were in the range of similar sites, the submerged Alas permafrost degradation rates were up to 170% faster. Remote sensing analyses suggest that 54% of lagoons wider than 500 m along northeast Siberian and northwest American coasts originated in thermokarst basins. Given the abundance of thermokarst basins and lakes along parts of the Arctic coastline, their effect on subsea permafrost degradation must be similarly prevalent.

Plain Language Summary Permafrost is defined as any ground or rock colder than 0°C for two or more consecutive years. In unglaciated regions of Siberia during the last ice age, the ground froze 1 km deep. When the ice sheets and glaciers melted at the end of the last Ice Age, millions of square kilometers of this cold permafrost were inundated with seawater on shallow Arctic shelves, creating subsea permafrost. Even today, new permafrost is submerged because of coastal erosion. Once submerged, heat and salt flow thaw the permafrost. However, the rate of subsea permafrost thaw partially depends on its temperature, ice content, and sediment type. Some permafrost areas called Alases already experienced deep thaw and refreezing from Arctic lake formation and drainage. On the southern coastline of the Bykovsky Peninsula in Siberia, we carried out non-invasive marine geophysical surveys parallel to the coastline to estimate how fast permafrost thaws beneath a submerged Alas next to a lagoon and permafrost areas without Alases. We discovered that subsea permafrost degradation was up to 170% faster beneath the submerged Alas nearshore. To highlight the broader relevance of these Alas-lagoon landscapes along the Arctic coastline, we map out Arctic lagoons.

1. Introduction

Subsea permafrost degradation rates are poorly constrained, mostly because we lack observational data. However, numerous modeling studies demonstrate that the degradation rate varies with sediment properties and porewater salinity (Frederick & Buffett, 2015; Nicolsky & Shakhova, 2010; Nicolsky et al., 2012; Overduin et al., 2019) and bottom water conditions (Dmitrenko et al., 2011; Golubeva et al., 2018; Harrison & Osterkamp, 1978). Repeated borehole observations close to the mouth of the Lena River suggest that degradation rates since the 1980s are increasing (Shakhova et al., 2017), which may have implications for shallow gas and carbon entrapped in ice-bearing permafrost (IBP) or shallow metastable inter-pore gas hydrates (Shakhova et al., 2019). Gas released from the dissociation of gas hydrates must bypass numerous physical and microbial sinks. Analyses of atmospheric methane fluxes (Kirschke et al., 2013; Saunois et al., 2020) and global hydrate distribution (Ruppel, 2015) rule out subsea permafrost-associated gas hydrate forcing for currently observed climate warming (Ruppel & Kessler, 2017). Therefore, the mobilization of subsea permafrost organic carbon could be of greater importance (Sayedi et al., 2020; Wild et al., 2018).

Thermokarst is the process by which the thawing of ice-rich permafrost creates new landforms. These landforms are often depressions occupied by *thermokarst lakes*. When these lakes drain, the resulting topographic lows are called *Alases*. Thermokarst lakes and Alases become part of the marine environment because of transgressions and ingressions (Grosse et al., 2007) or through the development of channels (Romanovskii et al., 2000). If a thermokarst lake does not completely drain during the land to sea transition, then the talik underneath the lake can refreeze if a negative temperature profile develops in the sediment (Romanovskii et al., 2000). However, the newly formed frozen sediment can re-thaw later as the chemical degradation lags behind sediment refreezing (Angelopoulos, Overduin, Westermann, et al., 2020). Submerged thermokarst lake taliks may facilitate open talik development for gas migration (Frederick & Buffett, 2014). Nicolsky et al. (2012) modeled subsea permafrost on the East Siberian Arctic Shelf for the last several glacial cycles and demonstrated that open taliks can develop beneath thermokarst depressions in sediments with low porosity or in fault zones with high geothermal heat fluxes.

When thermokarst lakes drain, taliks can refreeze quickly under sub-aerial conditions, as much as 53 m in 157 yr (Ling & Zhang, 2004). O'Neill et al. (2020) provide a review of recent terrestrial talik research (2010–2019) and key terminology. Loss of high Pleistocene ground ice contents through thermokarst is generally not replaced by Holocene ice re-accumulation (Jorgenson & Shur, 2007). Therefore, relatively young drained lake basins have different permafrost characteristics compared to Yedoma remnants. For example, Alas deposits can hold three times more organic carbon per unit volume compared to Yedoma deposits (Jongejans et al., 2018) and trap large amounts of methane (Kraev et al., 2019). The high organic carbon contents are concentrated in lacustrine deposits, while the underlying taberal deposits tend to contain less organic carbon per unit volume than the original Yedoma (Kholodov et al., 2003; Shmelev et al., 2017). Snow can accumulate in topographic lows, leading to warmer ground temperatures (Kaverin et al., 2018). In cryopeg formations beneath a migrating river channel in northern Alaska, Stephani et al. (2020) showed that the epigenetic permafrost that formed beneath freshly exposed surfaces was ice-poor. However, the total volumetric ice content in an old Alas can be similar to that of Yedoma deposits due to large amounts of pore and segregated ice, especially in northeastern Siberia (Strauss et al., 2013; Ulrich et al., 2014). The altered latent heat content in Alas-permafrost can affect thawing rates for the next thermokarst phase. This hysteresis has been demonstrated in the modeling of thaw/refreeze cycles for onshore permafrost (Eliseev et al., 2014). Depending on its age, Alas-permafrost can be warmer, less ice-rich, and potentially more organic carbon-rich.

In this study, the term *Yedoma* is used to describe ice-rich Pleistocene permafrost deposits with syngenetic ice wedges where an Alas has not formed (Strauss et al., 2017). Electrical resistivity surveying has been successfully applied to map the top of subsea IBP (Angelopoulos et al., 2019; Overduin et al., 2012, 2016; Sellmann et al., 1989), onshore cryopegs connected to sub-lagoon taliks (Pedrazas et al., 2020), and seawater intrusion beneath the base of thin coastal permafrost (Kasprzak et al., 2017). Offshore, former lake basins infilled with sediment were detected with seismic methods (Portnov et al., 2018; Rekant et al., 2015) and transient electromagnetic surveys detected the top of subsea IBP and possibly deep paleo-taliks beneath submerged thermokarst (Shakhova et al., 2017). In this study, we applied marine electrical resistivity surveying to test the following hypothesis: *Alas permafrost landscapes submerged by seawater are pre-conditioned to degrade faster than previously undisturbed Yedoma permafrost deposits*. The results have implications for subsea permafrost on Arctic shelves and along coastal stretches with abundant thermokarst terrain.

2. Study Area

The fieldwork took place on the Bykovsky Peninsula's southern coastline in northeastern Siberia in July 2017. Thermokarst processes here have a major impact on the landscape and lakes alone characterize approximately 15% of the peninsula (Grosse et al., 2008). Including drained lake basins, thermokarst-affected landscapes exceed 50% of the total land area (Grosse et al., 2005). Approximately 23% of the coastline is dominated by Alas terrain and 13% by sand bar or lagoon barriers (Lantuit, Atkinson, et al., 2011). Between

1951 and 2006, the mean erosion rate was more than twice as fast for Alas coastlines compared to Yedoma, possibly due to lower ice content and a lower cliff height to erode. However, the differential erosion rate can create embayments that reduce hydrodynamic forcing along Alas coastlines. Then, the erosion rate along Alas coastlines can decrease. The balance of these processes may explain why the Alas coastline is not further inland than the Yedoma for the southern coastline.

3. Methods

In our study area, we aimed to quantify relative thaw rates of the different terrain units once submerged, providing an insight into the priming of subsea permafrost degradation by prior thermokarst lagoon development along the Arctic coast. To quantify the abundance of these features, we mapped thermokarst lagoons along Arctic coasts in the Canadian and Alaskan Chukchi and Beaufort seas, as well as the northeastern Siberian seas.

3.1. Arctic Lagoon Mapping and Remote Sensing

We manually mapped the number and distribution of lagoons wider than 500 m along the Arctic coast from the Taimyr Peninsula in Russia to the Tuktoyaktuk Peninsula in Canada. Our study area includes the Laptev, East Siberian, Chukchi, and Beaufort sea coasts. The mapping was conducted in Google Earth Engine and QGIS3.6 using Sentinel-2 imagery. We created a mosaic covering the entire coastal study domain and consisting of August–September 2018 median pixel values for a false color near-infrared, red, green band combination (8-4-3) at 10 m pixel resolution. We visually identified thermokarst lagoons according to the following criteria:

1. Located in a thermokarst environment
2. Had a round to oval-shaped depression with a discernible shoreline
3. At least intermittent connection with the sea through (a) a visible channel with a maximum length of 1 km, (b) separation only by a narrow sand barrier; or (c) high likelihood of regular water exchange via spring tides or storm surges if the maximum elevation difference to the sea is <1.5 m.

Elevation differences between land and sea were measured using the ArcticDEM digital elevation model (DEM) and its hillshade (HSarcticDEM) (Porter et al., 2018). In the Sentinel Hub Playground (https://apps.sentinel-hub.com/sentinel-playground) the "Moisture Index" (band combination (B8A − B11)/(B8A + B11)) and "Geology" layers (band combination 12-4-2) were used to visually determine the nature of barriers between coastal water bodies and the sea. Interconnected lagoons were defined as one system.

3.2. Electrical Resistivity Surveys

We performed four electrical resistivity surveys parallel to the southern coastline of the Bykovsky Peninsula in July 2017 (Figure 1). We extrapolated all onshore terrain units to offshore and assumed that our offshore surveys parallel to shore traversed all the units. An additional transect perpendicular to the Yedoma shoreline combined with a terrestrial survey is presented in Angelopoulos et al. (2019). The profiles were collected with an IRIS Syscal Pro Deep Marine system. The system was equipped with an echo-sounder to measure water depths and apparent resistivity data was collected approximately every 5 m. The geoelectric cable consisted of two current electrodes and eleven potential electrodes arranged in a reciprocal Wenner-Schlumberger array with a 10 m electrode separation. The array was quasi-symmetrical and each vertical sounding had alternate electrode pairs that were slightly off center. Ten apparent resistivity readings were taken at each sounding location. Conductivity, depth, and temperature casts were taken to constrain the water layer resistivity in the inversions. The depth to IBP was interpreted where the maximum rate of change of the natural logarithm of inverted resistivity vs. depth occurred. The depth of investigation (DOI) provides an estimate of the depth to which the inverted electrical resistivity can be considered reliable (Vest Christiansen & Auken, 2012). The laterally constrained 1D inversions (Auken et al., 2005) and IBP determination are described in the Supporting Information.

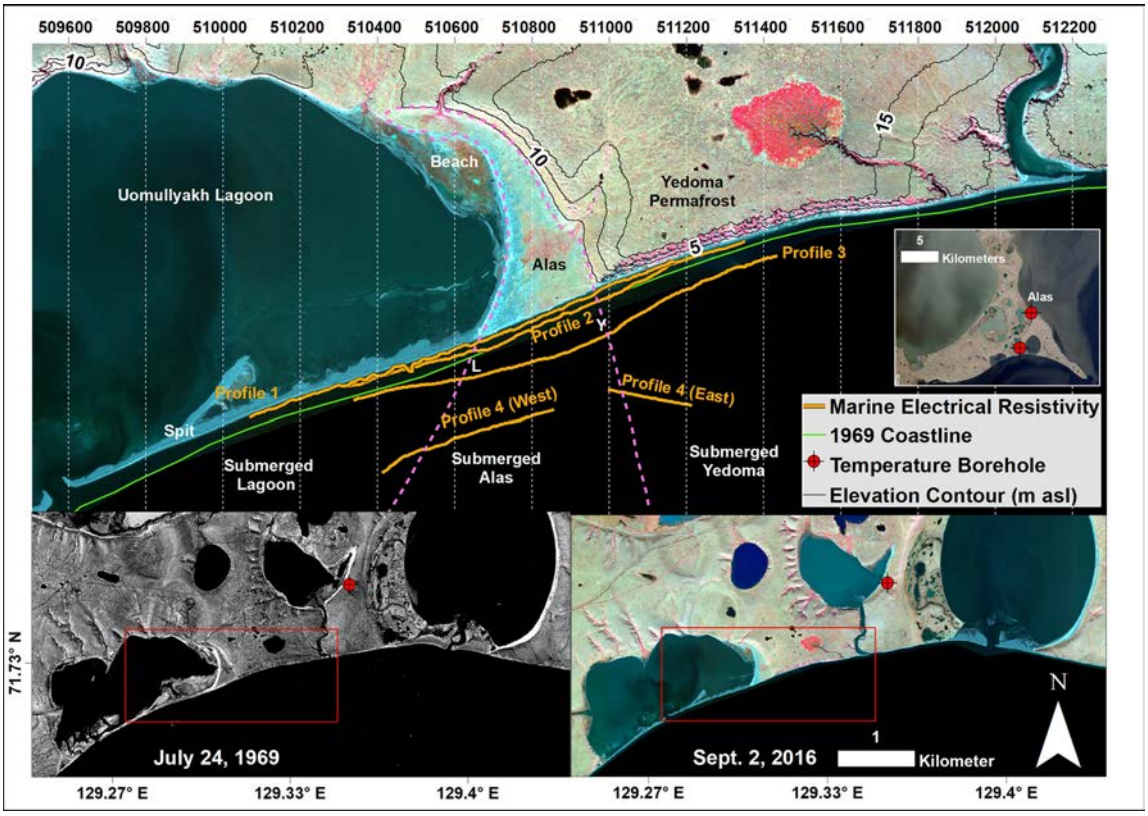

Figure 1. Top: Electrical resistivity survey locations from July 2017 superimposed on a high resolution satellite image (30 cm ground resolution WorldView-3 image from September 2, 2016 (DigitalGlobe©)). For context, the 1969 coastline and Yedoma temperature borehole (Schirrmeister et al., 2018) are also shown. The lagoon/Alas and Alas/Yedoma boundaries are extrapolated offshore and denoted "L" and "Y" respectively in Figure 3. To ease interpretation of the electrical resistivity profiles (Figure 3), easting (m) indicators are shown every 200 m. Bottom left: 1969 CORONA satellite image of the study area with the fieldwork map extent outline in the red rectangle. This is preferentially shown instead of an image available from 1951 because of better resolution. Bottom right: 2016 satellite image (WorldView-3) of the study area with the fieldwork map extent outline in the red rectangle.

4. Results

4.1. Arctic Lagoon Mapping and Remote Sensing

Of all 469 mapped lagoons, 253 (54%) originated in thermokarst basins (Figure 2). Most of the thermokarst lagoons (117) were located along the Beaufort Sea coastline. Along the coast of the Laptev Sea, 81 lagoons were mapped, 20 of which were thermokarst lagoons. In addition, all lagoons identified in the Lena River Delta originated from tapped thermokarst lakes. The observations showed that thermokarst lagoons were mainly restricted to lowland areas and were most abundant in delta regions. Six lagoons were identified on the Bykovsky Peninsula, all of them located in the south of the peninsula. Five of the six originated from thermokarst basins. Figure S1 shows all 469 lagoons mapped along the Arctic coast between the Taimyr Peninsula and the Tuktoyaktuk Peninsula west of the Mackenzie Delta. The Beaufort Sea coast featured the most lagoons (153), but was also the longest coastline investigated.

4.2. Submerged Yedoma Deposits

Offshore of the Bykovsky Peninsula's southern coastline, the most highly resistive subsurface layers were observed beneath submerged Yedoma (Figure 3). For each profile, there was a clear lateral transition in resistivity and depth to IBP at the submerged Alas/Yedoma transition. Similar to Angelopoulos et al. (2019),

Figure 2. Arctic coastline map of the 253 thermokarst lagoons along the Arctic coast between the Taimyr Peninsula (Siberia) and the Tuktoyaktuk Peninsula (Northwest Territories, Canada); number of lagoons in brackets.

the transition to IBP occurred between 16 and 130 Ωm. Within the frozen sediment body, the resistivity increased to 250 Ωm for profiles 1 and 2, but exceeded 500 Ωm for profile 3. For profile 3, the DOI was slightly below the depth to IBP and above the highly resistive zone in the submerged Yedoma. Along profile 4, the farthest from shore, the maximum resistivity of the IBP was only 75 Ωm. The depth to IBP increased from 1 to 2 m within 10 m of the coastline, to 8 m at 110 m offshore, and finally to 12 m at 300 m from the shoreline (Figure S2).

4.3. Submerged Alas and Lagoon Deposits

For profile 1, there was a clear distinction between the submerged Alas and the submerged lagoon deposits. Beginning at the submerged Alas/Yedoma boundary, the depth to IBP increased from approximately 5 to 15 m toward the lagoon/Alas boundary (Figure 3). Beneath the submerged lagoon deposits, the depth to IBP increased with distance away from the Alas. Furthermore, the unfrozen to frozen transition occurred at a

10.1029/2021GL093881

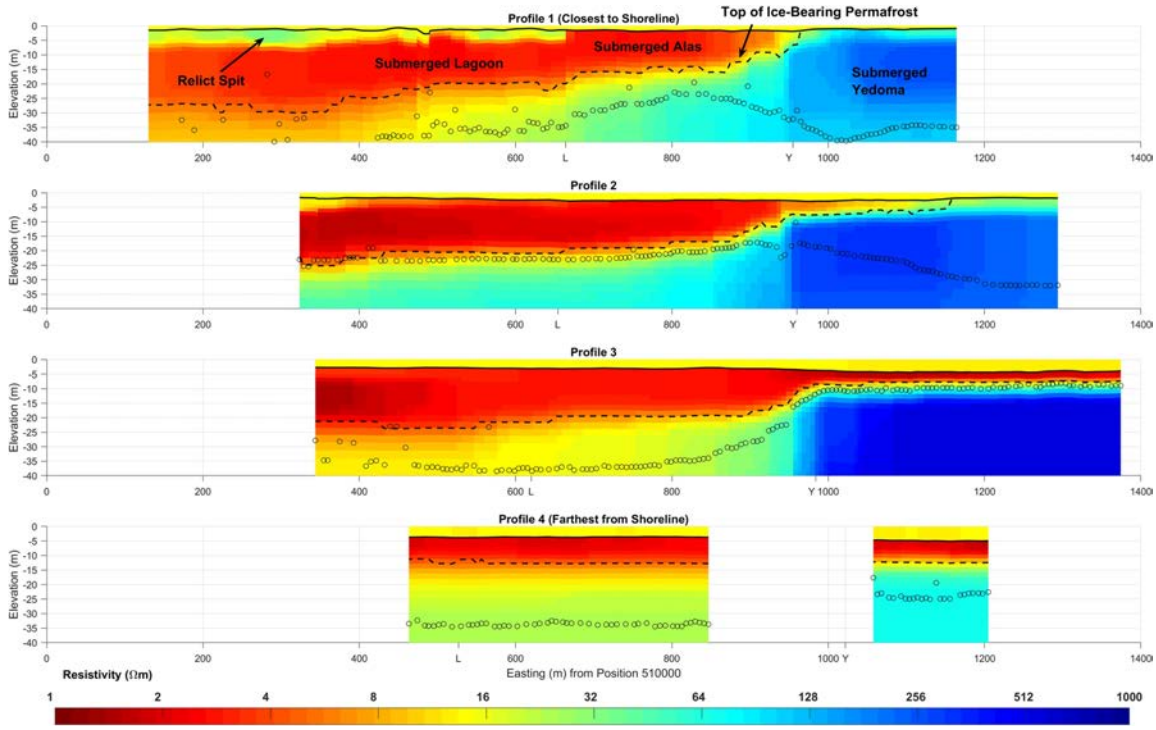

Figure 3. Electrical resistivity of four surveys parallel to shore in July 2017. The surveys traverse submerged lagoon, as well as submerged Alas and Yedoma terrain. The boundaries between each unit were extrapolated offshore as shown in Figure 1. On the *X* axis of the profiles, "L" denotes the lagoon to Alas boundary and "Y" the Alas to Yedoma boundary. The thick black line is the water depth, the dotted black line is the interpreted depth to the top of ice-bearing permafrost (IBP), and the black circles indicate the depth of investigation (DOI).

lower resistivity (around 8 Ωm) compared to the submerged Alas and Yedoma. In addition, a relatively high resistivity feature (up to 30 Ωm) 5 m thick was detected just below the seabed for the submerged lagoon. For both the Alas and the lagoon, the depth to IBP was above the DOI. Along profile 2, both the Alas and lagoon segments were similar. From the westernmost edge of the survey line to 800 m, the depth to IBP was 19 m and the frozen sediment had a maximum resistivity of 75 Ωm. The depth to IBP was slightly above the DOI for most of the profile west of the Yedoma. Along profile 3, the depth to IBP was 19 m in the Alas and as deep as 24 m in the lagoon, but the profile drifted toward the shoreline past the lagoon boundary (Figure 1). For both submerged landscape units, the depth to IBP was above the DOI. For profile 4, the IBP depth was 12 m in both the submerged lagoon and Alas. While the resistivity at the unfrozen to frozen interface was similar to profile 3, the depth to IBP was shallower despite being more than 100 m further offshore. The data residual for each sounding of all profiles was less than 1.0 assuming an uncertainty level of 5% on the apparent resistivity.

Overall, there was a strong linear fit between IBP depth and the natural logarithm of offshore distances less than 120 m for the Alas, but not for the lagoon, which yielded a negative correlation (Figure S2). When considering the natural logarithm of all offshore distances, both landscape units yielded weak linear fits with IBP depths. For coastal erosion rates of 0.25 and 0.50 m/yr, the maximum IBP degradation rate was 0.16–0.32 m/yr for the Alas at a 30 m offshore distance compared to 0.06–0.12 m/yr for Yedoma, representing an increase of up to 170% for the Alas. This disparity was present up to 120 m from shore.

10.1029/2021GL093881

5. Discussion

The depth to IBP beneath submerged Yedoma increased logarithmically with distance offshore and thus inundation time. The warm discharge of the Lena River results in faster IBP degradation rates in this area compared to the western Laptev Sea (Angelopoulos, Overduin, Miesner, et al., 2020). Since the coastline cuts approximately perpendicular across terrain unit boundaries, relative differences in degradation rates between submerged Yedoma and Alas therefore hold, irrespective of the coastal erosion rate. As shown in Figure 1, the 1969 coastline intersects profile 2, showing that the Alas was submerged after coastal erosion. The coastal erosion rate was approximately 0.5 m/yr for the Alas coastline from 1969 to 2017, corresponding to 48 yr of inundation. For further offshore distances (profiles 3 and 4), there is more uncertainty regarding the lagoon/Alas and Alas/Yedoma boundaries, as well as the Alas inundation history. Lower lying Alases could have been submerged earlier from rising sea levels (Gavrilov et al., 2006; Romanovskii et al., 2000), but this does not contradict the high rate of subsea IBP degradation for the submerged Alas deposits close to shore (up to 19 m in 48 yr). Shakhova et al. (2017) showed that the depth to IBP for submerged Yedoma permafrost offshore of Muostakh Island's north tip increased from 4.2 m after 49 yr of inundation (1982 borehole) to 8.6 m after 81 yr of inundation (2014 borehole).

The high rate of subsea IBP degradation for submerged Alas deposits within 30 m of the coastline suggests that conditions prior to submergence favor thawing. This may be partially due to a warmer ground thermal regime upon submergence, as borehole measurements showed that the average ground surface temperature in an Alas depression from 2012 to 2015 was −7°C compared to −10°C for Yedoma (Figure S3). However, this effect is less important than the reduced latent heat content associated with relatively ice-poor refrozen talik deposits. In this region, the total ice content (segregated ice + wedge ice) can reach up to 87% by volume for Yedoma deposits (Fuchs et al., 2020; Günther et al., 2015). The Alas had been sub-aerially exposed since at least 1951 (year of oldest available image), but partial lake drainage and lagoon formation likely occurred centuries earlier (Jenrich et al., 2021). The Stefan solution for permafrost formation (Riseborough et al., 2008) yields a sub-aerial refrozen talik down to 21 m in just 66 yr and 37 m in 200 yr, using a ground temperature of −7°C, a volumetric ice content of 50%, and a frozen sediment thermal conductivity of 2.6 W/(mK). The conductivity is representative for sediment in the East Siberian Arctic seas (Chuvilin et al., 2020). We conclude that the deep IBP (19 m within 30 m of shore) is indicative of marine-induced thaw and not relict thaw from the original thermokarst lake. We further suggest that in addition to warmer sediment temperatures and potentially low ice contents in the Alas, salt intrusion from lagoon-Alas interaction could precondition the sediment for rapid thaw.

Lateral seawater intrusion beneath a thin permafrost base was interpreted by electrical resistivity surveys several decameters inland in Svalbard (Kasprzak et al., 2017), leading to the concept of an onshore-permafrost wedge (Kasprzak, 2020). Due to seawater intrusion, this concept explains that the thickness of onshore permafrost increases with distance from the coastline. On the Bykovsky Peninsula, we suspect that lateral saltwater intrusion from the lagoon occurred beneath the sub-aerial Alas during refreezing. The driftwood on the Alas surface (Figure 1) indicates that it is also susceptible to storm surges and tidal flooding from the lagoon. A borehole drilled in the center of Uomullyakh Lagoon in April 2017 showed unfrozen hypersaline sediment down to a depth of 20 m below the top of the bedfast ice (1.2 m thick), despite temperatures as low as −4.4°C (Jenrich et al., 2021). Below 20 m, the temperature was as cold as −5.0°C and below the freezing point estimated from porewater electrical conductivity. The nearly uniform salt distribution vs. depth is not indicative of slow vertical diffusive salt transport (Harrison & Osterkamp, 1982). The Alas is part of the same basin and should have similar sediment properties conducive to density-driven water flow. The depth to IBP in the borehole was deeper than the maximum depth of the Yedoma (15 m below sea level), indicating that all the massive ice melted during the thermokarst lake phase. The IBP discovered in the borehole was characterized by sands underlying the Yedoma. Although remnants of the Yedoma can exist below drained lake basins (Kholodov et al., 2003), the lower resistivity of the IBP below the Alas deposits compared to Yedoma indicates that the submerged Yedoma IBP has a higher ice content than the Alas IBP. The lateral intrusion of saltwater into an Alas that starts to refreeze could create saline sub-aerial permafrost and cryopegs. Even if the saline Alas layers freeze, thawing would still be faster because of the reduced freezing point of the porewater and a higher unfrozen water content at temperatures below the freezing point (Nicolsky & Shakhova, 2010). The re-worked Alas deposits might also be more susceptible to convective salt transport offshore. As observed in Prudhoe Bay, Alaska, the convective transport of salt to the phase boundary can greatly increase the subsea permafrost degradation rate (Osterkamp, 2001; Osterkamp et al., 1989).

The Alas IBP depth showed a strong linear fit with the natural logarithm of offshore distances, but only less than 120 m from shore. For offshore distances greater than 200 m, the depth to IBP in the Alas was only 12 m compared to 19 m for offshore distances between 90 and 120 m (Figure S2). This is possible because the terrain unit extrapolation shown in Figure 1 is more unreliable at large distances from shore. However, if the terrain unit extrapolation is correct, we attribute the aforementioned finding to the fact that the submerged Alas more than 200 m offshore was pre-conditioned with salt and low ice content to a shallower depth or not at all. After a partially frozen saline layer thaws, the IBP degradation rate slows considerably. At this point, numerical models suggest that the IBP can degrade from salt diffusion from the overlying saline sediment (Figure S4). After enough time, the 0°C isotherm will catch up to the thawing front to accelerate IBP degradation. In Tiksi Bay, the mean annual bottom water temperature is above 0°C. The thermal models are described in the supporting information and are based on CryoGrid2 (Westermann et al., 2013) adapted for salt diffusion (Angelopoulos et al., 2019).

The interpreted IBP depths beneath the submerged lagoon were the deepest, based on the assumption that an unfrozen to frozen transition occurred at the maximum rate of change of the natural logarithm of inverted electrical resistivity vs. depth. It is possible that the transition was the shift from unfrozen saline ground to less saline, but still unfrozen ground. The very low resistivity transition to IBP (8 Ωm) is corroborated by Overduin et al. (2012) and Wu et al. (2017), who demonstrated that the bulk resistivity of hypersaline sediment can be 2–3 Ωm at the freezing point. Furthermore, IBP depths beneath the submerged lagoon were complicated by the spit, which moves along with the retreating coast. In profile 1, the high resistivity feature just below the seabed was likely relict IBP aggradation from the spit's position in earlier years. Cooling from the sub-aerially exposed spit could have also created permafrost upwards from the bottom of the talik. In the eastern Beaufort Sea, Ruppel et al. (2016) attributed shallower and thicker IBP to the presence of barrier islands. Permafrost aggradation also occurs below tidal flats, like in the Kara Sea (Vasiliev et al., 2017), as well as emerging polar coasts from isostatic rebound (Boisson et al., 2020). However, it is unlikely that the Alas was once submerged and uplifted, because the Bykovsky Peninsula lies in an area of tectonic subsidence (Morgenstern et al., 2020).

Spits and barrier islands may be important controls on subsea IBP preservation in the Arctic where large lagoons (>500 m) are widespread, like in the Beaufort Sea (Figure S1). The capacity for thermokarst-affected landscapes to increase subsea permafrost degradation is most significant where thermokarst lagoons and Alases interact with each other, such as along some stretches of the Laptev and Beaufort seas (Figure 2). Higher elevated Alas-rich coastlines with comparatively few lagoons like in Eastern Siberia may experience slower subsea permafrost degradation rates, but still thaw faster than Yedoma dominated coastal stretches.

6. Conclusions

We performed marine electrical resistivity surveys parallel to the southern coastline of the Bykovsky Peninsula to map the depth to the top of subsea IBP. The resistivity data indicate that the subsea permafrost degradation rate was up to 170% faster below submerged Alas deposits compared to submerged Yedoma permafrost. The deeper IBP table observed beneath submerged Alases adjacent to thermokarst lagoons is consistent with our hypothesis. While subsea permafrost thaw is generally slower than thaw beneath thermokarst lakes, reworked low-lying Alas deposits are primed for rapid degradation upon marine inundation. Arctic coastal erosion rates are also increasing, leading to faster inundation of terrestrial permafrost (Jones et al., 2018; Lantuit, Overduin, et al., 2011). The thermokarst lake phase can generate deep taliks that facilitate subsea open talik development through bottom-up thawing, providing conduits for gas migration from degrading gas hydrates (Malakhova, 2016; Malakhova & Eliseev, 2018). We suggest that low-lying thermokarst-affected landscapes adjacent to lagoons are susceptible to more rapid top-down thaw once they become part of the marine environment. While the more rapid thaw we observed occurred in the uppermost 20 m, subsea permafrost is estimated to contain 500 Gt of carbon not embedded in hydrates in the upper 25 m of sediment (Shakhova et al., 2010; Zimov et al., 2006). Given the abundance of thermokarst lagoons in this large portion of the Arctic, as revealed by our remote sensing effort, large-scale thermal assessments of subsea permafrost should consider reworked sediments beneath thermokarst depressions in numerical models. The presence of salt in IBP reduces the energy required for phase change, and thus submerged refrozen marine sediments are also pre-conditioned to degrade faster than submerged Yedoma deposits. Along Arctic coastal stretches of ice-rich permafrost, young Alases with low ice content, as well as Alases lying in thermokarst lagoon basins, are potential hot spots for rapid subsea permafrost degradation.

Data Availability Statement

The PANGAEA portal provides access to the apparent electrical resistivity data and water depths (https://doi.pangaea.de/10.1594/PANGAEA.934169), as well as the KML files for the Arctic lagoon mapping (https://doi.pangaea.de/10.1594/PANGAEA.934158). The borehole temperature data is available from the Arctic Data Center Portal of the Geophysical Institute, University of Alaska Fairbanks. The Yedoma borehole data can be accessed from https://permafrost.gi.alaska.edu/site/by1 and the Alas borehole data from https://permafrost.gi.alaska.edu/site/by3.

Acknowledgments
This research was funded by the PETA-CARB project (ERC grant # 338335) and the German Federal Ministry of Education and Research (grant # 03F0764B). The authors received additional support from the European Union's Horizon 2020 Research and Innovation Programme under grant agreement # 773421 (Nunataryuk). Maren Jenrich and Jens Strauss received support from NERC-BMBF (project CACOON) under grant agreement # 03F0806A for the Arctic lagoon mapping. On the expedition, we appreciated help from Bennet Juhls (Alfred Wegener Institute), Georgii Maksimov (Melnikov Permafrost Institute, Yakutsk, Russia), as well as Vladimir Olenchenko and Alexey Faguet (Institute of Petroleum Geology and Geophysics, Novosibirsk, Russia). The authors also thank Jens Tronicke (University of Potsdam) for helpful discussions on electrical resistivity. Open access funding enabled and organized by Projekt DEAL.

References

Angelopoulos, M., Overduin, P. P., Miesner, F., Grigoriev, M. N., & Vasiliev, A. A. (2020). Recent advances in the study of Arctic submarine permafrost. *Permafrost and Periglacial Processes*, *31*(3), 442–453. https://doi.org/10.1002/ppp.2061

Angelopoulos, M., Overduin, P. P., Westermann, S., Tronicke, J., Strauss, J., Schirrmeister, L., et al. (2020). Thermokarst lake to lagoon transitions in eastern Siberia: Do submerged taliks refreeze? *Journal of Geophysical Research: Earth Surface*, *125*, e2019JF005424. https://doi.org/10.1029/2019JF005424

Angelopoulos, M., Westermann, S., Overduin, P., Faguet, A., Olenchenko, V., Grosse, G., & Grigoriev, M. N. (2019). Heat and salt flow in subsea permafrost modeled with CryoGrid2. *Journal of Geophysical Research: Earth Surface*, *124*(4), 920–937. https://doi.org/10.1029/2018JF004823

Auken, E., Christiansen, A. V., Jacobsen, B. H., Foged, N., & Sørensen, K. I. (2005). Piecewise 1D laterally constrained inversion of resistivity data. *Geophysical Prospecting*, *53*(4), 497–506. https://doi.org/10.1111/j.1365-2478.2005.00486.x

Boisson, A., Allard, M., & Sarrazin, D. (2020). Permafrost aggradation along the emerging eastern coast of Hudson Bay, Nunavik (northern Québec, Canada). *Permafrost and Periglacial Processes*, *31*(1), 128–140. https://doi.org/10.1002/ppp.2033

Chuvilin, E., Bukhanov, B., Grebenkin, S., Tumskoy, V., Shakhova, N., Dudarev, O., et al. (2020). Thermal properties of sediments in the East Siberian Arctic Seas: A case study in the Buor-Khaya Bay. *Marine and Petroleum Geology*, *123*, 104672. https://doi.org/10.1016/j.marpetgeo.2020.104672

Dmitrenko, I. A., Kirillov, S. A., Tremblay, L. B., Kassens, H., Anisimov, O. A., Lavrov, S. A., et al. (2011). Recent changes in shelf hydrography in the Siberian Arctic: Potential for subsea permafrost instability. *Journal of Geophysical Research*, *116*(C10), C10027. https://doi.org/10.1029/2011JC007218

Eliseev, A. V., Demchenko, P. F., Arzhanov, M. M., & Mokhov, I. I. (2014). Transient hysteresis of near-surface permafrost response to external forcing. *Climate Dynamics*, *42*(5–6), 1203–1215. https://doi.org/10.1007/s00382-013-1672-5

Frederick, J., & Buffett, B. (2014). Taliks in relict submarine permafrost and methane hydrate deposits: Pathways for gas escape under present and future conditions. *Journal of Geophysical Research: Earth Surface*, *119*(2), 106–122. https://doi.org/10.1002/2013JF002987

Frederick, J., & Buffett, B. (2015). Effects of submarine groundwater discharge on the present-day extent of relict submarine permafrost and gas hydrate stability on the Beaufort Sea continental shelf. *Journal of Geophysical Research: Earth Surface*, *120*(3), 417–432. https://doi.org/10.1002/2014JF003349

Fuchs, M., Nitze, I., Strauss, J., Günther, F., Wetterich, S., Kizyakov, A., et al. (2020). Rapid fluvio-thermal erosion of a Yedoma permafrost cliff in the Lena River Delta. *Frontiers of Earth Science*, *8*(336). https://doi.org/10.3389/feart.2020.00336

Gavrilov, A., Romanovskii, N., & Hubberten, H. (2006). Paleographic scenario of the postglacial transgression on the Laptev Sea shelf. *Kriosfera Zemli (Earth's Cryosphere)*, *10*(1), 39–50.

Golubeva, E., Platov, G., Malakhova, V., Kraineva, M., & Iakshina, D. (2018). Modelling the long-term and interannual variability in the Laptev Sea hydrography and subsea permafrost state. *Polarforschung*, *87*, 195–210.

Grosse, G., Romanovsky, V., Walter, K., Morgenstern, A., Lantuit, H., & Zimov, S. (2008). Distribution of thermokarst lakes and ponds at three Yedoma sites in Siberia. In D. Kane, & K. Hinkel (Eds.), *Proceedings: Ninth International Conference on Permafrost* (pp. 551–556). Institute of Northern Engineering, University of Alaska Fairbanks. Retrieved form https://epic.awi.de/id/eprint/19086/

Grosse, G., Schirrmeister, L., Kunitsky, V. V., & Hubberten, H.-W. (2005). The use of CORONA images in remote sensing of periglacial geomorphology: An illustration from the NE Siberian coast. *Permafrost and Periglacial Processes*, *16*(2), 163–172. https://doi.org/10.1002/ppp.509

Grosse, G., Schirrmeister, L., Siegert, C., Kunitsky, V. V., Slagoda, E. A., Andreev, A. A., & Dereviagyn, A. Y. (2007). Geological and geomorphological evolution of a sedimentary periglacial landscape in Northeast Siberia during the Late Quaternary. *Geomorphology*, *86*(1), 25–51. https://doi.org/10.1016/j.geomorph.2006.08.005

Günther, F., Overduin, P. P., Yakshina, I. A., Opel, T., Baranskaya, A. V., & Grigoriev, M. N. (2015). Observing Muostakh disappear: Permafrost thaw subsidence and erosion of a ground-ice-rich island in response to Arctic summer warming and sea ice reduction. *The Cryosphere*, *9*(1), 151–178. https://doi.org/10.5194/tc-9-151-2015

Harrison, W. D., & Osterkamp, T. E. (1978). Heat and mass transport processes in subsea permafrost 1. An analysis of molecular diffusion and its consequences. *Journal of Geophysical Research*, *83*(C9), 4707–4712. https://doi.org/10.1029/JC083iC09p04707

Harrison, W. D., & Osterkamp, T. E. (1982). Measurements of the electrical conductivity of interstitial water in submarine permafrost. In H. M. French (Ed.), *Proceedings of the Fourth Canadian Permafrost Conference* (pp. 229–237). National Research Council of Canada. Retrieved from http://pubs.aina.ucalgary.ca/cpc/CPC4-229.pdf

Jenrich, M., Angelopoulos, M., Grosse, G., Overduin, P. P., Schirrmeister, L., Nitze, I., et al. (2021). Thermokarst Lagoons: A Core-based Assessment of Depositional Characteristics and an Estimate of Carbon Pools on the Bykovsky Peninsula. *Frontiers in Earth Science*, *9*. https://doi.org/10.3389/feart.2021.637899

Jones, B. M., Farquharson, L. M., Baughman, C. A., Buzard, R. M., Arp, C. D., Grosse, G., et al. (2018). A decade of remotely sensed observations highlight complex processes linked to coastal permafrost bluff erosion in the Arctic. *Environmental Research Letters*, *13*(11), 115001. https://doi.org/10.1088/1748-9326/aae471

Jongejans, L. L., Strauss, J., Lenz, J., Peterse, F., Mangelsdorf, K., Fuchs, M., & Grosse, G. (2018). Organic matter characteristics in Yedoma and thermokarst deposits on Baldwin Peninsula, west Alaska. *Biogeosciences*, *15*(20), 6033–6048. https://doi.org/10.5194/bg-15-6033-2018

Jorgenson, M. T., & Shur, Y. (2007). Evolution of lakes and basins in northern Alaska and discussion of the thaw lake cycle. *Journal of Geophysical Research*, *112*(F2). F02S17. https://doi.org/10.1029/2006JF000531

Kasprzak, M. (2020). Seawater intrusion on the Arctic Coast (Svalbard): The concept of onshore-permafrost wedge. *Geosciences*, *10*(9), 349. https://doi.org/10.3390/geosciences10090349

Kasprzak, M., Strzelecki, M. C., Traczyk, A., Kondracka, M., Lim, M., & Krzysztof, M. (2017). On the potential for a bottom active layer below coastal permafrost: The impact of seawater on permafrost degradation imaged by electrical resistivity tomography (Hornsund, SW Spitsbergen). *Geomorphology*, *293*, 347–359. https://doi.org/10.1016/j.geomorph.2016.06.013

Kaverin, D. A., Melnichuk, E. B., Shiklomanov, N. I., Kakunov, N. B., Pastukhov, A. V., & Shiklomanov, A. N. (2018). Long-term changes in the ground thermal regime of an artificially drained thaw-lake basin in the Russian European north. *Permafrost and Periglacial Processes*, *29*(1), 49–59. https://doi.org/10.1002/ppp.1963

Kholodov, A., Rivkina, E., Gilichinsky, D., Fyodorov-Davydov, D., Gubin, S., Sorokovikov, V., et al. (2003). Estimation of the organic carbon input into Arctic Ocean due to erosion of Laptev and East-Siberian seashore. *Cryosphere Earth*, *7*(3), 3–12.

Kirschke, S., Bousquet, P., Ciais, P., Saunois, M., Canadell, J. G., Dlugokencky, E. J., et al. (2013). Three decades of global methane sources and sinks. *Nature Geoscience*, *6*(10), 813–823. https://doi.org/10.1038/ngeo1955

Kraev, G., Rivkina, E., Vishnivetskaya, T., Belonosov, A., van Huissteden, J., Kholodov, A., et al. (2019). Methane in gas shows from boreholes in epigenetic permafrost of Siberian Arctic. *Geosciences*, *9*(2), 67. https://doi.org/10.3390/geosciences9020067

Lantuit, H., Atkinson, D., Paul Overduin, P., Grigoriev, M., Rachold, V., Grosse, G., & Hubberten, H.-W. (2011). Coastal erosion dynamics on the permafrost-dominated Bykovsky Peninsula, north Siberia, 1951–2006. *Polar Research*, *30*(1), 7341. https://doi.org/10.3402/polar.v30i0.7341

Lantuit, H., Overduin, P. P., Couture, N., Wetterich, S., Aré, F., Atkinson, D., et al. (2011). The Arctic coastal dynamics database: A new classification scheme and statistics on Arctic permafrost coastlines. *Estuaries and Coasts*, *35*(2), 383–400. https://doi.org/10.1007/s12237-010-9362-6

Ling, F., & Zhang, T. (2004). Modeling study of talik freeze-up and permafrost response under drained thaw lakes on the Alaskan Arctic Coastal Plain. *Journal of Geophysical Research*, *109*(D1), D01111. https://doi.org/10.1029/2003JD003886

Malakhova, V. (2016). On the thermal influence of thermokarst lakes on the subsea permafrost evolution. In *22nd International Symposium on Atmospheric and Ocean Optics: Atmospheric Physics* (Vol. 10035). International Society for Optics and Photonics. https://doi.org/10.1117/12.2248714

Malakhova, V., & Eliseev, A. (2018). Influence of rift zones and thermokarst lakes on the formation of subaqueous permafrost and the stability zone of methane hydrates of the Laptev Sea shelf in the Pleistocene. *Ice and Snow*, *58*(2), 231–242. https://doi.org/10.15356/2076-6734-2018-2-231-242

Morgenstern, A., Overduin, P. P., Günther, F., Stettner, S., Ramage, J., Schirrmeister, L., et al. (2020). Thermo-erosional valleys in Siberian ice-rich permafrost. *Permafrost and periglacial processes*. *32*, 59–75. https://doi.org/10.1002/ppp.2087

Nicolsky, D., Romanovsky, V. E., Romanovskii, N. N., Kholodov, A. L., Shakhova, N. E., & Semiletov, I. P. (2012). Modeling sub-sea permafrost in the East Siberian Arctic Shelf: The Laptev Sea region. *Journal of Geophysical Research*, *117*(F3), F03028. https://doi.org/10.1029/2012JF002358

Nicolsky, D., & Shakhova, N. (2010). Modeling sub-sea permafrost in the East Siberian Arctic Shelf: The Dmitry Laptev strait. *Environmental Research Letters*, *5*, 015006. https://doi.org/10.1088/1748-9326/5/1/015006

O'Neill, H. B., Roy-Leveillee, P., Lebedeva, L., & Ling, F. (2020). Recent advances (2010–2019) in the study of taliks. *Permafrost and Periglacial Processes*. *31*, 346–357. https://doi.org/10.1002/ppp.2050

Osterkamp, T. E. (2001). Sub-sea permafrost. In J. H. Steele, S. A. Thorpe, & K. K. Turekian (Eds.), *Encyclopedia of ocean sciences* (Vol. 5, pp. 2902–2912). Academic Press. https://doi.org/10.1006/rwos.2001.0008

Osterkamp, T. E., Baker, G. C., Harrison, W. D., & Matava, T. (1989). Characteristics of the active layer and shallow subsea permafrost. *Journal of Geophysical Research*, *94*(CII), 16227–16236. https://doi.org/10.1029/JC094iC11p16227

Overduin, P. P., Schneider von Deimling, T., Miesner, F., Grigoriev, M., Ruppel, C., Vasiliev, A., et al. (2019). Submarine permafrost map in the Arctic modeled using 1D transient heat flux (SuPerMAP). *Journal of Geophysical Research: Oceans*, *124*(6), 3490–3507. https://doi.org/10.1029/2018JC014675

Overduin, P. P., Westermann, S., Yoshikawa, K., Haberlau, T. S., Romanovsky, V., & Wetterich, S. (2012). Geoelectric observations of the degradation of nearshore submarine permafrost at Barrow (Alaskan Beaufort Sea). *Journal of Geophysical Research: Earth Surface*, *117*(F2), F02004. https://doi.org/10.1029/2011JF002088

Overduin, P. P., Wetterich, S., Günther, F., Grigoriev, M. N., Grosse, G., Schirrmeister, L., et al. (2016). Coastal dynamics and submarine permafrost in shallow water of the central Laptev Sea, East Siberia. *The Cryosphere*, *10*(4), 1449–1462. https://doi.org/10.5194/tc-10-1449-2016

Pedrazas, M. N., Cardenas, M. B., Demir, C., Watson, J. A., Connolly, C. T., & McClelland, J. W. (2020). Absence of ice-bonded permafrost beneath an Arctic lagoon revealed by electrical geophysics. *Science Advances*, *6*(43), eabb5083. https://doi.org/10.1126/sciadv.abb5083

Porter, C., Morin, P., Howat, I., Noh, M.-J., Bates, B., Peterman, K., et al. (2018). *ArcticDEM, Harvard Dataverse, V1*. Polar Geospatial Center, University of Minnesota. Retrieved from https://www.pgc.umn.edu/data/arcticdem/ [accessed January 2019]

Portnov, A., Mienert, J., Winsborrow, M., Andreassen, K., Vadakkepuliyambatta, S., Semenov, P., & Gataullin, V. (2018). Shallow carbon storage in ancient buried thermokarst in the South Kara Sea. *Scientific Reports*, *8*, 2045–2322. https://doi.org/10.1038/s41598-018-32826-z

Rekant, P., Bauch, H. A., Schwenk, T., Portnov, A. D., Gusev, E., Spiess, R., et al. (2015). Evolution of subsea permafrost landscapes in Arctic Siberia since the Late Pleistocene: A synoptic insight from acoustic data of the Laptev Sea. *arktos*, *1*(1), 1–15. https://doi.org/10.1007/s41063-015-0011-y

Riseborough, D., Shiklomanov, N., Etzelmüller, B., Gruber, S., & Marchenko, S. (2008). Recent advances in permafrost modelling. *Permafrost and Periglacial Processes*, *19*(2), 137–156. https://doi.org/10.1002/ppp.615

Romanovskii, N. N., Hubberten, H.-W., Gavrilov, A. V., Tumskoy, V. E., Tipenko, G. S., Grigoriev, M. N., & Siegert, C. (2000). Thermokarst and land-ocean interactions, Laptev Sea region, Russia. *Permafrost and Periglacial Processes*, *11*, 137–152. https://doi.org/10.1002/1099-1530(200004/06)11:2<137::aid-ppp345>3.0.co;2-l
Ruppel, C. D. (2015). Permafrost-associated gas hydrate: Is it really approximately 1% of the global system? *Journal of Chemical & Engineering Data*, *60*, 429–436. https://doi.org/10.1021/je500770m
Ruppel, C. D., Herman, B. M., Brothers, L. L., & Hart, P. E. (2016). Subsea ice-bearing permafrost on the U.S. Beaufort margin: 2. borehole constraints. *Geochemistry, Geophyics, Geosystems*, *17*, 4333–4353. https://doi.org/10.1002/2016GC006582
Ruppel, C. D., & Kessler, J. D. (2017). The interaction of climate change and methane hydrates. *Review of Geophysics*, *55*(1), 126–168. https://doi.org/10.1002/2016RG000534
Saunois, M., Stavert, A. R., Poulter, B., Bousquet, P., Canadell, J. G., Jackson, R. B., et al. (2020). The global methane budget 2000–2017. *Earth System Science Data*, *12*(3), 1561–1623. https://doi.org/10.5194/essd-12-1561-2020
Sayedi, S. S., Abbott, B. W., Thornton, B. F., Frederick, J. M., Vonk, J. E., Overduin, P., et al. (2020). Subsea permafrost carbon stocks and climate change sensitivity estimated by expert assessment. *Environmental Research Letters*, *15*(12), 124075. https://doi.org/10.1088/1748-9326/abcc29
Schirrmeister, L., Grigoriev, M., Strauss, J., Grosse, G., Overduin, P. P., Kholodov, A., et al. (2018). Sediment characteristics of a thermokarst lagoon in the northeastern Siberian Arctic (Ivashkina Lagoon, Bykovsky Peninsula). *arktos*, *4*. https://doi.org/10.1007/s41063-018-0049-8
Sellmann, P. V., Delanney, A. J., & Arcone, S. A. (1989). *Coastal submarine permafrost and bedrock observations using DC resistivity*. National Technical Information Service. Retrieved from https://apps.dtic.mil/sti/pdfs/ADA210784.pdf
Shakhova, N., Semiletov, I., & Chuvilin, E. (2019). Understanding the permafrost-hydrate system and associated methane releases in the Siberian Arctic Shelf. *Geosciences*, *9*(6), 251. https://doi.org/10.3390/geosciences9060251
Shakhova, N., Semiletov, I., Gustafsson, O., Sergienko, N., Lobkovsky, L., Dudarev, O., et al. (2017). Current rates and mechanisms of subsea permafrost degradation in the East Siberian Arctic Shelf. *Nature Communications*, *8*, 15872. https://doi.org/10.1038/ncomms15872
Shakhova, N., Semiletov, I., Leifer, I., Salyuk, A., Rekant, P., & Kosmach, D. (2010). Geochemical and geophysical evidence of methane release over the East Siberian Arctic Shelf. *Journal of Geophysical Research*, *115*(C8), C08007. https://doi.org/10.1029/2009JC005602
Shmelev, D., Veremeeva, A., Kraev, G., Kholodov, A., Spencer, R. G., Walker, W. S., & Rivkina, E. (2017). Estimation and sensitivity of carbon storage in permafrost of north-eastern Yakutia. *Permafrost and Periglacial Processes*, *28*(2), 379–390. https://doi.org/10.1002/ppp.1933
Stephani, E., Drage, J., Miller, D., Jones, B. M., & Kanevskiy, M. (2020). Taliks, cryopegs, and permafrost dynamics related to channel migration, Colville River Delta, Alaska. *Permafrost and Periglacial Processes*, *31*(2), 239–254. https://doi.org/10.1002/ppp.2046
Strauss, J., Schirrmeister, L., Grosse, G., Fortier, D., Hugelius, G., Knoblauch, C., et al. (2017). Deep Yedoma permafrost: A synthesis of depositional characteristics and carbon vulnerability. *Earth-Science Reviews*, *172*, 75–86. https://doi.org/10.1016/j.earscirev.2017.07.007
Strauss, J., Schirrmeister, L., Grosse, G., Wetterich, S., Ulrich, M., Herzschuh, U., & Hubberten, H.-W. (2013). The deep permafrost carbon pool of the Yedoma region in Siberia and Alaska. *Geophysical Research Letters*, *40*(23), 6165–6170. https://doi.org/10.1002/2013GL058088
Ulrich, M., Grosse, G., Strauss, J., & Schirrmeister, L. (2014). Quantifying wedge-ice volumes in Yedoma and thermokarst basin deposits. *Permafrost and Periglacial Processes*, *25*(3), 151–161. https://doi.org/10.1002/ppp.1810
Vasiliev, A., Melnikov, V., Streletskaya, I., & Oblogov, G. (2017). Permafrost aggradation and methane production in low accumulative laidas (tidal flats) of the Kara Sea. *Doklady Earth Sciences*, *476*, 1069–1072. https://doi.org/10.1134/S1028334X17090203
Vest Christiansen, A., & Auken, E. (2012). A global measure for depth of investigation. *Geophysics*, *77*(4), WB171–WB177. https://doi.org/10.1190/geo2011-0393.1
Westermann, S., Schuler, T. V., Gisnås, K., & Etzelmüller, B. (2013). Transient thermal modeling of permafrost conditions in southern Norway. *The Cryosphere*, *7*(2), 719–739. https://doi.org/10.5194/tc-7-719-2013
Wild, B., Shakhova, N., Dudarev, O., Ruban, A., Kosmach, D., Tumskoy, V., et al. (2018). Organic matter across subsea permafrost thaw horizons on the East Siberian Arctic Shelf. *The Cryosphere Discuss*. https://doi.org/10.5194/tc-2018-229
Wu, Y., Nakagawa, S., Kneafsey, T. J., Dafflon, B., & Hubbard, S. (2017). Electrical and seismic response of saline permafrost soil during freeze-thaw transition. *Journal of Applied Geophysics*, *146*, 16–26. https://doi.org/10.1016/j.jappgeo.2017.08.008
Zimov, S. A., Schuur, E. A., & Chapin, F. S. (2006). Permafrost and the global carbon budget. *Science*, *312*(5780), 1612–1613. https://doi.org/10.1126/science.1128908

C

Microbial methane cycling in sediments of Arctic thermokarst lagoons

Sizhong Yang[1,2*], Sara E. Anthony[3*], Maren Jenrich[4,5], Michiel H. in 't Zandt[6,7], Jens Strauss[4], Pier Paul Overduin[4], Guido Grosse[4,5], Michael Angelopoulos[4], Boris K. Biskaborn[8], Mikhail N. Grigoriev[9], Dirk Wagner[1,5], Christian Knoblauch[10,11], Andrea Jaeschke[3], Janet Rethemeyer[3], Jens Kallmeyer[1], and Susanne Liebner[1,12]

[1] GFZ German Research Center for Geosciences, Helmholtz Centre Potsdam, Section Geomicrobiology, Potsdam, Germany

[2] Cryosphere Research Station on the Qinghai-Tibet Plateau, State Key Laboratory of Cryospheric Science, Northwest Institute of Eco-Environment and Resources, Chinese Academy of Sciences, Lanzhou, China

[3] Institute of Geology and Mineralogy, University of Cologne, Cologne, Germany

[4] Permafrost Research Section, Alfred Wegener Institute Helmholtz Center for Polar and Marine Research, Potsdam, Germany

[5] Institute of Geosciences, University of Potsdam, Potsdam, Germany

[6] Department of Microbiology, RIBES, Radboud University, Nijmegen, the Netherlands

[7] Netherlands Earth System Science Center, Utrecht University, Utrecht, the Netherlands

[8] Polar Terrestrial Environmental Systems Section, Alfred Wegener Institute Helmholtz Center for Polar and Marine Research, Potsdam, Germany

[9] Laboratory of General Geocryology, Melnikov Permafrost Institute, Siberian Branch of the Russian Academy of Sciences, Yakutsk, Russia

[10] Institute of Soil Science, Universität Hamburg, Hamburg, Germany

[11] Center for Earth System Research and Sustainability, Universität Hamburg, Hamburg, Germany [12] Institute of Biochemistry and Biology, University of Potsdam, Potsdam, Germany

[*] contributed equally to this work

This chapter is published in:

Global Change Biology - DOI: 10.1111/gcb.16649, 2023

AUTHOR CONTRIBUTIONS

M. Jenrich created Figure 1, calculated the extend of pan-Arctic lagoons and contributed in revising and reviewing the manuscript draft.

Received: 1 July 2022 | Accepted: 27 January 2023

DOI: 10.1111/gcb.16649

Global Change Biology WILEY

RESEARCH ARTICLE

Microbial methane cycling in sediments of Arctic thermokarst lagoons

Sizhong Yang[1,2] | Sara E. Anthony[3] | Maren Jenrich[4,5] | Michiel H. in 't Zandt[6,7] | Jens Strauss[4] | Pier Paul Overduin[4] | Guido Grosse[4,5] | Michael Angelopoulos[4] | Boris K. Biskaborn[8] | Mikhail N. Grigoriev[9] | Dirk Wagner[1,5] | Christian Knoblauch[10,11] | Andrea Jaeschke[3] | Janet Rethemeyer[3] | Jens Kallmeyer[1] | Susanne Liebner[1,12]

[1]GFZ German Research Center for Geosciences, Helmholtz Centre Potsdam, Section Geomicrobiology, Potsdam, Germany

[2]Cryosphere Research Station on the Qinghai-Tibet Plateau, State Key Laboratory of Cryospheric Science, Northwest Institute of Eco-Environment and Resources, Chinese Academy of Sciences, Lanzhou, China

[3]Institute of Geology and Mineralogy, University of Cologne, Cologne, Germany

[4]Permafrost Research Section, Alfred Wegener Institute Helmholtz Center for Polar and Marine Research, Potsdam, Germany

[5]Institute of Geosciences, University of Potsdam, Potsdam, Germany

[6]Department of Microbiology, RIBES, Radboud University, Nijmegen, the Netherlands

[7]Netherlands Earth System Science Center, Utrecht University, Utrecht, the Netherlands

[8]Polar Terrestrial Environmental Systems Section, Alfred Wegener Institute Helmholtz Center for Polar and Marine Research, Potsdam, Germany

[9]Laboratory of General Geocryology, Melnikov Permafrost Institute, Siberian Branch of the Russian Academy of Sciences, Yakutsk, Russia

[10]Institute of Soil Science, Universität Hamburg, Hamburg, Germany

[11]Center for Earth System Research and Sustainability, Universität Hamburg, Hamburg, Germany

[12]Institute of Biochemistry and Biology, University of Potsdam, Potsdam, Germany

Correspondence

Sizhong Yang, GFZ German Research Center for Geosciences, Helmholtz Centre Potsdam, Section Geomicrobiology, Telegrafenberg, 14473 Potsdam, Germany.
Email: syang@gfz-potsdam.de

Sara E. Anthony, Department of Landscape Ecology, University of Rostock, 18059 Rostock, Germany.
Email: sara.anthony@uni-rostock.de

Susanne Liebner, Institute of Biochemistry and Biology, University of Potsdam, 14476 Potsdam, Germany.
Email: sliebner@gfz-potsdam.de

Present address

Sara E. Anthony, Department of Landscape Ecology, Faculty of Agricultural and Environmental Sciences, University of Rostock, Rostock, 18059, Germany

Abstract

Thermokarst lagoons represent the transition state from a freshwater lacustrine to a marine environment, and receive little attention regarding their role for greenhouse gas production and release in Arctic permafrost landscapes. We studied the fate of methane (CH_4) in sediments of a thermokarst lagoon in comparison to two thermokarst lakes on the Bykovsky Peninsula in northeastern Siberia through the analysis of sediment CH_4 concentrations and isotopic signature, methane-cycling microbial taxa, sediment geochemistry, lipid biomarkers, and network analysis. We assessed how differences in geochemistry between thermokarst lakes and thermokarst lagoons, caused by the infiltration of sulfate-rich marine water, altered the microbial methane-cycling community. Anaerobic sulfate-reducing ANME-2a/2b methanotrophs dominated the sulfate-rich sediments of the lagoon despite its known seasonal alternation between brackish and freshwater inflow and low sulfate concentrations compared to the usual marine ANME habitat. Non-competitive methylotrophic methanogens dominated the methanogenic community of the lakes and

Sizhong Yang and Sara E. Anthony are joint first authors.

Michiel H. in 't Zandt, Soil Biology Group, Wageningen University, Wageningen, the Netherlands

Funding information
Alfred Wegener Institute Helmholtz Centre for Polar and Marine Research; Bundesministerium für Bildung und Forschung, Grant/Award Number: CarboPerm 03F0764A, CarboPerm 03F0764F, KoPf 03G0836A and KoPf 03G0836D; National Natural Science Foundation of China, Grant/Award Number: 42271155; Chinese Academy of Sciences; Deutsche Bundesstiftung Umwelt, Grant/Award Number: Characterisation of organic carbon and estimation; Deutsche Forschungsgemeinschaft, Grant/Award Number: Baltic TRANSCOAST Research Training Group, GRK2000 and Cluster of Excellence CLICCS at Universität Hamburg; Deutsche GeoForschungsZentrum, GFZ; FP7 Ideas: European Research Council, Grant/Award Number: PETA-CARB 338335; Helmholtz Gemeinschaft (HGF), Grant/Award Number: Impulse and Networking Fund (#ERC-0013) and Helmholtz Young Investigators Group (VH-NG-919)

the lagoon, independent of differences in porewater chemistry and depth. This potentially contributed to the high CH_4 concentrations observed in all sulfate-poor sediments. CH_4 concentrations in the freshwater-influenced sediments averaged $1.34 \pm 0.98\,\mu mol\,g^{-1}$, with highly depleted $\delta^{13}C$-CH_4 values ranging from −89‰ to −70‰. In contrast, the sulfate-affected upper 300 cm of the lagoon exhibited low average CH_4 concentrations of $0.011 \pm 0.005\,\mu mol\,g^{-1}$ with comparatively enriched $\delta^{13}C$-CH_4 values of −54‰ to −37‰ pointing to substantial methane oxidation. Our study shows that lagoon formation specifically supports methane oxidizers and methane oxidation through changes in pore water chemistry, especially sulfate, while methanogens are similar to lake conditions.

KEYWORDS
^{13}C, ANME, AOM, coastal permafrost, methanotrophs, methylotrophic methanogenesis, MOB, permafrost thaw, sulfate-methane transition zone, sulfate reduction

1 | INTRODUCTION

Northern permafrost contains an estimated 1035 ± 150 PG of organic carbon within the top three meters (Hugelius et al., 2014), which is more than 30% of total terrestrial soil organic carbon (Strauss et al., 2021) and disproportionally high, given its limited coverage of 15%–22% of the terrestrial area (Schuur et al., 2015). The warming climate has triggered permafrost degradation with a variety of consequences for the landscape (Biskaborn et al., 2019), including top-down thaw, increasing active layer over long term, thermo-erosion along coasts, rivers, and lake shores, rapid thawing associated with thermokarst processes (Strauss et al., 2017; Turetsky et al., 2020) and significant land subsidence (Anders et al., 2020; Antonova et al., 2018). Thermokarst develops in the lowland areas of ice-rich permafrost, and typically results in formation of thermokarst ponds or lakes (Bouchard et al., 2016) and reassembly of permafrost microbiomes (Ernakovich et al., 2022). Thermokarst landscapes are estimated to cover approximately 20%–40% of permafrost regions (Olefeldt et al., 2016; Strauss et al., 2017). Thermokarst lakes are hotspots of CH_4 emission (Pellerin et al., 2022; Walter Anthony et al., 2016), especially those lakes that formed in organic-rich Yedoma permafrost, which contains approximately 40% of total permafrost carbon. As CH_4 *has* approximately 34 times the global warming potential of carbon dioxide (CO_2) over 100 years (Dean et al., 2018; Myhre et al., 2013), excessive CH_4 emissions from thermokarst landscapes can yield disproportionate CO_2 equivalents and feedback to the climate system (Serikova et al., 2019; Walter Anthony et al., 2018).

Marine systems only contribute 1%–2% of global CH_4 emissions even though they cover approximately 70% of the earth's surface, due to effective reduction of CH_4 emissions through anaerobic methane oxidation coupled with sulfate reduction termed S-AOM (Hinrichs & Boetius, 2002; Knittel et al., 2019; Wallenius et al., 2021). S-AOM consortia, symbiosis between anaerobic methanotrophic archaea (ANMEs) and sulfate-reducing bacteria, are widespread in marine systems, although ANMEs are very slow growing (Knittel & Boetius, 2009). There are three main clades of marine ANMEs: ANME-1, ANME-2 (further split into subclusters ANME-2a/2b and ANME-2c), and ANME-3. The differentiation between the clades is based on their relation to already cultivated methanogens, for example the ANME-2 clade is closely related to *Methanosarcinales* (Hinrichs et al., 1999; Knittel et al., 2005; Timmers et al., 2015). Because ANME organisms are ubiquitous in marine environments where CH_4 and sulfate are present, they potentially also establish in Arctic lagoons.

Thermokarst lagoons represent a transitional state between freshwater thermokarst lakes and a fully marine environment. The functionality of thermokarst lagoons in carbon turnover and greenhouse gas release has received little attention so far despite their importance in coastal carbon dynamics (In 't Zandt et al., 2020) and widespread occurrence along Arctic coasts (Angelopoulos et al., 2021). Lagoon formation occurs when intrusion of marine water introduces high concentrations of ions, especially sulfate, to the geochemical profiles of previous freshwater lakes (Spangenberg et al., 2021). Vertical diffusion of these salts also changes the ion composition of the freshwater sediments, creating a salt gradient across several meters of sediment (Angelopoulos et al., 2020). The sediment geochemistry of thermokarst lagoons largely depend on their hydrological connection with the sea. For example, open lagoons have a constant exchange with the sea leading to a more stable mixing regime and higher salinity and sulfate concentrations, while semi-closed lagoons have a seasonal connection that is often interrupted during winter months due to ice thickening resulting in seasonally more variable environmental conditions (Jenrich et al., 2021; Schirrmeister et al., 2018).

One impact of marine-water intrusion could be a change in methane production pathway and the methanogenic community. Methanogenesis is accomplished through three main pathways: hydrogenotrophic, which utilizes hydrogen and carbon dioxide; acetoclastic, which utilizes acetate; and methylotrophic, which uses simple methylated compounds, such as methanol or methylamines (Liu & Whitman, 2008; Sollinger & Urich, 2019). Acetoclastic and hydrogenotrophic methanogenesis are more susceptible to competition (Froelich et al., 1979; Jørgensen, 2006), such as from sulfate reducing bacteria (SRB), whereas methylotrophic methanogens are thought to be non-competitive and therefore could continue under conditions unacceptable for the other two pathways (Liu & Whitman, 2008; Lyu et al., 2018). Indeed, recent studies have shown methylotrophic methanogenesis occurring in sulfate-rich areas, for example in the sulfate–methane transition zone of estuaries (Maltby et al., 2018; Sela-Adler et al., 2017).

We investigated sediments of two thermokarst lakes and a thermokarst lagoon on the Bykovsky Peninsula in northeastern Siberia as a natural laboratory for the impacts of marine-water intrusion on methane cycling through the analysis of sediment CH_4 concentrations and isotopic signature, methane-cycling microbial taxa, sediment geochemistry, and lipid biomarkers.

2 | MATERIALS AND METHODS

2.1 | Site description

The study area is located on the Bykovsky Peninsula, southeast of the Lena Delta in the Buor-Khaya Gulf of the Laptev Sea in northeastern Siberia, Russia (Figure 1). Three of the water bodies on the peninsula were selected for this study: two freshwater thermokarst lakes, Lake Golzovoye (also anglicized as Goltsovoye, abbreviated as LG in this study) and Northern Polar Fox Lake (LNPF) and one thermokarst lagoon, Polar Fox Lagoon (PFL). Initial thermokarst lake formation occurred between 12,500 and 9400 years cal BP (calibrated, before present), before the peninsula itself was shaped (Grosse et al., 2007). Lake Golzovoye is relatively young, and formed approximately 8000 years cal BP (Jongejans et al., 2020). Northern Polar Fox Lake and Polar Fox Lagoon lie within the same partially drained thermokarst basin (Angelopoulos et al., 2020), with the lake to the north of the lagoon. The basin may have gone through repeated draining events between initial formation and present (Grosse et al., 2007; Jenrich, 2020). The channel between the lagoon and Tiksi Bay likely only formed within the last 2000 years cal BP. Thus, we view Northern Polar Fox Lake and Polar Fox Lagoon as two successive stages in the transition of coastal thermokarst landscapes into marine environments. The lagoon in its present state is a nearly closed system with a wide, shallow, and winding channel supplying it with water from Tiksi Bay during the summer, with large seasonal variation in salinity and ion concentrations such as sulfate and chloride (Angelopoulos et al., 2020; Spangenberg et al., 2021). The mean annual electrical conductivity of Tiksi Bay is 7.1 mS cm^{-1}, but values as high as 15 mS cm^{-1} have been observed in winter (Angelopoulos et al., 2020).

2.2 | Field work and sampling

During a drilling campaign on the Bykovsky Peninsula in April 2017, cores PG2420, PG2426, and PG2423 were retrieved from LG, LNPF, and PFL, with drilling depths from the sediment surface of 5.2, 5.4, and 6.1 m, respectively. Water height above sediment surface was 510, 560, and 310 cm for LG, LNPF and PFL, respectively. The cores were recovered with a hammer-driven 60 mm Niederreiter piston corer (UWITEC™) in overlapping sections retrieved in 3-m-core barrels. All cores consisted of unfrozen sediment at time of sampling. After retrieval, the cores were cut into 10 cm liner segments. The cores were cut with an electric saw. To avoid contamination, the saw blade was wiped with ethanol in between the cuttings and handling was done using nitrile gloves. The segments were packed in N_2-flushed, vacuum sealed opaque bags and were stored at approximately 4°C (pore water analysis) or frozen (molecular analysis, lipid biomarkers, bulk analysis) before processing. Samples were frozen at −20°C on-site and were kept frozen until further processing in the lab starting in September 2019. Sampling for sediment CH_4 concentrations and isotopes as well as molecular work was done in a cleaned and weather-protected tent at the coring site without time delay after a core was retrieved. Defined sediment plugs (3 cm^3) were obtained from the edges of the 10 cm core slices using cut syringes and placed into 20 mL vials containing saturated NaCl (gas analysis) or into sterile 15 mL falcon tubes (molecular work). A total of 139 of the 10 cm segments were used for analyses: 41 from LG, 39 from LNPF, and 59 from PFL.

2.3 | Porewater sampling and analysis

Porewater samples were extracted using a hydraulic press in an anoxic glovebox and then filtered through a 0.45 μm microporous membrane. pH was measured with a WTW MultiLab 540 probe (WTW, Germany). Samples were analyzed by suppressed ion chromatography for all major cations and anions. Alkalinity was measured by colorimetric titration. Dissolved iron (ferric and ferrous) concentrations in pore water were measured via spectrophotometry by the ferrozine method (Viollier et al., 2000), with a detection limit of 0.25 μM. Samples were measured at GFZ German Research Centre for Geosciences.

2.4 | CH_4 concentrations and carbon isotopes

Concentrations of CH_4 were determined by static headspace gas chromatography (GC7890, Agilent Technologies, USA) with a flame

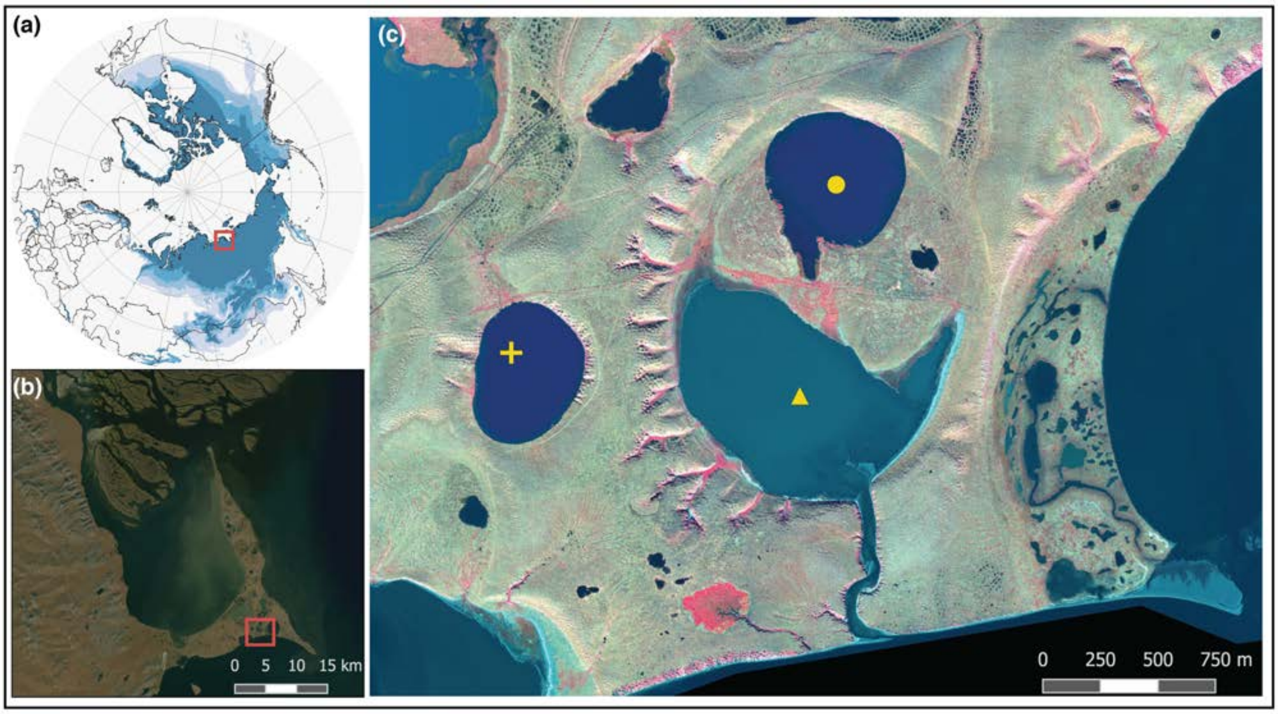

FIGURE 1 Location and map of the study site showing (a) location with respect to the Northern Hemisphere and permafrost extent regions (b) location with respect to the Bykovsky Peninsula, and (c) relative location of the lakes and the lagoon. Note the small channel at the bottom of PFL connecting to Tiksi Bay. Symbols show location of coring sites: Triangle—Polar Fox Lagoon; Circle—Northern Polar Fox Lake; Cross—Lake Golzovoye. Map in (a) based on Brown et al. (1997), (b) ESRI Satellite World Imagery, and (c) based on WorldView-3 false color satellite image (8–5–3), acquired 2016-09-02 (©DigitalGlobe). Map lines delineate study areas and do not necessarily depict accepted national boundaries.

ionizing detector (FID). Before each GC measurement, the instrument was checked against standard gasses and was newly calibrated if necessary. Plug samples were mixed into a slurry before analysis, and concentrations are presented in units of micromoles of CH_4 per gram of whole sediment plug ($\mu mol\,g^{-1}$). A sediment plug was defined as 3 cm^3 of the in-situ mixture of sediment, pore water, and pore gas. Stable carbon isotope signatures of CH_4 were analyzed by isotope-ratio mass spectrometry (Delta V plus, Thermo Scientific, Dreieich, Germany) coupled to a GC-Isolink/Trace-GC (Thermo Scientific, Dreieich, Germany) at Universität Hamburg. Values are expressed relative to Vienna Peedee belemnite (VPDB) using IAEA NGS3, (−73.3‰ VPDB) as external standards. The analytical error of these analyses was ±0.2‰.

2.5 | Bulk parameters

Samples were analyzed for total carbon (TC), total organic carbon (TOC), total nitrogen (TN), and total sulfur (TS) at the University of Cologne. For analysis of TC, TN, and TS, 20–30 mg aliquots of dry sample were combined with 20 mg of tungsten trioxide (an oxidation catalyst) and were measured on an Elementar Micro Vario elemental analyzer. For TOC measurements, samples were first processed to remove inorganic carbon by adding 1% HCl to 20–50 mg of dry bulk sample for 1 h at 60°C, and then allowed to continue to react overnight at room temperature. Samples were then thoroughly rinsed with 18.2 MΩ purified water until pH was back to neutral values and dried in the oven at 60°C. Afterwards, 20 mg of tungsten oxide were added to each and samples were analyzed using the same Elementar Micro Vario elemental analyzer.

2.6 | Lipid biomarker indices

Lipid extraction was performed to obtain *n*-alkanes for use in several biomarker indices to characterize the origin of organic matter in the lakes. Samples (6–10 g dry weight) were extracted following the method of Bligh and Dyer (1959). The total lipid extracts were then separated into neutral lipid, glycolipid and phospholipid fractions using hand-packed SiOH columns and eluting with dichloromethane, acetone, and methanol, respectively. The neutral fractions (containing *n*-alkanes) were further separated using activated SiO_2 column chromatography and *n*-hexane as eluent. The *n*-alkanes were measured on a gas chromatograph equipped with an on-column injector and flame ionization detector (GC-FID, 5890 series II, Hewlett Packard, USA). A fused silica capillary column (Agilent DB-5MS; 50 m × 0.2 mm; film thickness: 0.33 µm) was used with helium as carrier gas. *n*-Alkane identification and quantification was performed using an external standard mixture of C_{21}-C_{40} *n*-alkanes (PN 04071, Sigma-Aldrich).

Detailed information about the indices used can be found in the corresponding references, but briefly:

The carbon preference index (CPI) indicates the maturity of the organic matter, where higher values are generally indicative of less degraded organic matter. Crude oil, for example, has a CPI value of approximately 1. The CPI is calculated after Marzi et al. (1993):

$$CPI_{23-33} = \frac{\Sigma \text{ odd } C_{23-31} + \Sigma \text{ odd } C_{25-33}}{2 \bullet \Sigma \text{ even } C_{24-32}}.$$

The proxy P_{aq} was proposed by Ficken et al. (2000) and first applied to permafrost by Zheng et al. (2007). The P_{aq} expresses the portion of organic matter derived from submerged or floating macrophytes ($P_{aq} > 0.4$) as opposed to emergent and terrestrial plant input ($P_{aq} < 0.4$). We used the general trend of P_{aq} rather than the absolute values due to the proxy being applied to permafrost regions only recently, and not developed for this soil type

$$P_{aq} = \frac{C_{23} + C_{25}}{C_{23} + C_{25} + C_{29} + C_{31}}.$$

2.7 | DNA extraction and Illumina sequencing of amplicons and metagenomic DNA

Total nucleic acids were extracted in duplicate using the PowerSoil-Kit (MO-BIO, Qiagen) according to the manufacturer's protocol. The concentration of DNA extracts was checked via gel electrophoresis and on a Qubit fluorometer (Invitrogen).

Amplicon libraries were prepared with the barcoded primer pair Uni515-F/Uni806-R to cover both bacterial and archaeal 16S rRNA genes (Caporaso et al., 2011). Each sample was run in technical duplicate. The 50 μL PCR reactions contained 10x Pol Buffer C (Roboklon GmbH), 25 mM $MgCl_2$, 0.2 mM deoxynucleoside triphosphate (dNTP) mix (ThermoFisher Scientific), 0.5 mM each primer (TIB Molbiol, Berlin, Germany) and 1.25 U of Optitaq Polymerase (Roboklon). The PCR program started with a denaturation step at 95°C for 10 min, followed by 35 cycles at 95°C for 15 s, annealing at 60°C for 30 s, extension at 72°C for 45 s and a final extension step at 72°C for 5 min. The tagged PCR products were then purified with the Agencourt AMPure XP kit (Beckman Coulter, Switzerland) and eluted in 30 μL DNA/RNA-free water. The purified product was quantified and then the equilibrated PCR product, together with positive and negative controls, were pooled. The sequencing was performed on an Illumina MiSeq system (paired-end, 2 × 300 bp) by Eurofins Scientific.

In addition to amplicon sequencing, metagenomic sequencing was done on six samples of sediment from the lagoon by using the Illumina HiSeq 2500 platform by Eurofins Scientific. These six samples are representative of the sulfate zone (combination of the 40, 100, and 130 cm core segments), the upper (190 cm core segment), middle (220 cm core segment), and bottom (250 cm core segment) of the sulfate–methane transition zone, freshwater sediment (combination of the 310, 420, and 480 cm core segments), and the talik (570 cm core segment).

2.8 | Amplicon and metagenomic data processing

For the amplicon data, raw sequences were processed according to Yang et al. (2021). The community composition was reported in ASV (amplicon sequence variants) tables using the DADA2 algorithm (Callahan et al., 2016) and the taxonomy was assigned against the SILVA138 database (https://www.arb-silva.de). In this study, special attention was paid to methanogens and aerobic/anaerobic methanotrophs. The ASV table was filtered by taxonomy to keep only methane producing archaea, and methanotrophic prokaryotes. The technical duplicates of each sample were merged. The resulting data set had 264 ASVs including methanogenic archaea, aerobic methane oxidizing bacteria (MOB) and anaerobic oxidizers of methane (AOM). A total of 23 samples (excluding technical duplicates) were analyzed: 7 each from LG and LNPF, and 9 from PFL.

Metagenomic data for the lagoon were processed including steps of quality control, assembly, and functional annotation according to the flow described by Kieser et al. (2020). Briefly, we performed quality control on Illumina data using the BBtools suite (https://sourceforge.net/projects/bbmap), and assembled with metaSpades (Nurk et al., 2017) with default settings. For the genes predicted by Prodigal (Hyatt et al., 2010), functional annotation was processed by eggNOG-mapper (v2) with DIAMOND (v0.8.22.84) (Buchfink et al., 2015) against the associated reference database eggNOG 5.0 (Cantalapiedra et al., 2021). The abundance of key functional genes (in transcripts per kilobase million, TPM) involved in methanogenesis, aerobic methane oxidation (MOB), dissimilatory nitrate reduction (DNR) and sulfate reduction (DSR) was compared to provide additional insight to the amplicon-derived data for the lagoon. To check the taxonomy bearing these genes, we taxonomically annotated the translated protein sequences of these genes using DIAMOND and compared against the UniProt90 reference database (https://www.uniprot.org).

2.9 | Network analysis

First, the ASVs with mean relative abundances of less than 0.05% across all samples were removed from downstream analysis. The resulting dataset was further filtered to only keep those ASVs with a Spearman correlation coefficient with an absolute value greater than 0.6 and a statistically significant p value of less than 0.01. These filtering steps removed poorly represented ASVs and reduced network complexity, facilitating the determination of the non-random co-occurrence of the core community. The network was then explored and visualized using the *igraph* package (v 1.2.5, Csardi & Nepusz, 2006). Community modularity was detected via a *walktrap* algorithm according to the internal ties and the pattern of ties between different groups with the *igraph* package.

To explore the association between network modularity and environment conditions, the ASV members were first used for correspondence analysis, and then the ordination object was fitted by the environmental variables with the *envfit* function in R package *vegan* (version 2.5–6) (Oksanen et al., 2019).

2.10 | Numeric and statistical analysis, and structural equation modeling

The contribution of different consortia to the total abundance and beta diversity (Bray–Curtis dissimilarity) was calculated with R package *otuSummary* (Yang, 2020). A constrained analysis, Canonical Correspondence Analysis, was used to explore the linkage between microbial community variation and environmental variables (which includes the sediment, pore water chemical composition, and CH_4 concentration and isotopic signatures) by using R package *vegan* (Oksanen et al., 2019). Variation partitioning was subsequently performed based on the returned canonical correspondence analysis object to resolve the explanatory power of pore water chemistry and sediment nutrient condition by using the *varpart* function in package *vegan*. In addition, structural equation modeling (SEM) was implemented with R package *lavaan* (v0.6.9) (Rosseel, 2012) in order to numerically estimate the observed relation between community structure and different environmental features and ecological functionality. Data visualization of environmental data, qPCR and bubble plot was performed with the *ggplot2* package (v3.3.2) (Wickham, 2016).

3 | RESULTS

3.1 | Geochemistry

The porewater and bulk geochemistry of the two freshwater lakes were very similar, though differences were seen in the CH_4 concentrations, CH_4 carbon isotopes, and iron profiles (Figure 2). While the pore water chemistry results of the lower half of the lagoon sediment were quite similar to the lakes, large differences in alkalinity, salinity, chloride and sulfate concentrations, pH, and $\delta^{13}C\text{-}CH_4$ were observed in the upper 300 cm. These results reflected the freshwater condition of the porewater of the lakes, LG and LNPF, and brackish condition pore water in the upper sediment (and surface water) of the lagoon, PFL, and demonstrated that the pore water in the deeper lagoon sediment was still in a freshwater condition. The C:N ratio was roughly similar over the entire sediment profiles of both lakes, ranging from 7–12. The C:N ratio of the upper 430 cm of sediment in the lagoon was similar to that of the lakes. However, from 430–510 cm the C:N ratio, and TOC and TN content of the lagoon were much higher than that of the lakes, and of the upper lagoon sediment.

The $\delta^{13}C\text{-}CH_4$ values in all three water bodies, except for in the sulfate-rich region of the lagoon, were highly depleted, indicating that the most dominant production pathways were either methylotrophic or hydrogenotrophic methanogenesis. Within the sulfate-rich region of the lagoon sediments, comparatively less negative, or heavy, $\delta^{13}C\text{-}CH_4$ values indicated high rates of methane oxidation.

3.2 | Biomarker indices

The upper 200 cm of sediment of each water body generally had higher P_{aq} values than the rest of the profile, indicating that those layers were composed of more submerged and floating plants, while the deeper sediments had a larger portion of emergent macrophytes and terrestrial plants. The CPI values for both lakes and the lagoon were similar for the top 100 cm, with values between 5.5–6.5, converging again at their respective maximum core depths with CPI values of 8–9. This indicated that the organic matter in the upper sediment column was slightly more degraded (lower CPI value) than that of the deeper sediment (higher CPI value). In-between these regions the CPI was quite different for each lake indicating differences in the maturity of the organic matter and decomposition processes, or changes in the vegetation cover. For example, PFL had very degraded organic matter at approximately 350 cm compared to the less degraded organic matter at approximately 410 cm. Interestingly, the highest Fe^{2+} concentration in the pore water of PFL was also observed at this depth. This potentially signifies very reduced conditions which may be slowing degradation.

3.3 | Microbial consortia of the methane cycle

Methane cycling microbes which were derived from amplicon sequencing were separated into three main groups: methanogens, aerobic methanotrophs (methane oxidizing bacteria: MOBs), and anaerobic methanotrophs (AOMs) (Figure 3). Across all samples, methanogens were dominated by the methylotrophic Methanomassiliicoccales and Methanofastidiosales, followed by the hydrogenotrophic *Methanoregula* and obligatory acetoclastic *Methanothrix* (commonly referred to as *Methanosaeta*). *Methanosarcina* (generally acetoclastic) were scattered in some samples with relatively low abundances. This, coupled with the isotope results, indicated that methylotrophic methanogenesis is the most dominant methane production pathway.

Of the anaerobic methanotrophs, ANME-2a/2b were very abundant in the sulfate-rich sediments of the lagoon (upper 300 cm). Members of the candidate family Methylomirabilaceae, such as Sh765B-TzT-35 and Z114MB74, generally prevailed across all samples but were almost absent from the upper 300 cm of sediment of the lagoon. Other members of this same family, such as "*Candidatus* Methylomirabilis oxyfera", have been shown to couple methane oxidation to nitrite reduction (Versantvoort et al., 2018). Canonical aerobic methane oxidizers (MOBs) had very low relative abundances except for the upper 10 cm of sediment of all

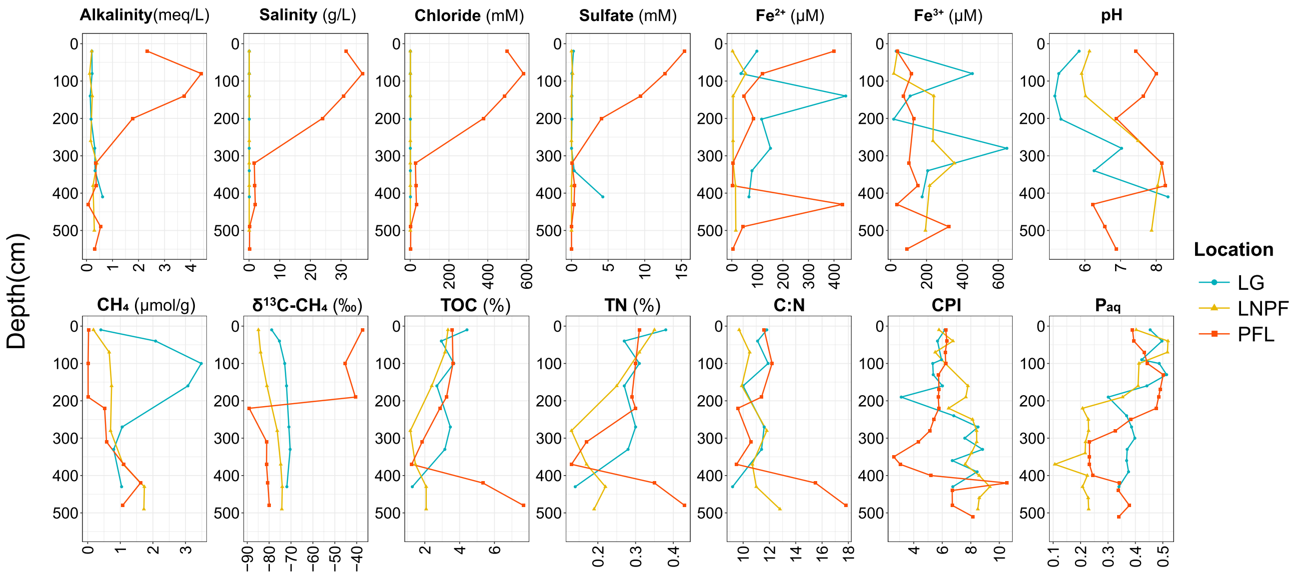

FIGURE 2 Porewater chemical features of sediments in three cores. The *y*-axis shows the depth from the sediment surface. Water height above sediment surface was 510, 560, and 310 cm for Lake Golzovoye (LG), Northern Polar Fox Lake (LNPF), and Polar Fox Lagoon (PFL), respectively. CPI, carbon preference index.

three water bodies. This indicated that aerobic methane oxidation was likely limited in the sediment column. Prevalent MOBs included mostly type I Gammaproteobacteria, such as members from *Crenothrix*, *Methylobacter*, and *Methyloprofundus* which had the highest relative abundance. Quantification of taxonomic and functional gene copy numbers through qPCR provided overall support of the relative abundances obtained from sequencing and downstream analysis. The qPCR method and results are presented in Data S1.

Metagenomic data of the lagoon sediments demonstrated a high ocurrence of genes responsible for dissimilatory sulfate reduction in the sulfate zone, and the key genes for methanogenesis (*mcrABG*) also exhibited slightly higher abundance in the sulfate zone (Figure 4). Genes which are involved in dimethylamine and trimethylamine metabolism (*mtbB* and *mttB*) were detected in the sulfate zone while the *mtmB* gene for monomethylamine metabolism was identified beneath the sulfate zone (Figure 4). The compositional variation of taxa annotated from the key genes supports this trend (Figure S1). The *pmoA* gene which is key for the canonical aerobic MOB occurred in low abundance in the two upper layers of the sulfate zone. In the sulfate zone of PFL, the *mcrABG* genes were highly associated with the taxonomic lineages of ANME-2a (ANME-2 cluster archaeon HR1, 47.4%–59.5%), followed by *Ca.* Methanoperedens (2.7%–19.3%) (Table S2). Aligned with the high occurrance of sulfate-dependent ANME2 lineage, abundant sulfate reducing genes and bacteria were also identified in the sulfate zone of the lagoon.

In the ordination space of the canonical correspondence analysis, the samples from 20–60 cm of the lagoon were generally separated from all other samples (the rest of the lagoon and the lakes) (Figure S2a). The environmental variables can explain approximately 74% of the total inertia (i.e., community variations) in the CCA analysis. The variation partition suggested that pore water chemistry was responsible for around 44% of total variance, followed by only 11% contribution by sediment features, which included TOC, TN, C:N, CPI, and P_{aq} (Figure S2b). The SEM further highlighted the strong influence of pore water chemistry on microbial assemblages versus the influence of sediment features (Figure 5). Methanogens and MOB respectively had positive and negative influences on the concentration and isotopic signature of sediment CH_4 underlining their direct role on the fate of CH_4.

3.4 | Co-occurrence and modularity

After quality filtering, 93 ASVs were used for network construction. These ASVs on average contributed 88.75% (min: 39.38%, first quartile Q_1: 88.95%, third quartile Q_3: 96.71%, max: 99.40%) to the total abundance (which constitutes 264 ASVs) and 75.05% (Q_1: 60.44%, Q_3: 90.99%) to the total Bray–Curtis dissimilarity (BC) (Table S3). Therefore, the subset of these ASVs largely represented the populations involved in methane cycling.

The species network consisted of 93 nodes (each node representing one ASV) and 1535 undirected edges (Figure 6). The density was 0.3588, the average path length was 1.716 edges with a diameter of 3 edges, and the average clustering coefficient transitivity was 0.6848. The centrality measures (degree, betweenness, closeness and eigen centrality) highlighted the importance of the lineages belonging to Methanomassiliicocales, *Methanoregula*, Methanofastidiosales and Methylomirabilaceae in the network involved in methane cycling.

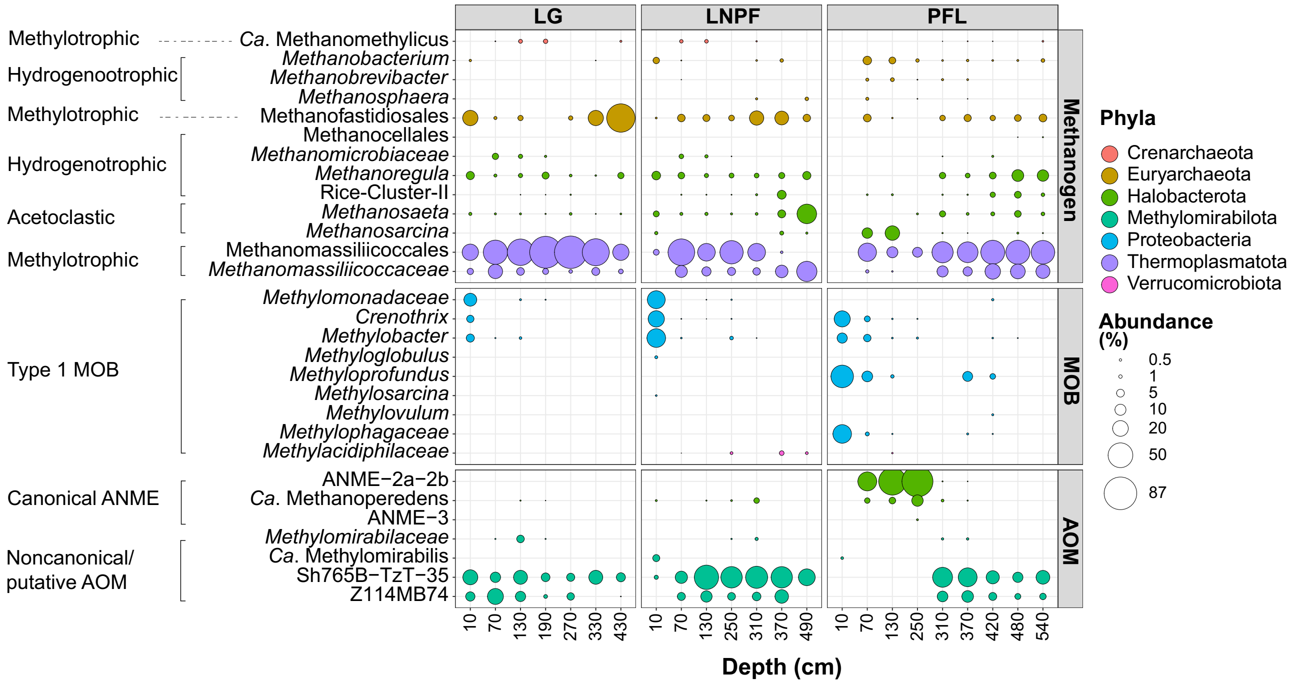

FIGURE 3 Bubble plot showing the relative abundance within the targeted subset of 264 ASVs (the abundance of all 264 ASVs sum up to 100%). The taxonomy was collapsed at genus level. If an assignment to the genus level was not possible the next higher assignable taxonomic level was used. LG: Lake Golzovoye, LNPF: Northern Polar Fox Lake, and PFL: Polar Fox Lagoon. AOM, anaerobic methane oxidizers; MOB, methane oxidizing bacteria.

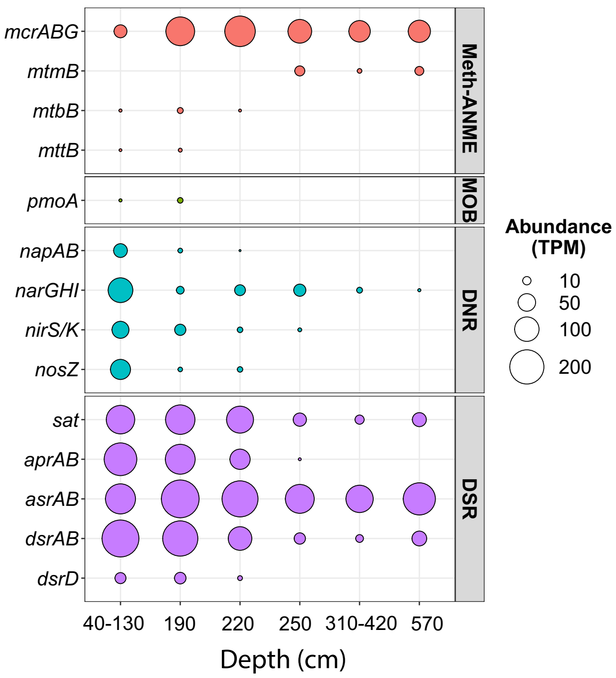

FIGURE 4 Abundance of key genes involved in methanogenesis/ANME, aerobic methane oxidization (MOB), dissimilatory nitrate reduction (DNR), and dissimilatory sulfate reduction (DSR) over six layers of Polar Fox Lagoon (PFL). The depths of 40–130 cm are in the sulfate zone; 190, 220 and 250 cm are in the upper, middle, and bottom of sulfate–methane transition zone; and depths from 310 cm and deeper are freshwater. ANME, anaerobic methanotrophic archaea.

Five modules were identified by the *walktrap* algorithm (modularity score = 0.204). With the members of each module an ordination showed that Module 1 and 4 are stretched along the first axis, suggesting association with marine-water sulfate, chloride, and alkalinity. In contrast, ASVs in Module 2, 3, and 5 are distant from the marine influenced samples, which showed stratified cluster features along axis CA2 (Figure 6; Figure S3). The distribution of different modules was likely structured by pore water chemistry. Module 2 occurred mainly in the surface samples (0–10 cm), while module 3 and 5 were distributed in down-core freshwater sediments. Across all modules, keystone taxa consisted of H_2-dependent methylotrophic methanogens which are mainly affiliated to Methanomassiliicocales or Methanofastidiosales. In Module 1 and 4, important components also include methane oxidizers like ANME-2a/b, *Candidatus* Methanoperedens and *Crenothrix*. Every module contains at least one methanogenic lineage. More specific information about which taxa were assigned to each module is available in Data S2.

4 | DISCUSSION

4.1 | Environmental conditions and history of the lagoon sediments

The porewater chemistry of the upper 300 cm of the lagoon sediments indicates that sulfate and other ions have diffused into

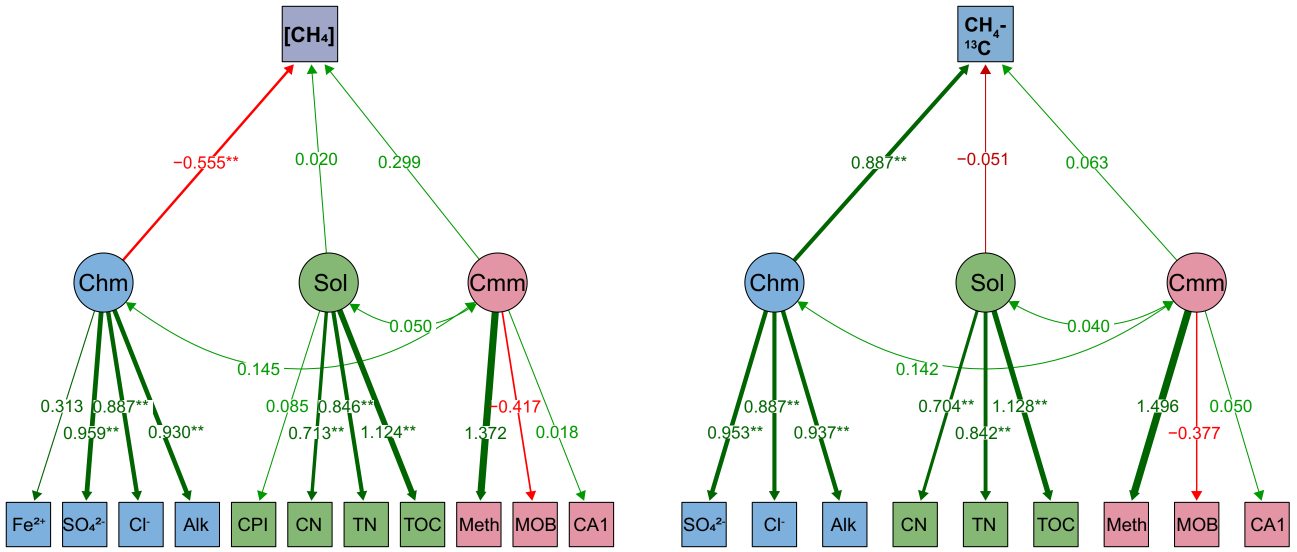

FIGURE 5 Structural equation modeling (SEM) showing the influence of latent variables, porewater chemistry (Chm), carbon and nitrogen (Sol), and Community (Cmm), on the sediment CH_4 concentration (left) and ^{13}C-CH_4 signature (right). Latent variables indicated with ovals and observed variables shown in rectangles. The residuals of observed variables is not shown here. Path coefficients standardized and significant at *p*-value <.05, and path width reflects the absolute value of standardized coefficients. The width of edges varies with absolute weights. Absolute weights under 0.3 become smaller in width. Edges with absolute weights under 0.01 were omitted. Meth: methanogen relative abundance, MOB: relative abundance of aerobic methane oxidizing bacteria, CA1: the first axis of corresponding analysis; Alk: alkalinity, [CH_4]: concentration of sediment methane (μmol g^{-1}). The Comparative Fit Indices (CFI) are 0.750 and 0.845 for the left and right analysis, respectively. The Root Mean Square Error of Approximation (RMSEA) are 0.234 and 0.235, respectively. The contribution of AOM had to be omitted in the SEM as the model did not converge due to many zero values of AOM over samples within the limited dataset.

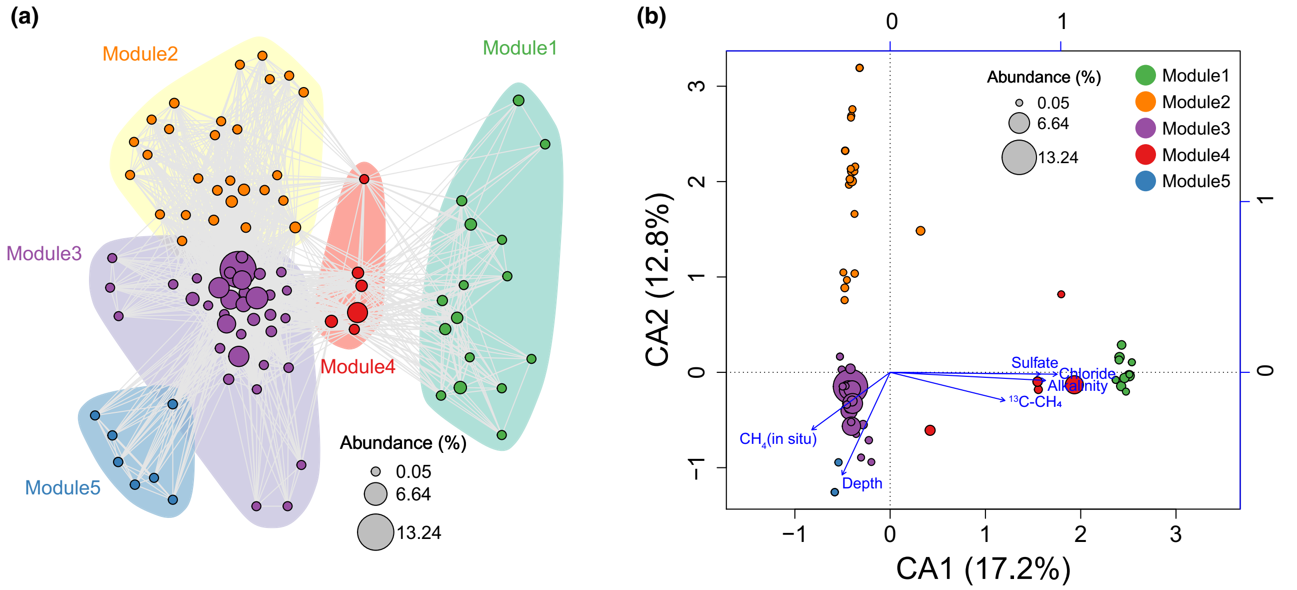

FIGURE 6 Network modules showing Modules for methane cycling consortia (a) and the association of each Module and environmental variables and features (b) in correspondence analysis ordination. Bubble size in network and ordination is corresponding to the mean relative abundance of each ASV.

sediments originally deposited under freshwater conditions, creating a marine-influenced gradient below which the porewater chemistry is comparable to the lakes. The seasonal intrusion of water from Tiksi Bay into the lagoon has fostered the formation of a sulfate zone from approximately 0–200 cm, followed by a sulfate–methane transition zone (SMTZ) from approximately 200–400 cm. This stresses the profound effect that infiltrating water from Tiksi Bay has on the porewater chemistry of the lagoon sediment, even though the lagoon is only connected to the bay during the ice-free summer months (Angelopoulos et al., 2020).

The trends in P_{aq} indicate that overall, organic matter was of a more terrestrial origin in deeper sediments of all studied water bodies, and has been slowly transitioning towards more submerged and floating plants in the shallower sediments. Though there are some differences in the C:N ratios, all three water bodies stay within a range of 8–18 over their entire profile, which indicates a similar, moderate, decomposition state of the organic matter within the sediments of all three lakes. This further supports that the sediment and organic matter composition of the lagoon was very similar to that of the freshwater lakes before marine water intrusion. This means that differences observed in the lagoon are more likely due to the marine water intrusion. This is also in line with the range found for a variety of permafrost deposits (5.4–72.6), as well as that found specifically in permafrost from the same region: approximately 5–30 (Walz et al., 2018). The C:N ratios could also indicate a large proportion of phytoplankton mixed into the sediments (Biskaborn et al., 2012; Vyse et al., 2020). The increase in CPI and C:N values in the range of 400–500 cm in the lagoon indicates that the organic matter there is less decomposed compared to the rest of the profile. This less degraded organic matter is possibly caused by partially refrozen sediment in the lagoon. For an explanation of coupled heat and salt flow in the sediment of this lagoon and consequences on frozen state of the sediment, see Angelopoulos et al. (2020).

4.2 | Lagoon formation promotes establishment of AOM consortia

The decrease of CH_4 concentration in the sulfate-rich upper part of the lagoon in conjunction with heavier isotopic values imply that thermokarst lagoons can establish a strong methane oxidation regime that reduces CH_4 concentrations compared to their freshwater analogs. Thermokarst lakes in the ice-rich permafrost lowland are generally hotspots of CH_4 emission (Walter et al., 2007; Walter Anthony et al., 2018), and our results from the sediment columns of the lakes, LG and LNPF, tend to agree with this given CH_4 concentrations of up to 2.21 μmol g^{-1} in LG, and up to 1.16 μmol g^{-1} in LNPF. The CH_4 present in the low sulfate sediment column of all three water bodies is likely a mixture of saturated or supersaturated porewater and small CH_4 gas bubbles. Calculations under the assumption that all measured CH_4 was dissolved in the porewater leads to concentrations of up to 17 mM in LG, much higher than the approximately 3.3–3.8 mM soluble at 1.51 bar (for 510 cm water depth) and 0–4°C in freshwater (Wiesenburg & Guinasso, 2002). In addition, ebullition was observed during sampling in the two freshwater lakes, but not in the lagoon. Bussmann et al. (2021) and Spangenberg et al. (2021) also saw extensive ebullition in LG during their sampling events. Evidence for the presence of CH_4 bubbles in the sediment or soil column have been observed in other studies, including in marine, lacustrine, and wetland environments (Pohlman et al., 2013; Thomsen et al., 2001; Tokida et al., 2005).

In comparison with the low sulfate sediment columns, the lagoon's maximum CH_4 concentration in the sulfate zone (0.02 μmol g^{-1}) was equivalent to only 0.4%–5% of the CH_4 concentrations of the rest of the lagoon sediment profile and of the concentrations along the entire profiles of both lakes. The reduction in porewater CH_4 concentration is concurrent with heavily enriched $\delta^{13}C$-CH_4 signatures (compared to the lakes), suggesting the occurrence of substantial CH_4 oxidation. In addition, Spangenberg et al. (2021) found that the CH_4 concentration in winter ice samples of the lagoon was as low as 10% of that in Lake Golzovoye (lagoon mean: 54.7 nM vs Golzovoye mean: 645 nM), indicating that CH_4 was still effectively attenuated in winter when the lagoon is disconnected from the bay. Angelopoulos et al. (2020) found that even though the lagoon was disconnected during the winter, continued growth of the ice cover would repel ion into the liquid phase and thus caused increased salinity in the shrinking water volume during the winter months, likely preserving the marine effect.

There is evidence that methane oxidation in the lagoon is performed by canonical anaerobic methanotrophic archaea, especially the ANME-2a/2b groups. Overall, a profound shift in CH_4 cycling consortia was observed between the freshwater lakes and the sulfate-affected portion of the lagoon, corresponding to changes in geochemical composition, in particular the high sulfate concentration and salinity. In the non-sulfate-affected region of the lagoon, the microbial community is roughly the same as in the lakes at that depth. The effect of the geochemical changes was reflected in the environmental partitioning and SEM analysis. Based on the porewater chemistry, such as the Fe^{2+} concentrations, the sediments in all three profiles below the redox boundary at about 10 cm are likely anoxic (Biskaborn et al., 2013). Previous studies working on the same lakes have also found that the sediments are anoxic except for limited oxygen availability in the top few centimeters (Jenrich, 2020; Schindler, 2019; Spangenberg et al., 2021). This would generally inhibit obligate aerobic methane oxidation below this point, providing space for the anaerobic methane oxidizing community to develop, which is supported by the amplicon sequencing and metagenomic results (Figures 3 and 4) and by overall low gene copy numbers of aerobic methane oxidizers (Figure S4). Accordingly, canonical aerobic MOBs are poorly represented in these thermokarst systems, especially in the zone of PFL where CH_4 concentrations and isotopes strongly point towards methane oxidation. The metagenomic and amplicon sequencing data support the presence of multiple types of AOMs in the lagoon. The most abundant (Figure 3) are the S-AOM ANME-2a/2b which are commonly found in classical marine environments. Their dominance is also supported by high sulfate reduction rates in the sulfate zone and SMTZ of the lagoon, which was previously shown to be at least one order of magnitude higher (ca. 50–420 nM cm^{-3} day^{-1}) than the rest of the profile and the freshwater lakes. Strong sulfate reduction in the sulfate zone of PFL could also be supported by the pronounced reduction of sediment CH_4 concentration and relatively enriched $\delta^{13}C$-CH_4 values (around −40‰) (Figure 2) and by substantially higher gene copy numbers of sulfate reducers in the lagoon (Figure S4).

The timing of the establishment of these marine ANME consortia in the lagoon is difficult to ascertain. As previously stated, the channel opened between the lagoon and Tiksi Bay approximately 2000 years ago, giving the upper limit of the time of establishment. The lower limit is unknown, but in recent studies of marine-water inundated coastal peatlands, no S-AOMs were observed even 25 years after inundation. One example comes from Weil et al. (2020), a study which included the 'Karrendorfer Wiesen', a formerly drained peatland re-wetted with marine water in 1993, which has no established S-AOM community even more than 25 years after the rewetting. In a rewetted coastal fen near Rostock in Germany with infrequent marine water intrusion events, only archaea from the so called ANME-2d group were found which are known to use nitrate as electron acceptor, but again no sulfate-driven ANMEs (like ANME 2a/2b) were observed (Wen et al., 2018). Another study in tropical coastal lagoons by Chuang et al. (2017) found very little methane oxidation activity even though sulfate and CH_4 concentrations were high.

Nitrate is also a viable terminal electron acceptor for AOM. Nitrate concentrations in the porewater, although very low in all three profiles, agree with nitrate concentrations in natural environments, which rarely exceed 50 μM (Schink, 2010). Porewater nitrate concentrations of the lagoon being below the detection limit may be a consequence of fast nitrate reduction, rather than a lack of nitrate production. This is supported the by high abundances of genes associated with denitrification and through occurrence of *Candidatus* Methanoperedens, known to couple AOM with nitrate reduction.

Ferric iron (Fe^{3+}), which is present in the low sulfate sediments of the lagoon, has also been highlighted as a potential alternative electron acceptor for methane oxidation in many other anoxic habitats (Ettwig et al., 2016; Rooze et al., 2016; Winkel et al., 2018). Such a pathway, according to a recent analysis on eutrophic coastal areas, can play an important role in mitigating CH_4 by coupling its oxidation with iron, manganese, or nitrate reduction beyond the sulfate zone in anoxic sediments due to eutrophication-associated hypoxia (Wallenius et al., 2021). Indeed, Hultman et al. (2015) found relatively high rates of iron reduction in permafrost and active zone soil incubations, indicating that iron reduction is an important process in permafrost areas. However, iron cycling is also intricately tied to methane release during thaw, with iron reduction processes causing increased emissions of methane in a thawing Palsa environment (Patzner et al., 2022). Thus, in order to fully understand the role iron plays in these environments, more targeted research is needed.

In addition to the results presented here, the work by Schindler (2019) utilizing ^{14}C-CH_4 labelling experiments also found clear evidence of AOM in the 0–200 cm lagoon sediments. Samples used by Schindler (2019) were from the cores as those used in this study. It is interesting that within the deeper sediments of LNPF and PFL, small pockets of known aerobic MOBs are present and seemingly coexisting with canonical AOM and methanogenic organisms, indicating that while this habitat is certainly not ideal for aerobic methanotrophs, it is also not completely inhospitable. As we did not perform any transcriptome analyses, we cannot make any inferences on the metabolic state of any specific group of methane oxidizers. Recent studies of other systems found evidence of methane oxidation in anaerobic sediment performed by lineages of canonical aerobic methanotrophs (MOB). For example, in their study of sub-Arctic lake sediments Martinez-Cruz et al. (2017) found that after a six-month incubation under anoxic conditions supporting methane oxidation, type I methanotrophs from the *Methylobacter* genus were the major driver of methane oxidation. This was similar to the findings of Su et al. (2015) in the anoxic sediments of a lake in Switzerland, where type I and type II aerobic methanotrophs were found to grow under both oxic and anoxic incubation conditions. In the lakes and lagoon, *Methylobacter*, and other type I methanotrophs are present, however they are most abundant in the top 10–20 cm of sediment and for the most part represent less than 1% of total abundance (Figure 3). *Crenothrix*, a known aerobic MOB, which could survive under slightly oxygen-deficient conditions in stratified lakes (Oswald et al., 2017), is also concentrated only within the top 10 cm of both lakes and the lagoon similar to other canonical MOB (Figure 3). Thus, while these organisms may be contributing to the total AOM process in sediments of all three water bodies, their contribution must be considered marginal relative to that of methanotrophic archaea (ANMEs) in the lagoon.

The abundant occurrence of the unclassified environmental groups Sh765B-TzT-35 and Z114MB74 (Figure 3) closely related with *Candidatus* Methylomirabilales, another known methane oxidizer (Ettwig et al., 2010), imply their ecological importance. The available genomes of Methylomirabilales demonstrated the existence of genes encoding particulate methane monooxygenase (pMMO) (Versantvoort et al., 2018). A recent stable isotope probing (SIP) study in wet forest soil showed that members of Sh765B-TzT-35 act as active anaerobic methanotrophs along with methylotrophic methanogens of *Methanomassiliicoccus*, which were proposed as positive biological indicators of methanotrophy and methanogenesis in wet forest soils (Nakamura, 2019). However, our understanding of the role of these clades is extremely poor and it remains open if Sh765B-TzT-35 and Z114MB74 members contribute to methane oxidation in the sediments of this study.

4.3 | Methylotrophic methanogens and the implications of their dominance

The methanogenic consortia were dominated by methylotrophic lineages, and their prevalence across all modules and depths (Figure 3) underscores the ecological importance of methylotrophic methanogenesis in all three water bodies. Methylotrophic methanogenesis has long been considered the least utilized methanogenesis pathway, with many studies instead focusing on hydrogenotrophic and acetoclastic methanogenesis. As Zalman et al. (2018) states, this thinking is so prevalent that rates of acetoclastic methanogenesis from mixed microbial communities have been determined by subtracting the rate of hydrogenotrophic methanogenesis from the total CH_4 production rate. This method is particularly problematic as methylotrophic methanogens do not appear to be affected by one of the most commonly used acetoclastic methanogenesis inhibitors, methyl fluoride (Penger et al., 2012). As described by Kurth et al. (2020) and Sollinger and Urich (2019), there are a wealth of substrates that various methylotrophic methanogens can and do utilize, many of which are non-competitive. Recent studies have also found that methylotrophic methanogenesis may be the dominant pathway in multiple environments. For example, Xiao et al. (2018) found methylotrophic methanogenesis to be the dominant CH_4 production pathway in sulfate-rich marine surface sediments from Aarhus Bay in Denmark. Zalman et al. (2018) found that Northern Minnesota peat bogs have a strong potential for methylotrophic methanogenesis based on the amounts of methylated substrate found there. Feldewert et al. (2020) suggested that methylotrophic methanogens are even able to outcompete hydrogenotrophic methanogens for H_2 when their habitats can provide sufficient methyl groups, even in the presence of sulfate. This study can now be added to the growing list of environments, both freshwater and marine, where methylotrophic methanogenesis is either found to be dominant, or found to have strong potential.

4.4 | Lagoon environments are unique from marine environments

The lagoon forms a microbial habitat unique not only from the freshwater sediments but also from marine sediments. In marine environments, ANME consortia are typically restricted to a SMTZ (Beulig et al., 2019; Egger et al., 2018; Nauhaus et al., 2002), whereas in the lagoon their abundance remains high in the sulfate zone above the observed SMTZ (Figure 3; Table S2). This could indicate that the location of the SMTZ in the lagoon is seasonally more variable than in marine sediments due to the dynamic nature of the lagoon (e.g., ice buildup and retreat, alternation between freshwater and brackish water inflow) but the reason for the spatially more spread ANME consortia in the lagoon in comparison with marine sediments would require further, more temporally resolved studies.

The observed prevalence of methanogens throughout the sulfate zone and SMTZ would have been a surprising finding under the classical understanding that sulfate reducers outcompete methanogens in high sulfate environments (e.g., Claypool and Kaplan (1974); Sansone and Martens (1981)). However, recent studies have also found co-habitation of methanogenesis and sulfate reduction in a few marine environments (Ozuolmez et al., 2015, 2020; Sela-Adler et al., 2017), as well as coastal marine sediments (Koebsch et al., 2019; Rooze et al., 2016). This finding is still an important distinction between classical marine environments and a lagoon environment. Mitterer (2010) proposed that the co-occurrence of methanogenesis and sulfate reduction is supported by the presence and utilization of non-competitive methanogenic substrates, such as methylamines and methylated sulfur compounds. Another potential explanation of these differences is the intrusion of freshwater in the lagoon and coastal marine environment. Compared with a lagoon system, marine sediments in the open ocean generally contain a higher sulfate content, while the organic matter is more diluted. It is therefore conceivable that marine sediment, aside from coastal regions, also has a reduced amount of available labile carbon. Previous paleoclimate reconstructions have shown that the sediments of the lakes and lagoons on the peninsula are mixtures of permafrost thawed in situ under the waterbody, permafrost eroded from shores by thermo-erosion, and lacustrine sedimentation that has accumulated over approximately 8000 years (Jongejans et al., 2020). The carbon densities in lagoons in Yedoma permafrost regions are on average 16.5 $kg\,m^{-3}$, which falls within the range of terrestrial Yedoma (8 $kg\,m^{-3}$) and thermokarst (24 $kg\,m^{-3}$) sediments in the Yedoma region (Jenrich, 2020; Vyse et al., 2021). The upper three to five meters of sediment contain a higher density of carbon than those below. Moreover, the organic carbon in thermokarst lagoons is strongly correlated with the origin of the organic matter and the depositional conditions (Jenrich et al., 2021; Jongejans et al., 2020). The quality of organic carbon is an important variable regulating microbial carbon turnover (Schuur et al., 2015; Wagner et al., 2005). Likely, thermokarst lakes and lagoons can provide sufficient labile organic carbon for microbial metabolism, in excess of what is usually available in marine environments, and which is another key precondition for the coexistence of sulfate reducing bacteria (SRB) and methanogens (Ozuolmez et al., 2015; Sela-Adler et al., 2017). Therefore, the lagoon provides a sulfate and carbon rich habitat distinctly different from generally carbon poor classical non-coastal marine systems, and based on the prevalence of non-competitive methylotrophic methanogens, may also contain a larger range of organic carbon compounds.

5 | CONCLUSION AND PERSPECTIVES

In Arctic coastal permafrost regions, the transition from thermokarst lakes to lagoons changes the ionic strength and oxidative capacity, and introduces new microbial species. Consequently, the initial geochemical and trophic stratification is reorganized which in turn induces profound shifts in the structure and functionality of the methane-cycling community, and influences carbon feedbacks in the lagoon by supporting a strong AOM community. The results of our study also indicate that, while considerably different from classical marine environments, lagoon environments can still be favorable habitats for canonical AOM consortia. In the lagoon system, a high load of organic carbon and non-competitive substrates further afford the co-existence of methanogens and other sulfate-reducing organisms. They are also an acceptable habitat for the establishment of new microbial communities (Module 1, Figure 7), and mixed communities (Module 4, Figure 7). Our study also shows that the original microbial community present before lagoon development persists under the new conditions (Modules

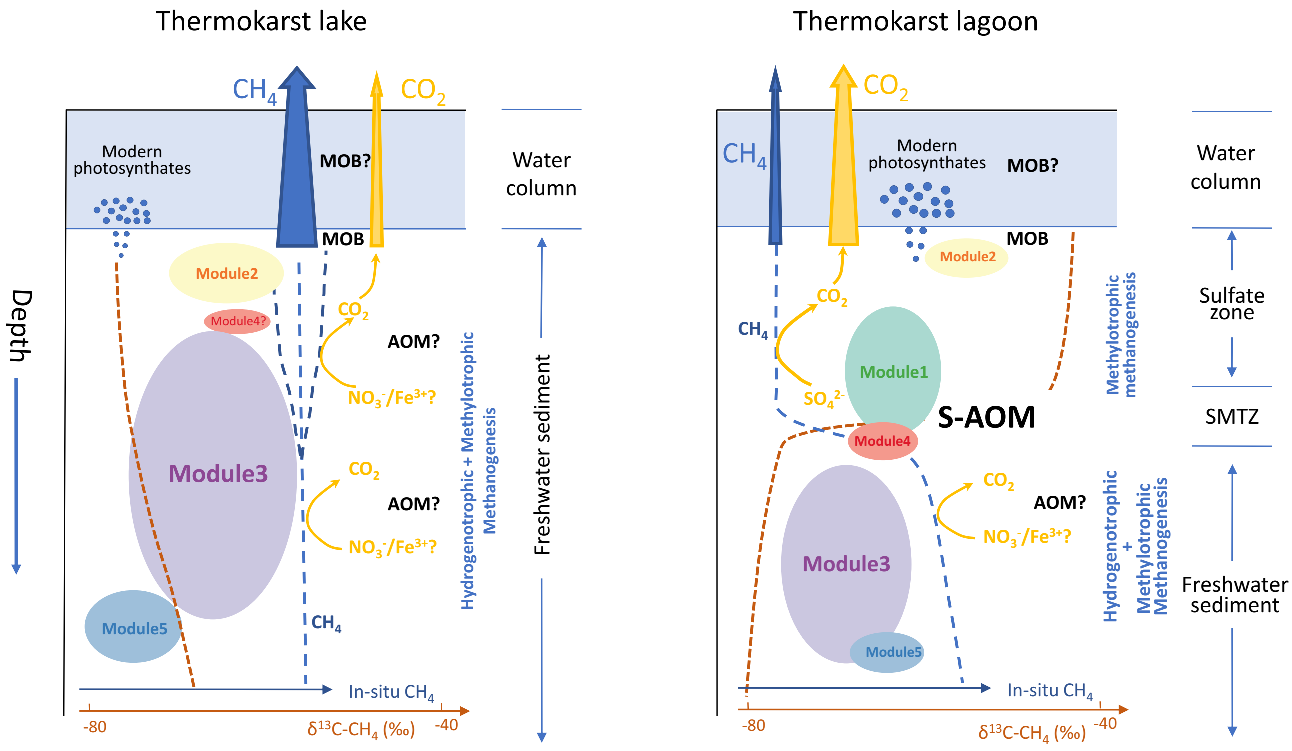

FIGURE 7 Schematic plot showing the stratified distribution of methane-cycling communities and processes in freshwater thermokarst lakes (left), and re-assembly of community and methane turnover pathways after thermokarst lakes turn into thermokarst lagoons (right). All Modules contain H_2-dependent methylotrophic methanogens. Module 1 is only found in the sulfate-zone of the lagoon, and is comprised of microbes preferring more marine conditions, especially marine AOMs. Module 4 has a smaller selection of AOM microbes, including one ASV of marine origin which is only found in the lagoon but is associated with the other microbes in the Module found also in the lakes. Modules 2, 3, and 5 are seen in both the lakes and lagoon and consist of varying types of methanogens, MOBs, and terrestrial-origin AOMs.

2, 3, and 5; Figure 7). Owing to effective methane oxidation, thermokarst lagoons mitigate sediment methane concentrations compared to freshwater thermokarst ecosystems. However, the impact of these local mitigations on the global permafrost methane flux is unknown.

An estimation of the current extent of pan-Arctic lagoons including lagoons along the coasts of the Laptev, East Siberia, Chuckhi, and Beaufort shelf seas, shows that these lagoons currently occupy an area of 2579 km^2 (Jenrich et al., 2022), which is roughly equivalent to the size of the country of Luxemburg. Although still comparatively small in area, thermokarst lagoons transform microbial methane cycling communities and will further expand in Arctic regions, especially along the Laptev Sea coast due to sea-level rise, accelerated permafrost thaw, intensified coastal erosion, and changing sea ice regimes. Pan-arctic lagoons may therefore be more relevant to the present-day and future permafrost carbon budget than is currently reflected in the literature, especially if they host a strong AOM community like shown here. Beyond that, thermokarst lagoon systems represent important natural laboratories for studying the effect of sea level rise on vulnerable, organic-rich coastal permafrost landscapes. Therefore, their potential to serve as habitat for efficient AOM-communities deserves more attention in the future.

ACKNOWLEDGMENTS

We thank Jan Kahl, Lutz Schirrmeister, and Axel Kitte for assisting with drilling during field work. We thank Daniela Warok for help with lipid biomarker analysis. We also thank Anke Saborowski for her contribution to the qPCR analysis. This study was supported by the Helmholtz Gemeinschaft (HGF) through funding for SL's Helmholtz Young Investigators Group (VH-NG-919). SY and SL were supported by the German Ministry of Education and Research as part of the projects CarboPerm (grant no. 03G0836A, 03G0836D), and KoPf (grant no. 03F0764A, 03F0764F). SY acknowledges the support from the National Natural Science Foundation of China (grant no. 42271155) and the Chinese Academy of Sciences. This study was conducted within the framework of the Research Training Group 'Baltic TRANSCOAST' funded by the DFG (Deutsche Forschungsgemeinschaft) under grant number GRK 2000 (www.baltic-transcoast.uni-rostock.de). This is Baltic TRANSCOAST publication no. GRK2000/0065. GG and JS were supported by ERC PETA-CARB (#338335) and the HGF Impulse and Networking Fund (#ERC-0013). MJ was supported by DBU grant (project "Characterisation of organic carbon and estimation of greenhouse gas emissions in a warming Arctic"). CK was supported by the Cluster of Excellence CLICCS (EXC2037/1) at Universität Hamburg funded by the German Research Foundation (DFG). Field work was supported by funds from AWI and GFZ as well as the ERC PETA-CARB project. Open Access funding enabled and organized by Projekt DEAL.

CONFLICT OF INTEREST STATEMENT

The authors have no conflicts of interest.

DATA AVAILABILITY STATEMENT

The data that support the findings of this study are openly available from two different repositories. Sequencing data and metadata were deposited in the European Nucleotide Archive (ENA) at https://www.ebi.ac.uk/ena/browser/view/PRJEB49195, reference number PRJEB49195 (Yang et al., 2022a). The sample accession numbers are listed in Table S1. The metagenomic data were deposited in the ENA at https://www.ebi.ac.uk/ena/browser/view/PRJNA821074, reference number PRJNA821074 (Berben et al., 2022). The geochemistry data were deposited in the GFZ Data Services' Geoscience Data Publisher at http://doi.org/10.5880/GFZ.3.7.2022.001, reference number GFZ.3.7.2022.001 (Yang et al., 2022b).

ORCID

Sizhong Yang https://orcid.org/0000-0001-8417-593X
Sara E. Anthony https://orcid.org/0000-0002-7945-4480
Maren Jenrich https://orcid.org/0000-0002-1330-7461
Michiel H. in 't Zandt https://orcid.org/0000-0002-0497-4502
Jens Strauss https://orcid.org/0000-0003-4678-4982
Pier Paul Overduin https://orcid.org/0000-0001-9849-4712
Guido Grosse https://orcid.org/0000-0001-5895-2141
Michael Angelopoulos https://orcid.org/0000-0003-2574-5108
Boris K. Biskaborn https://orcid.org/0000-0003-2378-0348
Mikhail N. Grigoriev https://orcid.org/0000-0003-1997-9506
Dirk Wagner https://orcid.org/0000-0001-5064-497X
Christian Knoblauch https://orcid.org/0000-0002-7147-1008
Andrea Jaeschke https://orcid.org/0000-0003-2518-2739
Janet Rethemeyer https://orcid.org/0000-0001-6698-4186
Jens Kallmeyer https://orcid.org/0000-0002-6440-1140
Susanne Liebner https://orcid.org/0000-0002-9389-7093

REFERENCES

Anders, K., Marx, S., Boike, J., Herfort, B., Wilcox, E. J., Langer, M., Marsh, P., & Höfle, B. (2020). Multitemporal terrestrial laser scanning point clouds for thaw subsidence observation at Arctic permafrost monitoring sites. *Earth Surface Processes and Landforms*, *45*(7), 1589–1600. https://doi.org/10.1002/esp.4833

Angelopoulos, M., Overduin, P. P., Jenrich, M., Nitze, I., Günther, F., Strauss, J., Westermann, S., Schirrmeister, L., Kholodov, A., Krautblatter, M., Grigoriev, M. N., & Grosse, G. (2021). Onshore thermokarst primes subsea permafrost degradation. *Geophysical Research Letters*, *48*(20), e2021GL093881. https://doi.org/10.1029/2021gl093881

Angelopoulos, M., Overduin, P. P., Westermann, S., Tronicke, J., Strauss, J., Schirrmeister, L., Biskaborn, B. K., Liebner, S., Maksimov, G., Grigoriev, M. N., & Grosse, G. (2020). Thermokarst Lake to lagoon transitions in eastern Siberia: Do submerged Taliks refreeze? *Journal of Geophysical Research: Earth Surface*, *125*(10), e2019JF005424. https://doi.org/10.1029/2019jf005424

Antonova, S., Sudhaus, H., Strozzi, T., Zwieback, S., Kääb, A., Heim, B., Langer, M., Bornemann, N., & Boike, J. (2018). Thaw subsidence of a Yedoma landscape in northern Siberia, measured in situ and estimated from TerraSAR-X interferometry. *Remote Sensing*, *10*(4), 494.

Berben, T., Forlano Bó, F., In 't Zandt, M. H., Yang, S., Liebner, S., & Welte, C. U. (2022). *Metagenomic sequencing of sediment of the polar fox lagoon*. Bykovsky Peninsula, Siberia, Russia https://www.ebi.ac.uk/ena/browser/view/PRJNA821074

Beulig, F., Roy, H., McGlynn, S. E., & Jorgensen, B. B. (2019). Cryptic CH_4 cycling in the sulfate-methane transition of marine sediments apparently mediated by ANME-1 archaea. *The ISME Journal*, *13*(2), 250–262. https://doi.org/10.1038/s41396-018-0273-z

Biskaborn, B. K., Herzschuh, U., Bolshiyanov, D., Savelieva, L., Zibulski, R., & Diekmann, B. (2012). Late Holocene thermokarst variability inferred from diatoms in a lake sediment record from the Lena Delta, Siberian Arctic. *Journal of Paleolimnology*, *49*(2), 155–170. https://doi.org/10.1007/s10933-012-9650-1

Biskaborn, B. K., Herzschuh, U., Bolshiyanov, D. Y., Schwamborn, G., & Diekmann, B. (2013). Thermokarst processes and depositional events in a Tundra Lake, Northeastern Siberia. *Permafrost and Periglacial Processes*, *24*(3), 160–174. https://doi.org/10.1002/ppp.1769

Biskaborn, B. K., Smith, S. L., Noetzli, J., Matthes, H., Vieira, G., Streletskiy, D. A., Schoeneich, P., Romanovsky, V. E., Lewkowicz, A. G., Abramov, A., Allard, M., Boike, J., Cable, W. L., Christiansen, H. H., Delaloye, R., Diekmann, B., Drozdov, D., Etzelmuller, B., Grosse, G., … Lantuit, H. (2019). Permafrost is warming at a global scale. *Nature Communications*, *10*(1), 264. https://doi.org/10.1038/s41467-018-08240-4

Bligh, E. G., & Dyer, W. J. (1959). A rapid method of total lipid extraction and purification. *Canadian Journal of Biochemistry and Physiology*, *37*(8), 911–917. https://doi.org/10.1139/o59-099

Bouchard, F., MacDonald, L. A., Turner, K. W., Thienpont, J. R., Medeiros, A. S., Biskaborn, B. K., Korosi, J., Hall, R. I., Pienitz, R., & Wolfe, B. B. (2016). Paleolimnology of thermokarst lakes: A window into permafrost landscape evolution. *Arctic Science*, *3*(2), 91–117.

Brown, J., Ferrians, O. J., Jr., Heginbottom, J. A., & Melnikov, E. S. (1997). *Circum-Arctic map of permafrost and ground-ice conditions*. Circum-Pacific Map 45. http://pubs.er.usgs.gov/publication/cp45

Buchfink, B., Xie, C., & Huson, D. H. (2015). Fast and sensitive protein alignment using DIAMOND. *Nature Methods*, *12*(1), 59–60. https://doi.org/10.1038/nmeth.3176

Bussmann, I., Fedorova, I., Juhls, B., Overduin, P. P., & Winkel, M. (2021). Methane dynamics in three different Siberian water bodies under winter and summer conditions. *Biogeosciences*, *18*(6), 2047–2061. https://doi.org/10.5194/bg-18-2047-2021

Callahan, B. J., McMurdie, P. J., Rosen, M. J., Han, A. W., Johnson, A. J., & Holmes, S. P. (2016). DADA2: High-resolution sample inference from illumina amplicon data. *Nature Methods*, *13*(7), 581–583. https://doi.org/10.1038/nmeth.3869

Cantalapiedra, C. P., Hernandez-Plaza, A., Letunic, I., Bork, P., & Huerta-Cepas, J. (2021). eggNOG-mapper v2: Functional annotation, orthology assignments, and domain prediction at the metagenomic scale. *Molecular Biology and Evolution*, *38*(12), 5825–5829. https://doi.org/10.1093/molbev/msab293

Caporaso, J. G., Lauber, C. L., Walters, W. A., Berg-Lyons, D., Lozupone, C. A., Turnbaugh, P. J., Fierer, N., & Knight, R. (2011). Global patterns of 16S rRNA diversity at a depth of millions of sequences per sample. *Proceedings of the National Academy of Sciences of the United States of America*, *108*(Suppl 1), 4516–4522. https://doi.org/10.1073/pnas.1000080107

Chuang, P. C., Young, M. B., Dale, A. W., Miller, L. G., Herrera-Silveira, J. A., & Paytan, A. (2017). Methane fluxes from tropical coastal lagoons surrounded by mangroves, Yucatán, Mexico. *Journal of Geophysical Research: Biogeosciences*, *122*(5), 1156–1174. https://doi.org/10.1002/2017jg003761

Claypool, G. E., & Kaplan, I. (1974). The origin and distribution of methane in marine sediments. In *Natural gases in marine sediments* (pp. 99–139). Springer.

Csardi, G., & Nepusz, T. (2006). The igraph software package for complex network research. *InterJournal, Complex Systems*, *1695*(5), 1–9. http://igraph.org

Dean, J. F., Middelburg, J. J., Röckmann, T., Aerts, R., Blauw, L. G., Egger, M., Jetten, M. S. M., de Jong, A. E. E., Meisel, O. H., Rasigraf, O., Slomp, C. P., In 't Zandt, M. H., & Dolman, A. J. (2018). Methane feedbacks to the global climate system in a warmer world. *Reviews of Geophysics*, *56*(1), 207–250. https://doi.org/10.1002/2017rg000559

Egger, M., Riedinger, N., Mogollón, J. M., & Jørgensen, B. B. (2018). Global diffusive fluxes of methane in marine sediments. *Nature Geoscience*, *11*(6), 421–425. https://doi.org/10.1038/s41561-018-0122-8

Ernakovich, J. G., Barbato, R. A., Rich, V. I., Schadel, C., Hewitt, R. E., Doherty, S. J., Whalen, E. D., Abbott, B. W., Barta, J., Biasi, C., Chabot, C. L., Hultman, J., Knoblauch, C., Vetter, M., Leewis, M. C., Liebner, S., Mackelprang, R., Onstott, T. C., Richter, A., ... Winkel, M. (2022). Microbiome assembly in thawing permafrost and its feedbacks to climate. *Global Change Biology*, *28*, 5007–5026. https://doi.org/10.1111/gcb.16231

Ettwig, K. F., Butler, M. K., Le Paslier, D., Pelletier, E., Mangenot, S., Kuypers, M. M., Schreiber, F., Dutilh, B. E., Zedelius, J., de Beer, D., Gloerich, J., Wessels, H. J., van Alen, T., Luesken, F., Wu, M. L., van de Pas-Schoonen, K. T., Op den Camp, H. J., Janssen-Megens, E. M., Francoijs, K. J., ... Strous, M. (2010). Nitrite-driven anaerobic methane oxidation by oxygenic bacteria. *Nature*, *464*(7288), 543–548. https://doi.org/10.1038/nature08883

Ettwig, K. F., Zhu, B., Speth, D., Keltjens, J. T., Jetten, M. S. M., & Kartal, B. (2016). Archaea catalyze iron-dependent anaerobic oxidation of methane. *Proceedings of the National Academy of Sciences of the United States of America*, *113*(45), 12792–12796. https://doi.org/10.1073/pnas.1609534113

Feldewert, C., Lang, K., & Brune, A. (2020). The hydrogen threshold of obligately methyl-reducing methanogens. *FEMS Microbiology Letters*, *367*(17), fnaa137. https://doi.org/10.1093/femsle/fnaa137

Ficken, K. J., Li, B., Swain, D. L., & Eglinton, G. (2000). An n-alkane proxy for the sedimentary input of submerged/floating freshwater aquatic macrophytes. *Organic Geochemistry*, *31*(7–8), 745–749. https://doi.org/10.1016/s0146-6380(00)00081-4

Froelich, P. N., Klinkhammer, G. P., Bender, M. L., Luedtke, N. A., Heath, G. R., Cullen, D., Dauphin, P., Hammond, D., Hartman, B., & Maynard, V. (1979). Early oxidation of organic matter in pelagic sediments of the eastern equatorial Atlantic: Suboxic diagenesis. *Geochimica et Cosmochimica Acta*, *43*(7), 1075–1090. https://doi.org/10.1016/0016-7037(79)90095-4

Grosse, G., Schirrmeister, L., Siegert, C., Kunitsky, V. V., Slagoda, E. A., Andreev, A. A., & Dereviagyn, A. Y. (2007). Geological and geomorphological evolution of a sedimentary periglacial landscape in Northeast Siberia during the Late Quaternary. *Geomorphology*, *86*(1–2), 25–51. https://doi.org/10.1016/j.geomorph.2006.08.005

Hinrichs, K. U., & Boetius, A. (2002). The anaerobic oxidation of methane: New insights in microbial ecology and biogeochemistry. In G. Wefer, D. Billett, D. Hebbeln, B. B. Jørgensen, M. Schlüter, & T. C. E. van Weering (Eds.), *Ocean margin systems* (pp. 457–477). Springer.

Hinrichs, K. U., Hayes, J. M., Sylva, S. P., Brewer, P. G., & DeLong, E. F. (1999). Methane-consuming archaebacteria in marine sediments. *Nature*, *398*(6730), 802–805. https://doi.org/10.1038/19751

Hugelius, G., Strauss, J., Zubrzycki, S., Harden, J. W., Schuur, E. A. G., Ping, C. L., Schirrmeister, L., Grosse, G., Michaelson, G. J., Koven, C. D., O'Donnell, J. A., Elberling, B., Mishra, U., Camill, P., Yu, Z., Palmtag, J., & Kuhry, P. (2014). Estimated stocks of circumpolar permafrost carbon with quantified uncertainty ranges and identified data gaps. *Biogeosciences*, *11*(23), 6573–6593. https://doi.org/10.5194/bg-11-6573-2014

Hultman, J., Waldrop, M. P., Mackelprang, R., David, M. M., McFarland, J., Blazewicz, S. J., Harden, J., Turetsky, M. R., McGuire, A. D., Shah, M. B., VerBerkmoes, N. C., Lee, L. H., Mavrommatis, K., & Jansson, J. K. (2015). Multi-omics of permafrost, active layer and thermokarst bog soil microbiomes. *Nature*, *521*(7551), 208–212. https://doi.org/10.1038/nature14238

Hyatt, D., Chen, G. L., Locascio, P. F., Land, M. L., Larimer, F. W., & Hauser, L. J. (2010). Prodigal: Prokaryotic gene recognition and translation initiation site identification. *BMC Bioinformatics*, *11*(1), 119. https://doi.org/10.1186/1471-2105-11-119

In 't Zandt, M. H., Liebner, S., & Welte, C. U. (2020). Roles of thermokarst lakes in a warming world. *Trends in Microbiology*, *28*(9), 769–779. https://doi.org/10.1016/j.tim.2020.04.002

Jenrich, M. (2020). *Thermokarst lagoons—carbon pools and panarctic distribution*. University of Potsdam, Potsdam, Germany.

Jenrich, M., Angelopoulos, M., Grosse, G., Overduin, P. P., Schirrmeister, L., Nitze, I., Biskaborn, B. K., Liebner, S., Grigoriev, M., Murray, A., Jongejans, L. L., & Strauss, J. (2021). Thermokarst lagoons: A core-based assessment of depositional characteristics and an estimate of carbon pools on the Bykovsky Peninsula. *Frontiers in Earth Science*, *9*, 637899. https://doi.org/10.3389/feart.2021.637899

Jenrich, M., Nitze, I., Laboor, S., Angelopoulos, M., Grosse, G., & Strauss, J. (2022). *Spatial extent of thermokarst lagoons along pan-Arctic coasts—an upscaling approach*. https://doi.org/10.1594/PANGAEA.948267

Jongejans, L. L., Mangelsdorf, K., Schirrmeister, L., Grigoriev, M. N., Maksimov, G. M., Biskaborn, B. K., Grosse, G., & Strauss, J. (2020). n-Alkane characteristics of thawed permafrost deposits below a thermokarst lake on Bykovsky Peninsula, Northeastern Siberia. *Frontiers in Environmental Science*, *8*, 118. https://doi.org/10.3389/fenvs.2020.00118

Jørgensen, B. B. (2006). Bacteria and marine biogeochemistry. In H. D. Schulz & M. Zabel (Eds.), *Marine Geochemistry* (pp. 169–206). Springer Berlin Heidelberg. https://doi.org/10.1007/3-540-32144-6_5

Kieser, S., Brown, J., Zdobnov, E. M., Trajkovski, M., & McCue, L. A. (2020). ATLAS: A Snakemake workflow for assembly, annotation, and genomic binning of metagenome sequence data. *BMC Bioinformatics*, *21*(1), 257. https://doi.org/10.1186/s12859-020-03585-4

Knittel, K., & Boetius, A. (2009). Anaerobic oxidation of methane: Progress with an unknown process. *Annual Review of Microbiology*, *63*(1), 311–334. https://doi.org/10.1146/annurev.micro.61.080706.093130

Knittel, K., Losekann, T., Boetius, A., Kort, R., & Amann, R. (2005). Diversity and distribution of methanotrophic archaea at cold seeps. *Applied and Environmental Microbiology*, *71*(1), 467–479. https://doi.org/10.1128/AEM.71.1.467-479.2005

Knittel, K., Wegener, G., & Boetius, A. (2019). Anaerobic methane oxidizers. In T. J. McGenity (Ed.), *Microbial communities utilizing hydrocarbons and lipids: Members, metagenomics and ecophysiology* (pp. 113–132). Springer International Publishing. https://doi.org/10.1007/978-3-030-14785-3_7

Koebsch, F., Winkel, M., Liebner, S., Liu, B., Westphal, J., Schmiedinger, I., Spitzy, A., Gehre, M., Jurasinski, G., & Köhler, S. (2019). Sulfate deprivation triggers high methane production in a disturbed and rewetted coastal peatland. *Biogeosciences*, *16*(9), 1937–1953.

Kurth, J. M., Op den Camp, H. J. M., & Welte, C. U. (2020). Several ways one goal-methanogenesis from unconventional substrates. *Applied Microbiology and Biotechnology*, *104*(16), 6839–6854. https://doi.org/10.1007/s00253-020-10724-7

Liu, Y., & Whitman, W. B. (2008). Metabolic, phylogenetic, and ecological diversity of the methanogenic archaea. *Annals of the New York Academy of Sciences*, *1125*(1), 171–189. https://doi.org/10.1196/annals.1419.019

Lyu, Z., Shao, N., Akinyemi, T., & Whitman, W. B. (2018). Methanogenesis. *Current Biology*, *28*(13), R727–R732. https://doi.org/10.1016/j.cub.2018.05.021

Maltby, J., Steinle, L., Löscher, C. R., Bange, H. W., Fischer, M. A., Schmidt, M., & Treude, T. (2018). Microbial methanogenesis in the sulfate-reducing zone of sediments in the Eckernförde Bay, SW Baltic Sea. *Biogeosciences*, *15*(1), 137–157. https://doi.org/10.5194/bg-15-137-2018

Martinez-Cruz, K., Leewis, M. C., Herriott, I. C., Sepulveda-Jauregui, A., Anthony, K. W., Thalasso, F., & Leigh, M. B. (2017). Anaerobic oxidation of methane by aerobic methanotrophs in sub-Arctic lake sediments. *Science of the Total Environment*, *607-608*, 23–31. https://doi.org/10.1016/j.scitotenv.2017.06.187

Marzi, R., Torkelson, B. E., & Olson, R. K. (1993). A revised carbon preference index. *Organic Geochemistry*, *20*(8), 1303–1306. https://doi.org/10.1016/0146-6380(93)90016-5

Mitterer, R. M. (2010). Methanogenesis and sulfate reduction in marine sediments: A new model. *Earth and Planetary Science Letters*, *295*(3–4), 358–366. https://doi.org/10.1016/j.epsl.2010.04.009

Myhre, G., Shindell, D., Bréon, F., Collins, W., Fuglestvedt, J., Huang, J., Koch, D., Lamarque, J., Lee, D., & Mendoza, B. (2013). Anthropogenic and natural radiative forcing, climate change 2013: The physical science basis. In T. F. Stocker, D. Qin, G.-K. Plattner, M. Tignor, S. K. Allen, J. Boschung, A. Nauels, Y. Xia, V. Bex, & P. M. Midgley (Eds.), *Contribution of working group I to the fifth assessment report of the intergovernmental panel on climate change* (pp. 659–740). Cambridge University Press.

Nakamura, F. M. (2019). *Microcosms and the role of active microbiota on methane cycle in soils under forest and pasture of eastern Amazon*. Universidade de São Paulo.

Nauhaus, K., Boetius, A., Kruger, M., & Widdel, F. (2002). In vitro demonstration of anaerobic oxidation of methane coupled to sulphate reduction in sediment from a marine gas hydrate area. *Environmental Microbiology*, *4*(5), 296–305. https://doi.org/10.1046/j.1462-2920.2002.00299.x

Nurk, S., Meleshko, D., Korobeynikov, A., & Pevzner, P. A. (2017). metaSPAdes: A new versatile metagenomic assembler. *Genome Research*, *27*(5), 824–834. https://doi.org/10.1101/gr.213959.116

Oksanen, J., Blanchet, F. G., Friendly, M., Kindt, R., Legendre, P., McGlinn, D., Minchin, P. R., O'Hara, R. B., Simpson, G. L., Solymos, P., Stevens, M. H. H., Szoecs, E., & Wagner, H. (2019). *Vegan: Community ecology package. R Package Version 2.5-6*. https://CRAN.R-project.org/package=vegan

Olefeldt, D., Goswami, S., Grosse, G., Hayes, D., Hugelius, G., Kuhry, P., McGuire, A. D., Romanovsky, V. E., Sannel, A. B., Schuur, E. A., & Turetsky, M. R. (2016). Circumpolar distribution and carbon storage of thermokarst landscapes. *Nature Communications*, *7*(1), 13043. https://doi.org/10.1038/ncomms13043

Oswald, K., Graf, J. S., Littmann, S., Tienken, D., Brand, A., Wehrli, B., Albertsen, M., Daims, H., Wagner, M., Kuypers, M. M., Schubert, C. J., & Milucka, J. (2017). Crenothrix are major methane consumers in stratified lakes. *The ISME Journal*, *11*(9), 2124–2140. https://doi.org/10.1038/ismej.2017.77

Ozuolmez, D., Moore, E. K., Hopmans, E. C., Sinninghe Damste, J. S., Stams, A. J. M., & Plugge, C. M. (2020). Butyrate conversion by sulfate-reducing and methanogenic communities from anoxic sediments of Aarhus Bay, Denmark. *Microorganisms*, *8*(4), 606. https://doi.org/10.3390/microorganisms8040606

Ozuolmez, D., Na, H., Lever, M. A., Kjeldsen, K. U., Jorgensen, B. B., & Plugge, C. M. (2015). Methanogenic archaea and sulfate reducing bacteria co-cultured on acetate: Teamwork or coexistence? *Frontiers in Microbiology*, *6*, 492. https://doi.org/10.3389/fmicb.2015.00492

Patzner, M. S., Logan, M., McKenna, A. M., Young, R. B., Zhou, Z., Joss, H., Mueller, C. W., Hoeschen, C., Scholten, T., Straub, D., Kleindienst, S., Borch, T., Kappler, A., & Bryce, C. (2022). Microbial iron cycling during palsa hillslope collapse promotes greenhouse gas emissions before complete permafrost thaw. *Communications Earth & Environment*, *3*(1), 76. https://doi.org/10.1038/s43247-022-00407-8

Pellerin, A., Lotem, N., Walter Anthony, K., Eliani Russak, E., Hasson, N., Roy, H., Chanton, J. P., & Sivan, O. (2022). Methane production controls in a young thermokarst lake formed by abrupt permafrost thaw. *Global Change Biology*, *28*(10), 3206–3221. https://doi.org/10.1111/gcb.16151

Penger, J., Conrad, R., & Blaser, M. (2012). Stable carbon isotope fractionation by methylotrophic methanogenic archaea. *Applied and Environmental Microbiology*, *78*(21), 7596–7602. https://doi.org/10.1128/AEM.01773-12

Pohlman, J. W., Riedel, M., Bauer, J. E., Canuel, E. A., Paull, C. K., Lapham, L., Grabowski, K. S., Coffin, R. B., & Spence, G. D. (2013). Anaerobic methane oxidation in low-organic content methane seep sediments. *Geochimica et Cosmochimica Acta*, *108*, 184–201. https://doi.org/10.1016/j.gca.2013.01.022

Rooze, J., Egger, M., Tsandev, I., & Slomp, C. P. (2016). Iron-dependent anaerobic oxidation of methane in coastal surface sediments: Potential controls and impact. *Limnology and Oceanography*, *61*(S1), S267–S282. https://doi.org/10.1002/lno.10275

Rosseel, Y. (2012). Lavaan: An R package for structural equation modeling. *Journal of Statistical Software*, *48*(2), 1–36.

Sansone, F. J., & Martens, C. S. (1981). Methane production from acetate and associated methane fluxes from anoxic coastal sediments. *Science*, *211*(4483), 707–709. https://doi.org/10.1126/science.211.4483.707

Schindler, M. (2019). *Microbial process rates in thermokarst lake sediments from Bykovsky Peninsula, Northern Siberia*. University of Tübingen, Tübingen.

Schink, B. (2010). Anaerobic transformation processes, microbiology. In J. Reitner & V. Thiel (Eds.), *Encyclopedia of Geobiology* (pp. 48–52). Springer.

Schirrmeister, L., Grigoriev, M. N., Strauss, J., Grosse, G., Overduin, P. P., Kholodov, A., Guenther, F., & Hubberten, H.-W. (2018). Sediment characteristics of a thermokarst lagoon in the northeastern Siberian Arctic (Ivashkina lagoon Bykovsky Peninsula). *Arktos*, *4*(1), 1–16. https://doi.org/10.1007/s41063-018-0049-8

Schuur, E. A., McGuire, A. D., Schadel, C., Grosse, G., Harden, J. W., Hayes, D. J., Hugelius, G., Koven, C. D., Kuhry, P., Lawrence, D. M., Natali, S. M., Olefeldt, D., Romanovsky, V. E., Schaefer, K., Turetsky, M. R., Treat, C. C., & Vonk, J. E. (2015). Climate change and the permafrost carbon feedback. *Nature*, *520*(7546), 171–179. https://doi.org/10.1038/nature14338

Sela-Adler, M., Ronen, Z., Herut, B., Antler, G., Vigderovich, H., Eckert, W., & Sivan, O. (2017). Co-existence of Methanogenesis and sulfate reduction with common substrates in sulfate-Rich estuarine sediments. *Frontiers in Microbiology*, *8*(766), 766. https://doi.org/10.3389/fmicb.2017.00766

Serikova, S., Pokrovsky, O. S., Laudon, H., Krickov, I. V., Lim, A. G., Manasypov, R. M., & Karlsson, J. (2019). High carbon emissions from thermokarst lakes of Western Siberia. *Nature Communications*, *10*(1), 1552. https://doi.org/10.1038/s41467-019-09592-1

Sollinger, A., & Urich, T. (2019). Methylotrophic methanogens everywhere—physiology and ecology of novel players in global methane cycling. *Biochemical Society Transactions*, *47*(6), 1895–1907. https://doi.org/10.1042/BST20180565

Spangenberg, I., Overduin, P. P., Damm, E., Bussmann, I., Meyer, H., Liebner, S., Angelopoulos, M., Biskaborn, B. K., Grigoriev, M. N., & Grosse, G. (2021). Methane pathways in winter ice of a thermokarst lake–lagoon–coastal water transect in North Siberia. *The Cryosphere*, *15*(3), 1607–1625. https://doi.org/10.5194/tc-15-1607-2021

Strauss, J., Abbott, B., Hugelius, G., Schuur, E. A. G., Treat, C., Fuchs, M., Schädel, C., Ulrich, M., Turetsky, M. R., Keuschnig, M., Biasi, C., Yang, Y., & Grosse, G. (2021). Permafrost. In FAO & ITPS (Ed.), *Recarbonizing global soils—A technical manual of recommended management* practices (Vol. 2, p. 251). Food & Agriculture Organization. https://doi.org/10.4060/cb6378en

Strauss, J., Schirrmeister, L., Grosse, G., Fortier, D., Hugelius, G., Knoblauch, C., Romanovsky, V., Schädel, C., Schneider von Deimling, T., Schuur, E. A. G., Shmelev, D., Ulrich, M., & Veremeeva, A. (2017). Deep Yedoma permafrost: A synthesis of depositional characteristics and carbon vulnerability. *Earth-Science Reviews*, *172*, 75–86. https://doi.org/10.1016/j.earscirev.2017.07.007

Su, Y., Zheng, X., Chen, Y., Li, M., & Liu, K. (2015). Alteration of intracellular protein expressions as a key mechanism of the deterioration of bacterial denitrification caused by copper oxide nanoparticles. *Scientific Reports*, *5*, 15824. https://doi.org/10.1038/srep15824

Thomsen, T. R., Finster, K., & Ramsing, N. B. (2001). Biogeochemical and molecular signatures of anaerobic methane oxidation in a marine sediment. *Applied and Environmental Microbiology*, *67*(4), 1646–1656. https://doi.org/10.1128/AEM.67.4.1646-1656.2001

Timmers, P. H., Widjaja-Greefkes, H. C., Ramiro-Garcia, J., Plugge, C. M., & Stams, A. J. (2015). Growth and activity of ANME clades with different sulfate and sulfide concentrations in the presence of methane. *Frontiers in Microbiology*, *6*, 988. https://doi.org/10.3389/fmicb.2015.00988

Tokida, T., Miyazaki, T., Mizoguchi, M., & Seki, K. (2005). In situ accumulation of methane bubbles in a natural wetland soil. *European Journal of Soil Science*, *56*(3), 389–396. https://doi.org/10.1111/j.1365-2389.2004.00674.x

Turetsky, M. R., Abbott, B. W., Jones, M. C., Anthony, K. W., Olefeldt, D., Schuur, E. A. G., Grosse, G., Kuhry, P., Hugelius, G., Koven, C., Lawrence, D. M., Gibson, C., Sannel, A. B. K., & McGuire, A. D. (2020). Carbon release through abrupt permafrost thaw. *Nature Geoscience*, *13*(2), 138–143. https://doi.org/10.1038/s41561-019-0526-0

Versantvoort, W., Guerrero-Cruz, S., Speth, D. R., Frank, J., Gambelli, L., Cremers, G., van Alen, T., Jetten, M. S. M., Kartal, B., Op den Camp, H. J. M., & Reimann, J. (2018). Comparative genomics of Candidatus Methylomirabilis species and description of Ca. Methylomirabilis Lanthanidiphila. *Frontiers in Microbiology*, *9*, 1672. https://doi.org/10.3389/fmicb.2018.01672

Viollier, E., Inglett, P. W., Hunter, K., Roychoudhury, A. N., & Van Cappellen, P. (2000). The ferrozine method revisited: Fe(II)/Fe(III) determination in natural waters. *Applied Geochemistry*, *15*(6), 785–790. https://doi.org/10.1016/s0883-2927(99)00097-9

Vyse, S. A., Herzschuh, U., Andreev, A. A., Pestryakova, L. A., Diekmann, B., Armitage, S. J., & Biskaborn, B. K. (2020). Geochemical and sedimentological responses of arctic glacial Lake Ilirney, chukotka (far East Russia) to palaeoenvironmental change since ~51.8 ka BP. *Quaternary Science Reviews*, *247*, 106607. https://doi.org/10.1016/j.quascirev.2020.106607

Vyse, S. A., Herzschuh, U., Pfalz, G., Pestryakova, L. A., Diekmann, B., Nowaczyk, N., & Biskaborn, B. K. (2021). Sediment and carbon accumulation in a glacial lake in Chukotka (Arctic Siberia) during the late Pleistocene and Holocene: Combining hydroacoustic profiling and down-core analyses. *Biogeosciences*, *18*(16), 4791–4816. https://doi.org/10.5194/bg-18-4791-2021

Wagner, D., Lipski, A., Embacher, A., & Gattinger, A. (2005). Methane fluxes in permafrost habitats of the Lena Delta: Effects of microbial community structure and organic matter quality. *Environmental Microbiology*, *7*(10), 1582–1592. https://doi.org/10.1111/j.1462-2920.2005.00849.x

Wallenius, A. J., Dalcin Martins, P., Slomp, C. P., & Jetten, M. S. M. (2021). Anthropogenic and environmental constraints on the microbial methane cycle in coastal sediments. *Frontiers in Microbiology*, *12*, 631621. https://doi.org/10.3389/fmicb.2021.631621

Walter Anthony, K., Daanen, R., Anthony, P., Schneider von Deimling, T., Ping, C.-L., Chanton, J. P., & Grosse, G. (2016). Methane emissions proportional to permafrost carbon thawed in Arctic lakes since the 1950s. *Nature Geoscience*, *9*, 679–682. https://doi.org/10.1038/ngeo2795

Walter Anthony, K., Schneider von Deimling, T., Nitze, I., Frolking, S., Emond, A., Daanen, R., Anthony, P., Lindgren, P., Jones, B., & Grosse, G. (2018). 21st-century modeled permafrost carbon emissions accelerated by abrupt thaw beneath lakes. *Nature Communications*, *9*(1), 3262. https://doi.org/10.1038/s41467-018-05738-9

Walter, K. M., Edwards, M. E., Grosse, G., Zimov, S. A., & Chapin, F. S., 3rd. (2007). Thermokarst lakes as a source of atmospheric CH4 during the last deglaciation. *Science*, *318*(5850), 633–636. https://doi.org/10.1126/science.1142924

Walz, J., Knoblauch, C., Tigges, R., Opel, T., Schirrmeister, L., & Pfeiffer, E.-M. (2018). Greenhouse gas production in degrading ice-rich permafrost deposits in northeastern Siberia. *Biogeosciences*, *15*(17), 5423–5436. https://doi.org/10.5194/bg-15-5423-2018

Weil, M., Wang, H., Bengtsson, M., Köhn, D., Günther, A., Jurasinski, G., Couwenberg, J., Negassa, W., Zak, D., & Urich, T. (2020). Long-term rewetting of three formerly drained peatlands drives congruent compositional changes in pro-and eukaryotic soil microbiomes through environmental filtering. *Microorganisms*, *8*(4), 550.

Wen, X., Unger, V., Jurasinski, G., Koebsch, F., Horn, F., Rehder, G., Sachs, T., Zak, D., Lischeid, G., & Knorr, K.-H. (2018). Predominance of methanogens over methanotrophs in rewetted fens characterized by high methane emissions. *Biogeosciences*, *15*(21), 6519–6536.

Wickham, H. (2016). *ggplot2: Elegant graphics for data analysis*. Springer-Verlag New York http://ggplot2.org

Wiesenburg, D. A., & Guinasso, N. L. (2002). Equilibrium solubilities of methane, carbon monoxide, and hydrogen in water and sea water. *Journal of Chemical & Engineering Data*, *24*(4), 356–360. https://doi.org/10.1021/je60083a006

Winkel, M., Mitzscherling, J., Overduin, P. P., Horn, F., Winterfeld, M., Rijkers, R., Grigoriev, M. N., Knoblauch, C., Mangelsdorf, K., Wagner, D., & Liebner, S. (2018). Anaerobic methanotrophic communities thrive in deep submarine permafrost. *Scientific Reports*, *8*(1), 1291. https://doi.org/10.1038/s41598-018-19505-9

Xiao, K. Q., Beulig, F., Røy, H., Jørgensen, B. B., & Risgaard-Petersen, N. (2018). Methylotrophic methanogenesis fuels cryptic methane cycling in marine surface sediment. *Limnology and Oceanography*, *63*(4), 1519–1527. https://doi.org/10.1002/lno.10788

Yang, S. (2020). otuSummary: Summarizing OTU table regarding the composition, abundance and beta diversity of abundant and rare biospheres. verion 0.1.1. https://github.com/cam315/otuSummary

Yang, S., Anthony, S. E., Jenrich, M., In 't Zandt, M. H., Strauss, J., Overduin, P. P., Grosse, G., Angelopoulos, M., Biskaborn, B. K., Grigoriev, M. N., Wagner, D., Knoblauch, C., Jaeschke, A., Rethemeyer, J., Kallmeyer, J., & Liebner, S. (2022a). *Sequencing data of sediments from Arctic thermokarst lakes and lagoons on the Bykovsky Peninsula, Siberia*. https://www.ebi.ac.uk/ena/browser/view/PRJEB49195

Yang, S., Anthony, S. E., Jenrich, M., In 't Zandt, M. H., Strauss, J., Overduin, P. P., Grosse, G., Angelopoulos, M., Biskaborn, B. K., Grigoriev, M. N., Wagner, D., Knoblauch, C., Jaeschke, A., Rethemeyer, J., Kallmeyer, J., & Liebner, S. (2022b). *Geochemistry of sediments from Arctic thermokarst lakes and lagoons on the Bykovsky Peninsula, Siberia*. https://doi.org/10.5880/GFZ.3.7.2022.001

Yang, S., Liebner, S., Svenning, M. M., & Tveit, A. T. (2021). Decoupling of microbial community dynamics and functions in Arctic peat soil exposed to short term warming. *Molecular Ecology*, *30*(20), 5094–5104. https://doi.org/10.1111/mec.16118

Zalman, C. A., Meade, N., Chanton, J., Kostka, J. E., Bridgham, S. D., & Keller, J. K. (2018). Methylotrophic methanogenesis in sphagnum-dominated peatland soils. *Soil Biology and Biochemistry*, *118*, 156–160. https://doi.org/10.1016/j.soilbio.2017.11.025

Zheng, Y., Zhou, W., Meyers, P. A., & Xie, S. (2007). Lipid biomarkers in the Zoigê-Hongyuan peat deposit: Indicators of holocene climate changes in West China. *Organic Geochemistry*, *38*(11), 1927–1940. https://doi.org/10.1016/j.orggeochem.2007.06.012

SUPPORTING INFORMATION

Additional supporting information can be found online in the Supporting Information section at the end of this article.

How to cite this article: Yang, S., Anthony, S. E., Jenrich, M., in 't Zandt, M. H., Strauss, J., Overduin, P. P., Grosse, G., Angelopoulos, M., Biskaborn, B. K., Grigoriev, M. N., Wagner, D., Knoblauch, C., Jaeschke, A., Rethemeyer, J., Kallmeyer, J., & Liebner, S. (2023). Microbial methane cycling in sediments of Arctic thermokarst lagoons. *Global Change Biology*, *29*, 2714–2731. https://doi.org/10.1111/gcb.16649

D

Organic Carbon, Mercury, and Sediment Characteristics along a land – shore transect in Arctic Alaska

Frieda P. Giest[1,2], Maren Jenrich[1,3*], Guido Grosse[1,3], Benjamin M. Jones[4], Kai Mangelsdorf[5], Torben Windirsch[1,a], Jens Strauss[1]

[1] Alfred Wegener Institute, Helmholtz Centre for Polar and Marine Research, Permafrost Research Section, Potsdam, Germany

[2] University of Potsdam, Institute of Environmental Science and Geography, Potsdam, Germany

[3] University of Potsdam, Institute of Geosciences, Potsdam, Germany

[4] Institute of Northern Engineering, University of Alaska Fairbanks, Fairbanks, Alaska, USA

[5] German Research Centre for Geosciences GFZ, Helmholtz Centre Potsdam, Organic Geochemistry Section, Potsdam, Germany

[a] now at Research Institute for Sustainability Helmholtz Centre Potsdam, Potsdam, Germany

* *Correspondence to*: Maren Jenrich

This chapter is in submission in:

EGU - Biogeosciences

AUTHOR CONTRIBUTIONS

J. Strauss, M. Jenrich and F. Giest designed this study. J. Strauss, G. Grosse, and M. Jenrich, developed the overall coring plans for the Perma-X Lagoons field campaign and conducted the fieldwork in 2022. B. M. Jones provided guidance on site selection, field assistance, and logistical support for the expedition. J. Strauss, M. Jenrich and F. Giest did the subsampling for all cores. F. Giest carried out the laboratory analyses. K. Mangelsdorf supported the biomarker interpretation. F. Giest wrote the first draft of the manuscript. All co-authors contributed within their specific expertise to data interpretation as well as manuscript writing.

Organic Carbon, Mercury, and Sediment Characteristics along a land – shore transect in Arctic Alaska

Frieda P. Giest[1,2], Maren Jenrich[1,3*], Guido Grosse[1,3], Benjamin M. Jones[4], Kai Mangelsdorf [5], Torben Windirsch[1,a], Jens Strauss[1]

[1]Alfred Wegener Institute, Helmholtz Centre for Polar and Marine Research, Permafrost Research Section, Potsdam, Germany
[2]University of Potsdam, Institute of Environmental Science and Geography, Potsdam, Germany
[3]University of Potsdam, Institute of Geosciences, Potsdam, Germany
[4]Institute of Northern Engineering, University of Alaska Fairbanks, Fairbanks, Alaska, USA
[5]German Research Centre for Geosciences GFZ, Helmholtz Centre Potsdam, Organic Geochemistry Section, Potsdam, Germany
[a] now at Research Institute for Sustainability Helmholtz Centre Potsdam, Potsdam, Germany

**Correspondence to*: Maren Jenrich (maren.jenrich@awi.de)

Abstract. Climate warming in the Arctic results in thawing permafrost and associated processes like thermokarst, especially in ice-rich permafrost regions. Since permafrost soils are one of the largest organic carbon reservoirs of the world, their thawing could lead to the release of greenhouse gases, further exacerbating climate warming. To enhance predictions of potential future impacts of permafrost thaw, we studied how soil characteristics change in response to permafrost landscapes affected by thermokarst processes in an Arctic coastal lowland. We analysed six sediment cores from the Arctic Coastal Plain of northern Alaska, each representing a different landscape feature along a gradient from upland to thermokarst lake and drained basin to thermokarst lagoons in various development stages. For the analysis, a multiproxy approach was used including sedimentological (grain size, bulk density, ice content), biogeochemical (total organic carbon (TOC), TOC density (TOCvol), total nitrogen (TN), stable carbon isotopes ($\delta^{13}C$), TOC/TN ratio, mercury (Hg)), and lipid biomarker (n-alkanes, n-alkanols, average chain length (ACL), P_{aq}, P_{wax}, carbon preference index (CPI), higher plant alcohol index (HPA)) parameters. The results showed highest TOC contents in samples of the thermokarst lake and the drained thermokarst lake basin. Lowest TOC contents were measured in the samples of the semi-drained thermokarst lagoon. The comparison of unfrozen and frozen deposits showed significantly higher TOCvol and TN in the unfrozen deposits. Indicated by the ACL, $\delta^{13}C$ and the P_{aq}, P_{wax} we found a stronger influence of aquatic organic matter (OM) in the OM composition in the soils covered by water, compared to those not covered by water. Moreover, it was indicated by the results of the $\delta^{13}C$, TOC/TN ratio, and the CPI that the saline deposits contain stronger degraded OM than the deposits not influenced by saltwater. Additionally, we found positive correlations between the TOC and TOCvol and the Hg content in the deposits. The results indicate that thermokarst-influenced deposits tend to accumulate Hg during thawed periods and thus contain more Hg than the upland permafrost deposits that have not been impacted by lake formation. Our findings offer valuable insights into the dynamics of carbon storage and vulnerability to decomposition in coastal permafrost landscapes, reflecting the interplay of environmental factors, landform characteristics, and climate change impacts on Arctic permafrost environments.

1 Introduction

Climate warming represents one of the most pressing global environmental challenges of our time. Arctic regions are currently changing rapidly, since they experience some of the highest rates of impacts from climate change (Intergovernmental Panel on Climate Change (IPCC), 2022, 2023). Surface air temperatures in the Arctic increased up to four times the rate the global mean air temperature did over the last decades, a phenomenon referred to as Arctic amplification (Ballinger et al., 2023; Cohen et al., 2020; Rantanen et al., 2022). The local drivers of this amplification include the decrease of sea ice and snow cover, resulting in a decreased albedo, and a shift of cloudiness over the Arctic (Ballinger et al., 2023). Moreover, there are remote drivers which contribute to the amplification, including an increased total water vapour in the Arctic atmosphere, due to an increased evapotranspiration and atmospheric moisture transport from the mid-latitudes and tropics, and accelerated heat from the atmosphere and the ocean (Cohen et al., 2020). As a result, surface temperatures in the Arctic during the winters in 2016 and 2018 were 6 °C above the average temperatures between 1981–2010 (Intergovernmental Panel on Climate Change (IPCC), 2022).

One impact of this warming is the thaw of permafrost, which underlies large areas of the Arctic (Biskaborn et al., 2019; Smith et al., 2022). In some locations a total increase of 2–3 °C in the last 30 years was found within 10–20 m soil depth. Permafrost has been identified as a large and vulnerable reservoir of organic carbon (OC) and due to climate change is considered a potential major future carbon source in the earth system (Hugelius et al., 2014; Mishra et al., 2021; Schuur et al., 2022). It is estimated that terrestrial deposits in permafrost regions store approximately 1460–1600 Gt carbon, which is about twice as much as is currently present in the atmosphere (Schuur and Mack, 2018; Strauss et al., 2024a). As permafrost thaws, the soils can turn from a carbon sink to a carbon source (Schuur et al., 2009). Increased temperatures cause an acceleration of microbial activity and thus an increased decomposition of organic carbon in the deposits, leading to the release of greenhouse gases in the form of carbon dioxide and methane with the potential to further exacerbate climate change (Miner et al., 2022). In order to analyse the quality of organic matter (OM) in the different soils lipid biomarkers can be used. Indices like the average chain length of *n*-alkanes (ACL), the carbon preferences index (CPI), and the higher plant index (HPA) can provide information about the source of the OM, as well as the level of degradation (Jongejans et al., 2020, 2021; Strauss et al., 2015).

Another consequence of permafrost thaw is the change of the landscape, for example due to melting ground ice causing surface subsidence and the development of thermokarst features (Grosse et al., 2013; Kokelj and Jorgenson, 2013). Around 20 % of the permafrost regions are affected by thermokarst processes, including the formation of thermokarst lakes and drained lake basins (Grosse et al., 2013; Jones et al., 2022; Olefeldt et al., 2016). In a coastal environment, increased coastal and riverbank erosion, sea level rise, higher water temperatures, and a reduced sea ice cover can lead to the inundation of thermokarst lakes and drained thermokarst lake basins by ocean water and the formation of thermokarst lagoons (Jenrich et al., 2021; Schirrmeister et al., 2018). These features add another complex setting of biogeochemical and hydrochemical processes in the transitional stage between terrestrial and marine environments, to the already diverse thermokarst landscapes (Schirrmeister et al., 2018).

In addition to the influence of permafrost thaw and the formation of thermokarst features on organic carbon characteristic in the permafrost and thawed soils, changes in other biogeochemical characteristics may also occur, e.g. through the relocation and release of mercury (Hg). It was found that considerable amounts of Hg accumulated in the ice-rich permafrost region (Rutkowski et al., 2021). Since permafrost soils sequestered Hg bound in organic matter over centuries, it is estimated that the amount of Hg retained in permafrost regions is twice as high as in all other soils, the atmosphere, and the ocean combined (Schuster et al., 2018). Therefore, Hg is a notable environmental concern in the Arctic region for both humans and wildlife, as elevated exposure can impact human health and have negative effects on the ecosystems (Rydberg et al., 2010; Smith-Downey et al., 2010).

In this study, we use a multiproxy approach to characterise OC in different landscape features of a coastal permafrost lowland along a gradient from upland to thermokarst-affected terrains (lakes and drained basins) to thermokarst lagoons representing a transition from terrestrial to marine environments on the Arctic Coastal Plain of northern Alaska. We aim to answer how OC characteristics and correlating biogeochemical parameters change with permafrost degradation and coastal saltwater inundation.

2 Study area and study sites

The study area is located in the Arctic coastal plain of northern Alaska, north of the Teshekpuk Lake (figure 1). The North Slope, an area framed by the Brooks Range in the south and the Beaufort Sea in the north, encompasses a diverse geology including deposits originated in the North American craton, passive margin sediments, rift sediments, pelagic sediments, volcaniclastics and deposits from the foreland basin (Jorgenson et al., 2011). Surface deposits in the study area consist of glacio-marine silts, marine sands, alluvial sands and silts from the Holocene and mid-Quaternary epochs (Jorgenson and Grunblatt, 2013).

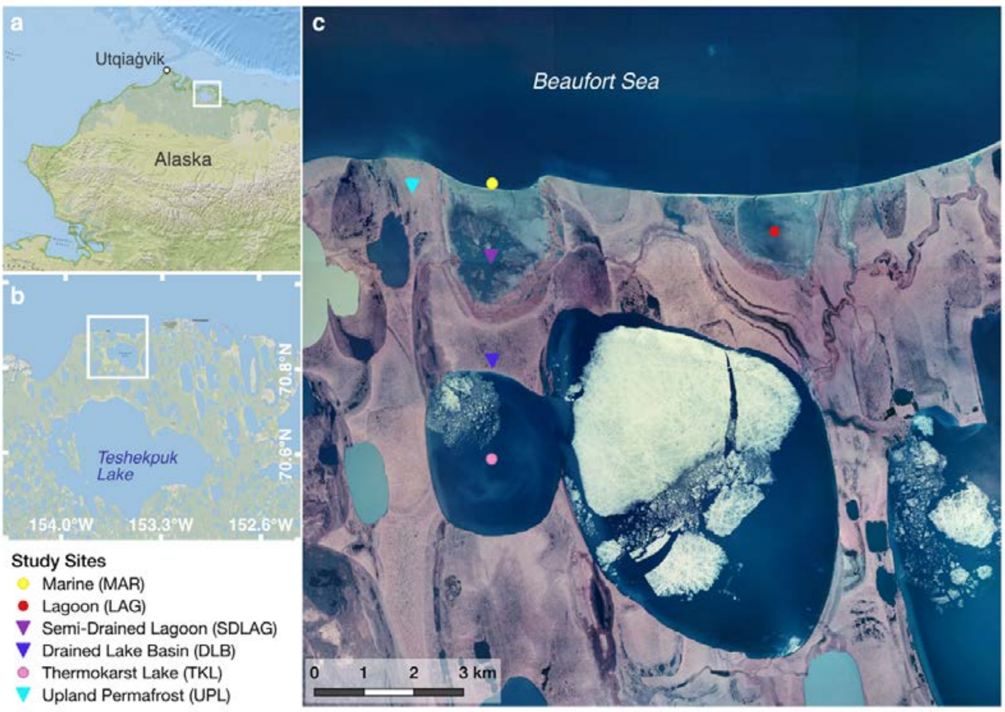

Figure 1: Map of the study sites located north of the Teshekpuk Lake in northern Alaska (a, b). Close-up of the study area, with the coring locations marked as dots (unfrozen deposits) and triangles (frozen deposits) (c). Sources: a, b: ESRI, c: Color infrared ortho aerial image (U.S. Geological Survey, Earth Explorer, 2002).

The climate in the region is cold and arid, with a mean annual temperature of -12 °C and a mean annual precipitation of 115 mm per year (Jorgenson et al., 2011). The soil composition in the area is intrinsically tied to the presence of continuous permafrost, with an interplay of low temperatures, impeded drainage, freeze-thaw dynamics, cryoturbation, and ground ice aggregation, collectively shaping its characteristic. The presence of 200 to 400 m thick continuous permafrost also led to the formation and preservation of one of the largest wetland complexes in the Arctic, which despite the cold and arid climate also lead to the accumulation of high OC contents in the soils (Jorgenson et al., 2011; Wendler et al., 2014). Moreover, the landscape is continuously transformed by thawing permafrost and melting ground ice, leading to ground subsidence and the formation of numerous thermokarst lakes and drained lake basins (Arp et al., 2011; Fuchs et al., 2019; Jones and Arp, 2015; Jorgenson and Shur, 2007; Wolter et al., 2024). Coastal erosion along the Beaufort Sea coast in this area is among the highest observed in the Arctic, resulting in the drainage of lakes and formation of thermokarst lagoons and embayments, and is currently accelerating further (Jones et al., 2009, 2018; Jones and Arp, 2015).

3 Material and Methods

3.1 Fieldwork

The fieldwork was performed during a joint German-US expedition to the Teshekpuk Lake area in Alaska in April 2022. For this study six soil cores were selected following a transect from inland to coast, with all core sites being located in close distance to each other (Figure 1). All sample sites represent different landscape features of a coastal thermokarst affected permafrost landscape scape, with the chosen transect describing the transformation pathway from a terrestrial permafrost landscape into a marine environment, following thaw and erosion processes (Jenrich et al., 2021). Three of the cores were frozen: from a permafrost upland (UPL; length 203 cm), a drained thermokarst lake basin (DLB; length 219 cm), and a semi-drained lagoon (SDLAG; length 183 cm). Three other cores were unfrozen: from a thermokarst lake (TKL; length 50 cm), a thermokarst lagoon (LAG; length 31 cm), and marine deposits (MAR; length 12 cm) (figure S1 in the supplements). For reference, all subsample depths are given in centimetres below surface level (cm b.s.l.). The unfrozen sediment cores were sampled using a Push Corer [Ø 6 cm], the frozen sediment cores were sampled using a SIPRE Corer [Ø 7.6 cm]. The frozen sediment cores were kept frozen, while thawed samples were packed and cooled for transport to AWI Potsdam for further analysis.

3.2 Laboratory analysis

In the laboratory, a multi-proxy approach was applied, including sedimentological, biogeochemical and lipid biomarker analysis. The cores were subsampled in intervals of 5 to10 cm. For the biomarker analysis, three to four samples of the longer, frozen cores and one to two samples of the shorter, unfrozen cores were selected, evenly distributed over the length of the cores. In preparation for further analysis all samples were freeze-dried and weighed before and after this process. A more detailed description of the methods used in the laboratory is given in the supplements (Sect. S1 in the supplements).

3.2.1 Sedimentological analysis

The sedimentological analysis included the measurement of water-/ice content, bulk density, and grain size composition.
The water-/ice content was calculated as the difference between wet and dry weight of each sample.
The bulk density (BD) was calculated using equation 1 (Strauss et al., 2012), where the porosity (n) of the soil was calculated as the ratio of the pore volume and the total volume of the samples. It was assumed that samples with a water-/ice content of ≥ 20 % were water-/ice saturated (Strauss et al., 2012), thus the water-/ice content equals the pore volume. Moreover, an ice density at -10 °C of 0.918 g cm^{-3} and a water density at 0 °C of 0.999 g cm^{-3} was used (Harvey, 2019). The dry mineral density (ρ_s) was considered to be 2.65 g cm^{-3} (Rowell, 1994).

$$BD = (n - 1) \cdot (-\rho_s)$$
(1)

Grain size distribution (GSD) measurement was carried out using a Malvern Mastersizer 3000 with a Malvern Hydro LV wet-sample dispersion unit, measuring in a range between 0.01–1000 µm. All grain size statistics were calculated using the software GRADISTAT (Blott and Pye, 2001).

3.2.2 Biogeochemical analysis

For biogeochemical analysis, all samples were homogenised using a planetary mill [FRITSCH pulverisette 5]. The determination of the total organic carbon content (TOC) was carried out using an ELEMENTAR soliTOC cube elemental analyser, measuring TOC and total inorganic carbon (TIC) via pyrolysis and gas analysis. Using a temperature ramping program to distinguish between TOC and TIC, the device was heated to 400 °C for 230 seconds (TOC), and subsequently heated to 600 °C for 120 seconds (TIC). Third heating stage was 900 °C for 150 seconds to ensure complete combustion of inorganic carbon compounds.
The carbon density (TOCvol) of each sample was determined using the bulk density and the TOC content. It was calculated using the following equation (2) (Strauss et al., 2015).

$$TOC_{vol}[kg\ m^{-3}] = BD[kg\ m^{-3}] \cdot \frac{TOC\ [wt\%]}{100}$$
(2)

The total nitrogen (TN) content was measured using an ELEMENTAR rapid MAX N exceed elemental analyser with a peak combustion temperature of 900 °C.
From the measured TOC and TN contents the TOC/TN ratio was calculated. This ratio provides information on the sources and the degradation level of the organic matter (OM) in the sediment, with high values indicating a higher share of terrestrial source material or well-preserved OM and low values indicating a higher share of aquatic sources or a high level of degradation of OM (Andersson et al., 2012; Meyers, 1997).
The measurement of the total mercury (Hg) content of the sediment samples was carried out using the direct mercury analyzer DMA-80 EVO.
The measurement of the $\delta^{13}C$ ratio, as a paleoenvironmental indicator, can also provide information on the sources of OM and its degree of decomposition. It is mainly determined by photosynthetic processes, but also by other factors like atmospheric CO_2, temperature, and water stress (Andersson et al., 2012). As the

first step of the analysis, carbonates were removed from the samples using hydrochloric acid. Subsequently, the measurement was carried out using a ThermoFisher Scientific Delta-V-Advantage gas mass spectrometer with a FLASH elemental analyser EA 2000 and a CONFLO IV gas mixing system. The isotope ratio was determined in relation to the Vienna Pee Dee Belemnite standard [‰ vs VPDB].

3.2.3 Lipid biomarker analysis

Measurement

Subsamples for lipid biomarker analysis were freeze-dried and homogenised. Lipid biomarkers were then extracted from approximately 8 g of sample material using accelerated solvent extraction (ASE; ThermoFisher Scientific Dionex ASE 350) with dichloromethane/methanol (DCM/MeOH 99:1). During extraction, samples were held in a static phase for 20 min at 75.5 °C and 5 MPa. For the subsequent analysis, 5α-androstane as a reference for n-alkanes in the aliphatic fraction, and 5a-androstan-17-one as a reference for n-alkanols in the neutral NSO-fraction were added. Resolved samples were then fractionated into an aliphatic, aromatic and NSO fraction using a medium pressure liquid chromatography (MPLC) system (Radke et al., 1980). Subsequently, the NSO fraction was separated into an acidic and neutral polar fraction by a manual KOH column separation. In preparation for the measurement the neutral NSO fraction was silylated by adding 50 µl DCM and 50 µl N-Methyl-N-(trimethylsilyl)trifluoroacetamide (MSTFA) and heated at 75 °C for one hour. The measurement of n-alkanes in the aliphatic fraction and n-alkanols in the neutral NSO fraction was performed using gas chromatography-mass spectrometry (GC-MS; Thermo Scientific ISQ 7000 Single Quadrupole Mass Spectrometer with a Thermo Scientific Trace 1310 Gas Chromatograph). The GC-MS system was operated with a transfer line temperature of 320 °C and an ion source temperature of 300 °C. Ionisation was achieved using an ionisation energy of 70 eV at 50 µA. The full scan mass spectra (m/z 50 to 600 Da, 2.5 scans s^{-1}) was analysed using the software XCalibur. The n-alkanes and n-alkanols were quantified by comparing their peak areas with those of the internal standards.

Biomarker indices

In total, five indices were calculated from the measured lipid biomarker concentrations. Three of these indices, calculated from the n-alkane concentrations, provide information on respective sources of the OC. The first index was the average chain length (ACL) of n-alkanes C_{23-33}, calculated following equation 3 where i is the carbon number and C is the concentration (Poynter and Eglinton, 1990; Strauss et al., 2015).

$$ACL = \frac{\sum i \cdot C_i}{\sum C_i} \tag{3}$$

A change of the ACL can indicate a change of the OC sources and thus a change of input vegetation type to the soil profile (Schäfer et al., 2016). The long chain odd-numbered n-alkanes are mainly produced by terrestrial higher plants like bryophytes (n-C_{23} & n-C_{25}), leaf waxes (n-C_{27} to n-C_{29}), and grasses (n-C_{31} to n-C_{33}) (Haugk et al., 2021; Zech et al., 2010).

The second and third indices are the P_{aq} (ratio of aquatic to terrestrial plant material, equation 4) and the P_{wax} (ratio of terrestrial plant waxes to total hydrocarbons, equation 5), two ratios that can be used as proxies for the intensity of aquatic influence on the sediments and to differentiate between aquatic and terrestrial plant input (Thomas et al., 2023; Zheng et al., 2007).

$$P_{aq} = \frac{C_{23}+C_{25}}{C_{23}+C_{25}+C_{29}+C_{31}} \quad (4)$$

$$P_{wax} = \frac{C_{27}+C_{29}+C_{31}}{\sum odd\ C_{23-31}} \quad (5)$$

With the P_{aq}, developed by Ficken et al. (2000) it is possible to distinguish between submerged and floating macrophytes, with values between 0.4 and 1, emergent macrophytes, with values between 0.1 and 0.4, and terrestrial plants, values < 0.1, as a source for OC in the soil. Since this index and its thresholds were developed in tropical regions, the P_{wax} was additionally used in this study, as seen in Jongejans et al. (2020). The P_{wax}, developed by Zheng et al. (2007), indicates the relative proportion of waxy hydrocarbons from emergent macrophytes and terrestrial plants to total hydrocarbons (Zheng et al., 2007).

The following two indices are used to provide information on the level of degradation of the OC in the soils. The first index is the Carbon preference index (CPI) of n-alkanes, introduced by Bray and Evans (1961). As a measure of alteration of OC, values of the CPI decrease with the degradation of OC in the soil (Marzi et al., 1993; Strauss et al., 2015). The calculation in this study was carried out using the equation introduced by Marzi et al. (1993), with a chain length interval of C_{23-33} (equation 6).

$$CPI_{23-33} = \frac{\sum odd\ C_{23-31} + \sum odd\ C_{25-33}}{2 \cdot \sum even\ C_{24-32}} \quad (6)$$

The second index as a measure of level of degradation of OC, introduced by Poynter (1989) is the higher plant alcohol index (HPA). As a basis of this index, it is assumed that the input ratio of n-alkanols and n-alkanes into a sedimentary environment is constant. Therefore, the ratio should depend on the extent of degradation, and since the n-alkanols are preferentially degraded over the n-alkanes or degraded to n-alkanes due to defunctionalisation, the ratio decreases with ongoing degradation (Poynter and Eglinton, 1990). The index was calculated using the following equation (7) (Poynter and Eglinton, 1990).

$$HPA = \frac{\sum(n-alkanols\ C_{24}, C_{26}, C_{28})}{\sum(n-alkanols\ C_{24}, C_{26}, C_{28}) + \sum(n-alkanes\ C_{27}, C_{29}, C_{31}} \quad (7)$$

3.3 Statistical analysis

The statistical analysis of the data included the analysis of central tendencies of the measured parameters across the different cores, and the comparison of unfrozen and frozen deposits, as well as saltwater influenced sites, and those not influenced by saltwater. Central tendencies analysis across the different cores was only applied to the SDLAG, TKL, DLB, and UPL cores, since the LAG and MAR cores had a too small sample size. After testing and disproving a normal distribution of the data, the nonparametric Kruskal-Wallis rank sum test was chosen to compare the data of the four different sites. For an additional pair-wise comparison of cores the Mann-Whitney-Wilcoxon test was used. In addition, it was tested if there are statistically significant differences between deposits that are influenced by saltwater (MAR, LAG, SDLAG) and deposits that are not influenced by saltwater (DLB, TKL, UPL) and the frozen (SDLAG, DLB, UPL) and unfrozen (MAR, LAG, TKL) cores, using the Mann-Whitney-Wilcoxon test. All tests of the central tendency analysis were carried out using R (script in Sect S4.1 & S4.2 in the supplements).

To test the data for existing correlations between the different measured parameters, a correlation matrix was created in R (script in Sect. S4.3 in the supplements). The calculation of the correlation was carried out after Pearson. The finished plot of the correlation matrix only shows correlations with a significance of $p < 0.05$.

4 Results

4.1 Sedimentology

The upland permafrost core (UPL) is generally dominated by silt, with a percentage share varying between 63.48 % and 77.5 %. The grain size distribution (GSD) over the whole length of the core is dominated by a peak in the area of fine sands and silts (figure 2). The sediment samples of the thermokarst lake (TKL) are dominated by silt, with a share ranging between 73.55 % and 80.37 %. The GSD is relatively homogenous over the length of the core, with a peak between silt and clay and a slight shift towards coarser deposits between 10–16 cm b.s.l. (figure 2). The drained lake basin core (DLB) is dominated by silt, ranging between 73.31 % and 79.91 %, with sand being represented with only between 2.3 % and 6.7 %. The GSD varies very little throughout the core, with mean grain sizes between 5.7 µm and 6.74 µm (figure 4) and a peak of the GSD at fine grain sizes between silt and clay (Figure 2). The GSD of the semi-drained lagoon (SDLAG) has a shift from higher shares of larger grain sizes peaking in the range of fine sand and silt in the deeper part of the core up to 100 cm b.s.l., to smaller grain sizes with a peak between silt and clay in the upper part of the core. The deposits of the intact lagoon (LAG) are dominated by silt and the GSD shows a peak at finer grain sizes between clay and silt (figure 2). The deposits (one sample) of the marine core (MAR) include a bigger sand portion of 58.5 % and show the coarsest grain sizes among the six studied cores with a mean grain size of 33.31 µm (figure 4).

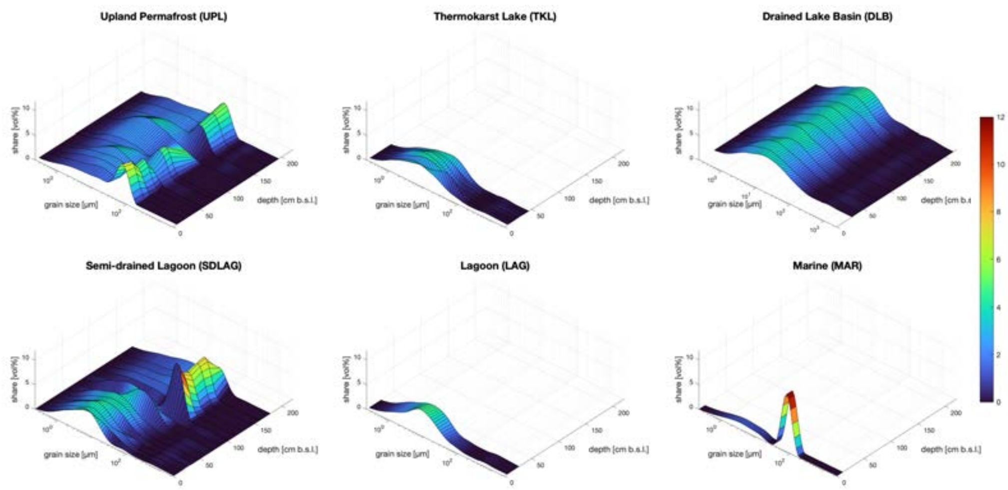

Figure 2: Three-dimensional grain size distributions over depth [cm] of a land-sea transect with a) upland Permafrost, b) thermokarst lake, c) drained lake basin, d) semi-drained lagoon, e) intact lagoon and f) marine

profiles. The Colours represent the share [%] of the grain sizes [µm] with dark blue representing 0 % and red representing 10 %.

4.2 Biogeochemistry

The DLB core shows the strongest variations in the TOC content, ranging from 2.94 wt% to 37.62 wt%, with a mean of 7.57 wt% (median 3.26 wt%) (figure 3). The UPL core also shows strong variations in the TOC content, peaking at 20.42 wt% at a depth of 56 cm b.s.l., with a mean of 4.66 wt% (figure 3). In contrast, the TKL sediment core shows a smaller range in the TOC content, between 4.63 wt% and 6.23 wt% (mean 5.37 wt%) (figure 3). It is significantly higher than the TOC content in the upper part of the UPL deposits. The two samples from the LAG plot within the lower end of the range of the TKL deposits, with TOC contents of 4.63 wt% and 4.09 wt% (figure 3). Above 40 cm the TOC content of the SDLAG core varies between those of the UPL and TKL deposits, below it has a consistently lower TOC contents than the other deposits, with a mean of 2.37 wt%, which is significantly lower than in the DLB and TKL samples (figure 3). Additionally, the sample of the MAR deposits has a very low TOC content of 1.3 wt% (figure 3).

The highest TOCvol was determined in the TKL deposits, with a mean of 48.02 kg m^{-3} (figure 4). It is significantly higher than in the SDLAG deposits (mean 32.23 kg m^{-3}) and the DLB deposits, with the lowest mean of 25.06 kg m^{-3}, both with strong variations in the TOCvol over depth (figure 3 & 4). The strongest variation in the TOCvol is shown by the UPL core, ranging between 6.79 kg m^{-3} and 119.7 kg m^{-3} (figure 3). The mean TOCvol of the UPL deposits of 36.66 kg m^{-3} is relatively high (figure 4). The TOCvol of the marine sample is again relatively low with 20.86 kg m^{-3}(figure 4).

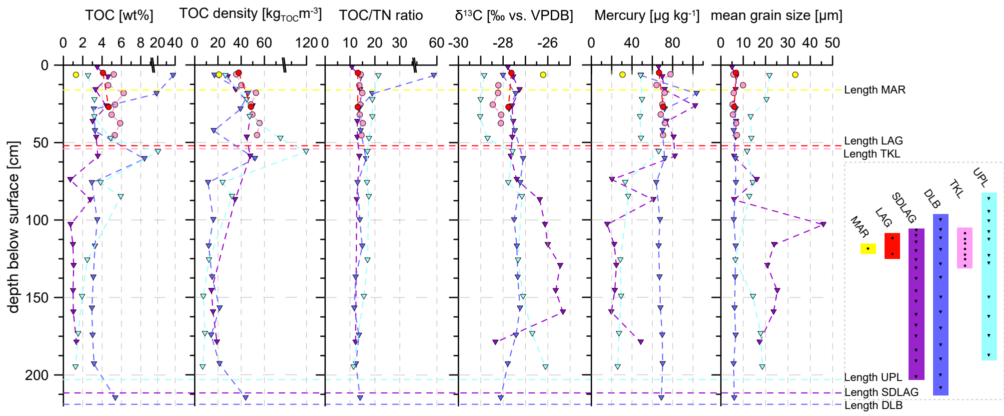

Figure 3: Summary of the biogeochemical parameters total organic carbon (TOC) in weight percent[wt%], TOC density [$kg_{TOC}m^{-3}$], total organic carbon/total nitrogen ratio (TOC/TN ratio), stable carbon isotope ratio ($\delta^{13}C$) per mil relative to Vienna PeeDee Belemnite standard [‰ vs. VPDB], Mercury]µg kg^{-1}] and mean grain size [µm] of the UPL, TKL, DLB, SDLAG, LAG, and MAR profiles, with circles for unfrozen sediments and triangles for frozen sediments. Core abbreviations: UPL: upland permafrost; TKL: thermokarst lake; DLB: drained lake basin; SDLAG: semi-drained lagoon; LAG: lagoon; MAR: marine. Split x axis for TOC, TOC density and TOC/TN ratio.

The TOC/TN ratio is highest in the UPL deposits (mean 17.23), which is significantly higher than in all thermokarst influenced deposits (figure 4). The lowest TOC/TN ratios were measured in both lagoonal

sites, with a mean of 13.1 in the SDLAG core (figure 4). The TOC/TN ratios of the SDLAG core are additionally significantly lower than TOC/TN ratios of the TKL deposits, with a mean of 14.39 (figure 4). The DLB core shows the highest ratio of 58.46 in the uppermost sample and a strong decrease in the deeper samples resulting in a mean of 17.5 (median 13.95) (figure 3 & 4). The TN content of the MAR sample below the detection limit resulted in no TOC/TN ratio.
Strongest variations in the $\delta^{13}C$ ratio were measured in the UPL (–26.1 to –29 ‰) and SDLAG (–25.3 to –28.3 ‰) deposits (figure 3). It is lowest, around –29 ‰, in the upper 50 cm of the UPL core and increases in the deeper part of the core (mean –27.8 ‰) (figure 3). Both the DLB (mean –27.5 ‰) and the SDLAG (mean –26.9 ‰) deposits have significantly higher $\delta^{13}C$ ratios than the TKL deposits, with the lowest mean $\delta^{13}C$ ratio of –28.2 ‰ (figure 4).
The mercury (Hg) analysis of the different cores shows that the thermokarst influenced deposits have higher Hg concentrations compared to the UPL deposits. Significant differences in the Hg content were observed between the DLB and UPL deposits, as well as between the TKL and UPL deposits, with the UPL samples having significantly lower Hg concentrations (figure 4). The median Hg content of the TKL samples (70.63 µg kg^{-1}) is nearly twice as high as the median of the UPL samples (36.34 µg kg^{-1}). Furthermore, the Hg levels of the two samples of the LAG core are in the same range as in the TKL samples (figure 3). The SDLAG profile shows the largest variations in the Hg content across the samples and has no significant differences to the other cores (figure 3 & 4).

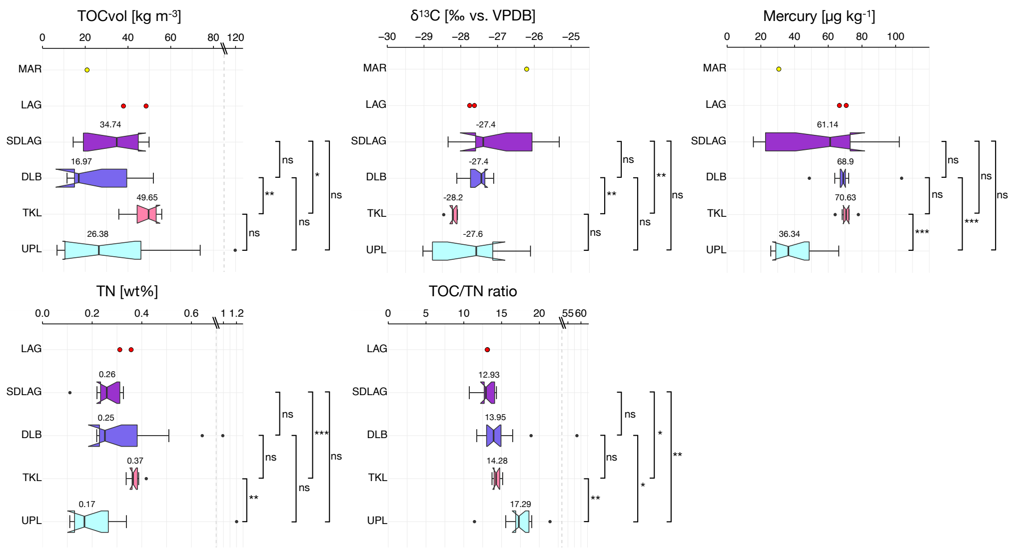

Figure 4: Boxplots of the biogeochemical parameters total organic carbon density (TOCvol) [kg$_{TOC}$m^{-3}], stable carbon isotope ratio ($\delta^{13}C$) per mil relative to Vienna PeeDee Belemnite standard [‰ vs. VPDB], Mercury [µg kg^{-1}], total nitrogen (TN) in weight percent [wt%], and total organic carbon/total nitrogen ratio (TOC/TN ratio) of the SDLAG, DLB, TKL, and UPL profiles and MAR and LAG as individual samples. The whiskers display the data range (outliers as black points) and the boxes show the interquartile range (25-75 %). The black vertical line marks the median and the notches represent the 95 % confidence interval. The bars right of the boxes show the statistical significance of differences between the profiles (ns = not significant; * = p < 0.05; ** = p < 0.01; *** = p < 0.001). Core abbreviations: UPL: upland permafrost; TKL: thermokarst lake; DLB: drained lake basin; SDLAG: semi-drained lagoon; LAG: lagoon; MAR: marine. Split x axis for TOCvol, TN, TOC/TN ratio.

4.3 Biomarker

4.3.1 Organic carbon source indicating indices

The average chain lengths of n-alkanes (ACL) are highest in the three samples of the UPL core, with the highest value of 28.73 in the sample from the middle part (figure 5). Lowest values have been detected for the LAG and the MAR samples, with the lowest from the MAR core (26.2) at a depth of 6.25 cm b.s.l. (figure 5). All cores with more than one sample show higher ACL values in deeper part of the core (figure 5).

As shown in figure 5, the highest P_{aq} values were measured in the MAR sample and the uppermost DLB sample, both having a P_{aq} of 0.66. The MAR sample also has the lowest P_{wax} of 0.52 indicating together with the P_{aq} an aquatic influence on the OM composition (figure 5). Also, the uppermost DLB sample shows a relatively low P_{wax} of 0.56 (figure 5). Other samples with high P_{aq} and low P_{wax} are both LAG samples, with a P_{aq} between 0.61 and 0.64 and a P_{wax} between 0.54 and 0.55, and the uppermost SDLAG sample with a P_{aq} of 0.62 and a P_{wax} of 0.53 (figure 5). The highest P_{wax} values were calculated for all UPL samples, ranging between 0.76 and 0.74 (figure 5). At the same time, they show the lowest P_{aq} values, varying between 0.31 and 0.39 (figure 5). Another sample with a high P_{wax} of 0.73 and a low P_{aq} of 0.41 is the DLB sample from a mean depth of 65.25 cm b.s.l. (figure 5). Overall, the data shows two end members, the marine sample with the most aquatic OM source and the upland permafrost samples with the most terrestrial OM source with the samples from the other location distributed between the two.

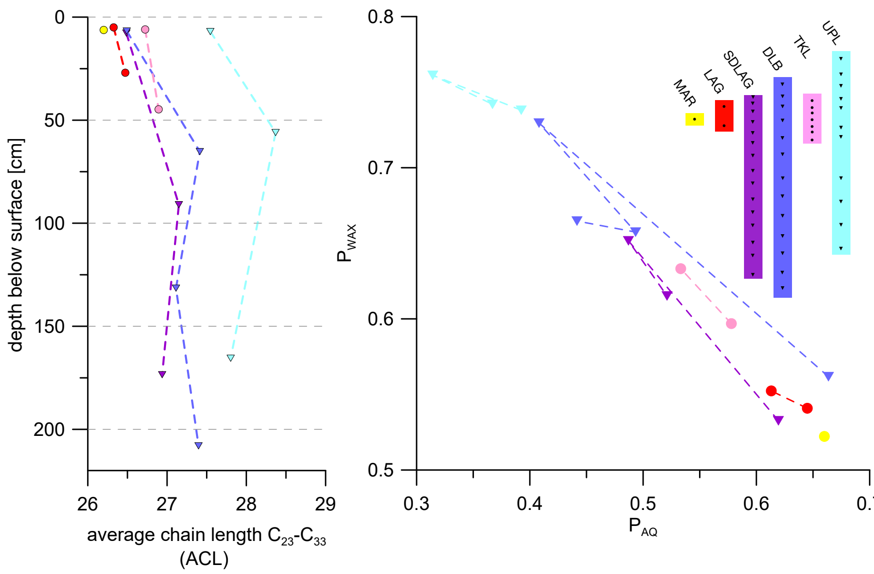

Figure 5: Organic carbon sources are indicated by the n-alkane indices average chain length (ACL) and the proxies P_{AQ}, for aquatic OM, and P_{WAX}, for terrestrial OM, with circles representing unfrozen sediments and triangles representing frozen sediments. Core abbreviations: UPL: upland permafrost; TKL: thermokarst lake; DLB: drained lake basin; SDLAG: semi-drained lagoon; LAG: lagoon; MAR: marine.

4.3.2 Organic carbon quality indicating indices

The carbon preference index of n-alkanes (CPI) shows the widest range in the samples of the DLB core, ranging between 7.88 in the deepest sample and the overall highest value of 12.31, calculated for the sample from a depth of 65.25 cm b.s.l. (figure 6). The lowest CPI values of 5.67 and 6.51 were measured in the LAG samples (figure 6).

The higher plant index (HPA) varies between 0.46 in the deepest SDLAG sample, and 0.81 in the deeper LAG sample (figure 6). The patterns of the HPA over depths in UPL, DLB and SDLAG samples are similar to the pattern of the CPI in terms of values increasing or decreasing over depth within each site (figure 6). In contrast, the patterns of the HPA over depth of TKL and LAG are reversed compared to the CPI, with an increasing value from the deeper sample to the uppermost one (figure 6).

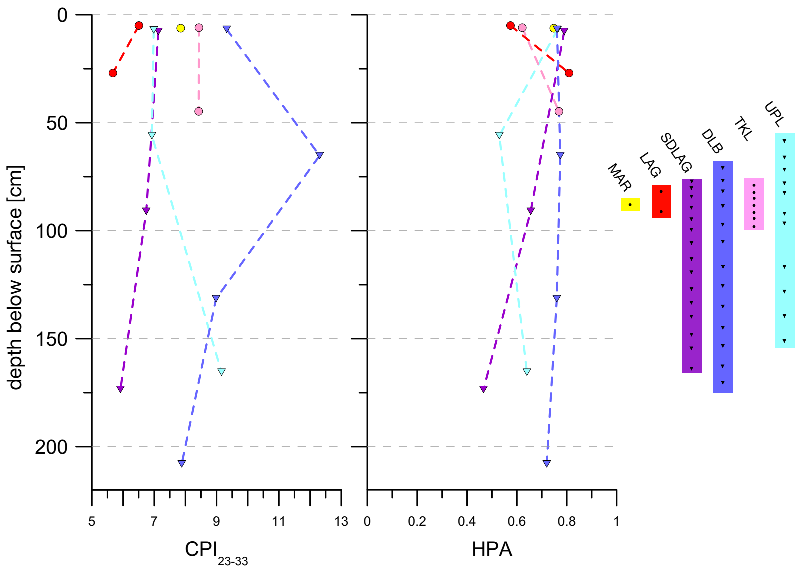

Figure 6: Organic carbon quality is indicated by the lipid-biomarker indices carbon preference index (CPI) and higher plant index (HPA), with circles for unfrozen sediments, triangles for frozen sediments. Core abbreviations: UPL: upland permafrost; TKL: thermokarst lake; DLB: drained lake basin; SDLAG: semi-drained lagoon; LAG: lagoon; MAR: marine.

5 Discussion

5.1 Organic carbon

5.1.1 Organic carbon characteristics

The total range of TOC contents, as well as the TOCvol, of all samples is wide (TOC: 0.72–37.62 wt%; TOCvol: 6.79–119.7 kg m^{-3}) (figures 3 & 4), but comparable to other studies that include permafrost and thermokarst features (TOC: 0.2–43 wt%; TOCvol: 2.8–93.5 kg m^{-3}) (Strauss et al., 2015). A reason for this variability is probably the heterogeneity of the organic source material from the different permafrost and thermokarst landscape features including well-preserved peat, paleosoils and marine influenced coastal areas. The large range of the TOC content (2.94–37.62 wt%) in the DLB core is likely caused by such a mixture of permafrost soils and thermokarst lake origin with different material type input and decomposition processes. Additionally, post-drainage peat accumulation that caused the high TOC contents in the upper soil of the DLB, has been previously shown in other drained thermokarst lake basin studies as well (Fuchs et al., 2019; Jones et al., 2012; Lenz et al., 2016). The large, often flat-bottomed drained lake basins provide perfect conditions for the formation of wetlands, through which most become vegetated in 5–10 years after the drainage event and accumulate peat 10–20 years after (Bockheim et al., 2004; Jones et al., 2012). Compared to the mean TOCvol of permafrost deposits from the Yedoma region (19 kg m^{-3}) and of thermokarst deposits (33 kg m^{-3}) (Strauss et al., 2013), the mean TOCvol of the cores of this study are relatively high (UPL: 37 kg m^{-3}; TKL: 48 kg m^{-3}; DLB: 25 kg m^{-3}; SDLAG: 32 kg m^{-3}), revealing a large pool of carbon in all deposits studied (figure 4). The high TOCvol in the TKL deposits, significantly higher than in the SDLAG and DLB deposits, are likely the result of an interplay of various factors. It might be partially related to the relocation of organic matter (OM) e.g., due to erosion, leading to OC accumulation in the basin and thaw subsidence progression due to ground ice loss (Lenz et al., 2016). Additionally, it is likely that there is a higher input of Holocene OC and an increased primary productivity in the lake stimulated by nutrient release from thawing permafrost (Strauss et al., 2015). The accumulation of OC might be further accelerated by slow decomposition rates in the cold and anaerobic lake environment (Strauss et al., 2015). The lower TOCvol in the refrozen thermokarst features (SDLAG & DLB) might partially be influenced by ground ice accumulation after the drainage of the water bodies. In case of the SDLAG deposits, the lower TOCvol is combined with a low mean TOC content (2.37 wt%), which might be also influenced by a decrease of the primary productivity with the transition from thermokarst lake to lagoon, since strong seasonal fluctuations of the salt content, the lowered, fluctuating water level to almost drainage, and the bedfast ice formation in winter, shortens the period of biological production. Moreover, there might have been decomposition of OM in the SDLAG deposits all year round when the lagoon had more water or rather was in the state of a thermokarst lake, which also could have led to a decreased TOC content.

The analysis of the OC and lipid biomarkers in the deposits shows that they contain OM from different sources, likely additionally influenced by parameters such as salinity, temperature, and water availability. This results in two end members for the sample set, MAR and UPL, with the other sites aligning between. It nicely depicts the transformation processes of soil OM over the course of landscape development from dry terrestrial permafrost over thermokarst lakes, saltwater exposure and finally a marine state (Jenrich et al., 2021). One indicator for the source of OM is the TOC/TN ratio, with lower values indicating a stronger aquatic influence and higher values indicating a stronger terrestrial influence (Meyers, 1997). The highest mean TOC/TN ratio was measured in the UPL deposits (17.2), significantly higher than in the three thermokarst landscape features included in the statistical analysis, indicating the strongest terrestrial influence on the OM composition of the UPL core (figure 3 & 4). The lowest mean TOC/TN ratios, significantly lower than in the UPL and TKL deposits, were measured in the LAG and SDLAG samples (13.1), indicating the strongest aquatic influence on those deposits, e.g. from algae and bacteria. The largest variation of the TOC/TN ratio is shown in the DLB core (11.7–58.5), indicating different sources of OM during the different stages of the thermokarst lake evolution. Since the TOC/TN ratio can also be influenced by other processes like the level of degradation of OM, we also analysed the n-alkane distribution in the samples and calculated the P_{aq} and P_{wax} as indicators of the source of OM. The results of these parameters also show the two end members (figure 5) with the highest ACL values and highest P_{wax}, thus the strongest terrestrial influence on the OM composition in the UPL deposits and the strongest aquatic influence on the

OM composition in the marine sample, with the lowest ACL and a high P_{aq}. It is also shown in figure 5 that all thermokarst deposits (LAG, SDLAG, DLB & TKL) align between the two end members, thus are stronger influenced by aquatic OM than the UPL samples. Moreover, figure 5 hints on a change of source of OM in the SDLAG, DLB and UPL profiles from the upper soil compared to the samples between 50 and 100 cm b.s.l. and between 100 and 200 cm b.s.l. This might not be influenced by different stages of the thermokarst lake evolution, but rather by changes of hydrological conditions at the time of deposition, or by the relocation of OM, for example due to cryoturbation or roots, since both the terrestrial endmember UPL and the thermokarst features show that changes.

5.1.2 Organic carbon degradation

On the basis of the TOC/TN and the $\delta^{13}C$ ratios, as well as the biomarker indices CPI and HPA the level of degradation of the OM stored in the soils is discussed (figure 3, 4 & 6).

The decomposition of OM releases carbon as CO_2 and CH_4 and portions of nitrogen as N_2O from the soils to the atmosphere (Schuur et al., 2022; Strauss et al., 2024b; Voigt et al., 2020). Deposits containing further degraded OM have lower TOC/TN ratios than those containing fresh OM due to a larger share of nitrogen in the soils (Andersson et al., 2012; Weintraub and Schimel, 2005). Thus, in addition to the OM sources the TOC/TN ratios also contain a component dependent on the OM decomposition level. As seen above, the TOC/TN ratios in the UPL deposits were significantly higher compared to the thermokarst influenced deposits (SDLAG, TKL, DLB), which was interpreted as a higher terrestrial character of the OM in the UPL samples. However, it is also likely that parts of the differences derive from the fact that the thermokarst deposits contain stronger degraded OM, due to longer unfrozen periods. The mean TOC/TN ratio of the UPL (17.23) is in the lower range of the ratios measured by Routh et al. (2014) in Arctic peat soils (15–25) and lower than the mean TOC/TN measured by Fuchs et al. (2019) in upland permafrost samples in the Teshekpuk region (21.3). However, they are higher than the mean TOC/TN ratio measured by Haugk et al. (2021) in Siberia (13.2). The mean TOC/TN ratios in the TKL (14.4) and the DLB (17.5) profiles are slightly higher than those measured by Fuchs et al. (2019) with a mean TOC/TN ratio in the upper 100 cm of the soils of 12.6 in TKL deposits and 16.6 of DLB deposits. These rather high values, compared to literature, found in all profiles indicate a relatively high level of preservation of the accumulated OM, leading to a likely good quality for future degradation and therefore a vulnerability to decomposition after thaw.

The carbon isotopic signal is also influenced by both factors: OM sources and OM degradation. Terrestrial material usually shows lighter and marine OM heavier $\delta^{13}C$ signals and due to the preferred release of $^{12}CO_2$ during degradation, the residual OM becomes isotopically heavier (Andersson et al., 2012). In the uppermost samples (down to 50 cm) the data resembled the two-end member model of the OM sources with the UPL samples showing the lightest $\delta^{13}C$ values (stronger terrestrial character) and the MAR sample exhibiting the heaviest signal (marine influenced) (figure 3). The other samples show intermediate data resembling supply of different OM sources and/or different level of degradation. In the deeper part the picture is less clear. The UPL samples are isotopically heavier plotting in the range of the DLB data, whose $\delta^{13}C$ signal is relatively constant throughout the whole core. This could indicate a higher level of degradation of OM in the deeper UPL deposits. The deeper SDLAG samples are, with exception of the deepest sample, isotopically significantly heavier which could indicate a stronger aquatic/marine influence in the lagoon during time of deposition rather than a stronger degradation of the OM.

Also, the CPI depends on both the source of OM and the level of OM maturation. The original odd-over even carbon number predominance of the indigenous *n*-alkanes in a sample is determined by the source material and is changing to lower values during OM maturation. Here, the wide range of different CPIs most likely rather resemble the various mixtures of OM at the different sites. This is supported by findings of Jongejans et al. (2021), also reporting that the CPI represents rather the source OM in such relatively young sediments. The HPA shows a very narrow band of values for all samples. In the uppermost sample of the TKL and LAG, samples show a shift to lower values which could indicate a higher degradation of the OM in the surface sediments. The UPL and SDLAG samples show lower HPA values in the deeper part of the core which might point to periods of stronger degradation in the past. However, the material shows low variability in the HPA values overall, plotting in the upper scale of the parameter and therefore indicating relatively less degraded OM. Thus, with ongoing climate warming and thawing of the deeper permafrost layers, the preserved OM of good quality could become available to decomposition, leading to increased emissions of greenhouse gases.

5.2 Additional Parameters

Processes that have an influence on OC characteristics in soils can also have effects on other parameters. To identify such associations, a correlation matrix was computed integrating the measured biogeochemical and sedimentological parameters (figure 7). TOC content and TOCvol are positively correlated with the Hg content in the samples. In general, sources for Hg, accumulating in Arctic soils, can be both natural and anthropogenic. Natural sources, contributing to the increase of atmospheric Hg and subsequent deposition into soils, include boreal forest fires and volcanic activity. Anthropogenic input has significantly intensified due to industrialization and expanding land use (Jonsson et al., 2017). A reason for the positive correlation of the TOCvol with Hg is presumably that approximately 70 % of the Hg in the Arctic tundra is derived from gaseous elemental Hg, which is ubiquitously present in the atmosphere (Obrist et al., 2017). Since the deposition of gaseous elemental Hg is strongly influenced by the Hg uptake of vegetation, sites with a higher input of OM and therefore higher TOCvol also accumulate higher levels of Hg bound in the plant matter (Obrist et al., 2017). The Hg content in the deposits is furthermore negatively correlated with the $\delta^{13}C$ ratio. This correlation indicates that there are higher mercury contents in the deposits with OM from a terrestrial or mixed terrestrial/aquatic source. For example, the marine influenced MAR sample with the highest $\delta^{13}C$ signal shows the lowest HG content and the upper UPL samples with the lower $\delta^{13}C$ signal shows higher HG contents than the lower UPL samples with the higher $\delta^{13}C$ signal (figure 3). The same can be observed for the SDLAG samples. Additionally, the Hg content correlates negatively with the mean grainsize. This is displayed in the mercury contents in the fine-grained freshwater thermokarst features (mean DLB: 69.87 $\mu g\ kg^{-1}$; mean TKL: 70.74 $\mu g\ kg^{-1}$) that are significantly higher than in the UPL deposits (mean UPL: 40.16 $\mu g\ kg^{-1}$) (figure 4). A reason for this could be that the thermokarst processes might affect the distribution and accumulation of Hg due to the release of Hg from previously freeze-looked Hg-containing OM in the soil upon decomposition (Schuster et al., 2018). Additionally, thermokarst, erosion and an increased soil water movement in a thickening active layer, all triggered by permafrost thaw, can increase the transport of Hg from the soils to Arctic surface waters, resulting in higher Hg concentrations in lacustrine and post-drainage sediments (Rydberg et al., 2010), which is also indicated by the data of this study. Especially in the SDLAG core the correlation of thermokarst processes with OC and sediment characteristics and the Hg content is visible. The GSD shows a peak at coarser grain sizes, between fine sand and silt, similar to the UPL deposits in the deeper half of the core below 100 cm b.s.l. (figure 2). The upper half of the core shows a peak at finer grain sizes similar to the thermokarst features, indicating lacustrine deposits (figure 2). This shift indicates that there is less influence of thermokarst processes in the deeper half of the core. Additionally, there are lower Hg contents in the deeper part (15.57–48.65 µg kg^{-1}) akin to the Hg content in the UPL deposits and accompanied by low TOC contents (0.74–1.35 wt%) (figure 3). In contrast, the thermokarst influenced upper half of the core show higher Hg concentrations (20.27–102.17 µg kg^{-1}), similar to the Hg concentrations in the other thermokarst features, accompanied by higher TOC contents (0.72–4.65 wt%) (figure 3).

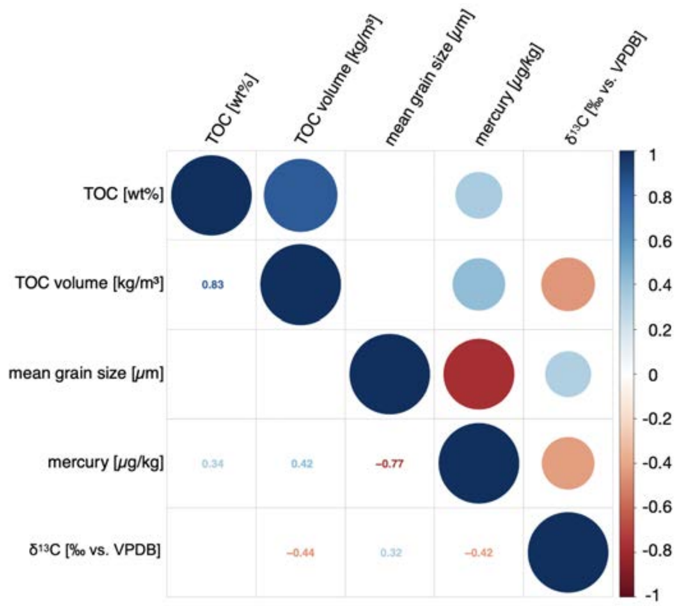

Figure 7: Correlation matrix of sedimentological and biogeochemical parameters. Strong positive correlations in dark blue, strong negative correlations in dark red. TOC: total organic carbon content in weight percent; TOC volume: organic carbon density; $\delta^{13}C$: stable carbon isotope ratio in per mil relative to Vienna PeeDee Belemnite standard.

5.4 Influence of salinity and soil condition on the biogeochemical soil characteristics

The statistical analysis for differences between frozen (UPL, DLB, SDLAG) and unfrozen (TKL, LAG, MAR) as well as saline (SDLAG, LAG, MAR) and non-saline (UPL, TKL, DLB) deposits shows for most parameters only low variation (figures 8 & 9). However, significant differences were found for ACL, $\delta^{13}C$, TOC/TN ratio and CPI for the saline/non-saline sites and for TOCvol, TN, ACL and $\delta^{13}C$ for the frozen/unfrozen sites.

Both, the comparison of the saline/non saline and the frozen/unfrozen deposits show significant differences for the ACL of *n*-alkanes. Since the ACL is influenced by the source of OM in the soil, this likely indicates that the input of OM is influenced by the salinity and whether the soils are frozen or unfrozen. It is significantly lower in the saline (26.48) and unfrozen deposits (median ACL 26.47) compared to the non-saline (27.4) and frozen deposits (median ACL 27.27) (figure 8 & 9) indicating a stronger aquatic influence on the OM composition in the saline and/or unfrozen deposits. In case of the comparison of the saline/non-saline deposits this is accompanied by significantly higher $\delta^{13}C$ ratios and lower TOC/TN in the saline deposits (median δ13C: –27.47; median TOC/TN: 13.1) compared to the non-saline deposits (median δ13C: –27.58; median TOC/TN: 14.76) (figure 8), supporting the presence of a stronger aquatic OM proportion in the saline deposits. The CPI values are higher in the non-saline samples, which could resemble different odd over even carbon number predominance distribution of *n*-alkanes in the aquatic/marine vs. terrestrial organic biomass. All three parameters, the $\delta^{13}C$, the TOC/TN ratio, and the CPI, might additionally indicate more fresh, undegraded OM in the non-saline deposits, which is likely influenced by a decreased input of fresh OM in the saline environments due to a decreased primary productivity, an increased microbial activity, since the salinity in the soil water leads to a depression of its freezing point, thus a longer unfrozen period, and less retention of fresh OM in the coarse marine sediments (Bischoff et al., 2018; Jongejans, 2022).

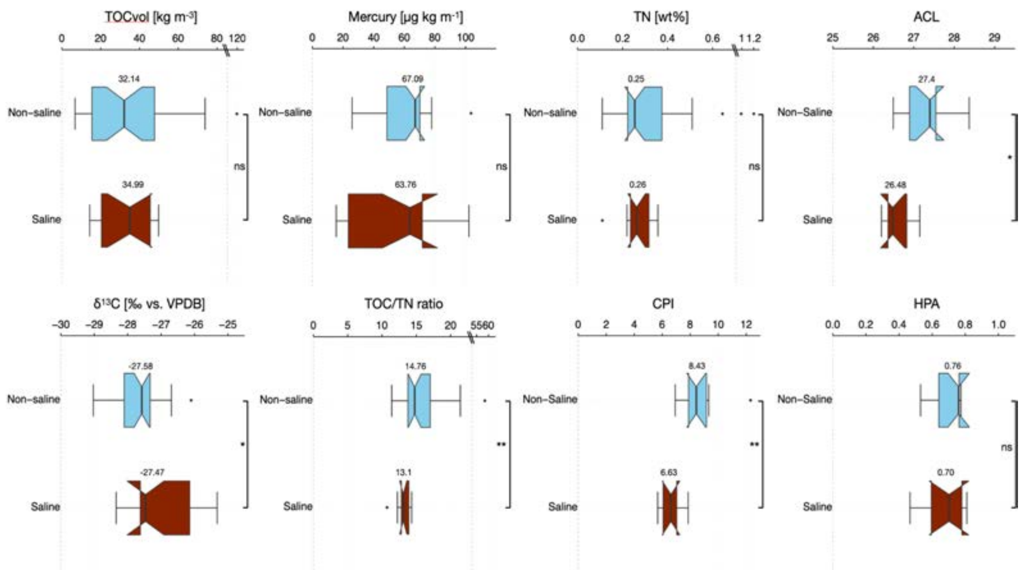

Figure 8: Boxplots of the biogeochemical parameters total organic carbon density (TOCvol) [$kg_{TOC}m^{-3}$], Mercury [µg kg^{-1}], total nitrogen (TN) in weight percent [wt%], average chain length of *n*-alkanes (ACL), stable carbon isotope ratio ($\delta^{13}C$) per mil relative to Vienna PeeDee Belemnite standard [‰ vs. VPDB], total organic carbon/total nitrogen ratio (TOC/TN ratio), carbon preference index (CPI), and higher plant alcohol index (HPA) of profiles in non-saline [blue] (including upland permafrost, thermokarst lake sediments, and drained lake basin sediments) and saline [red] (including semi-drained lagoon sediments, lagoon sediments, and marine sediments) soil settings. The whiskers display the data range (outliers as black points), and the boxes show the interquartile range (25–75 %). The black vertical line marks the median and the notches represent the 95 % confidence interval. The bars right of the boxes show the statistical significance of differences between the groups (ns = not significant; * = $p < 0.05$; ** = $p < 0.01$; *** = $p < 0.001$).

Moreover, the comparison of the frozen and unfrozen deposits shows significant differences in the TOCvol and the TN content. The frozen deposits have significantly lower TOCvol (median 24 kg m^{-3}) and TN (median 0.24 wt%) compared to the unfrozen deposits (median TOCvol 48.41 kg m^{-3}; median TN

0.36 wt%) (figure 9). The higher TN content in the unfrozen deposits is likely influenced by erosion processes, reactivated soil water movement in thawed permafrost, as well as surface runoff from nitrogen-rich upland permafrost and the refrozen thermokarst features, leading to the deposition of nitrogen in the aquatic systems (Strauss et al., 2024b). Furthermore, if bioavailable, the increased TN content in thawed permafrost soils could potentially enhance the ecosystem productivity, thereby influencing the increased TOCvol in the unfrozen deposits. Also, the significantly lower δ^{13}C values in the unfrozen deposits potentially indicates a higher input of fresh OM to the unfrozen thermokarst environments. Additionally, thaw subsidence progression in the unfrozen deposits and the accumulation of ground ice in the (re)frozen deposits likely have an influence on the TOCvol (Strauss et al., 2015).

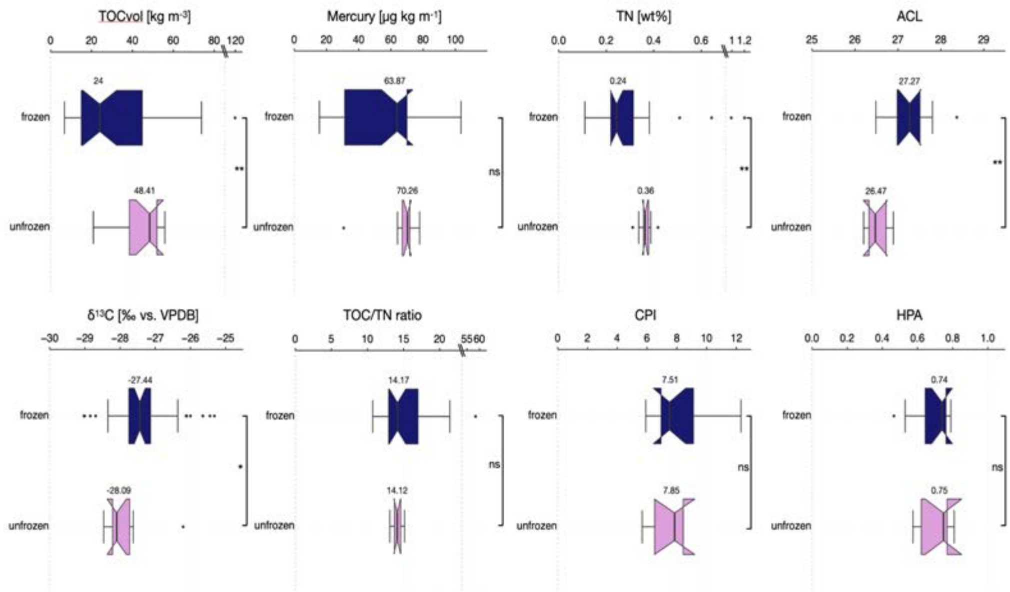

Figure 9: Boxplots of the biogeochemical parameters total organic carbon density (TOCvol) [$kg_{TOC}m^{-3}$], Mercury [µg kg^{-1}], total nitrogen (TN) in weight percent [wt%], average chain length of *n*-alkanes (ACL), stable carbon isotope ratio (δ^{13}C) per mil relative to Vienna PeeDee Belemnite standard [‰ vs. VPDB], total organic carbon/total nitrogen ratio (TOC/TN ratio), carbon preference index (CPI), and higher plant alcohol index (HPA) of frozen profiles [dark blue] (including upland permafrost, drained lake basin sediments, and semi-drained lagoon sediments) and unfrozen [pink] (including thermokarst lake sediments, lagoon sediments, and marine sediments) soil profiles. The whiskers display the data range (outliers as black points), and the boxes show the interquartile range (25–75 %). The black vertical line marks the median and the notches represent the 95 % confidence interval. The bars right of the boxes show the statistical significance of differences between the groups (ns = not significant; * = $p < 0.05$; ** = $p < 0.01$; *** = $p < 0.001$).

The HPA data are quite similar for the frozen/unfrozen and saline/non-saline sites and plot in the upper range of the parameter scale. This could indicate a comparable level of degradation between all sites and the potential to act as a good substrate for greenhouse gas production when actively metabolized. No significant differences were additionally identified for the Hg content. This might be influenced by the way Hg accumulates in sedimentary deposits. We see evidence that thawing permafrost initiates the reactivation and accumulation of Hg in thermokarst affected deposits. Unlike other measured parameters, these processes are not necessarily reversed upon refreezing of the deposits, but instead tend to pause until repeated thawing of the soils. Consequently, the amount of Hg in the soils is likely to increase with every thermokarst lake and thawing cycle the deposits undergo, without the current soil condition and other properties such as salinity, having a major influence accumulative effect.

6 Conclusion

The analysis of the six sediment cores from a thermokarst-affected coastal lowland in North Alaska showed that the OC characteristics in deposits of the different landscape features are diverse. The highest TOC contents were measured in the drained lake basin and thermokarst lake deposits, likely caused by an increased primary productivity and Holocene OC input. This is also reflected by the analysis of the quality of OC, with high CPI values indicating fresh, undegraded OM in both profiles. The deposits of a semi-drained thermokarst lagoon had significantly lower TOC contents than the freshwater-influenced thermokarst deposits. Additionally, there were significant differences in the CPI, $\delta^{13}C$, and TOC/TN ratio between saline and non-saline deposits, indicating a domination of aquatic OM in the saline deposits, and moreover likely indicating a higher level of fresh, undegraded OM in the non-saline deposits. The intrusion of saltwater to the deposits seems to lead to a lower quality of OM in the soils, likely influenced by a lower input of fresh OM due to a decreased primary productivity, and potentially enhanced by degradational processes. Indicated by the ACL and P_{aq}, P_{wax}, all thermokarst-influenced deposits showed a stronger aquatic influence on the OM composition than the upland permafrost deposits. Besides the differences in the source of OM, the comparison of unfrozen and frozen deposits showed higher TOCvol and TN contents in the unfrozen deposits. This is also likely influenced by differences in the level of primary productivity, depositional- and degradational processes. Thus, our findings provide valuable insights into the dynamics of carbon storage and vulnerability to decomposition in response to environmental changes in a coastal permafrost landscape, since they reflect the complex interplay of environmental factors, landform characteristics and impacts of climate change on these dynamic Arctic landscapes. The integration of carbon dioxide and methane emission measurements in further studies could complement the findings and provide an even more comprehensive picture of carbon fluxes across the geomorphological, hydrological, and ecological diverse landscapes of Arctic coastal lowlands and the influence of permafrost thaw and saltwater intrusion on the deposits.

The Supplement related to this article is available online at doi: *link will follow*

Author contributions. J. Strauss, M. Jenrich and F. Giest designed this study. J. Strauss, G. Grosse, and M. Jenrich developed the overall coring plans for the Perma-X Lagoons field campaign and conducted the fieldwork in 2022. B. M. Jones provided guidance on site selection, field assistance, and logistical support for the expedition. J. Strauss, M. Jenrich and F. Giest did the subsampling for all cores. F. Giest carried out the laboratory analyses. K. Mangelsdorf supported the biomarker interpretation. F. Giest wrote the first draft of the manuscript. All co-authors contributed within their specific expertise to data interpretation as well as manuscript writing.

Acknowledgements. We acknowledge support by the Deutsche Bundestiftung Umwelt to MJ. BMJ was supported by U.S. National Science Foundation awards OPP-1806213 and OPP-2336164. We thank Justin Lindemann, Jonas Sernau, Antje Eulenberg and Mikaela Weiner for their support and assistance in the lab. AWI base funds were used for facilitating the expedition and laboratory analyses. The Teshekpuk Lake Observatory managed by BMJ was used as a base during the expedition. We thank Ukpeaġvik Iñupiat Corporation for the logistical support, especially for the fixing of snow machines in remote areas. We further thank the Iñupiat community for allowing us to do work on their land.

References

Andersson, R. A., Meyers, P., Hornibrook, E., Kuhry, P., and Mörth, C.: Elemental and isotopic carbon and nitrogen records of organic matter accumulation in a Holocene permafrost peat sequence in the East European Russian Arctic, J Quaternary Science, 27, 545–552, https://doi.org/10.1002/jqs.2541, 2012.

Arp, C. D., Jones, B. M., Urban, F. E., and Grosse, G.: Hydrogeomorphic processes of thermokarst lakes with grounded-ice and floating-ice regimes on the Arctic coastal plain, Alaska, Hydrological Processes, 25, 2422–2438, https://doi.org/10.1002/hyp.8019, 2011.

Ballinger, T. J., Bigaalke, S., Walsh, J. E., Brettschneider, B., Thoman, R. L., Bhatt, U. S., Hanna, E., Hanssen-Bauer, I., Kim, S.-J., Overland, J. E., and Wang, M.: NOAA Arctic Report Card 2023: Surface Air Temperature, https://doi.org/10.25923/X3TA-6E63, 2023.

Bischoff, N., Mikutta, R., Shibistova, O., Dohrmann, R., Herdtle, D., Gerhard, L., Fritzsche, F., Puzanov, A., Silanteva, M., Grebennikova, A., and Guggenberger, G.: Organic matter dynamics along a salinity gradient in Siberian steppe soils, Biogeosciences, 15, 13–29, https://doi.org/10.5194/bg-15-13-2018, 2018.

Biskaborn, B. K., Smith, S. L., Noetzli, J., Matthes, H., Vieira, G., Streletskiy, D. A., Schoeneich, P., Romanovsky, V. E., Lewkowicz, A. G., Abramov, A., Allard, M., Boike, J., Cable, W. L., Christiansen, H. H., Delaloye, R., Diekmann, B., Drozdov, D., Etzelmüller, B., Grosse, G., Guglielmin, M., Ingeman-Nielsen, T., Isaksen, K., Ishikawa, M., Johansson, M., Johannsson, H., Joo, A., Kaverin, D., Kholodov, A., Konstantinov, P., Kröger, T., Lambiel, C., Lanckman, J.-P., Luo, D., Malkova, G., Meiklejohn, I., Moskalenko, N., Oliva, M., Phillips, M., Ramos, M., Sannel, A. B. K., Sergeev, D., Seybold, C., Skryabin, P., Vasiliev, A., Wu, Q., Yoshikawa, K., Zheleznyak, M., and Lantuit, H.: Permafrost is warming at a global scale, Nat Commun, 10, 264, https://doi.org/10.1038/s41467-018-08240-4, 2019.

Blott, S. J. and Pye, K.: GRADISTAT: a grain size distribution and statistics package for the analysis of unconsolidated sediments, Earth Surf Processes Landf, 26, 1237–1248, https://doi.org/10.1002/esp.261, 2001.

Bockheim, J. G., Hinkel, K. M., Eisner, W. R., and Dai, X. Y.: Carbon Pools and Accumulation Rates in an Age-Series of Soils in Drained Thaw-Lake Basins, Arctic Alaska, Soil Science Soc of Amer J, 68, 697–704, https://doi.org/10.2136/sssaj2004.6970, 2004.

Bray, E. E. and Evans, E. D.: Distribution of n-paraffins as a clue to recognition of source beds, Geochimica et Cosmochimica Acta, 22, 2–15, https://doi.org/10.1016/0016-7037(61)90069-2, 1961.

Cohen, J., Zhang, X., Francis, J., Jung, T., Kwok, R., Overland, J., Ballinger, T. J., Bhatt, U. S., Chen, H. W., Coumou, D., Feldstein, S., Gu, H., Handorf, D., Henderson, G., Ionita, M., Kretschmer, M., Laliberte, F., Lee, S., Linderholm, H. W., Maslowski, W., Peings, Y., Pfeiffer, K., Rigor, I., Semmler, T., Stroeve, J., Taylor, P. C., Vavrus, S., Vihma, T., Wang, S., Wendisch, M., Wu, Y., and Yoon, J.: Divergent consensuses on Arctic amplification influence on midlatitude severe winter weather, Nat. Clim. Chang., 10, 20–29, https://doi.org/10.1038/s41558-019-0662-y, 2020.

Ficken, K. J., Li, B., Swain, D. L., and Eglinton, G.: An n-alkane proxy for the sedimentary input of submerged/floating freshwater aquatic macrophytes, Organic Geochemistry, 31, 745–749, https://doi.org/10.1016/S0146-6380(00)00081-4, 2000.

Fuchs, M., Lenz, J., Jock, S., Nitze, I., Jones, B. M., Strauss, J., Günther, F., and Grosse, G.: Organic Carbon and Nitrogen Stocks Along a Thermokarst Lake Sequence in Arctic Alaska, JGR Biogeosciences, 124, 1230–1247, https://doi.org/10.1029/2018JG004591, 2019.

Grosse, G., Jones, B., and Arp, C.: 8.21 Thermokarst Lakes, Drainage, and Drained Basins, in: Treatise on Geomorphology, Elsevier, 325–353, https://doi.org/10.1016/B978-0-12-374739-6.00216-5, 2013.

Harvey, A.: Properties of Ice and Supercooled Water, in: CRC Handbook of Chemistry and Physics, CRC Press, Boca Raton, FL, 2019.

Haugk, C., Jongejans, L. L., Mangelsdorf, K., Fuchs, M., Ogneva, O., Palmtag, J., Mollenhauer, G., Mann, P. J., Overduin, P. P., Grosse, G., Sanders, T., Tuerena, R. E., Schirrmeister, L., Wetterich, S., Kizyakov, A., Karger, C., and Strauss, J.: Organic matter characteristics of a rapidly eroding permafrost cliff in NE Siberia (Lena Delta, Laptev Sea region), Biogeochemistry: Organic Biogeochemistry, https://doi.org/10.5194/bg-2021-331, 2021.

Hugelius, G., Strauss, J., Zubrzycki, S., Harden, J. W., Schuur, E. A. G., Ping, C.-L., Schirrmeister, L., Grosse, G., Michaelson, G. J., Koven, C. D., O'Donnell, J. A., Elberling, B., Mishra, U., Camill, P., Yu, Z., Palmtag, J., and Kuhry, P.: Estimated stocks of circumpolar permafrost carbon with quantified uncertainty ranges and identified data gaps, Biogeosciences, 11, 6573–6593, https://doi.org/10.5194/bg-11-6573-2014, 2014.

Intergovernmental Panel on Climate Change (IPCC): The Ocean and Cryosphere in a Changing Climate: Special Report of the Intergovernmental Panel on Climate Change, 1st ed., Cambridge University Press, https://doi.org/10.1017/9781009157964, 2022.

Intergovernmental Panel on Climate Change (IPCC): Climate Change 2022 – Impacts, Adaptation and Vulnerability: Working Group II Contribution to the Sixth Assessment Report of the Intergovernmental Panel on Climate Change, 1st ed., Cambridge University Press, https://doi.org/10.1017/9781009325844, 2023.

Jenrich, M., Angelopoulos, M., Grosse, G., Overduin, P. P., Schirrmeister, L., Nitze, I., Biskaborn, B. K., Liebner, S., Grigoriev, M., Murray, A., Jongejans, L. L., and Strauss, J.: Thermokarst Lagoons: A Core-Based Assessment of Depositional Characteristics and an Estimate of Carbon Pools on the Bykovsky Peninsula, Front. Earth Sci., 9, 637899, https://doi.org/10.3389/feart.2021.637899, 2021.

Jones, B. M. and Arp, C. D.: Observing a Catastrophic Thermokarst Lake Drainage in Northern Alaska, Permafrost & Periglacial, 26, 119–128, https://doi.org/10.1002/ppp.1842, 2015.

Jones, B. M., Arp, C. D., Jorgenson, M. T., Hinkel, K. M., Schmutz, J. A., and Flint, P. L.: Increase in the rate and uniformity of coastline erosion in Arctic Alaska, Geophysical Research Letters, 36, 2008GL036205, https://doi.org/10.1029/2008GL036205, 2009.

Jones, B. M., Farquharson, L. M., Baughman, C. A., Buzard, R. M., Arp, C. D., Grosse, G., Bull, D. L., Günther, F., Nitze, I., Urban, F., Kasper, J. L., Frederick, J. M., Thomas, M., Jones, C., Mota, A., Dallimore, S., Tweedie, C., Maio, C., Mann, D. H., Richmond, B., Gibbs, A., Xiao, M., Sachs, T., Iwahana, G., Kanevskiy, M., and Romanovsky, V. E.: A decade of remotely sensed observations highlight complex processes linked to coastal permafrost bluff erosion in the Arctic, Environ. Res. Lett., 13, 115001, https://doi.org/10.1088/1748-9326/aae471, 2018.

Jones, B. M., Grosse, G., Farquharson, L. M., Roy-Léveillée, P., Veremeeva, A., Kanevskiy, M. Z., Gaglioti, B. V., Breen, A. L., Parsekian, A. D., Ulrich, M., and Hinkel, K. M.: Lake and drained lake basin systems in lowland permafrost regions, Nat Rev Earth Environ, 3, 85–98, https://doi.org/10.1038/s43017-021-00238-9, 2022.

Jones, M. C., Grosse, G., Jones, B. M., and Walter Anthony, K.: Peat accumulation in drained thermokarst lake basins in continuous, ice-rich permafrost, northern Seward Peninsula, Alaska, J. Geophys. Res., 117, 2011JG001766, https://doi.org/10.1029/2011JG001766, 2012.

Jongejans, L. L.: Ablagerung von organischem Kohlenstoff in eisreichem PermafrostOrganic matter stored in ice-rich permafrost: future permafrost thaw and greenhouse gas release: zukünftige Permafrosttauen und Treibhausgasemissionen, Universität Potsdam, https://doi.org/10.25932/PUBLISHUP-56491, 2022.

Jongejans, L. L., Mangelsdorf, K., Schirrmeister, L., Grigoriev, M. N., Maksimov, G. M., Biskaborn, B. K., Grosse, G., and Strauss, J.: n-Alkane Characteristics of Thawed Permafrost Deposits Below a Thermokarst Lake on Bykovsky Peninsula, Northeastern Siberia, Front. Environ. Sci., 8, 118, https://doi.org/10.3389/fenvs.2020.00118, 2020.

Jongejans, L. L., Liebner, S., Knoblauch, C., Mangelsdorf, K., Ulrich, M., Grosse, G., Tanski, G., Fedorov, A. N., Konstantinov, P. Ya., Windirsch, T., Wiedmann, J., and Strauss, J.: Greenhouse gas production and lipid biomarker distribution in Yedoma and Alas thermokarst lake sediments in Eastern Siberia, Global Change Biology, 27, 2822–2839, https://doi.org/10.1111/gcb.15566, 2021.

Jonsson, S., Andersson, A., Nilsson, M. B., Skyllberg, U., Lundberg, E., Schaefer, J. K., Åkerblom, S., and Björn, E.: Terrestrial discharges mediate trophic shifts and enhance methylmercury accumulation in estuarine biota, Sci. Adv., 3, e1601239, https://doi.org/10.1126/sciadv.1601239, 2017.

Jorgenson, M. T. and Grunblatt, J.: Landscape-Level Ecological Mapping of northern Alaska and Field Site Photography, Arctic Landscape Conservation Cooperative, U.S. Fish and Wildlife Service, Fairbanks, Alaska, 2013.

Jorgenson, M. T. and Shur, Y.: Evolution of lakes and basins in northern Alaska and discussion of the thaw lake cycle, J. Geophys. Res., 112, 2006JF000531, https://doi.org/10.1029/2006JF000531, 2007.

Jorgenson, M. T., Shur, Y., Osterkamp, T., Ping, C.-L., and Kanevskiy, M.: Part 1: Environment of the Beaufort Coastal Plain, in: Coastal Region of Northern Alaska - Guidebook to Permafrost and related features, Guidebook 10-1, edited by: Jorgenson, M. T., Division of Geological & Geophysical Surveys, 1–39, 2011.

Kokelj, S. V. and Jorgenson, M. T.: Advances in Thermokarst Research, Permafrost & Periglacial, 24, 108–119, https://doi.org/10.1002/ppp.1779, 2013.

Lenz, J., Jones, B. M., Wetterich, S., Tjallingii, R., Fritz, M., Arp, C. D., Rudaya, N., and Grosse, G.: Impacts of shore expansion and catchment characteristics on lacustrine thermokarst records in permafrost lowlands, Alaska Arctic Coastal Plain, Arktos, 2, 25, https://doi.org/10.1007/s41063-016-0025-0, 2016.

Marzi, R., Torkelson, B. E., and Olson, R. K.: A revised carbon preference index, Organic Geochemistry, 20, 1303–1306, https://doi.org/10.1016/0146-6380(93)90016-5, 1993.

Meyers, P. A.: Organic geochemical proxies of paleoceanographic, paleolimnologic, and paleoclimatic processes, Organic Geochemistry, 27, 213–250, https://doi.org/10.1016/S0146-6380(97)00049-1, 1997.

Miner, K. R., Turetsky, M. R., Malina, E., Bartsch, A., Tamminen, J., McGuire, A. D., Fix, A., Sweeney, C., Elder, C. D., and Miller, C. E.: Permafrost carbon emissions in a changing Arctic, Nat Rev Earth Environ, 3, 55–67, https://doi.org/10.1038/s43017-021-00230-3, 2022.

Mishra, U., Hugelius, G., Shelef, E., Yang, Y., Strauss, J., Lupachev, A., Harden, J. W., Jastrow, J. D., Ping, C.-L., Riley, W. J., Schuur, E. A. G., Matamala, R., Siewert, M., Nave, L. E., Koven, C. D., Fuchs, M., Palmtag, J., Kuhry, P., Treat, C. C., Zubrzycki, S., Hoffman, F. M., Elberling, B., Camill, P., Veremeeva, A., and Orr, A.: Spatial heterogeneity and environmental predictors of permafrost region soil organic carbon stocks, Sci. Adv., 7, eaaz5236, https://doi.org/10.1126/sciadv.aaz5236, 2021.

Obrist, D., Agnan, Y., Jiskra, M., Olson, C. L., Colegrove, D. P., Hueber, J., Moore, C. W., Sonke, J. E., and Helmig, D.: Tundra uptake of atmospheric elemental mercury drives Arctic mercury pollution, Nature, 547, 201–204, https://doi.org/10.1038/nature22997, 2017.

Olefeldt, D., Goswami, S., Grosse, G., Hayes, D., Hugelius, G., Kuhry, P., McGuire, A. D., Romanovsky, V. E., Sannel, A. B. K., Schuur, E. A. G., and Turetsky, M. R.: Circumpolar distribution and carbon storage of thermokarst landscapes, Nat Commun, 7, 13043, https://doi.org/10.1038/ncomms13043, 2016.

Poynter, J.: Molecular stratigraphy: The recognition of paleo-climate signals in organic geochemical data, School of Chemistry, University of Bristol, Bristol, 324 pp., 1989.

Poynter, J. and Eglinton, G.: 14. Molecular Composition of three Sediments from Hole 717C: The Bengal Fan, Proceedings of the Ocean Drilling Program, Scientific Results, 116, 155–161, 1990.

Radke, Matthias., Willsch, Helmut., and Welte, D. H.: Preparative hydrocarbon group type determination by automated medium pressure liquid chromatography, Anal. Chem., 52, 406–411, https://doi.org/10.1021/ac50053a009, 1980.

Rantanen, M., Karpechko, A. Yu., Lipponen, A., Nordling, K., Hyvärinen, O., Ruosteenoja, K., Vihma, T., and Laaksonen, A.: The Arctic has warmed nearly four times faster than the globe since 1979, Commun Earth Environ, 3, 10, https://doi.org/10.1038/s43247-022-00498-3, 2022.

Routh, J., Hugelius, G., Kuhry, P., Filley, T., Tillman, P. K., Becher, M., and Crill, P.: Multi-proxy study of soil organic matter dynamics in permafrost peat deposits reveal vulnerability to climate change in the European Russian Arctic, Chemical Geology, 368, 104–117, https://doi.org/10.1016/j.chemgeo.2013.12.022, 2014.

Rowell, D. L.: Soil Science, 0 ed., Routledge, https://doi.org/10.4324/9781315844855, 1994.

Rutkowski, C., Lenz, J., Lang, A., Wolter, J., Mothes, S., Reemtsma, T., Grosse, G., Ulrich, M., Fuchs, M., Schirrmeister, L., Fedorov, A., Grigoriev, M., Lantuit, H., and Strauss, J.: Mercury in Sediment Core Samples From Deep Siberian Ice-Rich Permafrost, Front. Earth Sci., 9, 718153, https://doi.org/10.3389/feart.2021.718153, 2021.

Rydberg, J., Klaminder, J., Rosén, P., and Bindler, R.: Climate driven release of carbon and mercury from permafrost mires increases mercury loading to sub-arctic lakes, Science of The Total Environment, 408, 4778–4783, https://doi.org/10.1016/j.scitotenv.2010.06.056, 2010.

Schäfer, I. K., Lanny, V., Franke, J., Eglinton, T. I., Zech, M., Vysloužilová, B., and Zech, R.: Leaf waxes in litter and topsoils along a European transect, SOIL, 2, 551–564, https://doi.org/10.5194/soil-2-551-2016, 2016.

Schirrmeister, L., Grigoriev, M. N., Strauss, J., Grosse, G., Overduin, P. P., Kholodov, A., Guenther, F., and Hubberten, H.-W.: Sediment characteristics of a thermokarst lagoon in the northeastern Siberian Arctic (Ivashkina Lagoon, Bykovsky Peninsula), Arktos, 4, 1–16, https://doi.org/10.1007/s41063-018-0049-8, 2018.

Schuster, P. F., Schaefer, K. M., Aiken, G. R., Antweiler, R. C., Dewild, J. F., Gryziec, J. D., Gusmeroli, A., Hugelius, G., Jafarov, E., Krabbenhoft, D. P., Liu, L., Herman-Mercer, N., Mu, C., Roth, D. A., Schaefer, T., Striegl, R. G., Wickland, K. P., and Zhang, T.: Permafrost Stores a Globally Significant Amount of Mercury, Geophysical Research Letters, 45, 1463–1471, https://doi.org/10.1002/2017GL075571, 2018.

Schuur, E. A. G. and Mack, M. C.: Ecological Response to Permafrost Thaw and Consequences for Local and Global Ecosystem Services, Annu. Rev. Ecol. Evol. Syst., 49, 279–301, https://doi.org/10.1146/annurev-ecolsys-121415-032349, 2018.

Schuur, E. A. G., Vogel, J. G., Crummer, K. G., Lee, H., Sickman, J. O., and Osterkamp, T. E.: The effect of permafrost thaw on old carbon release and net carbon exchange from tundra, Nature, 459, 556–559, https://doi.org/10.1038/nature08031, 2009.

Schuur, E. A. G., Abbott, B. W., Commane, R., Ernakovich, J., Euskirchen, E., Hugelius, G., Grosse, G., Jones, M., Koven, C., Leshyk, V., Lawrence, D., Loranty, M. M., Mauritz, M., Olefeldt, D., Natali, S., Rodenhizer, H., Salmon, V., Schädel, C., Strauss, J., Treat, C., and Turetsky, M.: Permafrost and Climate Change: Carbon Cycle Feedbacks From the Warming Arctic, Annu. Rev. Environ. Resour., 47, 343–371, https://doi.org/10.1146/annurev-environ-012220-011847, 2022.

Smith, S. L., O'Neill, H. B., Isaksen, K., Noetzli, J., and Romanovsky, V. E.: The changing thermal state of permafrost, Nat Rev Earth Environ, 3, 10–23, https://doi.org/10.1038/s43017-021-00240-1, 2022.

Smith-Downey, N. V., Sunderland, E. M., and Jacob, D. J.: Anthropogenic impacts on global storage and emissions of mercury from terrestrial soils: Insights from a new global model, J. Geophys. Res., 115, 2009JG001124, https://doi.org/10.1029/2009JG001124, 2010.

Strauss, J., Schirrmeister, L., Wetterich, S., Borchers, A., and Davydov, S. P.: Grain-size properties and organic-carbon stock of Yedoma Ice Complex permafrost from the Kolyma lowland, northeastern Siberia, Global Biogeochemical Cycles, 26, 2011GB004104, https://doi.org/10.1029/2011GB004104, 2012.

Strauss, J., Schirrmeister, L., Grosse, G., Wetterich, S., Ulrich, M., Herzschuh, U., and Hubberten, H.: The deep permafrost carbon pool of the Yedoma region in Siberia and Alaska, Geophysical Research Letters, 40, 6165–6170, https://doi.org/10.1002/2013GL058088, 2013.

Strauss, J., Schirrmeister, L., Mangelsdorf, K., Eichhorn, L., Wetterich, S., and Herzschuh, U.: Organic-matter quality of deep permafrost carbon – a study from Arctic Siberia, Biogeosciences, 12, 2227–2245, https://doi.org/10.5194/bg-12-2227-2015, 2015.

Strauss, J., Fuchs, M., Hugelius, G., Miesner, F., Nitze, I., Opfergelt, S., Schuur, E., Treat, C., Turetsky, M., Yang, Y., and Grosse, G.: Organic matter storage and vulnerability in the permafrost domain, in: Reference Module in Earth Systems and Environmental Sciences, Elsevier, B9780323999311001641, https://doi.org/10.1016/B978-0-323-99931-1.00164-1, 2024a.

Strauss, J., Marushchak, M. E., Van Delden, L., Sanders, T., Biasi, C., Voigt, C., Jongejans, L. L., and Treat, C.: Potential nitrogen mobilisation from the Yedoma permafrost domain, Environ. Res. Lett., 19, 043002, https://doi.org/10.1088/1748-9326/ad3167, 2024b.

Thomas, C. L., Jansen, B., Czerwiński, S., Gałka, M., Knorr, K.-H., Van Loon, E. E., Egli, M., and Wiesenberg, G. L. B.: Comparison of paleobotanical and biomarker records of mountain peatland and forest ecosystem dynamics over the last 2600 years in central Germany, Biogeosciences, 20, 4893–4914, https://doi.org/10.5194/bg-20-4893-2023, 2023.

Voigt, C., Marushchak, M. E., Abbott, B. W., Biasi, C., Elberling, B., Siciliano, S. D., Sonnentag, O., Stewart, K. J., Yang, Y., and Martikainen, P. J.: Nitrous oxide emissions from permafrost-affected soils, Nat Rev Earth Environ, 1, 420–434, https://doi.org/10.1038/s43017-020-0063-9, 2020.

Weintraub, M. N. and Schimel, J. P.: Nitrogen Cycling and the Spread of Shrubs Control Changes in the Carbon Balance of Arctic Tundra Ecosystems, BioScience, 55, 408, https://doi.org/10.1641/0006-3568(2005)055[0408:NCATSO]2.0.CO;2, 2005.

Wendler, G., Moore, B., and Galloway, K.: Strong Temperature Increase and Shrinking Sea Ice in Arctic Alaska, TOASCJ, 8, 7–15, https://doi.org/10.2174/1874282301408010007, 2014.

Wolter, J., Jones, B. M., Fuchs, M., Breen, A., Bussmann, I., Koch, B., Lenz, J., Myers-Smith, I. H., Sachs, T., Strauss, J., Nitze, I., and Grosse, G.: Post-drainage vegetation, microtopography and organic matter in Arctic drained lake basins, Environ. Res. Lett., 19, 045001, https://doi.org/10.1088/1748-9326/ad2eeb, 2024.

Zech, M., Buggle, B., Leiber, K., Marković, S., Glaser, B., Hambach, U., Huwe, B., Stevens, T., Sümegi, P., Wiesenberg, G., and Zöller, L.: Reconstructing Quaternary vegetation history in the Carpathian Basin, SE-Europe, using n-alkane biomarkers as molecular fossils: Problems and possible solutions, potential and limitations, E&G Quaternary Sci. J., 58, 148–155, https://doi.org/10.3285/eg.58.2.03, 2010.

Zheng, Y., Zhou, W., Meyers, P. A., and Xie, S.: Lipid biomarkers in the Zoigê-Hongyuan peat deposit: Indicators of Holocene climate changes in West China, Organic Geochemistry, 38, 1927–1940, https://doi.org/10.1016/j.orggeochem.2007.06.012, 2007.

E

Effect of Sea Water Inundation on CO_2 and CH_4 Production of Thawing Coastal Permafrost near Utqiagvik, Alaska

Madina Lucia Dolle[1], Mèlissa Laurent[1*], Jörg Schaller[2], Fabian Seemann[1,3], Maren Jenrich[1,3], Jens Strauss[1], and Claire Treat[1,4]

[1]Alfred Wegener Institute Helmholtz Centre for Polar and Marine Research, Permafrost Research Section, Telegrafenberg, Potsdam, Germany

[2]Leibniz-Center for Agricultural Landscape Research (ZALF), Müncheberg, Germany

[3]Institute of Geosciences, University of Potsdam, Potsdam, Germany

[4]Center for Landscape Research in Sustainable Agricultural Futures, Aarhus University, Denmark

This chapter is under review in:

Permafrost and Periglacial Processes

AUTHOR CONTRIBUTIONS

J. Strauss, M. Laurent and Claire C. Treat conceptualized the study. J. Strauss and M. Jenrich collected the samples during the expedition in 2022. M. Dolle conducted the experiment, supported by M. Laurent. M. Dolle carried out the data analysis and wrote the R script. M. Dolle and F. Seemann made the figures. M. Dolle wrote the original draft with contributions from all the co-authors. M. Laurant led the editing during the reviewing process.

Effect of Sea Water Inundation on CO_2 and CH_4 Production of Thawing Coastal Permafrost near Utqiaġvik, Alaska

Madina Lucia Dolle[1,*], Mélissa Laurent[1,*], Fabian Seemann[1,3], Jörg Schaller[2], Fabian Seemann[1,3], Maren Jenrich[1,3], Jens Strauss[1], and Claire Treat[1,4]

[1]Alfred Wegener Institute Helmholtz Centre for Polar and Marine Research, Permafrost Research Section, Telegrafenberg, Potsdam, Germany
[2]Leibniz-Center for Agricultural Landscape Research (ZALF), Müncheberg, Germany
[3]Institute of Geosciences, University of Potsdam, Potsdam, Germany
[4]Center for Landscape Research in Sustainable Agricultural Futures, Aarhus University, Denmark

Correspondence: Mélissa Laurent (melissa.laurent@awi.de)

Abstract. Rising sea levels and changing marine dynamics are increasing the inundation of previously terrestrial permafrost, accelerating thaw and altering microbial carbon cycling. On the Arctic Coastal Plain of Alaska, permafrost features like drained lake basins (DLBs) and uplands (ULs), offer distinct redox conditions and formation histories that may influence the carbon cycling response to sea water inundation. This study investigates changes in CO_2 and CH_4 production during potential seawater inundation using ex-situ anaerobic incubations of soils from a DLB and a UL near Utqiaġvik, Alaska. Results showed that CO_2 and CH_4 production was respectively up to 2.2 and 3.3 times higher in the DLB site than in the UL site with the salt-less control treatment. The addition of artificial sea water inhibited CH_4 production at both sites. CO_2 production increased in the active and permafrost layers of the UL site, decreased in surface layers of both sites, and remained unaffected by saltwater treatments in the permafrost layers of the DLB site, likely due the presence of marine sediments in DLB. Carbon availability, microbial adaptation and electron acceptors are potential factors for the CO_2 and CH_4 response. Overall, the results of this study showed that anaerobic CO_2 production responded differently to sea water at different landscape positions and formation histories while CH_4 was inhibited independently of the landscape position. Those results highlight the need to consider local hydrology and landscape history in future GHG projections for coastal permafrost.

1 Introduction

Coastal permafrost (PF) regions are highly dynamic environments at the land-ocean interface. Coastal PF areas are characterized as environments exposed to both terrestrial and marine influences, extending up to ... km inland and representing 34% of all global coasts (Lantuit et al., 2012). Climate change impacts coastal PF at the sea site by rising sea levels, increasing open water seasons, warming and thawing PF on - and offshore. But it also has consequences on terrestrial coastal PF for example with rising coastal erosion rates and more extreme storm events (Lantuit et al., 2012; Fritz et al., 2017; Tanski et al., 2019; Irrgang et al., 2022). With more frequent storm surges and sea-level rise, an increasing area of coastal PF becomes inundated and exposed to thaw. On the Arctic Coastal Plain of Alaska, the study region of this study, inundations cause shoreline retreats of up to 25 m yr^{-1} (Gibbs and Richmond, 2017; Jorgenson and Brown, 2005). This inundation process can represent the first step of forming a PF lagoon where long-term terrestrial PF transforms into subsea PF (Angelopoulos et al., 2020; Jenrich et al., 2021).

The rapid changes in coastal PF due to climate change also affect carbon cycle (Irrgang et al., 2022). PF regions store 50 % of global terrestrial carbon (1,460 - 1600 Pg terrestrial carbon in PF regions Strauss et al. (2024)). When PF thaws, organic carbon stored in PF soils is destabilized, accelerating the release of greenhouse gases (GHGs) such as carbon dioxide (CO_2) and methane (CH_4) into the atmosphere (Schuur et al., 2022). However, CO_2 and CH_4 response to climate change in these environments remain understudied (Jenrich et al., 2025).

In terrestrial PF soils, the release of CO_2 and CH_4 to the atmosphere is heavily affected by soil moisture and drainage (Lee et al., 2012; Sturtevant and Oechel, 2013; Treat et al., 2015; Laurent et al., 2023). On the Arctic Coastal Plain of Alaska, carbon cycling is closely linked to the small-scale topography which creates a heterogeneous soil environment (Taş et al., 2018; Eckhardt et al., 2019). The landscape is dominated by drained thaw lake basins (DLBs) and relatively higher lying interstitial tundra (Hinkel et al., 2003). At these two landscape positions, soil moisture forms two different soil environments: 1) well drained soils with prevailing aerobic conditions such as uplands (ULs) and 2) poorly drained soils with prevailing anaerobic conditions such as DLBs. For carbon cycling microbes, anoxic conditions mean that oxygen is not available as electron acceptor for energy production. Thus, other electron acceptors need to be used by microbes for carbon cycling. The choice of elecetron acceptor used for the reaction depends on the redox-conditions of the soil. Under anoxic conditions nitrogen is used first, then iron, followed by sulfate (${SO_4}^{2-}$), and finally CO_2 allowing for methanogenesis (Reddy and DeLaune, 2008). Therefore CH_4 is usually produced under anaerobic conditions when all the other electron acceptor pools are depleted (Reddy and DeLaune, 2008). Under oxic conditions, oxygen is used as an electron acceptor resulting in CO_2 production.

Until now, most of climate models do not include changes in local hydrology in GHG emission projections following permafrost thaw Andresen et al. (2020). However, sea water inundations alter soil properties, promote anaerobic conditions in sediments, and facilitates the transport of labile carbon substrates from land to sea (Tanski et al., 2019). Although anoxic conditions are known to enhance CH_4 production, the increase of salinity inhibits methanogenesis (Shahariar et al., 2021; Yang et al., 2023; Jenrich et al., 2025). ${SO_4}^{2-}$ contained in sea water is thermodynamically more favorable and therefore will be preferentially used as electron acceptor than methanogenesis. However, a few studies have shown that in relatively newly flooded lowlands, CH_4 production can be established under brackish conditions (Yang et al., 2023). Under aerobic conditions mimicking coastal erosion, CO_2 production was found to be increased by sea water addition, while CH_4 was produced only in neglectable amounts (Tanski et al., 2019). The increased CO_2 production was associated with sea water discriminating against high-molecular carbon increasing less complex carbon for GHG production (Dou et al., 2008; Tanski et al., 2019). On the other hand, in terrestrial PF inundated for multiple centuries microbial abundance decreased hinting that sea water can act as a stress factor for terrestrial microbial communities (Mitzscherling et al., 2017) which might lower CO_2 as well as CH_4 production.

During the Holocene, the Utqiaġvik peninsula underwent multiple marine regressions and transgressions, leading to the deposition of marine sediments now overlain by terrestrial layers (Eisner et al., 2005; Jorgenson and Brown, 2005). These paleoenvironmental processes shaped the current landscape, as reflected in the landscape positions of DLBs and ULs. DLBs, being topographically lower, are more likely to have permafrost influenced by marine deposits, while only deeper permafrost in ULs may contain marine sediments. The environmental conditions prevailing during sediment deposition shape microbial communities and influence their responses to thaw (Holm et al., 2020). Additionally, marine sediment geochemistry, such as higher salinity and $SO_4{}^{2-}$ pool likely affect carbon production as well Tanski et al. (2019). In a warming Arctic, sea water intrusion may affect differently permafrost carbon response depending on its marine influence, yet the role of microscale landscape and sediment history in GHG production during sea water inundations remains underexplored.

In our study, we investigated the carbon cycling response to sea water inundation considering different landscape histories. We simulated permafrost thaw under a salinity gradient for two cores corresponding to two main landscape features in the Utqiaġvik peninsula: an UL and a DLB core. To cover the vertical heterogeneity of the cores we incubated four layers with distinct sedimentary composition under three water saltwater treatments and measured CO_2 and CH_4 production. We hypothesized that (1) the landscape history will result in different GHG production under sea water treatments, with higher CH_4 production from initially wetter site; (2) CH_4 will decrease with increase of salinity independently of the site history while CO_2 production will vary based on the landscape history.

2 Material and Methods

To assess the research question, an *ex-situ* anaerobic incubation with two PF cores representing a former anoxic and oxic soil environment was conducted at 10°C for 368 days. To determine CO_2 and CH_4 production under different salt contents, three salt treatments were applied to incubation samples: a control treatment without salt added, a brackish water treatment and a sea water treatment.

2.1 Site Description and Sampling

The sampling site was located on the Utqiaġvik, formerly known as Barrow, Peninsula (the northernmost place of the United States of America; north of 71° latitude, Fig. 1 a) which is part of the Arctic Coastal Plain of Alaska. Historically, the Arctic Coastal Plain was shaped by multiple marine regressions during the late Cenozoic. Thus, the basis of the Utqiaġvik Peninsula form Quaternary marine sediments that are covered by marine sands and silts (Eisner et al., 2005; Jorgenson and Brown, 2005). The peninsula topography is flat and mostly covered by thaw lakes, DLBs and interstitial polygonal tundra (Hinkel et al., 2003; Frohn et al., 2005; Lara et al., 2015). Underlying is continuous PF with an average active layer depth of 37 cm (Hinkel et al., 2003). The mean annual temperature in Utqiagvik, which lays about 12 km west of the sampling site, is -10.2 °C with a maximum of 5.4 °C in July and a minimum of - 24.4 °C in February (Alaska Climate Research Center (2023), period from 1991 to 2020). The precipitation at the sampling site is dominated by snow with a mean annual precipitation of 136.9 mm as rainfall and 1,160 mm as snow (Alaska Climate Research Center (2023), period from 1991 to 2020). The dominant vegetation depends on the landscape feature. The polygonal uplands are mainly composed of *Carex* and *Luzula*, while the DLB is dominated by *Carex, Eriophorum* and *Sphagnum* mosses (Lara et al., 2015; Wolter et al., 2024).

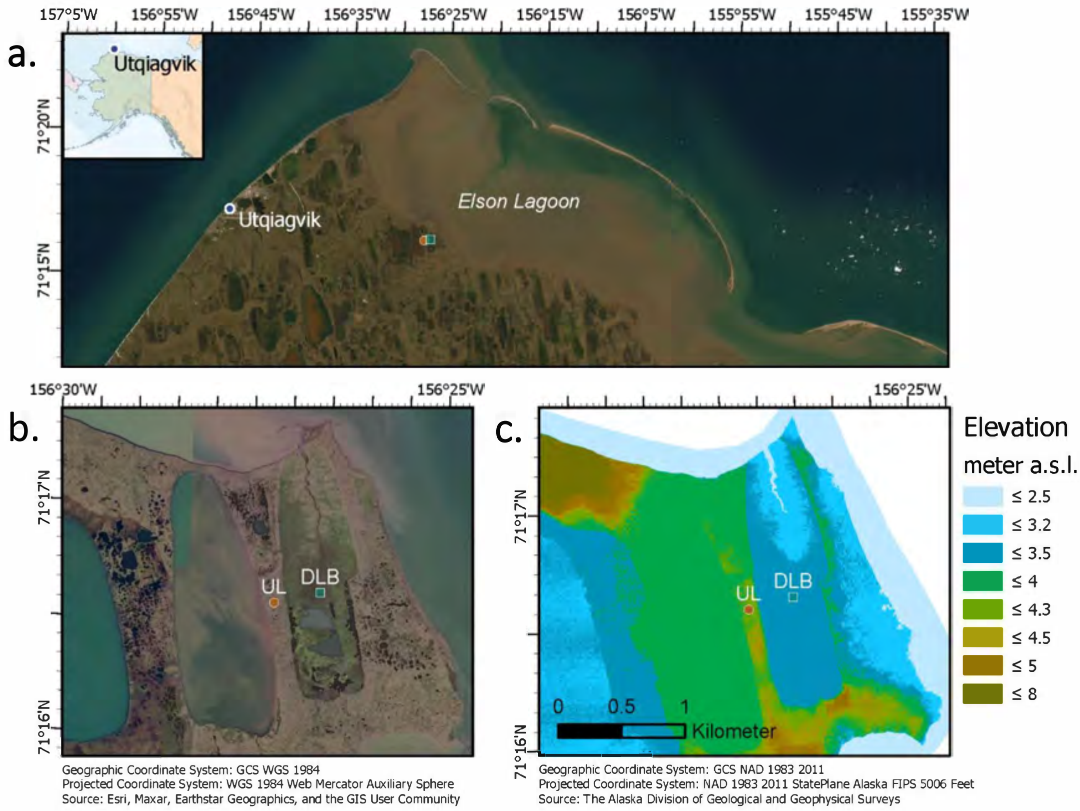

Figure 1. Sampling sites of the two PF cores. Panels a and b show satellite images of the sampling area at different scales. Panel c shows the elevation above sea level (a.s.l.). DLB refers to the landscape position drained lake basin and UL refers to upland. Map was created with ArcGIS.

Two PF soil cores were taken in April 2022 during the 2022 Alaska NorthSlope sampling campaign of the Alfred-Wegener-Institute (AWI) Potsdam. To represent the two most abundant landscape positions of the Arctic Coastal Plain, one 142 cm long core was sampled at a DLB connected to the Elson Lagoon via a small stream (DLB core; N 71.27720°; W 156.44311°; elevation: 3 m a.s.l.). A second core of 204 cm was sampled about 300 m westwards and about 1 m higher within interstitial tundra (UL core; N 71.27637°; W 156.45296°; elevation: 4 m a.s.l.) (Fig. 1 b and c). Since the expedition happened in winter, it was not possible to measure the active layer thickness at both sites. Therefore, we used the values from Nyland et al. (2021)

monitored in Utqiagvik (N 71.31667°; W 156.5833°) between 2017 and 2021 to assess the active layer thickness for both sites (i.e. ranging from 34 cm to 43 cm). For sampling, snow was removed from the sampling sites, then cores were drilled with a modified "Snow, Ice and PF-Establishment" (SIPRE) corer (Jon Holmgren's Machine Shop, Alaska, USA; diameter: 7.5 cm). A visual description of both cores can be found in the Supplementary Information (Fig. S2). Core segments were wrapped in plastic foil, labeled and stored frozen during the transport to AWI Potsdam.

2.2 Subsampling

Subsampling of the two cores took place in a cold lab at -4 °C. Sampling depths were selected to capture the vertical heterogeneity of the cores and therefore different responses to permafrost thaw and the treatments. After splitting the upper meter of each core in half lengthwise, four layers initially chosen based on the vertical permafrost distribution: the top of the active layer corresponding to the first 10 to 15 cm of the cores (AL1) (vegetation removed); the transition zone (bottom of the active layer: AL2); middle of the permafrost layer (PF1) and the bottom of the permafrost (PF2) (Tab. 1). Due to differences in geological history, the soil horizons of the two cores (UL and DLB) were not identical across the depth profile. In the UL core a thick peat layer extended from 0 to 33 cm, followed by a silty, organic-rich layer from 33 to 84 cm, interrupted by ice bands. The bottom 15 cm consisted of alternating grey silt and ice bands. In the DLB, the upper 22 cm also consisted of peat, followed by a sandy silt layer extending from 22 to 71 cm, then a thin silt layer, and finally a layer of peaty silt. From 91 to 107 cm, alternating light and dark grey layers were observed (Fig. S2). To ensure that each individual layer represented a consistent soil horizon, while also allowing for comparisons across cores at equivalent positions (surface layer (AL1), permafrost table (AL2), and permafrost (PF1, PF2)), slightly different depth ranges were subsampled for the same positions (Tab. 1).
The subsampled layers were split into two parts with the smaller part used for pore water and sediment analysis and the bigger part for the incubation. To ensure that the incubations were running properly (i.e., no contamination) we had four methodological replicates per layer and treatment.

2.3 Pore Water and Sediment Analyses

2.3.1 Pore Water Analysis

Electrical conductivity, pH and dissolved organic carbon (DOC) content were measured in pore water extracted with a Rhizon soil moisture samplers with a membrane filter length of 5 cm (poresize 0.15 μm, Rhizosphere Research Products, Netherlands). Electrical conductivity and pH were measured right after water extraction. For that around 3.5 mL of pore water were filled into a small glass vessel. First, the electrical conductivity was measured with a conductivity pocket meter with a reference temperature of 25 °C (Cond 340i, WTW, Germany). Next, the pH was measured with a potentiometer (Multilab 540, WTW, Germany).
Leftover pore water was acidified with a 30 % HCl solution in a ratio of 1 μL : 1 mL pore water to inhibit biological processes. Acidified samples were stored at 4 °C until DOC measurement conducted by catalytic combustion at 630 °C (TOC-VCPH,

Shimadzu, Japan).

SO_4^{2-} and Cl^- anions were measured with ion chromatography (ICS 2100, Dionex/Thermo Fisher Scientific, Germany).

2.3.2 Sediment Analysis

For sediment analysis, samples were freeze-dried (Sublimator 3-4-5, Zirbus Technology, Germany) and milled (Pulverisette 5, Fritsch, Germany) to a particle size smaller 2 mm.

Total carbon (TC), total organic carbon (TOC) and total inorganic carbon contents were determined with a total organic carbon analyzer (soliTOC Cube, Elementar, Germany). Total nitrogen (TN) contents were measured with a nitrogen analyzer (rapid Max N exceed, Elementar, Germany).

Sedimentological data from the same cores and acquired with the same methodology from Seemann et al. (2025) were added to our sedimentological data to have a higher vertical resolution and additional soil parameters (^{14}C ages and grain size distribution, 2). The Radiocarbon dating was conducted by the AWI MICADAS laboratory (Mollenhauer et al., 2021) for nine samples (four from the UL and five from the DLB). Plant remains were selected for most of the samples. However, no plant remain was found for UL PF2, therefore, bulk sediment was used. The Calib 8.20 and the IntCal20 calibration curve were used to calibrate the data (Reimer et al., 2020; Stuiver and Reimer, 1993).

Before analyzing the samples for grain size distribution, the organic matter was removed by adding hydrogen peroxide for four weeks. The grain size distribution was measured with a Malvern Mastersizer 3000 laser particle size analyzer (measuring range 0.01–1000 μm) and analyzed with GRADISTAT 8.0 (Blott and Pye, 2001).

2.4 Incubation

The incubation was designed to mimic a sea water inundation at two typical landscape positions on the Arctic Coastal Plain. Thus, soil samples of two PF cores were incubated for 368 days under dark and anaerobic conditions at 10 °C. To test the effect of sea water on CO_2 and CH_4 production, three salt treatments were applied in the incubation: a control treatment (sterilized tap water), a brackish water treatment and a sea water treatment. These treatments were applied across four depths for each core. Additionally, four blanks for each core were added: one corresponding to each treatment and an additional empty one. In total, the incubation comprised 104 samples (Fig. S1). The duration of the incubation and the temperature were chosen to unsure that the carbon response to the sea water treatments – specifically methanogenesis – will be captured.

For the incubation set-up an anoxic glovebox was used during sample preparation to ensure oxygen-free conditions. The samples were thawed overnight at 4°C. The thawed samples were homogenized in the glovebox, by gently kneading them. Then, 6 to 10 g of wet sample material was weighed into sterilized 120 mL glass incubation bottles. Water was added in a ratio of 1:1 (volume water: weight wet sample) according to the treatment to form a slurry. Lastly, incubation bottles were closed with a rubber septum and crimped with an aluminium cap.

The salt water treatments, artificial brackish water and sea water, were manufactured using the protocol of Koch et al. (2014): For the sea water treatment a total of 42.84 g salts and for the brackish water treatment a total of 15.45 g salts were added to one liter of MilliQ water (exact chemical composition in Tab. S1). The salt content in the sea water treatment was 34.5-34.8

mg·L^{-1} which is slightly higher than the normal salt content of 28-32 mg·L^{-1} observed near the sampling location (Guéguen et al., 2005). In the brackish water treatment the salt content was 12.6 mg·L^{-1}.

Table 1. Sampling depth and soil horizon description for each site.

Site	Layer	Sampling depth (cm)	Soil horizon
Upland	AL1	0–10	Light brown peat
	AL2	33–45	Medium grey silt, organic intrusion
	PF1	74–84	Medium grey silt, organic intrusion
	PF2	88–103	Grey silt, ice-rich
Drained Lake Basin	AL1	0–15	Peat
	AL2	22–45	Fine sandy silt
	PF1	69.5–79	Fine sandy silt
	PF2	95–107	Dark and light grey

2.5 Gas Measurements

To measure the CO_2 and CH_4 production in incubation bottles, 5 mL headspace gas was extracted and the CO_2 and CH_4 concentration was measured by a gas chromatograph (Nexis GC-2030, Shimadzu, Japan) with a flame ionization detector (FID) including a jetanizer (FID temperature: 400 °C, makeup flow rate (N_2): 26.2 mL/minute, air flow rate: 200 mL/minute). The minimum concentration measurable by the GC (detection limit) due to the calibration was 10 ppm.
Gas extraction was conducted using a 5 mL air tight glass syringe (SGE Analytical Science, Australia). In total 5.5 mL of head space gas were extracted during sampling of which 0.5 mL were used for flushing the needle tip. To minimize the pressure disturbance due to the extraction of 5.5 mL gas from the sample, 5.5 mL N_2 was added after head space gas extraction.
To avoid excessive over-pressure within the incubation bottles that could affect microbial activity, samples were flushed the following measurement day when they exceeded 10,000 ppm.
In the first week, CO_2 and CH_4 production was measured every one to two days. Then, every 7 to 10 days until day 100 and every one to two month after day 100.

2.6 Data Processing and Analysis

Data processing, analysis and plotting was conducted with R (4.3.1, R Core Team (2023)) in RStudio (2023.06.1+524, Posit team (2023)).

2.6.1 Data Processing

Raw GC data was transformed into daily production rates and cumulative productions in μg C per gram dryweight (g^{-1} DW) and also normalized per gram carbon (g^{-1} TOC) following the approach of Robertson et al. (1999). Thereby, gas concentrations in ppm were converted to μg CO_2-C or μg CH_4-C using the Ideal Gas Law assuming a laboratory sampling temperature of 20°C. Additionally, gas concentrations were corrected for sampling dilution (5.5 mL) and the gas fraction dissolved in the water using Henry's Law. Gas production was then calculated as difference between gas concentrations of two consecutive measurements. The gas production was divided by the number of days between the measurements to obtain the production rates. The cumulative production was calculated from the sum of the gas production over the incubation time.

For quality control, two procedures were added to data processing. Firstly, all CO_2 and CH_4 production rates below the mean change rate of procedural blank samples were excluded as not detectable. Secondly, a visual check for anomalies was conducted. Atypical samples were excluded if the anomaly was high in context with other replicates and measurements and if the GC chromatogram or a sampling note indicated a mistake. Finally, processed data (Dolle et al., 2024) was saved for data analysis.

2.6.2 Data Analysis

To assess differences between the landscape positions, only the control treatment was used. Two-way analysis of variances (ANOVAs) were conducted with cumulative CO_2 and CH_4 production at the end of the incubation. Since ANOVA requirements were not met in some cases, data was logarithmic transformed before ANOVAs. As posthoc test, pairwise t-tests with Bonferroni adjustment were carried out. Additionally, CH_4 lag times were determined as defined from Treat et al. (2015) as the time needed to reach the max. CH_4 production rate.

For comparison of treatment effects, a response factor per layer and treatment was calculated by normalizing the median production of a sample to the median production of the respective layer control treatment samples and subtracting one (which is the median production of the control treatment). Thus, a response factor of 0 represents the median cumulative production of the control treatment. A response factor smaller 0 means a lower production than the control treatment and a response factor higher 0 means a higher production than the control treatment. Significance in differences in CO_2 and CH_4 response between treatments (control treatment vs. brackish water and sea water treatment) was tested by paired t-tests.

3 Results

3.1 Pore Water and Sediment Parameters

Pore water and sediment parameters of the two PF cores differed greatly (Fig. 2). Pore water pH and electrical conductivity were stable at the UL site (5.2 to 5.6 and 0.2 to 0.6 mS/cm, respectively). Conversely, at the DLB site pH increased with depth with an acidic pH at the surface (4.7) and values around 8 in the PF layers. Electrical conductivity was higher than in UL and ranged from 1.2 mS/cm near the surface to 10.2 mS/cm near one meter depth. Both profiles showed a similarly high DOC (about 430 mg/L) in the surface layer but developed differently below that. The UL profile peaked (roughly 700 mg/L) below the PF table in a depth of around 50 cm and then decreased back to about 400 mg/L. Contrasting, at the DLB site DOC increased with depth (from 60 to 530 mg/L). Cl^- content was a magnitude higher at the DLB site (359 to 999 mg/L) than at

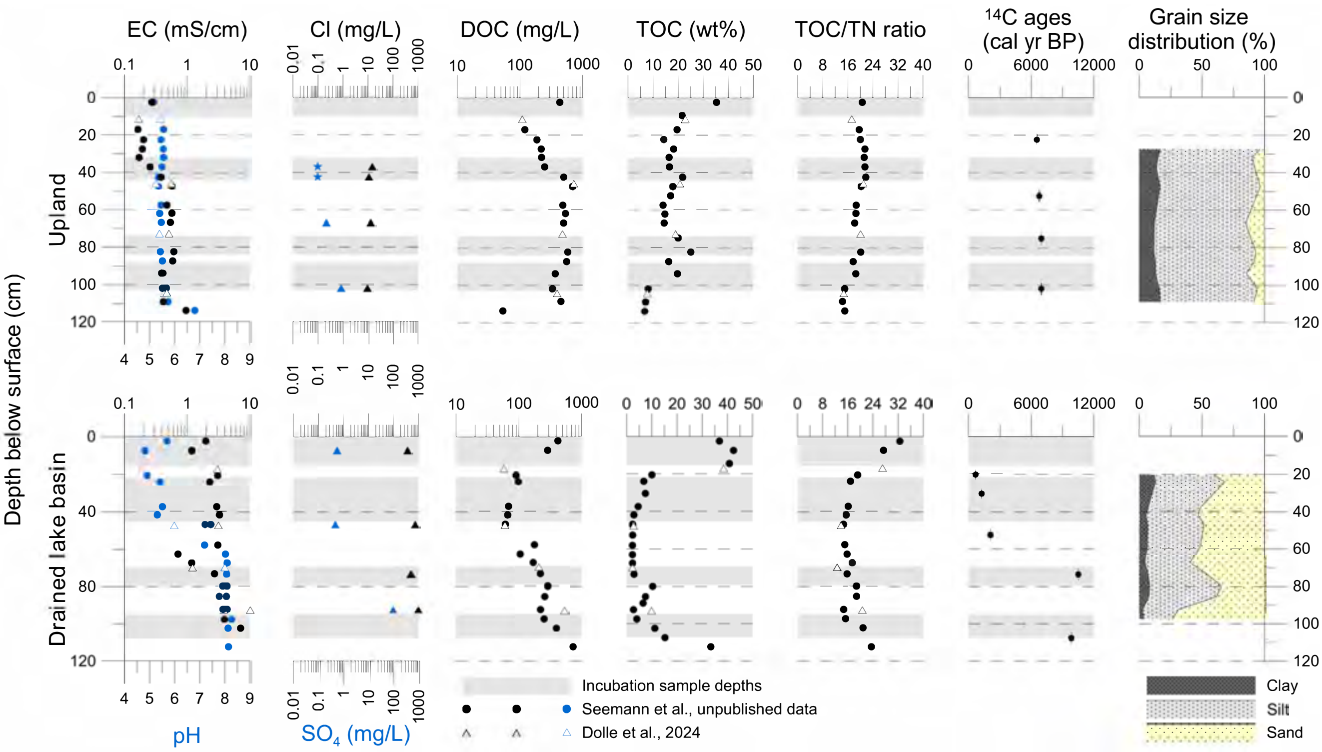

Figure 2. Soil parameters of both cores. Electrical conductivity (EC), pH, Chloride content (Cl), Sulfate content (SO_4^{2-}) and dissolved organic carbon (DOC) were measured in pore water. Total organic carbon content (TOC), TOC/total nitrogen content (TN) ratio, ^{14}C ages and grain sizes are sediment-based. Asterisks mark results below the detection limit of 0.1 mg/L. Please note that the SO_4^{2-} and Cl values at 75 cm for the DLB are similar, and therefore overlap.

the UL site (9.4 to 14.7 mg/L). SO_4^{2-} was similar in the active layers at both sites (max. 1 mg/L), but was substantially higher in DLB PF layers (98 and 548 mg/L).

Sediment TOC showed a more organic rich soil profile at the UL site compared to the DLB site. Both cores had an organic rich (higher 30 %) surface layer. TOC decreased to less than 10 % at the DLB site until about 80 cm deep where an increase in TOC was visible. At the UL site, TOC decreased more continuously from 35 % in the surface layer to about 10 % at a depth of 115 cm. TOC/TN ratios, were relatively stable in the UL core (around 20) while at the DLB, they fluctuated from 35 in the surface layer to 12 in layers below. ^{14}C ages indicated much younger C in the layer up to 55 cm at the DLB site than at the UL (676 $\pm$ 53 yr BP to 2,103 $\pm$ 239 yr BP an 6533 $\pm$ 142 yr BP, DLB and UL site respectively). In deeper layers, carbon from DLB ($\sim$10,000 yr BP) was substantially older compared to the upper layers and the UL core ($\sim$7,300 yr BP). The grain size distribution showed a highly silty (73 to 81 %) soil profile at the UL site and a more sand (32 to 74 %) dominated profile at the DLB site.

In conclusion, the two landscape positions showed two distinct soil conditions across depths. The UL profile was relatively

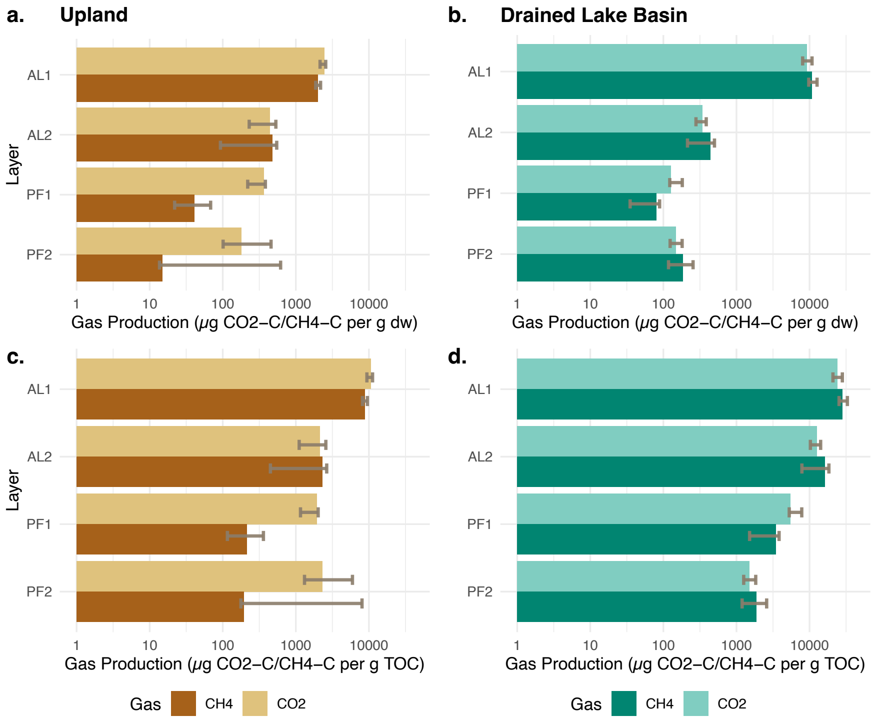

Figure 3. Cumulative anoxic CO_2 and CH_4 production by depth at day 368 of the incubation in the control treatment (no salt added). Panels a and b show the gas production on a dry weight basis. Panels c and d show the gas production on a carbon basis. The bar represents the median of 4 replicates. Error bars show the range of the 4 replicates (min. to max.). Please note the logarithmic x-axis.

homogeneous across the whole depth, with lower than DLB values for electrical conductivity, pH and $SO_4{}^{2-}$. While in the DLB profile, layers differed more in their soil parameters with a clear differentiation in pH, electrical conductivity, Cl^-, $SO_4{}^{2-}$ at a depth of 60 cm.

3.2 Landscape Position Effect on CO_2 and CH_4 Production

3.2.1 Cumulative Gas Production at the Incubation End

After 368 days, the general trend was that cumulative CO_2 and CH_4 production decreased with depth at both sites (Fig. 3). On a dry weight basis (Fig. 3 a and b), gas production in the AL1 layer was 4 to 5-times higher at the DLB site (9,270 CO_2-C g^{-1} DW and 10,900 CH_4-C g^{-1} DW) than at the UL site (2,440 CO_2-C g^{-1} DW and 2,010 CH_4-C g^{-1} DW). In all layers below, the production of CO_2 and CH_4 production decreased at both sites. CO_2 production ranged from 178 to 442 μg CO_2-C g^{-1} DW at the UL site and from 128 to 343 CO_2-C g^{-1} DW at the DLB site. CH_4 production ranged from 14.8 to 475 CH_4-C g^{-1} DW at the UL and from 80.3 to 439 CH_4-C g^{-1} DW at the DLB site. One layer created an exception to the depth trend on a dry weight basis: the PF1 layer at the DLB site where the lowest CO_2 (median: 128 μg C g^{-1} DW) and CH_4 production (median:

Table 2. Landscape position effect: ANOVA results for importance of the effects site and layer and the interaction effect of site and layer on cumulative CO_2 and CH_4 production on a DW and carbon basis at incubation end.

	CO_2				CH_4			
	DW		TOC		DW		TOC	
Effect	p-value	sign.	p-value	sign.	p-value	sign.	p-value	sign.
Site	8.72×10^{-1}		2.11×10^{-8}	***	2.00×10^{-3}	**	9.40×10^{-7}	***
Layer	2.02×10^{-17}	***	3.51×10^{-12}	***	9.43×10^{-11}	***	9.31×10^{-8}	***
Site:Layer	8.98×10^{-7}	***	2.78×10^{-7}	***	1.61×10^{-1}		2.27×10^{-1}	

[**] p-value < 0.01, significant; [***] p-value < 0.001, highly significant

80.3 μg C g^{-1} DW) of that site was observed (Fig. 3 b).

On a carbon basis, cumulative median CO_2 and CH_4 production were higher at the DLB site than the UL site (Fig. 3 c and d). The CO_2 production ranged from 1,930 to 10,700 μg CO_2-C g^{-1} TOC at the UL site and from 1,510 to 24,300 μg CO_2-C g^{-1} TOC at the DLB site (Fig. 3 c and d). 193 to 8,780 μg CH_4-C g^{-1} TOC and 1890 to 28,300 μg CH_4-C g^{-1} TOC were produced at the UL and DLB site, respectively. At the UL site, the PF2 layer created an exception from the depth trend on a carbon basis. Here, CO_2 and CH_4 production were similar to the PF1 layer of that core (Fig. 3 c).

ANOVA results (Tab. 2) suggested that both site and depth were important controls in regulating CO_2 and CH_4 production. For CO_2 production, depth was the most important factor, but also the interaction between site and depth had a significant impact on CO_2 production. For CH_4 production, depth was again the most important factor. Site also played a significant role in CH_4 production, while there was no significant interaction between site and depth for CH_4 production.

Overall, gas production generally decreased with depth at both sites. At the DLB site, cumulative CO_2 and CH_4 production on a carbon basis were higher at the UL site. Depth and site were important factors for cumulative CO_2 and CH_4 production according to the ANOVA.

3.2.2 CH_4 Production dynamic throughout the Incubation

When assessing gas production dynamics (Tab. 3), differences in CH_4 production between the two landscape positions became evident. At the DLB site, CH_4 production was stronger than at the UL site. This can be seen in the max. CH_4 production rates that were up to 10 times higher on a dry weight basis and up to 25 times higher on a carbon basis at the DLB site than at the UL site. Furthermore, the time to reach maximum CH_4 production rates, the CH_4 lag time, was shorter at the DLB site than at the UL site. In the AL1 layer, the DLB site had a CH_4 lag time (90 days) that was about half as long as the UL site (147 days). In the AL2 layer, the DLB core reached max. CH_4 production rate fastest (30 days) while it took 330 days in the UL core to reach its maximum. In PF layers, both sites showed similar CH_4 lag times.

Additionally to a higher and faster CH_4 production at the DLB site, this site also produced more CH_4 than CO_2. The higher CH_4 production can be seen in Fig. 3 (B and D) and was also reflected in min. CO_2:CH_4-ratios (Tab. 3). Min. CO_2:CH_4 ratios at the DLB site were about 0.6 with the PF1 layer as an exception. While at the UL site, CO_2:CH_4 ratios were about 1 in AL1

Table 3. Max. CH_4 production rates, CH_4 lag time, min. CO_2:CH_4 rates with the control treatment at both sites. The numbers represent the median values with the minimum and maximum values in parentheses for N = 4.

	Depth	**max. CH_4 production rate**		**CH_4 Lag Time**	**min. CO_2:CH_4**	
	(cm)	(g dw)	(g TOC)	(days)	(ratio)	(day)
Upland	0-10 (AL1)	10.2 [8.49, 10.7]	44.4 [37.2, 46.7]	147 [68.0, 292]	1.21 [1.07, 1.27]	368 [368, 368]
	33-45 (AL2)	3.67 [0.563, 5.15]	17.7 [2.72, 24.9]	330 [292, 368]	0.958 [0.918, 2.47]	368 [368, 368]
	74-84 (PF1)	0.272 [0.106, 0.555]	1.43 [0.561, 2.93]	297 [191, 368]	7.05 [5.41, 17.5]	368 [368, 368]
	88-103 (PF2)	0.0878 [0.0693, 5.07]	1.14 [0.900, 65.9]	191 [104, 292]	9.37 [0.714, 12.7]	292 [292, 368]
Drained Lake Basin	0-15 (AL1)	79.0 [77.7, 115]	205 [202, 298]	90.0 [85.0, 126]	0.591 [0.466, 0.716]	103 [85.0, 194]
	22-45 (AL2)	4.56 [3.77, 5.30]	168 [139, 195]	30.5 [27.0, 34.0]	0.597 [0.572, 0.661]	124 [43.0, 194]
	69.5-79 (PF1)	1.17 [0.332, 1.85]	50.3 [14.3, 79.7]	292 [229, 368]	1.62 [1.31, 3.49]	292 [229, 368]
	95-107 (PF2)	2.03 [1.77, 2.16]	20.6 [18.0, 22.0]	209 [95.0, 292]	0.577 [0.507, 0.631]	209 [126, 292]

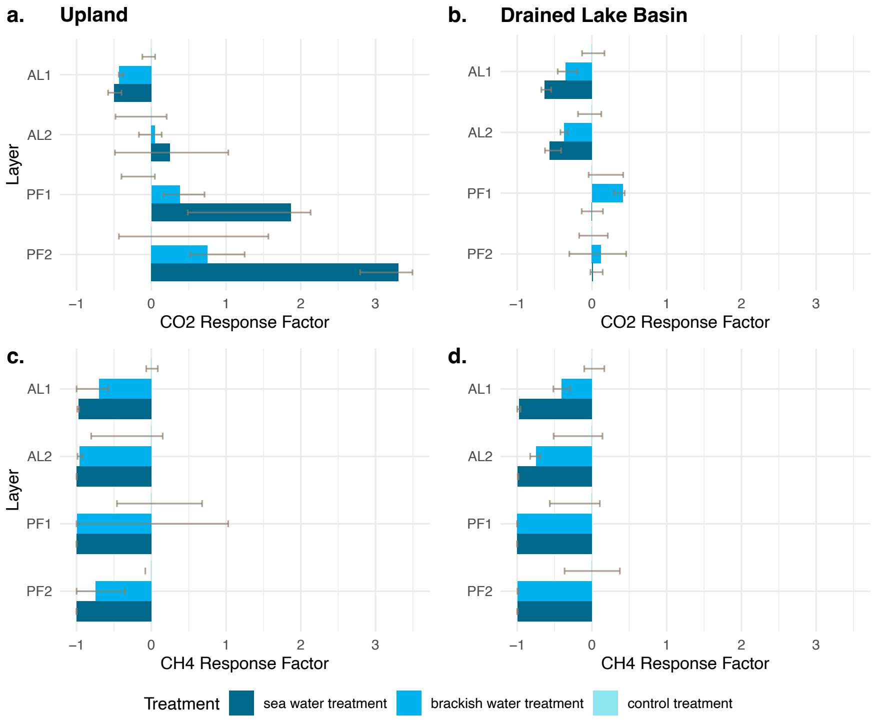

Figure 4. CO_2 and CH_4 response to sea water treatments relative to the production under the control treatment. Panels a and b show the CO_2 response. Panels c and d show the CH_4 response. Bars represent the median over 4 replicates. Error bars indicate min to max of 4 replicates. For non-detectable CH_4 productions (DLB upl and UL PF layers with sw treatment) a production of 0 was assumed to calculate the response factor. Asterisks mark significant differences in the response factors to the control treatment.

and AL2 layers and 7 to 9 in PF layers. Here again, the DLB site was faster in reaching min. CO_2:CH_4 ratios than the UL site. The DLB site, reached min. CO_2:CH_4 ratios in 103 to 124 days in AL1 and AL2 layers and 209 to 292 days in PF layers. While the UL site needed until the end of the incubation to reach its min. CO_2:CH_4 ratios. This also indicated that min. CO_2:CH_4 ratios at the UL site might not have been reach after 368 days.

To sum up, the active layers had higher max. CH_4 production rates and shorter lag times than for PF layers at both sites. However, the DLB site showed faster and greater CH_4 production at all depths compared to the UL site.

3.3 Salt Water Effect on CO_2 and CH_4 Production

3.3.1 Response Factor at the Incubation End

The response of CO_2 and CH_4 production to salt water at the incubation end compared to the median cumulative production of the control treatment is shown in Fig. 4.

Based on the CO_2 response factor at the end of the incubation (Fig. 4 a-b), there were three response groups to differentiate layers: Firstly, the three lower layers (AL2, PF1 and PF2) of the UL site where the CO_2 production increased in general with salt water treatments. This increase was significantly higher in the PF2 layer of the UL site where the sea water treatment produced 3.5 times more CO_2 ($p = 0.017$) than the control treatment. Secondly, AL1 layers at both sites and the AL2 layer of the DLB site where CO_2 production lowered up to 0.6 times with salt water addition. This decrease in CO_2 production compared to the control treatment was significant with the sea water treatment in all three layers (UL AL1 layer: $p = 0.021$, DLB AL1 layer: $p = 0.001$, DLB AL2 layer: $p = 0.007$). Thirdly, the PF layers at the DLB site where there was no significant difference in CO_2 production between salt water treatment and the control treatment. Although no significant difference was measured between DLB PF1 under brackish treatment and the control, the response factor was positive and of the same order of magnitude as that of UL PF1 for the same treatment.

CH_4 production reacted differently than the CO_2 production under salt water treatments. In all layers of both sites, CH_4 production was inhibited with salt water treatments and CH_4 was more inhibited with the sea water treatment than with the brackish water treatment if CH_4 was produced at all (Fig. 4 c-d, Fig. S6).

3.3.2 Gas Production with Salt Treatments throughout the Incubation

The strongest response in CO_2 production can be seen in the PF2 layer of the UL core (Fig. 5) with a response factor of 4.5 at around 200 days with the sea water treatment. That layer also showed the strongest response with the brackish water treatment with a response factor of about 2 after 50 days.

In general, all layers showed an initial peak in the CO_2 response factor with the brackish water treatment during the incubation. The time needed until this initial peak differed between the sites and layers. At the DLB site, the initial CO_2 response peak with brackish water appeared quickly after the incubation started, while it needed 30-50 days at the UL site for the response to show (Fig. 5). In the UL PF layers, the brackish water peak was followed by a CO_2 response peak with the sea water treatment.

The CH_4 production with salt treatments in PF layers at both sites was low to non-detectable (Fig. 6). In active layers, CH_4 production decreased with both salt treatments at the start of the incubation. After that initial decrease in CH_4 production, the response became attenuated in the brackish water treatment towards the end of the incubation while with the sea water treatment CH_4 inhibition lasted throughout the whole incubation.

4 Discussion

4.1 Soil characteristics

At the DLB site, pH, electrical conductivity, SO_4^{2-} and Cl^- content (Fig. 2) indicate that especially the PF layers likely had contact with sea water before this incubation. The sea water contact could have been caused by re-mobilized saline deposits (Jones et al., 2023) or by inundation. In this study, the gap of 8000 yr in the radiocarbon dating (Fig. 2), as well as the inverse age at 110 cm compared to 79 cm indicate potential cryoturbation events, supporting re-mobilized saline deposits more than

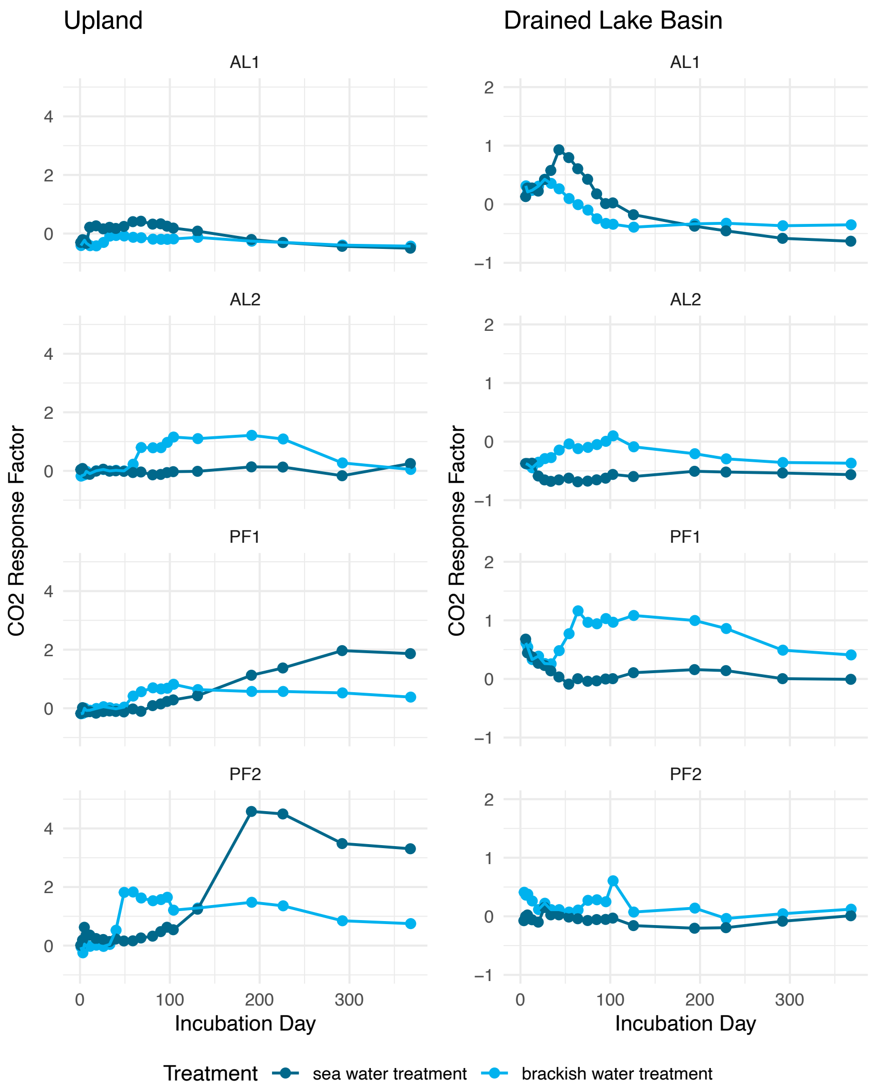

Figure 5. Median CO_2 response factors to salt treatments throughout the incubation at both sites. Please note the different y-axis.

sea water intrusion. In thermokarst lagoons, pore water hydrochemistry is highly variable due to complex freezing and brine exclusion mechanisms which lead to the formation of hypersaline layers (Angelopoulos et al., 2020; Jenrich et al., 2021). However, pH and electrical conductivity of DLB PF layers are similar to brackish core sections of Siberian thermokarst lagoon sediments (Jenrich et al. (2021): pH median 7.5 and 8, electrical conductivity median 3.3 mS/cm under brackish conditions; Yang et al. (2023): pH 6-8). The maximum DOC values at the DLB site are 1.5 times higher than values found in the above mentioned lagoons (Jenrich et al. (2021): max. 282 mg/L). Similarly high DOC values were found in a young (approx. 500

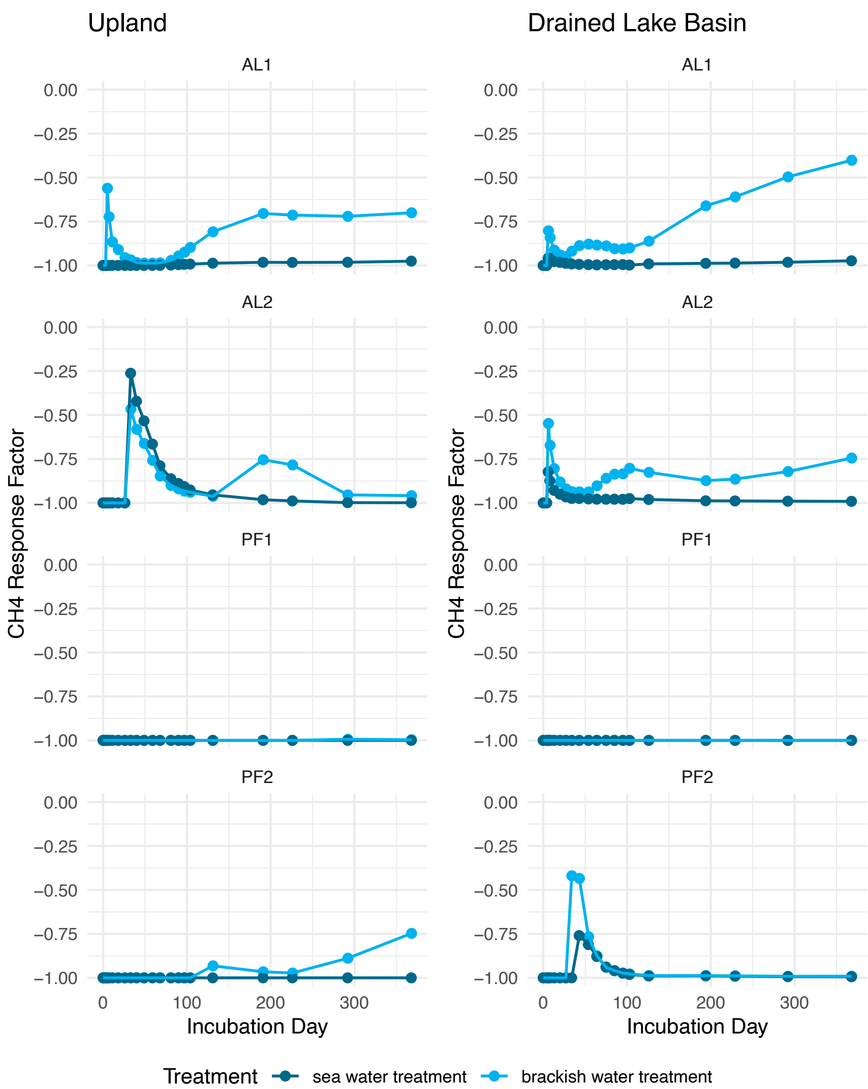

Figure 6. Median CH_4 response factors to salt treatments throughout the incubation at both sites.

years BP) DLB near Drew Point, about 100 km further south east at the Beaufort Sea coast (Bristol et al. (2021): up to 585 mg/L). As sediment parameters, TOC and TOC:TN at the DLB site are within the range of values observed in other DLBs in Alaska (Fuchs et al., 2019; Bristol et al., 2021; Jongejans et al., 2018).

The UL site exhibits a clearly different soil environment compared to the DLB site concerning the pore water and sediment parameters (Fig. 2). The parameters confirm the UL site as a primary surface, meaning that the landscape was not affected by thaw lake formation (Bristol et al., 2021). The pH (about 5 to 5.5) is acidic and falls within values observed in Alaskan polygonal tundra (Taş et al., 2018; Roy Chowdhury et al., 2015) and peat (Treat et al., 2014). DOC ranges similarly to the primary surface in Bristol et al. (2021) even though near Drew Point the high variability of DOC was observed over a depth of 3 meters at the primary surface site. TOC at the UL site decreases with depth (about 35 % to 10 %). It has a surface organic-rich layer that is on the lower end when compared to other Alaskan peat carbon contents (Treat et al. (2014): 44.8-16.8 %, Fuchs et al. (2019): 42 %, Taş et al. (2018): 40.1 %, Roy Chowdhury et al. (2015): 45.6%, Herndon et al. (2015): 38.9 %). TOC:TN ratio is relatively stable at 20 throughout the total core and similar to ratios in the upper meter of other tundra peat sites (Treat et al. (2014): 23.3-24.5, Fuchs et al. (2019): average 20 in depth 40 to 120 cm, Roy Chowdhury et al. (2015): 17-26) but slightly higher than TOC:TN ratios observed in primary surface (Bristol et al. (2021): 14-18).

To sum up, the soil characteristics at the UL and the DLB (Fig. 2) reveal distinct patterns dependent on landscape history and position. The active layer of the DLB compares well to other DLBs on the Alaskan North Slope. The PF layers have been inundated by marine waters before this study as characteristic for the Utqiaġvik Peninsula (Eisner et al., 2005; Jorgenson and Brown, 2005). At the UL site, soil characteristics are similar to other primary surfaces in the region with PF layers unaffected by earlier thawing.

4.2 Landscape Position Effect

4.2.1 Carbon Availability

A decrease in anaerobic CO_2 and CH_4 production with depth in PF soils is often linked to a decrease in carbon availability and quality (Treat et al., 2015; Waldrop et al., 2023). In this study, high TOC content in the AL1 layers (UL 35 %, DLB 40 %) coincides with the highest CO_2 and CH_4 production. Additionally, the DLB site with a 5% higher TOC content has a 4-time higher gas production than the UL site in that layer. In AL2, PF1 and PF2 layers, TOC is higher in the UL core which is concurrent with higher CO_2 productions than in the DLB core on a dry weight basis (Fig. 2, Fig. 3 a-b). This is in accordance with with previous studies showing the importance of soil carbon quantity for CO_2 production (Schädel et al., 2014; Treat et al., 2015; Lapham et al., 2020).

On a carbon basis, PF layers at the UL site produce very similar amounts of CO_2 and CH_4 after 368 days (Fig. 3 c). The CO_2 production is even similarly high as in the AL2 layer. As this site has been unaffected by former PF thaw, an initial burst of labile carbon may have become available upon PF thaw (Vonk et al., 2013; Drake et al., 2015). Labile carbon may then have acted as a driver of CO_2 production in PF layers of the UL site. This effect is supported by the initially higher CO_2 production of the PF layers compared to the AL2 layer (Fig. S4). After thaw, the PF layers of the DLB core exhibited a burst of CO_2 production as well. However, when normalized to carbon content, this production was two to five times lower than that observed in AL2 from the same core (Fig. S3). As previously mentioned, the PF layers in the DLB core were likely affected by cryoturbation, indicating past thaw events. This prior thaw exposure may have reduced the lability of the carbon Ping et al. (2015); Schuur et al. (2008), potentially explaining the lower CO_2 production compared to the UL layer. The results shown in this study are in accordance with the already established correlation betweenCO_2 production and organic carbon quantity/quality.

4.2.2 Microbial Adaptation

Prevailing anoxic soil conditions drive CH_4 production in PF soils (Laurent et al., 2023; Galera et al., 2023). As the DLB lies relatively lower than the UL site, water-logged anoxic conditions will be more apparent especially in the active layers at the DLB site (Sturtevant and Oechel, 2013). Thus, the microbial communities at the DLB site could be more adapted to anoxic conditions that were mimicked in the incubation than the microbial community at the UL site. This study support the idea of anoxic conditions driving CH_4 production with the higher CH_4 and CO_2 production on a carbon basis at the DLB than the UL site. Additionally, the high max. CH_4 production rates and low CO_2:CH_4 ratios (Fig. 3, Tab.3) also highlight the influence of already adapted microbial community to anoxic conditions.

With the DLB site being more adapted to anoxic soil conditions, the reduced CH_4 production on a dry weight basis in the PF1 layer at the DLB site (Fig. 3 b) is unexpected. Here, the former sea water contact of the PF layers might be an important control. Indeed, the electrical conductivity in the PF layers of DLB indicates brackish conditions in these layers. The high SO_4^{2-} content in the PF1 layer at the DLB site (999 mg/L; Fig. 2) can explain the low CH_4 production as SO_4^{2-} reduction is energetically more favorable than methanogenesis (Koch et al., 2009). This is consistent with (Yang et al., 2023), where they found that CH_4 production decreases with salinity, but was not fully inhibited for low-lying flooded area under brackish conditions. The increase of SO_4^{2-} in the soil leads to an increase of SO_4^{2-}-reducing bacteria (SBR) which can be competitors for methanogenesis (Gutekunst et al., 2022; Yang et al., 2023). To limit this competition, methanogens use mainly CO_2 or methanol metabolism pathways instead of organic compounds such as acetate (Söllinger and Urich, 2019; Yang et al., 2023).

Overall, CO_2 and CH_4 production with the control treatment can be interpreted as an interaction of microbial adaptation to anoxic soil conditions, carbon availability and sea water exposure which combined form the landscape position effect.

4.3 Salt Water Effect

4.3.1 Carbon Availability

CO_2 production increased with sea water addition at both sites in certain layers (Fig. 4). The same effect was observed in thawing coastal PF samples from thermokarst lake and thermokarst lagoon sediments on the Bykovsky Peninsula, Siberia, Russia under anaerobic conditions (Jenrich et al., 2025) and from the Yukon Coast, Canada under aerobic conditions (Tanski et al., 2019, 2021). As this effect has been observed under aerobic and anaerobic conditions, prevailing oxygen availability does not seem to be decisive for CO_2 production with salt water. Instead, a higher carbon availability due to the sea water addition is discussed as a possible reason for higher CO_2 production with sea water (Tanski et al., 2021; Lapham et al., 2020; Tanski et al., 2019). Sea water can cause complex carbon compounds to flocculate increasing the mobility of less complex carbon (Dou et al., 2008) that could then be available for CO_2 production (Tanski et al., 2021; Lapham et al., 2020; Tanski et al., 2019).

Conversely, the lack of response to sea water addition at the DLB site likely reflects its history of prior marine inundation and associated long-term changes in soil chemistry (Fig. 2). These pre-incubation conditions may have already changed the carbon availability, minimizing the effect of additional salt inputs. This is supported by significantly higherCO_2-C per g TOC under control conditions at DLB compared to UL (Fig. 3c-d), indicating that carbon was initially more available at DLB. In contrast, the UL site, which was not exposed to marine inundation, showed a stronger response, suggesting that sea water addition could have had a more pronounced effect on carbon mobilization and therefore explain the CO_2 response in AL2, PF1 and PF2 layers at the UL site (Fig. 4).

The overall decrease in CO_2 production observed in UL AL1 (Fig. 4) may be explained by the presence of a peat layer (Fig. 2, Fig. S1). In organic-rich soils (TOC > 20%), carbon is typically more available, often resulting in higher CO_2 production rates Treat et al. (2015). Therefore, in such peat layers, carbon availability might not be the limiting factor, and redox conditions could play a more dominant role in controlling CO_2 production.

4.3.2 Electron Acceptors and Microbial Adaptation

In non-PF coastal environments, an inhibition of CH_4 production with sea water is observed as well (Gutekunst et al., 2022; RoyChowdhury et al., 2018). This CH_4 response is likely linked to the role of electron acceptors in sea water (Gutekunst et al., 2022; RoyChowdhury et al., 2018; Koch et al., 2009). As ${SO_4}^{2-}$ reduction is energetically more favorable than methanogenesis, the addition of ${SO_4}^{2-}$ with the salt water treatments can hinder CH_4 production. In layers where CH_4 production was least inhibited by the brackish water treatment at the end of the incubation (meaning UL AL1 layer and DLB AL1 and AL2 layers), the initial ${SO_4}^{2-}$ concentrations were the lowest (Fig. 2). This could result in a smaller ${SO_4}^{2-}$ pool for these layers and therefore, explainCH_4 production at the end of the incubation period. The CH_4 lag time could thus represent the time needed to deplete ${SO_4}^{2-}$ as energy source.

This ${SO_4}^{2-}$ reduction could also explain the initial peak in CO_2 production that happened in AL1 layers with sea and brackish water treatment (Fig. 5, Fig. S5). Now, when assuming a depletion of ${SO_4}^{2-}$ as electron acceptor with the brackish water treatment within incubation duration it is possible to explain the stronger response in CO_2 (positively) and CH_4 (negatively) in AL1 layers with the higher amount of ${SO_4}^{2-}$.

At the DLB site, the PF most likely had contact with sea water before (Fig. 2) making it reasonable to assume that microbes are adapted to brackish water conditions. The addition of sea water did not seem to change any relevant factors for CO_2 production leading to almost no differences between all three treatments. That CH_4 was produced with the control treatment and that at least twice as much CH_4 was produced in DLB compared to UL PF layers (Fig. 3) indicates that active methanogens were present in the brackish water affected PF layers even though CH_4 production was inhibited when ${SO_4}^{2-}$ was present. Other studies observed a similar behaviour from low saline former PF environments, where CH_4 production declines significantly after sea water addition (Yang et al., 2023; Jenrich et al., 2025).

Not only the availability of ${SO_4}^{2-}$ is changed with the addition of salt water, but also the availability of other nutrients and pore water pH can be impacted by the treatments applied in this study. For example, the biogeochemical cycle of chloride on the Arctic Coastal Plain is linked to iron and humic substance cycling (Zlamal et al., 2017). It is even discussed if organohalide respiration could inhibit CH_4 production similar to Fe(III) reduction (by reducing H_2 levels) (Zlamal et al., 2017). Additionally, pH drives microbial communities in PF (Gray et al., 2014; Waldrop et al., 2023) with methanogens being most productive at ranging between 6.5 and 7 (Wang et al., 1993; Wagner et al., 2017). These complex biogeochemical couplings make it impossible to pinpoint the exact cause for CO_2 and CH_4 response to sea water within the scope of this study.

Furthermore, it is essential to consider the impact of rewetting and thawing on the CO_2 production. In the majority of the treatments, a peak in CO_2 production was observed at the beginning of the incubation. Many studies have shown that CO_2 exhibit a positive response following rewetting events (Kurganova et al., 2007; Deppe et al., 2010; Kim et al., 2012). The addition of water can facilitate the breakdown of the soil aggregates and make the organic matter mater more available for microbial communities (Van Gestel et al., 1993; Grogan et al., 2004; Kim et al., 2012).

In summary, the salt water effect on CO_2 and CH_4 production under anaerobic conditions can not solely be explained by a change in carbon availability. A key role is also played by the change in soil redox-conditions due to salt addition, which shifts the availability of electron acceptors. Additionally, other biogeochemical aspects such as pH and nutrient availability could additionally affect the CO_2 and CH_4 response to salt water.

4.4 Challenges in Comparing CO_2 and CH_4 Production Across Studies: Limitation, Implications and future Research

Directly comparing CO_2 and CH_4 production with other research is challenging due to the limited number of comparable incubation studies and the varying framework parameters used in these investigations (e.g. temperature, units, incubation duration; Tab. S2 and S3). Cumulative CO_2 and CH_4 production with the control treatment in mineral (TOC below 30%) and organic (TOC higher 30%) layers are within the same range as the anaerobic gas production observed at 15°C from moist acidic Alaskan PF soils incubated for 500 days (Tab. S2, Lee et al. (2012)). Compared to anoxic PF incubations on a pan-arctic scale, median CO_2 production rates are at least two times lower in this incubation at the respective landscape positions (Tab. S2, Treat et al. (2015): 52.1 μg g^{-1} C $^{d-1}$ (UL); 125 μg g^{-1} C $^{d-1}$ (DLB)). Median CH_4 production rates on the other hand are at least 4 times higher than max. production rates at the DLB (Tab. S2, Treat et al. (2015): 0.6 μg g^{-1} C $^{d-1}$ (DLB)) while they seem to be lower at the UL site (Tab. S2, Treat et al. (2015): 8.2 μg g^{-1} C $^{d-1}$ (UL)). The anaerobic CO_2 production with sea water (Fig. S5) is generally lower than CO_2 production with sea water at 4°C under aerobic conditions (Tab. S3, Tanski et al. (2021)).

This study investigated the production of CO_2 and CH_4 under anaerobic conditions mimicking PF thaw accompanied by sea water inundation. However, the actual amount of carbon GHG released to the atmosphere is also impacted by factors not covered in this study. For example, the transport process of GHG from soil to the atmosphere by exudation through plants or by ebullition can have a significant impact on the GHG flux (Eckhardt et al., 2019; Jentzsch et al., 2024; Rosentreter et al., 2023). During transport CH_4 can be oxidized to CO_2 within the sediment and water column in thaw lakes (De Jong et al., 2018; Lotem et al., 2023) as well as in marine environments (Yang et al., 2023; Uhlig et al., 2018). Additionally, soil temperature sensitivity (De Jong et al., 2018; Treat et al., 2014; Lapham et al., 2020; Zona et al., 2009), effects of freeze-thaw events (Schimel and Mikan, 2005; Roy Chowdhury et al., 2015), influences of water-level changes (Eckhardt et al., 2019) and effects of sea water composition (Dou et al., 2008) are aspects not within the scope of this study. Nevertheless, CO_2 and CH_4 production form the basis of GHG fluxes and ex-situ incubations have shown to effectively reproduce in-situ anaerobic carbon cycling dynamics, such as CO_2 and CH_4 productions (Hodgkins et al., 2015; Wilson et al., 2021). Finally, it is important to note that this study is based on only two soil cores. Although these were selected to represent the two most common landscape features in the area, they do not encompass the full heterogeneity of the permafrost landscape. Therefore, based on the results from this case study, we recommend further investigations into the effects of sea water inundation across a wider range of permafrost landforms, including sites with diverse landscape histories.

5 Conclusions

The results of this case-study show that sea water inundation of terrestrial PF has differing effects on CO_2 and CH_4 production. The CH_4 production decreases with the increase of salt concentration even when the microbial community was already adapted to brackish conditions, i.e., equal production of CO_2 and CH_4. The addition of ${SO_4}^{2-}$ is likely to explain this behavior, as it favors ${SO_4}^{2-}$ reduction over methanogenesis. Thus, our findings highlight that redox-conditions seem to be a stronger controlling factor than microbial adaptation for CH_4 production. The response of CO_2 is more variable and appears to be contingent on the site history. In particular, no response to the salt addition was observed for the layers that have been exposed to sea water intrusion before this incubation. However, for non-marine-affected soils, the salt addition may intensify the carbon availability as well as nutrient availability and lead to a positive feedback in CO_2 production. Here we highlight the effect of salt on CH_4 and CO_2 production in a controlled ex-situ experiment where soil dynamics are not considered. In future studies, it is therefore necessary to examine the effect of sea level rise on GHG production under conditions closer to reality, where vertical and lateral soil dynamics are taken into account.

Data availability. The data sets used in this paper are available at doi: 10.1594/PANGAEA.969147 and doi: 10.1594/PANGAEA.969148.

Author contributions. JS, ML and CCT conceptualized the study. JS and MJ collected the samples during the expedition in 2022. MD conducted the experiment, supported by ML. MD carried out the data analysis and wrote the R script. MD and FS made the figures. MD wrote the original draft with contributions from all the co-authors. ML led the editing during the reviewing process.

Competing interests. The authors declare that they have no conflict of interest.

Acknowledgements. Funding for this study was provided by European Research Council Starting Grant 851181 (FluxWIN). Authors would like to thank Guido Grosse and Benjamin Jones for leading the Arctic field campaign in April 2022 and for their participation in the coring; Justin Lindemann, Antje Eulenburg, Daniel Warner and all AWI Potsdam lab technicians for their help with lab work; Lars Johann Ebel for the soil parameter figure and the reviewers for their helpful comments.

References

Alaska Climate Research Center: Climate Data for Utqiakvik. Periode: 1991 - 2020., https://akclimate.org/data/data-portal/, 2023.

Andresen, C. G., Lawrence, D. M., Wilson, C. J., McGuire, A. D., Koven, C., Schaefer, K., Jafarov, E., Peng, S., Chen, X., Gouttevin, I., et al.: Soil moisture and hydrology projections of the permafrost region–a model intercomparison, The Cryosphere, 14, 445–459, 2020.

Angelopoulos, M., Overduin, P. P., Westermann, S., Tronicke, J., Strauss, J., Schirrmeister, L., Biskaborn, B. K., Liebner, S., Maksimov, G., Grigoriev, M. N., and Grosse, G.: Thermokarst Lake to Lagoon Transitions in Eastern Siberia: Do Submerged Taliks Refreeze?, Journal of Geophysical Research: Earth Surface, 125, e2019JF005 424, https://doi.org/10.1029/2019JF005424, 2020.

Blott, S. J. and Pye, K.: GRADISTAT: a grain size distribution and statistics package for the analysis of unconsolidated sediments, Earth surface processes and Landforms, 26, 1237–1248, 2001.

Bristol, E. M., Connolly, C. T., Lorenson, T. D., Richmond, B. M., Ilgen, A. G., Choens, R. C., Bull, D. L., Kanevskiy, M., Iwahana, G., Jones, B. M., and McClelland, J. W.: Geochemistry of Coastal Permafrost and Erosion-Driven Organic Matter Fluxes to the Beaufort Sea Near Drew Point, Alaska, Frontiers in Earth Science, 8, 598 933, https://doi.org/10.3389/feart.2020.598933, 2021.

De Jong, A. E. E., In 'T Zandt, M. H., Meisel, O. H., Jetten, M. S. M., Dean, J. F., Rasigraf, O., and Welte, C. U.: Increases in temperature and nutrient availability positively affect methane-cycling microorganisms in Arctic thermokarst lake sediments, Environmental Microbiology, 20, 4314–4327, https://doi.org/10.1111/1462-2920.14345, 2018.

Deppe, M., Knorr, K.-H., McKnight, D. M., and Blodau, C.: Effects of short-term drying and irrigation on CO_2 and CH_4 production and emission from mesocosms of a northern bog and an alpine fen, Biogeochemistry, 100, 89–103, 2010.

Dolle, M. L., Laurent, M., Vollmer, J., and Treat, C. C.: Gas production (CO_2 + CH_4) of an one year anaerobic incubation with salt water from two permafrost cores near Utqiagvik, Alaska [dataset], https://doi.org/10.1594/PANGAEA.969148, 2024.

Dou, F., Ping, C., Guo, L., and Jorgenson, T.: Estimating the Impact of Seawater on the Production of Soil Water-Extractable Organic Carbon during Coastal Erosion, Journal of Environmental Quality, 37, 2368–2374, https://doi.org/10.2134/jeq2007.0403, 2008.

Drake, T. W., Wickland, K. P., Spencer, R. G. M., McKnight, D. M., and Striegl, R. G.: Ancient low–molecular-weight organic acids in permafrost fuel rapid carbon dioxide production upon thaw, Proceedings of the National Academy of Sciences, 112, 13 946–13 951, https://doi.org/10.1073/pnas.1511705112, 2015.

Eckhardt, T., Knoblauch, C., Kutzbach, L., Holl, D., Simpson, G., Abakumov, E., and Pfeiffer, E.-M.: Partitioning net ecosystem exchange of CO_2 on the pedon scale in the Lena River Delta, Siberia, Biogeosciences, 16, 1543–1562, https://doi.org/10.5194/bg-16-1543-2019, 2019.

Eisner, W. R., Bockheim, J. G., Hinkel, K. M., Brown, T. A., Nelson, F. E., Peterson, K. M., and Jones, B. M.: Paleoenvironmental analyses of an organic deposit from an erosional landscape remnant, Arctic Coastal Plain of Alaska, Palaeogeography, Palaeoclimatology, Palaeoecology, 217, 187–204, https://doi.org/10.1016/j.palaeo.2004.11.025, 2005.

Fritz, M., Vonk, J. E., and Lantuit, H.: Collapsing Arctic coastlines, Nature Climate Change, 7, 6–7, https://doi.org/10.1038/nclimate3188, 2017.

Frohn, R. C., Hinkel, K. M., and Eisner, W. R.: Satellite remote sensing classification of thaw lakes and drained thaw lake basins on the North Slope of Alaska, Remote Sensing of Environment, 97, 116–126, https://doi.org/10.1016/j.rse.2005.04.022, 2005.

Fuchs, M., Lenz, J., Jock, S., Nitze, I., Jones, B. M., Strauss, J., Günther, F., and Grosse, G.: Organic Carbon and Nitrogen Stocks Along a Thermokarst Lake Sequence in Arctic Alaska, Journal of Geophysical Research: Biogeosciences, 124, 1230–1247, https://doi.org/10.1029/2018JG004591, 2019.

Galera, L. D. A., Eckhardt, T., Beer, C., Pfeiffer, E., and Knoblauch, C.: Ratio of In Situ CO_2 to CH_4 Production and Its Environmental Controls in Polygonal Tundra Soils of Samoylov Island, Northeastern Siberia, Journal of Geophysical Research: Biogeosciences, 128, e2022JG006 956, https://doi.org/10.1029/2022JG006956, 2023.

Gibbs, A. E. and Richmond, B. M.: National Assessment of Shoreline Change — Summary Statistics for Updated Vector Shorelines and Associated Shoreline Change Data for the North Coast of Alaska, US-Canadian Border to Icy Cape, Report, US Geological Survey, Reston, VA, https://pubs.usgs.gov/of/2017/1107/, 2017.

Gray, N. D., McCann, C. M., Christgen, B., Ahammad, S. Z., Roberts, J. A., and Graham, D. W.: Soil geochemistry confines microbial abundances across an arctic landscape; implications for net carbon exchange with the atmosphere, Biogeochemistry, 120, 307–317, https://doi.org/10.1007/s10533-014-9997-7, 2014.

Grogan, P., Michelsen, A., Ambus, P., and Jonasson, S.: Freeze–thaw regime effects on carbon and nitrogen dynamics in sub-arctic heath tundra mesocosms, Soil Biology and Biochemistry, 36, 641–654, 2004.

Gutekunst, C. N., Liebner, S., Jenner, A.-K., Knorr, K.-H., Unger, V., Koebsch, F., Racasa, E. D., Yang, S., Böttcher, M. E., Janssen, M., Kallmeyer, J., Otto, D., Schmiedinger, I., Winski, L., and Jurasinski, G.: Effects of brackish water inflow on methane-cycling microbial communities in a freshwater rewetted coastal fen, Biogeosciences, 19, 3625–3648, https://doi.org/10.5194/bg-19-3625-2022, 2022.

Guéguen, C., Guo, L., and Tanaka, N.: Distributions and characteristics of colored dissolved organic matter in the Western Arctic Ocean, Continental Shelf Research, 25, 1195–1207, https://doi.org/10.1016/j.csr.2005.01.005, 2005.

Herndon, E. M., Mann, B. F., Roy Chowdhury, T., Yang, Z., Wullschleger, S. D., Graham, D., Liang, L., and Gu, B.: Pathways of anaerobic organic matter decomposition in tundra soils from Barrow, Alaska, Journal of Geophysical Research: Biogeosciences, 120, 2345–2359, https://doi.org/10.1002/2015JG003147, 2015.

Hinkel, K. M., Eisner, W. R., Bockheim, J. G., Nelson, F. E., Peterson, K. M., and Dai, X.: Spatial Extent, Age, and Carbon Stocks in Drained Thaw Lake Basins on the Barrow Peninsula, Alaska, Arctic, Antarctic, and Alpine Research, 35, 291–300, https://doi.org/10.1657/1523-0430(2003)035[0291:SEAACS]2.0.CO;2, 2003.

Hodgkins, S. B., Chanton, J. P., Langford, L. C., McCalley, C. K., Saleska, S. R., Rich, V. I., Crill, P. M., and Cooper, W. T.: Soil incubations reproduce field methane dynamics in a subarctic wetland, Biogeochemistry, 126, 241–249, https://doi.org/10.1007/s10533-015-0142-z, 2015.

Holm, S., Walz, J., Horn, F., Yang, S., Grigoriev, M. N., Wagner, D., Knoblauch, C., and Liebner, S.: Methanogenic response to long-term permafrost thaw is determined by paleoenvironment, FEMS Microbiology Ecology, 96, fiaa021, https://doi.org/10.1093/femsec/fiaa021, 2020.

Irrgang, A. M., Bendixen, M., Farquharson, L. M., Baranskaya, A. V., Erikson, L. H., Gibbs, A. E., Ogorodov, S. A., Overduin, P. P., Lantuit, H., Grigoriev, M. N., and Jones, B. M.: Drivers, dynamics and impacts of changing Arctic coasts, Nature Reviews Earth & Environment, 3, 39–54, https://doi.org/10.1038/s43017-021-00232-1, 2022.

Jenrich, M., Angelopoulos, M., Grosse, G., Overduin, P. P., Schirrmeister, L., Nitze, I., Biskaborn, B. K., Liebner, S., Grigoriev, M., Murray, A., Jongejans, L. L., and Strauss, J.: Thermokarst Lagoons: A Core-Based Assessment of Depositional Characteristics and an Estimate of Carbon Pools on the Bykovsky Peninsula, Frontiers in Earth Science, 9, 637 899, https://doi.org/10.3389/feart.2021.637899, 2021.

Jenrich, M., Angelopoulos, M., Liebner, S., Treat, C., Knoblauch, C., Yang, S., Grosse, G., Giebeler, F., Jongejans, L. L., Grigoriev, M., et al.: Greenhouse Gas Production and Microbial Response During the Transition From Terrestrial Permafrost to a Marine Environment, Permafrost and Periglacial Processes, 36, 63–82, 2025.

Jentzsch, K., Männistö, E., Marushchak, M. E., Korrensalo, A., van Delden, L., Tuittila, E.-S., Knoblauch, C., and Treat, C. C.: Seasonal controls on methane flux components in a boreal peatland–combining plant removal and stable isotope analyses, EGUsphere, 2024, 1–32, 2024.

Jones, B. M., Kanevskiy, M. Z., Parsekian, A. D., Bergstedt, H., Ward Jones, M. K., Rangel, R. C., Hinkel, K. M., and Shur, Y.: Rapid Saline Permafrost Thaw Below a Shallow Thermokarst Lake in Arctic Alaska, Geophysical Research Letters, 50, e2023GL105 552, https://doi.org/10.1029/2023GL105552, 2023.

Jongejans, L. L., Strauss, J., Lenz, J., Peterse, F., Mangelsdorf, K., Fuchs, M., and Grosse, G.: Organic matter characteristics in yedoma and thermokarst deposits on Baldwin Peninsula, west Alaska, Biogeosciences, 15, 6033–6048, https://doi.org/10.5194/bg-15-6033-2018, 2018.

Jorgenson, M. T. and Brown, J.: Classification of the Alaskan Beaufort Sea Coast and estimation of carbon and sediment inputs from coastal erosion, Geo-Marine Letters, 25, 69–80, https://doi.org/10.1007/s00367-004-0188-8, 2005.

Kim, D.-G., Vargas, R., Bond-Lamberty, B., and Turetsky, M.: Effects of soil rewetting and thawing on soil gas fluxes: a review of current literature and suggestions for future research, Biogeosciences, 9, 2459–2483, 2012.

Koch, B. P., Kattner, G., Witt, M., and Passow, U.: Molecular insights into the microbial formation of marine dissolved organic matter: recalcitrant or labile?, Biogeosciences, 11, 4173–4190, https://doi.org/10.5194/bg-11-4173-2014, 2014.

Koch, K., Knoblauch, C., and Wagner, D.: Methanogenic community composition and anaerobic carbon turnover in submarine permafrost sediments of the Siberian Laptev Sea, Environmental Microbiology, 11, 657–668, https://doi.org/10.1111/j.1462-2920.2008.01836.x, 2009.

Kurganova, I., Teepe, R., and Loftfield, N.: Influence of freeze-thaw events on carbon dioxide emission from soils at different moisture and land use, Carbon balance and management, 2, 1–9, 2007.

Lantuit, H., Overduin, P. P., Couture, N., Wetterich, S., Aré, F., Atkinson, D., Brown, J., Cherkashov, G., Drozdov, D., Forbes, D. L., Graves-Gaylord, A., Grigoriev, M., Hubberten, H.-W., Jordan, J., Jorgenson, T., Ødegård, R. S., Ogorodov, S., Pollard, W. H., Rachold, V., Sedenko, S., Solomon, S., Steenhuisen, F., Streletskaya, I., and Vasiliev, A.: The Arctic Coastal Dynamics Database: A New Classification Scheme and Statistics on Arctic Permafrost Coastlines, Estuaries and Coasts, 35, 383–400, https://doi.org/10.1007/s12237-010-9362-6, 2012.

Lapham, L. L., Dallimore, S. R., Magen, C., Henderson, L. C., Powers, L. C., Gonsior, M., Clark, B., Côté, M., Fraser, P., and Orcutt, B. N.: Microbial Greenhouse Gas Dynamics Associated With Warming Coastal Permafrost, Western Canadian Arctic, Frontiers in Earth Science, 8, 15, 2020.

Lara, M. J., McGuire, A. D., Euskirchen, E. S., Tweedie, C. E., Hinkel, K. M., Skurikhin, A. N., Romanovsky, V. E., Grosse, G., Bolton, W. R., and Genet, H.: Polygonal tundra geomorphological change in response to warming alters future CO2 and CH4 flux on the Barrow Peninsula, Global Change Biology, 21, 1634–1651, https://doi.org/10.1111/gcb.12757, 2015.

Laurent, M., Fuchs, M., Herbst, T., Runge, A., Liebner, S., and Treat, C. C.: Relationships between greenhouse gas production and landscape position during short-term permafrost thaw under anaerobic conditions in the Lena Delta, Biogeosciences, 20, 2049–2064, https://doi.org/10.5194/bg-20-2049-2023, 2023.

Lee, H., Schuur, E. A. G., Inglett, K. S., Lavoie, M., and Chanton, J. P.: The rate of permafrost carbon release under aerobic and anaerobic conditions and its potential effects on climate, Global Change Biology, 18, 515–527, https://doi.org/10.1111/j.1365-2486.2011.02519.x, 2012.

Lotem, N., Pellerin, A., Anthony, K. W., Gafni, A., Boyko, V., and Sivan, O.: Anaerobic oxidation of methane does not attenuate methane emissions from thermokarst lakes, Limnology and Oceanography, p. lno.12349, https://doi.org/10.1002/lno.12349, 2023.

Mitzscherling, J., Winkel, M., Winterfeld, M., Horn, F., Yang, S., Grigoriev, M. N., Wagner, D., Overduin, P. P., and Liebner, S.: The development of permafrost bacterial communities under submarine conditions: Bacteria in Submarine Permafrost, Journal of Geophysical Research: Biogeosciences, 122, 1689–1704, https://doi.org/10.1002/2017JG003859, 2017.

Mollenhauer, G., Grotheer, H., Gentz, T., Bonk, E., and Hefter, J.: Standard operation procedures and performance of the MICADAS radiocarbon laboratory at Alfred Wegener Institute (AWI), Germany, Nuclear Instruments and Methods in Physics Research Section B: Beam Interactions with Materials and Atoms, 496, 45–51, 2021.

Nyland, K. E., Shiklomanov, N. I., Streletskiy, D. A., Nelson, F. E., Klene, A. E., and Kholodov, A. L.: Long-term circumpolar active layer monitoring (CALM) program observations in Northern Alaskan tundra, Polar Geography, 44, 167–185, 2021.

Ping, C., Jastrow, J., Jorgenson, M., Michaelson, G., and Shur, Y.: Permafrost soils and carbon cycling, Soil, 1, 147–171, 2015.

Posit team: RStudio: Integrated Development Environment for R, Posit Software, PBC, Boston, MA, http://www.posit.co/, 2023.

R Core Team: R: A Language and Environment for Statistical Computing, R Foundation for Statistical Computing, Vienna, Austria, https://www.R-project.org/, 2023.

Reddy, K. R. and DeLaune, R. D.: Biogeochemistry of wetlands: science and applications, CRC Press, Boca Raton, ISBN 978-1-56670-678-0, 2008.

Reimer, P. J., Austin, W. E., Bard, E., Bayliss, A., Blackwell, P. G., Ramsey, C. B., Butzin, M., Cheng, H., Edwards, R. L., Friedrich, M., et al.: The IntCal20 Northern Hemisphere radiocarbon age calibration curve (0–55 cal kBP), Radiocarbon, 62, 725–757, 2020.

Robertson, G. P., Coleman, D., Bledsoe, C., and Sollins, P.: Standard soil methods for long-term ecological research, Oxford University Press, ISBN 0-19-512083-3, 1999.

Rosentreter, J. A., Laruelle, G. G., Bange, H. W., Bianchi, T. S., Busecke, J. J., Cai, W.-J., Eyre, B. D., Forbrich, I., Kwon, E. Y., Maavara, T., et al.: Coastal vegetation and estuaries are collectively a greenhouse gas sink, Nature Climate Change, 13, 579–587, 2023.

Roy Chowdhury, T., Herndon, E. M., Phelps, T. J., Elias, D. A., Gu, B., Liang, L., Wullschleger, S. D., and Graham, D. E.: Stoichiometry and temperature sensitivity of methanogenesis and CO2 production from saturated polygonal tundra in Barrow, Alaska, Global Change Biology, 21, 722–737, https://doi.org/10.1111/gcb.12762, 2015.

RoyChowdhury, T., Bramer, L., Hoyt, D. W., Kim, Y.-M., Metz, T. O., McCue, L. A., Diefenderfer, H. L., Jansson, J. K., and Bailey, V.: Temporal dynamics of CO2 and CH4 loss potentials in response to rapid hydrological shifts in tidal freshwater wetland soils, Ecological Engineering, 114, 104–114, https://doi.org/10.1016/j.ecoleng.2017.06.041, 2018.

Schimel, J. P. and Mikan, C.: Changing microbial substrate use in Arctic tundra soils through a freeze-thaw cycle, Soil Biology and Biochemistry, 37, 1411–1418, https://doi.org/10.1016/j.soilbio.2004.12.011, 2005.

Schuur, E. A., Abbott, B. W., Commane, R., Ernakovich, J., Euskirchen, E., Hugelius, G., Grosse, G., Jones, M., Koven, C., Leshyk, V., Lawrence, D., Loranty, M. M., Mauritz, M., Olefeldt, D., Natali, S., Rodenhizer, H., Salmon, V., Schädel, C., Strauss, J., Treat, C., and Turetsky, M.: Permafrost and Climate Change: Carbon Cycle Feedbacks From the Warming Arctic, Annual Review of Environment and Resources, 47, 343–371, https://doi.org/https://doi.org/10.1146/annurev-environ-012220-011847, publisher: Annual Reviews Type: Journal Article, 2022.

Schuur, E. A. G., Bockheim, J., Canadell, J. G., Euskirchen, E., Field, C. B., Goryachkin, S. V., Hagemann, S., Kuhry, P., Lafleur, P. M., Lee, H., Mazhitova, G., Nelson, F. E., Rinke, A., Romanovsky, V. E., Shiklomanov, N., Tarnocai, C., Venevsky, S., Vogel, J. G., and Zimov,

S. A.: Vulnerability of Permafrost Carbon to Climate Change: Implications for the Global Carbon Cycle, BioScience, 58, 701–714, https://doi.org/10.1641/B580807, 2008.

Schädel, C., Schuur, E. A. G., Bracho, R., Elberling, B., Knoblauch, C., Lee, H., Luo, Y., Shaver, G. R., and Turetsky, M. R.: Circumpolar assessment of permafrost C quality and its vulnerability over time using long-term incubation data, Global Change Biology, 20, 641–652, https://doi.org/10.1111/gcb.12417, 2014.

Seemann, F., Jenrich, M., Lindemann, J., Eulenburg, A., Weiner, M., Mollenhauer, G., Meyer, H., Overduin, P. P., Grosse, G., Jones, B., and Strauss, J.: Sediment and pore water investigations in thermokarst terrain near Utqiagvik, Alaska [dataset], https://doi.org/10.1594/PANGAEA.974136, pANGAEA, 2025.

Shahariar, S., Farrell, R., Soolanayakanahally, R., and Bedard-Haughn, A.: Elevated salinity and water table drawdown significantly affect greenhouse gas emissions in soils from contrasting land-use practices in the prairie pothole region, Biogeochemistry, 155, 127–146, 2021.

Söllinger, A. and Urich, T.: Methylotrophic methanogens everywhere—physiology and ecology of novel players in global methane cycling, Biochemical Society Transactions, 47, 1895–1907, 2019.

Strauss, J., Fuchs, M., Hugelius, G., Miesner, F., Nitze, I., Opfergelt, S., Schuur, E., Treat, C., Turetsky, M., Yang, Y., and Grosse, G.: Organic matter storage and vulnerability in the permafrost domain, in: Reference Module in Earth Systems and Environmental Sciences, p. B9780323999311001641, Elsevier, ISBN 978-0-12-409548-9, https://doi.org/10.1016/B978-0-323-99931-1.00164-1, 2024.

Stuiver, M. and Reimer, P. J.: Extended 14C data base and revised CALIB 3.0 14C age calibration program, Radiocarbon, 35, 215–230, 1993.

Sturtevant, C. S. and Oechel, W. C.: Spatial variation in landscape-level CO2 and CH4 fluxes from arctic coastal, Global Change Biology, 19, 2853–2866, https://doi.org/10.1111/gcb.12247, 2013.

Tanski, G., Wagner, D., Knoblauch, C., Fritz, M., Sachs, T., and Lantuit, H.: Rapid CO_2 Release From Eroding Permafrost in Seawater, Geophysical Research Letters, 46, 11 244–11 252, https://doi.org/10.1029/2019GL084303, 2019.

Tanski, G., Bröder, L., Wagner, D., Knoblauch, C., Lantuit, H., Beer, C., Sachs, T., Fritz, M., Tesi, T., Koch, B. P., Haghipour, N., Eglinton, T. I., Strauss, J., and Vonk, J. E.: Permafrost Carbon and CO2 Pathways Differ at Contrasting Coastal Erosion Sites in the Canadian Arctic, Frontiers in Earth Science, 9, 630 493, https://doi.org/10.3389/feart.2021.630493, 2021.

Taş, N., Prestat, E., Wang, S., Wu, Y., Ulrich, C., Kneafsey, T., Tringe, S. G., Torn, M. S., Hubbard, S. S., and Jansson, J. K.: Landscape topography structures the soil microbiome in arctic polygonal tundra, Nature Communications, 9, 777, https://doi.org/10.1038/s41467-018-03089-z, 2018.

Treat, C. C., Wollheim, W. M., Varner, R. K., Grandy, A. S., Talbot, J., and Frolking, S.: Temperature and peat type control CO2 and CH4 production in Alaskan permafrost peats, Global Change Biology, 20, 2674–2686, https://doi.org/10.1111/gcb.12572, 2014.

Treat, C. C., Ernakovich, J., Iversen, C. M., Lupascu, M., McGuire, A. D., Norby, R. J., Roy Chowdhury, T., Richter, A., Šantrůčková, H., Schädel, C., Schuur, E. A. G., Sloan, V. L., Turetsky, M. R., and Waldrop, M. P.: A pan-Arctic synthesis of CH_4 and CO_2 production from anoxic soil incubations, Global Change Biology, 21, 2787–2803, https://doi.org/10.1111/gcb.12875, 2015.

Uhlig, C., Kirkpatrick, J. B., D'Hondt, S., and Loose, B.: Methane-oxidizing seawater microbial communities from an Arctic shelf, Biogeosciences, 15, 3311–3329, https://doi.org/10.5194/bg-15-3311-2018, 2018.

Van Gestel, M., Merckx, R., and Vlassak, K.: Microbial biomass responses to soil drying and rewetting: the fate of fast-and slow-growing microorganisms in soils from different climates, Soil Biology and Biochemistry, 25, 109–123, 1993.

Vonk, J. E., Mann, P. J., Davydov, S., Davydova, A., Spencer, R. G. M., Schade, J., Sobczak, W. V., Zimov, N., Zimov, S., Bulygina, E., Eglinton, T. I., and Holmes, R. M.: High biolability of ancient permafrost carbon upon thaw, Geophysical Research Letters, 40, 2689–2693, https://doi.org/10.1002/grl.50348, 2013.

Wagner, R., Zona, D., Oechel, W., and Lipson, D.: Microbial community structure and soil pH correspond to methane production in Arctic Alaska soils, Environmental Microbiology, 19, 3398–3410, https://doi.org/10.1111/1462-2920.13854, 2017.

Waldrop, M. P., Chabot, C. L., Liebner, S., Holm, S., Snyder, M. W., Dillon, M., Dudgeon, S. R., Douglas, T. A., Leewis, M.-C., Walter Anthony, K. M., McFarland, J. W., Arp, C. D., Bondurant, A. C., Taş, N., and Mackelprang, R.: Permafrost microbial communities and functional genes are structured by latitudinal and soil geochemical gradients, The ISME Journal, https://doi.org/10.1038/s41396-023-01429-6, 2023.

Wang, Z., Delaune, R., Patrick Jr, W., and Masscheleyn, P.: Soil redox and pH effects on methane production in a flooded rice soil, Soil Science Society of America Journal, 57, 382–385, 1993.

Wilson, R. M., Zayed, A. A., Crossen, K. B., Woodcroft, B., Tfaily, M. M., Emerson, J., Raab, N., Hodgkins, S. B., Verbeke, B., Tyson, G., Crill, P., Saleska, S., Chanton, J. P., Rich, V. I., IsoGenie Project Coordinators, and IsoGenie Project Field Team: Functional capacities of microbial communities to carry out large scale geochemical processes are maintained during ex situ anaerobic incubation, PLOS ONE, 16, e0245 857, https://doi.org/10.1371/journal.pone.0245857, 2021.

Wolter, J., Jones, B. M., Fuchs, M., Breen, A., Bussmann, I., Koch, B., Lenz, J., Myers-Smith, I. H., Sachs, T., Strauss, J., et al.: Post-drainage vegetation, microtopography and organic matter in Arctic drained lake basins, Environmental Research Letters, 19, 045 001, 2024.

Yang, S., Anthony, S. E., Jenrich, M., in 't Zandt, M. H., Strauss, J., Overduin, P. P., Grosse, G., Angelopoulos, M., Biskaborn, B. K., Grigoriev, M. N., Wagner, D., Knoblauch, C., Jaeschke, A., Rethemeyer, J., Kallmeyer, J., and Liebner, S.: Microbial methane cycling in sediments of Arctic thermokarst lagoons, Global Change Biology, 29, 2714–2731, https://doi.org/10.1111/gcb.16649, 2023.

Zlamal, J. E., Raab, T. K., Little, M., Edwards, R. A., and Lipson, D. A.: Biological chlorine cycling in the Arctic Coastal Plain, Biogeochemistry, 134, 243–260, 2017.

Zona, D., Oechel, W., Kochendorfer, J., Paw U, K., Salyuk, A., Olivas, P., Oberbauer, S., and Lipson, D.: Methane fluxes during the initiation of a large-scale water table manipulation experiment in the Alaskan Arctic tundra, Global Biogeochemical Cycles, 23, 2009.

ACKNOWLEDGEMENTS - DANKSAGUNG

The journey to completing this thesis has been filled with challenges and triumphs, made possible by the support of many incredible people.

First and foremost, my deepest gratitude goes to my supervisor, Jens Strauß. Thank you for encouraging me to embark on this PhD journey in the first place, for trusting me with the planning of my first Arctic expedition, and for your unwavering day-to-day support and guidance. Completing my PhD would not have been possible without you!

Guido Große, thank you for your invaluable support, for including me in the Alaska expedition, for patiently proofreading manuscripts, for sharing your innovative ideas and visions, and for giving me the opportunity to work at AWI.

Susanne Liebner, thank you for introducing me to the fascinating world of microorganisms, for allowing me to use your GC lab and glovebox, and especially for your help with data interpretation, your insightful ideas for improving the structure of my manuscripts, and your warm, encouraging words during challenging times.

Anne Morgenstern, thank you for standing by me and supporting me during my difficult times with Long COVID, as well as for the helpful personal conversations. That has meant so much to me.

Christian Knoblauch, I deeply appreciate your guidance in planning and analyzing the incubation experiments and your contributions to the many publications. To all of the aforementioned, thank you for serving on my PhD committee, for your direction, constructive feedback, and guidance.

Josefine Lenz, thank you for introducing me to the world of outreach with *Permafrost im Wandel*. From Explore Science to the WWF Student Academy and the Week of the Environment, I thoroughly enjoyed the many events we participated in together. Your dedication and enthusiasm in bringing permafrost science to everyone inspired me immensely. Thank you for that!

Mike Angelopoulos, thank you for sharing your enthusiasm for lagoons, for continuously motivating me, believing in my abilities, and offering your professional guidance whenever I needed it. It has been a joy to collaborate and publish with you, especially as you ensured I was always up to date.

Juliane Wolter, I am so grateful for our exciting statistics and data analysis talks and brainstorming sessions. I learned so much from you!

A heartfelt thank-you goes to the amazing lab technicians for their assistance in analyzing the countless samples. Special thanks to Justin Lindemann, Jonas Sernau, Antje Eulenberg, and Oliver Burckhardt for your active and dedicated support.

I would also like to express my gratitude to the Deutsche Bundestiftung Umwelt (DBU). Without the PhD scholarship, this dissertation would not have been possible. A personal thank-you goes to my mentor, Dr. Volker Berding, and his assistant, Mrs. Heike Stock, for their warm and understanding support, particularly during my extended illness with Long COVID.

In this context, I also want to thank my friends and colleagues from the PhD representatives' group (Promovierenden-Vertretung). Your commitment, good spirit, and enjoyable meetings made a significant impact. I am proud of what the improvements we achieved together, and I will always cherish the memories of this time.

A huge thank-you goes to Dustin Whalen and Aude Flamand. Without your expertise, logistical support, and hands-on help, the 2021 Canada expedition—right in the midst of the pandemic—would not have been possible.

I am also grateful to POLMAR for supporting my studies and funding my participation in numerous courses and conferences.

Many thanks to my wonderful office colleagues Loeka Jongejans, Torben Windirsch-Woiwode, Lydia Stolpmann, Fabian Seemann, Frieda Giest, Fiona Giebeler, Verena Bischoff, and Bennett Stolze for creating a warm and friendly atmosphere, for the fun and deep conversations, and for your support whenever I needed it. Without you, the everyday PhD routine would have been much more monotonous and challenging! Thanks to Annabeth McCall, Verena, and Constance Lefebvre for the fun post-conference vacation in the Yukon. I'll never forget our adventurous kayak tour and the wilderness camping.

Special thanks to my colleagues Moein and Philip for the enjoyable times we shared, especially during the early days of our PhDs and throughout the journey. I still fondly remember our afternoons by the Havel. To all colleagues who became dear friends, I am grateful for the friendships we built beyond work.

Finally, I would like to extend my heartfelt thanks to my friends. These four years of my PhD have been a true rollercoaster, but you were my anchors. You caught me when I fell, celebrated my successes with me, and brought so much color and joy to my everyday life. I am so fortunate to have you all in my life!

Jacob, a special thank-you goes to you for your help with programming, your patience in explaining, and our many valuable personal conversations. Over the last four years, our friendship has deepened a lot, and I am very grateful for that.

Der letzte und größte Dank geht an meine Familie. Danke Mama, dass du immer für mich da bist, für dein unendliches Vertrauen in mich und die Liebe die du mir gibst. Danke, dass du mich in allem unterstützt, dich für mich einsetzt und keine Mühen scheust mein Leben einfacher zu machen. Ich könnte mir keine bessere Mutter wünschen. Danke auch an meine Brüder Lieven und Johannes und meine Schwestern Sarah und Reni für das füreinander da sein.

EIDESSTATTLICHE ERKLÄRUNG

Hiermit erkläre ich, dass ich die vorliegende Arbeit selbstständig verfasst und keine anderen als die angegebenen Hilfsmittel und Quellen verwendet habe.

Ich habe die kumulative Dissertation am Alfred-Wegener-Institut Helmholtz Zentrum für Polar- und Meeresforschung in Potsdam erarbeitet und in englischer Sprache verfasst. Diese Dissertation wird erstmalig und ausschließlich an der Universität Potsdam eingereicht.

Die dem Promotionsverfahren zugrundeliegende Promotionsordnung vom September 2013 ist mir bekannt.

Potsdam, November 2024

Maren Jenrich